Imperial College London

Development of instrumentation for autofluorescence spectroscopy and its application to tissue autofluorescence studies and biomedical research

João Luis Lagarto

Photonics Group

Department of Physics

Imperial College London

Thesis submitted in partial fulfilment of the requirements
for the degree of Doctor of Philosophy (Ph.D.)
Imperial College of Science, Technology and Medicine

Abstract

Autofluorescence spectroscopy is a promising non-invasive label-free approach to characterise biological samples and has shown potential to report structural and biochemical changes occurring in tissue owing to pathological transformations.

This thesis discusses the development of compact and portable single point fibre-optic probe-based instrumentation for time-resolved spectrofluorometry, utilising spectrally resolved time-correlated single photon counting (TCSPC) detection and white light reflectometry. Following characterisation and validation, two of these instruments were deployed in clinical settings and their potential to report structural and metabolic alterations in tissue associated with osteoarthritis and heart disease was investigated.

Osteoarthritis is a chronic and progressive disease of the joint characterised by irreversible destruction of articular cartilage for which there is no effective treatment. Working with the Kennedy Institute of Rheumatology, we investigated the potential of time-resolved autofluorescence spectroscopy as a diagnostic tool for early detection and monitoring of the progression of osteoarthritis. Our studies in enzymatically degenerated porcine and murine cartilage, which serve as models for osteoarthritis, suggest that autofluorescence lifetime is sensitive to disruption of the two major extracellular matrix components, aggrecan and collagen. Preliminary autofluorescence lifetime data were also obtained from *ex vivo* human tissue presenting naturally occurring osteoarthritis. Overall, our studies indicate that autofluorescence lifetime may offer a non-invasive readout to monitor cartilage matrix integrity that could contribute to future diagnosis of early cartilage defects as well as monitoring the efficacy of therapeutic agents.

This thesis also explored the potential of time-resolved autofluorescence spectroscopy and steady-state white-light reflectometry of tissue to report structural and metabolic changes associated with cardiac disease, both *ex vivo* and *in vivo*, in collaboration with clinical colleagues from the National Heart and Lung Institute. Using a Langendorff rat model, the autofluorescence signature of cardiac tissue was investigated following different insults to the heart. We were able to correlate and translate results obtained from *ex vivo* Langendorff data to an *in vivo* myocardial infarction model in rats, where we report structural and functional alterations in the infarcted and remote myocardium at different stages following infarction. This investigation stimulated the development of a clinically viable instrument to be used in open-chest surgical procedures in humans, of which progress to date is described.

The impact of time-resolved autofluorescence spectroscopy for label-free diagnosis of diseased would be significantly enhanced if the cost of the instrumentation could be reduced below what is achievable with commercial TCSPC-based technology. The last part of this thesis concerns the development of compact and portable instrumentation utilising low-cost FPGA-based circuitry that can be used with laser diodes and photon-counting photomultipliers. A comprehensive description of this instrument is presented together with data from its application to both fluorescence lifetime standards and biological tissue. The lower potential cost of this instrument could enhance the potential of autofluorescence lifetime metrology for commercial development and clinical deployment.

Author declaration

All the work presented in this thesis was performed by the author, with the following exceptions:

- In Chapter 3, solutions of malate dehydrogenase and lactate dehydrogenase for NADH protein binding experiments were prepared by Dr Benjamin Dyer.
- In Chapter 5, porcine cartilage extracts were prepared for autofluorescence lifetime measurements by Dr Mohammad Nickdel.
- In Chapter 5, all animal work concerning the murine osteoarthritis model (section 5.6) was carried out by Dr Mohammad Nickdel, including histology images.
- In Chapter 5, human cartilage samples treated with retinoic acid were prepared by Dr Hugh Manning (section 5.7.2.1).
- In Chapter 6, all animal work for Langendorff autofluorescence lifetime measurements was carried out by Dr Benjamin Dyer.
- In Chapter 6, myocardial infarction induction surgeries were realised by Dr Markus Sikkel and Adam Mills.
- In Chapter 6, i*n vivo* measurements of myocardial infarction were realised in collaboration with Dr Benjamin Dyer.
- In Chapter 6, collagen quantification through histology was realised by Dr Benjamin Dyer.

Copyright declaration

Acknowledgements

Firstly, I would like to thank my supervisors Paul and Chris for giving me the opportunity to work on this project and for their invaluable help, guidance and advice over its course. I would also like to extend my thanks to Nick, Alex and Yoshi for their expertise on heart and cartilage matters.

Within the Photonics Group I am particularly grateful to Cliff, for introducing me to time-resolved autofluorescence and for passing on his knowledge on TCSPC. A big thanks to all friends and colleagues at Imperial that have shared long days in the lab and long nights in the pub, and also to Simon and Martin, without whom this project would take another three years (at least) to complete.

A special thanks to Ben for the long (and dark) days in the lab, during which I was presented with useful English lessons. At the NHLI, I would also like to acknowledge Markus, Maeve, Laura, Matt and Adam for their help during this project.

Outside Imperial, I would like to thank all my friends, both in London and elsewhere. Special thanks to the boys and girls in Lisbon for their support and friendship throughout the years. To my family, a big thanks for their support and encouragement.

Finally, a very big “thankyou” to Marta for embarking in this adventure 3 years ago. I couldn’t have done it without her patience, support and encouragement.

To my parents

Table of Contents

List of Figures

List of Tables

List of Abbreviations

ADAMTS	A Disintegrin And Metalloproteinase with ThromboSpondin Motifs
ADC	Analog-to-digital converter
ADP/ATP	Adenosine diphosphate/triphosphate
AFL	Autofluorescence lifetime
AMC	Age matched controls
APD	Avalanche photodiode
ASIC	Application specific integrated circuits
AUC	Area under the curve
CAD	Coronary artery disease
CCD	Charge-coupled device
CE	Collection efficiency
CFD	Constant fraction discriminator
CML	Current-mode logic
CMOS	Complementary metal–oxide–semiconductor
CT	Computerised tomography
CW	Continuous wave
DAC	Digital-to-analog converter
DAPI	4′,6-Diamidino-2-phenylindole dihydrochloride
DCM	Digital Clock Managers
DDP	2,6-dimethyldifuro-8-pyrone
DFD	Digital frequency domain
DLL	Dynamic-Link Library
ECM	Extracellular matrix
ETC	Electron transport chain
FAD/FADH2	Oxidised/reduced flavin adenine dinucleotide
FDG-PET	Fludeoxyglucose positron emission tomography
FIFO	First In First Out
FLIM	Fluorescence lifetime imaging microscopy
FOD	First order derivative
FPGA	Field Programmable Gate Array
FRET	Förster Resonant Energy Transfer
FWHM	Full width at half maximum
GAG	Glycosaminoglycan
GDP/GTP	Guanine diphosphate/triphosphate

GUI	Graphic User Interface
HDL	Hardware description language
IGD	Interglobular domain
IR	Infrared
IRF	Instrument response function
ISC	Intersystem crossing
KH	Krebs-Henseleit
LAD	Left anterior descending
LDA	Linear discriminant analysis
LDH	Lactate dehydrogenase
LED	Light emitting diode
LGE-CMR	Late gadolinium enhancement cardiac magnetic resonance
LipDH	Lipoamide dehydrogenase
LPF	Low-pass filter
LV	Left ventricle
LVPECL	Low-voltage positive emitter-coupled logic
LVTTL	Low-voltage transistor-transistor logic
MCP-PMT	Microchannel plate photomultiplier tube
MDH	Malate dehydrogenase
MI	Myocardial infarction
MI-HF	Myocardial infarction heart failure
MMP	Matrix Metalloproteinases
MPE	Maximum permissible exposure
MRI	Magnetic resonance imaging
NAD^+/NADH	Oxidised/reduced nicotinamide adenine dinucleotide
$NADP^+$/NADPH	Oxidised/reduced nicotinamide adenine dinucleotide phosphate
ND	Neutral density
NHLI	National Heart and Lung Institute
NMR	Nuclear magnetic resonance
OA	Osteoarthritis
OCT	Optical coherence tomography
OS	Operating-system
PBS	Phosphate buffered saline
PC	Principal components
PCA	Principal component analysis
PDC	Pyruvate-dehydrogenase complex

PECL	Positive Emitter-Coupled Logic
PET	Positron emission tomography
PMT	Photomultiplier tube
PSR	Picrosirius red
RF	Radio-frequency
RLD	Rapid lifetime determination
ROC	Receiver operator characteristic
ROI	Region of interest
RV	Right ventricle
SD	Standard deviation
SNR	Signal-to-noise ratio
SPAD	Single photon avalanche diode
TAC	Time-to-amplitude converter
TCA	Tricarboxylic acid cycle
TCSPC	Time-correlated single photon counting
TDC	Time-to-digital converter
TNF	Tumour necrosis factor
TRFS	Time-resolved fluorescence spectroscopy
TTL	Transistor-Transistor Logic
TTS	Transit-time-spread
UI	User interface
USB	Universal Serial Bus
UV	Ultraviolet
VHDL	VHSIC Hardware Description Language
VHSIC	Very High Speed Integrated Circuit

Publications and presentations

Journal Publications

BT Dyer, **J Lagarto**, P French, Dunsby, NS Peters, C Dunsby, AR Lyon (2014). Time-resolved autofluorescence spectroscopy as a label-free method to characterise acute changes in ex vivo models of cardiac disease. Heart, 100 (Suppl 4), A13–A13.

Contributions to this work: designed the experiments; data collection and analysis. (Chapter 6)

João Lagarto, Benjamin T. Dyer, Clifford Talbot, Markus Sikkel, Nicholas Peters, Paul French, Alexander Lyon and Chris Dunsby, "Application of time-resolved autofluorescence to label-free in vivo optical mapping of changes in tissue matrix and metabolism associated with myocardial infarction and heart failure", *Biomedical Optics Express*, Jan. 2015.

Contributions to this work: wrote the paper; designed the experiments; data collection and analysis. (Chapter 6)

Dyer, B., **Lagarto, J.**, Sikkel, M., French, P., Dunsby, C., Peters, N., & Lyon, A. (2014). 186 The Application of Autofluorescence Lifetime Metrology as a Novel Label-free Technique for the Assessment of Cardiac Disease". Heart, 100 (Suppl 3), A104–A104.

Contributions to this work: designed the experiments; data collection and analysis. (Chapter 6)

D. J. Kelly, S. C. Warren, S. Kumar, **J. L. Lagarto**, B. T. Dyer, A. Margineanu, E. W.-F. Lam, C. Dunsby, and P. M. W. French, "An automated multiwell plate reading FLIM microscope for live cell autofluorescence lifetime assays," *J. Innov. Opt. Health Sci.*, vol. 07, no. 05, p. 1450025, Sep. 2014.

Contributions to this work: data collection. (Chapter 3)

H. B. Manning, M. B. Nickdel, K. Yamamoto, **J. L. Lagarto**, D. J. Kelly, C. B. Talbot, G. Kennedy, J. Dudhia, J. Lever, C. Dunsby, P. French, and Y. Itoh, "Detection of cartilage matrix degradation by autofluorescence lifetime.," *Matrix Biol.*, vol. 32, no. 1, pp. 32–8, Jan. 2013.

Contributions to this work: data analysis. (Chapter 5)

Presentations and proceedings

J. Lagarto, C. B. Talbot, B. Dyer, D. J. Kelly, M. Nickdel, M. B. Sikkel, J. Dudhia, Y. Itoh, N. S. Peters, A. R. Lyon, C. Dunsby, P. M. W. French, "Compact and portable hyperspectral autofluorescence lifetime point probe system applied to the study of disease", Photon 14, London, United Kingdom, 2014. Oral presentation by J. Lagarto.

J. Lagarto, C. B. Talbot, B. Dyer, D. J. Kelly, M. Nickdel, M. B. Sikkel, J. Dudhia, Y. Itoh, N. S. Peters, A. R. Lyon, C. Dunsby, P. M. W. French, "A compact and portable hyperspectral autofluorescence lifetime point probe system applied to the study of cardiac disease and arthritis", Laser Europe 2014, Amsterdam, The Netherlands, 2014. Oral presentation by J. Lagarto.

J. Lagarto, C. B. Talbot, B. Dyer, D. J. Kelly, M. Nickdel, M. B. Sikkel, J. Dudhia, Y. Itoh, N. S. Peters, A. R. Lyon, C. Dunsby, P. M. W. French, "A compact and portable hyperspectral autofluorescence lifetime point probe system applied to the study of cardiac disease and arthritis", BiOS 2014 SPIE Photonics West, San Francisco, California, United States, 2014. Oral presentation by J. Lagarto.

Mohammad B. Nickdel, **João L. Lagarto**, Douglas J. Kelly, Hugh B. Manning, Kazuhiro Yamamoto, Clifford B. Talbot, Christopher Dunsby, Paul French, Yoshifumi Itoh, "Autofluorescence lifetime metrology for label-free detection of cartilage matrix degradation", BiOS 2014 SPIE Photonics West, San Francisco, California, United States, 2014. Oral presentation by Mohammad B. Nickdel.

Benjamin T. Dyer, **J. Lagarto**, M. B. Sikkel, C. B. Talbot, N. S. Peters, A. R. Lyon, P. M. French, C. Dunsby, "Application of autofluorescence lifetime metrology as a label-free technique to assess heart disease", BiOS 2014 SPIE Photonics West, San Francisco, California, United States, 2014. Oral presentation by Benjamin T. Dyer.

S. Coda, D. Kelly, **J. Lagarto**, H. Manning, R. Patalay, H. Sparks, A. Thompson, S. Warren, J. Dudhia, G. Kennedy, M. Nickdel, C. Talbot, K. Yamamoto, M. Neil, Y. Itoh, J. McGinty, G. Stamp, A. Thillainayagam, C. Dunsby, and P. French, "Autofluorescence lifetime imaging and metrology for medical research and clinical diagnosis" in Optics in the Life Sciences, OSA Technical Digest (online) (Optical Society of America, 2013), paper MT3C.4. Oral presentation by S. Coda.

M. Nickdel, **J. L. Lagarto**, D. J. Kelly, H. B. Manning, K. Yamamoto, C. B. Talbot, J. Dudhia, C. Dunsby, P. M. W. French, Y. Itoh, "Detection of cartilage matrix degradation by autofluorescence lifetime", Spring Meeting of the British-Society-for-Matrix-Biology, Oxford, England, Vol. 94, 5, A12-A13, 2013. Oral presentation by M. Nickdel.

J. Lagarto, M. Nickdel, B. Dyer, C. Talbot, C. Dunsby, P. French, "Development of autofluorescence lifetime instrumentation and its application to the study of disease", Biophotonics 2013, Island of Ven, Sweden, 2013. Poster presentation by J. Lagarto.

1 Thesis overview

Autofluorescence spectroscopy is a promising technique for the characterization of biological tissues and has showed potential for *in vivo* clinical diagnosis of many diseases. It can exploit the photo-physical properties of endogenous molecules to provide information about structural, functional and biochemical changes that occur in biological tissue and thus provides label-free molecular contrast without issues of toxicity associated with the introduction of exogenous labels. In particular, time-resolved fluorescence spectroscopy can improve the specificity of autofluorescence measurements by resolving the autofluorescence intensity decay characteristics and thus provide an additional source of contrast. Autofluorescence lifetime measurements of endogenous fluorophores, such as collagen, NADH and FAD, may present a convenient non-invasive approach to probe pathological transformations. Historically, autofluorescence lifetime studies have been mainly undertaken in cuvette-based instruments, partly due to limitations of the instrumentation required to analyse the autofluorescence signal. In recent years, however, the growing clinical interest has stimulated the development of new compact and portable fibre-optic based fluorescence lifetime instrumentation, which has been increasingly applied to studies of biological tissue and has shown potential for medical applications of tissue diagnosis.

This thesis aims to investigate the potential of autofluorescence lifetime metrology to readout intrinsic contrast and discriminate between healthy and diseased tissues. In particular, the application of a new compact and portable instrument that combines time-resolved spectrofluorometry and steady-state diffuse reflectance spectroscopy is reported, to investigate the clinical diagnostic potential of autofluorescence and diffuse reflectance in osteoarthritis and heart disease.

Osteoarthritis is a chronic and degenerative disease characterised by progressive loss of function of the joints and for which there is currently no effective treatment available. With current diagnostic techniques, osteoarthritis can only be detected at late stages of disease progression, when the degradation of the cartilage is no longer reversible. Building on earlier work in our group, this thesis describes collaborative work with the Kennedy Institute of Rheumatology to investigate the potential of autofluorescence lifetime measurements to read out early changes in the cartilage matrix due to degradation. If the efficiency and practicality of this approach can be demonstrated, autofluorescence lifetime metrology could find clinical applications in this area, including earlier detection and monitoring of osteoarthritis progression and evaluation of therapeutic intervention.

Heart disease is the leading cause of death in the developed world, for which myocardial infarction is a major contributor. This thesis describes collaborative work with the National Heart and Lung

Institute to explore the potential of autofluorescence lifetime measurements to report structural and metabolic alterations in the myocardium owing to pathological transformations associated with heart failure, with a view to developing a new label-free cardiac diagnostic tool.

This thesis begins with an introduction to the most relevant concepts for this research. **Chapter 2** provides a background overview of the physics underlying fluorescence and the properties of fluorescence emission, with particular emphasis on fluorescence lifetime, for which the most commonly employed measurement and data analyses techniques are described. In **Chapter 3**, the concept of autofluorescence, i.e. naturally occurring fluorescence in biological specimens, is reviewed, including a brief overview of the most relevant endogenous fluorophores for our studies. To establish baseline values for our investigation of osteoarthritis and heart disease, the autofluorescence properties of collagen, NADH and FAD were characterised, since these correspond to the predominant fluorophores in articular cartilage (collagen type II) and in cardiac tissue (NADH and FAD).

Chapter 4 introduces the field of optical tissue spectroscopy, providing a comprehensive description of the techniques used in our studies, i.e. steady-state and time-resolved fluorescence spectroscopy and diffuse reflectance spectroscopy, along with a comparison with other optical techniques commonly employed in biomedical research. In this chapter, the development of a single-point fibre-optic probe-based instrument that combines spectrally-resolved autofluorescence lifetime spectroscopy and white light reflectometry is also discussed. A detailed description of this instrument and its characterisation is followed by comparison with a well-characterised system previously developed in our laboratory. Two of these new instruments were developed during this PhD and subsequently applied to osteoarthritis and heart disease studies, presented in **Chapters 5** and **6**, respectively.

Chapter 5 describes the application of autofluorescence lifetime measurements to *in vitro* and *ex vivo* studies of articular cartilage, with a view to developing a new diagnostic tool for early detection of osteoarthritis. These studies, which were realised in enzymatically degenerated porcine and murine cartilage, suggest that the autofluorescence lifetime of cartilage is sensitive to disruption of the extracellular matrix components, aggrecan and collagen. Autofluorescence lifetime data were also obtained from *ex vivo* human tissue presenting naturally occurring osteoarthritis and the preliminary results of this investigation are also presented.

Chapter 6 discusses the application of time-resolved autofluorescence spectroscopy and steady-state white-light reflectometry to the study of cardiac disease, both *ex vivo* and *in vivo*. Here, an investigation of the autofluorescence and diffuse reflectance signatures of cardiac tissue is presented,

in an *ex vivo* Langendorff rat model and in an *in vivo* myocardial infarction rat model, where we observed structural and energetic changes in the infarcted and remote non-infarcted myocardium at different stages of disease progression. This investigation prompted the development of a clinically viable instrument to be used in open chest surgical procedures in humans, of which progress to date is described.

The remainder of this thesis concerns the development and application of a low-cost instrument for autofluorescence lifetime measurements of biological tissue. **Chapter 7** presents a detailed description and characterisation of the detection methodology employed in this instrument, along with preliminary data obtained from lifetime measurements of reference fluorophores. In **Chapter 8**, the development and application of a complete low-cost system is discussed, including excitation and detection setups. Preliminary autofluorescence lifetime data obtained from *ex vivo* lamb kidneys are presented, together with a comparison against a well-characterised time-resolved spectrofluorometer. The advantages and limitations of this instrument relative to our "gold-standard" instrument are addressed, including a discussion on future work required to develop a clinical prototype.

Finally, **Chapter 9** summarises the key results presented throughout this thesis and the main conclusions that can be drawn from our investigations, including the potential clinical impact and suggestions on future work.

The work presented in this thesis resulted in 5 journal publications, 7 oral communications and 1 poster presentation.

2 Introduction to fluorescence

The use of fluorescence in biomedical research has had a remarkable growth in the past 30 years and, accordingly, fluorescence microscopy and spectroscopy are now extensively used in various fields such as flow cytometry, DNA sequencing and medical diagnostics. In this thesis, we discuss the development and clinical application of biomedical spectroscopy instrumentation, with particular emphasis to fluorescence measurements of osteoarthritis and heart disease. Given its importance to our work, this chapter aims to outline the underlying principles of fluorescence, including means of quantification of a fluorescence signal. Here, particular relevance is given to fluorescence lifetime, as this is a key optical readout in our investigations. This includes a review of the most common fluorescence lifetime measurement techniques, both in time-domain and frequency-domain.

Outline

- Introduction to fluorescence.
- Means of quantification of a fluorescence signal.
- Description of fluorescence lifetime measurement techniques.
- Summary

2.1 Fluorescence

Fluorescence is the spontaneous emission of a photon when an electron in a molecule relaxes to its ground state from an excited energy level. This principle is illustrated in the Jablonski diagram in Figure 2.1.

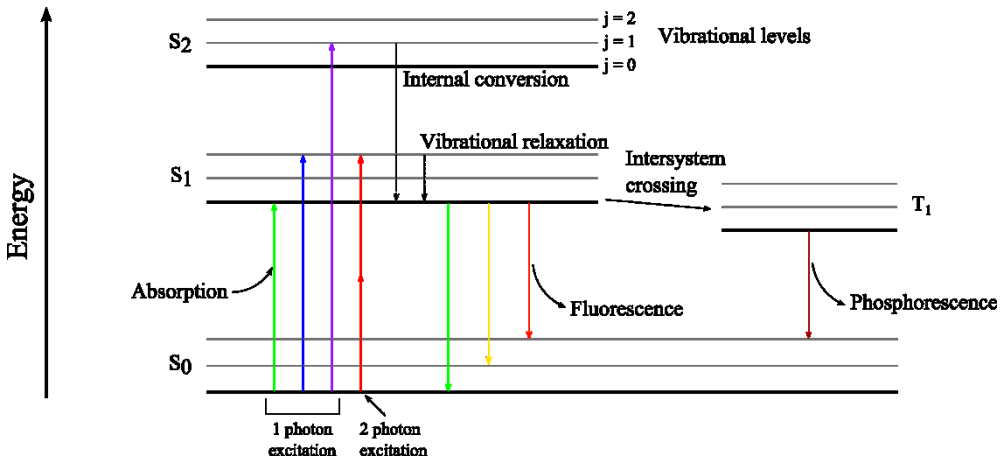

Figure 2.1 Jablonski diagram showing possible transitions between molecular energy states. Adapted from [1].

The process is initiated with promotion of an electron usually from the ground state (S_0) to an excited singlet state. Fluorescent molecules are usually excited to higher vibration levels of S_1 or S_2,

depending on the excitation energy. The energy necessary to excite electrons from the ground state is primarily obtained by absorption of either a single photon or by the simultaneous absorption of multiple photons, each having a fraction of the energy of the transition, as illustrated in Figure 2.1.
Once excited, there are a number of radiative and non-radiative routes by which electrons can return to the ground state (not necessarily to the vibrational level j = 0). When excited to upper vibrational levels of an excited state, the molecule can quickly relax to the lowest vibrational level of that state (j = 0, see Figure 2.1) through a non-radiative process known as vibrational relaxation. It is also possible for electrons to decay non-radiatively between vibrational levels of different excited states. This process is known as internal conversion and is more likely to occur when the difference of energy between the two excited states is smaller. Given that both internal conversion and vibrational relaxation occur within 10^{-12} seconds or less, these processes usually precede the subsequent decay to the ground state [1].

Transition from the lowest vibrational level of S_1 (i.e. j = 0) to the ground state S_0 can occur radiatively by emission of a photon. This process is known as fluorescence and typically occurs in a time scale of 10^{-9} seconds. Alternatively, the molecule can undergo an intersystem crossing (ISC) to a triplet state, as illustrated in Figure 2.1, from which it can also radiatively decay to the ground state S_0 (phosphorescence). Transitions from the triplet excited state T_1 to the ground singlet state S_0 are forbidden, because they require a spin reversal. Hence, phosphorescence emission is much slower than fluorescence, typically occurring on a microsecond timescale. Molecules can also relax non-radiatively to the ground state, also referred to as quenching. The rate k_{nr} at which this relaxation occurs depends on the surrounding environment. In this case, energy can be dissipated as heat to the environment or transferred with other molecules, e.g. Förster Resonant Energy Transfer (FRET).

2.2 Properties of fluorescence

The fluorescence light that originates from fluorescent molecules is characterised by several intrinsic properties, including intensity, wavelength, polarisation and lifetime. Given that the fluorescence emission is dependent on the electronic configuration of the fluorophore and its surrounding environment, fluorescence measurements can provide means of contrast between different molecular species or environments and therefore, in the context of medical diagnostics, between healthy and diseased tissues. The following sections provide a brief overview of the most fundamental fluorescence properties.

2.2.1 Intensity and quantum yield

Fluorescence intensity is the most widely investigated fluorescence parameter in biomedical applications, given the simplicity of the instrumentation required to realise a fluorescence intensity measurement. The fluorescence intensity depends on the absorbed radiation, fluorophore

concentration and quantum yield, ϕ, of the specimen under investigation, which can be described by the number of fluorescent photons emitted (N_e) relative to the number of absorbed photons (N_a), as defined in equation 2.1.

$$\phi = \frac{N_e}{N_a} \tag{2.1}$$

Alternatively, the quantum yield can also be reported as a function of the radiative and non-radiative decay rates, k_f and k_{nr}, respectively.

$$\phi = \frac{k_f}{k_f + k_{nr}} \tag{2.2}$$

As k_f and k_{nr} are dependent on the electronic configuration and on the immediate vicinity of the fluorophore, respectively, measurements of the quantum yield represent a direct approach to obtain information regarding the local molecular environment. The quantum yield is typically measured by comparing the fluorescence intensity of the specimen under investigation to that of a sample of known quantum yield. However, such measurements are more commonly employed in cuvette-based systems as they can be difficult to realise in biological specimens given that the amount of radiation absorbed by a specimen can vary with a number of factors including fluorophore concentration, excitation light intensity and geometry, re-absorption of the emitted fluorescence and heterogeneity in the absorption and scattering properties of the sample. Furthermore, the intensity of the detected fluorescence signal can also vary with instrumentation, e.g. transmission of optical components or quantum efficiency of the detectors. Therefore, measurements of fluorescence intensity are often challenging to compare between instruments and samples, particularly in biological specimens, and thus other fluorescence parameters may also be recorded in parallel to fluorescence intensity to increase the specificity of the measurements.

2.2.2 Excitation and emission spectra

The wavelength of a fluorescence photon (λ_f) is determined by the energy difference (ΔE) between the two electronic states involved in the transition and can be defined as shown in equation 2.3, where h is Planck's constant and c is the speed of light.

$$\lambda_f = \frac{hc}{\Delta E} \tag{2.3}$$

As described in section 2.1, after excitation, electrons may undergo a series of processes by which energy is lost, before emission of a fluorescence photon occurs. Hence, the energy of the emitted photon is necessarily lower than the excitation energy and thus the fluorescence emission wavelength is red-shifted relative to the excitation wavelength (Stokes' shift). Furthermore, the fluorescence emission spectrum of a fluorophore typically has similar yet "mirrored shape" of the excitation spectra, as result of similar vibrational level structure for ground and first excited states.

The wavelengths at which a fluorophore may be excited and emit fluorescence light depend on the electronic configuration of the molecules. In turn, the electronic structure depends on the chemical structure of the molecule and on its local environment. Hence, measurements of the fluorescence excitation and emission spectra can report on these parameters and are typically employed in the context of biomedical research to differentiate healthy from diseased tissues, as for example in references [2]–[4].

2.2.3 Polarisation

The absorption efficiency of a fluorophore depends on its orientation relative to the excitation light polarisation. A fluorophore absorbs light more efficiently when its dipole moment is parallel to the electric field of the excitation light. If one considers a fluorophore with the dipole orientation parallel to the linearly polarised excitation light, the corresponding fluorescence light will have identical polarisation orientation, provided that the molecule remains stationary throughout the lifetime of the excited state. If the molecule rotates, light is emitted with a different orientation relative to the excitation. If we now consider a fluorescence sample containing a large number of randomly oriented molecules, illumination with linearly polarised light will preferentially excite a population of molecules with a particular orientation, while others will be excited less efficiently, resulting in an uneven distribution of the fluorescence intensity with degree of polarisation. Further depolarisation can occur as result of the rotational mobility and collisions between molecules. The degree of polarisation of the fluorescence emission is usually termed fluorescence anisotropy, r, which can be calculated as shown in equation 2.4, using the fluorescence intensity detected at parallel ($I_{||}$) and perpendicular ($I_{\perp}$) orientations relative to the excitation light polarisation. The parameter G describes the variation of the optical detection efficiency of one fluorescence polarisation state over the other.

$$r = \frac{I_{||} - GI_{\perp}}{I_{||} + 2GI_{\perp}} \tag{2.4}$$

The fluorescence anisotropy of a freely rotating molecule is typically described by a single exponential decay function. In a biological sample containing various different molecular species, the anisotropy decay can be described by a sum of exponentials, as defined in equation 2.5,

$$r(t) = \sum_{i=1}^{n} r_{0i} e^{-t/\theta_i} \tag{2.5}$$

where r_0 is the anisotropy at the time of excitation and θ is the rotational correlation time. For single photon excitation, the initial anisotropy r_0 can be described as a function of the angle α between the absorption and emission dipole moments of a fluorophore, as in equation 2.6.

$$r_0 = \frac{2}{5}\left(\frac{3\cos^2\alpha - 1}{2}\right) \tag{2.6}$$

In turn, the rotation correlation time, θ, depends not only on the fluorophore itself but also on its surrounding environment, as defined in equation 2.7, where η is the viscosity of the environment, T is the temperature, K is the Boltzmann constant and V is volume of the molecule, which is considered to be approximately spherical.

$$\theta = \frac{\eta V}{KT} \tag{2.7}$$

Overall, fluorescence anisotropy measurements are sensitive to both intrinsic fluorophore properties and the local environment and thus they can report on e.g. the viscosity of the environment [5], [6], molecular conformations [7] or protein binding state [8], [9].

In order to realise quantitative fluorescence anisotropy measurements, a fluorescence sample of randomly oriented fluorophores requires excitation with linearly polarised light and detection at parallel and perpendicular orientations. If the sample is excited using unpolarised light or if the fluorescence detection is not polarisation-resolved, the polarisation state of the measured fluorescence signal will be averaged. In contrast, one can also realise fluorescence measurements at a particular angle relative to the excitation orientation ($\alpha = 54.7^{o}$, typically termed magic angle) such that the contribution of anisotropy to the fluorescence signal is eliminated. This is particularly relevant for cuvette-based fluorescence lifetime measurements of fluorophores, for which the contribution of fluorescence anisotropy can lead to errors it is not taken into account.

2.2.4 Lifetime

Of all parameters described in this section, the fluorescence lifetime assumes the greatest relevance in our investigations and thus it will be described in greater detail, including measurement and data analysis techniques (see sections 2.3 and 2.4, respectively). The fluorescence emitted by an ensemble

of identical fluorophores in a homogeneous environment decays exponentially with time, following a delta excitation function, as defined in equation 2.8,

$$I(t) = I_0 e^{-t/\tau} \tag{2.8}$$

where I_0 is the initial intensity and τ is the fluorescence lifetime, defined as the average time an electron remains in an excited state before decaying back to the ground state. The fluorescence lifetime can be described as a function of the radiative and non-radiative decay rates, k_f and k_{nr}, respectively, as indicated in equation 2.9.

$$\tau = \frac{1}{k_f + k_{nr}} \tag{2.9}$$

From equations 2.2 and 2.9, we can rewrite the quantum yield, ϕ, as a function of the fluorescence lifetime.

$$\phi = k_f \tau \tag{2.10}$$

Similarly to the quantum yield, equation 2.9 suggests that fluorescence lifetime is dependent on the electronic conformation of the fluorophore and its local environment. An important advantage of fluorescence lifetime over quantum yield measurements is that lifetime is inherently ratiometric, depending on the intensity decay profile over time rather than on the absolute intensity values. Hence, unlike quantum yield, fluorescence lifetime is relatively insensitive to artefacts affecting intensity measurements caused by e.g. uneven fluorophore concentration or heterogeneous absorption and scattering in the sample.

The fluorescence lifetime is sensitive to a number of environmental factors that affect the non-radiative decay rate k_{nr}, including viscosity [5], [6], temperature [5] or pH [10]. Fluorescence lifetime can also be sensitive to changes in the structural conformation of a molecule or protein binding state. For example, free NADH yields a short fluorescence lifetime of ~0.4 ns, which is attributed to a balance between the extended and folded conformations of the molecule. However, when bound to an enzyme, NADH exhibits a longer fluorescence lifetime (~1.5 ns [11]), resulting from the inability to fold [1]. The fluorescence properties of NADH and other endogenous fluorophores will be discussed in further detail in Chapter 3.

Altogether, given its sensitivity to changes in local environment and relative insensitivity to intensity based artefacts, fluorescence lifetime has been increasingly studied in the context of biomedical

research to readout contrast between healthy and diseased tissues, e.g. in various types of cancer [12]–[20] and cardiovascular disease [21]–[24].

2.3 Fluorescence lifetime measurement techniques

In general, fluorescence lifetime measurement techniques can be categorised as time-domain or frequency-domain, depending on the fluorescence excitation and detection strategies. In time-domain techniques, the fluorescence signal is recorded in time following excitation with a short optical pulse. In contrast, frequency-domain techniques measure the harmonic response of the system, from which lifetime information can be derived from the difference in phase and amplitude between a periodically modulated excitation signal (typically a sinusoidal waveform) and the resulting demodulated fluorescence emission. While both time- and frequency-domain methods can provide equivalent lifetime information, their implementation differs significantly, each having their respective merits and limitations with respect to cost, complexity and performance. Historically, time-domain implementations offered higher temporal resolution, yet they were more expensive given the necessity of having ultrafast laser sources to realise the acquisition and complex detection methodologies. However, significant advances in laser technology and microelectronics have prompted the development of new lower-cost excitation and detection strategies, e.g. [25]–[28], which narrowed the gap between time-domain and frequency-domain techniques, with respect to the cost of the implementation.

In the following sections, the most common time- and frequency-domain techniques utilised in fluorescence lifetime spectroscopy and imaging are briefly described, including their respective merits and limitations.

2.3.1 Time-domain methods

Time-domain fluorescence lifetime measurement techniques can be categorised according to whether they are photon counting techniques, such as time-correlated single photon counting (TCSPC), in which the time of arrival of single photons is recorded with respect to the excitation pulse, or sampling techniques, in which the fluorescence emission is recorded in two or more time gates following the excitation signal. In general, photon counting techniques can offer greater temporal resolution at the expense of acquisition time, given that detection is typically limited to one photon per excitation period and is realised on a point-by-point (or pixel-by-pixel) basis. In contrast, time gated methods offer fast acquisition times, allowing simultaneous acquisition of multiple pixels, which constitutes a great advantage for clinical imaging modalities, such as endoscopy.

2.3.1.1 Time-correlated single photon counting (TCSPC)

TCSPC is the most common and well-established method for fluorescence lifetime measurements. It is based on the principle that, at sufficiently low fluorescence rates, all individual photons can be

detected and their respective time of arrival measured relative to the laser excitation pulse. A diagram of this principle is shown in Figure 2.2.

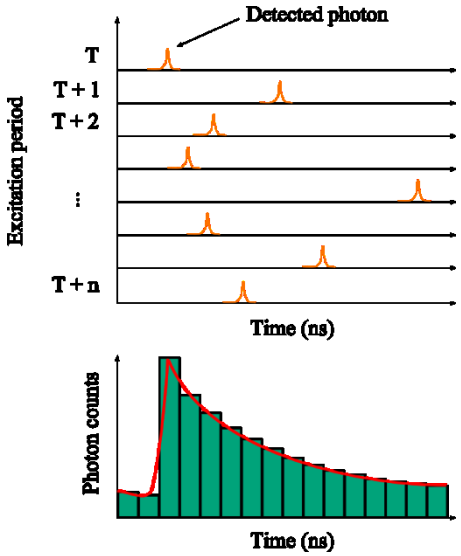

Figure 2.2 Working principle of TCSPC Photons are detected one at a time and their time of arrival measured relative to the excitation pulse. Hence, a histogram of photon arrival times can be generated, which can be fitted to an exponential function for determination of the lifetime parameters. Adapted from [29].

TCSPC utilises ultrashort excitation pulses at high repetition rates (in the MHz regime), photon counting detectors (typically photomultiplier tubes [PMT]) and sophisticated high-speed counting electronics to accurately measure the time of arrival of single photons. When a fluorescence photon hits the detector following an excitation pulse, the corresponding detector output signal pulse is delivered to the TCSPC card, where it is read out by a fast discriminator. Although a conventional leading-edge discriminator could be used to detect the signal, PMTs can present considerable amplitude jitter, due to the pseudo random amplification mechanism. For example, the voltage amplitude output by a cooled photon counting PMT (e.g. model PMC-100-1, Becker and Hickl GmbH, Germany) can vary from 50 to 200 mV, at 90% of the maximum gain [30]. If leading-edge discriminators were used to trigger upon such a signal, the amplitude jitter would introduce timing jitter potentially equivalent to the maximum pulse rise time. Hence, to obtain optimal temporal resolution over a wide range of pulse amplitudes, constant fraction discriminators (CFD) are used. In contrast to leading-edge discriminators, CFDs trigger at a constant fraction of the maximum pulse height, thus guaranteeing that all photons are detected at an equivalent time-point. Conventional CFD implementations, such as the one used in TCSPC, utilise zero-cross based triggering to achieve optimal resolution. The method is illustrated in Figure 2.3.

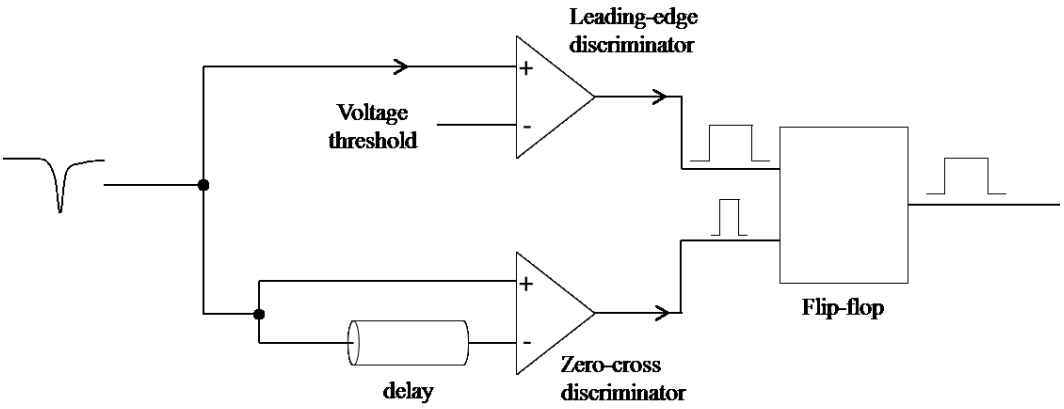

Figure 2.3 Schematic representation of a typical CFD implementation. The PMT pulse is split in two lines for threshold and zero-cross discrimination. The output pulses from both discriminators are fed to a flip-flop that will output a standard logic pulse (typically TTL) if the amplitude of the PMT pulse is greater than the threshold voltage.

In brief, the incoming pulse from the detector is split in two delay lines: one is connected to a leading-edge discriminator for comparison against a voltage threshold; the other is split again such that one of the lines is fed to the non-inverting input (V_+) of a comparator and the other line is delayed and fed to the inverting input (V_-). The second comparator effectively "sees" a bipolar pulse that is positive at the start and has a rapid transition to negative polarity and produces a logic pulse at the output upon the zero-cross transition. Ideally, the zero-cross point is independent of the pulse amplitude and therefore represents a precise time measurement of its arrival. Because the zero-cross point is within the voltage range of noise, a voltage threshold is implemented in the leading-edge discriminator to avoid random triggering due to noise. The output from each comparator is then fed to a flip-flop that will output a logic pulse if the amplitude of the PMT pulse is greater than the threshold voltage.

A second CFD exists in the TCSPC circuit to detect the laser excitation pulses which will serve as a timing reference from the light source. In conventional TCSPC setups (from Becker and Hickl), the output signals of the two CFDs are used as *Start* and *Stop* inputs of a time-to-amplitude converter (TAC) [29]. The working principle of a TAC is illustrated in Figure 2.4B. A TAC circuit is essentially a ramp generator that produces a voltage output that is linearly proportional to the time interval between the *Start* and *Stop* pulses. In a TCSPC setup the *Start* pulse is set by the detector while the *Stop* is set by laser sync pulse. This "reversed start-stop" configuration prevents a voltage build up in case that no photons are detected during an excitation period [29].

Finally, the output voltage from the TAC is directed to an analog-to-digital converter (ADC) and the resulting digital value - that effectively corresponds to the time of arrival of the photon - is assigned to a memory address, where detected photon events accumulate. The recordings are repeated for additional pulses until a satisfactory number of photons are recorded. The final output of the TCSPC readout is a histogram of photon arrival times that can be fitted to an exponential decay curve, from

which the lifetime parameters can be extracted. A schematic representation of a conventional TCSPC configuration is shown in Figure 2.4A. Other TCSPC configurations are possible, such as that used in PicoQuant TCSPC systems, which utilise a time-to-digital converter (TDC) instead of the TAC and ADC modules to immediately provide a digital representation of the time of arrival of single photons [31].

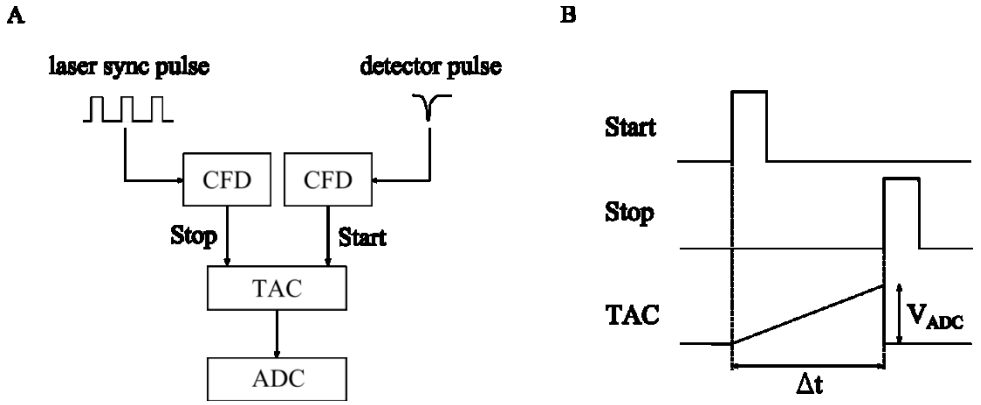

Figure 2.4 (A) Typical TCSPC implementation showing reversed *Start-Stop* configuration; (B) Timing diagram of a time-to-amplitude converter (TAC), where Δt refers to the time between the arrival of the Start and Stop signal and V_{ADC} refers to the voltage output of the TAC, which serves an input of the ADC.

TCSPC implementation of fluorescence lifetime measurements offers high photon efficiency at low count rates, high temporal resolution (down to 3 ps at 80 MHz) and high temporal accuracy and is widely regarded as a "gold-standard" method for fluorescence lifetime determination [1], [32]. Its major limitation concerns the relatively low count rates and, consequently, longer acquisition times, which are essentially imposed by the dead time of the electronics (typically greater than 100 ns) following the detection of a single photon. Indeed, in TCSPC the intensity of the fluorescence signal needs to be kept low (ideally 1 to 5% of the laser repetition rate) so that the probability of more than one photon arriving at the detector within the dead time of the electronics is close to zero. If the count rate of the fluorescence signal is such that multiple photons arrive within the dead time, photons arriving closer to the excitation pulse are preferentially read out by the TCSPC electronics over late-arriving photons. This effect is known as "photon pile-up" and ultimately can bias the fluorescence lifetime measurement towards shorter values.

TCSPC is commonly employed in laser scanning fluorescence lifetime imaging microscopes, as for example in references [32]–[36]. The acquisition time in these instruments is typically long compared to wide-field fluorescence lifetime imaging microscopy (FLIM) technologies, as the fluorescence intensity decay is collected on a pixel-by-pixel basis. TCSPC is also used to realise single-point detection [17], [37]–[39], which requires considerably reduced acquisition times, by integrating the

fluorescence intensity arising from a large volume of the sample. This approach is typically employed when spatial information is not required.

2.3.1.2 Time gating

An alternative approach to TCSPC measurements is based on gated detection of the fluorescence intensity signal at different time points relative to the excitation pulse. Typical time gating approaches utilise a single gate that samples the fluorescence intensity decay over a time interval of interest. The process is repeated at different delays relative to the excitation pulse, until a sufficient number of photons are detected (see Figure 2.5A). The resulting fluorescence decay curve yields as many points as the number of intervals sampled, as illustrated in Figure 2.5B. Unlike TCSPC, time gated detection is traditionally not a single photon counting technique and is more commonly employed in the context of wide-field microscopy [40]–[42] or endoscopy [22], [43], [44], making of use a gated image intensifier to provide snapshots of the fluorescence decay at different delays relative to the excitation pulse and a charge-coupled device (CCD) camera to record the fluorescence signal. This configuration allows FLIM acquisition at higher rates compared to TCSPC, since the fluorescence signal is acquired simultaneously for all pixels. Advances in microelectronics and complementary metal–oxide–semiconductor (CMOS) technology have permitted the development of time-gated detection architectures utilising e.g. Field Programmable Gate Arrays (FPGAs) or Single Photon Avalanche Diode (SPAD) arrays, both for imaging [45], [46] and single-point instruments [47]–[49], which constitute an attractive lower-cost alternative to the most traditional implementations.

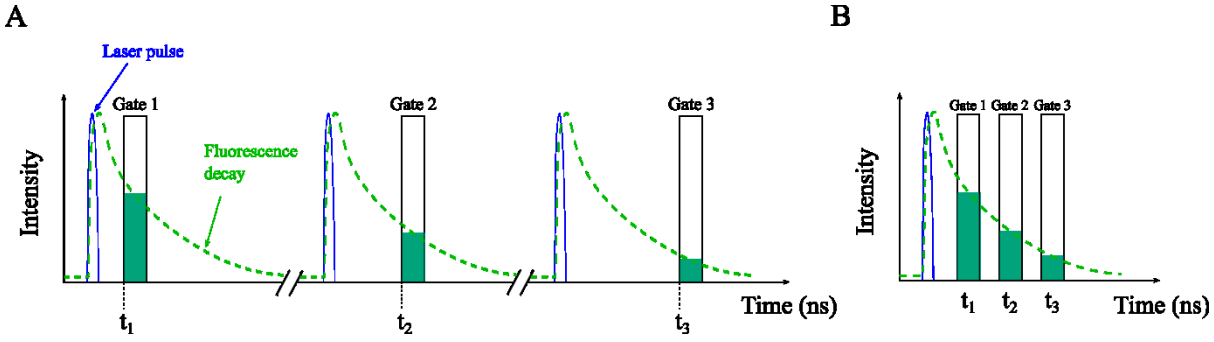

Figure 2.5 Schematic representation of a time gated fluorescence lifetime acquisition method, using three gates. (A) Temporal adjustment of the gates. (B) The reconstructed 3-point fluorescence decay profile, from all the measurements in each time gate.

A major limitation of time-gating refers to its relatively poor photon efficiency due to the low duty cycle of the detection, which translates into photons arriving outside the range of the detection gate not being recorded. To some extent, this limitation can be overcome by using wider gates, which maintain the ability to resolve complex decays and fast decay components due to the sub-100 ps rising and falling edge durations. An alternative method consists of generating gates of different widths, depending on their respective delay to the excitation pulse, i.e. shorter gates are generated closer to

the excitation pulse to resolve faster decays. This configuration was introduced by Grauw et al [25] applied to time-resolved confocal microscopy. Although this implementation does not strictly follow the classic time-gated fluorescence lifetime approach, as the different detection gates are generated sequentially within a single excitation period, it introduced the concept of time-gated single photon counting, which allows acquisition of data at greater speeds compared to TCSPC, given that the detection does not suffer from dead-time or photon pile-up limitations.

2.3.2 Frequency-domain methods

Frequency-domain fluorescence lifetime measurements concern the demodulation of a fluorescence signal following excitation with an intensity modulated light source. The principle of frequency-domain measurements is the following: if a fluorophore is illuminated with light modulated at an angular frequency ω (with $\omega = 2\pi f_{exc}$), described by a function $E(t)$, as defined in equation 2.12,

$$E(t) = E_{DC} + E_{pp}\sin(\omega t) \tag{2.12}$$

where E_{DC} and E_{pp} refer respectively to the DC component and peak-to-peak amplitude of the excitation waveform (see Figure 2.6), the corresponding fluorescence signal $F(t)$ will oscillate at the same angular frequency ω and exhibit a demodulation m and a phase shift φ relative to the excitation signal. Accordingly, the fluorescence signal can be described by equation 2.13, where F_{DC} and F_{pp} refer to the DC component and peak-to-peak amplitude of the signal, respectively.

$$F(t) = F_{DC} + F_{pp}\sin(\omega t + \varphi) \tag{2.13}$$

This principle is best illustrated in Figure 2.6. Historically, illumination is modulated by a sinusoidal waveform, although it is important to refer that any high frequency repetitive waveform can be used.

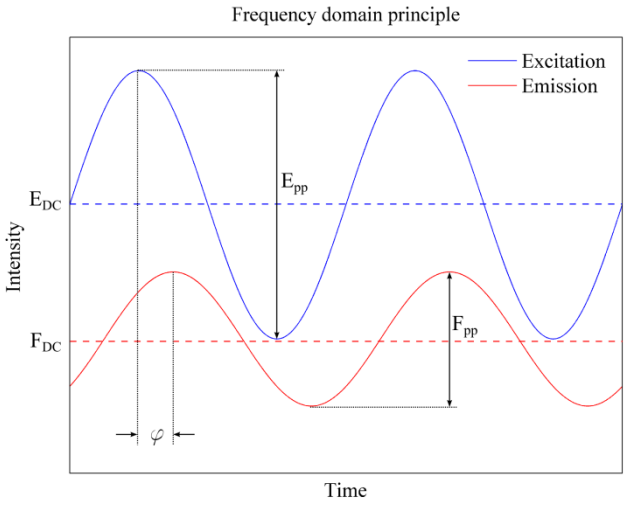

Figure 2.6 Basic principle of frequency-domain fluorescence lifetime measurements, showing phase delay φ and demodulation m (as defined in equation 2.14) of the fluorescence emission (in red) relative to the excitation signal (in blue).

The phase shift φ is caused by the time delay between absorption and subsequent emission of a fluorescence photon while the decrease in amplitude results from the finite nature of the lifetime of the sample [1]. The demodulation m of the fluorescence signal $F(t)$ relative to the excitation $E(t)$ is calculated as indicated in equation 2.14.

$$m = \frac{F_{pp}/F_{DC}}{E_{pp}/E_{DC}} \tag{2.14}$$

The fluorescence lifetime of the sample can be determined from measurements of the phase shift or the relative modulation of the signal. Accordingly, two apparent lifetime values can be determined, phase lifetime τ_φ and modulation lifetime τ_m, which can be calculated as indicated in equations 2.15 and 2.16, respectively. The derivation of these equations is provided in reference [50].

$$\tau_\varphi = \frac{\tan\varphi}{\omega} \tag{2.15}$$

$$\tau_m = \frac{1}{\omega}\sqrt{\frac{1}{m^2} - 1} \tag{2.16}$$

The apparent lifetimes τ_φ and τ_m are characteristic of the sample, but may not provide a complete description of the fluorescence intensity decay, since they represent a different weighted average of the decay times displayed by the sample [1]. Hence, in the case of a single exponential decay, τ_φ and τ_m will have the same value. For complex multiexponential decays, it may be necessary to repeat the measurements at multiple harmonics of the excitation frequency in order to obtain a more complete

description of the fluorescence decay, although this would also represent an increased acquisition time. For biomedical applications, in which long acquisition times are undesirable, it is common to realise the measurements at a single modulation frequency only.

Because frequency-domain measurements do not require fast photon counting detectors or picosecond optical pulses, they can be implemented as low-cost alternatives to the traditionally expensive time-domain methods, e.g. [51]–[55]. In the context of biomedical research, frequency-domain measurements have been employed in a number of applications including cancer investigations [56], [57] and stem cell differentiation [58]–[60].

2.4 Analysis of fluorescence lifetime data

As will be further discussed in Chapter 3, the fluorescence signal in biological tissue is typically complex due to the presence of multiple fluorophore species that give rise to complex intensity decay profiles. Hence, fluorescence from biological tissue is more commonly described by a multi-exponential decay model, as defined in equation 2.17,

$$I(t) = \sum_{i=1}^{n} a_i e^{-t/\tau_i} \tag{2.17}$$

where τ_i and a_i represent the fluorescence time and the pre-exponential factor of the ith component in the decay, respectively. From the decay parameters in equation 2.17, we can calculate the intensity weighted mean lifetime τ_{mean} as follows:

$$\tau_{mean} = \frac{\sum_{i=1}^{n} a_i {\tau_i}^2}{\sum_{i=1}^{n} a_i \tau_i} \tag{2.18}$$

For convenience, the fractional contribution, β_i, of the ith component to the overall decay can be calculated as shown in equation 2.19.

$$\beta_i = \frac{a_i \tau_i}{\sum_{k=1}^{n} a_k \tau_k} \tag{2.19}$$

The photon distribution in a fluorescence lifetime experimental measurement is the mathematical convolution of the sample's fluorescence intensity decay with the system's temporal instrument response function (IRF), which can be defined as the convolution of the excitation pulse shape, the bandwidth of the detector, e.g. due to the transit-time-spread (TTS) of a PMT, dispersion in the optical system and shape of the detection gate [29]. Hence, in order to be able to accurately fit a

complex decay model to the data, it is necessary to measure the temporal IRF of the system. In an ideal optical system, the IRF is recorded as an exact replica of the laser excitation pulse. Any deviations from this will cause broadening of the IRF. A common method for measuring the IRF is by recording the signal obtained from a sample with a very short fluorescence lifetime (ideally less than 100 ps) or, alternatively, the response of a scattering sample measured at the excitation wavelength.

There are a number of methods that can be employed to analyse fluorescence decay data, e.g. rapid lifetime determination (RLD) [61], Laguerre expansion [62] or phasor analysis [63], [64]. Another approach, and perhaps the most common to analyse fluorescence lifetime data, is to employ non-linear least squares fitting to minimise the goodness of fit chi-square value, χ^2, expressed as indicated in equation 2.20,

$$\chi^2 = \sum_{k=1}^{n} \frac{(I(t_k) - I_{model}(t_k))^2}{I(t_k)} \tag{2.20}$$

where n is the number of bins in the decay, I is the measured decay at each time delay and I_{model} is the model decay function convolved with the IRF. The fitting model can include the measured background offset, the after-pulsing probability of the detectors and incomplete decay estimation. All fluorescence lifetime data presented in this thesis were analysed using a non-linear least squares fitting routine from MATLAB (lsqnonlin function, R2011b, The Mathworks, Inc., USA), implemented in custom software written by our group, e.g. *FLIMfit* [42].

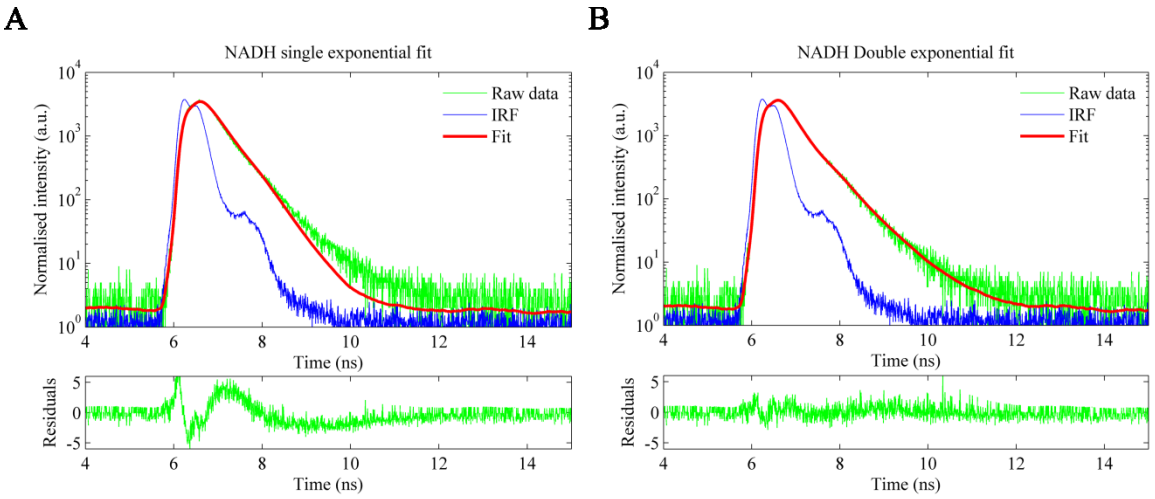

Figure 2.7 NADH fluorescence decays (~500,000 photons collected) fitted with (A) single and (B) double exponential models. Measurements were carried out at room temperature, in a cuvette-based system described in section 3.3.1.3, using TCPSC detection (4096 bins).

Figure 2.7 shows examples of single and double exponential fittings to NADH fluorescence decay data, excited at 375 nm using 40 MHz laser repetition rate. For the single exponential fitting, we measured a fluorescence lifetime of 0.41 ± 0.01 ns (χ^2 = 2.62 ± 0.08). Here, we observe a fluctuation in the residuals curve (Figure 2.7A, bottom), which indicates that a single exponential model cannot accurately describe the fluorescence intensity decay. In particular, we observe an underestimation of the fitting at around 10 ns, which effectively translates in lower sensitivity to long lifetime components.

The double exponential decay model (Figure 2.7B) was found to provide a better fit to the data relative to the single exponential decay model, with smaller weighted residuals randomly distributed around zero and a χ^2 closer to unity (χ^2 = 1.21 ± 0.03). The fluorescence intensity decays with a bi-exponential profile with lifetimes of 0.30 ± 0.01 ns (β_1 = 0.66 ± 0.03) and 0.70 ± 0.03 ns (β_1 = 0.34 ± 0.03), yielding a weighted mean fluorescence lifetime of 0.44 ± 0.01 ns. These results are in good agreement with reported NADH fluorescence lifetime values, at room temperature [8]. We note that the precision of the reported values is sufficient to provide a good description of the system, considering the total number of photons collected during a fluorescence lifetime acquisition (typically around 100,000 per second in a TCSPC-based setup), the temporal resolution of the TCSPC detection (typically ~10 ps) and the magnitude of the values.

It is important to note that the number of exponential components used in the fitting model is not necessarily the same as the number of fluorophores giving rise to the fluorescence signal. This is because a fluorescence decay fitting becomes increasingly more computationally intensive and sensitive to noise as the number of exponential components increases. For example, Köllner el al [65] estimated that only 185 photons are necessary to resolve a single exponential lifetime of 2.5 ns with 10% accuracy within an 8 ns acquisition window and 256 bins. In contrast, in a double exponential decay with individual lifetimes of 2 and 4 ns, acquisition period of 10 ns and 256 bins, one would need 400,000 photons to achieve the same accuracy, which emphasises the complexity of multi-exponential fluorescence lifetime decays, such as those typically found in tissue. Therefore, in most biological applications, the fluorescence decay is either described as a single or a double exponential decay model, depending on the number of photons collected during the acquisition. Alternatively, one could employ global binning, which combines data from several fluorescence decays to increase the total number of photons and thus reduce the uncertainty of the measurements. This approach is more commonly applied in the analysis of FLIM data, particularly in applications using FRET, e.g. [42], [66].

2.5 Summary

In this chapter, a brief overview of the fundamental principles of fluorescence was presented, including means of quantification of a fluorescence signal. Given its relevance to our investigations, discussion was particularly focussed on fluorescence lifetime. An overview of the most widely used fluorescence lifetime measurement techniques was presented, along with example applications in the context of biomedical research. In the following chapter, the underlying principles of fluorescence in biological tissue are presented, including a discussion of the most common endogenous fluorophores, which will serve as basis for the work presented in Chapter 5 and 6, concerning the application of fluorescence lifetime measurements to medical diagnosis in osteoarthritis and heart disease, respectively.

3 Tissue autofluorescence

In Chapter 2 we have reviewed the basic concepts of fluorescence including means of quantification, with particular emphasis on fluorescence lifetime. This chapter introduces the fundamentals of autofluorescence in biological tissue, including a brief overview of the most common endogenous fluorophores, namely Nicotinamide Adenine Dinucleotide (Phosphate) (NAD(P)H), Flavin Adenine Dinucleotide (FAD) and collagen. A characterisation of the steady-state and time-resolved fluorescence signal of these fluorophores is presented, which corresponds to the first step towards the application of autofluorescence measurements to the study of disease, more specifically osteoarthritis and heart disease, presented in Chapters 5 and 6, respectively.

Part of the work presented in this chapter resulted in the publication of 1 journal article (Kelly et al, *J. Innov. Opt. Health Sci.*, 2014).

Outline

- Introduction to autofluorescence.
- Overview of the most common endogenous fluorophores.
- Steady-state and time-resolved autofluorescence measurements of collagen type I, NADH nad FAD.
- Conclusions and summary.

3.1 Introduction

As discussed in Chapter 2, there are several ways to quantify a fluorescence signal and these have been widely investigated in biomedical research to provide means of contrast in biological samples. Contrast can be achieved either by employing exogenous markers that will tag specific molecules in a specimen or by exciting the intrinsic fluorescence that emanates naturally from within the specimen. This endogenous fluorescence, typically termed “autofluorescence”, originates in molecules that exist and can be intimately involved in important biological mechanisms and therefore can potentially provide a label-free read out of these mechanisms, including structural, functional and biochemical properties. For clinical applications, endogenous fluorescence has the additional advantage of being less invasive than exogenous labels, which can be harmful to the patient, thus making their application undesirable, particularly for *in vivo* studies [67]. Accordingly, autofluorescence has been increasingly investigated in biomedical applications to serve as a diagnostic tool, by providing label-free contrast between healthy and diseased tissues, as in references [3], [12]–[14], [17], [19], [38], [41], [68]–[81].

Autofluorescence can arise from multiple sources within a specimen, either from within cells (e.g. NAD(P)H, FAD or porphyrins) or from the extracellular matrix space (e.g. collagen and elastin). Accordingly, the autofluorescence emission spectrum of biological tissue is typically complex, often reflecting the presence of multiple fluorophores. The following section provides a brief overview of the most common endogenous fluorophores in biological specimens, with particular emphasis on those most relevant for our investigations of heart disease and osteoarthritis.

3.2 Endogenous fluorophores in biological tissue

3.2.1 Amino acid fluorescence

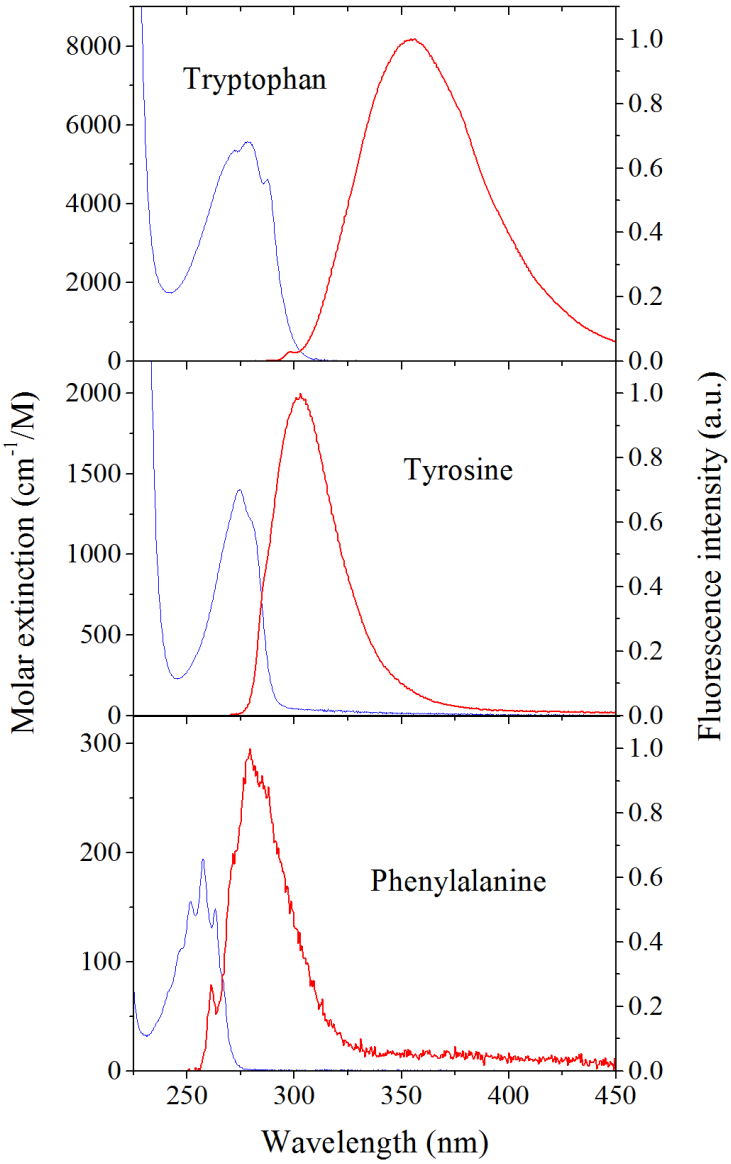

Figure 3.1 Optical absorption reported as molar extinction (in blue) and fluorescence emission spectra (in red) of Tryptophan, Tyrosine and Phenylalanine in water, retrieved from reference [82]. The fluorescence excitation spectra of these amino acids is identical to their absorption spectra [83]. The fluorescence emission spectra were acquired using excitation light at 270 nm, 260 nm and 240 nm, respectively.

There are three aromatic amino acid residues that can contribute to the intrinsic autofluorescence of proteins: tryptophan, tyrosine and phenylalanine [83]. Their absorption and fluorescence emission spectra are illustrated in Figure 3.1. Of the three, phenylalanine has the lowest quantum yield (~3% [1], [83]) and absorbs and emits at the shortest wavelengths. Thus, its contribution for protein fluorescence is typically negligible in the presence of tyrosine and tryptophan in the range of wavelengths typically used for excitation (between 280 and 300 nm) [1]. In this range of excitation wavelengths, protein fluorescence is typically dominated by tryptophan, due to its largest extinction coefficient and emission at longer wavelengths. The fluorescence properties of tryptophan and tyrosine are quite sensitive to the environment, with particular emphasis to their anisotropy and lifetime [1]. Hence, these properties are typically used to study protein structure and dynamics, e.g. NADH conformation upon binding to malate dehydrogenase (MDH) [84] and lactate dehydrogenase (LDH) [85]. The range of wavelengths necessary to excite these amino acids can limit their practical application in biomedical research, particularly for *in vivo* studies, due to the potential for light at this wavelength to produce malignancies in the tissue [86].

3.2.2 Cellular autofluorescence

Cellular autofluorescence typically exhibits a complex pattern with multiple fluorophores contributing to the signal, which originates predominantly from mitochondria and lysosomes [87]. In particular, the major contributors to the autofluorescence signal in mitochondria are NAD(P)H and FAD, two enzyme cofactors that are intimately involved in metabolic processes and therefore are of key interest for our investigations of the heart (see Chapter 6). Other endogenous fluorophores, such as keratin or porphyrins, can contribute to cellular autofluorescence and play relevant roles in the diagnosis of disease, e.g. [2], [88], [89]. For our studies, however, only NAD(P)H and FAD are of relevance, and thus they are discussed in further detail below.

3.2.2.1 NAD(P)H

Nicotinamide adenine dinucleotide (NAD^+/NADH) and nicotinamide adenine dinucleotide phosphate ($NADP^+$/NADPH) play a major role as intermediaries in cellular metabolism. The chemical structure of NAD^+/NADH and $NADP^+$/NADPH differs by the presence of a phosphate group (PO_4^{3-}) in the latter, which replaces a hydroxyl group (OH^-), as highlighted in red in Figure 3.2. They also have distinct roles in the cell: NAD^+/NADH drive the production of ATP in glycolysis and oxidative phosphorylation (as further discussed in Chapter 6) while $NADP^+$/NADPH play an active role in the defence against harmful reactive oxygen species [90].

The reduced and oxidised forms of these molecules present distinct absorption spectra: at excitation wavelengths typically used in biomedical research (i.e. $\lambda_{exc} > 340$ nm), only the reduced form is fluorescent [1]. In the 1960's, Chance et al [68] pioneered the application of this property to report the redox state of the cell and much work has been done on this field since then, e.g. [91]–[95]. NADH

and NADPH absorb strongly in the UV range of the spectrum - with maximum absorption at ~340 nm - to fluoresce in the visible range with maximum emission at ~450 nm. The fluorescence is attributed to the nicotinamide ring (see Figure 3.2) and presents identical properties in both NADH and NADPH, namely with respect to spectra, lifetime and anisotropy [9]. Thus these molecules are considered to be "spectroscopically" undistinguishable in their unbound form. For that reason, it is common to use the term "NAD(P)H" to refer to both molecules, if the origin of the fluorescence is unknown. However, a recent study by Blacker et al [11] has demonstrated that NADH and NAPDH yield different fluorescence lifetimes when bound to enzymes and thus these molecules can be distinguished accordingly.

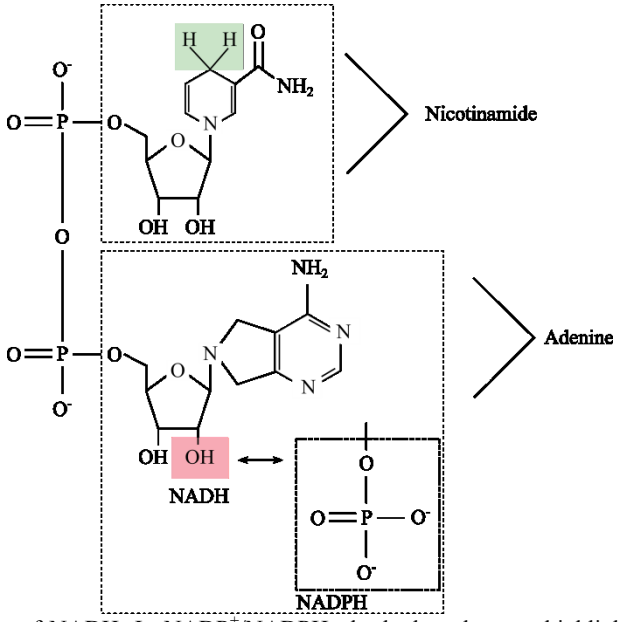

Figure 3.2 Chemical structure of NADH. In $NADP^+$/NADPH, the hydroxyl group highlighted in red is replaced by the phosphate group illustrated on the bottom right. In NAD^+/$NADP^+$, the two protons highlighted in green are lost. Adapted from [1].

Freely diffusing NAD(P)H (i.e. not bound to enzymes) in aqueous buffer can exist in two conformations at room temperature, extended and folded, which give rise to individual fluorescence lifetimes of ~300 ps and ~700 ps, respectively, yielding an average fluorescence lifetime of 400 to 500 ps [8]. NAD(P)H fluorescence is sensitive to protein binding and it is well-known that both the quantum yield and the fluorescence lifetime of NAD(P)H increase upon binding to enzymes (e.g. MDH and LDH) [1], [96]. NAD(P)H can exist in tissue in both free and enzyme-bound forms. Accordingly, its fluorescence lifetime in tissue is typically approximated by a double exponential decay model: a short lifetime component associated with free NAD(P)H and a long lifetime component associated with enzyme-bound NAD(P)H. Thus a change in average lifetime of NAD(P)H can report on binding fraction and binding state and so may be used to monitor cellular metabolism [11].

The fluorescence properties of NAD(P)H have been extensively investigated in the last 50 years and several studies have been published accordingly, e.g. [8], [96]–[99]. However, most of these studies are realised under different experimental conditions, with respect to their physiology (e.g. pH, temperature or buffer) or optical setup (e.g. excitation wavelengths), and therefore are difficult to compare, often showing inconsistent results, particularly with respect to the reported fluorescence lifetime values, e.g. [8] and [100] (0.44 ns and 0.52 ns, respectively). In the context of our investigations, given the importance of NADH to cellular metabolism, it is relevant to understand its autofluorescence signal and how this varies with protein binding state or under different physiological conditions, at the excitation and emission wavelengths used in our experiments in Chapter 6. Hence, in section 3.3 we present a characterisation of the NADH autofluorescence signature under a different set of environmental parameters (pH and temperature) and binding partners.

3.2.2.2 FAD

Similarly to the NAD^+/NADH redox couple, FAD and its reduced form $FADH_2$ are intimately involved in the production of ATP in the oxidative pathway of cellular metabolism (see Chapter 6). Conveniently, only the oxidised form is fluorescent, i.e. FAD. Hence, ratiometric measurements of NADH autofluorescence against that of FAD (the "redox ratio") can effectively provide a label-free readout of the oxidative state of the cells and infer about their metabolism, as for example in references [77], [91], [101], [102].

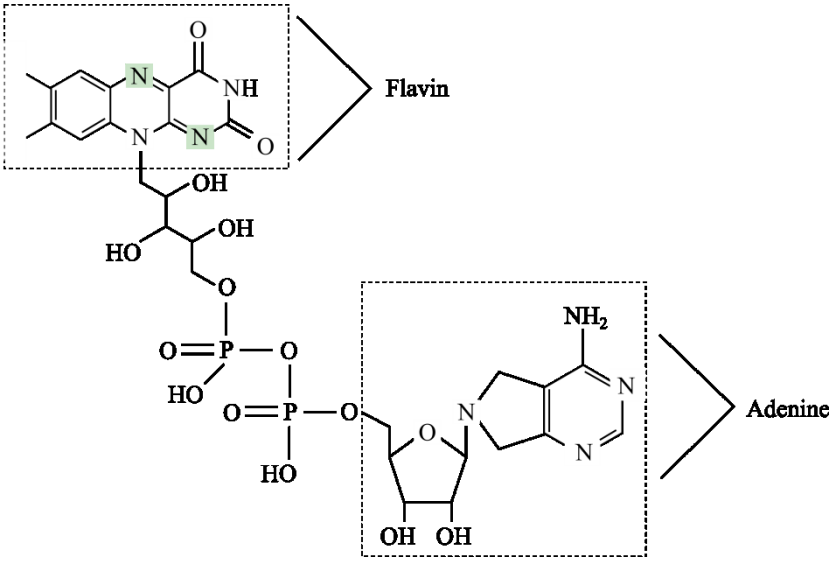

Figure 3.3 Chemical structure of FAD. The molecule is reduced to $FADH_2$ by coupling of two protons to the nitrogen atoms highlighted in green. Adapted from [1].

FAD is strongly fluorescent in the visible range of the spectrum, with absorption and emission maxima at ~450 nm and ~525 nm, respectively. The fluorescence lifetime of free FAD in aqueous buffer presents a complex multiexponential decay profile (up to four components have been reported [103]) that yield an average fluorescence lifetime of ~2.7 ns, at room temperature [103], [104]. When

the molecule is folded, the fluorescence arising from the flavin group (see Figure 3.3) is efficiently quenched by the adenine ring, giving rise to very short lifetimes (< 100 ps) [104], [105]. In contrast, two long lifetimes (of approximately 2 and 4 ns) have been attributed to the extended conformation of free FAD [105].

In tissue, FAD can be found in its free configuration or bound to proteins, such as lipoamide dehydrogenase (LipDH) [106] or d-amino acid oxidase [107], [108]. However, in contrast to NADH, the fluorescence lifetime of free FAD decreases upon binding [107], [108]. Accordingly, when the autofluorescence lifetime of FAD in tissue is described by a multiexponential decay model, the shorter lifetime components (< 1 ns) are associated with the protein-bound state, while longer lifetimes are associated with free FAD.

As with NADH, we have also measured the autofluorescence properties of free FAD under different physiological conditions. These results are presented in section 3.3.

3.2.3 Extracellular matrix autofluorescence

In biological tissue, the autofluorescence signal can also arise from extracellular space components, most notably from collagen and elastin fibres.

3.2.3.1 Collagens

Collagen is a structural protein that exists in tissues throughout the body. So far, 28 different types of collagen have been identified in vertebrates [109], although 80 to 90% of the collagen content is attributed to fibrillar collagen only, namely collagen types I, II, III and V [110], [111]. In particular, collagen types I and II are of importance for our investigations due to their role in heart disease and osteoarthritis, respectively, and thus discussion will be focussed on these molecules. Detailed information of other types of collagen is given in references [110]–[112]. Collagen type I is the predominant collagen in vertebrates and can be found in several tissues throughout the body, e.g. skin, bone, tendons or blood vessel walls [112], being also a major component of scar tissue [113], [114]. Collagen type II exists essentially in cartilaginous tissue and is the major constituent of articular cartilage (see Chapter 5).

Collagen molecules consist of three polypeptide chains arranged in a helical conformation (α-chains), of which composition and crosslinks can change with species and anatomic origin and suffer alterations during disease progression, healing or aging [115]. The fluorescence of collagens is attributed to aromatic amino acids (i.e. tryptophan, tyrosine and phenylalanine) that exist in the α-chains and to fluorescent crosslinks between collagen molecules [116]. At excitation wavelengths in the near-UV and visible ranges of the spectrum, the contribution of the aromatic amino acids to the fluorescence signal is negligible (see section 3.2.1), and thus the great majority of the fluorescence

arises from the crosslinks, such as pyridinoline (excitation/emission maxima: 295 nm/395 nm), pentosidine (335 nm/385 nm), vesperlysine (370 nm/470 nm) or crossline (380 nm/460 nm) [70], [117]–[120]. Given that collagen crosslinks and their relative proportion can vary between different types of collagen, tissue type or species, the fluorescence signal can vary accordingly. A previous study in our group [121] has demonstrated the heterogeneity of collagen fluorescence, by measurement of the fluorescence excitation and emission spectra of different types of collagen from different sources. According to this study, collagen fluorescence can be excited with wavelengths from ~280 nm up to 500 nm. This heterogeneity of the fluorescence signal appears to be corroborated by previous research of Marcu et al [122], in which they demonstrated the fluorescence lifetime variability of different types of collagen from various species and sources. In Table 3.1 we summarise the fluorescence lifetimes of collagen types I and II reported in previous studies. Given the great variability in the reported values and the importance of collagen for our studies, we measured the autofluorescence spectrum and lifetime of collagen type I from rat tail at the excitation and emission wavelengths used in our experiments. These results are presented in section 3.3.

Table 3.1 Reported fluorescence lifetimes for collagen types I and II. In all studies fluorescence was excited at 337 nm.

Collagen type	Source	Detection (nm)	Average lifetime (ns)	Reference
I	Bovine achiles tendon	390	5.20	[122]
I	Calf skin	390	1.45	[122]
I	Rat tail	390	1.05	[122]
I	Bovine tendon	380	5.44	[123]
I	Calf skin	420	2.55	[123]
II	Bovine nasal septum	390	6.10	[122]
II	Bovine tracheal cartilage	390	6.20	[122]
Unknown	Unknown	380	5.42	[124]

3.2.3.2 Elastin

Elastin is also a fibrillar protein that has a relevant structural function in the elasticity of tissues, including arteries, lungs and skin [125]. As with collagen, the fluorescence from elastin (in the near-UV and visible spectrum) is primarily attributed to crosslinks between elastin molecules and thus its fluorescence signal is typically complex and can vary with excitation and emission wavelength [118], [126]. A major contributor to the fluorescence signal is believed to be a tricarboxylic triamino pyridinium derivative, which exhibits fluorescence excitation and emission maxima at 325 nm and 400 nm, respectively [126]. Elastin molecules also contain tyrosine and phenylalanine [125], which can contribute to the fluorescence excitation and emission spectra at shorter wavelengths (< 300 nm). With respect to the fluorescence lifetime, elastin powder exhibits a complex decay profile with average lifetime ranging from ~1.5 to 2.5 ns (at λ_{exc} = 337 nm), which appears to dependent of the

emission wavelength [43], [124]. In contrast, a previous study by Konig et al [127] reported a longer fluorescence lifetime of ~5 ns for elastin excited at 390 nm.

3.3 Fluorescence lifetime measurements of collagen type I, NAD(P)H and FAD

Despite the numerous studies characterising NAD(P)H, FAD and collagen autofluorescence signal, the reported values are in some cases inconsistent and, given the heterogeneity and complexity of the signal, they can be difficult to compare, since most studies were realised under different experimental (e.g. pH, temperature or buffer) conditions and with different excitation/emission wavelengths. Given the importance of these fluorophores to our research, we characterised their autofluorescence signature under physiological conditions and using an optical setup that is similar to that used in our experiments of osteoarthritis and heart disease, which will be presented in Chapter 4.

3.3.1 Experimental methods

3.3.1.1 Materials

Solutions of β-NADH (N1161, Sigma-Aldrich, Germany) and FAD (F6625, Sigma-Aldrich, Germany) were prepared by diluting the respective powder in phosphate buffered saline (PBS) solution. Fresh solutions were prepared for each day of measurements. Rat tail collagen type I powder (C8897, Sigma-Aldrich, Germany) was used directly without further preparation.

3.3.1.2 Measurements of absorption and fluorescence emission spectra

Absorbance measurements were realised on a commercially available spectrophotometer (UV-3101PC, Shimadzu, Japan). Measurements of the autofluorescence emission spectra were carried out on a spectrofluorophotometer (RF-5301PC, Shimadzu, Japan) using 375 nm excitation light. Emission spectra were recorded from 400 to 700 nm. A 390 nm long-pass filter was placed at the entrance slit of the monochromator to prevent contamination of the fluorescence signal by the excitation light.

3.3.1.3 Measurements of fluorescence lifetime

Autofluorescence lifetime measurements were carried out on a previously described [128] home-built cuvette-based time-resolved spectrofluorometer. Its optical setup is illustrated in Figure 3.4. The system comprises three excitation light sources: a supercontinuum laser (SPC-400, Fianium, UK) providing picosecond pulses at 20 MHz, between 400 and 2000 nm (an infra-red filter is located immediately after the beam output to narrow the bandwidth to the visible range, i.e. 400 to 800 nm); a gain-switched laser diode (LDH-P-C-375B, PicoQuant GmbH, Germany) providing ~70 ps pulses at 375 nm with a maximum output power of 3.3 mW and adjustable repetition rate from 5 to 80 MHz, which was fixed to 40 MHz for the experiments described below; and a diode-pumped frequency-tripled Neodymium Vanadate laser (Vanguard 350-HM355, Spectra-Physics, USA) generating ~12 ps optical pulses at 80 MHz and 355 nm. We note the latter was not used in the experiments described below. For collagen and NADH measurements the 375 nm laser diode was used, operating at 20 and

40 MHz, respectively. In contrast, FAD measurements were realised using the supercontinuum source at 440 ± 5 nm. The system comprises two optical paths in the excitation arm. In the first path, light from the supercontinuum source is directed onto a prism and the resulting spectrum is focussed onto a mirror-slit arrangement, for wavelength and bandwidth selection [129]. The second path is used to allow an external beam (from the UV light sources) to be coupled into the system. The excitation light from one of the sources is then directed to a computer controlled shutter (SH05 shutter & SC10 controller, Thorlabs, Germany) and a rotatable filter wheel (Newport, USA) containing seven neutral density (ND) filters with optical transmissions of 100, 93, 79, 63, 50, 25, 10, and 1% to allow adjustment of the beam intensity. Finally, the excitation is passed through a Glan-Taylor polarising cube and directed onto a quartz cuvette containing the sample. Before reaching the cuvette, part of the excitation light (~4%) is diverted onto a spectrometer for verification of the excitation light wavelength. Detection of the fluorescence is realised at right angles relative to the excitation beam direction and one of two detection pathways can be used. In the first path - used in the experiments below - fluorescence or scattered light from the sample are imaged through a rotatable linear sheet polariser onto the input slit of a motorised monochromator (CM110, CVI Inc., USA) and detected by a cooled photon counting PMT (PMC-100-1, Becker and Hickl GmbH, Germany), which is connected to a TCSPC acquisition card (SPC-730, Becker and Hickl GmbH, Germany) that processes the time-resolved data. The polariser allows measurements to be realised horizontally, vertically or at the magic angle relative to the excitation light polarisation. In the experiments described below, all cuvette measurements were realised at the magic angle, to eliminate contributions of fluorescence anisotropy to the decay. The second detection arm was not used in these experiments. It consists of a 16-channel PMT (PML-SPEC, Becker and Hickl GmbH, Germany) that separates the fluorescence light according to its wavelength. This can then be connected to the TCSPC electronics to provide spectrally- and time-resolved information. We note that the first detection arm can also provide spectrally-resolved data by adjusting the monochromator centre wavelength. Collagen and NADH time-resolved measurements were realised with monochromator centre wavelength at 460 nm. For FAD, the monochromator centre wavelength was adjusted to 525 nm.

For tissue samples, the system also comprises suitable optics that divert the excitation beam onto a custom-made fibre-optic probe (FiberTech Optica, Canada) consisting of nineteen 200 μm core fibres: three fibres are used for excitation and sixteen fibres are used for collection of the fluorescence from the sample. At the sample end, the fibres have a hexagonal arrangement with the excitation fibres at the centre surrounded by the collection fibres. Fluorescence from the sample is collected by the sixteen fibres and delivered to the detection arm where the collection fibres are arranged in a line to facilitate light focussing onto the input slit of either the monochromator or the 16-channel PMT for detection. It should be noted that cuvette and fibre-optic measurements cannot be realised at the same time.

The whole system can be controlled using custom-written software in LabVIEW (LabVIEW, National Instruments, USA).

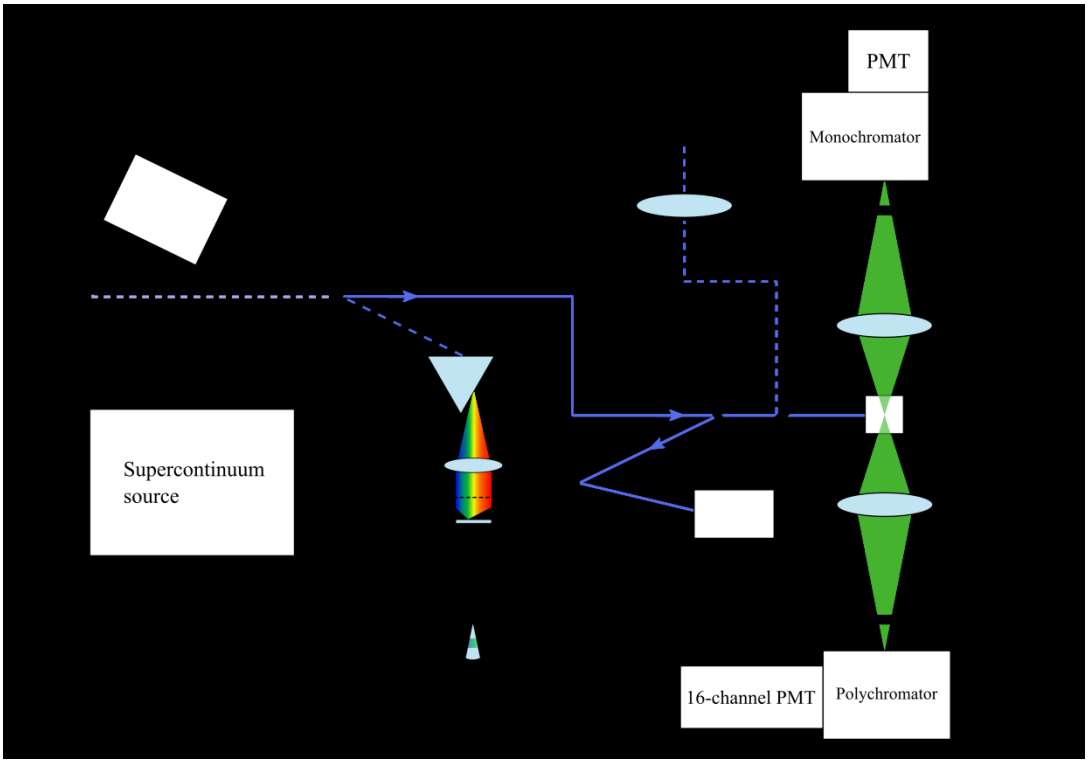

Figure 3.4 Optical setup of the cuvette based system, comprising three laser sources (355 nm, 375 nm and 400 – 700 nm) and two detection pathways. For tissue measurements, the beam can be diverted onto a fibre optic probe. Adapted from [128].

3.3.1.4 Fluorescence lifetime vs. temperature

The cuvette-based system presented above also comprises external temperature controlling facilities that allow one to change the temperature of the sample in the cuvette. Temperature calibration of the setup was realised using a quartz cuvette (identical to those used in our measurements) filled with water, of which temperature was monitored using a thermistor (Fluke 51 K/J Thermometer, Fluke, USA). Time-resolved autofluorescence measurements of NADH (50 µM, in PBS) and FAD (50 µM, in PBS) were realised between 25°C and 45°C in incrementing steps of 2°C. To prevent photobleaching artefacts in the measurements, for each temperature, the sample in the cuvette was replaced by an aliquot of the stock solution. The temperature of the new aliquot was allowed to stabilise for 15 minutes before realising the fluorescence acquisition.

3.3.1.5 Fluorescence lifetime vs. pH

With respect to time-resolved measurements of NADH, two protocols were followed. In "protocol 1", buffer solutions were prepared from pH tablets (BDH buffer solution, VWR) diluted in PBS, from which NADH solutions at different pH were prepared. These measurements were realised at 25°C. In "protocol 2", the pH of an NADH solution in PBS was adjusted between 4 and 10 using HCl (0.1M) and NaOH (0.1M) solutions. The pH of the solutions was monitored using a handheld pH-meter

(VWR, USA). These measurements were realised at 37°C. For FAD measurements, solutions were prepared according to "protocol 2".

3.3.1.6 NADH protein binding experiments

To verify the variation in the autofluorescence signal of NADH upon binding to enzymes, we have acquired porcine heart malate dehydrogenase (MDH) and lactate dehydrogenase (LDH) from Sigma-Aldrich. MDH and LDH are enzymes that bind to NADH during cellular metabolism in the mitochondria, as further discussed in Chapter 6. Stock solutions of NADH, MDH and LDH were prepared in PBS. MDH was used without further purification. LDH was prepared as described in [130]. Concentrations were calculated based on absorption measurements performed using a spectrophotometer (UV3101-PC, Shimadzu, Japan). The molar extinction coefficients used were as follows: 6.3×10^3 $M^{-1}.cm^{-1}$ (at 340 nm) for NADH [84]; 7.2×10^4 $M^{-1}.cm^{-1}$ (at 280 nm) for MDH [84]; 16.3×10^4 $M^{-1}.cm^{-1}$ (at 280 nm) for LDH [85]. Final solutions for time-resolved measurements were made up with NADH concentration held constant at 25 μM, whilst the concentrations of MDH and LDH were adjusted to obtain ratios of 0:1 to 4:1 relative to the concentration of NADH. All measurements were realised at 37°C and at the magic angle orientation, relative to the excitation light polarisation.

3.3.2 Results and discussion

3.3.2.1 Collagen type I

Figure 3.5 shows the fluorescence emission spectrum of collagen type I powder extracted from rat tail, using 375 nm excitation light at 20 MHz. The spectrum indicates an emission maximum at 437 nm, which, considering the excitation wavelength used in these measurements, is consistent with the presence of the crosslinks vesperlysine and/or crossline [1], [118], [131]. We note that in collagen, different excitation wavelengths can give rise to different fluorescence emission spectra derived from the various sources of fluorescence that exist in a collagen scaffold, as previously discussed. This may explain the difference between this spectral profile and those from other references, e.g. [70].

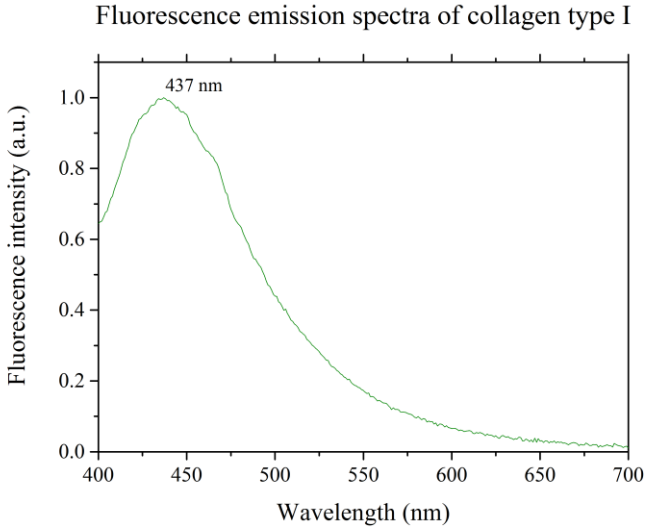

Figure 3.5 Fluorescence emission spectra of collagen type I powder excited at 375 nm showing an emission peak at 437 nm. Measurements were carried out between 400 and 700 nm, in 1 nm intervals.

With respect to the autofluorescence lifetime of collagen type I, we measured a complex decay profile, with at least three exponential components that can potentially reflect the contribution of different crosslinks to the decay.

Table 3.2 summarises the autofluorescence lifetime parameters measured for collagen type I (fitted with a triple exponential decay model) at three distinct emission wavelengths, which are of interest for our studies (see Chapter 4). The results show that the mean autofluorescence lifetime is similar at different detection wavelengths (~ 6 ns). The results also indicate the presence of short (~200 to 300 ps) and long (~8 to 9 ns) lifetime components in all decays. In particular, the presence of a long lifetime component in collagen as previously been reported by others [73], [124]. In general, our results are within the range of previously published values for collagen, as indicated in Table 3.1. We note, however, the shorter autofluorescence lifetime of collagen type I powder from rat tail measured by Marcu et al (see Table 3.1) relative to our results. This difference is likely to be due to the different excitation wavelength used in their measurements (337 nm) in comparison to that used in our experiments (375 nm). An alternative explanation consists in the extraction method that collagen fibrils may have been subjected to, which involves chemical treatment of the collagenous tissue that can potentially affect the biochemical properties of the specimen and, accordingly, its autofluorescence lifetime. Furthermore, the structural composition of collagen fibrils can change with disease or stage of maturation, which would also give rise to different autofluorescence lifetimes.

In summary, our results demonstrate that collagen type I powder yields a long autofluorescence lifetime of ~6 ns when excited at 375 nm. This is considerably longer than those measured for NADH

and FAD (see below) and therefore fluorescence lifetime may represent a convenient approach to distinguish these fluorophores in a complex autofluorescence signal.

Table 3.2 Fluorescence lifetime parameters of collagen type I powder from rat tail, excited at 375 nm and 20 MHz laser repetition rate.

	Detection centre wavelength (nm)		
	410 nm	**455 nm**	**525 nm**
β_1	0.11	0.15	0.12
τ_1 **(ns)**	0.28	0.37	0.20
β_2	0.29	0.38	0.37
τ_2 **(ns)**	3.29	3.70	3.58
β_3	0.60	0.47	0.51
τ_3 **(ns)**	8.63	9.27	8.91
τ_{mean} **(ns)**	6.16	5.82	5.87

3.3.2.2 NADH

3.3.2.2.1 Absorption and fluorescence emission spectra

The absorbance spectrum of free NADH in solution (see Figure 3.6, blue curve) presents a double peak profile with local maxima at 260 and 339 nm, which is in agreement with previous absorbance studies of NADH [132]. In contrast, its oxidised form (NAD^+) presents a single maximum at 260 nm and one can take advantage of this difference to monitor the oxidative state of the tissue, as firstly demonstrated by Chance et al [68]. The autofluorescence emission spectrum of NADH (see Figure 3.6, red curve) indicates a single peak at ~460 nm, which is also in agreement with previous observations e.g. [70], [96].

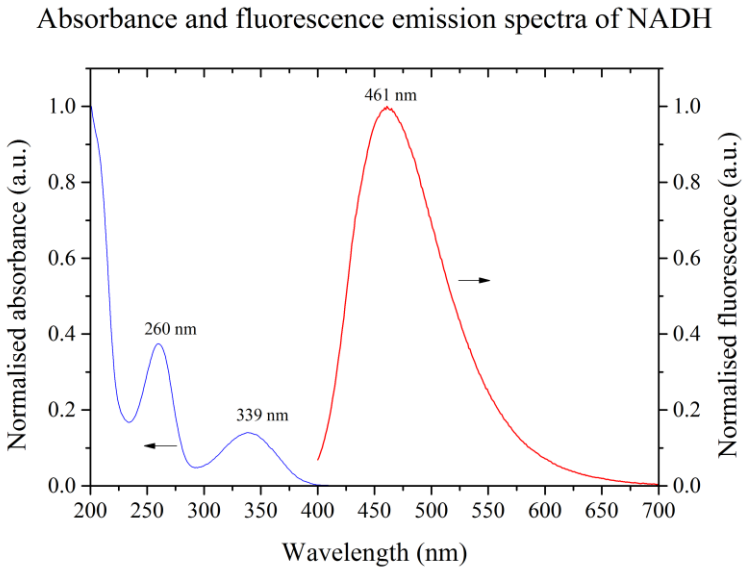

Figure 3.6 Absorbance (blue) and fluorescence (red) emission spectra of free NADH in solution, measured with 1 nm spectral resolution. Fluorescence emission spectrum was measured using 375 nm excitation. Measurements were realised at room temperature and pH 7.4. Black arrows indicate curves y-axis.

3.3.2.2.2 Changes in NADH autofluorescence with temperature

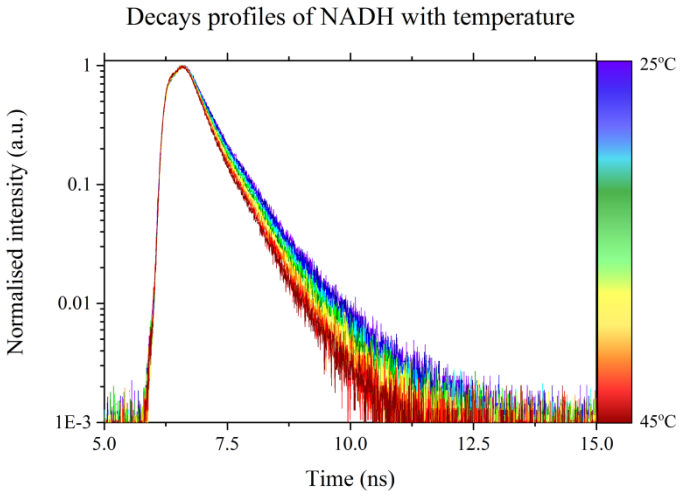

Figure 3.7 NADH fluorescence decay profiles with temperature.

The temperature dependence of NADH autofluorescence was investigated using excitation light at 375 nm and 40 MHz repetition rate. Detection of the fluorescence signal was realised at 460 nm and at the magic angle to eliminate contributions from fluorescence anisotropy. The autofluorescence lifetime data - fitted to a double exponential decay model - presented in Figure 3.7 and Figure 3.8 indicate that the mean autofluorescence lifetime of NADH decreases linearly with temperature, at an average rate of 4 ps/^{o}C, which is in agreement with previous observations, albeit those experiments were realised at a lower temperature [97]. This decrease in the mean autofluorescence lifetime can be traced back to decreases in the short and long lifetime components (see Figure 3.8A) and an increase in the contribution of the short component to the overall fluorescence decay (see Figure 3.8B). In particular, the long lifetime decreases approximately 1.5 times faster than the short lifetime component. The values measured at 25^{o}C are in good agreement with previously reported values, e.g [8], [96], [97], [130]. At 37^{o}C we measured a mean autofluorescence lifetime of 359 ps, a short lifetime of 214 ps and long lifetime of 524 ps.

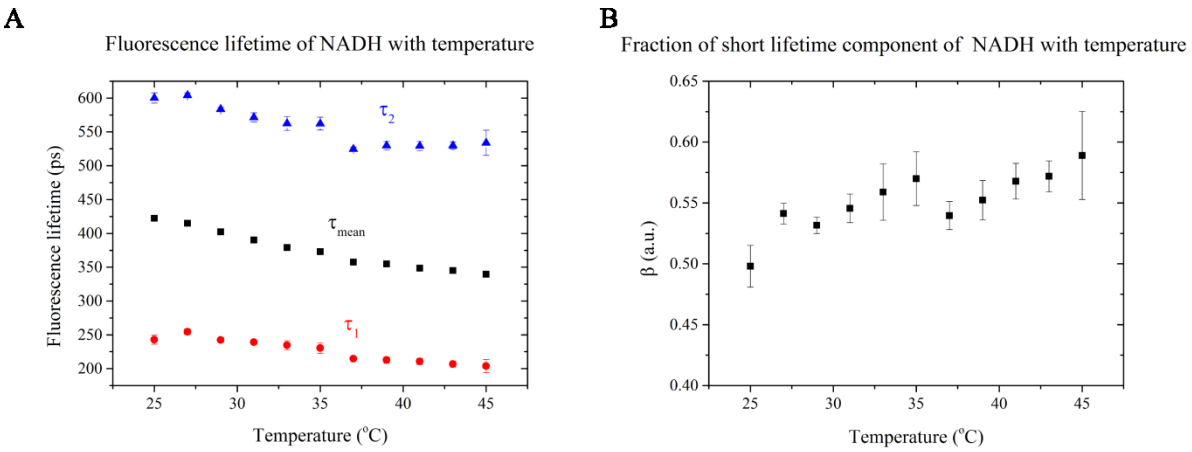

Figure 3.8 Variation of NADH (A) mean fluorescence lifetime, short and long lifetime components with temperature and (B) contribution of the short lifetime component to the fluorescence decay with temperature.

Along with the autofluorescence lifetime, we have also measured a decrease in the NADH autofluorescence intensity of approximately 25% over the range of temperatures studied (see Figure 3.9). In particular, the quantum yield of NADH at 37°C is about 80% of that at 25°C. These results are in agreement with previous studies [97], [100] and may be the result of conformational changes of NADH.

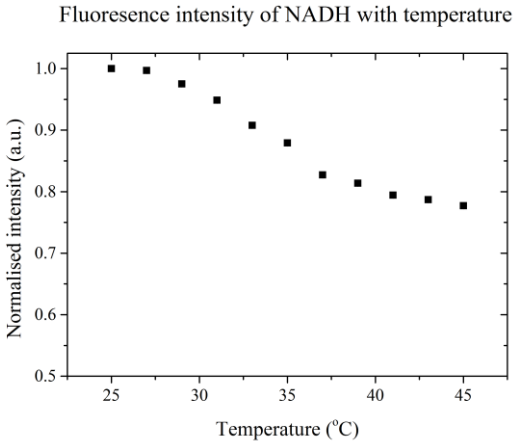

Figure 3.9 Variation of NADH autofluorescence signal as a function of temperature.

3.3.2.2.3 Changes in NADH autofluorescence with pH

During aerobic respiration, the movement of electrons in the inner mitochondrial membrane promotes the pumping of protons from the matrix into the intermembrane space. This creates a pH gradient across the inner mitochondrial membrane, with greater pH in the matrix (~8) relative to the cytosol (~7) [133]. The electrochemical gradient between mitochondrial matrix and intermembrane space promote the flow of protons back into the matrix with concomitant production of ATP (see Chapter 6). Disruption of cellular metabolism will therefore affect the flow of protons across the membrane and the pH of mitochondria will change accordingly [134]. It is therefore relevant to characterise the NADH autofluorescence as a function of pH and understand if the degree of potential changes is relevant in a physiological environment.

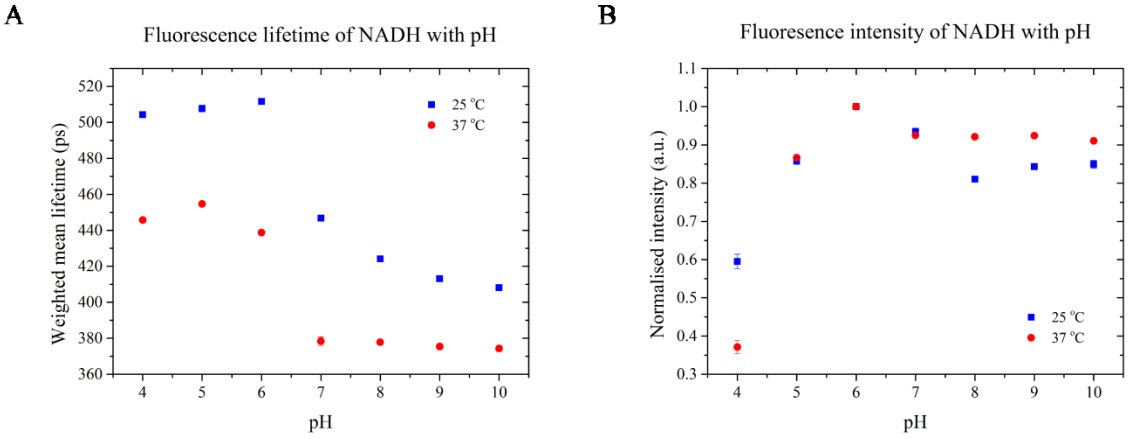

Figure 3.10 Variation of NADH (A) mean autofluorescence lifetime and (B) intensity with pH, at 25 and 37°C. Solutions were prepared as described in section 3.3.1.5, i.e. solutions measured at 25°C were prepared with BDH buffer solutions (protocol 1) and the pH of the solutions measured at 37°C were adjusted using NaOH and HCl (protocol 2).

Figure 3.10 shows the variation of NADH autofluorescence lifetime (Figure 3.10A) and intensity (Figure 3.10B) with pH, at 25 and 37°C, following adjustment of the pH according to protocols 1 and 2, respectively (see section 3.3.1.5). Despite the fact we have followed different protocols to adjust the pH of the solutions, the results show similar variations: at both 25 and 37°C, the autofluorescence lifetime is longer at lower pH, showing an abrupt decrease of ~70 ps between pH 6 and 7. At pH 7, there is also a difference of ~70 ps between measurements at 25 and 37°C, which is in good agreement with the difference observed in the results presented in the previous section (~80 ps, see Figure 3.8A), at pH 7.4, given the variation in pH between the two datasets (pH 7 and pH 7.4). A previous study by Ogikubo et al [135] has demonstrated that the mean autofluorescence lifetime of NADH decreases with increasing pH (~40 ps from pH 5 to 9). Our measurements indicate a decrease of ~90 ps between pH 5 and 9 at both 25 and 37°C, although in the latter this variation occurs predominantly between pH 5 and 7 (see Figure 3.10A, red squares). Similar changes to those reported in Figure 3.10 can be observed in short and long lifetimes of NADH (see Figure 3.11A, measurements at 37°C only, following protocol 2), for which we measured consistently longer lifetime values for pH lower than 7. The contribution of short lifetime to the decay (see Figure 3.11B) appears to decrease consistently with increasing pH, suggesting a conformational change in NADH molecules (i.e. less extended, more folded). Similar variations were observed for solutions prepared according to protocol 1 (data not shown).

Finally, with respect to the autofluorescence intensity (see Figure 3.10B), measurements at both temperatures show similar variations, with maximum fluorescence intensity at pH 6. At physiological levels (from pH 7 to 8) we observe little variation of the autofluorescence signal, particularly at 37°C, which is also apparent in lifetime data (see Figure 3.10A), suggesting that the conformation of NADH is more stable at this temperature.

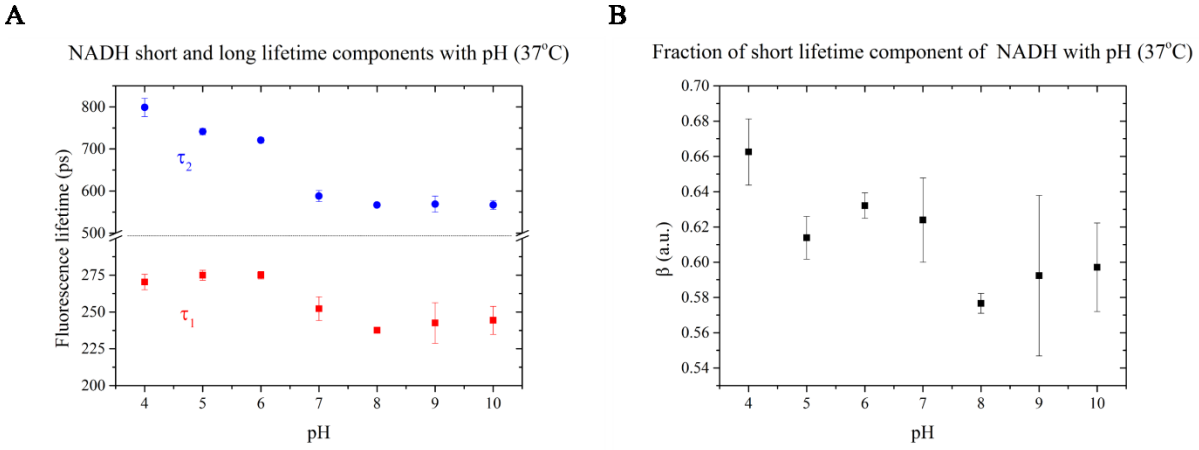

Figure 3.11 Variation of NADH (A) short and long lifetimes and (B) fraction of the short lifetime component with pH, measured at 37°C. pH of the solutions was adjusted according to protocol 2.

3.3.2.2.4 Protein binding

Protein binding studies of NADH are relevant for understanding the complex autofluorescence signal arising from metabolically active specimens, such as cardiac tissue (see Chapter 6). In the context of cellular metabolism, NADH can bind to different enzymes, such as MDH or LDH, which take part in the aerobic and anaerobic metabolic pathways, respectively.

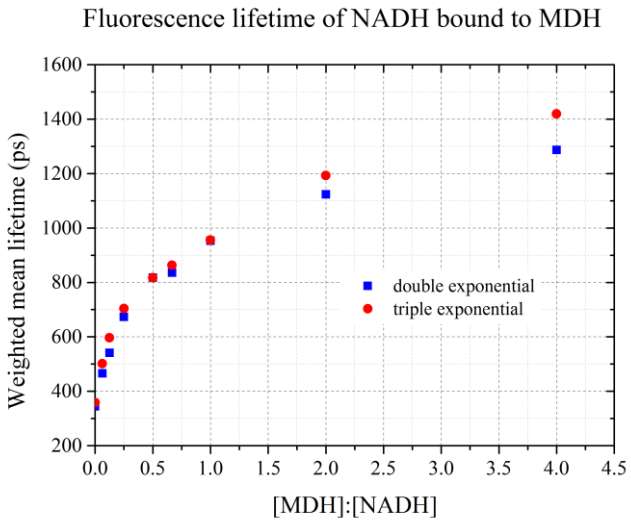

Figure 3.12 Weighted mean fluorescence lifetime of NADH bound to MDH using a double and a triple exponential model to fit data. In the latter, the long component τ_3 was fixed at 4500 ps, which was the long fluorescence lifetime component measured for the protein alone.

Figure 3.12 shows the mean autofluorescence lifetime of NADH in solution with increasing MDH concentration, fitted with double and triple exponential decay models. We note that based on previous observations by others [130], we would expect the mean autofluorescence lifetime to stabilise with increasing MDH concentration, provided that only NADH is fluorescent. Interestingly, we found that exciting MDH with 375 nm light produces a complex fluorescence decay profile (~1/10 of NADH total fluorescence signal for approximately the same concentration) with two lifetime components (~500 ps [80%] and ~4500 ps [20%]) yielding an average lifetime of ~ 3 ns, which is consistent with the observations of Torikata et al [84], albeit they used different excitation and emission wavelengths (295 nm and 340 nm, respectively). This finding contradicts the results of Yu et al [130], in which they have observed no background fluorescence from MDH, using two-photon excitation (λ_{exc} = 750 nm).

In order to accommodate for the MDH fluorescence, we fit the NADH-MDH binding data to a triple exponential decay model, fixing the long lifetime component to the value of the long lifetime component measured for MDH fluorescence, i.e. τ_3 = 4.5 ns, while leaving all other parameters free. We note that in our measurements, we now have two fluorophores contributing to the decay, i.e. NADH and MDH, with at least two components each. Fitting four exponentials to the data did not produce meaningful results (data not shown) likely due to the number of photons detected in our measurements being insufficient to accurately describe such a complex decay profile. Hence we

decided to add only the long MDH lifetime component to the fitting model, noting that the proximity of the shorter MDH lifetime to the expected values of free NADH makes it difficult to separate them. The resulting mean autofluorescence lifetime is shown in Figure 3.12 (red circles). More interestingly, the values of τ_1 and τ_2 and their relative contributions for the decay are illustrated in Figure 3.13. In particular, τ_2 reaches a saturation plateau when the concentration of NADH is approximately 1.5 times that of MDH.

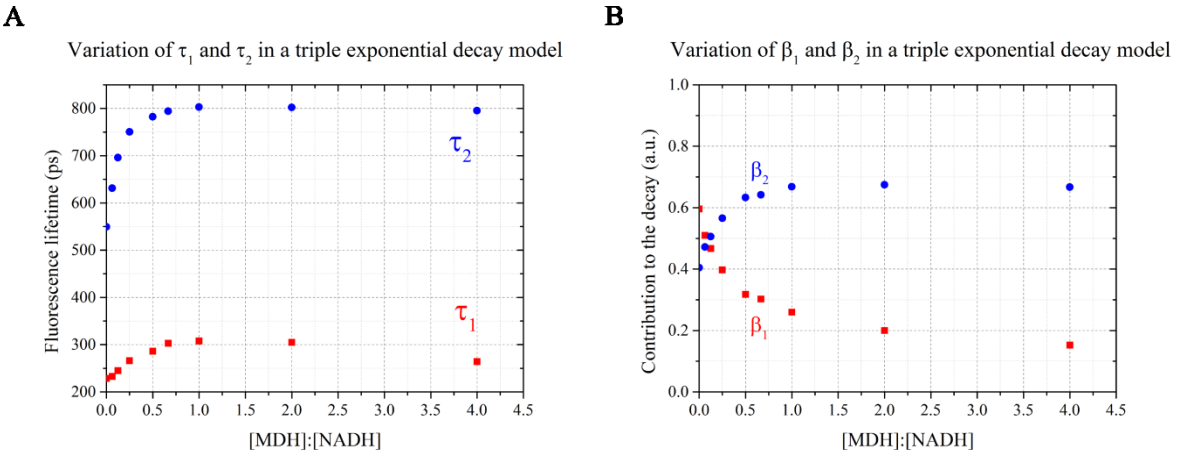

Figure 3.13 (A) Variation of NADH τ_1 and τ_2 in a triple exponential decay model, with τ_3 fixed at 4500 ps. (B) Contribution of τ_1 and τ_2 to the fluorescence decay.

With respect to the background fluorescence produced by MDH, we observe an increased contribution of the long component τ_3 to the overall fluorescence, as demonstrated in Figure 3.14, which we provisionally attribute to MDH as a function of its concentration. This result supports the explanation that this background fluorescence decay is "masking" a stabilisation of the mean autofluorescence lifetime that was previously reported by others, but was not observed in our measurements.

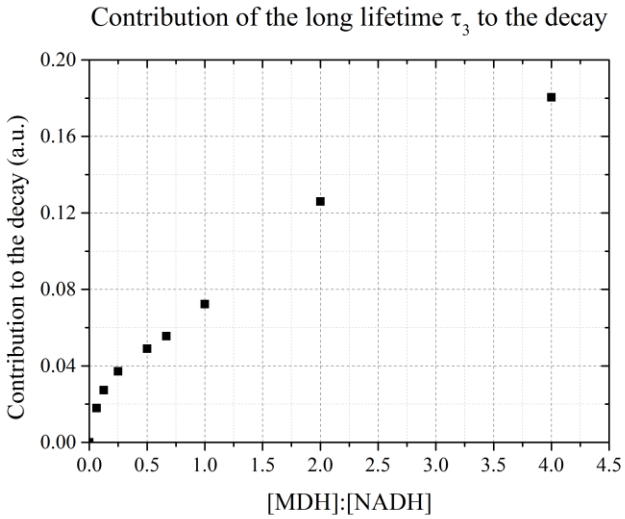

Figure 3.14 Contribution of the long lifetime component to the decay, showing an increase with protein concentration.

It is challenging to identify the reasons why our results are so distinct from those presented by Yu et al [130]. There are many studies in the literature reporting MDH fluorescence, e.g. [84], [99], albeit

using excitation at much shorter excitation wavelengths (typically ~280 nm) than that used in our measurements (375 nm). At 280 nm, fluorescence arises from aromatic amino acids present in MDH, predominantly tryptophan. Indeed, the absorbance spectrum of MDH (see Figure 3.15) resembles that of tryptophan (see Figure 3.1), although MDH appears to fluoresce at much longer wavelengths. Using excitation light at 375 nm we did not observe fluorescence from tryptophan, tyrosine or phenylalanine, suggesting that their contribution to MDH autofluorescence excited at that wavelength is small. Fluorescence studies of NADH bound to MDH (or other enzymes) using 375 nm excitation light or similar are scarce, which makes it even more challenging to interpret our results. An alternative explanation to intrinsic protein fluorescence would be a possible contamination of the protein itself, despite it being acquired with nominal purity of 99.9%. However, in a previous study [136] the protein was used as acquired, i.e. without further purification, and no background fluorescence was reported using 340 nm excitation light. To summarise, we observe background fluorescence in our NADH-MDH measurements and its origin remains unclear. Further measurements would be necessary to understand our results and eventually identify the source of the background fluorescence decay. For example, time-resolved fluorescence anisotropy could provide leads regarding whether this is intrinsic MDH fluorescence or another contaminant, which could potentially result from the protein extraction process. An alternative approach could utilise mass spectrometry to determine the molecular composition of the solution. In any case, our simplistic triple exponential fitting (see Figure 3.13) give us an idea of how the fluorescence lifetime of NADH varies when bound to MDH relative to its free form. In addition to these results, we have also observed a ~2-fold increase in the autofluorescence intensity of NADH bound to MDH (at MDH:NADH = 0.5) relative to free NADH (data not shown), which is in agreement with previous studies [96].

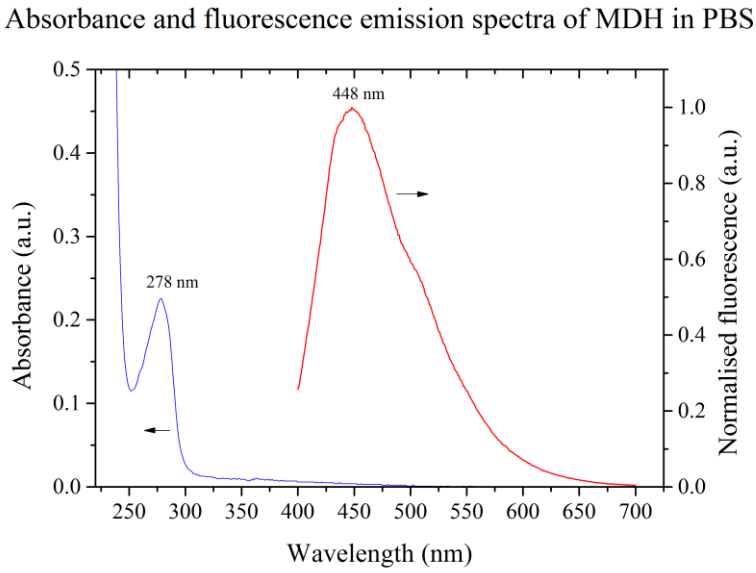

Figure 3.15 Absorbance (blue) and fluorescence (red) emission spectra of 120 μM MDH in PBS. Fluorescence emission spectrum was measured using 375 nm excitation light. Black arrows indicate curves y-axis.

We also investigated the NADH autofluorescence signature bound to LDH. In this case, the protein was prepared as described in [130], i.e. the protein was dialysed three times prior to being used. However, we encountered similar issues to those described above for MDH, i.e. related to background fluorescence, and thus the results for LDH are summarised in Figure 3.16, illustrating the variation of NADH fluorescence lifetime with increasing LDH concentration, fitted to a double exponential model. In general, the fluorescence decay of NADH bound to LDH appears to be more complex than that bound to MDH, since even a triple exponential model did not seem to produce an accurate fitting. With respect to the fluorescence lifetime, we observe similar values to those measured with NADH and MDH binding.

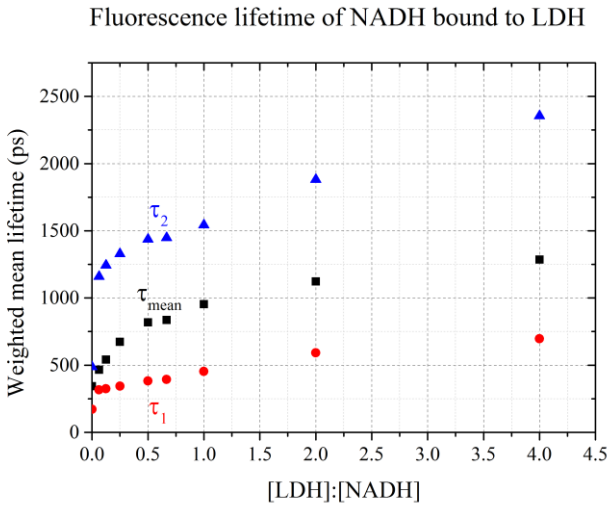

Figure 3.16 Fluorescence lifetime of NADH bound to LDH. Data fitted to a double exponential decay model.

3.3.2.3 FAD

3.3.2.3.1 Absorption and fluorescence emission spectra

The absorption spectra of free FAD in solution (see Figure 3.17, blue curve) presents two peaks at 377 nm and 454 nm, in agreement with previous observations, e.g. [70], [137]. The fluorescence emission spectrum (see Figure 3.17, red curve) indicates that FAD fluorescence is considerably red-shifted relative to NADH or collagen fluorescence, with an emission peak at ~525 nm, which is also consistent with previous results [70].

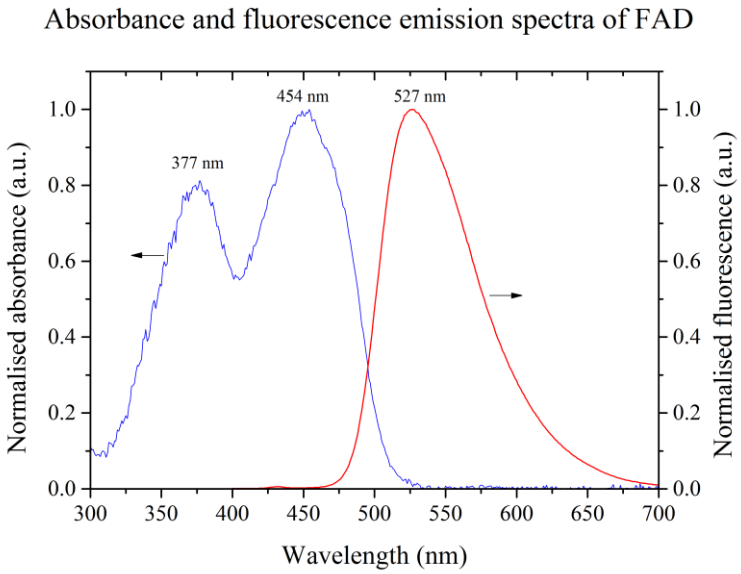

Figure 3.17 Absorbance (blue) and fluorescence (red) emission spectra of free FAD in solution. Fluorescence emission spectrum was measured using 375 nm excitation. Black arrows indicate curves y-axis.

3.3.2.3.2 Changes in FAD autofluorescence with temperature

The temperature dependence of FAD was investigated using excitation and emission close to the absorption and emission maxima (see Figure 3.17), more specifically at 440 nm and 525 nm, respectively. We chose to excite at 440 nm (and not 450 nm) since this is the excitation wavelength used in the instrument developed for osteoarthritis and heart disease studies (see Chapters 4, 5 and 6).

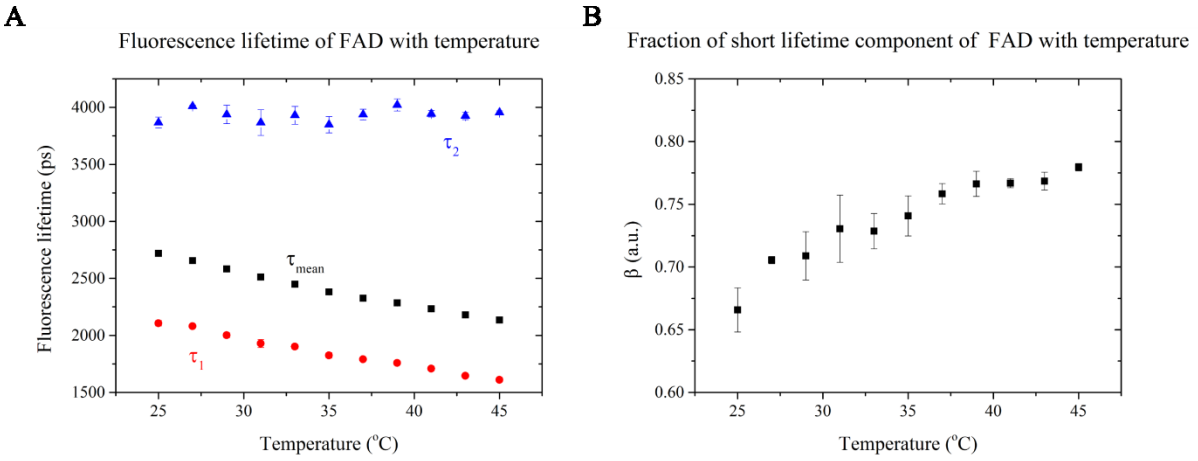

Figure 3.18 Variation of FAD (A) mean fluorescence lifetime and individual lifetime components with temperature. (B) Contribution of the short lifetime component to the decay.

The variation of autofluorescence lifetime with temperature is presented in Figure 3.18, for a double exponential fit. At room temperature, we measured a mean autofluorescence lifetime of 2720 ± 3 ps, which is in good agreement with previously reported values [39], [103]. The two long components resolved by our measurements (τ_1 = 2107 ± 24 ps; τ_2 = 3867 ± 47 ps) have previously been associated with the extended conformation of FAD [105]. We note that the presence of additional ultrafast decay components (<100 ps) due to intramolecular electron transfer between the flavin and adenine rings in folded conformation have previously been reported by others, e.g. [103], [105], [138]. However,

given the long full width at half maximum (FWHM) of the IRF (~250 ps) and the relatively low number of photons detected in our measurements, it is challenging to resolve such short lifetime components and thus our results represent a more simplistic description of the fluorescence decay of FAD.

The results presented in Figure 3.18A show a decrease in the mean lifetime of FAD of approximately 30 ps/^{o}C, which is consistent with previous observations [105]. The short lifetime τ_1 appears to be most sensitive, while the long lifetime component τ_2 remains mostly unchanged from 25 to 45^{o}C. At 37^{o}C, the values of τ_1 (1790 ± 12 ps) and τ_2 (3937 ± 47 ps) yield a mean autofluorescence lifetime of 2326 ± 3 ps. The decrease in the mean autofluorescence lifetime can also be traced back an increase in the contribution of the short lifetime component to the decay (see Figure 3.18B). We also observe a slight increase in the autofluorescence intensity of FAD with increasing temperature (see Figure 3.19).

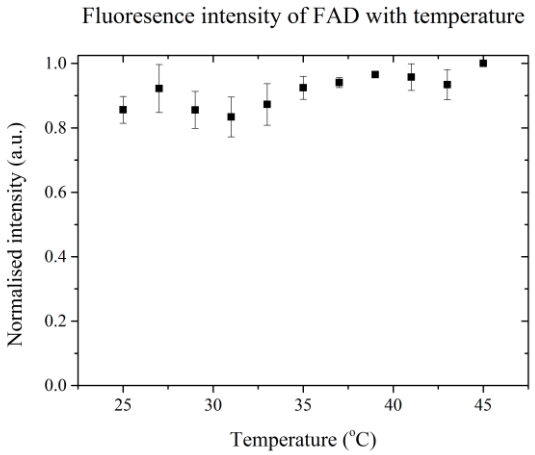

Figure 3.19 Variation of FAD autofluorescence intensity as a function of temperature.

3.3.2.3.3 Changes in FAD autofluorescence with pH

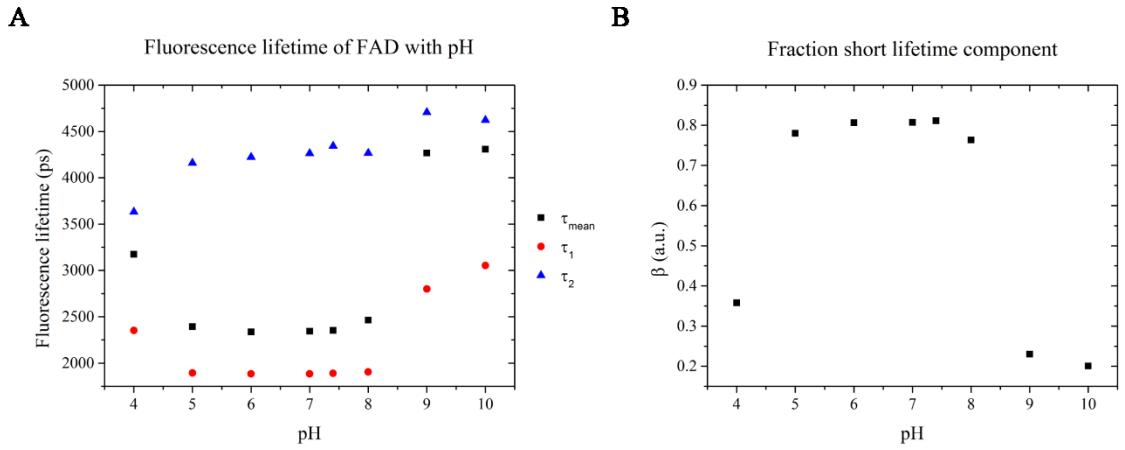

Figure 3.20 Variation of FAD (A) mean fluorescence lifetime, short and long lifetime components and (B) contribution of the short lifetime component to the fluorescence decay with pH.

FAD autofluorescence lifetime results with varying pH are presented in Figure 3.20. All measurements were realised at 37^{o}C. In general, at physiological pH (i.e. between 7 and 8) we do not

observe significant variations in any of the lifetime parameters, which is in agreement with previous studies of FAD autofluorescence with pH [103]. Changes occur predominantly at extreme pH levels, for which we observe an increase in the mean autofluorescence lifetime and in the short lifetime τ_1, and a decrease in its contribution to the fluorescence decay (see Figure 3.20). At pH 7.4, we measured a mean autofluorescence lifetime of 2355 ps, which is in good agreement with measurements in the previous section, at 37^{o}C (i.e. 2326 ps), given the magnitude of the values and other sources of errors that can potentially affect the accuracy of the measurement, such as temperature. With respect to the fluorescence intensity (see Figure 3.21), we do not observe significant variations within physiological pH levels.

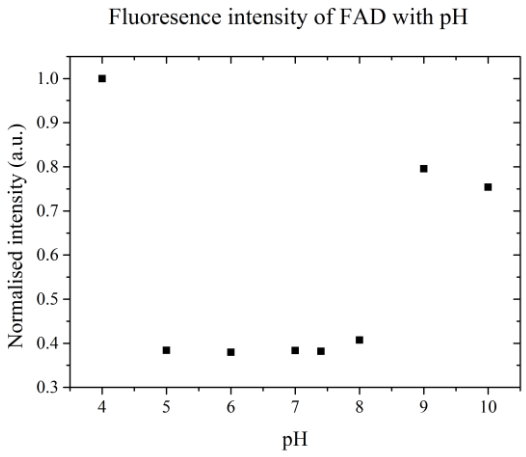

Figure 3.21 Variation of FAD autofluorescence signal as a function of pH.

3.4 Conclusions and summary

In this chapter, we presented a brief description of the most common endogenous fluorophores that exist in biological tissue and a characterisation of the autofluorescence signature of the most relevant fluorophores for our studies, namely collagen type I, NADH and FAD. The interest in these fluorophores rests in the possibility of making use of their autofluorescence properties to report on the functional and structural composition of the tissue without using exogenous labels that could potentially introduce toxicity and alter the chemical environment of the sample under investigation.

Many fluorophores can be encountered in biological specimens, including different types of collagen, elastin, NAD(P)H, FAD, porphyrins and keratin, among others [70], [118]. Accordingly, the autofluorescence spectra of biological specimens typically present complex profiles reflecting the contribution from multiple fluorescence sources. Furthermore, some of these fluorophores have broadly overlapping emission spectra, e.g. collagen and NADH, making it challenging to discern the origin of the signal using spectral measurements. Autofluorescence lifetime can provide an alternative route to distinguish endogenous fluorophores with similar spectral profiles but different fluorescence decay characteristics. A good example is collagen type I and free NADH, whose emission spectra

broadly overlap and yet their distinct autofluorescence lifetimes allows one to clearly distinguish them, as demonstrated by our measurements (~6 ns and 0.4 ns, respectively).

As already mentioned, collagen type I, NADH and FAD are of particular interest to us, given their contribution to the autofluorescence signal, particularly in cardiac tissue. Collagen type I powder yields a complex and long autofluorescence lifetime (~6 ns). Although this value is within the range of reported values for collagen fluorescence lifetime, we note that collagen structural composition can change with collagen and tissue type and with extraction process used for purification. Furthermore, the autofluorescence emission changes with excitation and thus the combination of all these factors makes it challenging to validate our results against other published values. However, it seems relatively well-established that collagen yields a long fluorescence lifetime component (~9 ns) with a number of publications pointing out similar results, e.g. [73], [124].

With respect to NADH, our measurements are in good agreement with previously published data, e.g. [8], [96], [97]. Free NADH in solution yields a double exponential fluorescence decay, with mean autofluorescence lifetime between 400 and 500 ps and individual lifetimes of 200 to 300 ps and 600 to 800 ps, which are attributed to the extended and folded conformations of the molecule, respectively. These values were found to decrease with increasing temperature and thus, at 37^{o}C, the mean autofluorescence lifetime of free NADH is ~350 ps. We have also studied the variation of NADH autofluorescence lifetime with pH, having observed little variation within the physiological pH range. In biological tissue, NADH can exist free or bound to enzymes. Enzyme-bound NADH was found to yield a longer fluorescence lifetime compared to freely diffusing NADH, which is consistent with previous studies, e.g. [8], [96]. However, our experiments do not allow us to draw any further conclusions regarding the fluorescence dynamics of enzyme bound NADH, given the fluorescence background observed, which contaminated our measurements. Once the origin of this fluorescence background is identified, work could be focused on characterisation of the autofluorescence spectral and lifetime properties of NADH bound to different enzymes with a view to understand how the resulting values fit in the autofluorescence signal of biological tissue. It would also be interesting to undertake temperature and pH experiments of NADH bound to enzymes. Given that the mitochondrial pH can change upon metabolic dysfunction, such experiments could help us to understand the variations in the autofluorescence signal observed in metabolically active tissue.

We have also investigated the fluorescence signature of free FAD with varying temperature and pH. The fluorescence decay of free FAD is complex, possibly with more than two exponential components. In our studies, we have identified two long components with lifetimes of ~2.1 ns and ~4 ns (at room temperature), both of which associated with the open conformation of FAD. Shorter lifetime components, such as those reported in references [103], [105], have not been observed, likely

due to the inability of our system to resolve such ultra-short (tens of ps) decays, given the longer IRF FWHM (~250 ps) and the low photon counts. Unlike NADH, we have not undertaken protein bound studies of FAD and therefore future work could be focussed on the characterisation of the autofluorescence properties of FAD bound to enzymes, e.g. succinate, which are in general less studied than those for protein bound NADH.

The intrinsic complexity of the autofluorescence signal due to the presence of multiple fluorophores is further emphasised by the complexity of the autofluorescence signal emanating from each fluorophore, as demonstrated throughout this chapter. One way of simplifying the fluorescence signal arising from multiple fluorophores is to realise spectrally resolved detection, i.e. detection at different wavelengths that maximise collection from one specific fluorophore but not from the other. In the following chapter, we present an instrument that realises spectrally- and time-resolved detection of the fluorescence, which will then be utilised for studies of osteoarthritis (Chapter 5) and heart disease (Chapter 6).

4 Tissue spectroscopy

As discussed in Chapters 2 and 3, the optical properties of biological tissue can reveal changes in biochemical composition, metabolism and morphology owing to pathological transformations. Optical techniques, such as fluorescence or diffuse reflectance spectroscopy, have been widely employed in the study of biological tissue and, consequently, have shown potential for medical applications of tissue diagnosis. This chapter introduces the concept of tissue spectroscopy and presents the fundamentals of optical spectroscopy techniques, including fluorescence and reflectance spectroscopy, which are of particular interest for this thesis. It also describes the development of instrumentation for autofluorescence spectroscopy with a particular emphasis on measurements of autofluorescence lifetime. Two fibre-optic probe-based instruments providing spectrally resolved TCPSC-based autofluorescence lifetime measurements have been developed to be deployed at the National Heart and Lung Institute (NHLI) and at the Kennedy Institute of Rheumatology for systematic studies of heart disease and osteoarthritis, respectively, in collaboration with clinical colleagues. A comprehensive description of the development and characterisation of these instruments are presented together with data from its application to measurements of fluorescence lifetime standards.

Outline

- Introduction to tissue spectroscopy, including time-resolved, steady state fluorescence spectroscopy and white light reflectometry.
- Development of time-resolved spectrofluorometer for single point fibre-optic probe based measurements of biological tissue.
- Characterisation and calibration of the instrument developed.
- Fluorescence lifetime measurements of reference fluorophores.
- Conclusion and summary.

4.1 Introduction to tissue spectroscopy

In recent years, optical spectroscopy techniques have become the basis of biomedical research in the development of non or minimally invasive tools for medical applications and clinical diagnosis [1], [139], [140]. The growing clinical interest in optical tools is primarily motivated by the potential that optical measurements offer to provide immediate biochemical, morphological and/or physiological information at relatively low cost that could enhance early detection of alterations in tissue associated to pathological transformations [118], in contrast to well-established clinical techniques, such as Computerised Tomography (CT), Magnetic Resonance Imaging (MRI) or Positron Emission

Tomography (PET), which, despite their recognised merits [141], [142], can still be expensive, time consuming and require the administration of exogenous probes to provide or optimise contrast, and thus introduce toxicity into the system that could potentially alter the biochemical environment. By providing *in situ* and real-time diagnostic information, optical measurements can effectively be regarded as "virtual biopsy" tools that can guide clinicians and significantly reduce treatment delays and costs associated with unnecessary surgical removal of tissue samples that can the impact the overall quality of care for patients [118], [139], [143], [144].

A number of optical techniques have been widely investigated as potential routes towards non-invasive optical-based study of biological tissue including diffuse reflectance [139], [145] and autofluorescence spectroscopy and imaging [146]–[150], confocal reflectance microscopy [151], [152], pump-probe spectroscopy [153], [154], optical coherence tomography (OCT) [155]–[157] and Raman spectroscopy [158]–[160]. These techniques share the same basic principle: light interacts with tissue at both molecular and tissue levels, giving rise to optical signals that are fingerprints for biomedical characterisation [118], [161]. Alterations in the local biochemical and structural composition will affect light-tissue interaction, giving rise to different optical readouts that provide means for contrast in tissue. Up to now, these optical techniques have been successfully employed in tissue diagnosis in a wide range of clinical applications, including blood oxygen saturation [162]–[164], heart disease [3], [95], [165]–[169], osteoarthritis [145], [170]–[172], atherosclerosis [22], [24], [69], [173]–[175] and various types of cancer [12]–[14], [16], [19], [38], [71], [154], [176]. Table 4.1 summarises the advantages and limitations of the techniques outlined above.

While all these techniques have merits and have shown potential in a wide range of clinical applications, none of them possess all the key features necessary to realise practical real-time clinical diagnosis, i.e. sensitivity, specificity, spatial and temporal resolution, data acquisition time, size and cost. An attractive pathway to overcome these limitations consists in combining these modalities to realise multimodal detection e.g. OCT and autofluorescence spectroscopy [177]–[179] or Raman and near-infrared autofluorescence spectroscopy [180], [181] to provide complementary information on morphological and biochemical properties of the tissue.

Table 4.1 Advantages and limitations of different optical spectroscopy techniques

Modality	Output	Advantages	Limitations	Examples of clinical applications
Diffuse reflectance	Tissue morphology and physiology	Simple to implement; Can be low cost;	Sensitive to intensity artefacts; Low molecular specificity;	Osteoarthritis [145], [172]; Colon cancer [182]; Oral cancer [183]; Lung cancer [184] Blood oxygenation [163];
Autofluorescence	Tissue morphology; Biochemical composition; Cellular metabolism; Protein crosslinking;	Steady-state or time-resolved modalities; Quantitative and qualitative information on biochemical composition;	Complexity of the autofluorescence signal;	Cardiac disease [3]; Breast cancer [12], [15], [102]; Skin cancer [35], [185]; Lung cancer [71]; Colon cancer [14]; Atherosclerotic plaques [21];
Confocal reflectance microscopy	Morphologic information	High resolution and high contrast; Can provide optical sectioning;	High cost; Depth of imaging is limited by optical penetration and SNR;	Skin cancer [186]–[188]
Pump-probe reflectance spectroscopy and microscopy	Morphologic and biochemical information	Optical sectioning in highly scattering samples; can provide information on the dynamics of non-fluorescent chromophores;	Insensitive to non-pigmented tissue; High cost;	Skin cancer [154], [189]; Ocular cancer [190];
OCT	Morphologic information	Commercially available; Fast data acquisition; High penetration depth;	No functional information	Ophthalmology [157]; Atherosclerotic plaques [174], [175]; Skin cancer [191]–[193];
Raman spectroscopy	Qualitative identification and quantitative determination of molecular species	High molecular specificity	Weak signal, requiring highly sensitive detection instrumentation; Complex data interpretation;	Breast cancer [158], [160]; Skin cancer [159], [194]; Colon cancer [195];

Autofluorescence spectroscopy is a promising tool for characterisation of biological tissues and has shown potential for *in vivo* clinical diagnosis in a number of applications, e.g. [14], [19], [196]. As discussed in Chapters 2 and 3, endogenous fluorescence can provide powerful means of achieving label-free optical contrast in biological tissue. Furthermore, autofluorescence measurements can report changes in structure, metabolism and protein crosslinking by resolving the characteristic spectral and temporal properties of the fluorescence emission from endogenous fluorophores, e.g.

NAD(P)H, FAD, collagen and elastin [70]. As consequence, there has been an increasing interest in the application of this technique in biomedical research and a number of instruments have been developed accordingly, using spectrally and/or time-resolved fluorescence detection alone, e.g. [13], [14], [17], [19], [40], [43], [197], or in a multimodal approach, in combination with other optical techniques for increased specificity of the detection [3], [19], [177]–[179], [181], [184], [198], [199]. Overall, autofluorescence spectroscopy is a promising non-invasive label-free approach to characterise biological tissue, representing an attractive opportunity for *in vivo* optical-based diagnosis. In this chapter, the development of a multimodal instrument that implements spectrally- and time-resolved autofluorescence spectroscopy and diffuse reflectance spectroscopy is presented, to be applied in tissue measurements of osteoarthritis and heart disease. Both autofluorescence and diffuse reflectance spectroscopy are described in detail below. It should be noted that these techniques can be applied via single point or imaging approaches with their respective merits and limitations: point spectroscopy suffers from lack of spatial resolution but yields a greater signal-to-noise ratio (SNR), while imaging modalities such as microscopy and endoscopy still have key issues to address related to data acquisition time, SNR, sample motion and others, before becoming practical to use in clinical settings [1], [44], [200], [201]. For this reason, we believe that single point observations are ideal to investigate the potential of time-resolved autofluorescence spectroscopy as label-free tools to aid clinical diagnosis of disease. Hence, only point spectroscopy will be discussed hereafter.

4.1.1 Fluorescence spectroscopy

Fluorescence measurements can be classified into two categories: steady-state and time-resolved. Both modalities have been extensively used in the study of biological tissue, both *ex vivo* and *in vivo*. In general, they share much of the same basic instrumentation, although steady-state fluorescence measurements are simpler to implement and therefore more commonly used [1], [202], [203].

4.1.1.1 Steady-state fluorescence measurements

Steady-state fluorescence spectroscopy refers to measurements performed with constant illumination and detection: the sample is illuminated with continuous wave (CW) radiation and the fluorescence intensity or reflected light spectrum collected at the same time. Figure 4.1 illustrates a typical configuration of a steady-state fluorescence spectrometer.

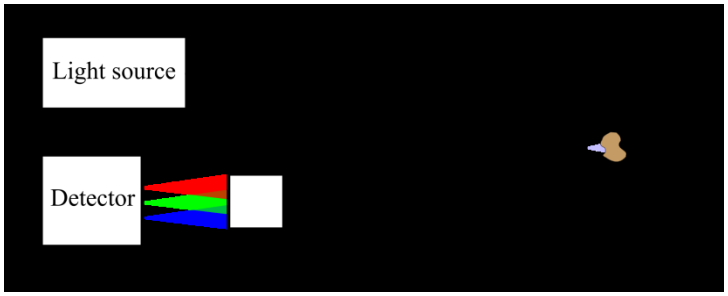

Figure 4.1 Basic configuration of a steady-state fluorescence spectroscopy instrument, utilising a fibre-optic probe for light delivery and collection.

Here, the sample is illuminated with a constant intensity of light provided typically by a lamp, a laser or an light emitting diode (LED) [1]. With respect to delivery and collection of light from the sample, two approaches may be considered. The first uses fibre-optic probes as light guides, as demonstrated in Figure 4.1. In this case, the fibre-optic is placed in contact or in close proximity to the biological specimen allowing interrogation of small areas of tissue. This is our preferred approach for single point fluorescence spectroscopy measurements. The second approach does not require contact with the sample, as excitation light is projected and collected from the sample via a series of lenses. This approach is usually preferred for imaging modalities, as it allows measurements of larger areas of tissue. Fluorescence from the sample is then delivered to the detection arm to be spectrally dispersed using dispersing elements before being directed to the detection element [1], [202]. Typical arrangements use a grating or a prism to separate out the fluorescence emission according to its wavelength and a CCD array to measure the light intensity at different wavelengths. Alternative configurations involve the use of dichroic mirrors and multiple single channel detectors like PMTs and inclusion of polarisers to realised polarisation-resolved measurements.

As discussed in Chapter 2, intensity-based measurements are sensitive to the concentration and distribution of fluorophores present in the tissue and therefore can be used to report the disease state of the tissue. A number of studies can be found in literature involving the application of steady-state fluorescence spectroscopy to clinical investigations of heart disease [3], [168], atherosclerosis [69] and cancer including skin [13], pancreas [176], [204], lung [12], [205], breast [12], cervix [206] and others [4], [13], [207], [208].

Overall, despite being relatively well-established, there are a number of factors hampering further widespread deployment of this approach into clinical investigations [203], [209]. Intensity-based artefacts in the fluorescence measurements can emerge from uneven excitation/collection efficiency e.g. due to tissue movement or surface profile, heterogeneous absorbing (e.g. variable haemoglobin concentration) and scattering properties or photobleaching. In addition, autofluorescence in biological tissue can exhibit complex emission profiles that arise from a multitude of fluorophores with broadly

overlapping fluorescence emission spectra present in the tissue, making it challenging to differentiate between different fluorophores based solely on spectral analysis [70], [140], [202].

4.1.1.2 Time-resolved fluorescence measurements

Time-resolved fluorescence spectroscopy (TRFS) aims to resolve the characteristic fluorescence intensity dynamics and thus provide additional information to that available from steady-state measurements alone [1]. TRFS is an inherently ratiometric technique that can overcome common problems associated with fluorescence measurements including variations in excitation/collection efficiency, fluorophore concentration and heterogeneous sample absorption and scattering [140]. Moreover, it is well suited to discriminate between fluorophores with overlapping fluorescence emission spectra but different decay times [148]. In addition, as discussed in Chapter 2, fluorescence lifetime can be sensitive to the microenvironment and therefore its measurement can provide a direct approach to probe environmental parameters such as temperature [210], oxygenation [211], pH [212] or calcium concentration [146], through the use of an appropriate fluorescent probe.

With respect to the instrumentation, TRFS is similar to the steady-state approach, although it requires a pulsed excitation light source and specialised time-resolved detection electronics to record the fluorescence intensity decay profiles. Figure 4.2 illustrates a basic TRFS configuration using TCSPC-based detection circuitry at multiple wavelengths. As previously discussed, fluorescence lifetime measurements can be conducted in either time-domain or frequency-domain, both with their own merits and limitations, although the first is more commonly implemented for TRFS of biological tissue, with a multitude of instruments available in literature. In a typical time-resolved single-point spectroscopy setup, measurements of tissue are carried out using a pulsed laser as excitation source operating in the MHz regime and single-photon counting detectors with TCSPC acquisition to record the temporal response of the fluorescence emission [17], [19], [39], [80], [213]. Alternative configurations are also possible utilising lasers that operate at low repetition rates (e.g. nitrogen laser) and fast digitisers (e.g. digital oscilloscopes) that record the fluorescence emission as a function of time, as in references [14], [16], [214]–[216]. In both cases, instruments typically record the fluorescence intensity decays in a number of spectral channels, thus providing both time- and spectrally-resolved information of the sample, which can enhance the specificity of the measurements and improve the ability to differentiate tissue states. For this reason, TRFS has increasingly been applied in clinical research in a number of fields, including cardiovascular applications [39], [169], [173], [214], [216], [217] and cancer studies of skin [17], [19], colon [14], [38], brain [76], [79], [218], lungs [16], [71] and cervix [206].

Overall, in recent years, TRFS has emerged as a potential diagnostic tool that can help to differentiate healthy from diseased tissues both *ex vivo* and *in vivo*. In particular, our group has explored this

technique in the investigation of osteoarthritis and myocardial infarction. This work will be described in detail in Chapters 5 and 6, respectively.

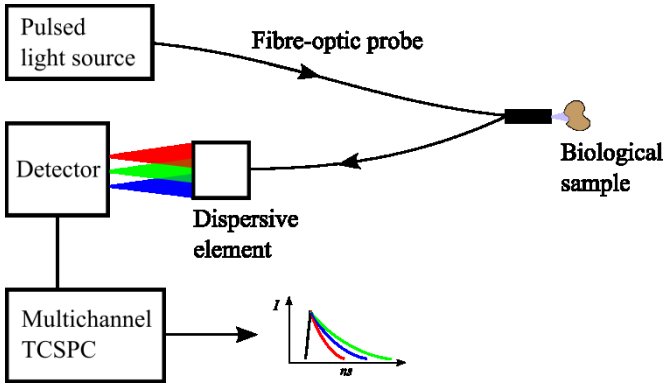

Figure 4.2 Basic configuration of a TRFS instrument, utilising a fibre-optic probe for light delivery and collection and multichannel TCPSC-based detection for recording of the fluorescence decay characteristics.

4.1.2 Diffuse reflectance spectroscopy

Diffuse reflectance spectroscopy is a well-established optical technique that measures the characteristic "reflectance" spectrum produced by the interaction of light with biological tissue. When light propagates through tissue, it is affected by multiple elastic scattering and absorption events. The radiation that emerges from these interactions provides quantitative information about tissue scatterers and absorbers from which physiological and morphological parameters can be derived. Because scattering and absorption properties can change upon pathological transformations in tissue, e.g. as result of alterations in cell density, diffuse reflectance represents a convenient non-invasive approach to read out changes in tissue properties. However, as with steady-state fluorescence spectroscopy, diffuse reflectance is affected by variations in illumination brightness and spectrum or detector sensitivity, and therefore it needs to be carefully calibrated. With respect to fluorescence spectroscopy, diffuse reflectance should not be regarded as a competing method but as complementary, potentially enhancing the specificity of the detection: while diffuse reflectance can read out the morphological and physiological state of the tissue, fluorescence measurements can report altered metabolism or protein crosslinking.

Typical diffuse reflectance setups utilise a broadband light source to illuminate the sample, a bifurcated fibre-optic probe to deliver and collect light from the sample and a spectrometer to detect the light at different wavelengths. Examples of such set-ups are given in references [182], [183], [219], [220]. In diffuse reflectance spectroscopy, the configuration of the fibre-optic probe is of particular importance, more specifically the arrangement of the collection fibres relative to the delivery fibres. This is because different arrangements select light that interacted with tissue in different manners, hence leading to light probing different regions of the sample. For example, the

greater is the distance between delivery and collection fibres, the greater will be the average propagation (or the mean distance) of light through the tissue, resulting in more scattering and absorption interactions and in a higher probability that the detected photons have probed deeper into the tissue. This is illustrated in Figure 4.3A, using two collection fibres at different distances relative to a single delivery fibre. This principle is also one of the strengths of diffuse reflectance spectroscopy, as it allows morphological and physiological studies of tissue at different depths e.g. using multiple collection fibres at various distances from the illumination fibre.

Overall, diffuse reflectance spectroscopy is a simple and non-invasive method that can be implemented with relatively inexpensive optical instrumentation. Hence, it represents a convenient approach to probe the morphological and physiological state of the tissue, having been applied in various biological and clinical studies including blood oxygenation [221], haemoglobin and myoglobin concentrations [222], skin [223], [224], heart [3], [164], [225], [226], osteoarthritis [145], [172], [227], [228] and cancer [19], [182], [183], [229].

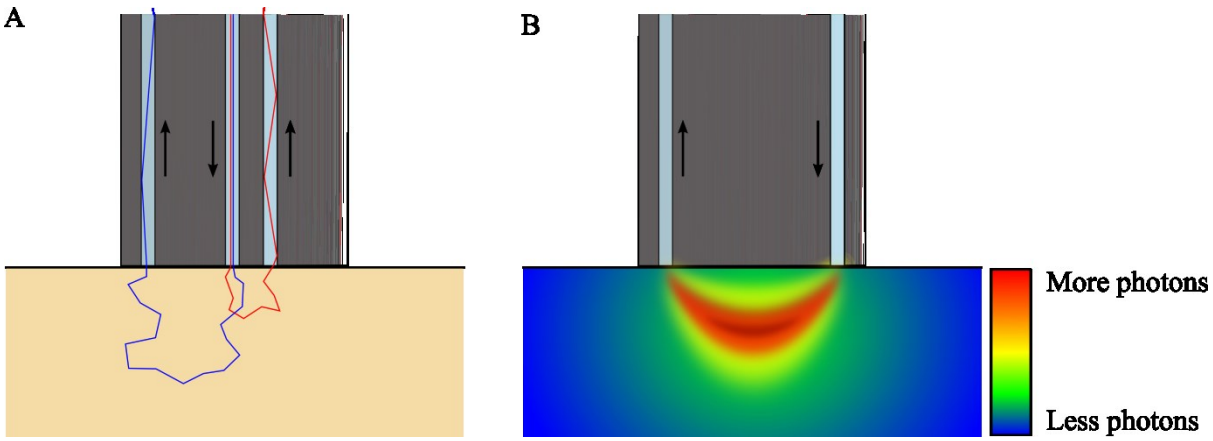

Figure 4.3 (A) Representation of the diffuse reflectance principle utilising a single illumination fibre (centre) and two collection fibres. Detected photons have undergone multiple interactions and travelled randomly in the tissue. Adjusting the distance between illumination and collection fibres, one can probe the tissue at different depths. (B) Schematic representation (pictorial guess, no simulation models involved) of the photon propagation probability in diffuse reflectance measurements.

4.2 Development of TCSPC-based time-resolved spectrofluorometer for single point measurements

As discussed previously, this study aims to translate well-established autofluorescence and diffuse reflectance technology into clinical investigation of heart disease and osteoarthritis. To explore the label-free optical readout provided by these methods, we have developed compact instrumentation combining time-resolved spectrofluorometry and white light reflectometry utilising a fibre-optic probe to realise single point measurements of tissue. Similar instruments have previously been presented. In particular, Mycek et al [14] pioneered the application of single-point spectrally- and time-resolved spectroscopy to *in vivo* studies of colon cancer, utilising a nitrogen laser to provide excitation and a fast digitiser to record the fluorescence decay profile. A more recent instrument was

published by Cheng et al [197], describing a new method to realise multispectral detection utilising a single PMT and a digitiser to record the fluorescence intensity decay. Although this method refers to an imaging modality, it has shown potential to discriminate healthy from disease tissues and a similar detection approach could be used for single point measurements. In our group, De Beule et al [17] developed an instrument for skin cancer autofluorescence studies that utilised a 16-channel PMT and TCSPC detection to realise single point spectrally and time-resolved fluorescence measurements at two excitation wavelengths (355 nm and 440 nm). This instrument was later improved by Thompson et al [19] to accommodate white light reflectometry instrumentation to realise multimodal spectrally- and time-resolved autofluorescence and diffuse reflectance spectroscopy detection of basal cell carcinomas. This section presents the development of a single point instrument similar in concept to that presented by Thompson et al, utilising a lower number of fluorescence detection channels, which benefits the SNR in our instrument, and a simplified and more compact optical instrument. A detailed description of the development, characterisation and calibration of this instrument is provided, including comparison against a well-characterised cuvette-based time-resolved spectrofluorometer previously developed in our laboratory and described in section 3.3.1.3.

4.2.1 Optical setup

This instrument was designed to discriminate and maximise the contrast between autofluorescence signals of endogenous fluorophores that play a major role in the clinical applications for which the instrument was primarily designed for, i.e. heart disease and osteoarthritis. As is further discussed in Chapter 6, NADH and FAD play an important role as electron donors in mitochondrial metabolism and therefore are of great significance in heart studies. In the case of osteoarthritis, we expect the autofluorescence signal to be predominantly from collagen type II, which fluoresces strongly in the short wavelength range of the visible spectrum.

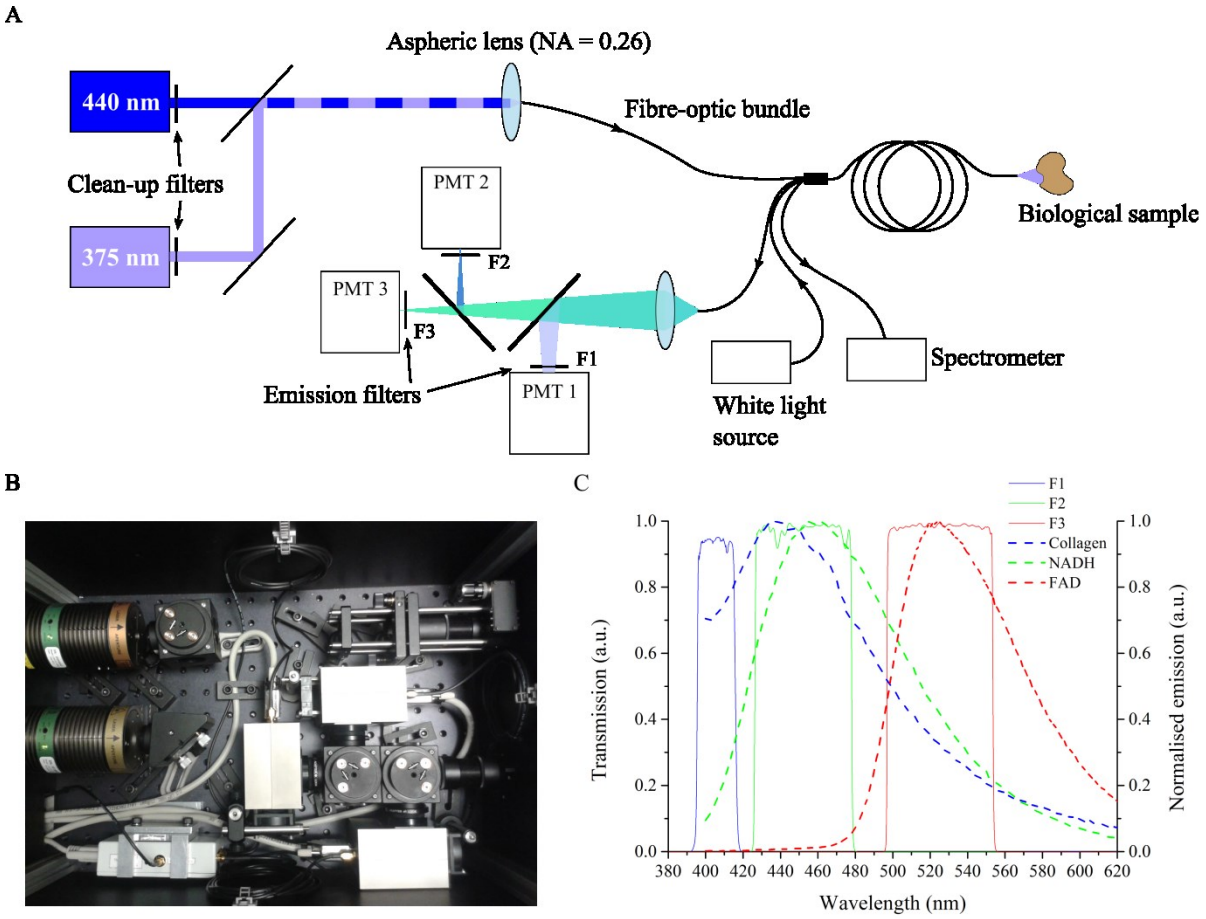

Figure 4.4 (A) Optical layout of single-point time-resolved spectrofluorometer. (B) Photograph of the optical layout. (C) Emission spectra of endogenous fluorophores of interest excited at 375 nm and plotted to show their relation to the spectral range of the detection channels of the fluorescence lifetime point probe system. Curves are normalised to their maximum amplitude. Data measured on a spectrofluorophotometer (RF-5301PC, Shimadzu, Japan). Solutions of β-NADH (N1161, Sigma-Aldrich, Germany) and FAD (F6625, Sigma-Aldrich, Germany) were prepared by diluting the respective powder in PBS solution. Collagen type-I powder from rat tail was acquired from Sigma (C8897, Sigma-Aldrich, Germany) and used directly without further preparation.

This system is configured as shown in Figure 4.4A. Excitation light is provided by two compact laser sources: a laser diode (LDH-P-C-375B, PicoQuant GmbH, Germany) providing 70 ps pulses at 375 ± 5 nm with an average output power of 3.3 mW; and a second laser diode (LDH-P-C-440B, PicoQuant GmbH, Germany) generating 90 ps pulses at 440 ± 5 nm, with 3.5 mW of average power. A single laser driver (Sepia II, PicoQuant GmbH, Germany) controls both lasers, allowing power control and adjustment of the repetition rate up to 80 MHz. The laser beams are combined using a dichroic mirror (Di01-R405, Semrock, USA) and subsequently coupled into a custom-made optical fibre bundle (FiberTech Optica, Canada) consisting of three excitation fibres and fourteen detection fibres arranged in a hexagonal structure around the excitation fibres, see Figure 4.6. There are also two extra fibres that are used for white light delivery and diffuse reflectance detection. Further characterisation of this fibre-bundle is presented below. Fluorescence light from the sample is collected by the detection fibres and directed to three spectrally resolved detection channels implemented using a set of dichroic mirrors and band-pass filters. When using 375 nm excitation, all three channels are active: the first

channel collects light from 400 to 420 nm (CH1); the second channel collects light from 430 to 480 nm (CH2); the third channel accepts light from 500 to 550 nm (CH3). When using 440 nm excitation light, only the third (500-550 nm) channel is active and, for convenience, this is referred as "channel 4" (CH4) hereafter. The detection band-pass filters used are shown in Figure 4.4C, alongside with the fluorescence emission spectra of fluorophores of interest, namely NADH, FAD and collagen type I. Each detection channel has a photon-counting photomultiplier (PMC-100-1, Becker-Hickl GmbH, Germany), which are controlled using DCC-100 modules (Becker-Hickl GmbH, Germany). The photomultipliers (PMT) are connected to a router (HRT-41, Becker-Hickl GmbH, Germany) that serialises the incoming signals for input to a time-correlated single photon counting (TCSPC) acquisition card (SPC-830, Becker-Hickl GmbH, Germany). The TCSPC system records the temporal fluorescence decay profile for each spectral channel. The instrument also comprises a white light source (HL-2000, Ocean Optics, USA) and a compact spectrometer (USB-2000+, Ocean Optics, USA) for diffuse reflectance measurements. The optical setup was assembled on a 30 × 45 cm^2 breadboard (Thorlabs, USA), which was enclosed and interlocked for safe use (see Figure 4.4B). Due to its compactness, the system could either be mounted on a portable trolley for ease of transportation within a clinical facility or simply sit on a bench (see Figure 4.5). The system is fully controlled via a custom application written in LabVIEW (LabVIEW, National Instruments, USA), which will be described in more detail below.

Figure 4.5 (A) Point probe system assembled on a trolley for ease of transportation between experimental settings within a facility. (B) System assembled on a bench at NHLI.

4.2.2 Fibre-optic probe

Our instrument utilises a custom-made fibre-optic bundle consisting of 19 multimode optical fibres, each one having 200 μm diameter core with a further 20 μm cladding and numerical aperture (NA) 0.22, with four individual branches at the proximal end and a common distal end, as illustrated in

Figure 4.4A. The 19 optical fibres are as follows: 3 are used for fluorescence excitation, 14 are used for fluorescence collection and the remaining 2 used for white light delivery or detection.

At the proximal end of the fluorescence excitation branch, light is coupled into a short length (~2 cm) of 600 μm fibre, which couples against three 200 μm closely packed excitation fibres that deliver the light into the sample, as illustrated in Figure 4.6A. The input end of the 600 μm fibre was cleaved at 8^{o} to minimise back-reflections from the fibre that would arise from a double pass of the excitation light in the delivery fibres, and would excite the sample twice. It is relevant to point out that at the beginning of our studies we utilised fibre-optic probes with flat inputs, i.e. not cleaved, and therefore back-reflections were observed in the fluorescence profiles acquired with this system (see Figure 4.12).

The arrangement of the fibres at the distal end can have a great impact on the fluorescence signal collected from the sample. Multiple designs have been studied and used in tissue spectroscopy applications, although, in general, all arrangements target maximisation of the SNR and precise target interrogation [230], [231]. Our fibre-probe uses a popular configuration in our group [19], [128] consisting of a hexagonal arrangement with the excitation fibres at the centre surrounded by the collection fibres (see Figure 4.6B). All optical fibres are fixed with epoxy glue inside a ~5 mm long medical grade stainless steel ferrule (see Figure 4.6C). The same hexagonal arrangement can be found at the proximal end of the fluorescence detection branch, yet without the excitation and white light delivery and collection fibres.

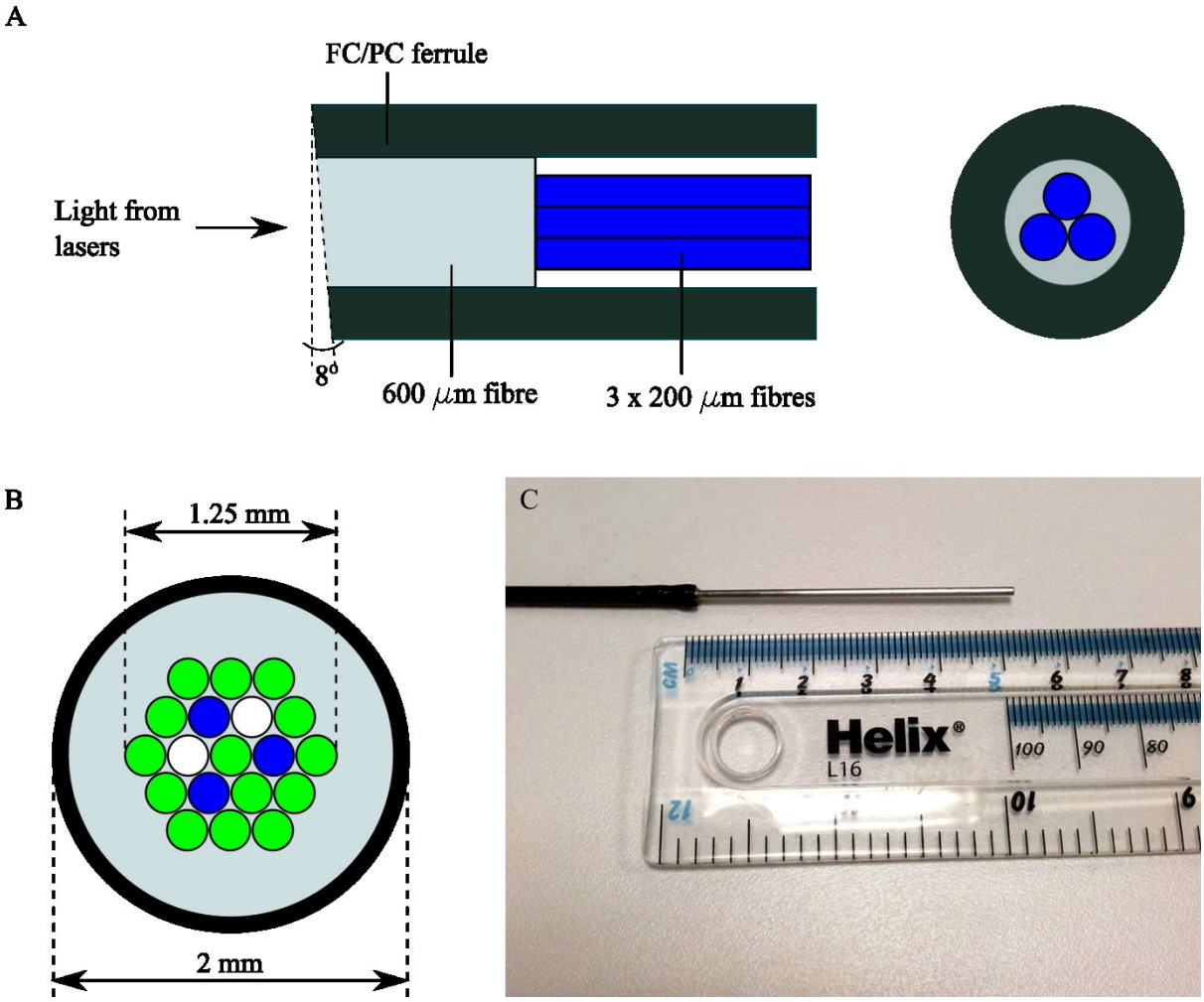

Figure 4.6 (A) Cross-section (left) and frontal (right) views of the proximal end of the fibre-bundle, at the fluorescence excitation branch. (B) Cross-section view showing arrangement of delivery and collection fibres at the distal end. Fluorescence excitation fibres are coloured blue, fluorescence collection fibres are coloured green and white light delivery and collection fibres are displayed in white. (C) Photograph of the distal end of the fibre bundle.

4.2.3 Control software

Our instrument is controlled by a custom LabVIEW (LabVIEW, National Instruments, USA) program that builds up on previously developed code in our laboratory. In particular, this software allows:

- Control of the lasers operation, including ON/OFF switch and optical power adjustment.
- Control of the white light source operation - the intensity of the light can only be adjusted manually.
- Interface with SPC-830 acquisition that allows data acquisition and real-time readout of the photon count rate.
- Interface with spectrometer.
- Configuration of the SPC-830 and DCC-100 modules.

Figure 4.7 shows the front panel of the graphical user interface.

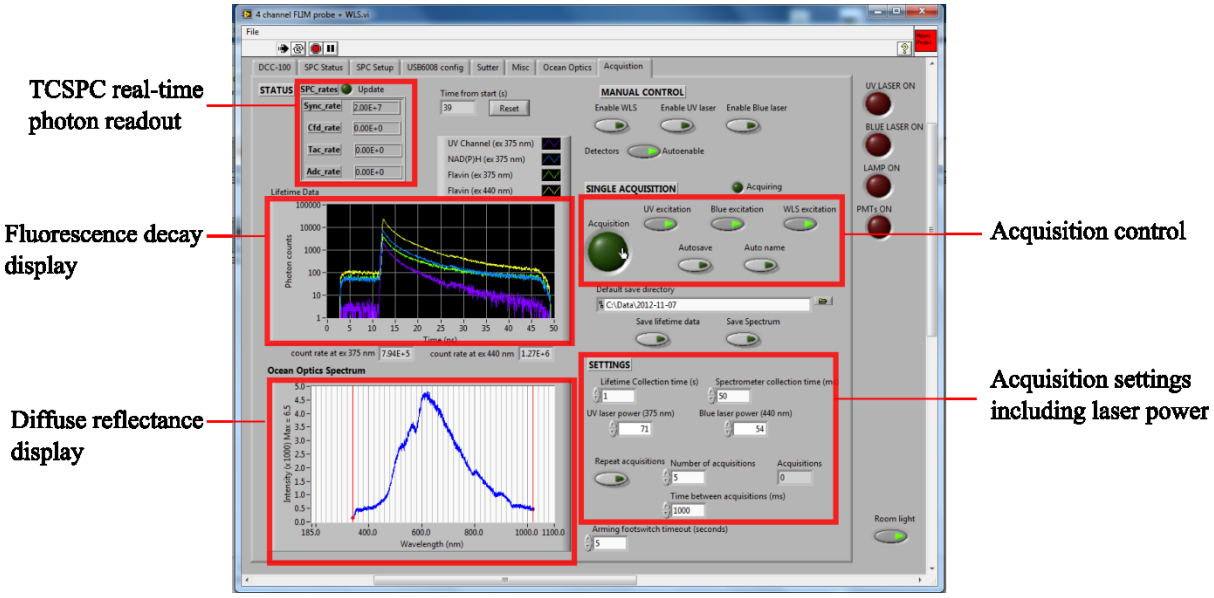

Figure 4.7 LabVIEW graphical user interface front panel of the time-resolved spectrofluorometer. This software is an upgrade of code that was previously developed in our laboratory.

The software allows either manual or automatic control of the lasers: the first is used for verification of the laser output and photon count rate; the second is for operation of the laser during an acquisition. The acquisition of a complete dataset - i.e. fluorescence and diffuse reflectance - occurs broadly in three sequential steps: 1) acquisition of fluorescence data using UV excitation; 2) acquisition of fluorescence data using blue excitation; 3) acquisition of diffuse reflectance data. These three steps are independent and any of them can be omitted via controls on LabVIEW interface. The integration time for fluorescence lifetime and diffuse reflectance measurements can also be adjusted independently. Finally, data are saved to two text files, containing fluorescence data from both excitation sources and reflectance data, respectively. Figure 4.8 shows the flow diagram of data acquisition.

Because this system is to be deployed in clinical settings, the software includes safety features to protect both the user and the equipment itself, as follows:

- Laser output power is limited to below the maximum permissible exposure (MPE) (see section 4.3.2) for an accidental exposure of up to 100 seconds.
- A software-controlled laser interlock prevents users to turn on the laser if the software is not loaded.
- If any of the PMTs overloads due to exposure to too much light, detection is automatically disabled and the lasers switched off.

The software also accommodates event-based structures for foot pedal inputs, which can facilitate the usage of the instrument by a clinician, in the case of having both hands occupied, e.g. in *in vivo* surgical procedures. In addition, the software also allows control of a white LED that can provide room illumination between measurements. Foot pedals and external illumination are controlled by software via an USB-6008 data acquisition card (NI-USB-6008, National Instruments, USA).

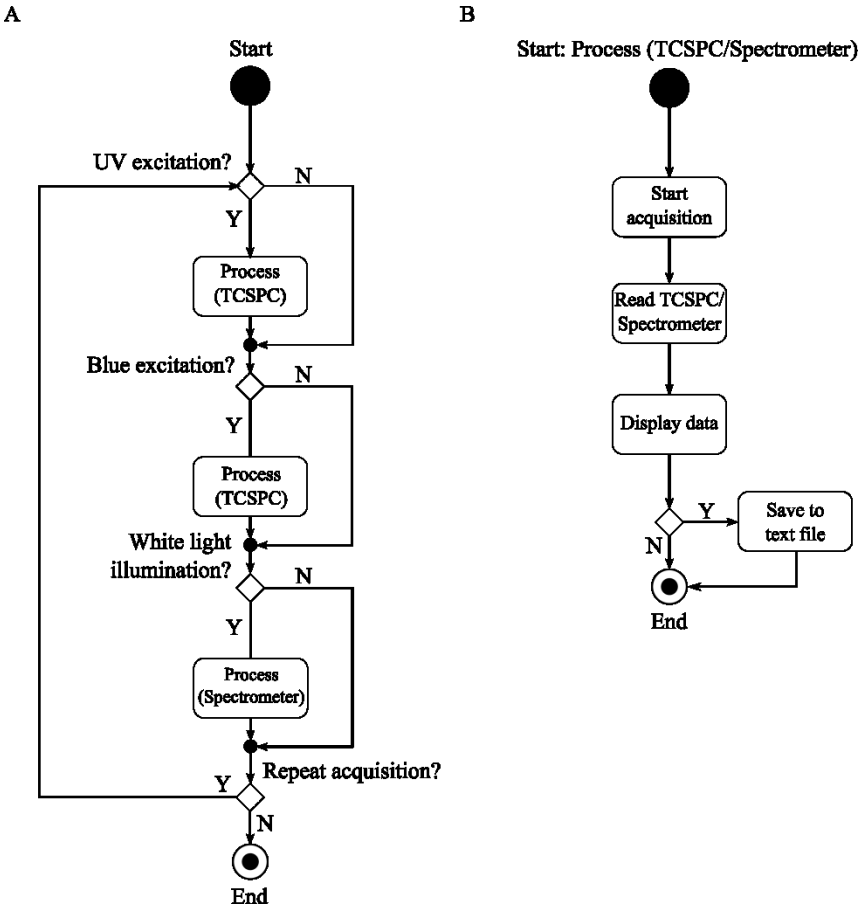

Figure 4.8 Flow diagram of the acquisition of (A) a complete dataset and (B) each individual dataset.

4.3 Instrument characterisation and calibration

4.3.1 Laser output

In laser diodes, the intensity of the laser emission is controlled by the electric current provided by the laser driver, i.e. increasing (or decreasing) the driving current will increase (decrease) the optical output power. In the Sepia II driver, the driving current can be adjusted using a voltage control, which is scaled from 0 to 100%, and can be adjusted in steps of 1%. However, due to the non-linear nature of laser diodes, adjustment of the input voltage does not correspond to a linear adjustment of the optical output power. Figure 4.9 shows calibration curves for both excitation wavelengths. For these measurements, a powermeter (Model 841-PE, Newport, USA) was positioned in front of the fibre-

optic bundle, therefore mimicking the experimental conditions of tissue measurements. This is of relevance, as the systems are to be deployed in clinical facilities and therefore need to be safe under all conditions of normal use. In particular, the system's optical output power must not exceed the MPE for the naked eye. The MPE was calculated to be 78.6 µW for 100 s of accidental exposure with 375 nm light and 986 µW for 0.25 s exposure (blinking reflex) with 440 nm light.

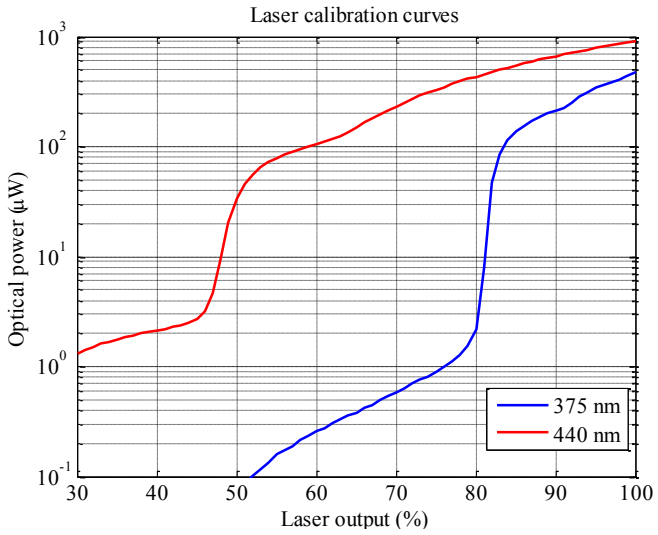

Figure 4.9 Calibration curves for both excitation wavelengths. Optical output power was measured after the fibre-optic bundle to replicate experimental conditions at clinical settings. Measurements are carried out with 1% interval in the laser output.

Although the power requirements may change from sample to sample, depending on its brightness, early measurements with reference dyes and biological samples showed that the average power typically used is well below the MPE for both excitation wavelengths. Therefore, the output power was limited in software to a maximum of approximately 25 µW for 375 nm excitation and 250 µW for 440 nm excitation. Restriction of the optical output power also has the advantage of limiting the width of the optical pulse. This is because gain-switched laser diodes inherently produce broader optical pulses as result of additional peaks in time, produced with increasing driving current [232]. Hence, operation at lower optical powers will effectively correspond to cleaner and narrower optical pulses, particular for operation close to the lasing threshold. Figure 4.10 shows IRF measurements with the 375 nm laser diode using a scattering sample of Ludox beads (420786-1L, Sigma-Aldrich, Canada), at 85 and 100% of the maximum laser output power.

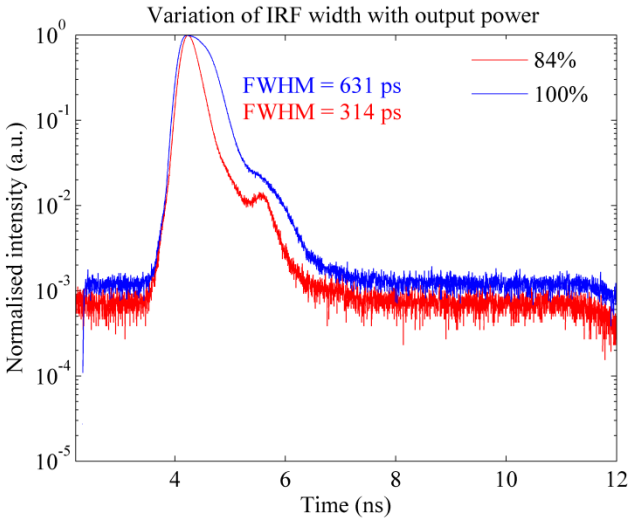

Figure 4.10 IRF measurements of a 375 nm laser diode at 80 MHz repetition rate of a scattering sample of Ludox beads. Measurements were realised in the cuvette-based system presented in Chapter 3, due to the impossibility of realising a similar measurement in the instrument presented in this chapter.

It was also observed that the lasers respond differently when switched on. In particular, we excited a sample of 4′,6-Diamidino-2-phenylindole dihydrochloride (DAPI, Sigma-Aldrich, USA) using 375 nm light and observed a gradual increase in the photon count rate until stabilisation was reached, approximately 40 seconds later, see Figure 4.11A. Similarly, a sample of Erythrosin B (Sigma-Aldrich, USA) was excited at 440 nm, although in this case we observed an immediate increase of the photon count rate (data not shown).

To confirm that this was a laser-induced artefact and not related to the sample, the experiment was repeated. However, instead of switching on the laser at the time of measurements, the laser was left on for a period while delivery of light to the sample was blocked. Upon removal of the light block and consequent excitation of DAPI, we observed an immediate increase in the detected photon count rate (see Figure 4.11B), suggesting that this behaviour is caused by some mechanism within the laser head, possibly related to temperature stabilisation. This behaviour was found to be independent of the laser driving current. Despite the variation of the photon count rate, we did not observe significant variations in the fluorescence lifetime of DAPI that can be attributed to this effect.

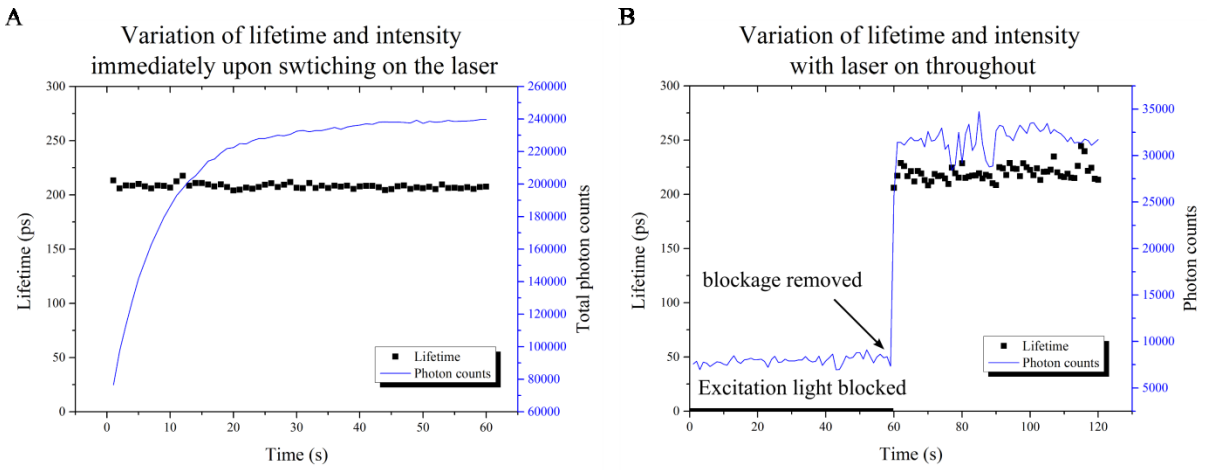

Figure 4.11 (A) Gradual increase of the photon count immediately upon switching on the laser. (B) Immediate increase in the photon count rate upon delivery of light into a sample of DAPI, having the laser on during the entire period of the experiment.

4.3.2 Instrument response function

4.3.2.1 Fluorescence lifetime

Ideally, the IRF is measured at the emission wavelength from a specimen providing an impulse shorter than the response time of the detection electronics. Therefore, the temporal response of our system was measured using reference fluorophores with known short decay characteristics. Figure 4.12 shows a typical IRF measurement using DAPI (Sigma-Aldrich, USA) with 375 nm excitation in all detection channels and Erythrosin B (Sigma-Aldrich, USA) with 440 nm excitation. At the measurement wavelengths, these reference dyes have lifetimes of approximately 200 ps, which is comparable to the pulse lengths of the lasers used.

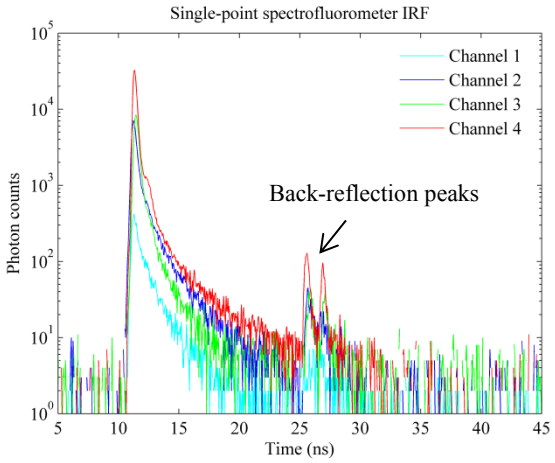

Figure 4.12 IRF measurements using DAPI (50 µM in water) and Erythrosin B (50 µM in water), at 20 MHz. The proximal end of fluorescence excitation branch was not cleaved in the probe used for these measurements, hence the presence of back-reflection peak approximately 13 ns after the main excitation peak.

From Figure 4.12, it is possible to observe the presence of additional peaks approximately 13 ns after the main peak, which is equivalent to an optical path length of 2.6 m in an optical fibre. This length corresponds to twice the length of the excitation arm of our optical fibre and therefore the additional peaks can be attributed to back-reflections in the excitation arm of the fibre-optic bundle. It is

noteworthy that these measurements were carried out using a fibre-optic bundle that was not angle cleaved at the proximal end of the fluorescence excitation branch. Figure 4.13 shows an Erythrosin B measurement at 5 MHz, using a fibre-optic bundle cleaved at 8° in the proximal end.

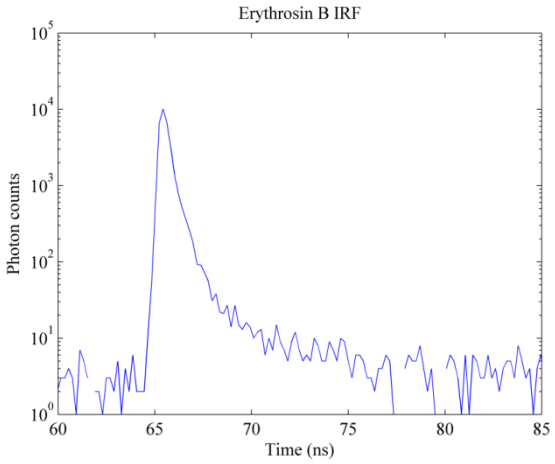

Figure 4.13 Fluorescence decay of Erythrosin B (50 μM in water) using 440 nm excitation at 5 MHz and a fibre-optic bundle cleaved at 8° to minimise back-reflections.

4.3.2.2 Diffuse reflectance

The white light source used for diffuse reflectance measurements consists of a halogen lamp that provides a continuous yet uneven spectrum of light, from the near-UV to the near infrared. Furthermore, one needs to consider that the efficiency of light transmission in the fibre-optic probe changes with wavelength. Thus, in order to retrieve the true reflectance spectrum of a sample, one needs to correct for these distortions by measuring the white light spectrum against a white reflectance target through the fibre-optic conduits. The true reflectance spectrum of a sample, I, can then be calculated according to equation 4.1, where I_0 and I_m correspond to the white light calibration spectrum and the measured sample spectrum, respectively.

$$I = \frac{I_m}{I_0} \tag{4.1}$$

Figure 4.14 shows the reflectance spectra of the white light source measured against a white reflectance standard (WS-1-SL, Labsphere, USA) and the uncorrected and corrected spectra of a healthy rat heart, measured *in vivo*.

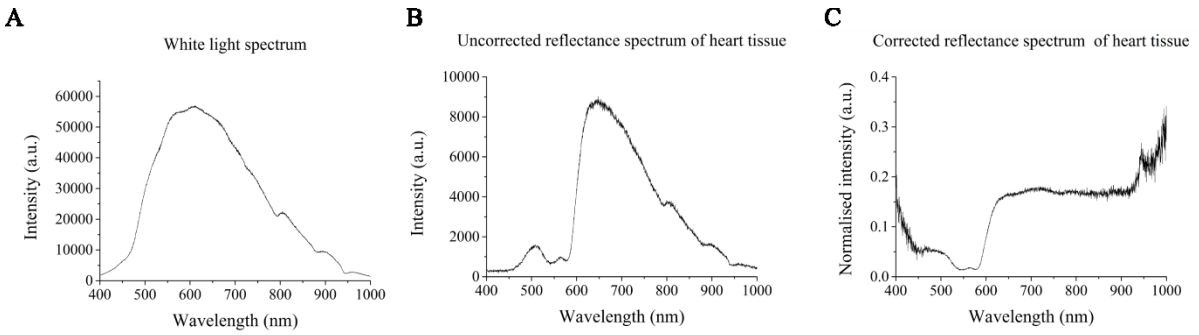

Figure 4.14 (A) Spectrum of white light source measured against a white light standard. (B) Uncorrected and (C) corrected spectra of healthy heart tissue measured *in vivo*, following equation 4.1.

4.3.3 Characterisation of fibre-optic probe

Using fibre-optic probes to deliver excitation light and collect fluorescence signal from biological samples is a well-established technique [19], [231], [150]. The fibre-optics arrangement can have a strong influence on the overall performance of the system and multiple designs have been studied and utilised depending on the end-application [231]. In the specific case of tissue measurements, it is important to maximise the volume of interrogated area as well as the collection efficiency (CE), as the autofluorescence signal is, typically, not abundant. The experimental CE of our fibre-optic probe was evaluated by measuring the fluorescence from a ~1.5 mm thick fluorescent slide (Chroma, USA) mounted on a z-translation stage (Thorlabs, USA) that allows fine adjustments of the height. The probe was mounted in a vertical position and kept fixed throughout the measurements whilst the sample z-position was adjusted in steps of 0.5 mm between each measurement. The experimental result (see Figure 4.15B) suggests that the fluorescence signal from a sample is maximised if the tip of the probe is positioned 1.5 to 2 mm away from the sample.

We compared this result against a theoretical model based on the fibre probe geometry illustrated in Figure 4.6B, consisting of three excitation fibres and fourteen collection fibres. At the sample plane, we can assume that the excitation light has a circular profile and the fluorescence signal can be detected from a circular region, as shown in Figure 4.15A. The overlapping area A between these two regions represents the effective region from where the fluorescence signal is collected and can be calculated from the following equation (see appendix A):

$$A = R^2 \cos^{-1}\left(\frac{d}{2R}\right) - d\sqrt{R^2 - \frac{d^2}{4}} \tag{4.2}$$

where d refers to the position of the collection fibre relative to the excitation fibre and R represents the radius of the circular region at the sample plane and is given by equation 4.3,

$$R = h \tan \alpha \tag{4.3}$$

where h distance from the tip of the probe to the sample and α is the angle of the acceptance cone of the optical fibres (see Figure 4.15A). To simulate the thickness of the slide (~1.5 mm), we will consider that for a given distance from the tip of the probe, the fluorescence emanates from multiple regions at different planes within the slide, and each plane is at a given distance from its surface. In our simulation, the fluorescent planes were separated by 100 µm. We have also considered the fibres to be separated from each other by a distance equal to two times the radius of a single fibre, which is a good approximation to the real case. Finally, because the intensity is inversely proportional to the square of the distance to the sample under investigation, the fluorescence intensity at the collection fibres scales with respect to excitation power by the overlapping area at the sample plane divided by the fourth power of the distance between probe and sample. Figure 4.15B shows the experimental and simulated curves of the variation of normalised collected fluorescence with distance from sample to the tip of the probe.

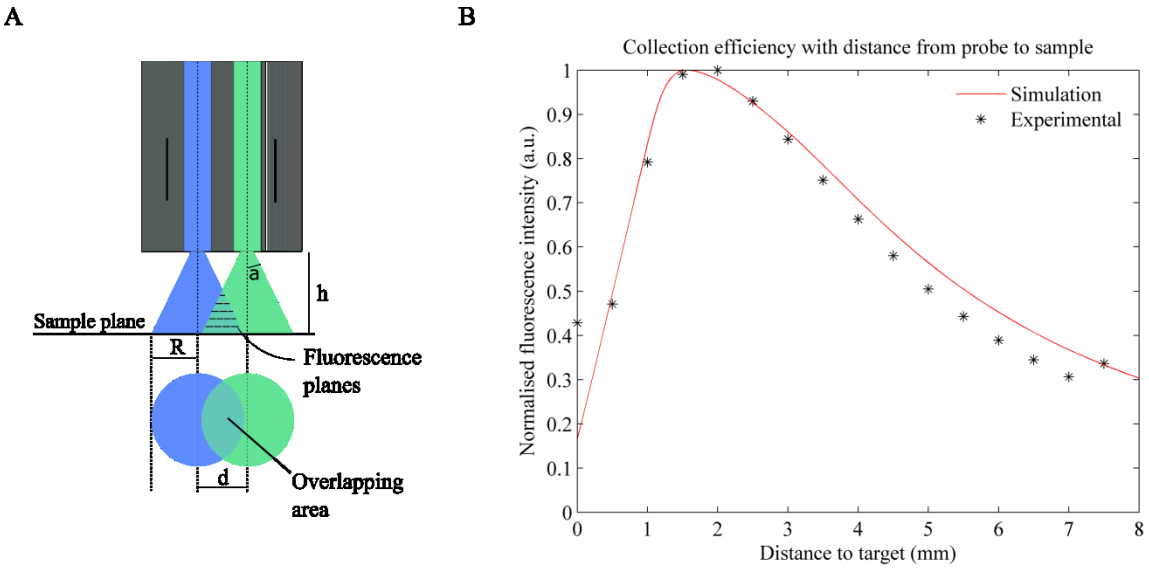

Figure 4.15 (A) Diagram of the theoretical model. (B) Variation of the collection efficiency of the probe with distance to the sample.

Although the proposed theoretical model consists of a rough approximation to the real physical case, the two curves are good agreement in respect to the position where the collection of fluorescence is maximised. The discrepancies observed, particularly at longer distances to the samples, may be attributed to heterogeneous spatial distribution of excitation light at the sample plane, resulting from multimode propagation of light in the delivery fibres. This contrasts with the top-hat profile of our simulations. It is important to note that this model only applies for a sample consisting of multiple thin layer of fluorophores rather than the whole excitation/detection volume. Moreover, optical scattering and absorption properties of the sample were not included in this model, which could influence fluorescence excitation and detection efficiency at different depths. For thick samples such as biological tissue, a more complex approach, e.g. using Monte Carlo methods to model the optical properties of the tissue, would yield more accurate results. However, despite the simplicity of our method, experimental results are in good agreement with simulation.

In a multimode fibre probe, it is not only important to assess the CE but also its temporal broadening, which can ultimately limit the temporal resolution of the TCSPC acquisition. When travelling inside a multi-mode fibre, light pulses are subjected to temporal broadening due to modal dispersion. The temporal broadening *T* can be estimated according to the following equation [232]:

$$T = \frac{n_1 l}{c}\left(\frac{n_1}{n_2} - 1\right) \tag{4.3}$$

where n_1 and n_2 refer to the refractive indexes of the fibre core and cladding respectively (n_1 = 1.48, n_2 = 1.46), l represents the fibre probe length (l = 1.3 m) and c refers to the speed of light. The temporal broadening caused by this fibre bundle is approximately 90 ps between excitation light coupling at the proximal end and delivery to the sample. Similarly, fluorescence light from the sample will be dispersed by the same amount when traveling towards the detectors. Hence, the overall temporal dispersion is approximately 180 ps.

4.3.4 Fluorescence lifetime measurements of reference fluorophores

In order to check the temporal accuracy of the instrument, a number of fluorescent dyes with single exponential decay characteristics were measured and compared against measurements in the cuvette-based spectrofluorometer, described in section 3.3.1.3.

All measurements were carried out using a laser repetition rate of 20 MHz. In the fibre-optic probe-based time-resolved spectrofluorometer, DAPI and Erythrosin B in solution were used as reference fluorophores for 375 nm and 440 nm excitation wavelengths, respectively. For the cuvette-based system measurements, a solution of Ludox beads (420786-1L, Sigma-Aldrich, Canada) was used to measure the IRF at the excitation wavelength. It is also important to point out that measurements in the cuvette-based system are carried out at the magic angle using vertically polarised excitation light, hence eliminating contribution of molecular reorientation to the fluorescence decay. A total of 3 acquisitions were taken for each fluorophore. All datasets were fitted to a single exponential decay model, as described in section 2.4. Results are presented in Table 4.2.

Table 4.2 Average lifetimes of reference fluorophores in solution measured in the cuvette- and fibre-optic based systems. All measurements were realised at room temperature. In the cuvette-based instrument, fluorescence was detected at 460 nm and 525 nm for UV and blue excitations, respectively.

		Literature	Cuvette-based instrument	Fibre-optic probe-based instrument		
Dyes	**Excitation λ (nm)**	**τ (ns)**	**τ (ns)**	**CH1 τ (ns)**	**CH2 τ (ns)**	**CH3/4 τ (ns)**
Stilbene-3 (in water)	375	1.2 – 1.4 [a]	1.20 ± 0.01	1.17 ± 0.02	1.17 ± 0.02	1.17 ± 0.03
POPOP (in Ethanol)	375	~1.3 [b]	1.33 ± 0.01	1.24 ± 0.02	1.24 ± 0.02	1.24 ± 0.02
Coumarin 6 (in Ethanol)	440	2.4 - 2.5 [c]	2.56 ± 0.01	-	-	2.48 ± 0.01
Coumarin 153 (in Ethanol)	440	4.3 [d] (in methanol)	4.64 ± 0.01	-	-	4.67 ± 0.02
Coumarin 314 (in Ethanol)	440	3.46 [e]	3.41 ± 0.01	-	-	3.45 ± 0.02

[a] from references [233], [234]; [b] from references [6], [235]; [c] from references [236], [237]; [d] from reference [238]; e from reference [239]

Overall, the fluorescence lifetimes extracted are in reasonable agreement between systems and with those found in literature. In particular, we measured shorter fluorescence lifetimes in the fibre-optic probe-based that are more discrepant for POPOP and Coumarin 6 from those measured with the cuvette-based system. The fibre-optic probe-based instrument does not have suitable optics to realise polarisation resolved measurements and thus the fluorescence reaches the detectors with an arbitrary orientation. As consequence, the fluorescence lifetimes extracted for this system can have contributions from different polarisation states, which could explain the shorter fluorescence lifetime measured for these dyes in comparison with cuvette-based measurements [240]. There are other factors that can influence the fluorescence decay in each system and eventually contribute to any deviations in the measured lifetime. The most relevant is related to the usage of non-ideal reference fluorophores in the analysis of fluorescence decay data measured using the fibre-optic probe-based instrument, which are not capable of describing the system's behaviour as accurately as a measurement of system IRF at the excitation wavelength. We also note that we have measured a longer fluorescence lifetime for Coumarin 153 relative to values reported in literature, although this difference may be attributed to the usage of different solvents.

4.4 Conclusions and summary

In this chapter, the development and characterisation of a compact and portable instrument was presented, combining spectrally resolved "gold-standard" TCSPC detection and white light reflectometry to realise single-point autofluorescence and reflectance measurements of biological tissue using a fibre-optic probe.

The whole system is based on two pulsed laser diodes emitting at wavelengths selected to excite endogenous fluorophores of interest, namely NADH, FAD and collagens, which can provide label-

free information of the structural and biochemical compositions of biological tissue. Moreover, the system utilises multichannel TCSPC detection to realise spectrally- and temporally-resolved autofluorescence measurements, offering the advantages of both steady-state and time-resolved techniques. The system also includes a white light source and a compact spectrometer to realise diffuse reflectance measurements which can provide label-free morphological and physiological information that is not available in the autofluorescence readout, therefore increasing the specificity of the detection. Hence, autofluorescence and diffuse reflectance spectroscopy techniques should be regarded as complementary methods to enhance the specificity of the detection. To facilitate light delivery and collection, the system comprises a flexible fibre-optic bundle that is easy to handle by clinicians and allows measurements from anatomical regions that are of difficult access.

A key point of this instrument is related to the fact that it provides single-point readouts rather than images. The usage of single point instruments yields some advantages relative to imaging systems, as follows:

- **Data acquisition time**. In an imaging system one fluorescence decay is recorded per pixel, whilst in point spectroscopy only a single decay is collected per acquisition. Hence, to achieve the same SNR, imaging systems require longer acquisition times than single point measurements. As result, single point measurements can more easily obtain sufficient photons to analyse complex fluorescence decay profiles, such as those typically found in tissue.
- **Sensitivity to motion**. Imaging modalities are more sensitive to motion, which can produce artefacts in the final results. This is of particular interest for *in vivo* clinical studies of the heart. Although some techniques have been developed to compensate for tissue motion, e.g. [200], [241], they also increase the complexity and cost of the instrumentation.
- **Complexity**. In general, imaging systems are more technically challenging to implement and require greater optimisation and fine-tuning [44].

The main disadvantage of point spectroscopy is clearly related to the lack of spatial resolution, although in some clinical applications this may not be necessary. Overall, because of the advantages outlined above, single-point spectroscopy offers a quicker pathway relative to image-based spectroscopy towards translation of clinical instrumentation from bench to bedside, where the clinical utility of the spectroscopic signals can be explored, which is the ultimate goal of this project.

As previously mentioned in this chapter, two of these instruments were developed to be deployed in clinical settings. The following chapters of this thesis will discuss the implementation of these instruments at the Kennedy Institute of Rheumatology for systematic studies of cartilage degradation

and at NHLI for studies of heart disease, with a particular emphasis for *in vivo* studies of myocardial infarction in rats. Concerning translation of this technology into clinical practice, Chapter 6 also discusses the adaptation of this system to be used in *in vivo* human clinical trials during surgical procedures.

5 Autofluorescence of articular cartilage

In this chapter the application of time-resolved autofluorescence spectroscopy and white light reflectometry to the study of articular cartilage is presented. This study was carried out in collaboration with Dr Yoshifumi Itoh's Group at the Kennedy Institute of Rheumatology from the University of Oxford.

The objective was to investigate the autofluorescence signature of articular cartilage and therefore demonstrate the potential of this technique as a clinically viable tool to study the development and diagnosis of osteoarthritis. Osteoarthritis (OA) is a chronic and progressive disease of the joint characterised by irreversible destruction of articular cartilage for which there is currently no effective treatment. Early detection of OA and its progression is therefore highly desirable but to date there are no appropriate non- or minimally-invasive techniques available. Our studies in enzymatically degenerated porcine and murine cartilage, which serve as models for OA, suggest that autofluorescence lifetime is sensitive to disruption of two major extracellular matrix components, aggrecan and collagen. Preliminary autofluorescence and diffuse reflectance data were also obtained from *ex vivo* human tissue presenting naturally occurring OA. Overall, these studies indicate that autofluorescence lifetime may offer a non-invasive readout to monitor cartilage matrix integrity that could contribute to future diagnosis of early cartilage defects as well as monitoring the efficacy of therapeutic agents.

Part of the work presented in this chapter resulted in the publication of 1 journal article (Manning et al, *Matrix Biology*, 2013) and 6 oral presentations.

Outline

- Introduction to articular cartilage and its underlying biology, including the role of aggrecan and collagen in osteoarthritis development.
- Autofluorescence measurements of porcine articular cartilage.
- Autofluorescence measurements of murine articular cartilage.
- Autofluorescence and diffuse reflectance measurements of human articular cartilage.
- Conclusions and summary.

5.1 Introduction

Arthritis is the biggest cause of pain and disability in the UK and each year 20% of the general population seeks treatment for this condition [242]. The most common form of arthritis is

osteoarthritis (OA) and it is estimated that a third of people aged 45 and over have sought treatment for this disease in recent years [242]. OA is a chronic and progressive disease of the joint characterised by degenerative morphological and structural alteration of the tissue, ultimately leading to erosion of articular cartilage that is typically accompanied by pain and occurs most frequently in the knee and hip joints [171], [243].

Articular cartilage is a vital tissue to maintain joint function. It is a specialised tissue with a single cell type, the chondrocyte, and is predominantly composed of extracellular matrix (ECM) components including type II collagen and aggrecan, with other minor components including small leucine rich proteoglycans and type IX and XI collagens [244]–[246]. The mechanical and structural properties of cartilage tissue are completely dependent of its ECM: aggrecan retains water in the cartilage, endowing it with the ability to resist compression, while collagen provides the tissue with structure and tensile strength [247]. It is believed that in early OA, aggrecan is depleted from the tissue first and collagen degradation follows. While aggrecan loss can be reversed, collagen degradation is mostly irreversible and results in major structural and functional damage to the tissue [248], which can ultimately result in the replacement of the tissue with a prosthetic joint.

Current diagnosis of OA traditionally rests on physical examination and imaging studies. Various symptoms can be associated with OA including pain, stiffness and decreased motion [243], [245]. However, the listed symptoms can also be associated with other diseases of the joint such as rheumatoid arthritis, gout or other conditions caused by traumatic injuries and therefore further evaluation is necessary [243]. Although current imaging modalities utilised to aid OA diagnosis, e.g. X-Ray imaging and Magnetic Resonance Imaging (MRI), can provide relevant structural information of the tissue, alterations associated with OA are often reported in the mid to late stages of the disease progression when changes in tissue are no longer reversible [171]. An alternative approach is to realise arthroscopic surgery, although this also suffers from the limitations outlined above and is more commonly employed as preventive treatment procedure. Hence, detection of early structural and biochemical changes in articular cartilage associated with OA would be highly desirable and could offer new prevention and treatment options.

The application of optical spectroscopy techniques to OA research is still at an early stage and only a few studies have been reported in recent years, mostly associated with diffuse reflectance spectroscopy. In particular, Oberg et al [145] introduced this technique as a way of quantifying cartilage thickness on the principle that optical absorption is different in cartilage and subchondral bone. Further improvements to this method have already been reported [172], [249] and have demonstrated promising results towards detection of OA-induced degradation in *ex vivo* human samples. Other relevant investigations include those by Kinnunen et al, in *ex vivo* human OA samples

[250] and in enzymatically digested bovine cartilage [251], in which they demonstrated that diffuse reflectance is sensitive to the level of degradation of articular cartilage. All studies aforementioned utilised white light illumination and detection in the visible range of the spectrum. There are also a few reports of near-infrared reflection spectroscopy applied to OA investigation using *ex vivo* animal models [227], [228], [252], [253] or *ex vivo* human samples [254]. Other optical spectroscopy techniques have also been applied to articular cartilage and OA research, reporting the application of steady-state fluorescence spectroscopy utilising exogenous labels to provide contrast [171], [243]. Overall, although the results of the studies outlined showed promise, intensity-based measurements alone can be sensitive to variations in the illumination pattern, background light, heterogeneous sample absorption and scattering and so are difficult to compare between samples and patients [140], [203]. Moreover, exogenous contrasting agents can potentially introduce toxicity and be harmful to the biological system and therefore their application is undesirable [70], [140].

As discussed in Chapter 4, autofluorescence lifetime spectroscopy is an inherently ratiometric technique and thus relatively insensitive to the artefacts outlined above. Furthermore, it has shown potential for tissue diagnosis in a number of applications, both ex vivo [17], [38], [176], [255] and in vivo [14], [19], [256], [257]. Here, we hypothesise that the fluorescence lifetime of articular cartilage changes with cartilage degradation and therefore it may be used to detect cartilage defects at early stages of disease progression. We report studies of the autofluorescence signature of articular cartilage both in healthy and diseased conditions that build on preliminary work carried out in our group [258], [259]. This includes autofluorescence lifetime studies of digested cartilage of both animal and human samples, *ex vivo* animal models and *ex vivo* human samples of naturally occurring OA.

5.2 Cartilage

Cartilaginous tissues can be found in many areas of the body, e.g. joints, ear, nose or bronchial tubes, and are classified histologically as hyaline, elastic and fibrocartilage, depending on their molecular composition [244]. Elastic cartilage can be found in e.g. ear and larynx whereas fibrocartilage is present in e.g. intervertebral disks. Hyaline cartilage is the most predominant form of cartilage and is most commonly associated with the skeletal system, being found on the articulating ends of the long bones. A comprehensive discussion of the different types of cartilage is outside the scope of this report and can be found in references [244], [260]. Because only hyaline articular cartilage is of interest for OA studies, it will be referred to as cartilage or articular cartilage hereafter.

Articular cartilage is a highly specialised connective and avascular tissue with unique biomechanical properties that provide a smooth, lubricated and wear-resistant surface for articulation, thus facilitating the transmission and distribution of loads, as well as great resilience and high compressive and shear resistance. It consists of a single type of cells, chondrocytes, that populate (at low density)

and are responsible for maintaining the integrity of an extensive ECM that is primarily composed of water, type II collagen and proteoglycans, with other noncollagenous proteins and glycoproteins present in lesser amounts [244], [245]. Because of its low cellularity, the ECM is relatively homogeneous throughout the cartilage, being mostly composed of a network of fibrillar collagens that give the tissue its shape, tensile strength and stiffness, whilst proteoglycans provide hydration to the tissue. This relatively simple composition is believed to be the cause of the limited regenerative capacity of articular cartilage [261]. Because cartilage is avascular, progenitor cells from blood cannot penetrate damaged regions and contribute for the healing process. Consequently, defects are not repaired and can contribute for further degradation, ultimately progressing to severe forms of OA [261], [262]. The following sections give an overview of the articular cartilage structure and composition.

5.2.1 Structure

Cartilage has a well-defined layered structure that can be functionally and morphologically divided in four zones (see Figure 5.1): the superficial or tangential zone; the middle zone; the deep zone; and the zone of calcified cartilage [245], [263]. The morphology of deeper layers in articular cartilage is substantially different than that of superficial layers, particularly in the pattern of fibrillar collagen.

The superficial layer has the highest collagen concentration found in articular cartilage and consists of densely packed collagen fibrils arranged tangentially to the articular surface and chondrocytes of elongated appearance. This composition provides most of the hard-wearing properties of cartilage, enabling it to resist the harsh environment imposed by articulation, thus shielding deeper layers from erosion.

The middle zone represents 40 to 60% of the cartilage thickness and is characterised by a less organised and dense distribution of the collagen fibrils, which are typically arranged obliquely relative to the articular surface. Chondrocytes in this layer are more rounded than in the superficial layer and can be more sparsely distributed. The middle layer has a greater compressive modulus than the superficial layer thus providing greater resistance against compressive forces.

Of all articular cartilage layers, the deep layer is the one that provides highest resistance against compressive forces, due to the perpendicular arrangement of the large collagen fibrils relative to the articular surface. The collagen fibrils penetrate the calcified cartilage layer through an irregular plane known as tidemark and eventually enter the subchondral bone where they are firmly attached. This feature is of utmost importance endowing articular cartilage the ability to resist shearing forces, which would otherwise tend to remove the cartilage away from the subchondral bone surface.

The size and thickness of articular cartilage varies significantly with species, going from ~100 μm in mice to ~3 mm in elephants [246]. For example, human articular cartilage is 2 to 4 mm thick, depending on its location in the body and the load that it is subjected to [245], [246], [264], [172].

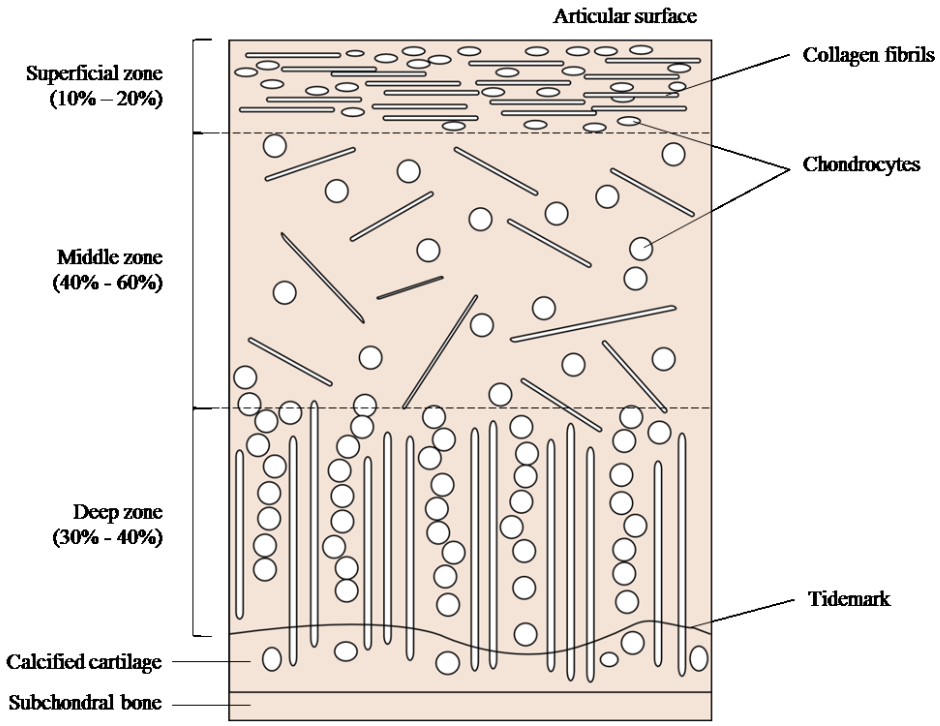

Figure 5.1 Simplified stratified structure of articular cartilage. Adapted from [245].

5.2.2 Composition

5.2.2.1 Chondrocytes

The chondrocyte is the only cell type found in healthy articular cartilage. Chondrocytes are believed have a critical role in the regulation of the ECM, including biosynthesis, maintenance and turnover of the ECM components, such as collagens and proteoglycans [265]. Despite their critical function, chondrocytes represent only up to 5% of the cartilage total volume, have no detectable proliferation and remain at a relatively low metabolic activity [266]. The low metabolism is believed to be essential to maintain the ECM integrity, although it is also pointed out as one of the causes of the limited regenerative capacity of cartilage [261].

5.2.2.2 ECM

The important biomechanical properties of articular cartilage are primarily sustained by the ECM major components: water, type II collagen and proteoglycans of which the most relevant and abundant is aggrecan. Other classes of molecules can be found in the ECM, although in minor concentrations and with lesser relevant functions. These include lipids, noncollagenous proteins or other types of collagens, such as type VI, IX, X and XI [247]. For our investigation, collagen fibrils and aggrecan

within the articular cartilage ECM are of particular relevance, as these molecules are intimately involved in key mechanisms of OA, as discussed below.

5.2.2.2.1 Collagens

Collagen is a key protein in musculoskeletal stability, providing the mechanical properties that permit connectivity between tissues. Different types of collagen are expressed in articular cartilage of which the most relevant is type II collagen, corresponding to over 90% of the total collagen content in healthy articular cartilage in adults [247]. Collagen fibrils exist in the ECM as heteropolymers consisting primarily of collagen type II filaments, with collagens IX and XI in lesser amounts. The structure of a collagen heterofibril is illustrated in Figure 5.2A. Other forms of collagen can be found in healthy cartilage, such as types VI and X, although these only represent a small fraction (less than 5%) of the overall collagen content [247], [267]. Interfibrillar connections are thought to be mediated by collagen type IX that covalently binds to the surface of collagen type II fibrils thus enforcing a mechanical restriction in the fibrillar network [245], [247], [267], [268]. Intra- and intermolecular crosslinks generate a dense collagen matrix that positively contributes to the tensile strength of the tissue and in which chondrocytes, proteoglycans and other ECM molecules are entrapped, see Figure 5.2B. The structural integrity of articular cartilage depends heavily on this extensive crosslinked collagen framework and its characteristic organisation in different layers of the tissue [269]. It is believed that loss of integrity of the fibrillar network is the key step for an irreversible degradation of articular cartilage in joints [245], [247]. Hence, monitoring the biological mechanisms involving the fibrillar collagen network is of utmost importance towards the validation of therapeutic agents for prevention and early treatment of OA.

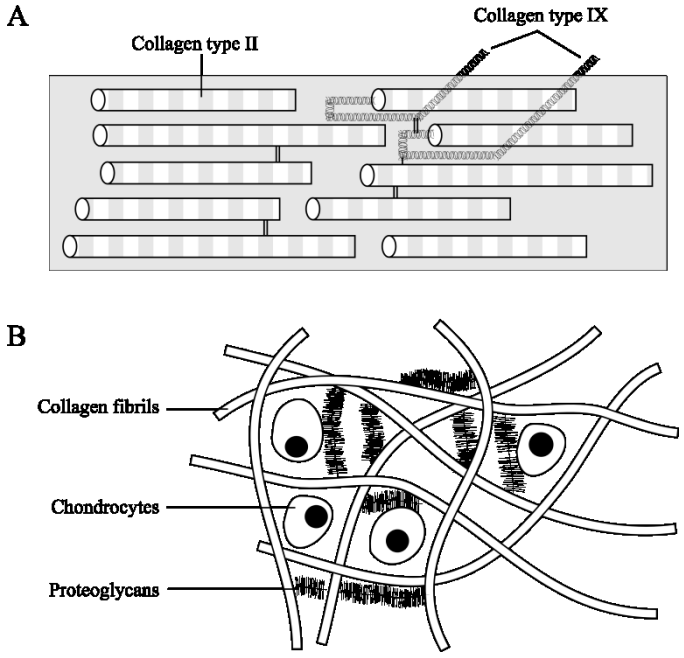

Figure 5.2 (A) Simplified structure of a collagen fibril. (B) Schematic representation of the arrangement of the ECM components in articular cartilage.

5.2.2.2.2 Aggrecan

Cartilage contains a variety of proteoglycans that are essential to maintain the integrity of the tissue and modulate its metabolism. Aggregan is by far the most abundant proteoglycan in articular cartilage, although a number of other proteoglycans exist in the ECM in much lower concentrations and thus are beyond the scope of this report.

Aggrecan is the major structural proteoglycan found in the cartilage ECM and consists of a central core protein to which glycosaminoglycan (GAG) chains are covalently linked [260], [270], [271]. The core protein contains three globular domains (G1, G2 and G3) and an interglobular domain (IGD) that spans about 150 amino residues (see Figure 5.3A) [260]. In articular cartilage, the G1 domain of aggrecan molecules binds non-covalently with hyaluronan to form very large and stable macromolecular complexes (see Figure 5.3B) that endow the articular cartilage with water absorbing properties [272]. This is because the highly negatively charged GAG chains are accompanied with positively charged ions, thus creating an ion concentration gradient between cartilage and surrounding tissue. Hence, there is a large osmotic swelling pressure that draws water into the cartilaginous tissue and forms a well-hydrated aggrecan-rich gel, which provides the tissue with important lubricant and shock absorbing properties [267], [273], [274]. In addition, together with the collagen fibrils, it forms a stiff and resistant network that provides the tissue with a great resistance to deformation. Maintenance of aggrecan content is therefore critical to the function of the tissue. Aggrecan depletion in articular cartilage has been associated with cleavage of the core protein in the IGD, first by Matrix Metalloproteinases (MMPs) followed by A Disintegrin And Metalloproteinase with ThromboSpondin Motifs (ADAMTSs) [272].

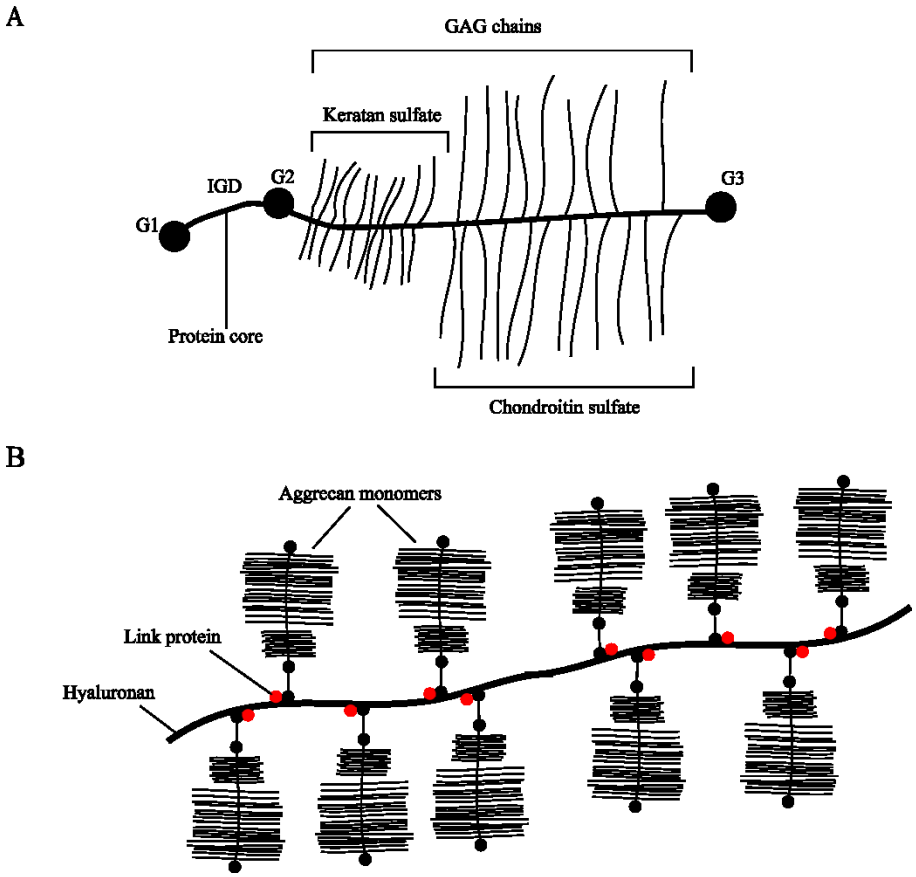

Figure 5.3 Simplified representations of (A) an aggrecan monomer structure and (B) a proteoglycan aggrecate.

5.3 Osteoarthritis (OA)

Osteoarthritis (OA) is a degenerative disease of the joint involving a number of biomechanical and biochemical abnormalities that cause progressive loss of structure and functionality of articular cartilage and ultimately degradation of the subchondral bone [275]. The precise mechanisms of cartilage degradation are still not yet fully understood and therefore OA remains a chronic disease for which there is little, if any, effective treatment [276], [277]. OA can affect any joint in the body, although joints under frequent high loads and stress are more likely to develop the condition, e.g. hip or knee. A number of factors have been associated with the development of the disease. These include age, gender (OA is more common in women), obesity, high physical activity, occupational activities involving frequent heavy weight lifting and previous traumatic injury [275], [276], [278], [279]. Figure 5.4 illustrates the difference between healthy and OA articular cartilage in a knee joint.

Overall, although the knowledge of clinical OA has grown in recent years, the biological mechanisms behind the genesis and development of the disease are still not completely understood, thus hampering the development and validation of effective therapeutic agents [245], [277]. The following sections describe the basic biological mechanisms involved in cartilage degradation during OA as well as the features of the several stages of disease progression.

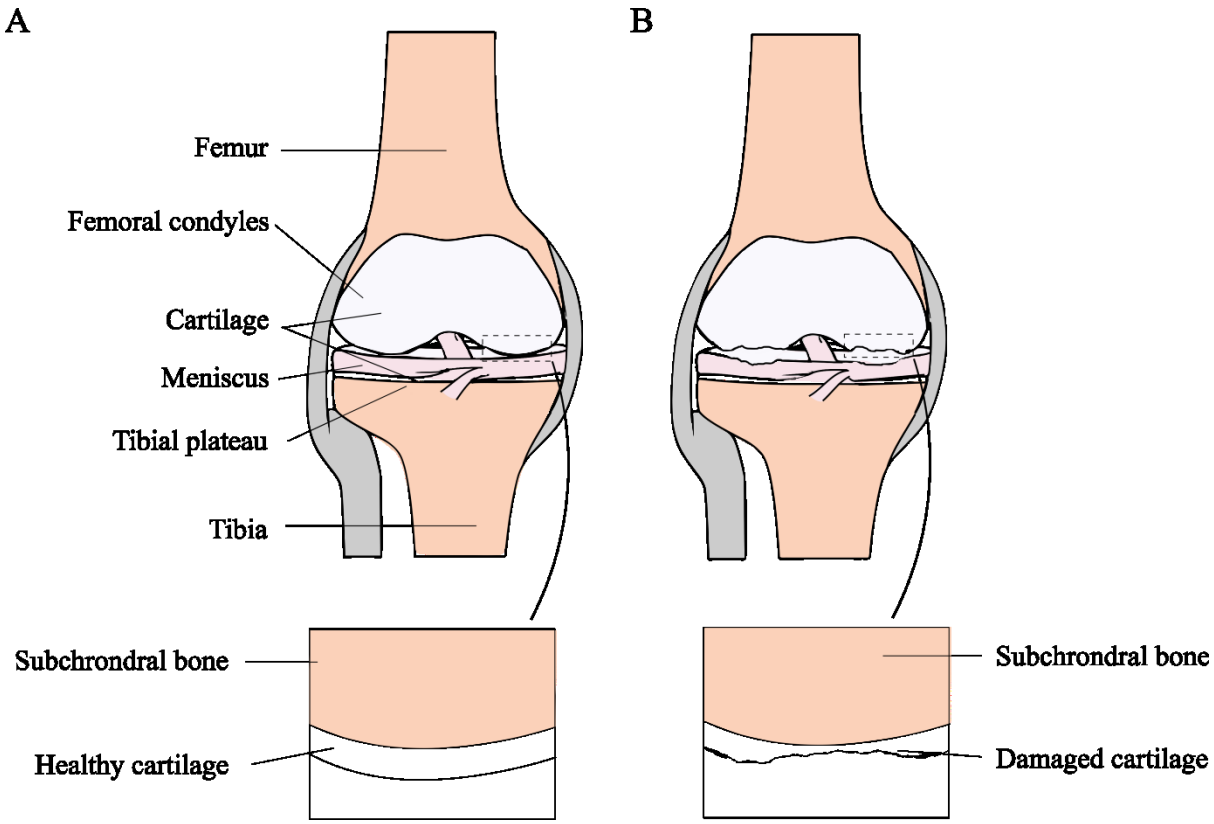

Figure 5.4 Simplified representation of (A) healthy knee joint and (B) OA knee joint. Panels at the bottom show the cross section view at the interface subchrondral bone-cartilage in femoral condyles.

5.3.1 Basic mechanisms of OA

Although OA is recognizably driven by mechanical abnormalities, it is believed that the degradation of the articular cartilage ECM is a chemically mediated process, resulting from the proteolytic activity of key digestive enzymes such as MMPs and ADAMTSs [280], [281].

In healthy articular cartilage, a balance between anabolic and catabolic processes maintains the integrity and homeostatic state of the tissue [265]. However, in OA, it has been demonstrated that the catabolism is enhanced over anabolism, due to the overexpression of MMPs and ADAMTSs by the chondrocytes that results in loss of collagen and proteoglycans [265], [281], [282]. There are multiple factors that can stimulate the overexpression or activation of digestive enzymes. These include mechanical loads, inflammatory reactions, reactive oxygen species and aging [245], [281]. In particular, inflammation of the synovial membrane is believed to be of great relevance in OA progression. Synovial inflammation is promoted by the accumulation of end-products of the digestive action of matrix components by MMPs and ADAMTSs. Cytokines and growth factors like tumour necrosis factor (TNF)-α, which are produced by the synovial membrane, have been shown to modulate chondrocyte metabolism by enhancing the biosynthesis of MMPs and ECM components and inhibiting the synthesis of MMP inhibitors [248]. This effectively results in a vicious cycle: cartilage degradation provokes synovial inflammation which, in turn, promotes further degradation.

In summary, chondrocytes are the primary cellular sources of digestive enzymes that degrade the cartilage ECM and their activity is believed to be regulated by inflammatory cytokines. In disease, collagen is primarily degraded by collagenases belonging to the MMPs family - particularly MMP-1 and MMP-3 - and aggrecan by MMPs and ADAMTSs [281], [282]. It is believed that aggrecan is depleted in the early stage of OA by the action of MMPs and aggrecanases belonging to the ADAMTSs family, which is followed by collagen degradation.

5.3.2 Disease progression

The pathological progression of OA is typically divided in three stages. In the first stage, commonly referred to as early OA, the matrix-network is degraded by proteolytic activity [248], [276]. As result of the proteoglycan digestion, the matrix becomes more permeable and the water content increases. Hence, the structure of the collagen network is damaged, which leads to reduced stiffness of the tissue [276]. This process is initiated by mechanical degradation of the most superficial layers of the cartilage. In moderate OA, the erosion of the articular surface is accompanied by the release of breakdown products into the synovial fluid and compensated by the upregulation of the chondrocyte metabolism that results in the overexpression of digestive enzymes and matrix components [248], [276]. Finally, in advanced OA, synovial inflammation occurs and catabolism becomes predominant over anabolism. In consequence, the cartilage structure is progressively lost. Ultimately, the subchondral bone is damaged, resulting in deposition of type I collagen - which is produced by the chondrocytes - and subsequent formation of fibrocartilage [276], [283].

5.4 Autofluorescence in articular cartilage

Autofluorescence in articular cartilage has been demonstrated to be primarily due to crosslinks between collagen molecules, in particular pyridinoline and pentosidine [70], [117]. Although these crosslinks provide an excitation band in the UV region of the spectrum, previous studies have demonstrated that articular cartilage can also be excited with wavelengths up to ~500 nm [121]. Collagen type II also contains a few aromatic amino acids, including 7 tryptophans, 10 tyrosines and 25 phenylalanines, that can contribute to the overall autofluorescence signal of cartilage, although in lesser amounts [284].

In terms of fluorescence lifetime, collagens – and collagen type II in particular – have been demonstrated to yield decay characteristics that are highly dependent not only of the excitation and emission wavelengths but also of the source of collagen itself [121]–[123]. Previous work in our group has demonstrated that human articular cartilage yields a mean lifetime of approximately 1.4 ns [258]. However, these measurements were realised in fixed tissue and therefore may not be representative of autofluorescence lifetime in untreated healthy cartilage. Recently, we have published a study of autofluorescence lifetime in porcine articular cartilage, for which we measured a much

longer fluorescence lifetime of approximately 10 ns [80]. The work presented in the following sections aims to build on this initial work and to develop a more comprehensive knowledge of the articular cartilage autofluorescence signature.

5.5 Autofluorescence lifetime of porcine articular cartilage

In order to test the hypothesis that autofluorescence lifetime is sensitive to cartilage degeneration we investigated the autofluorescence lifetime signature of articular cartilage from porcine trotter joints. Porcine articular cartilage has comparable mechanical properties and thickness to human articular cartilage [285], [286], thus representing a very convenient test sample for our investigations.

The following sections present the results of our investigations in healthy and digested porcine articular cartilage samples. It should be noted that the experiments reported here were realised *in vitro*. Therefore, they do not reproduce the harsh environment of the joint and should merely be regarded as proof of concept for our hypothesis.

5.5.1 Materials and methods

5.5.1.1 Sample preparation

Porcine articular cartilage samples were obtained from trotter joints of freshly slaughtered pigs delivered from the abattoir. Upon arrival, the trotters were immersed in 4% Virkon for disinfection for approximately 1 hour and then thoroughly washed in PBS. The skin was then removed from the top side of the trotter and an incision was made along the metacarpophalangeal joint intersection. The cartilage surface was exposed by cutting through the ligaments of the joint. For studies presented in sections 5.5.2.1 and 5.5.2.2, which will be referred to as "Protocol A" hereafter, fragments of cartilage tissue (approximately 5 mm x 5 mm x 1 mm) were removed from the surface of the joint using a scalpel. For studies presented in section 5.5.2.3, i.e. "Protocol B", cartilage was left attached to the metacarpal bone which was cut distally using a hacksaw. In both cases, cartilage samples were thoroughly washed in PBS before immediate use or storage at -80^{o}C for later use.

5.5.1.2 Instrumentation

The experiments described in this section were carried out using the cuvette-based time-resolved spectrofluorometer with the fibre-optic probe extension described in Chapter 3. Measurements of cartilage extracts (protocol A) were realised at 355 nm excitation light and 80 MHz repetition rate provided by the frequency tripled Nd:YVO4 laser (Vanguard, Spectra-Physics, USA) and fluorescence from the sample was measured at 420 nm. For autofluorescence lifetime measurements of localised lesions in the cartilage surface (protocol B), illumination light was delivered at 375 nm by the laser diode (LDH-P-C-375B, Picoquant GmbH, Germany) installed in the system, operating at 5

MHz. In this case, fluorescence from the sample was measured at the 460 nm. An explanation for alterations of excitation wavelength and repetition rate is provided below, in section 5.5.2.1.

5.5.1.3 Data analysis

5.5.1.3.1 Fluorescence decay analysis

Autofluorescence lifetime data of murine articular cartilage was fitted to a double exponential decay model, as discussed in section 2.4, using a scattering sample of Ludox beads (420786-1L, Sigma-Aldrich, Canada) to record the system IRF at the excitation wavelength.

5.5.1.3.2 Statistical analysis

All results are expressed as mean ± standard deviation (SD). Statistical analysis was computed using paired two-tailed Student t-tests, unless otherwise stated. The Student's t-test is a commonly used statistical tool that compares the means of two datasets relative to the variation in the data. If the p-value associated with the t-test is lower than a predefined threshold (typically $p < 0.05$), then the two datasets are considered to be different. If the p-value associated with the t-test is larger (i.e. $p > 0.05$), then one can conclude that the two datasets are not different. In our experiments, a p-value smaller than 0.05 was considered to be statistically significant. For convenience, the following notation was used to identify statistical significance between two sets of data: * $p < 0.05$; ** $p < 0.01$; *** $p < 0.001$; **** $p < 0.0001$.

5.5.2 Results and discussion

5.5.2.1 Healthy porcine articular cartilage

In order to be able to detect any changes in the fluorescence properties of cartilage following degradation, we first investigated the autofluorescence signature of healthy cartilage. Figure 5.5 shows the fluorescence emission spectrum and a typical fluorescence decay curve of a healthy porcine articular cartilage sample.

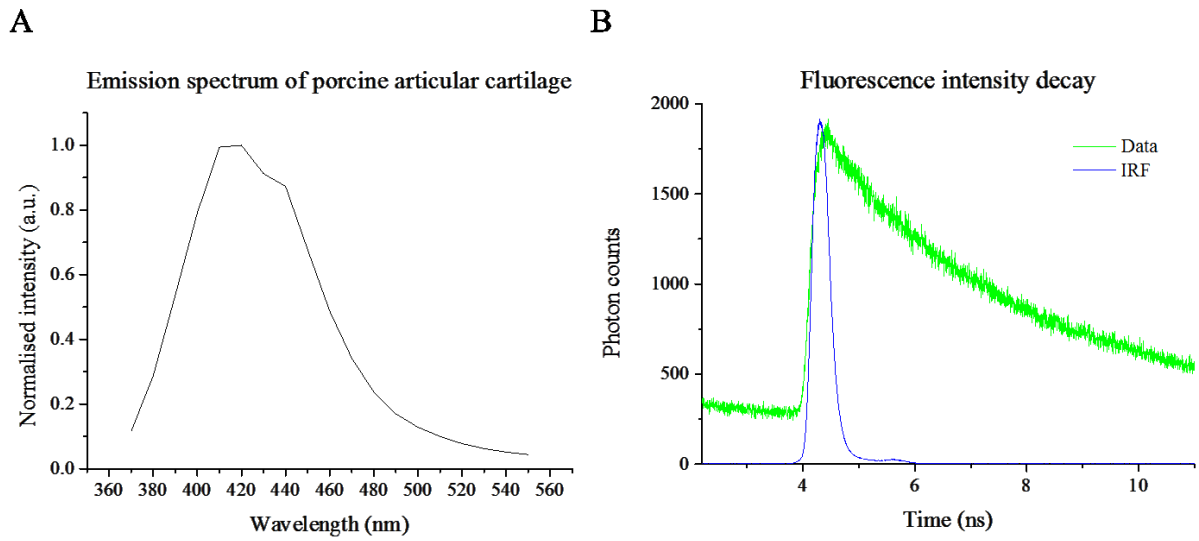

Figure 5.5 (A) Fluorescence emission spectrum and (B) representative fluorescence decay (measured at the maximum fluorescence emission peak) of a healthy articular cartilage explant excited at 355 nm. Measurements of the fluorescence emission spectrum were carried out betwwen 370 nm and 550 nm, in 10 nm intervals.

Figure 5.6 shows the distribution of the mean autofluorescence lifetime for articular cartilage measurements (n = 51). The autofluorescence lifetime was found to vary between different areas of cartilage and different cartilage pieces, suggesting a different structure or chemical environment, potentially related to the orientation of the collagen fibrils.

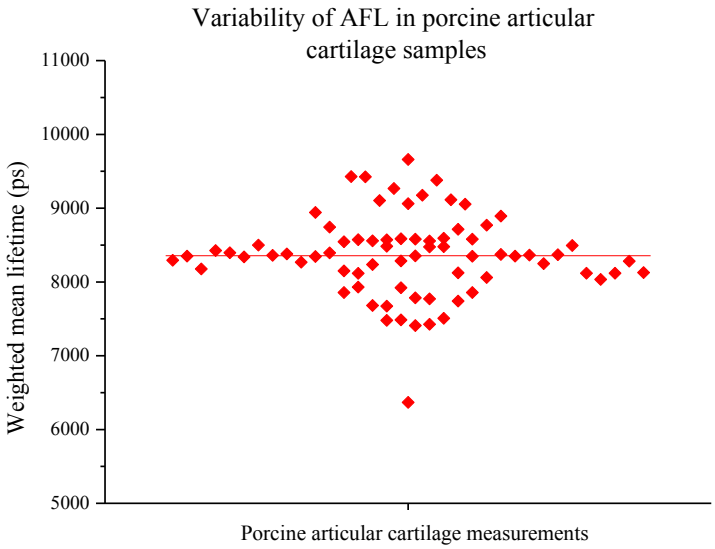

Figure 5.6 Dot plot showing the heterogeneous distribution of the autofluorescence lifetime in articular cartilage. Horizontal bar denotes average of measurements (n = 51). Data points are spread along the x-axis for better visualisation of each individual measurement, i.e. shape of the data in the x-axis carries no "physical meaning". Data were fitted to a double exponential decay model.

The temporal decay profile of each single point measurement was fitted to single, double and triple exponential decay models and the corresponding fitting parameters are presented in Table 5.1.

Table 5.1 Fitting parameters for single, double and triple exponential decay models, for a total of n = 51 measurements.

Parameter	Single exponential	Double exponential	Triple exponential
τ_1 (ns)	5.54 ± 0.24	1.53 ± 0.13	0.26 ± 0.09
β_1	-	0.18 ± 0.02	0.01 ± 0.01
τ_2 (ns)	-	9.87 ± 0.69	1.87 ± 0.09
β_2	-	0.82 ± 0.02	0.21 ± 0.02
τ_3 (ns)	-	-	11.79 ± 0.75
β_3	-	-	0.78 ± 0.02
τ_{mean} (ns)	-	8.37 ± 0.50	9.56 ± 0.57
χ^2	11.84 ± 2.60	1.32 ± 0.11	1.20 ± 0.11

Figure 5.7 shows a representative fluorescence lifetime curve fitted with double and triple exponential decay models.

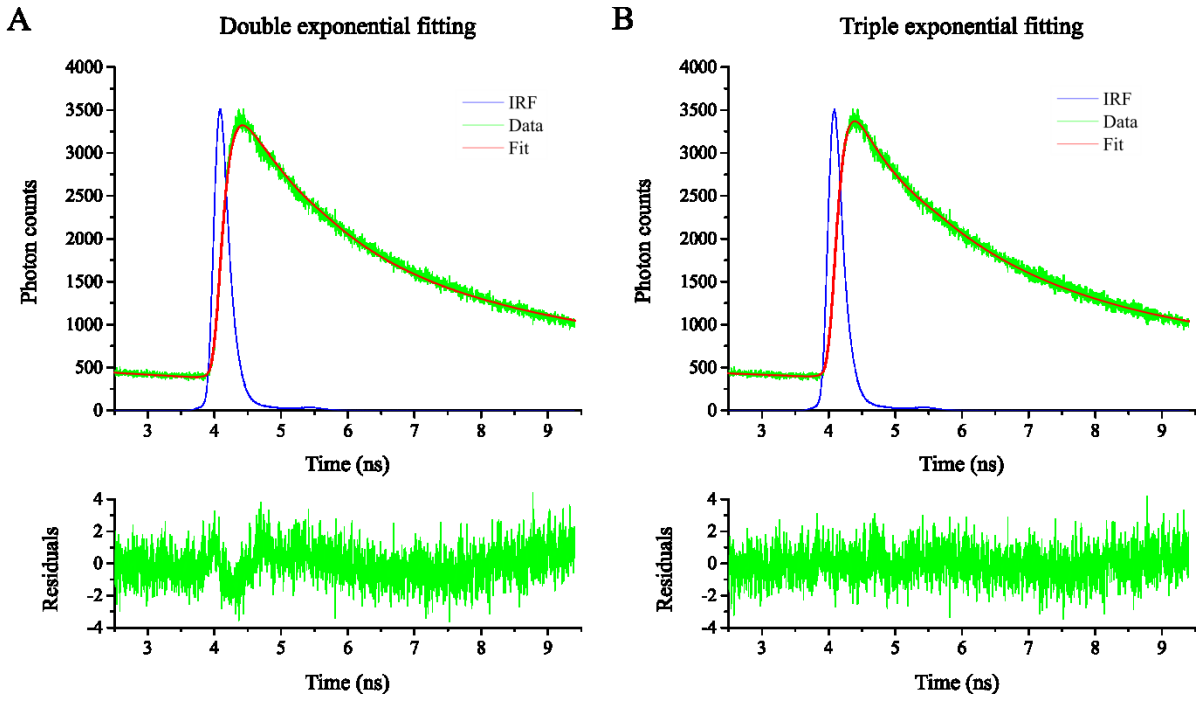

Figure 5.7 Fluorescence lifetime curve fitted with a (A) double exponential model and (B) a triple exponential model. Measurements were realised using 355 nm excitation light at 80 MHz repetition rate and detection at 420 nm.

It is clear that articular cartilage yields a complex fluorescence decay profile as the triple exponential decay model was found to provide a better fit to the data with smaller weighted residuals randomly distributed around zero and a χ^2 closer to unity, relative to the single and double exponential decay models (see Figure 5.7). However, as discussed in Chapter 2, fitting such complex decays requires the detection of a large number of photons in order to produce accurate results [65], which can be challenging particularly in measurements of tissue autofluorescence in clinical settings. Hence, for the results reported below, the autofluorescence lifetime curves of healthy or degenerated cartilage were fitted to double exponential models.

Fitting results in Table 5.1 also demonstrate the presence of a long lifetime component (> 10 ns) with a significant contribution to the overall decay, which translates into an incomplete decay at 80 MHz (see Figure 5.5B). Although the fitting routines can account for incomplete decays [287], it is relevant to note that measurements at high excitation repetition rates are less sensitive to long lifetime components. Furthermore, if the background light level is not correctly estimated, the routine can output biased results. Although the background estimation may not be an issue in a controlled environment e.g. in an optical laboratory, it can be challenging to quantify in clinical settings. Hence, only the first experiments here reported were realised at 80 MHz. For the remaining experiments we chose to use a lower repetition rate, 5 MHz, that allows recording of complete fluorescence decays in a single excitation period. Because the UV laser initially used has a fixed repetition rate of 80 MHz, we switched to a 375 nm laser diode with adjustable repetition rate as illumination source. Figure 5.8 shows the fluorescence emission spectrum and a typical fluorescence decay curve of a healthy porcine articular cartilage sample excited at 375 nm and 5 MHz laser repetition rate.

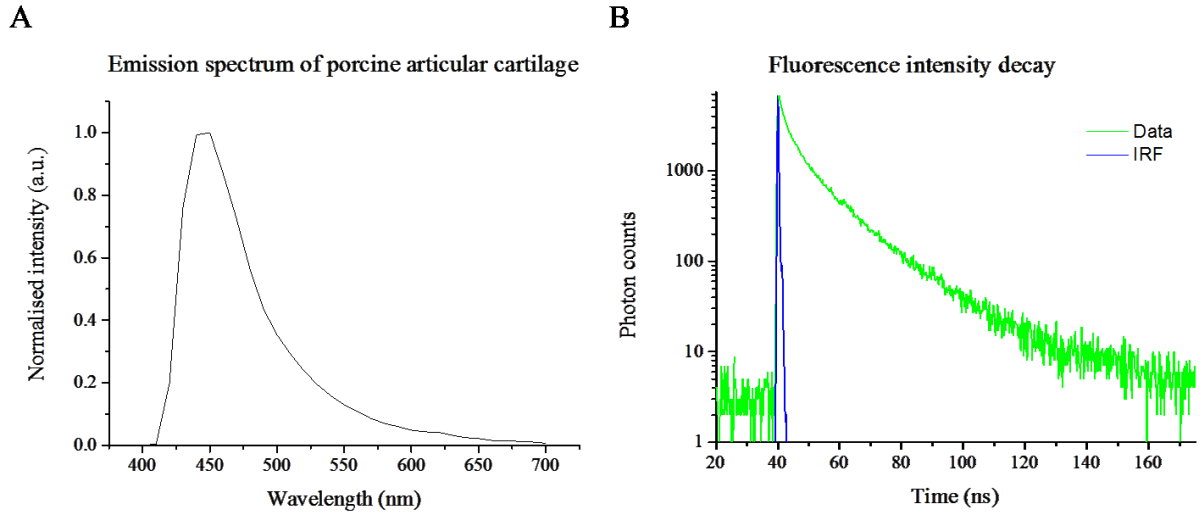

Figure 5.8 (A) Emission spectrum and (B) a representative fluorescence intensity decay curve (plotted in log scale) of a healthy porcine articular cartilage sample excited at 375 nm at 5 MHz repetition rate. The fluorescence emission spectrum was measured between 400 and 700 nm, in 10 nm steps.

Figure 5.8A shows that the fluorescence emission peak is red-shifted when the cartilage is excited at 375 nm relative to 355 nm excitation (see Figure 5.5A). A possible explanation is that these two wavelengths excite different collagen crosslinks, which may have different fluorescence properties, thus originating more fluorescence at different wavelengths. The weighted mean fluorescence lifetime extracted for untreated cartilage explants (n = 15) excited at 375 nm was 8.79 ± 0.55 ns, which is comparable to that measured with 355 nm excitation, given the great intra- and inter-sample variability (see Figure 5.6).

5.5.2.2 Enzymatically degenerated cartilage explants

As discussed previously in this chapter, in OA, cartilage degeneration is believed to be initiated by aggrecanolysis followed by collagenolysis. The present study aims to investigate the effect of

cartilage degeneration in the autofluorescence lifetime and to what extent this label-free optical technique can detect early changes in the cartilage ECM. Hence, it is relevant to study the autofluorescence lifetime signature at both stages of disease progression. To that effect, cartilage fragments were extracted from the surface of metacarpophalangeal trotter joints and treated with a set of different enzymes. Treatment was applied by immersing the samples in solution containing the enzyme, followed by incubation at 37^{o}C.

5.5.2.2.1 Effect of collagenase treatment in articular cartilage autofluorescence lifetime

There are a number of enzymes capable of breaking down collagen fibrils of which the most widely used in OA research is bacterial collagenase due to its wide availability and strong enzymatic activity [288]–[291]. To establish whether collagen cleavage has an effect on cartilage autofluorescence lifetime, frozen and thawed cartilage pieces (n = 5) were treated with 100 µg/ml bacterial collagenase at 37^{o}C for 24 hours. Control samples (n = 5) were immersed in TNC buffer and incubated under the same conditions. Autofluorescence lifetime measurements were carried out immediately after treatment and the resulting data fitted to a double exponential decay model.

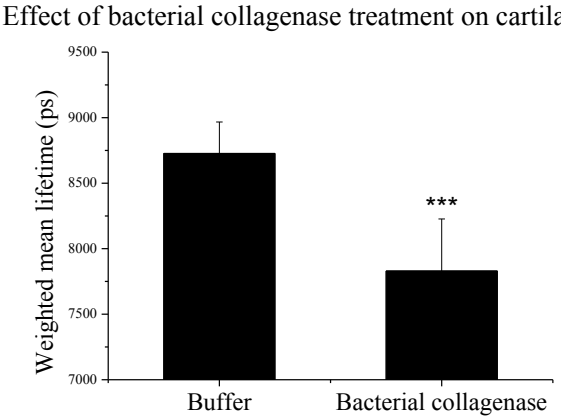

Figure 5.9 Effects of bacterial collagenase (100 µg/ml) treatment on articular cartilage mean AFL. (*** $p < 0.001$)

Results presented in Figure 5.9 indicate that enzyme treatment decreases the cartilage mean autofluorescence lifetime ($p = 0.0002$), which can be traced back to decreases in both the short ($p = 0.001$) and long ($p < 0.0001$) lifetime components and also in the relative contribution from the shorter component ($p = 0.0209$), see Figure 5.10.

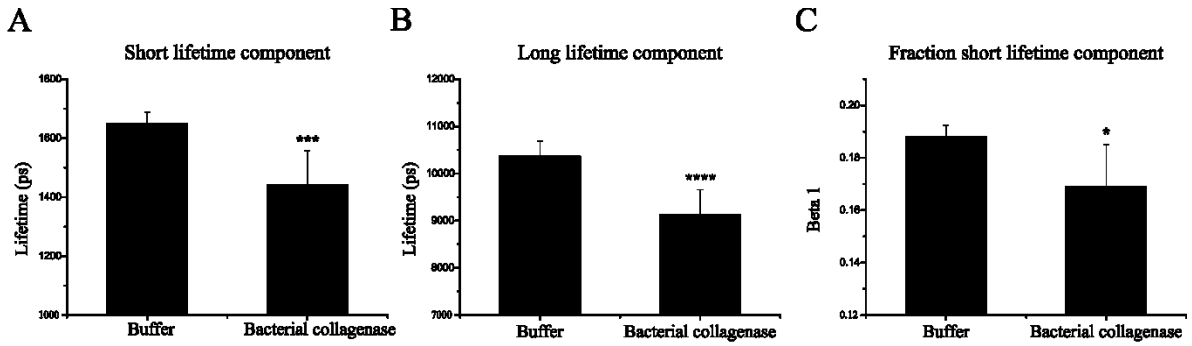

Figure 5.10 Effect of bacterial collagenase treatment in (A) short lifetime component; (B) long lifetime component; (C) relative contribution of short lifetime component.

Following these results, we investigated the dose and time dependency effect of bacterial collagenase treatment on cartilage autofluorescence lifetime. Results are presented in Figure 5.11.

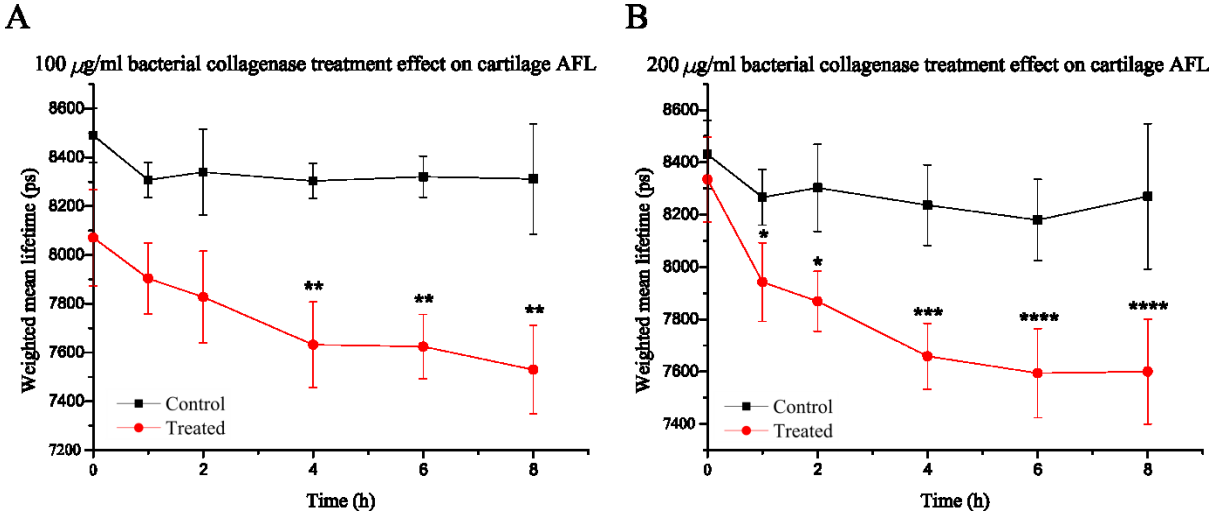

Figure 5.11 Dose and time dependency effect of bacterial collagenase treatment on articular cartilage mean autofluorescence lifetime. (A) Cartilage treated with 100 µg/ml bacterial collagenase; (B) Cartilage treated with 200 µg/ml bacterial collagenase. Due to the intra- and inter-sample variability, measurements at each time point (n=3) were compared against measurements at t = 0 hours, within the same group (Control or treated), using 2-way ANOVA. No statistical significance was found within the control group.

The results in Figure 5.11 confirm that bacterial collagenase treatment affects the articular cartilage autofluorescence lifetime in dose and time dependent manners. As expected, treatment at 200 µg/ml (see Figure 5.11B) degraded the cartilage more severely than treatment at a lower concentration. More interestingly, the mean fluorescence lifetime at the highest dose seem to have reached a saturation plateau after 6 hours of treatment, suggesting that the cartilage samples were completely degraded at that time.

We also investigated the role of mammalian collagenase, MMP-1, in articular cartilage degradation and its effect in the autofluorescence lifetime. As discussed previously in this study, OA is enhanced by the overexpression of MMPs by chondrocytes in the cartilage ECM. Furthermore, it has been

demonstrated that MMPs play an important role not only in breaking down collagen fibrils but also in the cleavage of the aggrecan core protein [282], [292]. Hence, based on previous results, it was expected that the fluorescence lifetime of cartilage would decrease following treatment with this enzyme. To demonstrate this effect, cartilage samples (n = 5) were treated with 500 μg/ml MMP-1 at 37°C for 48 hours. Control samples (n = 4) were immersed in TNC buffer for comparison. Results are presented in Figure 5.12.

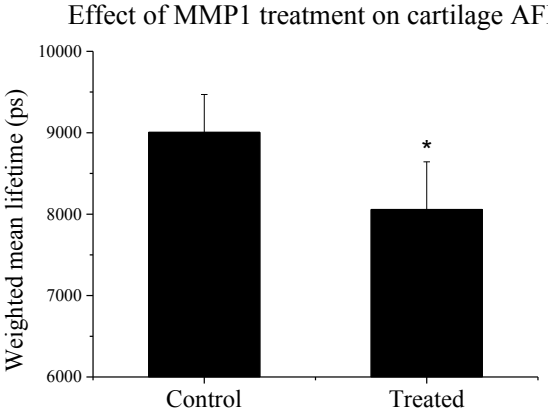

Figure 5.12 Mean autofluorescence lifetime variation with MMP-1 treatment. Raw data fitted with a double exponential decay model.

As expected, treatment with MMP-1 decreased the autofluorescence lifetime of cartilage ($p = 0.0249$), which translates a significant decrease in both short and long lifetime components (data not shown). This result demonstrates that treatment with MMP-1 significantly alters the fluorescence lifetime of cartilage, which is an important result for the validation of this tool, as MMP-1 is one of the key enzymes involved in cartilage degradation during OA.

5.5.2.2.2 Effect of aggrecan depletion in articular cartilage autofluorescence lifetime

To investigate the effect of aggrecan depletion in cartilage autofluorescence lifetime, we induced the removal of proteoglycans from fresh cartilage tissue using retinoic acid. Retinoic acid is a derivative of Vitamin A involved in the regulation of the development of all kinds of tissues. It has been demonstrated that retinoic acid modulates the synthesis of proteoglycans and is responsible for the irreversible depletion of aggrecan in articular cartilage ECM by enhancing the synthesis of endogenous aggrecanases, while maintaining the collagen content intact [273], [293]–[295].

Fresh cartilage explants (n = 5) were treated with 10 μM retinoic acid for 72 hours, following protocol A (see section 5.5.1). For pairwise comparisons, an equal number of cartilage pieces were immersed in buffer for the same period. Autofluorescence lifetime measurements were carried out immediately after treatment. Results - presented in Figure 5.13 - show that treatment with retinoic acid decreases the mean autofluorescence lifetime of cartilage in a significant manner ($p = 0.0002$). This result suggests that decrease in lifetime of degraded cartilage is not attributed exclusively to cleavage of

collagen, which is the main source of autofluorescence in cartilage tissue. Rather, the fluorescence lifetime is also sensitive to aggrecan depletion from the tissue and potentially reflects changes in the biochemical composition of the ECM. As previously discussed in this report, degradation of articular cartilage in OA is initiated with proteoglycan depletion, followed by cleavage of collagen fibrils. Hence, our results suggest that time-resolved measurements can read out cartilage defects even though the collagen network remains unaffected, which is an important step towards the validation of the technique to detect early signs of disease.

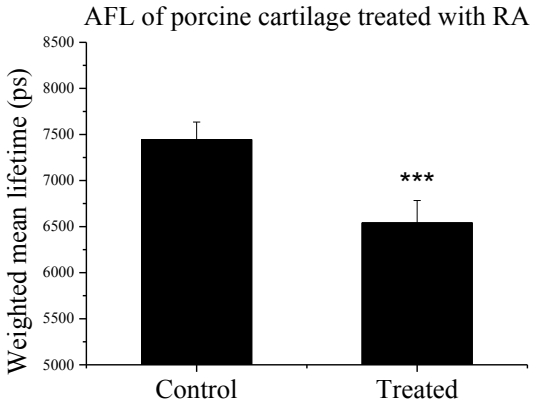

Figure 5.13 Autofluorescence lifetime of porcine articular cartilage treated with retinoic acid (n = 5).

5.5.2.3 Localised lesions following enzymatic treatment

In the previous section, it was demonstrated that autofluorescence lifetime is sensitive to local changes in the chemical environment of articular cartilage, following degradation induced by enzymatic treatment. Although this can be regarded as proof of concept for our hypothesis, degradation was induced in cartilage extracts, i.e. pieces of tissue removed from the surface of the cartilage. Thus, these samples were measured in an environment different from that found in joints. In order to proceed towards a more realistic model of OA, enzymatic degradation was induced in localised regions of a complete porcine metacarpophalangeal joint (protocol B, see section 5.5.1.2), in which healthy articular cartilage was still attached to the subchrondral bone. Given the dimensions of these samples (approximately 2 cm x 2 cm x 1 cm), this also constitutes an opportunity to investigate the discriminatory potential of time-resolved fluorescence measurements of damaged regions that are surrounded by healthier tissue using a fibre-optic probe. Localised lesions in the surface of fresh articular cartilage samples were induced by soaking circular pieces of filter paper (approximately 5 mm of diameter) in either buffer or digestive enzyme, as illustrated in Figure 5.14, followed by incubation at 37^{o}C. The following sections present the results of the application of different digestive enzymes in the articular cartilage surface.

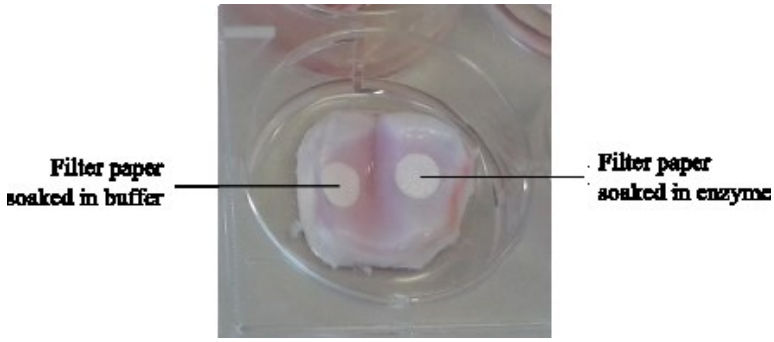

Figure 5.14 Method to induce localised lesions in the articular cartilage surface of a porcine metacarpophalangeal trotter joint, using 5 mm diameter circles of filter paper soaked in either buffer or enzyme.

5.5.2.3.1 Autofluorescence lifetime measurements of localised lesions following enzymatic treatment

To replicate the experiments presented in section 5.4.2.2 in a more physiological environment bacterial collagenase (500 μg/ml) and MMP-1 (500 μg/ml) were applied separately in different samples. To rule out any negative effect of the filter paper in the cartilage autofluorescence properties, a piece filter paper soaked in TNC buffer was also positioned in each sample, as illustrated in Figure 5.14. Autofluorescence lifetime measurements were carried on the region where the filter paper was applied, prior and after the application of enzyme and incubation at 37^{o}C for 24 hours, when localised degradation was clearly visible in the articular cartilage surface, see Figure 5.15.

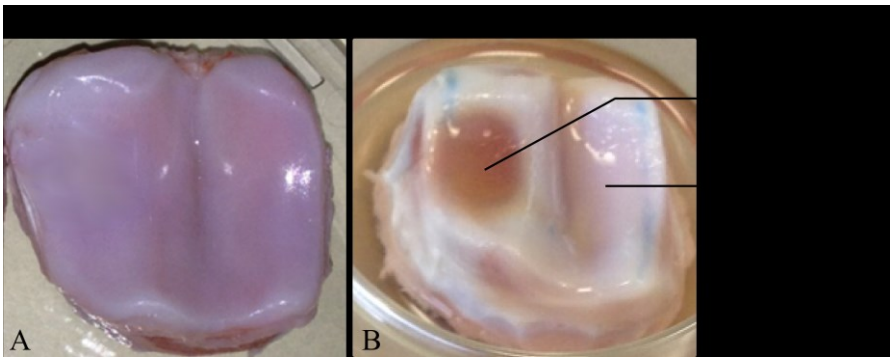

Figure 5.15 Representative images of cartilage samples (A) before and (B) after treatment for 24 hours at 37^{o}C with 500 μg/ml bacterial collagenase.

Figure 5.16 shows the mean autofluorescence lifetime of articular cartilage samples treated with bacterial collagenase and MMP-1.

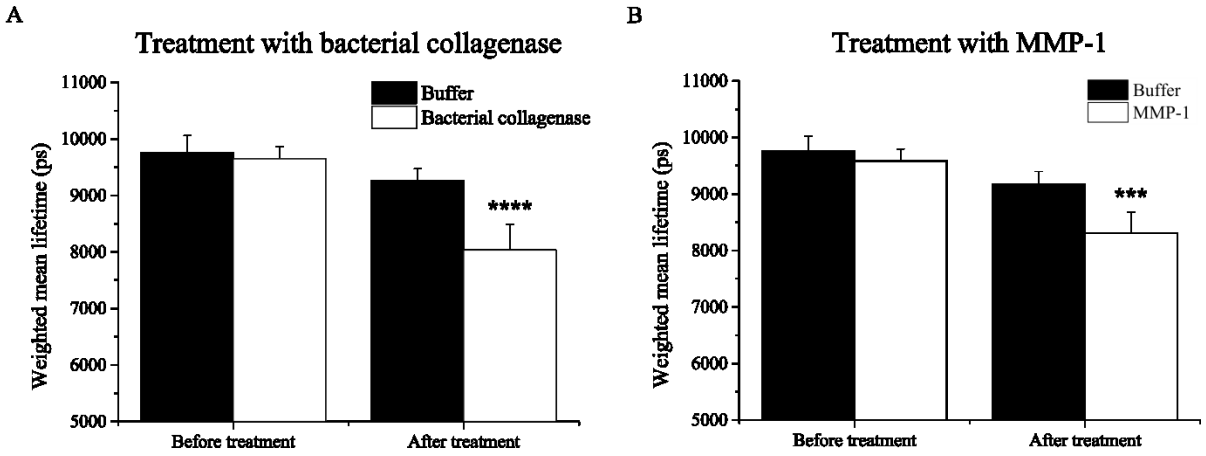

Figure 5.16 Mean autofluorescence lifetime of articular cartilage samples treated with (A) bacterial collagenase ($p < 0.0001$, $n = 9$) and (B) MMP-1 ($p = 0.0004$, $n = 9$). No statistical significance was found between groups prior to treatment. Statistical significances were computed between both groups at each time point using two-tailed t-tests. Data was fitted to a double exponential decay model.

Results presented in Figure 5.16 demonstrate that treatment with bacterial collagenase or MMP-1 decreases the autofluorescence lifetime of articular cartilage to a significant extent, thus confirming the results from previous experiments (see section 5.4.2.1). It is noteworthy that buffer alone seems to induce a decrease in autofluorescence lifetime, although at smaller scale relative to that induced by enzymatic treatment. A possible explanation lies on the fact that "treatment" in buffer can induce the release of proteoglycans from the tissue, albeit in much smaller proportion relative to enzymatic induction, and thus lead to minor changes in the mechanical properties of cartilage that will reflect on a variation of the autofluorescence lifetime [296].

To further investigate the sensitivity of autofluorescence lifetime measurements to changes in articular cartilage ECM, cartilage samples were treated following protocol B with bacterial collagenase at different doses, followed by incubation at 37^{o}C, for 16 hours. Although it is clear that the mean autofluorescence lifetime of articular cartilage decreases with an increasing concentration of bacterial collagenase (see Figure 5.17), this was only found to be significant for the most severe treatment, i.e. 1 mg/ml ($p < 0.0001$, $n = 6$) and not for treatment at lower doses. The same trends were found for individual lifetime components (data not shown). Because the mean autofluorescence lifetime has been shown to decrease in samples treated with 0.5 mg/ml bacterial collagenase for 24 hours (see Figure 5.16A), it is possible that treatment for 16 hours is not sufficient to induce damage in the cartilage surface to the point where a significant difference of the mean lifetime is observable.

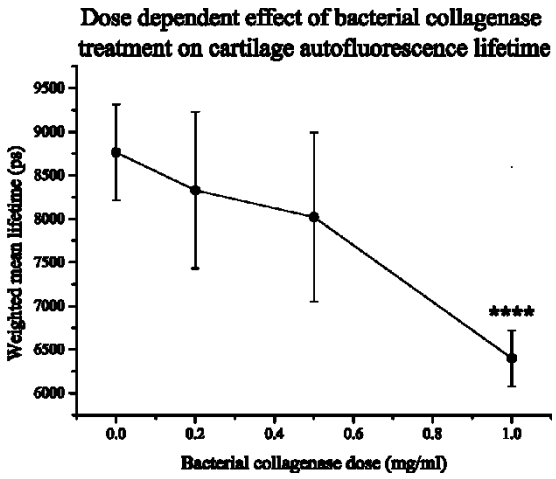

Figure 5.17 Mean autofluorescence lifetime variation following treatment (protocol B) with bacterial collagenase at different concentrations for 16 hours. Data fitted to a double exponential model.

Finally, to examine the effect of aggrecan release on the autofluorescence lifetime of articular cartilage, localised lesions in the cartilage surface were induced with trypsin. The end effect of treatment with trypsin is the same of that with retinoic acid, i.e. cleavage of proteoglycans and other minor proteins in the ECM while maintaining intact the collagen fibrils [227], [247], [267], [297]. The key difference is that trypsin is itself an enzyme and is directly involved in the breakdown of the proteoglycans, whilst retinoic acid promotes the release of endogenous enzymes. Figure 18 shows the results of articular cartilage treated with trypsin, following protocol B.

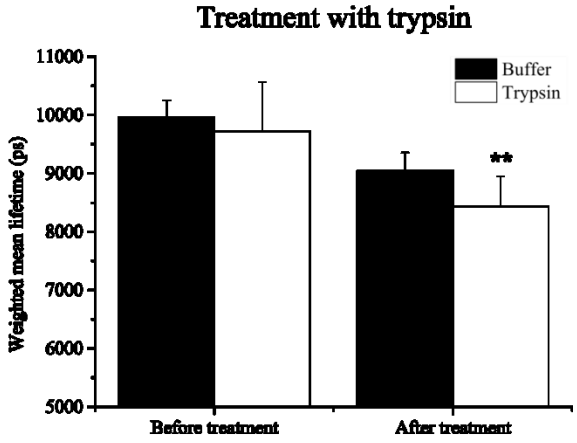

Figure 5.18 Mean autofluorescence lifetime of articular cartilage samples treated with 200 μg/ml trypsin ($p = 0.0072$, $n = 9$). Statistical significance was not found between Buffer and Trypsin groups before treatment. (** $p < 0.01$)

As in the case of treatment with retinoic acid (see Figure 5.13), removal of proteoglycans from the tissue with trypsin significantly changes the autofluorescence lifetime of the cartilage surface ($p < 0.01$). We also observed a decrease in the mean autofluorescence lifetime in regions where only buffer was applied which can be attributed to the release of proteoglycans from the tissue induced by the buffer, as discussed previously. However, our results demonstrate that this has a lower effect on the cartilage autofluorescence lifetime in comparison to treatment with trypsin.

5.5.2.3.2 Spatially-resolved autofluorescence lifetime measurements in degraded cartilage

Up to now, autofluorescence lifetime measurements in the articular cartilage surface were carried out only in areas where either buffer or digestive enzymes were applied, hence allowing one to classify the tissue as either healthy or damaged. Although the goal of the present study is to use autofluorescence lifetime as a predictor of the degenerative state of tissue and ultimately to validate this technique as clinical tool for the early diagnosis of OA, further validation is still required as it remains unclear if autofluorescence lifetime can discern areas of tissue that are closely located but were exposed to different degrees of degradation, as in naturally occurring OA. Hence, we have investigated the ability of time-resolved single point measurements to discriminate healthy from damaged cartilage over small areas of the joint, so that a transition from healthy to digested tissue could be observed through measurements of fluorescence lifetime. To that effect, we have interrogated the surface of cartilage samples in small steps using the fibre-optic probe, spanning both untreated and treated regions with bacterial collagenase (500 μg/ml) or MMP-1 (500 μg/ml), as illustrated in Figure 5.19A. Autofluorescence lifetime measurements of line profiles along the treated area are presented in Figure 5.19B. Ideally, a line profile measured as described here would show an inverted Gaussian-like curve for samples treated with bacterial collagenase and MMP-1: the lifetime would be of around 9 ns in the beginning and decrease until maximum degradation was reached, from where it would increase again to the baseline value, i.e. 9 ns. For the control sample, a constant autofluorescence lifetime would be expected over the interrogated area. Experimentally, a Gaussian-like profile was obtained in the sample treated with bacterial collagenase. In this case, the mean autofluorescence lifetime steadily decreases from approximately 9.2 ns down to a minimum of 7.8 ns, over a distance of approximately 6 mm, from where it increases again up to 8.6 ns. The curve extracted for MMP-1 treatment also shows a decrease in autofluorescence lifetime from the region of healthy tissue to the more degraded area, although this is less clear and pronounced relative to bacterial collagenase treatment. We have also observed a decrease in fluorescence lifetime in the presence of buffer, which is in agreement with our previous results. Surprisingly, the decrease in lifetime in observed in the second half of the line profile, potentially reflecting diffusion of the solution through the articular cartilage surface.

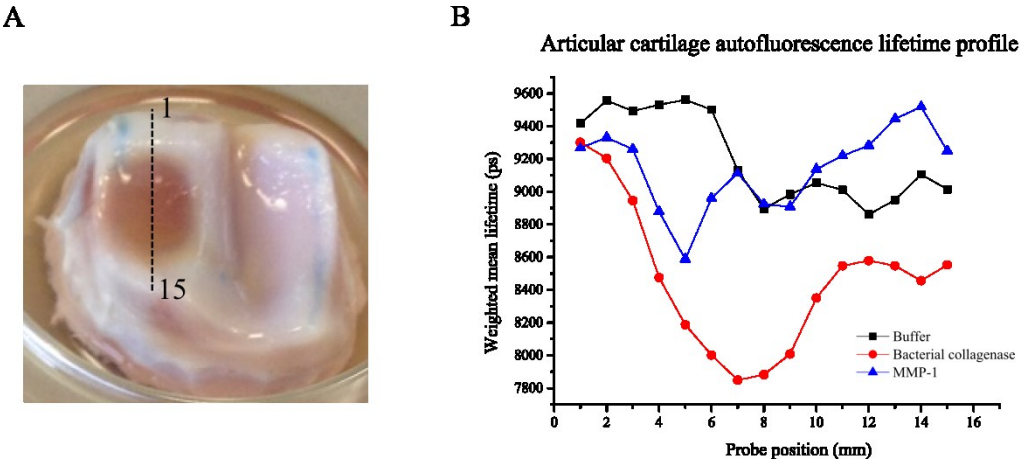

Figure 5.19 (A) Schematic of the experiment. Fifteen equidistant measurements were realised along the profile (represented by the dashed line) using the fibre-optic bundle. (B) Results for three different samples treated with buffer, bacterial collagenase (500 µg/ml) and MMP-1 (500 µg/ml). Measurements from 3 to 10 mm were realised in the treated area.

5.6 Autofluorescence lifetime of murine articular cartilage

In previous sections, it was demonstrated that autofluorescence lifetime can differentiate healthy from enzymatically degenerated cartilage. More interestingly, the mean autofluorescence lifetime appears to be sensitive to the level of degradation of the tissue, i.e. the greater the degradation, the shorter the lifetime (see Figure 5.11 and Figure 5.17). Although promising, these results were obtained *in vitro* and thus are still far from mimicking the natural degradation found in OA tissue. Hence, in order to approximate our studies to a realistic model of OA, we investigated the potential of autofluorescence lifetime to read out cartilage degradation in an OA mouse model of the knee joint. Experimental animal models of OA not only provide a more realistic and yet controlled environment, but also allow investigation of cartilage degradation from the earliest stages of disease progression.

Articular cartilage from mouse knee joints is identical in structure to what has been described previously in the present study. However, it differs significantly from human and porcine articular cartilage in terms of surface area and thickness [246]. This is relevant for our investigation as, in mice, the surface area of the knee joint covered by articular cartilage is equivalent to the area of tissue interrogated by our fibre-optic probe and therefore a single point measurement is likely to span areas of the cartilage that are at different stages of degradation. Although it is unlikely that our measurements can differentiate "healthy" from damaged cartilage in a single specimen, the autofluorescence lifetime extracted for these measurements will effectively correspond to the average lifetime over the interrogated area, hence providing an indication of the general state of degradation of the tissue and allowing different specimens to be compared.

The following sections present the results of our investigations in murine knee joints, first in enzymatically degraded samples - as proof of concept - followed by studies of disease progression in naturally occurring OA samples.

5.6.1 Materials and methods

All animal procedures were performed in accordance with current UK Home Office regulations for animal work, at the Kennedy Institute of Rheumatology.

5.6.1.1 Enzymatic degradation of knee joints

Healthy adult C57BL/6 mice were euthanized and their knee joints of both left and right back legs harvested and trimmed. Tibial plateaus were used for autofluorescence lifetime measurements of the articular cartilage. Enzymatic degradation was induced by immersing the tibial plateaus in solution containing the enzyme (or buffer in the case of control experiments), see Figure 5.20.

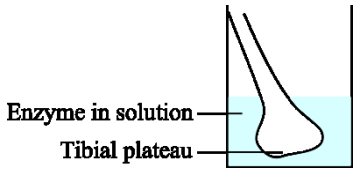

Figure 5.20 Schematic representations of the application of digestive enzymes in murine knee joints.

5.6.1.2 OA mouse model

Animal models are practical and clinically relevant approaches to investigate the natural progression of OA. There are several well-established animal models of OA, each one with own unique advantages and disadvantages. A comprehensive review of different OA models was recently published by Gregory et al [298]. For the purposes of our investigation it would be convenient to study a model involving cartilage of similar properties of that of humans and in which the disease could develop in a similar way, e.g. horse or dog. However, only mouse models of OA are studied at Kennedy Institute of Rheumatology. The specific model followed in our studies involves mechanical destabilisation of the joint via transection of medial meniscotibial ligament (see Figure 5.21), which results in medial and posterior rotation of the medial meniscus and ultimately leads to a mild form of OA. A more detailed description of this method can be found in reference [299].

In our studies, OA was induced in adult (10 weeks old) C57BL/6 mice (n = 24) by sectioning of the medial meniscotibial ligament of the right legs. Mice remained housed in standard cages with food and water available *ad libitum*, with maintenance of a thermo-neutral environment for up to 8 weeks after surgery. Mice were euthanized at weeks 4, 6, or 8 post-surgery (n = 8 at each time point) and their knee joints harvested and trimmed. Tibial plateaus were used for autofluorescence lifetime measurements of the articular cartilage. Left knees were used as controls having been subjected to no surgery or sham surgery, which included visualisation of the ligament with no transection.

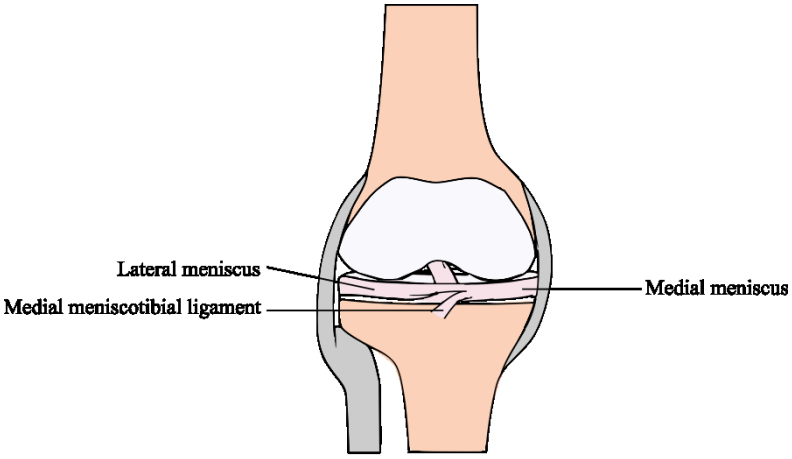

Figure 5.21 Schematic of the knee joint of the mouse

5.6.1.3 Instrumentation

Autofluorescence lifetime measurements were carried out in the cuvette-based system using the fibre-optic probe extension (see chapter 3). Excitation light was provided at 375 nm with 5 MHz repetition rate. Fluorescence from the specimens was measured at the emission peak wavelength, i.e. 460 nm (see Figure 5.22A). For each measurement, the tip of fibre probe was positioned at approximately 1 mm from the sample and at right angles relative to cartilage surface, as illustrated in Figure 5.22B.

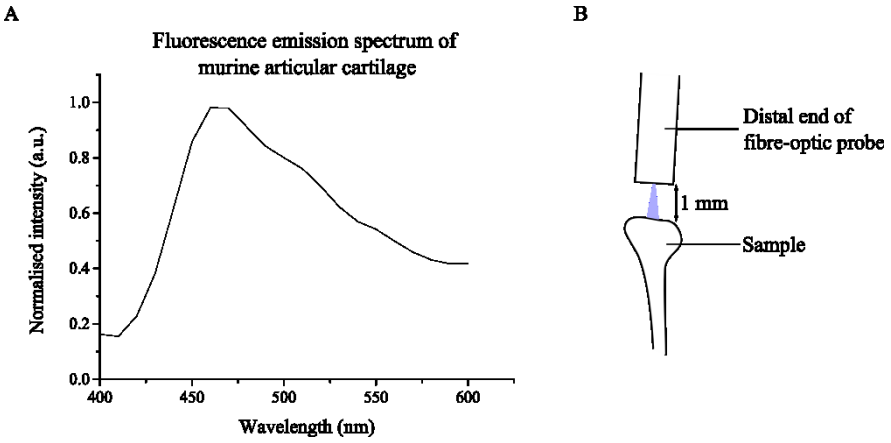

Figure 5.22 (A) Fluorescence emission spectrum of a healthy articular cartilage sample from a mouse knee joint excited at 375 nm. Measurements were carried out between 400 and 600 nm, in 10 nm steps. (B) Diagram illustrating the fibre-optic probe position relative to the sample in autofluorescence lifetime measurements.

5.6.1.4 Histology

Knee joints of mice were subjected to histological analysis to reveal pathological changes associated with OA development. Tissues were fixed in 4% paraformaldehyde, decalcified, dehydrated and then embedded in paraffin for sectioning. 8-µm thick coronal or sagittal sections of the joint were cut and stained with Safranin-O for demonstration of proteoglycan content [253], [299]–[301]. Sections were imaged using 40x magnification on an Olympus BH2 microscope.

5.6.1.5 Data analysis

5.6.1.5.1 Fluorescence decay analysis

Autofluorescence lifetime data of murine articular cartilage was fitted to a double exponential decay model, as discussed in section 2.4. The system IRF was measured at the excitation wavelength, i.e. 375 nm, using a scattering sample of Ludox beads.

5.6.1.5.2 Statistical analysis

All results are expressed as mean ± standard deviation (SD). Statistical analysis was computed using paired two-tailed Student t-tests. A p-value < 0.05 was considered to be statistically significant. For convenience, the following notation was used to identify statistical significance between two sets of data: * $p < 0.05$; ** $p < 0.01$; *** $p < 0.001$; **** $p < 0.0001$.

5.6.2 Results and discussion

5.6.2.1 Autofluorescence lifetime signature of murine articular cartilage

Prior to realising autofluorescence lifetime studies during natural progression of OA, we first characterised the autofluorescence properties of healthy knee joints in mice. To verify the variability among specimens and between left and right knee joints, the autofluorescence lifetime of untreated right and left knee joints freshly harvested from a number of animals (n = 5) was measured. Results presented in Figure 5.23 indicate that the mean autofluorescence lifetime does not differ significantly between knee joints. If we average all measurements from left and right knee joints (i.e. n = 10), we obtain an average autofluorescence lifetime of 6.25 ± 0.49 ns, which is considerably shorter than that extracted for porcine articular cartilage with a double exponential fitting, i.e. 8.38 ± 0.50 ns (see Figure 5.6 and Table 5.1). The reasons for this difference are unclear, although it is possible that it merely reflects a different crosslinking environment or different arrangement of the collagen fibrils between species. As mentioned previously, the articular cartilage of mice is very thin - approximately 100 μm [246] - and therefore it is also possible that light can penetrate through the various layers of the tissue that can present different autofluorescence lifetimes. It is relevant to note that such a thin layer of cartilage may allow excitation light to penetrate through the cartilage tissue and reach the subchondral bone, for which we measured an autofluorescence lifetime of 5.51 ± 0.46 ns (n = 5). Although this is unlikely to occur in healthy cartilage, it may occur in highly eroded samples, where the cartilage layer is thinner.

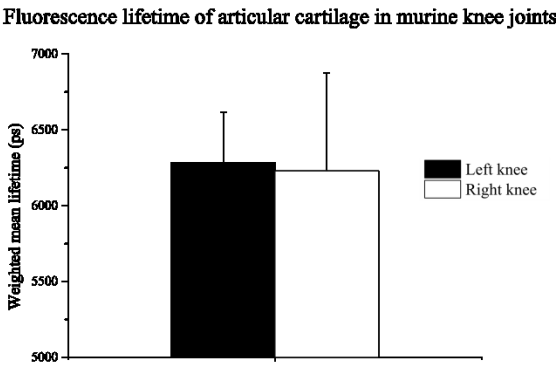

Figure 5.23 Variability of the mean autofluorescence lifetime of articular cartilage in mice, corresponding to an average of n = 5 measurements for both left and right knee joints (no statistical significant difference was found between groups).

Although it is expected that murine cartilage degradation produces the same effects in fluorescence lifetime as in the case of porcine samples, i.e. shorter autofluorescence lifetime indicates a greater degradation, this had not been confirmed experimentally. To examine the effects of murine cartilage degradation in the autofluorescence lifetime, these samples were treated with 200 μM MMP-1 for 24 hours, at 37°C incubation, as described in section 5.6.1.1. As expected, the results presented in Figure 5.24 demonstrate that the mean autofluorescence lifetime decreases significantly with MMP-1 treatment, with p-values of 0.0145 and 0.0012 for left and right knee joints, respectively, hence confirming the trends previously reported in section 5.5 for porcine articular cartilage specimens.

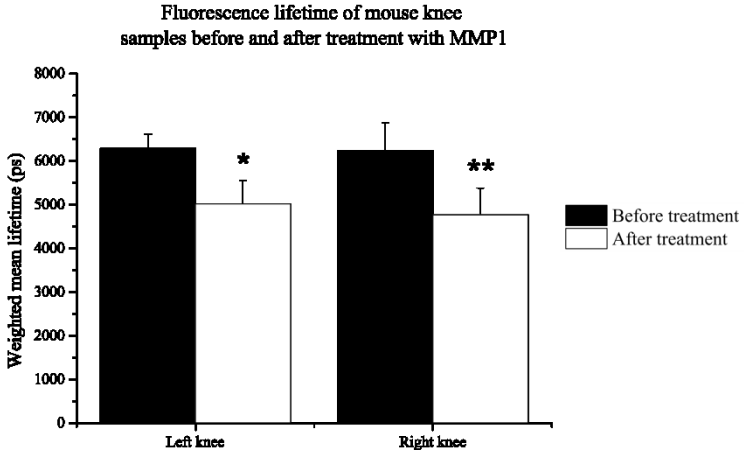

Figure 5.24 Decrease in the mean autofluorescence lifetime of murine articular cartilage upon treatment with MMP-1. Statistical significance was computed for measurements realised before and after treatment.

5.6.2.2 Autofluorescence lifetime in an OA model

As described in section 5.6.1.2, OA was induced in right knees via transection of the medial meniscotibial ligament, whilst left knees were used as controls. Autofluorescence lifetime measurements were carried out at weeks 4, 6 and 8 post-surgery in a total of 8 specimens per time point and three acquisitions per specimen. Inter animal variability was verified using control samples at each time point (see Figure 5.25). Despite the great variability between specimens, we observed

minimal differences between mean autofluorescence lifetimes at each time point after surgery (see horizontal bars in Figure 5.25).

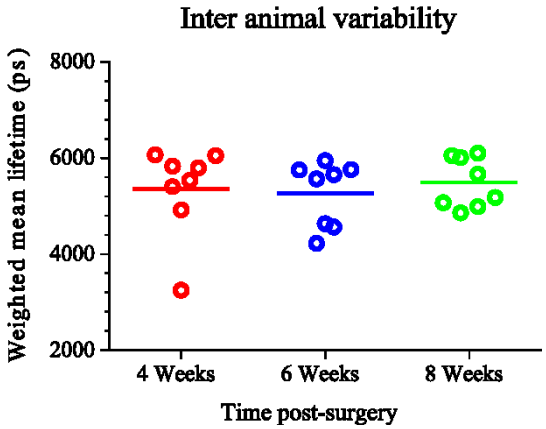

Figure 5.25 Inter-animal variability across control specimens at each time point post OA induction surgery. Each point measurement represents an average of three acquisitions.

Results of the autofluorescence lifetime data measured at each time point post-surgery are plotted in Figure 5.26.

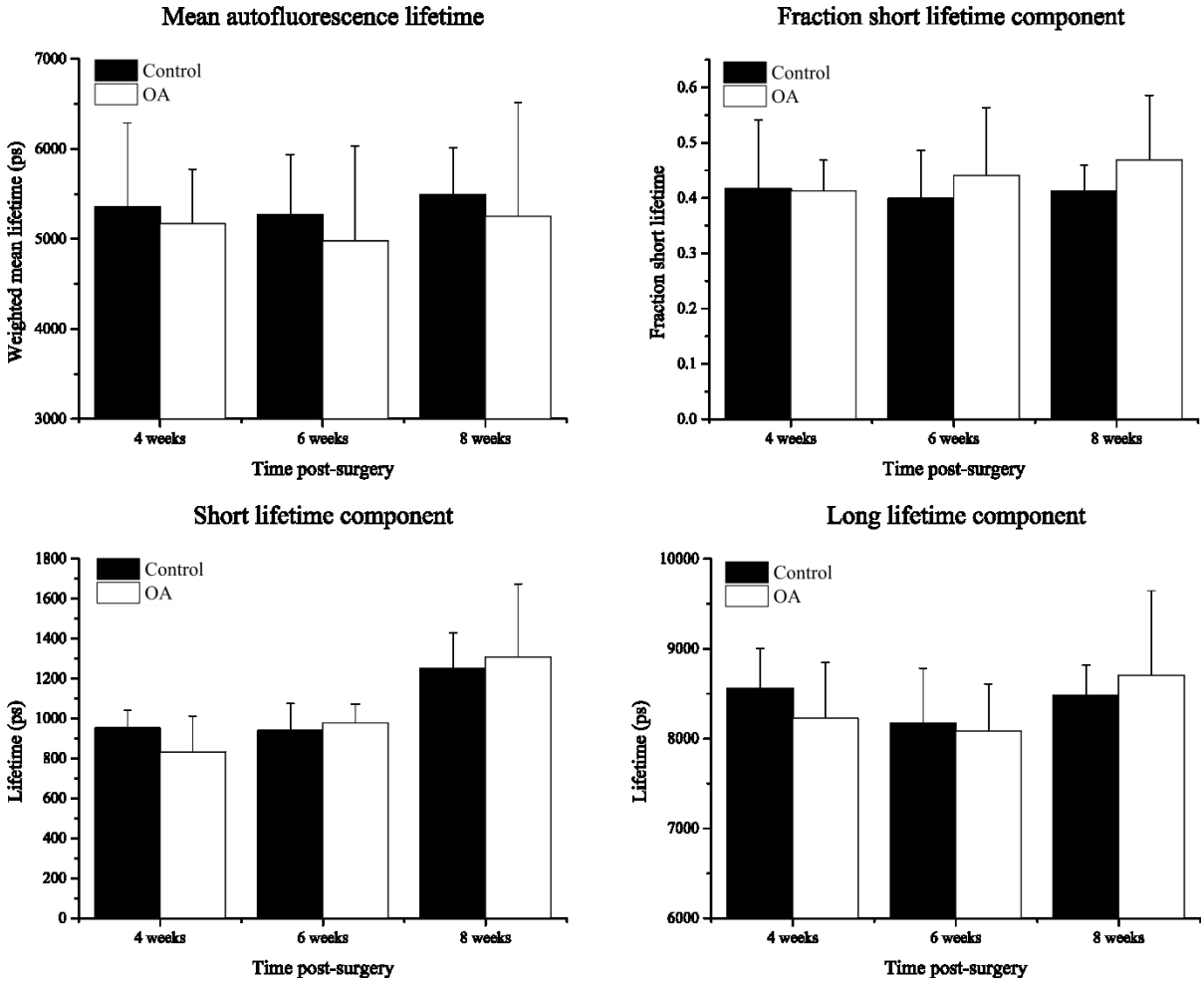

Figure 5.26 Autofluorescence lifetime results at each time point after OA induction surgery. Error bars show standard deviation (n = 8 specimens, per time point and group).

Overall, despite our success in reading out articular cartilage degeneration through enzymatic treatment, as demonstrated in section 5.6.2.1, we were unable to replicate those results in naturally occurring disease in mouse. Our results do not to demonstrate significant differences between healthy and OA joints in any of the lifetime parameters and time points, despite the obvious degradation that is observable in histology images (see Figure 5.27). Although surprising, there are a few possible explanations for these results. In OA, it is well-established that the medial meniscus is more commonly affected than the lateral meniscus [302]. This is because medial regions of the joint are subject to a heavier load relative to lateral regions, therefore suffering greater erosion. In terms of autofluorescence, this would be expected to effectively translate to one region yielding a shorter lifetime relative to the other. Because the samples under investigation have a relatively small surface area (approximately 2 mm x 2 mm), it is difficult to visually identify these regions at the surface of the tibial plateau. Furthermore, excitation light delivered by the fibre-optic probe diverges from the tip of the probe, making it even more challenging to discriminate between signals from medial and lateral regions. Hence, it is likely that the autofluorescence signal measured from our samples arise from both regions. This effect is not an issue for enzymatically degenerated cartilage as treatment is applied evenly to the whole cartilage (see Figure 5.20 and Figure 5.24).

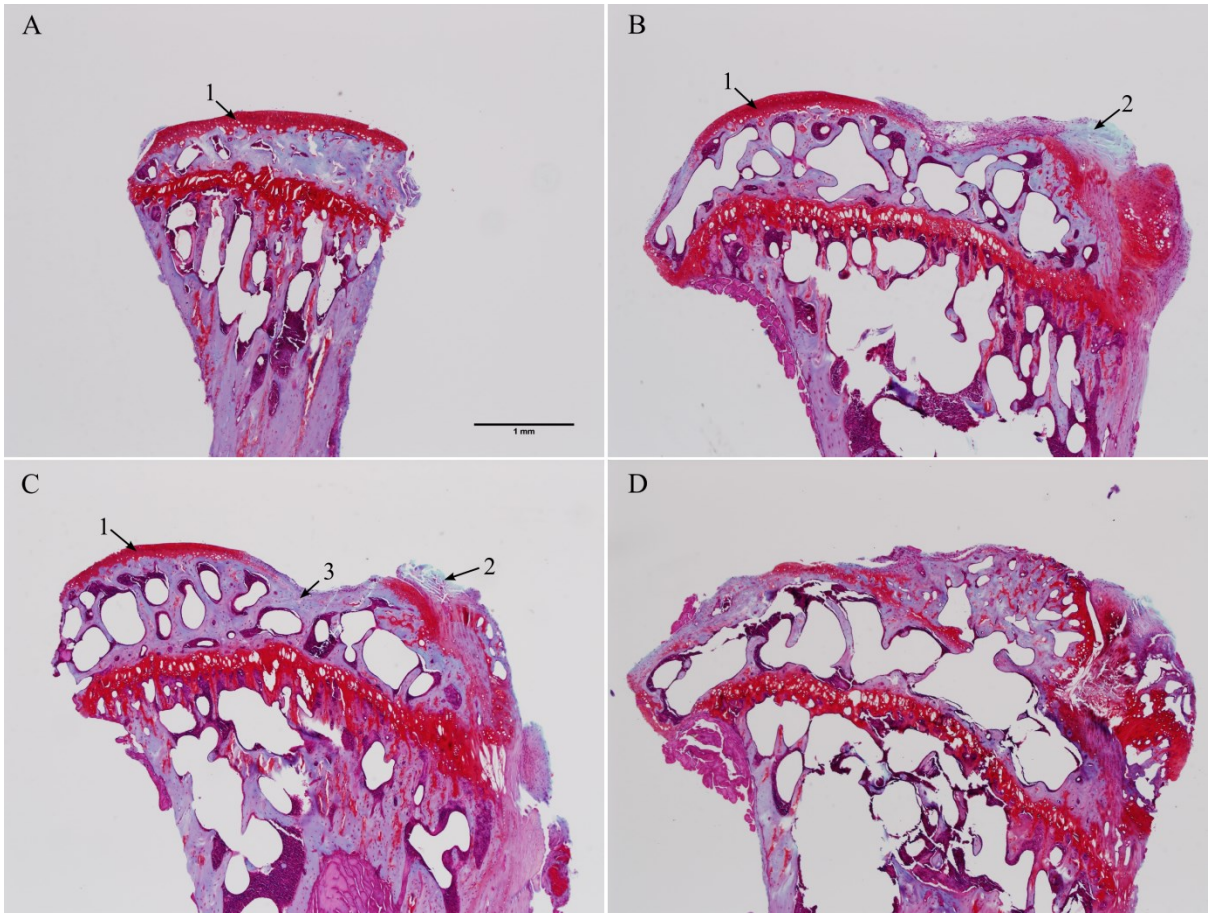

Figure 5.27 Representative histology images of a (A) healthy knee joint and OA joints at (B) 4 weeks, (C) 6 weeks and (D) 8 weeks post OA induction surgery. Samples were stained with Safranin-O, which is used to identify proteoglycans in cartilage tissue (stained red). Bone is coloured purple. Numbers in images indicate: 1 – Non- or minimally damaged cartilage; 2 - Fibrotic tissue; 3 - Subchondral bone.

Histology images indicate that OA is completely established at only 4 weeks after surgery and only residues of undamaged articular cartilage can be found in the majority of these samples (see Figure 5.27B). Furthermore, it is possible to observe that large areas of the cartilage surface are covered by fibrotic tissue, as result of an inflammatory process. It is unclear if the inflammation is a natural consequence of OA development in the joints or if it is induced by cutting of the meniscotibial ligament during surgery. Whatever the cause of the inflammation, this fibrotic tissue is primarily constituted of collagen type I, which presents a mean fluorescence lifetime of approximately 6 ns (as discussed in Chapter 3). This is comparable to that of healthy articular cartilage in mice and so the build-up of collagen type I may lead to changes in the autofluorescence lifetime of damaged cartilage that could mask any changes caused by degradation of the tissue. It is also possible that some regions at the surface of the joint are neither covered by cartilage or fibrotic tissue. In that case, excitation light is delivered directly to the subchondral bone (see Figure 5.27C), which yields a lifetime of approximately 5.5 ns, as mentioned previously.

To summarise, autofluorescence of articular cartilage from OA joints in this murine model appears to be modulated by several endogenous and exogenous factors: uneven tissue degradation; inflammation induced by surgery and/or disease; and autofluorescence from sources other than cartilage. It is interesting to consider that these factors raise questions for studies of human OA: is fibrotic tissue likely to mix-up the autofluorescence signal in human joints? Can medial and lateral regions of the knee joint be distinguished? Can cartilage fluorescence be distinguished from that of bone?

5.7 Autofluorescence lifetime in human articular cartilage

Up to now, it was demonstrated that autofluorescence lifetime spectroscopy can be employed to readout articular cartilage degradation when this is enzymatically induced. Unfortunately, as discussed in the previous section, this was not possible to validate in the "natural" occurring form of the disease in mice and it is important to establish whether autofluorescence lifetime readouts can successfully be applied in the diagnosis of OA in human joints. Validation of this method in mouse knee joints encountered a number of limiting factors including proliferation of collagen type I and other issues related to the size and thickness of articular cartilage in mice. We believe that in cartilage with larger surface area and thickness, as that of humans, it is likely that these limitations can be overcome. For example, in adult humans, the tibial plateau has a surface area of approximately 1600 mm^2 in healthy joints [303], thus different regions of cartilage can be easily distinguished using a fibre-optic probe. Furthermore, in the OA mouse model, even though the disease developed naturally, this was artificially induced, resulting in inflammation and proliferation of fibrotic tissue beyond what is expected to occur in OA human knee joints, as fibrosis is commonly associated with progressive degradation of the joint as part of the repairing process and therefore its presence is less prominent at early stages of the disease in humans [302], [304].

To investigate how autofluorescence lifetime is sensitive to the degradation of human articular cartilage, as proof of concept we first aimed to replicate the results obtained in porcine cartilage in human samples. Next, we investigated the potential of time-resolved autofluorescence spectroscopy combined with diffuse reflectance to discriminate healthy from damaged cartilage in frozen/thawed and freshly excised human knee joints. These experiments were realised at the Kennedy Institute of Rheumatology using one of the two portable single-point time-resolved spectrofluorometers developed for this project and previously presented in Chapter 4.

5.7.1 Materials and Methods

5.7.1.1 Sample preparation

5.7.1.1.1 Enzymatically treated samples

Specimens of intact metatarsophalangeal joints were obtained from one patient undergoing lower-limb amputation surgery at Charing Cross Hospital. After arrival, specimens were thoroughly washed in PBS to remove any residues of blood and other bodily fluids. A total of eight specimens were received – two specimens for each metatarsal head, with the exception of the first metatarsus. For pairwise comparison, one specimen of each metatarsal head was kept untreated whilst the other was treated with retinoic acid for proteoglycan removal. All samples were frozen at -80^{o}C and then thawed for autofluorescence and diffuse reflectance measurements.

5.7.1.1.2 Naturally occurring OA samples

Naturally occurring OA samples from the tibial plateau of human knee joints were provided by Professor Andrew Price from the University of Oxford. Samples were delivered to the Kennedy Institute of Rheumatology from 1 to 2 hours after being removed from patients undergoing knee joint replacement surgery. Upon arrival, all samples were washed in PBS to remove any residues of blood or other bodily fluids. Due to the impossibility of taking immediate measurements, some of the samples (n = 4) were stored at -80^{o}C until measurements were carried out. For the remaining samples (n = 2), autofluorescence measurements were realised immediately after arrival and also after storage at -80^{o}C and thawing, for comparison purposes.

5.7.1.2 Instrumentation

Experiments described in this section were carried out employing the single-point time-resolved spectrofluorometer presented in chapter 4, with the laser repetition rate adjusted to 5 MHz. Figure 5.28 shows the instrument deployed in a lab at the Kennedy Institute of Rheumatology. Due to technical problems at the time of the measurements, illumination at 440 nm was not used on the measurement of samples treated with retinoic acid.

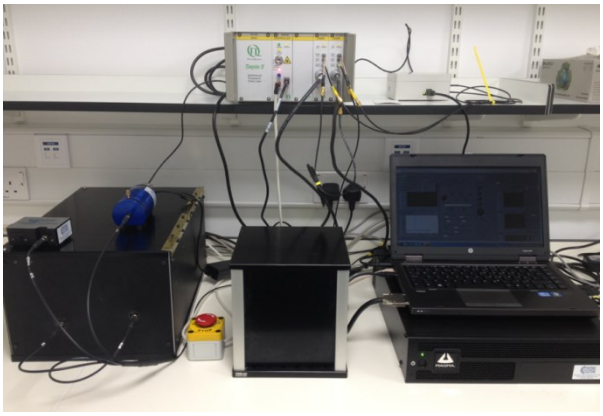

Figure 5.28 Single-point time-resolved spectrofluorometer deployed at the Kennedy Institute of Rheumatology.

5.7.1.3 Data analysis

5.7.1.3.1 Fluorescence decay analysis

Autofluorescence lifetime data of human cartilage from each detection channel were fitted to double exponential decay models, as discussed in section 2.4. The system response was measured using reference fluorophores with known decay characteristics: DAPI (Sigma-Aldrich, USA) for 375 nm excitation in all detection channels; and Erythrosin B (Sigma-Aldrich, USA) using 440 nm excitation. These reference dyes have lifetimes of approximately 200 ps, which are comparable to the pulse lengths of the lasers used.

5.7.1.3.2 Spectral analysis of diffuse reflectance data

As discussed in Chapter 4, diffuse reflectance spectroscopy is a well-established optical spectroscopy technique that has previously been used to characterise tissue optical properties such as absorption coefficient, reduced scattering coefficient, haemoglobin and myoglobin concentrations and total blood oxygenation [163], [223], [225]. However, in this study, we only intend to establish whether differences exist between the diffuse reflectance signals of healthy and damaged cartilage. For this comparison, all acquired spectra were normalised to the signal of the diffuse reflectance from a white reference target (WS-1-SL, Labsphere, USA). All diffuse reflectance values are reported in units of absorbance, calculated as follows:

$$A(\lambda) = -\log_{10}\left(\frac{I(\lambda)}{I_0(\lambda)}\right) \tag{5.1}$$

where A is the tissue absorbance, I is the measured spectrum and I_0 is the calibrated spectrum of the white light source.

5.7.1.3.3 Discriminant analysis

Differences between healthy and damaged regions (or specimens in the case enzymatically induced degradation) were quantified by discriminant analysis, following the implementation of a

classification algorithm that is conceptually similar to the ones described in references [4], [19], [24], [35], [180], employing principal component analysis (PCA) for feature selection followed by linear discriminant analysis (LDA) on the two most significant principal components (PC). The PCs are the underlying structure of a given set of data, corresponding to the principal directions in which the data varies. They are orthogonal and linear transformations of the original data points, and therefore the maximum number of PCs is determined by the number of dimensions *n* in the data [305]. The PCs are calculated through the eigenvectors and eigenvalues of the data covariance matrix. The eigenvector with the largest eigenvalue corresponds to the direction where data varies the most and is identified as the first principal component. The eigenvector with the second highest eigenvalue is orthogonal to the first, corresponding to the second principal component and so on. In the context of dimensionality reduction, the eigenvectors that correspond to the largest eigenvalues are typically a low-dimensional representation of the whole dataset and contain the most important variance of the data. For a more comprehensive description of PCA for dimensionality reduction, the reader is directed to references [305], [306].

Receiver operator characteristic (ROC) curves were generated from the scores of each classification. The performance of each classifier was measured by the area under the ROC curve (AUC).

5.7.1.3.4 Statistical analysis

All data results are expressed as mean ± standard deviation (SD). Statistical analysis of different groups was computed using a two-tailed Student t-test, unless otherwise stated. A p-value < 0.05 was considered to be statistically significant. For convenience, the following notation was used to identify statistical significance between two sets of data: * $p < 0.05$; ** $p < 0.01$; *** $p < 0.001$; **** $p < 0.0001$.

5.7.2 Results and discussion

5.7.2.1 Enzymatically treated samples

Figure 5.29A and Figure 5.29B show typical articular cartilage specimens from human metatarsophalangeal joints measured with our time-resolved point probe system. Figure 5.29C shows the autofluorescence lifetime variability in untreated specimens in all detection channels of the point probe system under UV excitation.

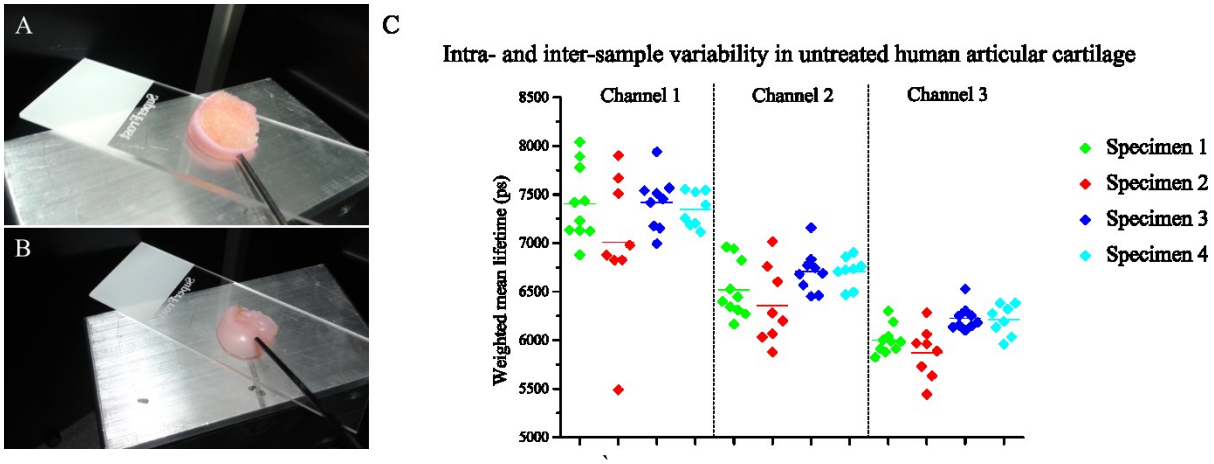

Figure 5.29 (A, B) Images of representative human metatarsophalangeal articular cartilage specimens. (C) Intra- and inter-sample variability of autofluorescence lifetime in untreated specimens. Different colours identify different specimens. Horizontal bars identify weighted mean fluorescence lifetime.

It is important to point out that although these samples were untreated and thus used as controls for enzymatically degraded samples, it is likely that they present some natural degradation, which can explain the lifetime variation, particularly in channel 1 (see Figure 5.29C). If we take the average lifetime of each specimen at each channel (i.e. n = 4 specimens), we obtain mean autofluorescence lifetimes of 7.30 ± 0.20 ns, 6.57 ± 0.19 ns and 6.08 ± 0.19 ns for channels 1, 2 and 3, respectively. It is interesting to observe that the autofluorescence lifetime appears to be wavelength dependent, which goes against previous findings in digested porcine cartilage explants [80]. Previous studies in our group [121] and others [122] have demonstrated that collagen yields a complex autofluorescence signature owing to the multitude of crosslinks present in the samples. Hence, it is possible that the variation of autofluorescence lifetime with emission wavelength can be attributed to different crosslinking environment in human samples with respect to porcine samples.

To verify the sensitivity of our instrument to cartilage degradation, specimens were treated with 10 μM retinoic acid for 72 hours, which induced the release of proteoglycans from the tissue. The results – presented in Figure 5.30 – indicate a consistent decrease in the autofluorescence lifetime in all detection channels, relative to control samples, which becomes more significant at longer wavelengths. P-values of 0.0127, 0.0280 and 0.0005 were extracted for channels 1, 2 and 3, respectively (n = 4). It is also interesting to observe that treatment with retinoic acid induces a shift in the autofluorescence emission spectrum towards longer wavelengths, see Figure 5.30B. It is possible that cartilage degradation induces the break-up of collagen crosslinks that fluoresce preferentially at shorter wavelengths, which would explain the shift in fluorescence emission. The shift in fluorescence emission wavelength can be quantified by calculating the ratio of fluorescence detected at shorter wavelengths with that detected at longer wavelengths, as defined in equation 5.2, where *F1* and *F3* denote the relative autofluorescence in channels 1 and 3, respectively.

$$R_{shift} = \frac{F1}{F1 + F3} \tag{5.2}$$

Empirically, the index R_{shift} is expected to decrease with increasing cartilage degradation. From the dataset presented in Figure 5.30B, we calculate an R_{shift} of 0.6 ± 0.02 for untreated samples and 0.5 ± 0.02 for treated samples, with a corresponding p-value of 0.0002 (n = 4). This result suggests that steady-state autofluorescence data may also provide means of label-free contrast in degenerated cartilage specimens.

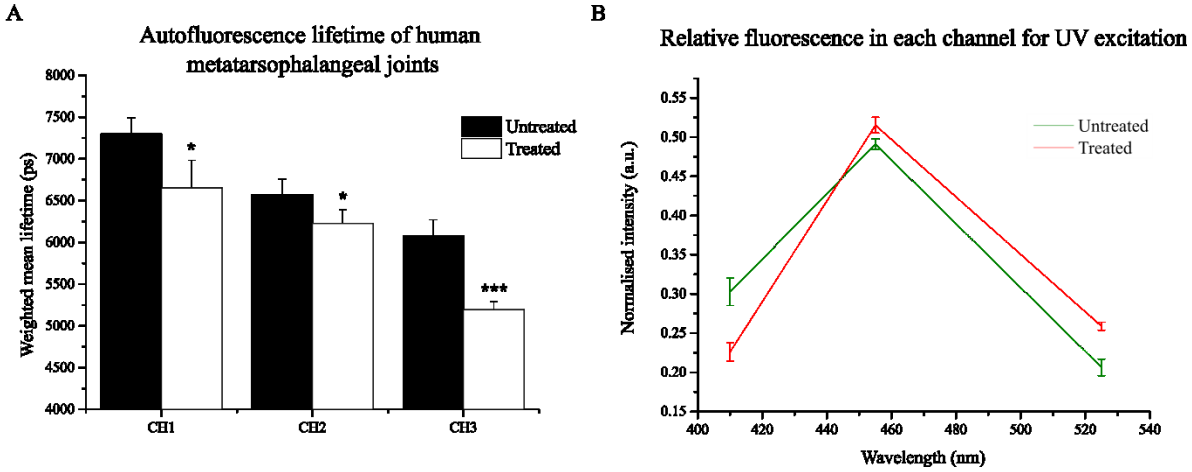

Figure 5.30 (A) Mean autofluorescence lifetime decrease with retinoic acid treatment. p-values of 0.0127, 0.0280 and 0.0005 were calculated for channels 1, 2 and 3, respectively, indicating statistical significance between measurements in untreated and treated samples. (B) Relative contribution of each spectral channel to the overall fluorescence signal under UV excitation.

Figure 5.31 presents the diffuse reflectance data of untreated (in green) and treated (in red) articular cartilage, indicating representative tissue absorbance spectral profiles, calculated as described in section 5.7.1.4. Our data show an overall increase in absorbance in retinoic acid treated samples, which is in general agreement with previous observations of diffuse reflectance data in the visible range of the spectrum in collagenase-treated bovine joints [251] and *ex vivo* human knee samples [172]. Changes in tissue reflectance upon cartilage degradation have been associated to both proteoglycan depletion and collagen disruption [227]. Our results suggest that removal of proteoglycans alone can affect the tissue optical scattering and absorption properties, possibly as a result of loss in water content that ultimately leads to an overall increase in tissue absorbance in the visible range of the spectrum. We also observe the presence of a pronounced absorbance peak at ~ 420 nm in treated samples, which is not as evident in untreated samples. Although we have not yet established the origin of the pronounced absorbance peak measured at around ~420 nm, this appears to be consistent with an absorbance maximum of oxygenated haemoglobin [307], [308]. Previous studies [145], [172] have demonstrated that the diffuse reflectance spectra of articular cartilage can

contain hallmark features of haemoglobin, particularly in regions where the cartilage is thinner, which has been attributed to the presence of blood in subchondral bone. In our case, removal of proteoglycans from the tissue may have altered the tissue scattering and absorption properties, which would facilitate light penetration into deeper regions of the cartilage tissue and eventually reach the subchondral bone. Additional studies are still required in order to validate this hypothesis.

Overall, if we calculate the relative changes in tissue absorbance as a ratio of the two curves, we verify that differences in the mean absorbance spectra are maximised in the short wavelength range of the spectrum and are minimised towards longer wavelengths, which is in agreement with previous diffuse reflectance studies in *ex vivo* human knee samples presenting naturally occurring degradation [172].

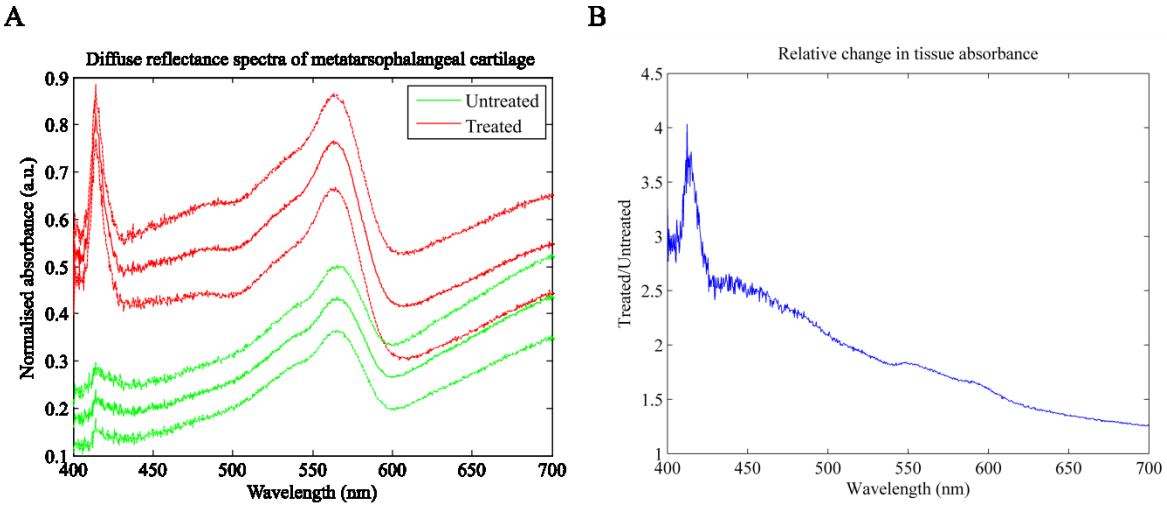

Figure 5.31 (A) Absorbance spectra between 400 and 700 nm of untreated (n = 8) and treated (n = 9) articular cartilage from metatarsophalangeal joints. Solid line shows average and dotted lines show standard deviation. (B) Relative changes in tissue absorbance, indicated as A(treated)/A(untreated).

In order to illustrate the potential of our instrument to distinguish untreated and treated human articular cartilage, a discrimination algorithm was implemented, employing PCA followed by LDA, as described in section 5.7.1.5. The algorithm was employed on the weighted mean fluorescence lifetime, relative contribution to the fluorescence signal of channels 1, 2 and 3, and average absorbance within 400 and 700 nm. Due to the low number of specimens available, each individual point measurement was used in this analysis providing a total of 35 measurements for untreated specimens and 34 measurements for treated specimens. Figure 5.32A shows the scores of the first two principal components separated by the decision line (in blue) produced by LDA analysis. From the classification, we extracted an AUC value of 0.991, and sensitivity and specificity of 100% and 97.1%, respectively, thus clearly demonstrating the capability of our system to distinguish untreated from digested samples.

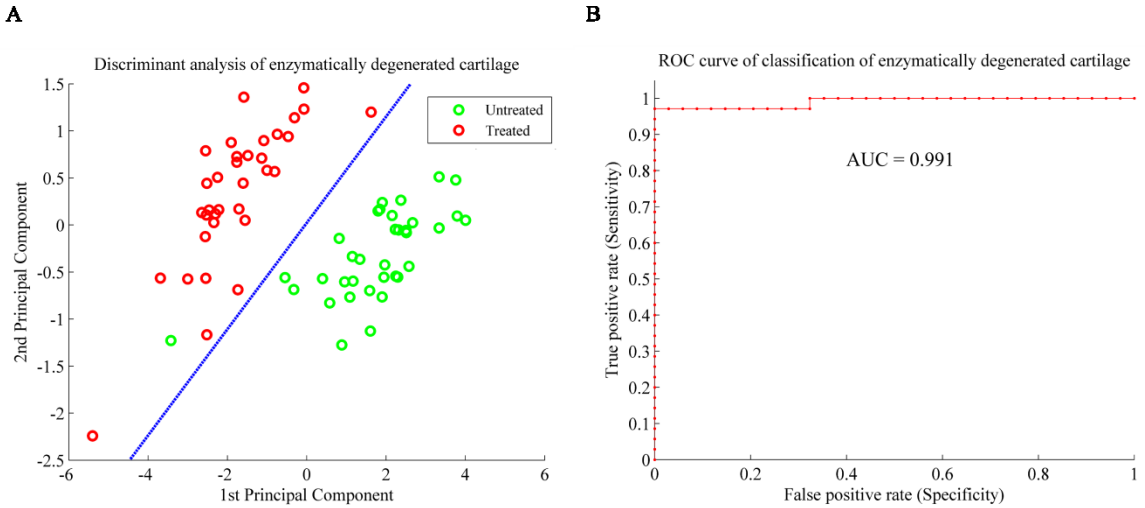

Figure 5.32 (A) Scatter plot of the first two PC from PCA analysis. Blue dotted line represents the decision line produced by LDA separating untreated (n = 35) from treated (n = 34) measurements. The most relevant parameters for the first and second principal components were CH1 τ_{mean} and CH1 R (ratio of the total fluorescence signal detected in channel 1, under UV excitation), respectively. (B) ROC curve for classification of enzymatically degenerated human cartilage.

5.7.2.2 Naturally occurring OA samples

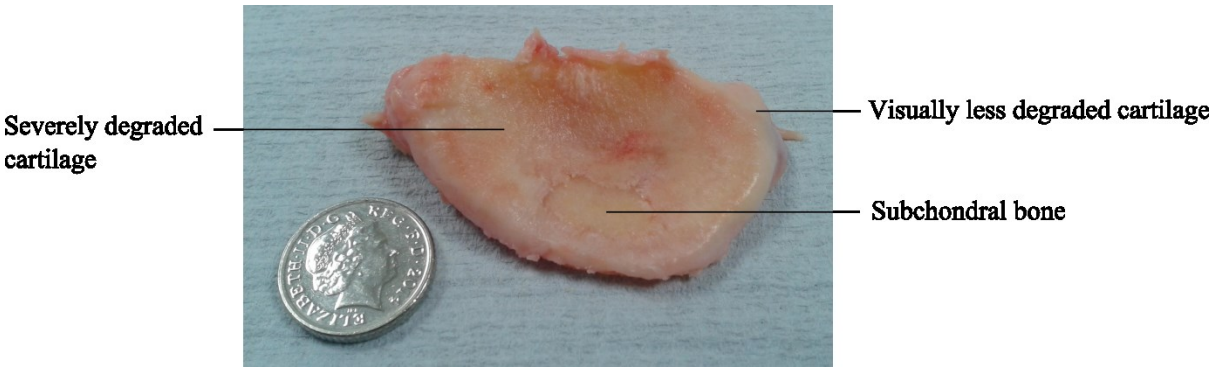

Figure 5.33 Human tibial plateau showing signs of severe OA. Subchondral bone is visible at the centre. Regions at the edge of the sample are apparently less degraded, i.e. tissue is visually more homogenous.

Data presented in this section were collected from samples obtained during routine knee replacement surgeries, therefore all samples presented hallmark features of late stages of OA and lacked minimally damaged or intact cartilage. In fact, patients with symptoms of early OA are less likely to be undergo this surgery and, consequently, these samples are much less frequent and, likewise, more precious. A human OA joint representative of those measured in this study is illustrated in Figure 5.33, showing hallmark characteristics of severe OA, with visible subchondral bone at the centre of the joint and no intact cartilage throughout.

Due to the large size of the samples and because it was challenging to distinguish regions at different levels of degradation (apart from bone), autofluorescence and diffuse reflectance measurements were taken from different regions of the surface of the tibial plateau (see Figure 5.34A). The goal was to

create lifetime (and diffuse reflectance) maps that could then be correlated to histology. Although lifetime and diffuse reflectance maps were created for all samples investigated, only one representative example is demonstrated here (see Figure 5.34). For the remaining samples, the average lifetime and diffuse reflectance and spectral curves for each region are presented.

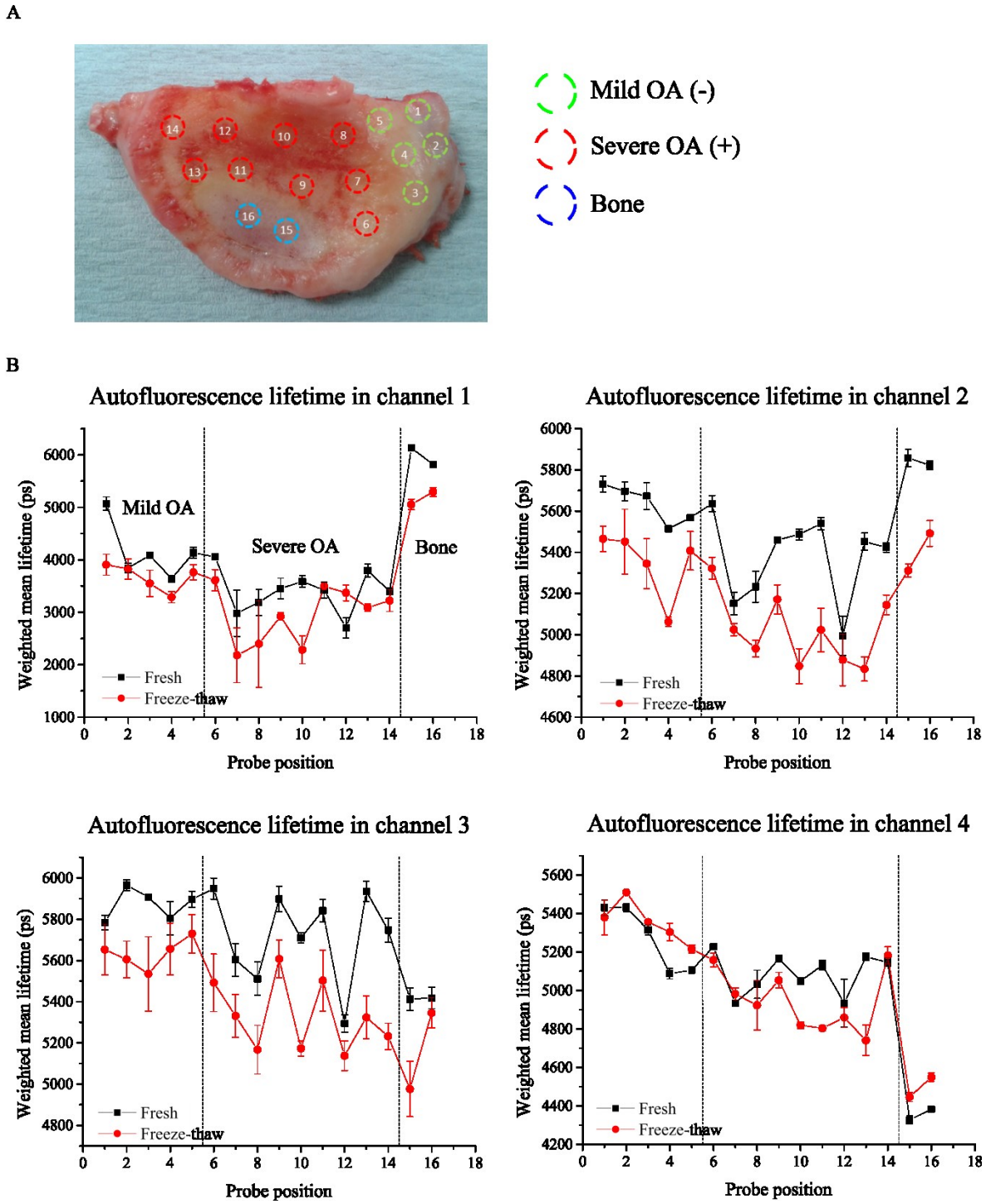

Figure 5.34 (A) Diagram showing approximate position of the fibre-optic probe at the time of measurements, which were realised immediately after extraction from the patient and after freezing and thawing. (B) Weighted mean autofluorescence lifetime in each region of the sample, for each spectral channel of the point probe system. Regions are identified by colour: green for apparently healthy; red for damaged; blue for bone.

Areas of the cartilage surface that were visually less degraded were identified as 'Mild OA', for comparison and potential discrimination from 'Severe OA' regions (see Figure 5.34A). It should be noted that this is merely a visual classification and therefore may not be a correct assessment of the real state of degradation of the tissue. However, we believe this is a comparable approach to that of surgical procedures, e.g. knee arthroscopies, which also require visual inspection of the tissue to resect. A similar approach was recently published by Brown et al [228].

The sample illustrated in Figure 5.34A was measured immediately upon receipt and after storage at -80°C, to verify the effect of freeze-thaw treatment on the autofluorescence lifetime. The first immediate conclusion that can be drawn is that the autofluorescence lifetime is consistently shorter after the freeze-thaw procedure. If we average all measurements, excluding those of subchrondral bone, we found a statistical significant decrease in the mean autofluorescence lifetime in detection channels 1, 2 and 3, with p-values of 0.0433, 0.0005 and 0.0001, respectively (n = 14, two-tailed Student t-tests). Previous studies by others have demonstrated that proteoglycans and collagen are not released from the tissue in significant amounts due to freezing at -80°C [309], [310], hence contradicting our findings. However, it has also been demonstrated that the formation of ice crystals can disrupt the ECM, which ultimately leads to alterations in the articular cartilage mechanical properties [310], [311]. It is possible that the decrease in autofluorescence lifetime results from a mixture of both processes. Furthermore, freeze-thaw at -80°C can affect the viability of chondrocytes [312] and further disrupt the ECM.

The average absorbance spectra for each of the regions identified in the sample illustrated in Figure 5.34A (measured fresh) are plotted in Figure 5.35.

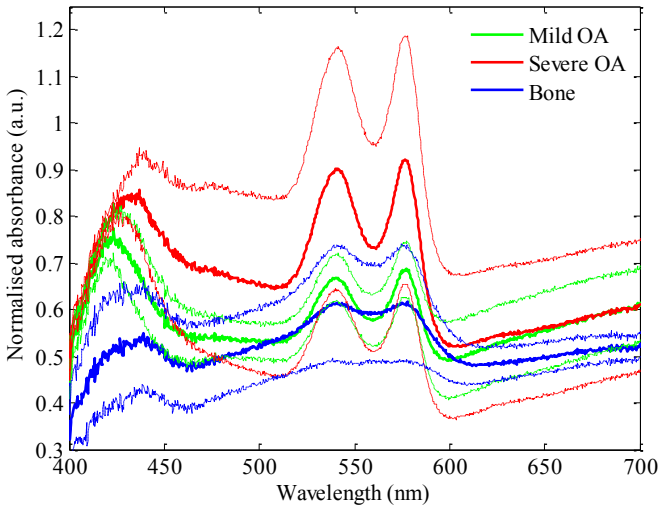

Figure 5.35 Normalised average absorbance spectra for 'Mild OA' (n = 5), 'Severe OA' (n = 8) and 'Bone' (n = 2) regions, calculated as described in section 5.7.1.4. Thick solid lines represent average and dashed lines represent standard deviation.

In the diffuse reflectance spectra measured from this sample, we observe hallmark characteristics of the haemoglobin spectra, with maximum absorbance peaks at ~420 nm, ~540 nm and ~576 nm. This is an expected result as, despite having been thoroughly washed with PBS, the specimen was measured fresh, i.e. immediately upon receipt, and therefore blood residues were still present in the tissue, as its colouration indicates (see Figure 5.34A). With respect to the amplitude of the curves, we observe that regions identified as "Severe OA" yield higher absorbance relative to 'Mild OA' regions, which is in agreement with previous results (see Figure 5.31) that showed that tissue absorbance increases with degradation.

Autofluorescence and diffuse reflectance results for each region in all specimens investigated were averaged and are presented in Figure 5.36. It is important to note that we were unable to identify 'Mild OA' regions in one sample, which explains the difference in the number of samples in each group.

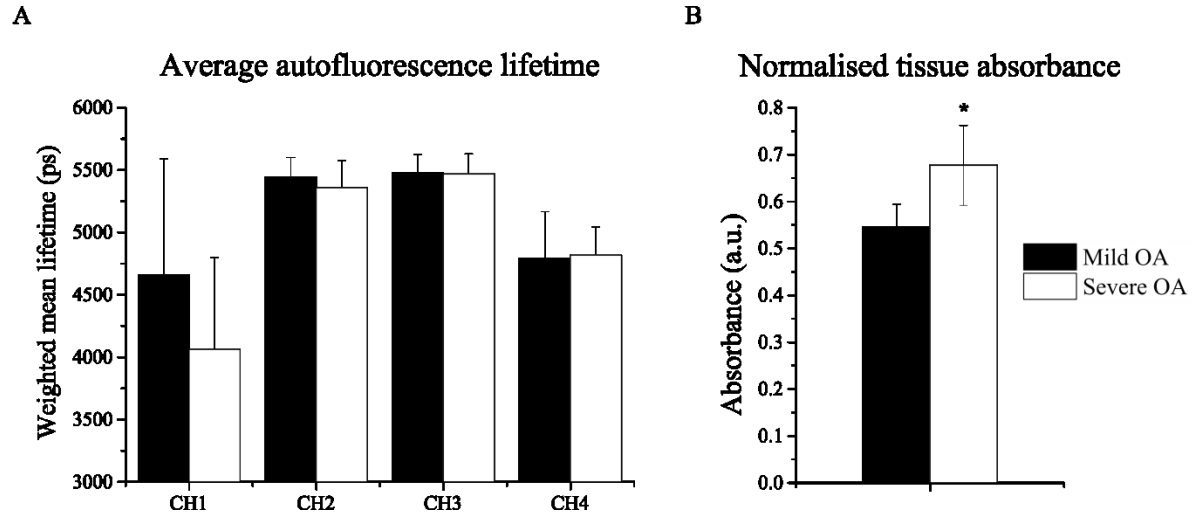

Figure 5.36 (A) Autofluorescence lifetime in each spectral channel of our time-resolved point probe instrument and (B) average tissue absorbance in 'Mild OA' (n = 5) and 'Severe OA' (n = 6) regions of human articular cartilage. Data from 'Healthy' group are extracted from articular cartilage measurements of metatarsophalangeal joints. * denotes statistical significance between 'Mild OA' and 'Severe OA', computed with two-tailed t-tests.

Results in Figure 5.36 indicate that lifetime-based parameters are unable to differentiate 'Mild OA' from 'Severe OA'. Diffuse reflectance parameters appear to be more sensitive to the degree of degradation of the tissue, where we found a statistically significant increase in the average tissue absorbance in "Severe OA" ($p = 0.0124$) relative to 'Mild OA' samples, which confirms our previous observations in digested human cartilage (see Figure 5.31). We also observe a decrease in contribution from short wavelengths to the overall fluorescence signal upon UV excitation in 'Severe OA' relative to 'Mild OA' samples, which effectively translates into a shift in the fluorescence emission towards longer wavelengths (see Figure 5.37). Since we have also observed the same effect upon proteoglycan removal via retinoic acid treatment (see Figure 5.30B), our results suggest that changes in fluorescence emission wavelength are associated with both proteoglycan depletion and break-up of collagen crosslinks that are responsible for fluorescence in that range of the spectrum. If

we quantify the shift in fluorescence emission wavelength through the index defined in equation 5.2, we obtain an R_{shift} of 0.3 ± 0.09 for 'Mild OA' (n = 5) and 0.2 ± 0.10 for 'Severe OA' (n = 6), and a corresponding p-value greater than 0.05, which indicates no significant difference between the two regions.

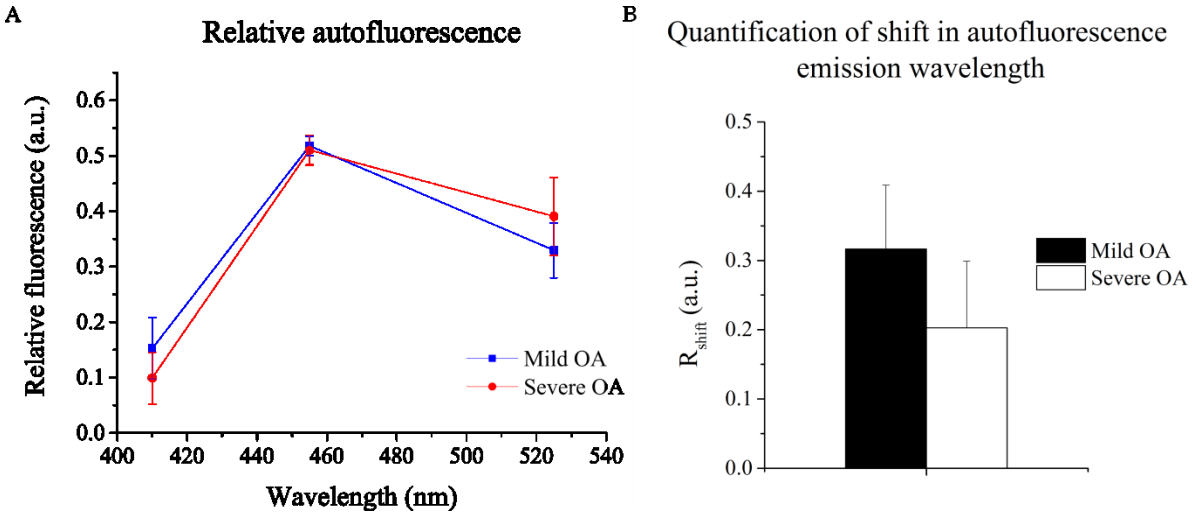

Figure 5.37 (A) Relative fluorescence intensity in each channel of the point probe system under UV light excitation and (B) quantification of the autofluorescence emission wavelength, calculated as defined in equation 4.2.

The results presented above suggest that diffuse reflectance parameters are more sensitive to the degree of degradation of the tissue compared to autofluorescence parameters. However, it should be noted that diffuse reflectance measurements are sensitive to intensity artefacts, which, in this case, are caused by the presence of blood residues in the tissue. As result, the diffuse reflectance spectra of these samples presented hallmark features of haemoglobin (see Figure 5.35). Since cartilage is an avascular tissue, blood is not expected to be present in an *in vivo* measurement. Therefore, it is possible that the diffuse reflectance results for these samples merely reflect the presence of blood in tissue rather than a characteristic cartilage degradation signature.

In summary, the results presented in this section suggest that further investigations are still necessary in order to validate autofluorescence and diffuse reflection spectroscopy as clinically viable tools for early detection of OA. In particular, it is of interest to correlate the autofluorescence and diffuse reflectance data with biochemical parameters extracted from histology. Unfortunately, histology results were not available in time for the present study.

5.8 Conclusions and summary

In this chapter, the application of autofluorescence and diffuse reflectance measurements to studies of articular cartilage was described, intended to show the potential of the technique as a tool for the study of the development and diagnosis of osteoarthritis.

The potential of autofluorescence lifetime to read out cartilage degradation was investigated *in vitro* in porcine cartilage and *ex vivo* in murine and human cartilage specimens. In general, our results indicated that healthy cartilage yields a long and complex fluorescence decay profile, with average lifetimes ranging from 8 - 10 ns, 5 - 6 ns and 5 - 7 ns in porcine, murine and human cartilage, respectively. The relatively long fluorescence lifetimes and corresponding wavelength dependency (in the case of human samples) can be attributed to the presence of collagen type II, which is the dominant source of autofluorescence in articular cartilage tissue. Previous studies in our group [121], [258] and others [122], [123] have demonstrated that collagen fluorescence characteristics are highly dependent not only of the excitation and emission spectra but also of the source of collagen itself. In particular, collagen type II from nasal septum and tracheal cartilage has been found to yield a complex fluorescence decay profile with lifetime of approximately 6 ns [122] - using 337 nm excitation - which is in general agreement with our results. The difference in autofluorescence lifetimes measured for each species may be related to the biochemical composition and structure of cartilage. It is well known that cartilage composition varies with species and mechanical load, which translates into different collagen arrangement, proteoglycan concentration and thickness [246], [313]. It is possible that the differences found in the average lifetime of cartilage of different species reflect variations in these parameters.

With respect to the effect of proteolytic activity on the cartilage autofluorescence, we observed significant differences in the autofluorescence lifetime of degenerated porcine cartilage upon enzymatic digestion of its two major components: collagen and aggrecan. In particular, the autofluorescence lifetime of articular cartilage was found to decrease with bacterial collagenase and MMP-1 treatment, which are enzymes that induce the cleavage of collagen fibrils and the depletion of proteoglycan from the tissue. More excitingly, we observed a similar decrease in autofluorescence lifetime of cartilage upon treatment with retinoic acid and trypsin, which are known to deplete the proteoglycan content from the tissue while maintaining the collagen network intact. These results are of particular interest for OA studies, as aggrecanolysis is believed to be the first step of cartilage degradation in the natural progression of the disease [245], [248]. The sensitivity demonstrated by autofluorescence lifetime measurements to read out aggrecan depletion in the absence of collagen disruption represents an important step towards the validation of this technique as a clinically viable tool for early detection of cartilage defects during OA. This is further emphasised by the fact that we were able to differentiate healthy from proteoglycan depleted cartilage in human samples. These results also suggest that changes in the autofluorescence lifetime of cartilage due to degradation cannot be exclusively attributed to the cleavage of collagen fibrils, but also reflect changes in the biochemical composition of the ECM due to the loss of proteoglycan content.

Unfortunately, despite we have observed similar effects to those discussed above in enzymatically digested murine cartilage, we were unable to replicate such findings in mouse knee joints presenting naturally occurring OA, most likely due to the poor spatial resolution of our instrument, given the sample size and heterogeneity of the degradation. In addition, histology images indicated proliferation of collagen type I, as result of the tissue healing process. Because collagen type I yields a long fluorescence lifetime (see Chapter 3), and is thus comparable to that of healthy murine cartilage, it is possible that its proliferation in OA samples masked any changes in the average lifetime that could be attributed to cartilage degradation.

We have also investigated the autofluorescence and diffuse reflectance signatures of articular cartilage from *ex vivo* human knee joints in which OA developed naturally. These samples were obtained from OA patients undergoing routine knee replacement surgery and therefore only a limited number of samples were available, all of which presenting hallmark characteristics of late stage OA. In order to investigate the sensitivity of our instrument to the level of degradation, we visually identified regions of the cartilage presenting 'Mild OA' or 'Severe OA' characteristics. Although these regions appeared to be visually distinguishable, our studies suggest that it is challenging to discriminate them using autofluorescence and diffuse reflectance parameters. Since we have demonstrated that both autofluorescence and diffuse reflectance can differentiate cartilage at different stages of degradation, with a particular emphasis for autofluorescence lifetime measurements, it is possible that, at the level of severe degradation presented by these samples, our measurements can no longer read out intrinsic contrast. This hypothesis appears to be corroborated by one of our studies of enzymatically induced degradation in porcine specimens (see Figure 5.11B), in which the autofluorescence lifetime decreases with treatment time until a saturation plateau is reached, suggesting that autofluorescence lifetime cannot read out contrast when the cartilage is severely damaged. Since all samples presenting naturally occurring OA showed signs of severe degradation, it is possible that we are observing a similar effect in these samples. Overall, further analysis is still required, particularly regarding the correlation of autofluorescence and diffuse reflectance data with biochemical and histological analyses of the cartilage. Unfortunately, these were not available in time for the present study, thus limiting further and thorough analysis on this topic.

One of the limitations of this study relates precisely to the fact that all samples of naturally occurring OA presented severe signs of degradation with little or no intact cartilage. Hence, we were unable to examine the autofluorescence and diffuse reflectance signals in early OA. However, the results presented in this chapter demonstrate that autofluorescence lifetime has the potential to readout early changes in cartilage matrix during OA, as a result of proteoglycan depletion. To further validate our instrument as a clinically viable tool for the diagnosis of OA, it is of key importance that future studies focus on characterising the autofluorescence and diffuse reflectance signatures in early stages

of disease progression in human samples. This may prove challenging, as samples presenting minor signs of natural degradation are scarce and therefore difficult to obtain. A potential solution would be to measure the autofluorescence signal from knee joints explanted from cadavers, as in reference [250].

Although both time-resolved and diffused reflectance spectroscopy were studied here, the latter was only used at a later stage of this investigation and therefore it is not possible to directly compare both techniques with respect to the detection of early cartilage degeneration. In summary, the work presented in this chapter demonstrated that both time-resolved autofluorescence spectroscopy and steady state white light reflectometry may offer a non-invasive readout to monitor cartilage matrix integrity that could contribute to future diagnosis of early cartilage defects as well as monitoring the efficacy of therapeutic agents. However, further investigations are still necessary in order to confirm our findings, with particular emphasis for studies at early stages of natural progression of OA. Based on this preliminary work, we believe that once the autofluorescence and diffuse reflectance signatures that accompany the progression of OA in a natural environment are well characterised, these techniques could be applied during arthroscopic procedures to study and possibly aid diagnosis of early OA in joints.

6 Autofluorescence and diffuse reflectance studies of cardiac tissue

In this chapter, the application of autofluorescence lifetime measurements and diffuse reflectance spectroscopy to the study of heart disease is presented, with a particular relevance to myocardial infarction studies, using the single point fibre-optic probe based instrument presented in Chapter 4. This work was carried out in collaboration with Dr Alexander Lyon's group at the National Heart and Lung Institute (NHLI) from Imperial College of London.

Cardiovascular disease is a leading cause of morbidity and mortality in the developed world. In particular, myocardial infarction is one of the most frequent and severe cardiovascular events and thus a major contributor to the death statistics. The objective of this investigation was to explore the potential of time-resolved spectrofluorometry and white light reflectometry to report structural and metabolic changes associated with cardiac disease, both *ex vivo* and *in vivo*, with a view to developing a new label-free cardiac diagnostic tool. Using a Langendorff rat model, the autofluorescence signature of cardiac tissue was investigated under different stress conditions, e.g. hypoxia and glucose privation. We were able to correlate and translate *ex vivo* findings to an *in vivo* myocardial infarction model in rats, where we observed structural and energetic changes in the infarcted and remote myocardium at different stages of disease progression. This work prompted the development of a clinically viable instrument to be used in open chest surgical procedures in humans, of which progress to date is described. Overall, our investigations indicate that autofluorescence lifetime may offer a label-free readout of energetic and structural alterations in the myocardium, which could contribute to future diagnosis of cardiac disease as well as monitoring the efficacy of therapeutic procedures, by means of a minimally-invasive catheter-based approach.

Part of the work presented in this chapter resulted in the publication of 1 journal article (Lagarto et al, *Biomedical Optics Express*, 2015) and 6 oral presentations.

Outline

- Introduction to the heart and its underlying biological mechanisms, including metabolic pathways and tissue remodelling upon myocardial infarction.
- Characterisation of the autofluorescence and diffuse reflectance signatures of cardiac tissue in an *ex vivo* Langendorff rat model, including hypoxia and glucose privation studies.
- *In vivo* autofluorescence and diffuse reflectance studies of a rat myocardial infarction model.

- Conclusions, including a brief description of the progress towards *in vivo* measurements of human hearts during surgery.

6.1 Introduction

Cardiovascular disease is a leading cause of morbidity and mortality in the developed world, for which myocardial infarction is the most frequent and severe contributor [314], [315]. Diseases of the myocardium such as left ventricular hypertrophy and heart failure are frequently characterised by disturbances in mitochondrial metabolism and energetic dysfunction, alterations in extracellular matrix (ECM) and interstitial fibrosis. There is growing evidence that these structural and functional abnormalities contribute to progression of contractile dysfunction and electrical instability, underpinning the progression to pump failure and malignant ventricular arrhythmias, the two leading causes of morbidity and mortality in patients with left ventricular hypertrophy and heart failure.

Currently, a number of clinical imaging tools are available to evaluate and monitor myocardium structure and function including FDG-PET, NMR spectroscopy and LGE-CMR [316]. Although well-established, these techniques have a number of limitations including low sensitivity and suboptimal spatial resolution, in addition to practical barriers including relatively high cost, limited availability and the limitations on the frequency of repeated measurements in the same individual, as they require the administration of a radionuclide (in the case of FDG-PET) or contrast agent (in the case of LGE-CMR) to provide or enhance contrast in tissue, which can potentially introduce toxicity in the biological system [70], [140]. New technologies with greater sensitivity to detect and monitor changes in myocardial metabolism and progression of fibrosis are needed, which may help guide treatment selection and stratification at an earlier stage, and also cross correlate structural and functional changes to provide new insights into the pathophysiology of myocardial disease. In recent years, advances in interventional and surgical techniques have allowed access to measurements and monitoring of cardiac function using electrodes, 3D echocardiography or pressure wires. However, none of these approaches directly evaluates the viability of the myocardium itself, but rather the gross and late impairment in electrical and mechanical activity at the level of the whole ventricular chamber. These macroscopic approaches, whilst offering new insights, generally do not provide accurate prognostic information or treatment targeting, which is now known to be best determined by myocardial structural and functional abnormalities and their inhomogeneity, and therefore more sophisticated tools are required. In particular, techniques employing a label-free method for *in situ* and real time characterization of cardiac tissue to identify the early alterations in the failing heart would represent a useful diagnostic advance to target early therapeutic intervention.

Autofluorescence spectroscopy is a promising tool for characterization of biological tissues and has shown potential for *in vivo* clinical diagnosis of diseased tissues and therefore optimization of

therapeutic procedures [203]. The application of optical spectroscopy to heart disease is still very limited and only a few *in vivo* studies have been reported. Many of these studies utilised diffuse reflectance spectroscopy to characterise the hemodynamic state of the heart by quantification of the tissue oxygenation and haemoglobin and myoglobin concentrations [163], [164], [219], [317]. Other studies used steady-state autofluorescence intensity or emission spectroscopy to report cardiac tissue viability and metabolic state [3], [92], [167]. However, intensity measurements alone are sensitive to variations in excitation efficiency, fluorophore concentration and heterogeneous sample absorption and scattering and so are difficult to compare between samples and patients [140]. Spectrally-resolved ratiometric measurements can provide quantitative readouts but their discrimination is limited by the broad overlapping fluorescence spectra of many tissue fluorophores [284].

As discussed in Chapter 4, time-resolved fluorescence spectroscopy (TRFS) is an inherently ratiometric technique that aims to improve the specificity of fluorescence measurements by resolving the fluorescence intensity decay characteristics and it is well suited to discriminate between fluorophores with overlapping emission spectra but different decay times [148]. With respect to cardiovascular research, although a number of studies employing autofluorescence lifetime measurements have been reported in isolated cardiac cells [39], [149] and in a number of other cardiovascular applications [24], [140], [216], its application to measurements of the heart remains limited [169]. In their work, Venius et al [169] undertook a preliminary *ex vivo* study of the human heart to characterise the autofluorescence lifetime signature of cardiac tissue excited at 405 nm with emission between 430 and 550 nm. This pioneering study of the application of TRFS in the field of cardiac research was conducted in a single human heart and therefore a systematic investigation and characterisation of the cardiac signature in different conditions or disease states remains to be done. Furthermore, measurements were realised *ex vivo* (12 – 24 hours *post-mortem*) and therefore it is possible that the cardiac signature at the time of measurements was significantly altered and not representative of the *in vivo* metabolically active signal.

In this chapter, we report the application of the fibre-optic based instrument presented in Chapter 4 to characterise the autofluorescence and diffuse reflectance signatures that accompany structural and functional changes in cardiac tissue and to investigate the potential of these optical techniques to provide label-free contrast in myocardial disease. We report *ex vivo* studies in a Langendorff rat model through which the metabolic state of the heart was modulated, permitting the characterisation of the cardiac signature under different stress conditions in a well-established and controlled environment. We also report *in vivo* longitudinal studies of myocardial infarction, in which we identify metabolic and structural alterations in the tissue at different stages of disease progression.

6.2 Heart anatomy and basic function

The heart is a muscular organ approximately the size of a closed fist with the primary function of pumping blood to the cells throughout the body. The human heart is located obliquely in the thorax between the lungs, posterior to the sternum and superior to the diaphragm, where it rests. It is enclosed within the pericardium, a double-layered sac that protects the heart and provides a lubricated surface that facilitates its motion in the cavity. The inner anatomy of the heart consists of four chambers (see Figure 6.1): two superior atriums and two inferior ventricles. The right atrium and ventricle are responsible for the pulmonary circulation: the superior and inferior venae cavae and the coronary sinus deliver oxygen-depleted blood to the right atrium; the blood then flows from the atrium into the ventricle, which is responsible for pumping it to the lungs through the pulmonary arteries. The blood is re-oxygenated in the lungs and delivered into the left atrium by the pulmonary veins. Finally, oxygenated blood is directed to the left ventricle to be pumped out of the heart via the aorta and to be delivered to tissues over the entire body. Since the pressure required to pump blood to the systemic circulation is considerably higher than for the pulmonary circulation, in a healthy human heart, the left ventricle presents a significantly thicker muscular wall than the right ventricle (~10 mm compared to ~2 mm [318], [319]).

The wall of the heart consists of three layers, arranged from outside to inside as follows: epicardium, myocardium and endocardium. The myocardium is the basic muscle of the heart and therefore the most relevant for our discussion. It consists of basic cardiac muscle cells known as myocytes, which are central to the contractile function and viability of the heart, and ECM components, such as collagen types I and III, which are responsible for supporting the muscle cells and vessels as well as providing tensile strength and resilience during diastolic and systolic cycles [113]. Alterations in the collagen network are important features of myocardial disease. In a healthy heart, there is a fine balance between collagen synthesis and uptake in the ECM that maintain the viability of the heart. Impairment of this process leads to changes in the concentration of collagen in the tissue, which can affect the mechanical properties of the heart [320].

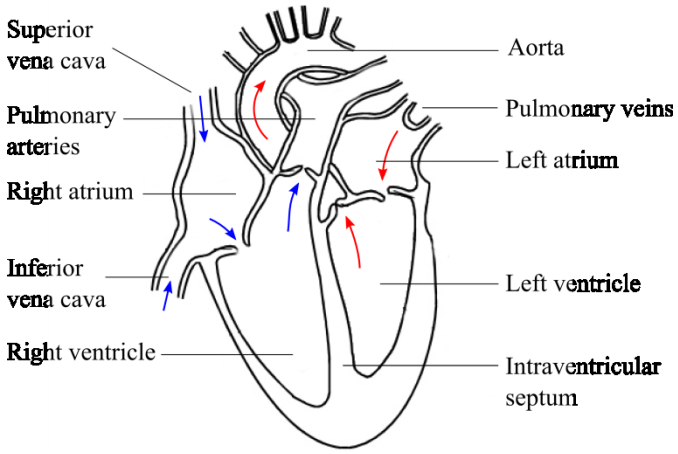

Figure 6.1 Coronal cross section view of the heart revealing atrial and ventricular chambers. Blue and red arrows indicate circulation of deoxygenated and oxygenated blood, respectively. Adapted from [321].

6.3 Metabolism in the heart

The contractile function of the heart is a process with extraordinary and continuous high energy demand. It consumes approximately 70% of the energy produced by the heart, while the remaining 30% is used in cellular processes such as ion pumps [322]. Because of this perpetual mechanical work, ATP - the fuel that drives all cellular processes - is consumed at a very fast rate and, accordingly, it can be exhausted within a few seconds if not replenished, since the heart has little capacity for energy storage [323]. Metabolic regulation is therefore essential and inevitably related to cardiac function: the amount of energy consumed during contraction must be restored during the cardiac relaxation period. Oxygen plays an important role in this cycle: the heart is essentially an aerobic organ, with little capacity to work sustainably under anaerobic conditions, and thus an adequate supply of oxygen (and nutrients) to the cardiac myocytes is essential to maintain function [324]. Indeed, impairment in the energy production-uptake regulation is associated with progressive loss of myocardial function that ultimately leads to heart failure [323]. This is primarily related to the decline in the activity of metabolic pathways that leads to diminished capacity for production of ATP. The reduced capacity for producing ATP results in dysregulation of cellular processes central to the contractile function, which in turn leads to an increase in the energy demand and, consequently, further loss of function.

The heart can produce ATP from different substrates including fatty acids, glucose or, to a lesser extent, amino acids [324], [325]. The preferential metabolic pathways to produce ATP are dependent on the availability of these substrates in blood and in the cells, coronary flow (i.e. blood circulation through the myocardium) and inotropic state [324].

In a healthy adult human heart, if the oxygen supply is sufficient, the dominant sources of energy are fatty acids, which are oxidised in the mitochondria via beta-oxidation. This corresponds to

approximately 70% of the total ATP production in the myocardium [326]. The remaining energy is mainly produced by oxidation of glucose by means of glycolysis in the cytosol and further breakdown of its by-product pyruvate in the pyruvate-dehydrogenase complex (PDC), which occurs in the inner mitochondrial membrane. The by-product of beta-oxidation and glycolysis (and PDC) is acetyl Coenzyme A (acetyl-CoA), which is the fuel of the Citric Acid cycle. Here, FAD and NAD^+ are reduced to produce $FADH_2$ and NADH, which will serve as electron donors in the electron transport chain (ETC). The movement of electrons through the protein complexes of the ETC promotes the movement of protons (H^+) from the mitochondrial matrix into the intermembrane space. As a result, a differential electrical charge is established across the inner mitochondrial membrane, which drives ATP synthesis in oxidative phosphorylation.

In contrast, if the oxygen supply is not adequate, e.g. during intense physical activity, glucose is converted into pyruvate - producing some ATP - which in turn is converted into lactate. This reaction is catalysed by lactate dehydrogenase (LDH). Lactate can be converted back to pyruvate (in the liver) at the expense of ATP. Although this process produces energy at a faster rate than the oxidative pathway, in the long term it is far less efficient energetically and therefore the heart cannot be sustained exclusively by this pathway.

In summary, aerobic cellular metabolism (or respiration) can be divided in three phases: 1) production of acetyl-CoA; 2) citric acid cycle; 3) respiratory chain, including electron transport chain and oxidative phosphorylation. The following sections provide a brief overview of each of the cardiac energy metabolic pathways, with particular emphasis for their energy yield and redox reactions.

6.3.1 Production of acetyl-CoA

The production of acetyl-CoA is the first step towards production of ATP in the mitochondria, in an aerobic environment. Acetyl-CoA derives primarily from the breakdown of fatty acids and glucose by means of beta-oxidation and glycolysis, respectively.

6.3.1.1 Beta-oxidation

Beta-oxidation is the process by which long fatty acid chains are degraded to generate acetyl-CoA. Initially, conversion of the fatty acid to a fatty acyl occurs in the cytosol of the cell, at the expense of two ATPs. The fatty acyl is then transported into the mitochondria to be further oxidised within the mitochondrial matrix. This process involves a series of sequential reactions that ultimately produce a two-carbon fragment in the form of an acetyl-CoA. The remaining fatty acid chain, now shorter by two carbons, will undergo a new cycle of beta-oxidation and the process repeats until all carbons are converted into acetyl-CoA. The number of acetyl-CoA molecules depends on the number of carbon atoms of the fatty acid undergoing oxidation. In addition, for each beta-oxidation cycle one molecule

of NADH and another of $FADH_2$ are formed, to be used later in the electron transport chain as electrons donors to produce ATP. Figure 6.2 summarises the beta oxidation pathway.

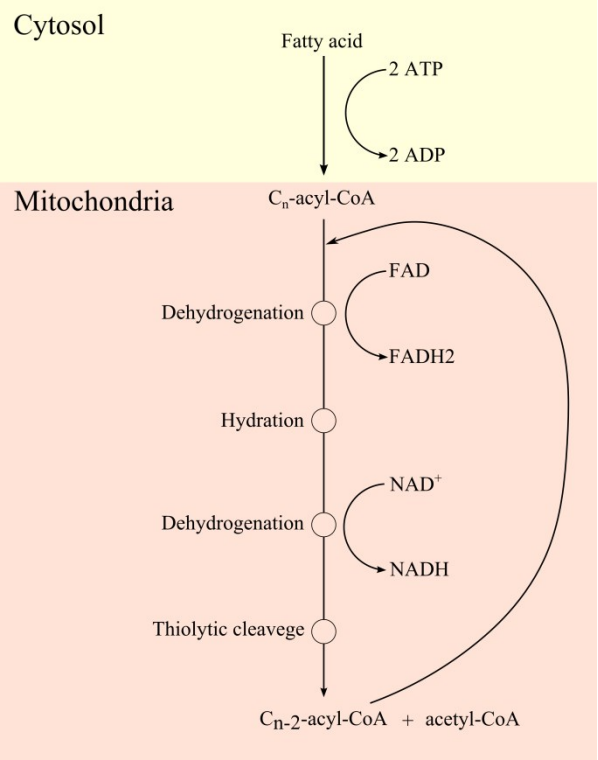

Figure 6.2 Simplified representation of the fatty acid beta-oxidation pathway where *n* represents the number of carbon atoms in the fatty acid. The cycle ends when all carbons are converted into acetyl-CoA, i.e. with n = 2. For each cycle, one molecule of NADH and $FADH_2$ are produced. Adapted from [327].

6.3.1.2 Glycolysis and pyruvate-dehydrogenase complex (PDC)

Glycolysis is the metabolic pathway by which one molecule of glucose is converted to two molecules of pyruvate, with concomitant generation of two moles of ATP. Unlike beta-oxidation, glycolysis occurs in the cytosol of the cell and does not require the presence of oxygen. Conversion of glucose to pyruvate occurs in two distinct phases: 1) an energy investment phase, in which a glucose molecule ($C_6H_{12}O_6$) is phosphorylated at the expense of two molecules of ATP and cleaved to form two three-carbon molecules (glyceraldehyde-3-phosphate, $C_3H_7O_6P$); 2) in the energy gain phase, these two molecules undergo a series of reactions to generate energy-rich compounds, which then transfer the high-energy phosphate to ADP, yielding ATP. The by-product of these reactions is pyruvate. Overall, the net yield of glycolysis per each molecule of glucose degraded is two molecules of ATP and two molecules of pyruvate. In addition, two molecules of NADH are generated during the energy gain phase, which will later be used in the electron transport chain.

In aerobic conditions, the pyruvates derived from glycolysis are transported into the mitochondria, where they undergo a series of oxidative decarboxylation reactions, catalysed by pyruvate dehydrogenase, to generate acetyl-CoA. These reactions also involve the generation of one molecule

of NADH per molecule of pyruvate. Figure 6.3 summarises the glucose metabolic pathway to generate acetyl-CoA.

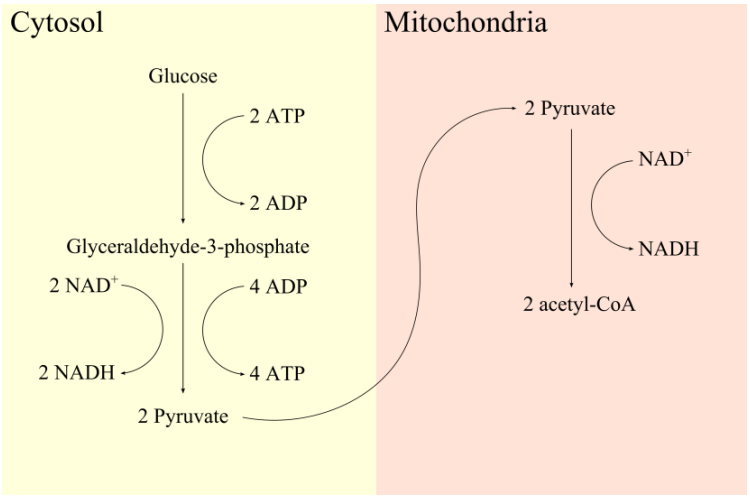

Figure 6.3 Simplified schematics of the aerobic glucose metabolic pathway to generate acetyl-CoA. Glycolysis occurs in the cytosol of the cells (left) and pyruvate is oxidised to acetyl-CoA by the PDC in mitochondria (right). Adapted from [327].

6.3.2 Citric acid cycle

The citric acid cycle, also known as Krebs cycle or tricarboxylic acid cycle (TCA), is the second stage of the metabolic pathway towards production of ATP and occurs in the mitochondrial matrix. It consists of a number of decarboxylation, oxidation and (de)hydration reactions by which a six-carbon complex, formed by the interaction of acetyl-CoA with oxaloacetate, is converted to a four-carbon molecule, resulting in the release of CO_2, while converting the energy of the acetyl group into ATP. In the process, three molecules of NADH and one molecule of $FADH_2$ are also generated, which will serve as electron donors in the electron transport system of the respiratory chain. The citric acid cycle is summarised in Figure 6.4. A brief overview of the reactions involved in the cycle is given below. For a more comprehensive discussion, the reader is directed to references [327], [328].

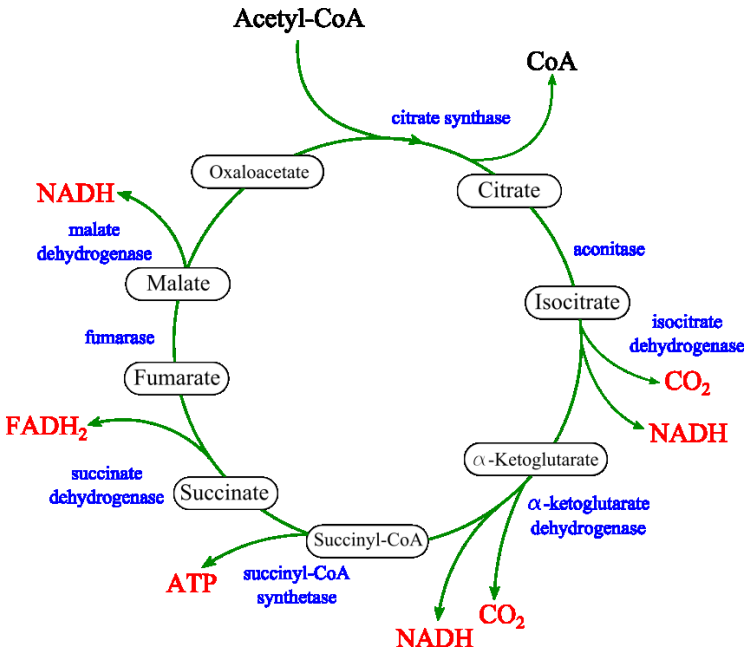

Figure 6.4 Schematic representation of the citric acid cycle, including by-products (in red) and enzyme complexes that catalyse each reaction (in blue). Adapted from [327].

The cycle initiates with a reaction catalysed by citrate synthase between acetyl-CoA and oxaloacetate to form citrate, a six-carbon complex with an unstable CoA group that is spontaneously hydrolysed.

The second reaction is catalysed by aconitase. Here, isomerisation of citrate occurs, by successive dehydration and hydration. This results in the delocalisation of a hydroxyl (OH) group to generate isocitrate.

The third reaction corresponds to the first oxidative decarboxylation in the cycle and it is catalysed by isocitrate dehydrogenase. This reaction involves oxidation of isocitrate to an intermediate compound (oxalosuccinate) and formation of NADH from NAD^+. This intermediate is immediately decarboxylated to generate α-ketoglutarate, which is accompanied by the release of a CO_2 molecule.

The fourth reaction consists in the decarboxylation of α-ketoglutarate, with removal of a CO_2 molecule and its replacement by a CoA complex. In the process, NADH is generated from NAD^+. This reaction yields succinyl-CoA.

The fifth reaction consists in the phosphorylation of succinyl-CoA, which loses the CoA complex to generate succinate. In this reaction, a molecule of guanine triphosphate (GTP) is synthesised from phosphorylation of guanine diphosphate (GDP). In turn, ATP is synthesised from dephosphorylation of GTP.

The sixth reaction of the cycle is catalysed by succinate dehydrogenase and involves the oxidation of succinate to fumarate and consequent reduction of FAD to generate $FADH_2$. FAD is covalently bound to succinate dehydrogenase, which in turn is bound to the mitochondrial inner membrane. The importance of this binding is related to the re-oxidation of $FADH_2$ in the mitochondrial electron transport chain, which is required for the enzyme to act again (see section 6.3.3).

The seventh reaction consists of the hydration of fumarate to yield malate and it is catalysed by fumarase hydratase.

The final reaction of the citric acid cycle corresponds to regeneration of oxaloacetate from dehydrogenation of malate and reduction of NAD^+ to generate NADH. This reaction is catalysed my malate dehydrogenase.

To summarise, for each mole of glucose, two moles of acetyl-CoA are generated, which corresponds to two citric acid cycles. This yields six moles of NADH, two moles of $FADH_2$ and two moles of ATP per each mole of glucose metabolised.

6.3.3 Respiratory chain: electron transport chain and oxidative phosphorylation

Up to now, we have reviewed the first two stages of cellular respiration, in which ATP is produced in small amounts and therefore not sufficient to maintain regular cellular function. Indeed, the production of acetyl-CoA and the citric acid cycle can be considered preparatory steps for the production of energy, which occurs in the final stage of cellular respiration. In this stage, re-oxidation of the reduced electron carriers NADH and $FADH_2$ will generate most of the energy necessary to synthesise ATP. It can be divided in two steps, illustrated in Figure 6.5: the ETC and oxidative phosphorylation.

The ETC is a metabolic pathway consisting of a series of oxidation and reduction reactions that drive ATP synthesis in oxidative phosphorylation. Here, NADH and $FADH_2$ are oxidised by four enzyme complexes that are bound to the inner membrane of the mitochondria and the resulting electrons are passed along these complexes by electron carriers. Complex I receives electrons from oxidation of NADH to NAD^+ and Complex II carries out a similar reaction from oxidation of $FADH_2$. This process is intimately related to the oxidation of succinate and consequent reduction of FAD to $FADH_2$ in the citric acid cycle (see section 6.3.2). The electrons generated from these reactions are passed onto coenzyme Q, which can move freely through the inner mitochondrial membrane. Coenzyme Q is then oxidised by Complex III, which in turn reduces cytochrome c. Finally, cytochrome c is oxidised by Complex IV and the final acceptor of the reducing equivalents is oxygen, hence producing water. The movement of electrons through the inner membrane causes protons (H^+) to be pumped out of the

mitochondrial matrix to the intermembrane space. Consequently, a net negative charge builds up in the matrix while a net positive charge builds up in the intermembrane space. This differential electrical charge establishes an electrochemical gradient that favours the flow of protons back into the mitochondrial matrix via a specific channel, known as Complex V or ATP synthase. The energy released by the movement of protons across the membrane drives the phosphorylation of ADP to ATP. This process, known as oxidative phosphorylation, is quite energetic: for each mole of NADH that is oxidised, 3 moles of ATP are synthesised; similarly, for each mole of $FADH_2$ oxidised, 2 moles of ATP are synthesised.

At this point, it is convenient to review the energetic yield of cellular respiration, for both glycolysis (Table 6.1) and beta-oxidation (Table 6.2) pathways. The total energetic yield per mole of glucose metabolised is 38 moles of ATP, which corresponds to approximately 6.3 ATP per carbon atom (see Table 6.1). Similarly, cellular respiration through beta-oxidation of a sixteen-carbon fatty acid yields 129 moles of ATP or approximately 8.1 ATP per carbon oxidised in CO_2 (see Table 6.2). Hence, the energetic yield per carbon oxidised to CO_2 is higher in beta-oxidation than in glycolysis. In the anaerobic pathway (see Table 6.3), ATP is once produced during glycolysis, hence the energetic yield is much lower than in the aerobic pathways.

Table 6.1 Energetic yield of aerobic cellular respiration through glucose ($C_6H_{12}O_6$) metabolism. All values are reported in moles.

	NADH	$FADH_2$	ATP	Total ATP synthesised
Glycolysis	2	0	2	$2 \times 3 + 2 = 8$
Pyruvate dehydrogenase complex	2	0	0	$2 \times 3 = 6$
Citric acid cycle	6	2	2	$6 \times 3 + 2 \times 2 + 2 = 24$
Total ATP synthesised	$10 \times 3 = 30$	$2 \times 2 = 4$	4	38 (6.3 ATP/carbon)

Table 6.2 Energetic yield of aerobic cellular respiration through beta-oxidation of a 16-carbon fatty acid (palmitate). All values are reported in moles.

	NADH	$FADH_2$	ATP	Total ATP synthesised
Beta-oxidation	7	7	-2	$7 \times 3 + 7 \times 2 - 2 = 33$
Citric acid cycle	24	8	8	$24 \times 3 + 8 \times 2 + 8 = 96$
Total ATP synthesised	$31 \times 3 = 93$	$15 \times 2 = 30$	6	129 (8.1 ATP/carbon)

Table 6.3 Energetic yield of anaerobic metabolism

	NADH	$FADH_2$	ATP	Total ATP synthesised
Glycolysis	0	0	2	2
Total ATP synthesised	-	-	2	2 (0.33 ATP/carbon)

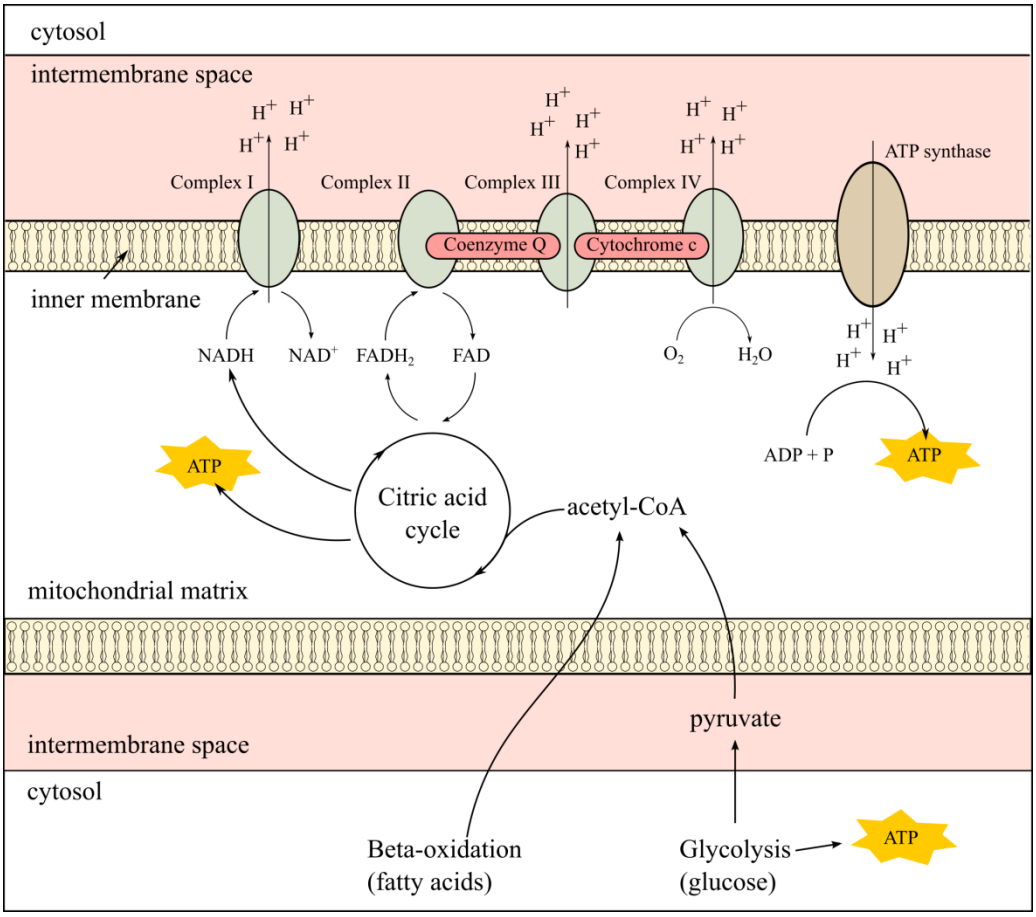

Figure 6.5 Summary of aerobic metabolic pathways for production of ATP.

6.4 Myocardial infarction and heart failure

Heart failure is one of the most concerning healthcare issues in the developed world with recognised medical, social and economic impact [315], [329], [330]. Heart failure is a chronic and progressive clinical syndrome characterised by inadequate cardiac pump function and subsequent inability to supply sufficient oxygenated blood to meet the demands of peripheral tissues throughout the body. The most common cause of heart failure is coronary artery disease (CAD) typically followed by myocardial infarction (MI). Myocardial infarction (MI) is one of the most severe and frequent cardiovascular injuries and is responsible for a high rate of hospitalisation and mortality [314], [315]. MI is characterised by progressive cell death of cardiac myocytes caused by impairment in the energy supply and demand, typically driven by rupture of an atherosclerotic plaque and consequent interruption of blood supply to the cardiac muscle [314]. Following MI, a number of repair mechanisms try to maintain the structural integrity and viability of the infarcted myocardium, including replacement of injured tissue by a fibrotic scar and remodelling of the remaining ventricle [331]–[333].

Ventricular remodelling is generally accepted as a determinant precursor of heart failure following MI, although it can also be developed as consequence of other cardiac disorders (e.g. hypertension or

inflammatory heart muscle disease) [334]. While the mechanisms of cardiac remodelling are not completely understood, they involve complex and dynamic functional, morphological and biochemical alterations that are not restricted to the region of infarction but can also affect the remote non-infarcted myocardium [335], [336]. In recent years, much investigation in heart failure following MI has been performed to characterise these changes. Reported changes include alterations of interstitial fibrosis throughout the heart affecting tissue compliance and contraction and relaxation [333], alteration of the electrical properties of the tissue [337] as well as alteration of the mitochondrial function and energy production of the failing heart [326]. Because structural and metabolic changes in heart failure can impact the autofluorescence signal of endogenous fluorophores of interest in the heart - namely collagen, NADH and FAD (see section 6.7) - these are described in further detail below.

6.4.1 Structural alterations in heart failure

After an acute myocardial injury such as myocardial infarction of the left ventricle, the wound-healing process is rapidly initiated, typically within a few hours after the injury occurs [338], and localised to the area of infarction [338], [339]. The initial remodelling phase consists in the repair of the wounded area via deposition of collagen types I and III and rearrangement of the collagenous matrix, i.e. scar formation, which is induced by the proliferation and upregulation of myofibroblasts [320]. Deposition of collagen types III and I has been observed only from two and four days post-infarction, respectively, and can still be observed after three months, particularly for the latter [320], [338], [339]. The deposition of collagen increases the tensile strength of the muscle allowing maintenance of the cardiac output. However, this also contributes to increased ventricular stiffness and reduced compliance, thus compromising ventricular function in the long term. This process is accompanied by significant dilation of the left ventricular chamber in response to loss of function of the muscle [335] and thinning and elongation of the infarcted area, which is associated with reduced number of cardiac myocytes in the muscle wall [340]. The extent of these repair mechanisms reflects the magnitude of the lesion, i.e. the greater the infarction, the greater the ventricular dilation and the thinner the muscle wall [335], [338].

Structural changes in the remote non-infarcted myocardium are not as well understood as in the infarcted region, although previous studies suggest that the increase in collagen content is less prominent and occurs at a later period [320], [333]. Remodelling of the non-infarcted myocardium can also include dilation of the ventricular chamber [341] and increased wall thickness, as result of increased left ventricle pressure overload [342].

6.4.2 Cardiac energetics in heart failure

As discussed above, after MI, the heart undergoes a number of structural alterations to compensate its inability to pump sufficient blood to meet the needs of the body. The increase in tensile strength as a

result of increased collagen content allows maintenance of the cardiac output with concomitant increase in energy consumption. Progressive loss of contractile function due to increased stiffness further increases the energy consumption as the heart tries to maintain the cardiac output. Eventually, the energy produced is not sufficient to meet the demand, resulting in dysregulation of cellular processes and further loss of function, ultimately leading to heart failure.

In heart failure, impairment in energy production-uptake is associated with alterations and dysregulation of metabolic pathways that lead to diminished capacity to produce ATP. It is generally accepted that in heart failure there is a switch in the favoured metabolic pathway from beta-oxidation to glycolysis [323], [343], which is associated with the down-regulation of the enzymes involved in the oxidation of fatty acids [344]. With an accelerated glycolytic rate, the heart can produce energy at a faster pace in order to meet the demand of cardiomyocytes at high workloads. However, with progressive ventricular remodelling, the energy produced during glycolysis becomes insufficient, leading to decreased efficiency.

Another important abnormality is associated with excessive formation of reactive oxygen species (ROS). ROS are inherent by-products of aerobic metabolism and their production is tightly regulated in the cells. An overproduction of ROS can inflict damage in lipids and proteins ultimately leading to reduced activity of enzyme complexes and ATP synthase in oxidative phosphorylation and other enzymes involved in the Citric Acid cycle [323], [343], [345]. Furthermore, the reduced coronary flow can limit the delivery of nutrients and oxygen to the cardiac myocytes. The latter is of particular relevance due to its central role in the production of ATP (see section 6.3.3). If the supply of oxygen is not adequate, the energetic efficiency of the oxidative pathway will be further reduced. Hence, the production of ATP will be mostly supported by the anaerobic pathway, which is not as energetically sustainable, as discussed above.

In summary, heart failure results from a series of cascading events that affect the structural and functional viability of the myocardium. Initially, increase in collagen content and consequent alteration of the mechanical and structural properties of the heart promotes the dysregulation of the energy production-uptake. The energy supplied to the cardiac muscle cells is not adequate to maintain sustainable contractile function, therefore contributing to further progression of dysfunction towards heart failure.

6.5 Autofluorescence of cardiac tissue

The autofluorescence signal of cardiac tissue is complex, emanating predominantly from metabolites NADH and FAD [149], [165], [346], [347], although other ECM fluorescent components can be present in lesser amounts, such as collagen types I and III and elastin [3], [73]. The fluorescence

excitation and emission peaks of these fluorophores are summarised in Chapter 3, together with their characteristic fluorescence lifetimes.

As discussed above, the concentration of these fluorophores are expected to change in disease. For example, after myocardial infarction, the autofluorescence signal from collagen is expected to increase due to scar formation in tissue. At the same time, changes in the metabolic pathways to produce ATP are likely to occur as result of mitochondrial dysfunction, which will affect the relative proportions of NADH and NAD^+ and, similarly, of $FADH_2$ and FAD. Hence, since the absolute concentrations of the reduced and oxidised forms of these molecules change in opposite directions in response to changes in metabolism, one can take advantage of the fact that only NADH and FAD are fluorescent at specific excitation wavelengths - e.g. 340 nm and 440 nm respectively - to quantify metabolic alterations. Indeed, the ratio of fluorescence intensity of NADH and FAD is known as the redox ratio and it represents the most common optical method to read out metabolic alterations in tissue [77].

With respect to the autofluorescence lifetime of cardiac tissue, it is more challenging to predict its signature in healthy and diseased myocardium. Collagen yields a long autofluorescence lifetime, and thus scar tissue formation can produce an increase in the mean autofluorescence lifetime of cardiac tissue. With respect to NADH and FAD autofluorescence, they can bind to multiple enzymes, yielding different and complex autofluorescence lifetimes for each binding partner [74], [84], [96], [130], [347]–[350]. Moreover, the binding partners or their relative proportions can change during disease progression or merely reflect alteration of the predominant metabolic pathway [39], [351]–[353], and thus further increasing the complexity of the decay.

A previous study by Venius et al [169] characterised the autofluorescence signature of different structures in the human heart *ex vivo*, namely the myocardium, conduction system and connective tissue. These structures were found to yield similar average fluorescence lifetimes of approximately 4 ns - using a tri-exponential model to fit the data - which was attributed to the presence of collagen in the tissue. It should be noted however that these measurements were realised *ex vivo* and therefore may not be representative of the *in vivo* metabolically active signal.

6.6 Ex vivo Langendorff studies of the heart

The Langendorff heart, established by Oscar Langendorff in 1897, is a technique that allows isolated perfusion of mammalian hearts. The basic principle of a Langendorff preparation remains mostly unchanged since its original demonstration. It consists in maintaining the cardiac activity of an explanted heart by perfusing a physiological salt solution retrogradely via the coronary arteries, down the ascending aorta, which is opposite to the blood flow in a living animal. This forces the aortic valve

to close under pressure and the solution not to enter the left ventricle. Instead, it is directed into the coronary arteries to perfuse the ventricles. Finally, the solution exits the coronary venous circulation via the coronary sinus to the right atrium [354].

The advantage of using a Langendorff setup is mostly associated with its simplicity and low cost preparation. Furthermore, it represents a very convenient method to study the biochemical, morphological or physiological response of the myocardium to different pathological conditions e.g. ischaemia or arrhythmia, that would otherwise be challenging to investigate in an *in vivo* experiment. Despite being a convenient method to study the myocardial properties, the heart is effectively isolated from other organs and tissues of the body, which may have a negative impact in the clinical relevance of any findings derived from this method. Furthermore, from our experience, the isolation of the heart is technically challenging and requires fine surgical skills. It also requires fine control of the instrumentation to balance all physiological parameters, i.e. perfusion pressure, temperature, oxygenation and salt concentration, which are essential to maintain stable and relevant cardiac activity.

Overall, the Langendorff heart preparation represents a convenient approach to investigate the autofluorescence and diffuse reflectance signatures of cardiac tissue. In particular, we used this method to establish the baseline autofluorescence signature of cardiac tissue not only in normal physiological conditions but also in response to physiological insults such as oxygen or glucose privation. These measurements, presented below, will serve to establish baseline readouts for *in vivo* experiments, presented in section 6.7.

6.6.1 Experimental methods

All work involving animal use was carried out under protocols approved and regulated under the Animals (Scientific Procedures) Act 1986 (Project Licenses PPL 70/7399 and 70/7419). All experiments presented below were realised using the hyperspectral point probe system described in Chapter 4.

6.6.1.1 Langendorff preparation

Adult male Sprague-Dawley rats (250–500 g) were anaesthetised by administration of 5% isoflurane and sacrificed by cervical dislocation. Hearts were rapidly explanted and immersed in oxygenated iced Krebs-Henseleit (KH) solution. The composition of the KH solution is as follows (values in mM): 118 NaCl; 4.7 KCl; 0.94 $MgSO_4$; 1 $CaCl_2$; 1.2 KH_2PO_4; 25 $NaHCO_3$; 11.5 $C_6H_{12}O_6$. Hearts were cannulated through the aorta for retrograde perfusion with oxygenated ($95\%O_2/5\%CO_2$) KH solution in a Langendorff apparatus (130105EZ-V, ADInstruments, USA) within 5 minutes from explantation. After cannulation, hearts were allowed to stabilise for 10 minutes prior to realise autofluorescence and diffuse reflectance measurements (see section 6.6.1.2). The flow rate was

maintained at 18 ml/min throughout the entire procedure. Hearts evidencing signs of ventricular fibrillation or with cardiac frequency outside the range 200 – 400 bpm were discarded. The experimental layout of the Langendorff system utilised in these experiments is illustrated in Figure 6.6. In brief, the apparatus comprises two columns that contain solutions to be delivered to the heart by means of a peristaltic pump that maintained the pumping pressure close to physiological levels. Column 1 consisted of oxygenated KH solution. Column 2 was used to provide an insult-solution to the heart. Three different solutions were investigated: 1) oxygenated KH solution, which served as control; 2) deoxygenated (95%N_2/5%CO_2) KH solution to induce a hypoxic state; 3) glucose-depleted oxygenated solution to induce energy substrate privation. In the latter solution, glucose was replaced by mannitol, a sugar alcohol with similar molecular weight to that of glucose and that is nearly metabolically inert to mammals [355]–[358]. The solutions were combined using a three-way tap that allowed perfusion with only one solution at a given time. Two bubble traps were positioned in the circuit to prevent air bubbles from entering the heart. The setup also included temperature controlling and monitoring facilities to ensure that the solutions were maintained at a constant temperature, hence keeping the temperature of the heart stable at 37.5 ± 1°C throughout the experiments.

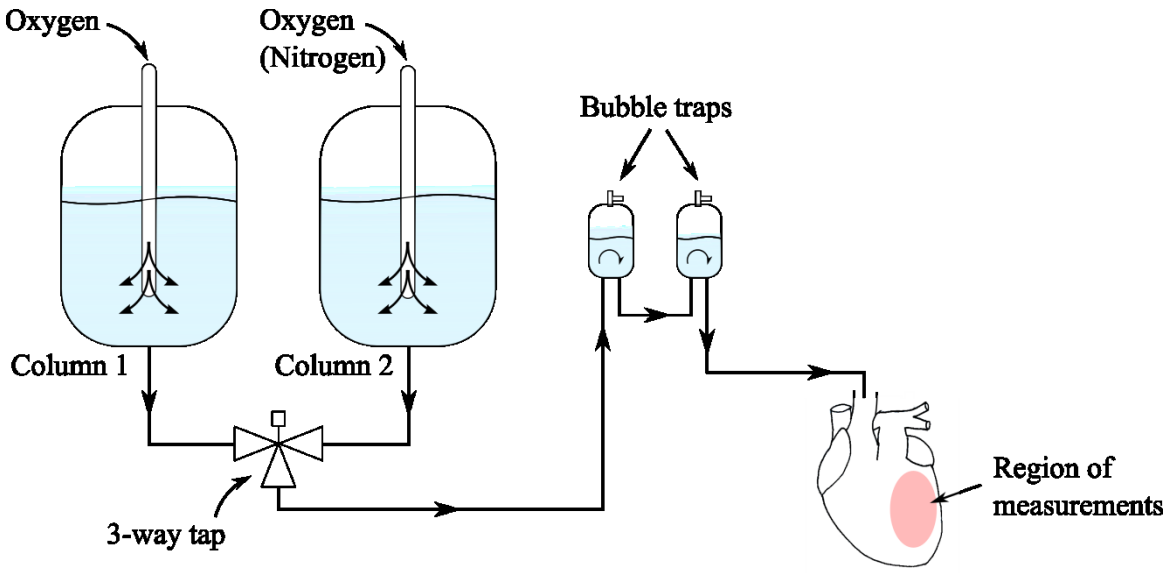

Figure 6.6 Schematic representation of the Langendorff model. A three-way tap positioned immediately after the reservoirs guaranteed that only one solution was delivered to the heart at a given time. Pink area indicates the region from where measurements were realised. Black arrows indicate direction of the flow.

6.6.1.2 Data collection

Autofluorescence and diffuse reflectance data were collected from the anterior wall of left ventricle (LV), as indicated in Figure 6.6. The fibre optic probe tip was positioned in gentle contact with the epicardial surface of the heart. Due to the natural movement of the heart, the pressure of the probe tip on the surface of heart varied slightly during each measurement and between consecutive measurements. We therefore ensured that the acquisition protocol would cover multiple heart beats so that any artefacts due to the motion of the heart during a measurement were averaged.

The experimental protocol was divided in three phases, with a total time of approximately 26 minutes:

1. 3 minutes of baseline measurements, during which the heart was perfused with KH solution (column 1).
2. 7.5 minutes of perfusion with insult-solution, provided by column 2. The insult-solution was either oxygenated KH solution (control), deoxygenated KH solution (hypoxia) or glucose-depleted solution (mannitol).
3. 15 minutes of reperfusion with KH solution from column 1.

Autofluorescence and diffuse reflectance data were acquired every 5 seconds. The integration times used in a single acquisition were 1 second for UV excitation, 1 second for blue excitation and 50 milliseconds for diffuse reflectance measurements with white light illumination.

6.6.1.3 Data analysis

6.6.1.3.1 Spectral analysis of autofluorescence data

In Langendorff measurements, autofluorescence intensity data in each spectral channel of the time-resolved spectrofluorometer was normalised to the average of the first minute of baseline measurements. Due to variations in the UV laser intensity, previously characterised in section 4.3.1, the first minute of acquisitions was discarded in the analysis of data. We have also calculated the fraction of the total autofluorescence signal in each spectral channel under UV excitation together with the ratio of autofluorescence signal between each of these channels. We excluded channel 4 from ratio calculations as this is sensitive to any small day-to-day changes in the fibre optic coupling efficiency and laser power differences between the two lasers of the instrument.

6.6.1.3.2 Fluorescence decay analysis

Autofluorescence lifetime data of cardiac tissue presents a complex profile due to the presence of multiple fluorophores, as discussed in section 6.5. Due to the limited number of photons in each spectral channel, we chose to fit a single exponential decay model to channel 1 data and a double exponential decay model to the remaining channels (see section 4.2.1 for a review of the wavelength ranges of each detection channel). Hence, for all detection channels but channel 1, we extracted four lifetime parameters, as defined in section 2.4: β_1, τ_1, τ_2 and τ_{mean}. For channel 1, data were fitted to a single exponential decay model with lifetime τ. The system response was measured using reference fluorophores with known decay characteristics: 4′,6-Diamidino-2-phenylindole dihydrochloride (DAPI) (Sigma-Aldrich, USA) for 375 nm excitation in all detection channels; and Erythrosin B (Sigma-Aldrich, USA) using 440 nm excitation.

Overall, for each acquisition, we collected a combined total of 19 lifetime and spectral parameters, as summarised in Table 6.4.

Table 6.4 List of spectroscopic parameters extracted from a single fluorescence lifetime acquisition

Channel	Index	Description
Channel 1	τ	Fluorescence lifetime
Channel 2	τ_{mean}	Weighted mean fluorescence lifetime
	τ_1	Short lifetime component
	τ_2	Long lifetime component
	β	Contribution of the first component
Channel 3	τ_{mean}	Weighted mean fluorescence lifetime
	τ_1	Short lifetime component
	τ_2	Long lifetime component
	β	Contribution of the first component
Channel 4	τ_{mean}	Weighted mean fluorescence lifetime
	τ_1	Short lifetime component
	τ_2	Long lifetime component
	β	Contribution of the first component
	CH1 R	Relative fluorescence in channel 1
	CH2 R	Relative fluorescence in channel 2
	CH3 R	Relative fluorescence in channel 3
	CH1 I/CH2 I	Fluorescence intensity in CH 1 / Fluorescence intensity in CH2
	CH2 I/CH3 I	Fluorescence intensity in CH 2 / Fluorescence intensity in CH3
	CH1 I/CH3 I	Fluorescence intensity in CH 1 / Fluorescence intensity in CH3

6.6.1.3.3 Diffuse reflectance data analysis

Diffuse reflectance data of cardiac tissue were analysed as discussed in section 5.7.1.3.2. All diffuse reflectance values are reported in units of absorbance, normalised to the diffuse reflectance signal from a white reference target (WS-1-SL, Labsphere, USA).

6.6.2 Results and discussion

6.6.2.1 Diffuse reflectance measurements

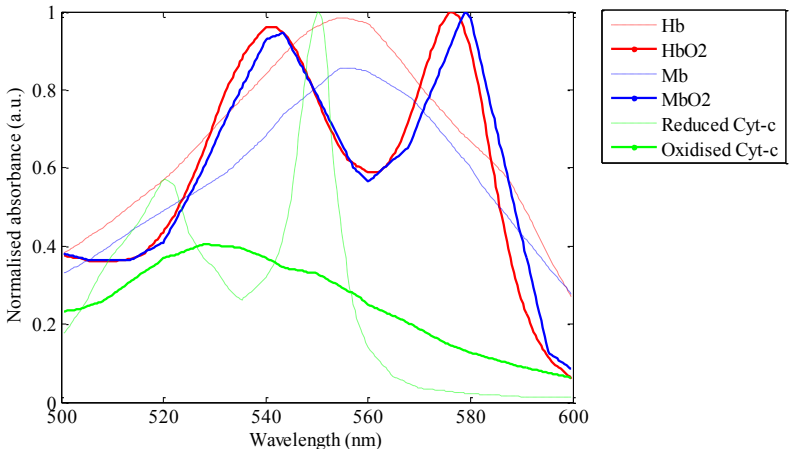

Figure 6.7 Absorbance spectra of key chromophores in cardiac tissue. The absorbance curves for human Hb and HbO_2 were obtained from [307]. The absorbance curves for oxidised and reduced horse cytochrome C were obtained from [359]. The absorbance curves for horse Mb and MbO_2 were obtained from [360]. The Hb and HbO_2, Mb and MbO_2 and reduced and oxidised cytochrome c pairs of curves were scaled in proportion with the largest of each curve being normalised to 1.

The diffuse reflectance spectrum is highly dependent on the absorption spectra of tissue chromophores. In cardiac tissue, the dominant chromophores are myoglobin, which is highly abundant in muscular tissue, and haemoglobin, which is present in red blood cells and is responsible for carrying oxygen to the tissues throughout the body. In a Langendorff preparation however, the heart is blood-free and therefore the contribution of haemoglobin to the diffuse reflectance spectra is negligible.

In the presence of oxygen, the absorption spectrum of myoglobin presents a double peak profile, with local maxima at ~544 nm and ~578 nm and minimum at ~560 nm [361]. In contrast, in the absence of oxygen it exhibits a broader spectral profile with a single maximum peak at ~555 nm [361], [362]. Other chromophores can also contribute to the absorption spectra of heart tissue such as mitochondrial cytochromes. In particular, cytochrome c plays an important role in the regulation of the mitochondrial respiratory chain, as discussed in section 6.3.3, and therefore can provide readouts of the metabolic activity. The absorption spectrum of reduced cytochrome c has a well-defined peak at ~550 nm [328]. The absorbance curves of the reduced and oxidised forms of these chromophores are presented in Figure 6.7.

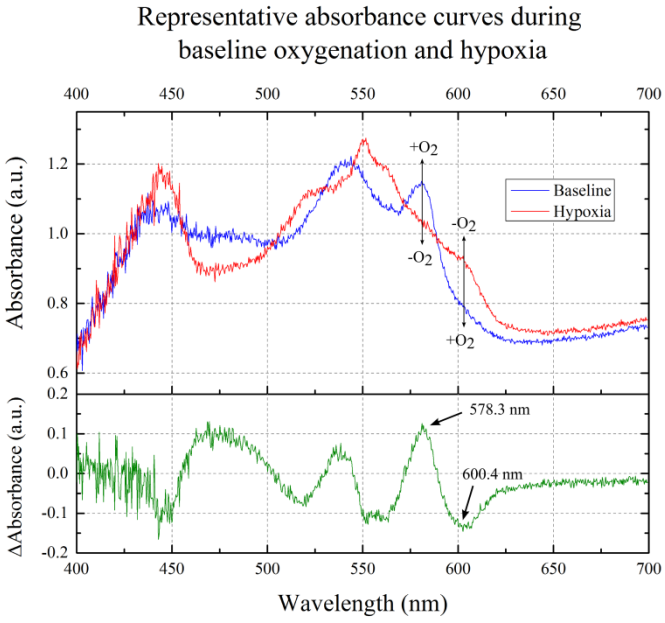

Figure 6.8 Representative absorbance spectra of oxygenated and hypoxic cardiac tissue obtained from the Langendorff setup. The bottom curve (in green) shows the difference between the two spectra, i.e. A(blue)-A(red). Black arrows indicate two wavelengths at which the differences between curves are maximised. Black lines indicate transition from $+O_2$ to $-O_2$.

Figure 6.8 shows representative absorption curves of well oxygenated and oxygen-depleted tissue, retrieved from measurements during baseline and hypoxia measurements in the Langendorff setup, respectively. The oxygenated curve (in blue) shows a double peak profile in the 500 – 600 nm band, with local maxima at ~543.9 and ~578.3 nm, calculated through the first order derivative (FOD), and are in excellent agreement with previously reported values [361]. The local minimum in this range

was found to be at ~568.8 nm, which is considerably red-shifted relative to the expected value of 560 nm (see Figure 6.7). It is possible that reduced cytochrome c (or even perhaps its oxidised form) is also contributing to the absorption spectrum of the tissue, which would produce a broadening of the peak at ~544 nm and a red-shift of the local minimum. It should be noted that the measurements quoted from literature were obtained from horse myoglobin, which can yield slight differences from the absorbance spectrum of myoglobin derived from other species [362].

With respect to the oxygen-depleted curve (in red), we observe a complex profile that does not resemble the deoxymyoglobin spectrum presented in Figure 6.7. Rather, it is interesting to observe a pronounced peak at ~550 nm and a smooth shoulder at ~520 nm, which are consistent with the presence of cytochrome c in the tissue. There is also a shoulder at ~560 nm that we attribute to the deoxygenated form of myoglobin, considering the proximity to its maximum peak (~555 nm). The increase in reduced cytochrome c absorbance is easily explained by the depletion of oxygen in the tissue. As discussed in section 6.3.3, cytochrome c is a key element in the respiratory chain, being reduced by complex III and oxidised by complex IV. Without oxygen, reduced cytochrome c accumulates in the mitochondria, hence explaining the peaks observed in the diffuse reflectance measurements during hypoxia.

Although diffuse reflectance measurements can be used to quantify myoglobin (and haemoglobin) concentrations [222], oxygen saturation [164], [360] and, eventually, report on the oxidative state of the tissue [163], in our experiments we used diffuse reflectance data to only verify the level of oxygenation of the tissue. It should be noted that we did not intend to quantify the oxygen saturation in tissue as e.g. pulse oximetry, which requires careful calibration. Rather, we aimed to read out any variations in tissue oxygenation to establish that all control and glucose-privation measurements were not influenced by this factor. The oxygen level of the tissue can be read out using the absorption values at key wavelengths, typically from the red and infra-red regions (e.g. 660 nm and 950 nm), where the differences between oxygenated and deoxygenated myoglobin/haemoglobin curves are maximised. In our case, since we are working in the visible spectrum, we calculated the difference between oxygenated and deoxygenated curves in the 400 – 700 nm band to find the wavelengths at which the difference is maximised (see Figure 6.8, bottom graph). From the calculated curve, we verify that difference between the two curves is maximised at 578.3 nm and 600.4 nm. Hence, by calculating the absorbance ratio at these wavelengths, i.e. A(578.3)/A(600.4), one can estimate the variation in tissue oxygenation throughout the experimental protocol. Figure 6.9 shows the average oxygenation level - calculated as described above - for control, hypoxia and glucose-privation (mannitol) experiments. As expected, the oxygenation level decreased in hypoxia experiments (red curve) when perfusion was switched from oxygenated to deoxygenated solutions, returning to the baseline levels upon re-oxygenation. The curves for control and mannitol experiments are flat, thus

indicating that the oxygenation level of the tissue was maintained approximately constant throughout the entire protocol. Hence, variations in the autofluorescence readout within this period for control or mannitol experiments cannot be attributed to variations of tissue oxygenation. The hypoxia curve (in red, Figure 6.9) also indicates that changes in tissue oxygenation are only observed approximately two minutes after switching the perfusion solutions. This is the time required for the solution in each column to reach the heart.

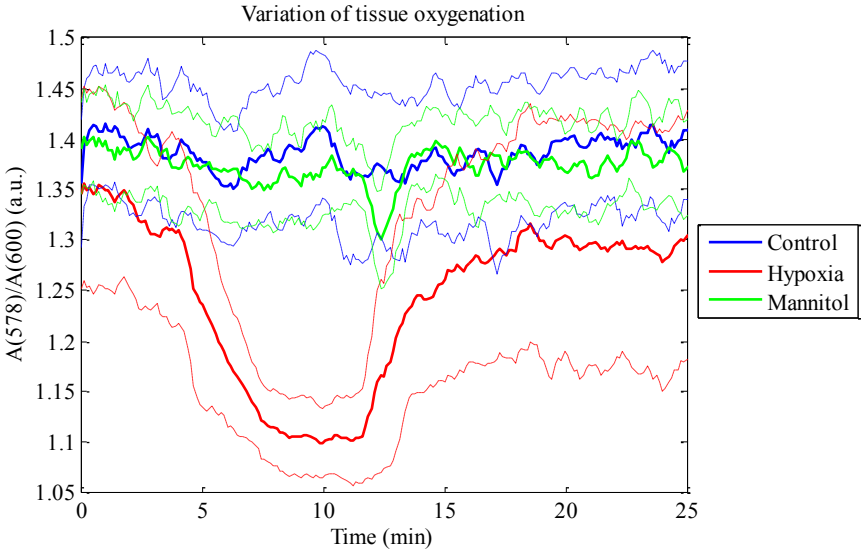

Figure 6.9 Variation of tissue oxygenation throughout the protocol. Dashed lines in grey indicate the switching time between perfusion solutions. Solid lines represent average and dashed lines represent standard deviation. The number of specimens studied is as follows: control (n = 4); hypoxia (n = 5); mannitol (n = 4).

6.6.2.2 *Autofluorescence spectral measurements*

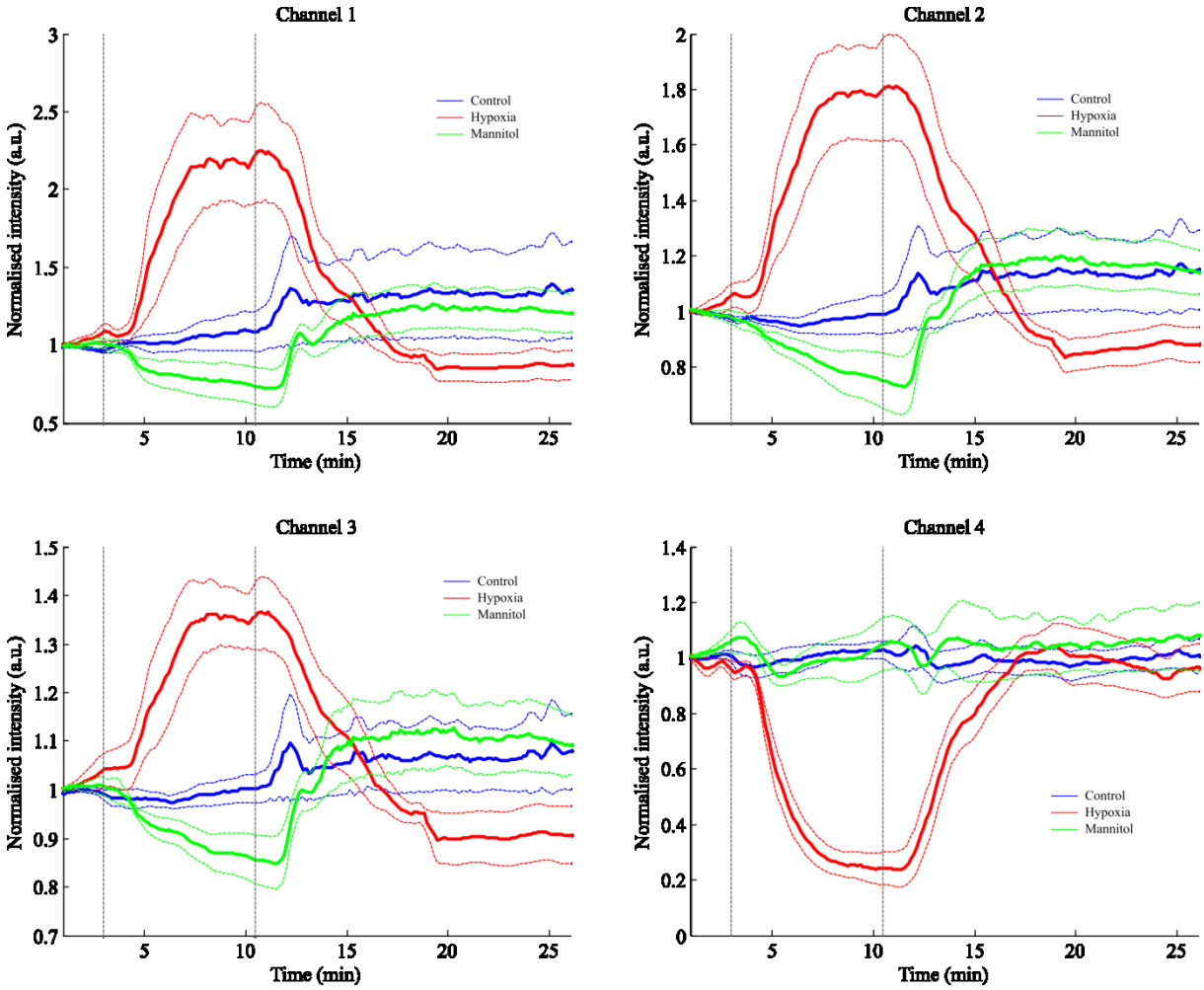

Figure 6.10 Normalised fluorescence intensity during control (blue), hypoxia (red) and mannitol (green) protocols. Curves are normalised to the average of the first minute of measurements. Vertical greyed dashed lines indicate the time when the perfusion solution was changed. Solid lines represent average and dashed lines represent standard deviation. The number of specimens studied for each group are as follows: control (n = 4); hypoxia (n = 5); mannitol (n = 4).

Figure 6.10 shows the variation of autofluorescence intensity in all spectral channels of the time-resolved spectrofluorometer, normalised to the average of the first minute of measurements. Interestingly, we verify that the fluorescence intensity increases slightly in control specimens, as function of the time. This is more evident in detection channels with UV excitation, i.e. channels 1, 2 and 3. Since these channels are primarily associated with NADH autofluorescence, the results suggest a small increase of NADH content over time. We also note an increase in fluorescence intensity upon switching the perfusion solution from column 2 to column 1. It is possible that this variation reflects uneven temperature: all components of the Langendorff setup were water jacketed, i.e. hot water circulated through the system to maintain its temperature. However, since the heating water warmed column 1 first and then column 2, it is expected a small decrease in temperature from columns 1 to 2, which could explain the small variation observed in the autofluorescence intensity curves of control specimens, given the variation of NADH quantum yield with temperature (see Chapter 3).

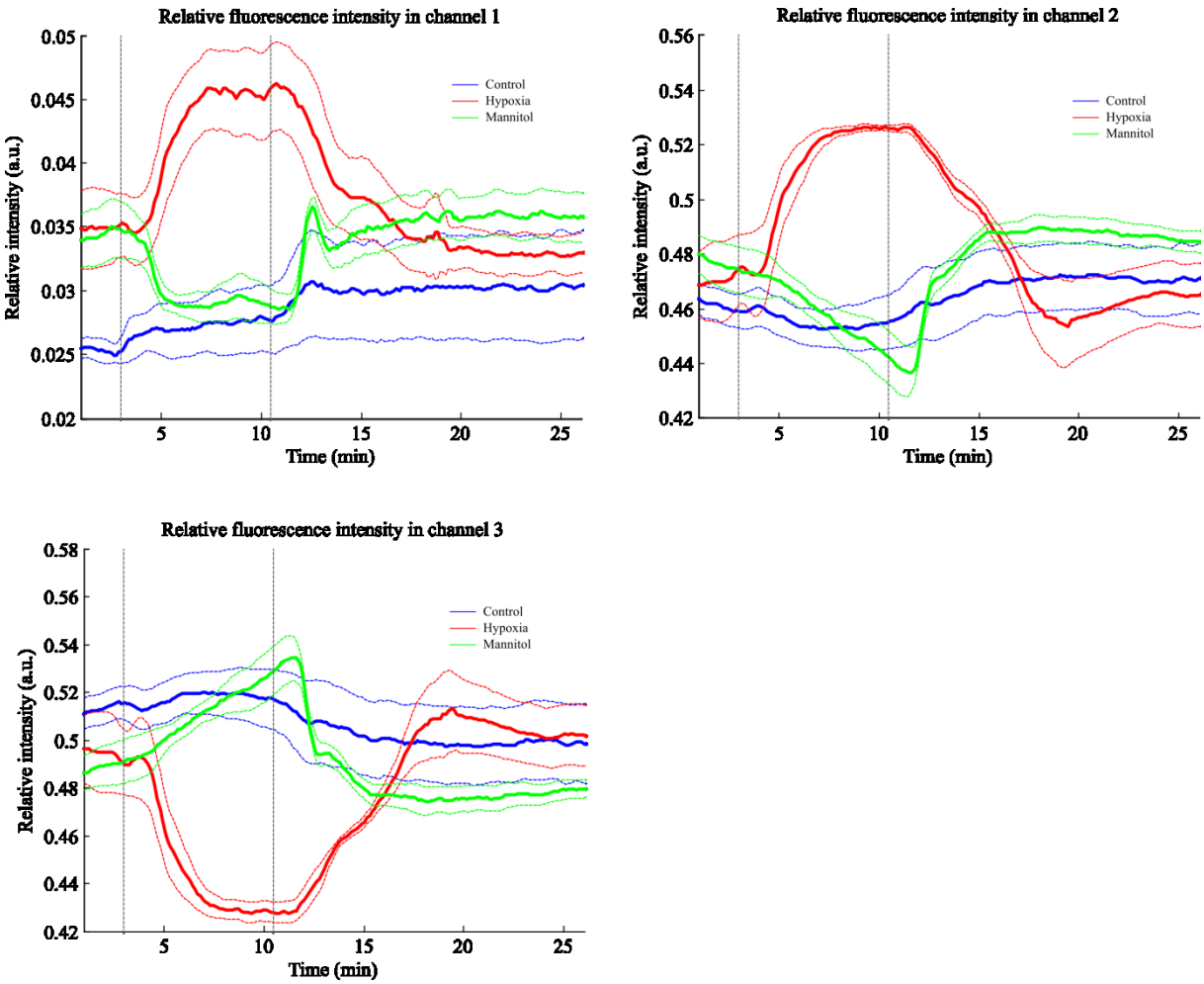

Figure 6.11 Fraction of autofluorescence signal in each detection channel under UV excitation: channel 1 (top left); channel 2 (top right); channel 3 (bottom left). Data show a shift in the fluorescence emission spectra towards shorter wavelengths during hypoxia (in red) and longer wavelengths during glucose deprivation (in green). Thick solid lines indicate mean and dashed lines indicate standard deviation. Vertical greyed lines indicate column switching time.

With respect to hypoxia, we observe an increase in the autofluorescence intensity of detection channels 1 to 3 dominated by NADH signal with concomitant decrease in the FAD signal, in channel 4. This also translates in a shift of fluorescence emission towards shorter wavelengths (see Figure 6.11), as channel 3 is a mixture of NADH and FAD fluorescence. These results are consistent with a decrease in aerobic metabolism and a switch to the dominance of glycolysis over oxidative phosphorylation. Since oxygen is the final electron acceptor in the electron transport chain (see section 6.3.3), removing it from the system effectively inhibits the oxidation of NADH and $FADH_2$, the transport of electrons to the membrane and, ultimately, the production of ATP in oxidative phosphorylation. Consequently, NADH and $FADH_2$ will accumulate in the tissue, explaining the increase in NADH signal and decrease in FAD signal. These metabolic alterations can also be read out by the optical redox ratio of NADH to FAD fluorescence in biological tissues. In our instrument, the redox ratio can be estimated from the ratio of the fluorescence intensities measured in channels 2 and 3, which, in healthy cardiac tissue, is equivalent to the ratio [NADH]/(α[NADH] + β[FAD]), where α and β represent the relative contributions of NADH and FAD respectively to channel 3

intensity under UV excitation. The results presented in Figure 6.12 show an increase in redox ratio in hypoxia specimens, which further confirms the accumulation of NADH and concomitant depletion of FAD. Upon perfusion with deoxygenated KH solution we observe an increase/decrease in NADH/FAD autofluorescence and increase in redox ratio until a stabilisation plateau is reached. It is possible that at this point the oxidative metabolic pathway is completely inhibited and thus ATP for the cardiac cells is synthesised only in glycolysis, which can occur in anaerobic conditions. However, as discussed in section 6.3, glycolysis has substantially lower energetic yield compared to oxidative phosphorylation and therefore the heart cannot be sustained exclusively by this pathway. This explains the decrease in heart rate (typically less than 200 bpm) measured for these hearts (data not shown). Maintenance of this pathway for a longer period would eventually result in unrecoverable cell damage and consequent death. It is also interesting to observe that upon reperfusion with oxygenated KH solution, the autofluorescence intensity in channels 1-3 slowly decreases and stabilise to values below the baseline. Moreover, the redox ratio decreases at a slower rate (~ 5 minutes, from 10 to 90%) than it initially increases after perfusion with deoxygenated solution (~ 2 min, from 90 to 10%). The reasons for this difference are unclear, although they are possibly related to the energetic dysfunction of the heart during hypoxia that may damage myocardial cells and slow down recovery to normal function. Similar patterns have been observed in ischaemia reperfusion models with respect to the diastolic pressure of the heart, which remains elevated after reperfusion [363] and may explain our results.

The results obtained with perfusion of mannitol are more complex to interpret than those for hypoxia. As discussed above, in a living body the main source of fuel to the heart are fatty acids. However, the heart has little capacity to store nutrients [324] and, therefore, in a Langendorff heart, the energy substrate is mainly supplied by the perfusion solution containing glucose. When the tissue is deprived of glucose, the substrate consumed to produce energy is not replenished, eventually leading to mitochondrial dysfunction likely due to high concentration of ROS [364]. Accordingly, the levels of ATP in tissue are expected to decrease, contributing to progressive myocardial cell death and concomitant impaired contractile function [365]. Our results presented in Figure 6.10 suggest an increased oxidative state of the tissue, with decreased NADH autofluorescence, which is consistent with increased production of ROS and with previous observations of glucose deprivation studies in cell lines [11]. The decrease in NADH fluorescence is also seen in the relative fluorescence signal in channel 3, which has contributions from both NADH and FAD, and the redox ratio (see Figure 6.12). It is interesting to observe that changes in autofluorescence intensity and the redox ratio due to glucose deprivation occur at a slower rate than changes caused by oxygen deprivation. Moreover, at the time of the second switch (reperfusion with glucose-based solution) the redox ratio was still decreasing, suggesting a progressive rather than abrupt decrease in metabolic rate. It is possible that some level of substrate was stored in the heart cells and used when there was no other source of

energy. Despite our results suggesting a predominance of oxidation over reduction, we found inconsistent FAD autofluorescence signatures in channel 4: only 1 out of 4 specimens showed an increase in autofluorescence; in the remaining 3 specimens the autofluorescence signal persisted mostly unchanged throughout the course of the experiments. This resulted in a flat mean autofluorescence intensity curve, as illustrated in Figure 6.10 (bottom right panel, green curve). It is possible that FAD autofluorescence is less sensitive to glucose deprivation than NADH. In that case, the redox ratio would merely indicate a decrease in NADH concentration but not an increase in FAD.

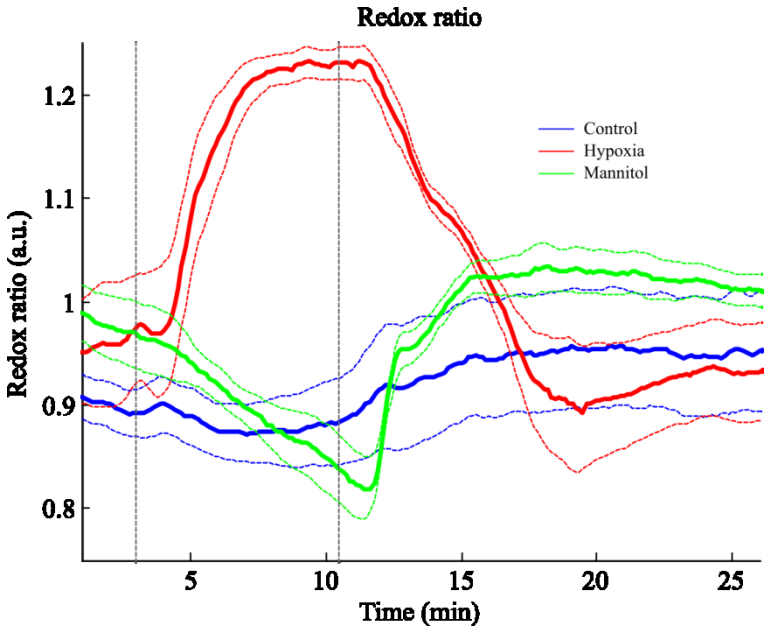

Figure 6.12 Redox ratio curves calculated as the ratio of fluorescence detection in channel 2 relative to channel 3. Greyed dashed lines indicate the time when the perfusion solution was changed.

6.6.2.3 Autofluorescence lifetime measurements

In the previous section we characterised the steady-state autofluorescence signature of cardiac tissue during hypoxia and glucose-deprivation. More interestingly, we were able to correlate changes in the autofluorescence intensity of NADH and FAD with alterations in the metabolic pathways. With respect to the time-resolved autofluorescence signature, rather than trying to explain the metabolic mechanisms behind changes in the decay characteristics, we only intend to characterise the autofluorescence lifetime signal during hypoxia and glucose deprivation. These measurements will serve to validate our *in vivo* results from a myocardial infarction heart failure model presented in section 6.7.

6.6.2.3.1 Channel 1 (λ_{exc}= 375 nm; λ_{em} from 400 to 420 nm; expected NADH fluorescence)

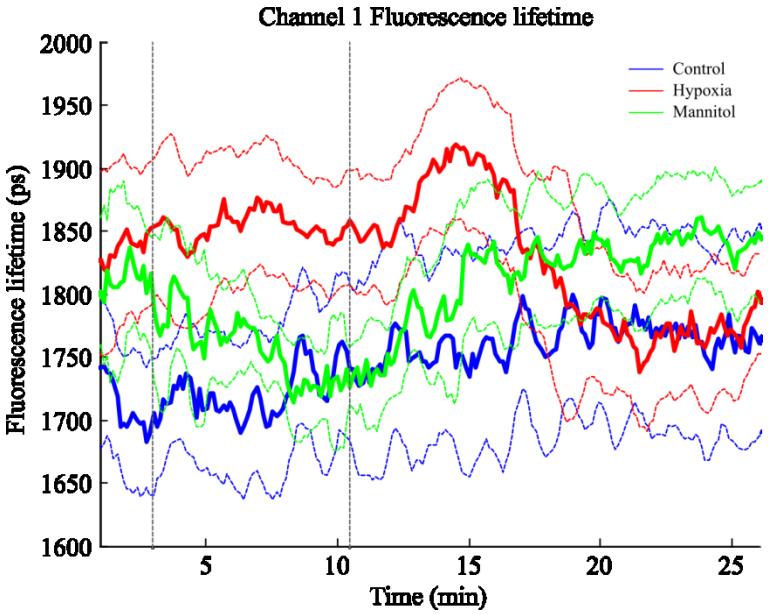

Figure 6.13 Autofluorescence lifetime in channel 1 during control, hypoxia and mannitol experimental protocols. Data were fitted to a single exponential decay model. Greyed dashed lines indicate the time when the perfusion solution was changed. Thick solid lines represent average and dashed lines represent standard deviation. The number of specimens studied for each group are as follows: control (n = 4); hypoxia (n = 5); mannitol (n = 4).

Figure 6.13 shows the autofluorescence lifetime curves measured in channel 1. As mentioned in section 6.6.1.4.2, channel 1 data were fitted to a single exponential decay model, due to the low number of photons detected in this channel during baseline measurements (~5000 photons), which may affect the precision of the resulting lifetime measurement. If we average the control measurements taken during the whole course of the experiments we calculate an average fluorescence lifetime of 1.75 ± 0.13 ns (n = 4). In healthy cardiac tissue, the fluorescence signal in this channel is dominated by short wavelength NADH. We note that despite the strong collagen fluorescence in this range, its presence in healthy myocardium is negligible compared to NADH, and so is its contribution to channel 1 fluorescence signal. Hence, any changes in the fluorescence lifetime in this channel reflect changes in NADH autofluorescence.

With respect to the hypoxia curve, we observe an increase in the autofluorescence lifetime after reperfusion with oxygenated KH solution, followed by a decrease until stabilisation is reached. A similar pattern can be observed in mean autofluorescence lifetime of channel 2 (see Figure 6.14A) although in this case changes during hypoxia are well pronounced. It is possible that a simplistic single exponential model used to describe the fluorescence decay in channel 1 is not sufficient to read out alterations in cardiac tissue metabolism. In contrast, the autofluorescence lifetime seems to decrease upon perfusion with mannitol, returning to baseline values upon reperfusion with glucose-based solution.

6.6.2.3.2 Channel 2 (λ_{exc}= 375 nm; λ_{em} from 430 to 480 nm; expected NADH fluorescence)

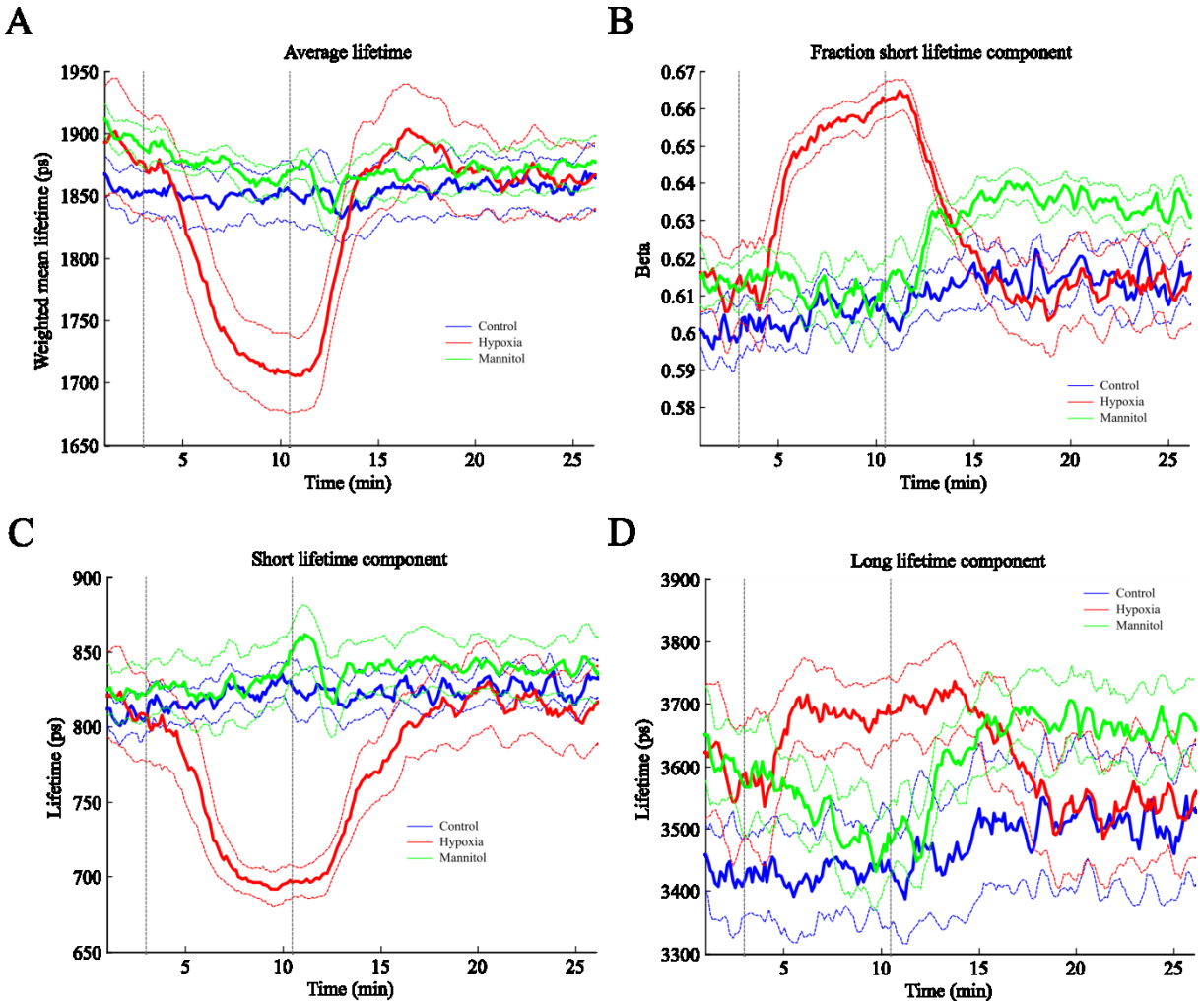

Figure 6.14 Autofluorescence lifetime measured in channel 2. (A) Weighted mean fluorescence lifetime; (B) Contribution of the short lifetime component to the decay, β_1; (C) Short lifetime component, τ_1; (D) Long lifetime component, τ_2. Data were fitted to a double exponential model.

Figure 6.14 shows the autofluorescence lifetime parameters in channel 2, extracted from a double exponential fitting model. In this channel, changes in the autofluorescence lifetime parameters can be better identified than in channel 1 due to higher signal and thus higher SNR, in particular for the hypoxia data. If we average the measurements taken during the whole course of control experiments, we calculate a mean lifetime (τ_{mean}) of 1.85 ± 0.04 ns, a short lifetime (τ_1) of 0.82 ± 0.02 ns, a long lifetime (τ_2) of 3.47 ± 0.16 ns and a fraction of the short lifetime component (β) of 0.61 ± 0.01 (n = 4).

During hypoxia we observe a decrease in the mean autofluorescence lifetime. This can be traced back to a decrease in the short lifetime (Figure 6.14C) and increases in the long lifetime (Figure 6.14D) and in the fraction of the short lifetime component (Figure 6.14B). In healthy cardiac tissue, channel 2 is primarily associated with NADH autofluorescence. In tissue, NADH can exist in its free form or bound to proteins. As discussed in Chapter 3, free NADH can exist in two conformations (extended and folded), which give rise to decay components at ~300 ps and ~700 ps, respectively. Moreover,

there are a multitude of enzymes to which NADH can bind depending on the metabolic pathway (e.g. MDH or LDH), yielding longer double exponential components, in the range ~1 to ~6 ns [1]. An accurate description of such complex autofluorescence signal would eventually require fitting at least four exponential components to the decay, which is not practical with respect to the number of photons required. Hence, NADH autofluorescence in biological tissue is typically described with a more simplistic double exponential model, in which the short lifetime component is typically associated with free NADH and the long lifetime component associated with protein bound NADH. In hypoxia, our results show an increase in the contribution of free NADH to the autofluorescence decay (see Figure 6.14B). Furthermore, the decrease in short lifetime suggests an increase in concentration of the extended conformation of the molecule, which is typically associated with the short lifetime component of free NADH. With respect to the long lifetime component, the results are more challenging to interpret. It is possible that these reflect an alteration in the binding state of NADH. In the oxidative pathway, NADH is bound to MDH in the citric acid cycle (see section 6.3.2). Upon inhibition of this pathway, glycolysis becomes the predominant pathway with oxidation of pyruvate to lactate, by action of LDH. Hence, alterations in the long lifetime may reflect a change in the relative proportions of LDH and MDH binding. Alternatively, Blacker et al [11] recently suggested that alterations in protein-bound lifetime component can be attributed to relative changes in the ratio of NADPH to NADH. Since NADPH plays an important role in the neutralisation of ROS in oxidative stress [366], it is possible that the increase in the long lifetime observed in our experiments reflect an increase in the ratio of NADPH to NADH autofluorescence.

Similarly to the steady-state autofluorescence data, changes in autofluorescence decay characteristics are less pronounced during perfusion with mannitol and concomitant glucose starvation than during hypoxia. Indeed, our results suggest that glucose deprivation does not induce alterations in the mean autofluorescence lifetime of NADH at this detection wavelength. Clear changes are only observed in the long lifetime, which shows a slight decrease upon perfusion with mannitol, returning to the baseline upon reperfusion with glucose. We also note a slight increase in the contribution of the short lifetime component to the autofluorescence decay after reperfusion with glucose-based solution. As explained above, it is possible that changes occurring after reperfusion are related to increased diastolic pressure due to loss of myocardial function during glucose deprivation. Overall, these results suggest that detection channel 2 is less sensitive to changes induced by glucose deprivation compared to channel 3 (see below).

6.6.2.3.3 Channel 3 (λ_{exc}= 375 nm; λ_{em} from 500 to 550 nm; expected NADH and FAD fluorescence)

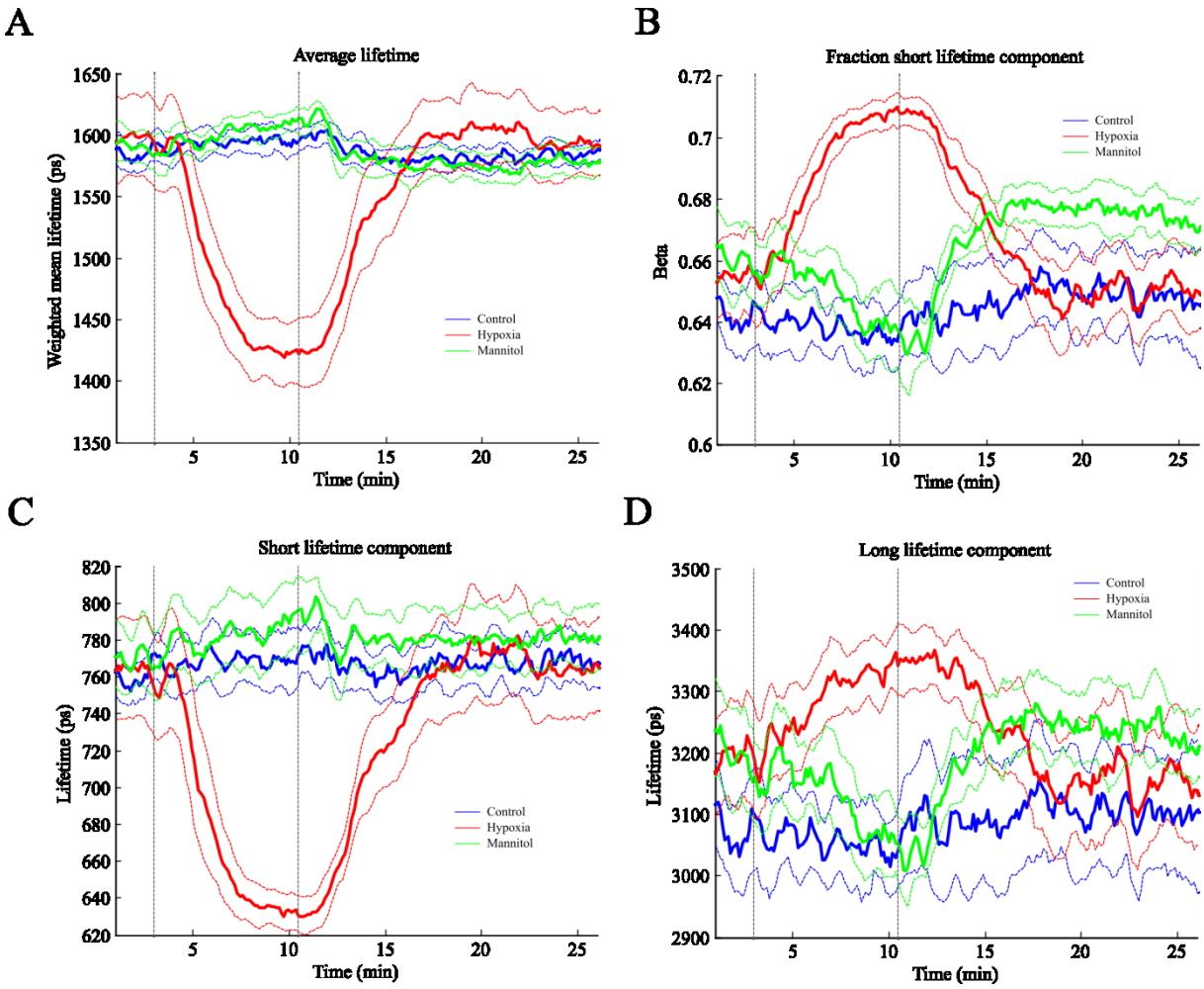

Figure 6.15 Autofluorescence lifetime measured in channel 3. (A) Weighted mean fluorescence lifetime; (B) Contribution of the short lifetime component to the decay, β_1; (C) Short lifetime component, τ_1; (D) Long lifetime component, τ_2. Data were fitted to a double exponential model.

Figure 6.15 presents the autofluorescence lifetime data for channel 3, following fitting with a double exponential decay model. The fluorescence lifetime patterns measured for this channel are similar to those of channel 2, particularly for hypoxia. This is an expected result, since this channel is dominated by NADH autofluorescence with a small contribution of FAD. With respect to control specimens, the average values of each parameter are as follows: τ_{mean} = 1.59 ± 0.01 ns; τ_1 = 0.77 ± 0.02 ns; τ_2 = 3.08 ± 0.15 ns; β = 0.65 ± 0.02 (n = 4). The average autofluorescence lifetime extracted for this channel is shorter than average channel 2 lifetime for control data, which can be traced back to decreases in both short and long lifetimes and increase in the contribution of the short lifetime component. This variation possibly reflects a greater contribution of FAD to the autofluorescence detected in this channel, given the shorter autofluorescence lifetime measured for channel 4 data (see following section). Alternatively, it is well established that the fluorescence emission spectrum of NADH can shift with protein binding and the magnitude of this shift depends on the enzyme it is

bound to. Since different binding partners can yield different fluorescence lifetimes, it is possible that the difference between channels 2 and 3 also reflect a different binding state of NADH.

Alterations in the autofluorescence signature of cardiac tissue induced by glucose deprivation are more clearly observed in this detection channel than in channel 2, although they are not as pronounced as changes induced by hypoxia. As in channel 2, we observe a decrease in the long lifetime upon privation of glucose. More interestingly, changes in the contribution of the short lifetime component are more evident in this channel: it decreases with glucose deprivation and slowly returns to the baseline values when glucose is restored to the system. The decrease in the contribution of the short component, along with the decrease in the autofluorescence signal in this channel (see section 6.6.2.2), suggests a decrease of NADH concentration and, perhaps, an increase in free FAD, given its long fluorescence lifetime compared to free NADH. An increase in FAD content would also explain the decrease in the long lifetime, since both the free and protein bound forms of the molecule yield shorter fluorescence lifetimes than those measured for this channel (see Chapter 3). However, further investigation is necessary in order to validate these results.

6.6.2.3.4 Channel 4 (λ_{exc}= 440 nm; λ_{em} from 500 to 550 nm; expected FAD fluorescence)

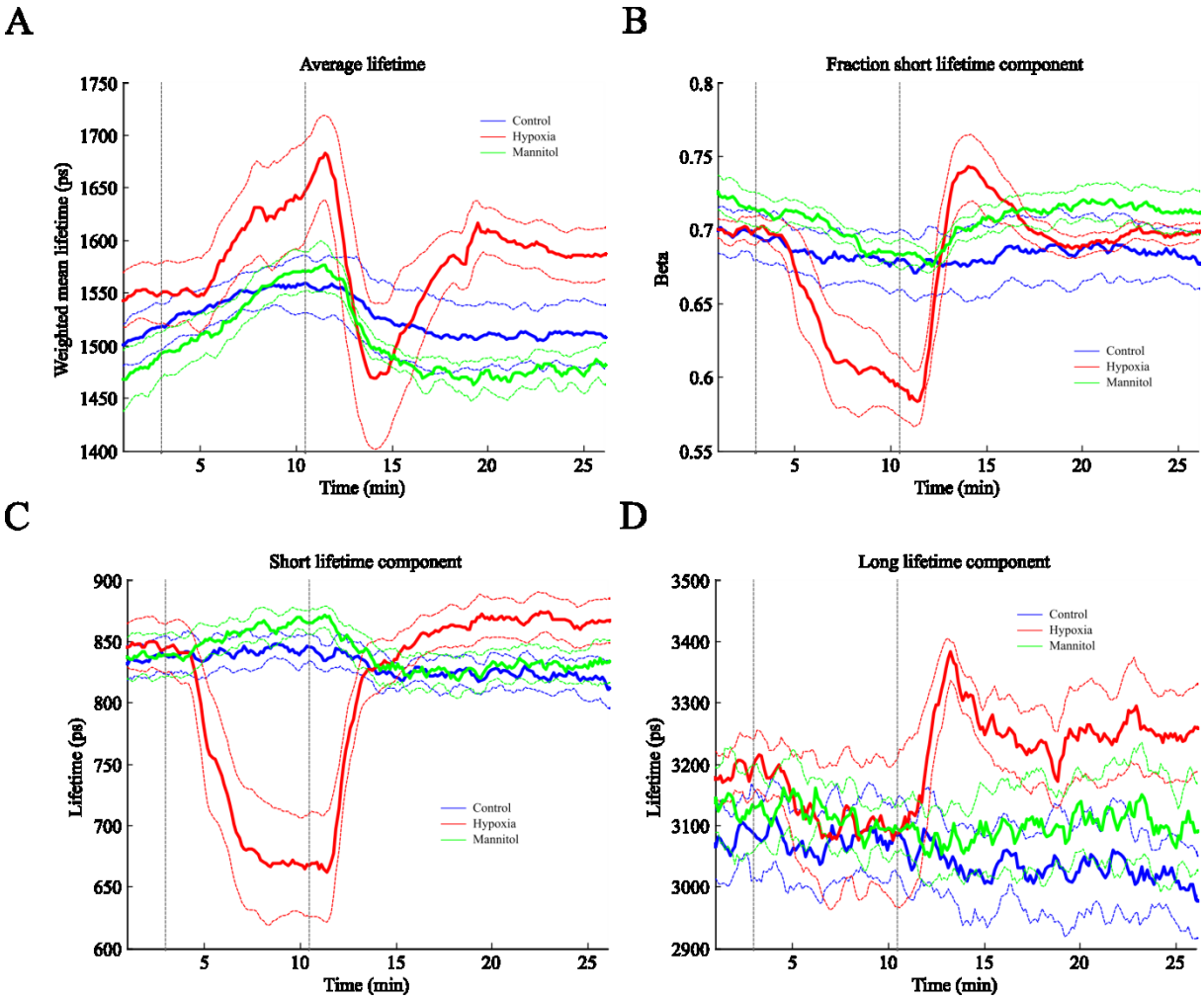

Figure 6.16 Variation of the autofluorescence lifetime signal measured in detection channel 4, i.e. using 440 nm excitation light, following oxygen or glucose deprivation. (A) Weighted mean fluorescence lifetime; (B) Contribution of the short lifetime component to the decay, β_1; (C) Short lifetime component, τ_1; (D) Long lifetime component, τ_2. Data were fitted to a double exponential model.

Figure 6.16 shows the variation of the autofluorescence decay properties of cardiac tissue in detection channel 4. Changes in this channel are more complex than in detection channels 2 and 3. In particular, we observed a variation of ~ 50 ps in the mean autofluorescence lifetime of control specimens and also in the baseline measurements across hypoxia, mannitol and controls protocols that are possibly related to variations in the temperature of the perfusion solution. If we average all measurements for control specimens (n = 4), we obtain the following values: τ_{mean} = 1.52 ± 0.05 ns; τ_1 = 0.83 ± 0.02 ns; τ_2 = 3.05 ± 0.11 ns; β = 0.69 ± 0.04. The proximity of these values with those measured for detection channel 3 - with exception to the short lifetime component τ_1 - could suggest similar species contributing equally to both decays. However, this is contradicted by the opposite steady-state and time-resolved autofluorescence signatures evidenced by channels 3 and 4 (see Figure 6.10, Figure 6.15 and Figure 6.16). Indeed, in healthy cardiac tissue, the autofluorescence signal in detection channel 4 is expected to arise predominantly from FAD, which is optimally excited at 440 nm. In

contrast, we expect only minimal autofluorescence from NADH at these excitation (440 nm) and emission wavelengths (500 to 550 nm).

The autofluorescence decay measured in this channel exhibits a complex signature during hypoxia. The average lifetime initially increases during oxygen deprivation due to decreases in τ_1 and β, followed by a rapid decrease upon reperfusion with oxygenated solution, with an undershoot relative to baseline. Finally, the average lifetime increases again to stabilise slightly above the baseline level. Changes in the average fluorescence lifetime after reperfusion can be traced back to rapid increases in the long lifetime and contribution of the short lifetime component. It is challenging to explain these alterations, particularly because we do not observe a similar pattern in any other autofluorescence parameter. Indeed, we have previously demonstrated that changes in the steady-state autofluorescence signal occur at a slower rate in reperfusion relative to the initial oxygen depletion and a similar pattern can be observed for the time-resolved properties of channels 2 and 3. It is possible that FAD autofluorescence decay properties are more sensitive to metabolic alterations in the myocardium than NADH autofluorescence, which would explain the differences observed. Moreover, in contrast with NADH, FAD autofluorescence derives from mitochondria only [328]. Therefore, these alterations may also indicate a rapid reestablishment of the oxidative pathway. This would not be observed in the NADH autofluorescence properties since NADH is present in both the aerobic and anaerobic pathways. However, this still requires validation.

It is also interesting to observe that both lifetime components decrease during hypoxia, although this is more pronounced in the short lifetime component. This result is particularly interesting in the context of metabolic remodelling post myocardial infarction, as discussed below. Overall, our results suggest an increase in free FAD content during hypoxia, given its longer fluorescence lifetime relative to protein-bound FAD (see Chapter 3).

Finally, our results do not suggest that there is a difference between control and mannitol groups. Although the average lifetime (see Figure 6.16A) appears to increase after perfusion with mannitol, this was already increasing during baseline and, in general, the pattern is similar to that of control specimens, suggesting an artefact in the measurements, likely due to variations in temperature. Furthermore, as discussed in the previous section, the FAD autofluorescence appears to be less sensitive to metabolic alterations due to glucose starvation than NADH autofluorescence, which could further explain the small variations observed in this channel.

To summarise, the results presented in this section demonstrate the potential of autofluorescence to readout metabolic changes in cardiac tissue *ex vivo*. In particular, we characterised the

autofluorescence signature of the myocardium following oxygen or glucose deprivation. The fluorescence intensity and lifetime trends observed upon hypoxia and glucose deprivation are summarised in Table 6.5. These measurements will serve to validate our autofluorescence lifetime results of an *in vivo* myocardial infarction heart failure model, presented in the following section.

Table 6.5 Summary of the trends observed during hypoxia and glucose deprivation relative to controls. In general, our instrument seems to be most sensitive to variations in tissue oxygenation relative to glucose deprivation. This is true for both steady-state and lifetime-based parameters. Variations in the autofluorescence parameters caused by glucose deprivation are, in general, less visible. Legend: (+) increase; (-) decrease; (0) no variation observed.

		Hypoxia	Glucose deprivation
Redox ratio		+	-
CH1	**Intensity**	+	-
	τ	0	0
CH2	**Intensity**	+	-
	τ_{mean}	-	0
	τ_1	-	0
	τ_2	+	-
	β_1	+	-
CH3	**Intensity**	+	-
	τ_{mean}	-	0
	τ_1	-	0
	τ_2	+	-
	β_1	+	-
CH4	**Intensity**	-	0
	τ_{mean}	+	0
	τ_1	-	0
	τ_2	-	0
	β_1	-	-

6.7 *In vivo* myocardial infarction heart failure model

6.7.1 Experimental methods

All work involving animal use was carried out under protocols approved and regulated under the Animals (Scientific Procedures) Act 1986 (Project Licenses PPL 70/7399 and 70/7419). All experiments below were realised using the hyperspectral point probe system described in Chapter 4.

6.7.1.1 MI induction surgery

Adult male Sprague-Dawley rats (Charles River UK, Ltd.) weighing 250-300g underwent proximal left anterior descending (LAD) coronary ligation to induce chronic myocardial infarction, as previously described [367]. Five percent isoflurane anaesthesia was used for induction and once the animal was intubated and ventilated, anaesthesia was maintained with 2% isoflurane and opiate

analgesia. Enrofloxacin (5 mg/kg) and 0.9% saline (10ml/kg) were administered preoperatively. Myocardial infarction heart failure animals (MI-HF) and their age-matched controls (AMC) were studied for *in vivo* epicardial autofluorescence and diffuse reflectance characteristics during a terminal procedure at 1, 2, 4 and 16 weeks post-MI surgical induction. The number of animals studied at each time point is presented in Table 6.6. The animals were anesthetised by placement in an anaesthetic chamber with 95%/5% O2 / isoflurane. A blunt catheter was passed into the trachea under direct visualisation and connected to a ventilator (Harvard Apparatus, USA). Anaesthesia was maintained with 98%/2% O2 / isoflurane using tidal volume of approximately 2 ml and a respiratory rate of approximately 90 cycles/min. Opiate analgesia was also given at appropriate dose for body weight. The heart and other internal organs were exposed via a laparotomy and sternotomy for spectroscopy measurements as described in section 6.6.6.2. At the end of the procedure the animal was sacrificed and its heart taken for representative histology.

Table 6.6 Number of animals studied at each time-point after MI induction surgery

Time post-surgery	AMC	MI-HF
1 week	3	3
2 weeks	4	3
4 weeks	4	3
16 weeks	6	6

6.7.1.2 Histology

Cardiac tissue sampled for histology was washed in sterile PBS, fixed in 10% paraformaldehyde for 48 hours and then processed for paraffin embedding. 6 μm thick sections were stained with picrosirius red (PSR) to demonstrate interstitial collagen content [368]. Whole sections were imaged using a 10x objective on a Zeiss Axio Observer inverted microscope with a fully motorized stage. Percentage interstitial fibrosis in each anatomical area of interest was quantified using Fiji image analysis software [369] by adjusting colour thresholds to calculate the area of tissue positively stained with PSR. Unfortunately, results from histology for 1, 2 and 4 weeks post-MI specimens were not available in time for this report.

6.7.1.3 Data collection

In each heart, autofluorescence and diffuse reflectance data were collected from four regions of interest (ROI) (see Figure 6.17): right ventricle (RV); left ventricle posterior wall (LV posterior), which represents the remaining viable myocardium in the presence of a large scar; left ventricle anterior wall/scar (LV anterior); and septum/scar border zone (border zone). In MI-HF hearts, the border zone was defined as the non-infarcted tissue at the boundary of the infarcted area – as determined visually – on the anterior wall. For pairwise comparison, we defined border zone as the septum in the AMC. All measurements were realised with the fibre optic probe in gentle contact with the epicardial surface of the heart (see Figure 6.18). As with Langendorff measurements, we ensured

that the fluorescence and diffuse reflectance data acquisition protocol covered multiple (typically 3-6) heart beats so that any artefacts due to the heart motion during a measurement were averaged. To further average over possible artefacts associated with the placement of the probe, we also repeated each measurement, including removal and replacement of the probe tip, at each ROI. From each ROI, we acquired 3 sets of autofluorescence and diffuse reflectance data from each of 3 random positions within the ROI, i.e. 9 measurements in total. The integration times used in a single acquisition were 1 second for UV excitation, 1 second for blue excitation and 50 milliseconds for diffuse reflectance measurements with white light illumination.

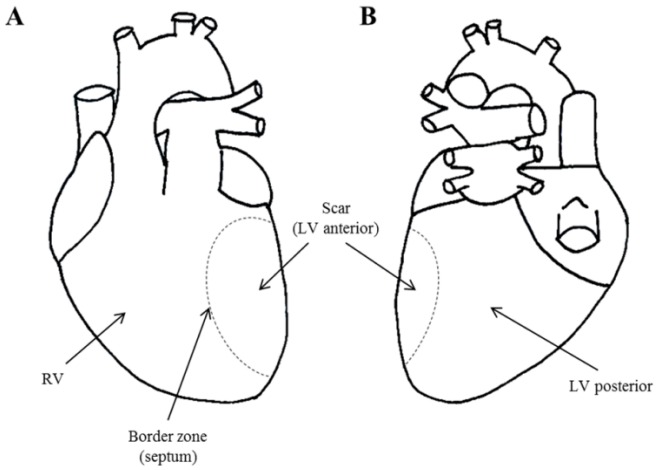

Figure 6.17 Diagram of the heart illustrating regions of interest (ROI) for our measurements: (A) anterior view; (B) posterior view. "RV" - right ventricle; "LV posterior" - left ventricle posterior wall; "LV anterior (scar)" - left ventricle anterior wall; and "border zone" - scar border zone or septum.

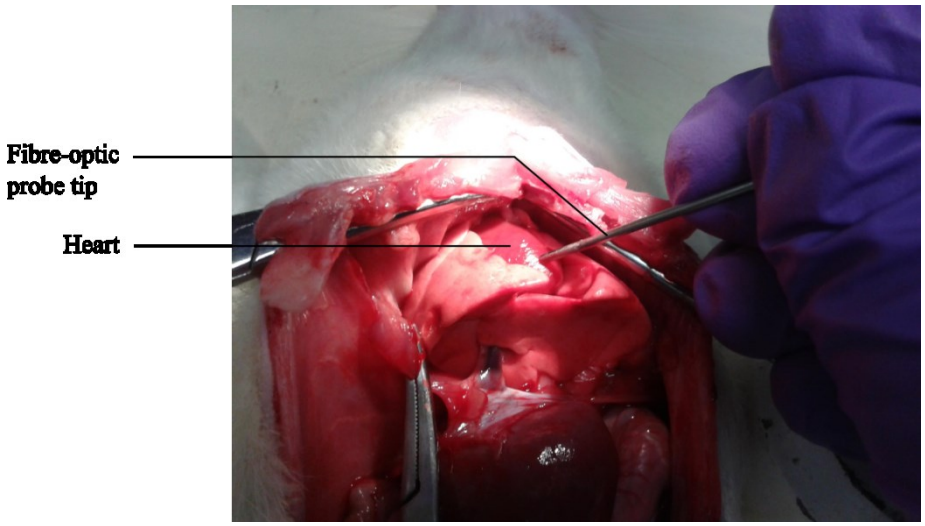

Figure 6.18 Photograph of the fibre-optic probe position at the time of measurements, showing the operator positioning the tip of the probe in contact with epicardial surface of the heart.

6.7.1.4 Data analysis

Spectral analysis of the recorded fluorescence data was realised as described in section 6.6.1.3.1. Analysis of fluorescence lifetime data was realised as described in section 6.6.1.3.2. Diffuse

reflectance data of cardiac tissue were analysed as discussed in section 5.7.1.3.2. All diffuse reflectance values are reported in units of absorbance, normalised to the diffuse reflectance signal from a white reference target (WS-1-SL, Labsphere, USA).

6.7.1.4.1 Linear discriminant analysis and principal component analysis

To quantify differences between AMC and MI-HF hearts, within the corresponding ROI, we implemented a classification algorithm that is conceptually similar to the ones described in references [4], [36], [370], employing principal component analysis (PCA) for feature selection followed by linear discriminant analysis (LDA) on the 5 most significant principal components (PC), using a 'leave-one-out' cross-validation approach that allows for each measurement to be classified as either AMC or MI-HF. A key point in our approach is that we focused on finding differences between equivalent regions of healthy and diseased hearts, rather than distinguishing between different regions within the same heart. This is because, in a potential cardiovascular procedure guided by fluoroscopy, the position of the probe within the heart would be known but not the condition of different regions of the heart. As a first step to generate a diagnostic algorithm to discriminate healthy and diseased heart in specific ROI, each individual point measurement was used in this analysis. Receiver operator characteristic (ROC) curves were generated from the scores of each classification. The performance of each classifier was measured by the area under the ROC curve (AUC).

6.7.1.4.2 Statistical analysis

Results are expressed as mean ± standard deviation (SD). Statistical analysis was computed using a two-tailed Student t-test. A p-value < 0.05 was considered to be statistically significant. For convenience, the following notation was used to identify statistical significance between two sets of data: * $p < 0.05$; ** $p < 0.01$; *** $p < 0.001$; **** $p < 0.0001$.

The discriminating power of each parameter for all ROI was calculated using the Cohen's *d* coefficient. The Cohen's *d* is an appropriate effect size measurement for the comparison between two means. It indicates the standardised difference between two means, and expresses this difference in standard deviation units. The Cohen's *d* coefficient can be defined in terms of population means μ and standard deviations *s*, as shown below:

$$d = \frac{|\mu_1 - \mu_2|}{\sigma} \tag{6.1}$$

where

$$\sigma = \sqrt{\frac{{s_1}^2 + {s_2}^2}{2}} \tag{6.2}$$

As an effect size measure, a larger Cohen's *d* represents a greater differentiation between two groups. Thus, it is traditionally presented as complementary to the report of results from a statistical significance test. Whereas the latter is used to suggest whether a difference exists between two groups, the Cohen's *d* reports the magnitude of this difference.

6.7.2 Results and discussion

In this section we describe the application of the instrument presented in Chapter 4 to explore the potential of time-resolved spectrofluorometry and white light reflectometry to provide label-free optical readouts in cardiac diagnosis. To this end, the autofluorescence and diffuse reflectance signatures of cardiac tissue were characterised at different time points following myocardial infarction, of which results are presented next.

6.7.2.1 1 week post-surgery

Cardiac occlusion of the left anterior descending (LAD) artery produced a transmural MI with formation of scar tissue in the anterior wall of the left ventricle in all specimens. At this time point, scar tissue was still in formation and thus not well identifiable through visual inspection. Compensatory hypertrophy of the remaining myocardium was confirmed by an increase, yet not significant ($p > 0.05$), in heart to body weight ratio in MI-HF animals (3.75 ± 0.22 g/kg, $n = 3$) compared to AMC animals (3.36 ± 0.17 g/kg, $n = 3$).

6.7.2.1.1 Diffuse reflectance measurements

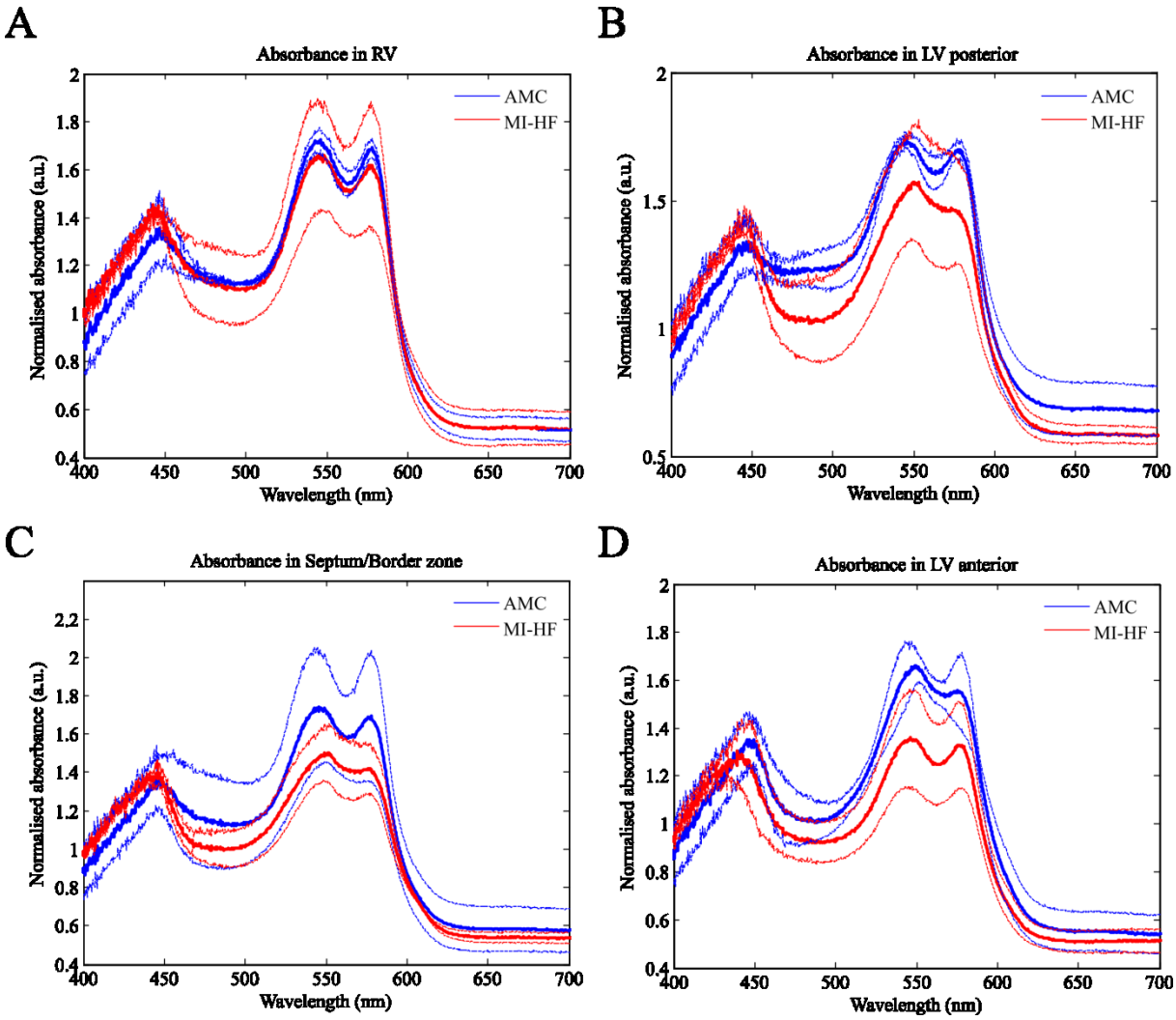

Figure 6.19 Diffuse reflectance spectra 1 week post-infarction in (A) RV, (B) LV posterior, (C) Border zone, (D) LV anterior. Ticked solid lines indicate average and dashed lines indicate +/- 1 SD.

Figure 6.19 presents the diffuse reflectance spectra of AMC and MI-HF hearts at 1 week post-infarction in all ROI, indicating the tissue absorbance between 400 and 700 nm, calculated as described in section 6.6.6.3. The data shows an overall decrease in tissue absorbance in MI-HF relative to AMC hearts, which is more pronounced in the LV anterior. All spectral profiles of AMC hearts (in blue) denote hallmark features of oxygenated haemoglobin/myoglobin, with a double peak profile in the 500 to 600 nm band, with local maxima at ~540 nm and ~580 nm (see Figure 6.7). With respect to MI-HF hearts, the double peak profile is also well identified in the remote RV and in the scar region (LV anterior). In the LV posterior and border zone regions the hallmark features of oxygenated haemoglobin/myoglobin are less pronounced and the ~540 nm peak is shifted to ~550 nm, indicating the additional presence of reduced cytochrome c or deoxygenated haemoglobin/myoglobin in the tissue.

6.7.2.1.2 Autofluorescence spectral measurements

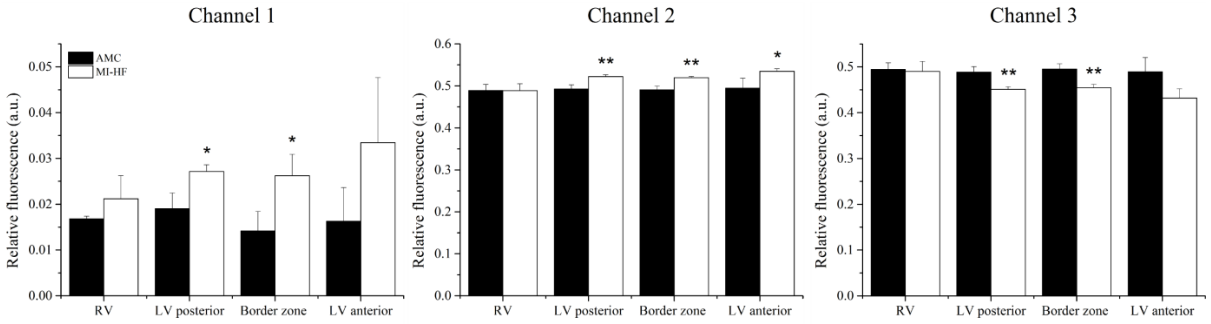

Figure 6.20 Relative autofluorescence contribution of each spectral detection channel in AMC and MI-HF hearts 1 week post-MI induction surgery, displayed by ROI.

Figure 6.20 and Figure 6.21 show the relative autofluorescence signal in each spectral detection channel for UV excitation displayed by ROI and wavelength, respectively. The results indicate a significant increase in the autofluorescence signal in channel 1 in all regions but RV, which can be clearly observed in Figure 6.21 as a shift in the fluorescence emission towards shorter wavelengths. Previous studies of MI models have demonstrated an increase in collagen content only 1 week after infarction [320], which is consistent with an increased fluorescence signal in detection channel 1, given the fluorescence emission spectrum of collagen type I, see Chapter 3. We also observe an increase in the relative contribution of channel 2 in LV posterior, border zone and LV anterior, which is also consistent with an increase in collagen type I content, given its broad fluorescence emission spectrum. A previous study of this model [3] also observed an increase in fluorescence in the wavelength range of detection channel 2, which was attributed to increased NADH content. Therefore, given the broad emission spectrum of collagen type I, the increase in the contribution of channel 2 in our instrument may be the result of an increase of collagen and/or NADH content in tissue.

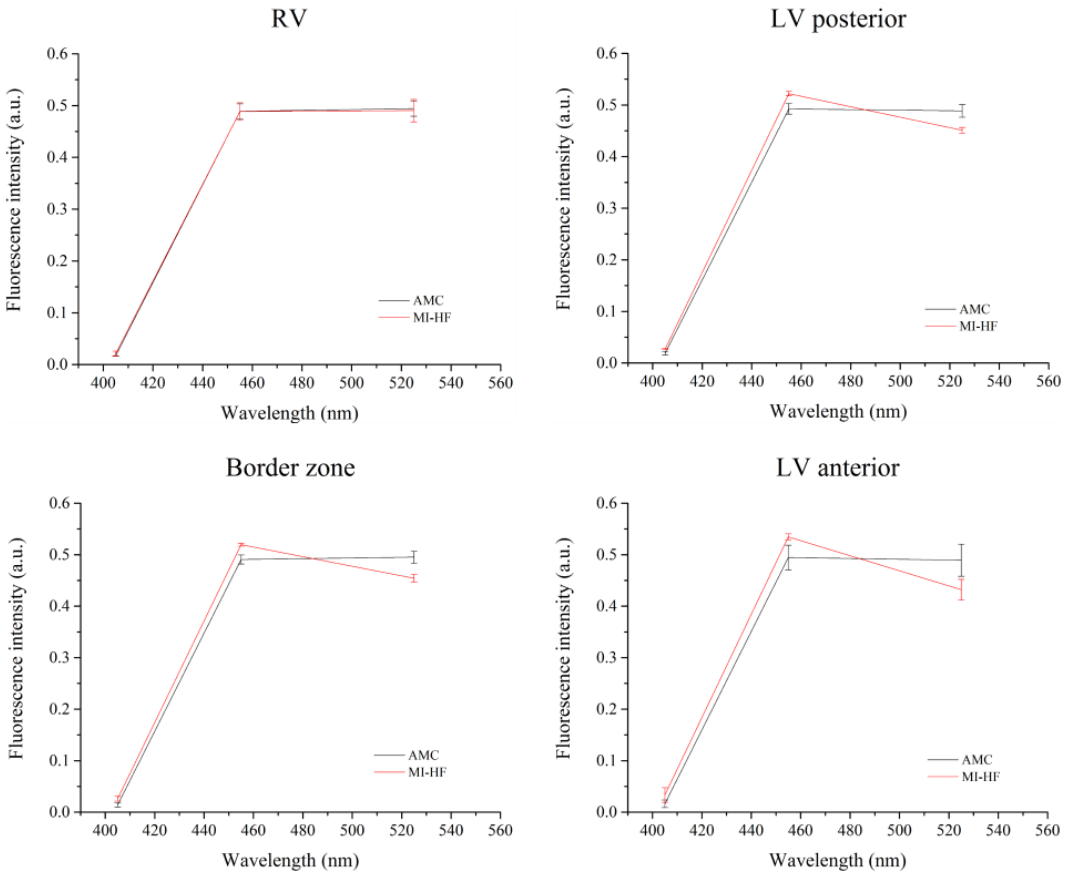

Figure 6.21 Relative autofluorescence in each region of interest for AMC and MI hearts, 1 week after MI surgery. Data show a shift in the autofluorescence emission spectra towards shorter wavelengths, which is consistent with increased collagen content.

6.7.2.1.3 Autofluorescence lifetime measurements

Results of autofluorescence lifetime measurements are plotted in Figure 6.22. In general, the data show an increase in the mean autofluorescence lifetime of MI-HF scar tissue (LV anterior) relative to healthy LV myocardium, which is statistically significant in channels 1 and 4. The increase in the mean autofluorescence lifetime can be traced back to an increase in the long decay component in channels 2, 3 and 4, not only in region of infarction, but for channels 2 and 3 also in remote LV posterior and border zone regions. Given the long fluorescence lifetime and broad emission spectrum of collagen type I (see Chapter 3) we provisionally attribute these changes to increase in interstitial collagen content resulting from the healing process, which confirms our steady-state fluorescence results (see previous section). More interestingly, in the remote non-infarcted LV posterior, we observe statistically significant decreases in τ_1 in channels 2, 3 and 4 and an increase in its contribution to the decay (β) in channels 2 and 3. These results are similar to those previously reported for Langendorff hearts during hypoxia (see section 6.6.2.3.1), and thus suggest alterations in tissue metabolism rather than increase in interstitial collagen content. Despite the fact that we only observe statistical significance in the changes for remote LV posterior and border zone, the value of τ_1 in channels 2, 3 and 4 is lower in all regions of MI-HF hearts relative to AMC, apart from one

exception (channel 2, RV). This is more apparent in detection channel 4 (see Figure 6.22, bottom row), which we associate with FAD autofluorescence.

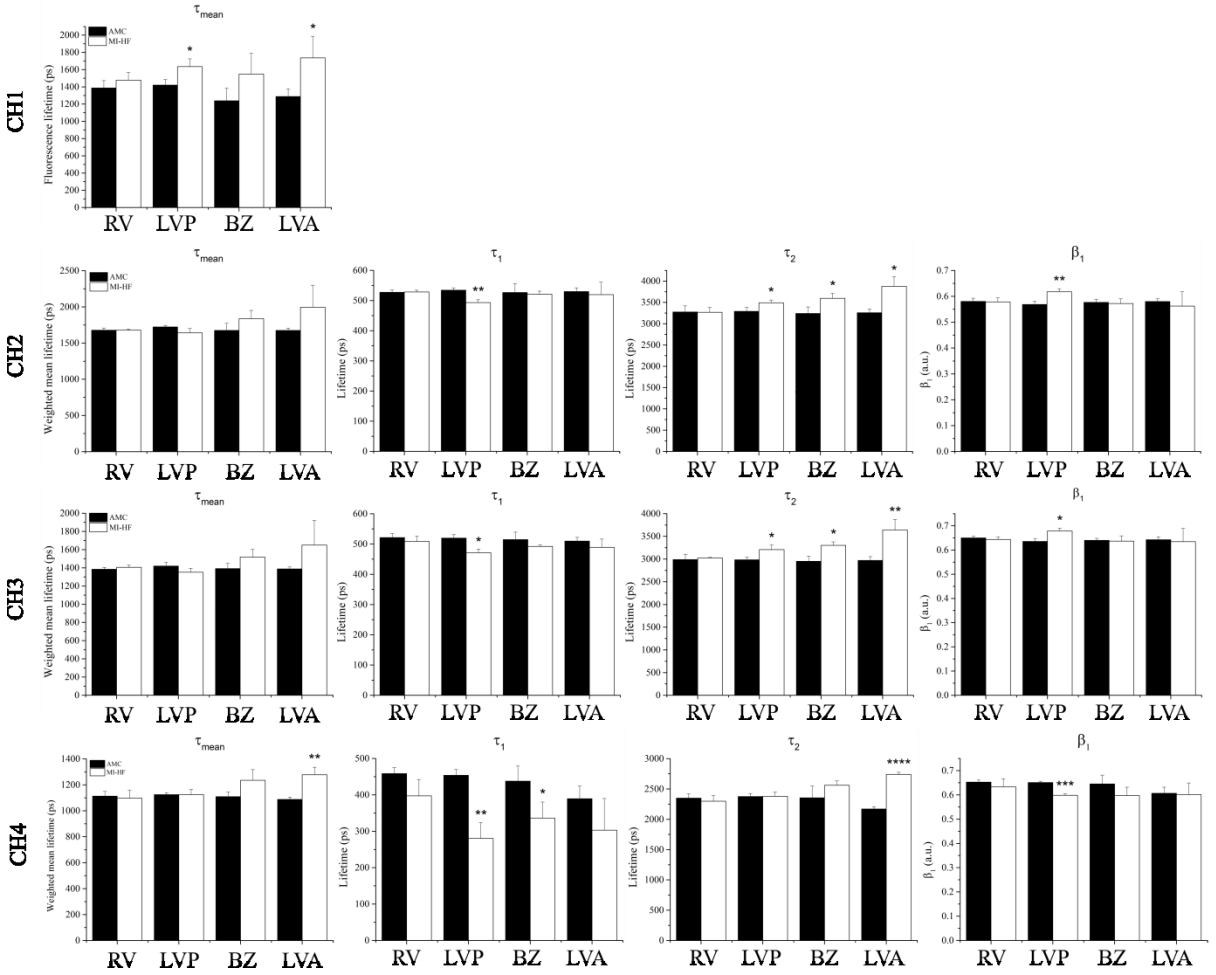

Figure 6.22 Autofluorescence lifetime parameters in each spectral detection channel, displayed by ROI, 1 week after MI induction. Results show a general increase in the mean autofluorescence lifetimes in the scar region of MI-HF relative to healthy AMC hearts, as a result of collagen deposition in this anatomical area. In detection channels 2, 3 and 4, we observe a decrease in the short lifetime component τ_1 in LV posterior of MI-HF hearts, which may indicate functional remodelling in this region. RV – Right ventricle; LVP – Left ventricle posterior wall; BZ – border zone/septum; LVA – Left ventricle anterior wall/scar region.

6.7.2.1.4 Discriminant analysis

In order to investigate the potential of our instrument to discriminate between healthy and infarcted hearts in each ROI, we employed PCA followed by LDA, as described in section 6.7.1.4.4. To this dataset, we applied the classification algorithm to all fluorescence parameters, both time-resolved and steady-state, for a combined total of 19 parameters, as indicated in Table 6.4. Figure 6.23 shows the scores of the first two PC for each ROI using all fluorescence parameters and Table 6.7 summarises results the discrimination algorithm. Despite the subtle differences evidenced in autofluorescence results, particularly in RV (see Figure 6.20, Figure 6.21 and Figure 6.22), classification results show that our instrument provides excellent discrimination between healthy and diseased hearts one week after MI, not only in the infarcted scar (LV anterior) in which differences were more pronounced but,

more interestingly, also in the border zone and remote-non infarcted myocardium, i.e. RV and LV posterior, yielding a diagnostic accuracy of 100% in all ROIs.

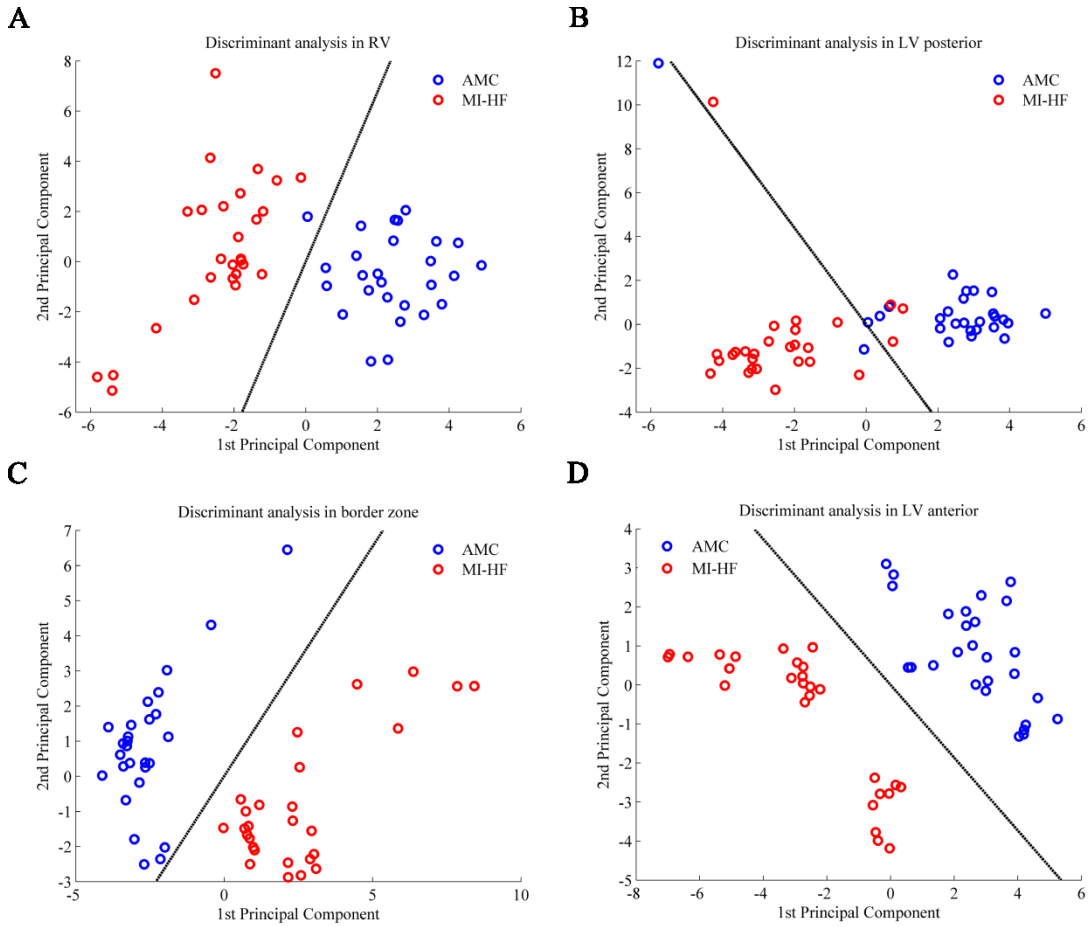

Figure 6.23 Results from PCA of all autofluorescence parameters measured 1 week post-MI for each ROI shown as scatter plots of the scores of the first two PC: a) RV, b) LV posterior, c) border zone and d) LV anterior. Black lines show the decision lines produced by LDA analysis. The most relevant parameters (in descending order of importance) for the first and second principal components (PC1 and PC2, respectively) were as follows (see Table 6.4 for the list of parameters): **RV** – PC1: CH3 τ_1 and CH4 β; PC2: CH3 R and CH2 I/CH3 I. **LV posterior** – PC1: CH3 R and CH2 I/CH3 I; PC2: CH2 τ_{mean} and CH3 τ_{mean}. **Border zone** – PC1: CH1 I/CH3 I and CH1 R; PC2: CH2 τ_1 and CH3 τ_1. **LV anterior** – PC1: CH2 I/CH3 I and CH1 I/CH3 I; PC2: CH2 τ_1 and CH3 τ_1.

Table 6.7 Classification results of the LDA-PCA based algorithm applied to 1 week data, using the five most relevant PC.

	RV	LV posterior	Border zone	LV anterior
Variance in data (%)	93.5	94.1	92.5	94.9
Sensitivity (%)	100.0	100.0	100.0	100.0
Specificity (%)	100.0	100.0	100.0	100.0
Diagnostic accuracy (%)	100.0	100.0	100.0	100.0
AUC	1.00	1.00	1.00	1.00

6.7.2.2 2 weeks post-surgery

Cardiac occlusion of the LAD artery produced a large transmural MI in the anterior wall of the left ventricle, with formation of well-defined scar tissue in 1 of 3 specimens 2 weeks post-MI induction, showing white colouration due to collagen deposition. In some cases, scar tissue was also visible in the posterior wall of the left ventricle, suggesting development of the MI also in this region. MI-HF

hearts showed an increased heart to body weight ratio (4.07 ± 0.80 g/kg, n = 3) relative to AMC hearts (3.11 ± 0.47 g/kg, n = 4), although this was not statistically significant.

6.7.2.2.1 Diffuse reflectance measurements

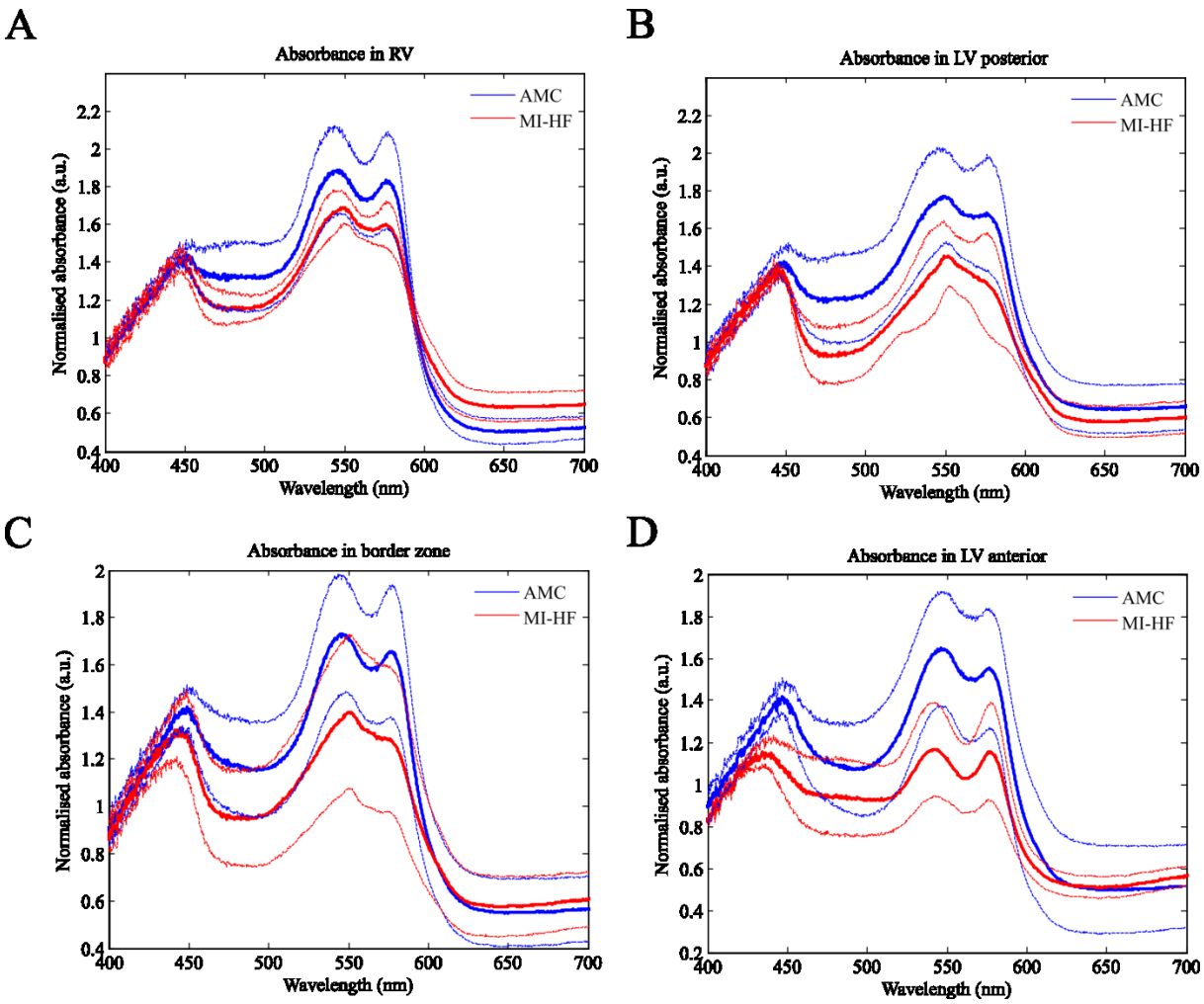

Figure 6.24 Diffuse reflectance spectra 2 weeks post-infarction in (A) RV, (B) LV posterior, (C) Border zone, (D) LV anterior. Ticked solid lines indicate average and dashed lines indicate +/- 1 SD.

Figure 6.24 shows the characteristic diffuse reflectance spectra of cardiac tissue 2 weeks after infarction, indicated as tissue absorbance. As in week 1 (see Figure 6.19), our data shows a decrease in tissue absorbance in MI-HF hearts, as a consequence of reduced haemoglobin and myoglobin concentration. AMC specimens show hallmark features of oxygenated haemoglobin/myoglobin in all ROI, with a characteristic local maxima at ~540 and 580 nm. The absorbance curves in RV and scar region of MI-HF hearts also present characteristic features of oxygenated haemoglobin and myoglobin, although this is more pronounced in the latter. The mean absorbance spectra of LV posterior and border zone in MI-HF hearts are similar, showing a single peak at ~ 550 nm and a smooth shoulder at 580 nm, consistent with the presence of cytochrome c and oxygenated haemoglobin/myoglobin, respectively (see Figure 6.7). With respect to LV posterior of MI-HF hearts, the shift from a double peak profile to a single peak can also be attributed to an increase in deoxy-

haemoglobin/myoglobin and concomitant decrease in tissue oxygenation. This is evident in the lower standard deviation curve of MI-HF hearts (see Figure 6.24B), in which we observe a single peak at ~550 nm and a shoulder at ~520 nm from reduced cytochrome c, accompanied by characteristic features of deoxygenated haemoglobin/myoglobin spectral profiles at ~560 nm and ~590 nm (see Figure 6.7).

6.7.2.2.2 Autofluorescence spectral measurements

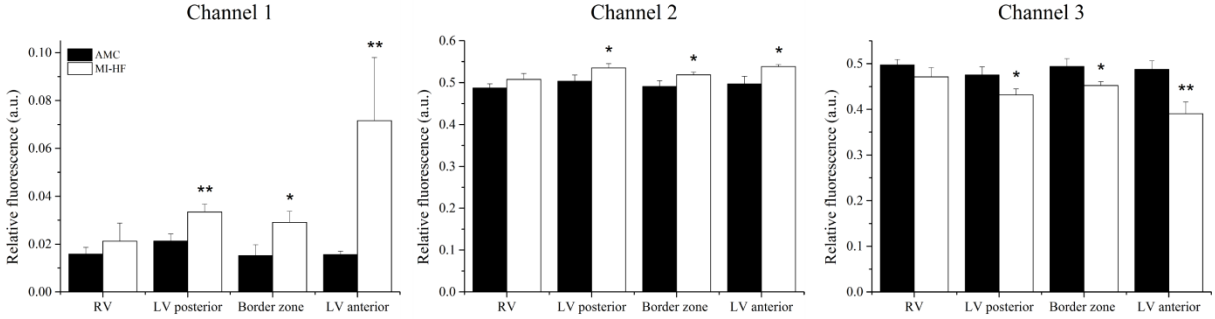

Figure 6.25 Relative autofluorescence contribution of each spectral detection channel in AMC and MI-HF hearts 2 weeks post-MI induction surgery, displayed by ROI.

Figure 6.25 shows the relative contribution of each detection channel active upon UV excitation to the total autofluorescence signal. The results indicate an increase in the contribution of channel 1 autofluorescence in MI-HF hearts, particularly in scar tissue (LV anterior), which is consistent with increased collagen deposition in this area following MI. This is more evident in Figure 6.26, as a blue-shift in the fluorescence emission wavelength of MI-HF hearts. We also observe a significant increase in channel 1 autofluorescence in LV posterior, which is consistent with the development of the MI into this region, as mentioned above, with consequent collagen proliferation and formation of scar tissue. As the total relative fluorescence signal must sum to one by definition, the increase in channel 1 contribution is obviously accompanied by a decrease in the contribution of channel 3, as demonstrated in Figure 6.25.

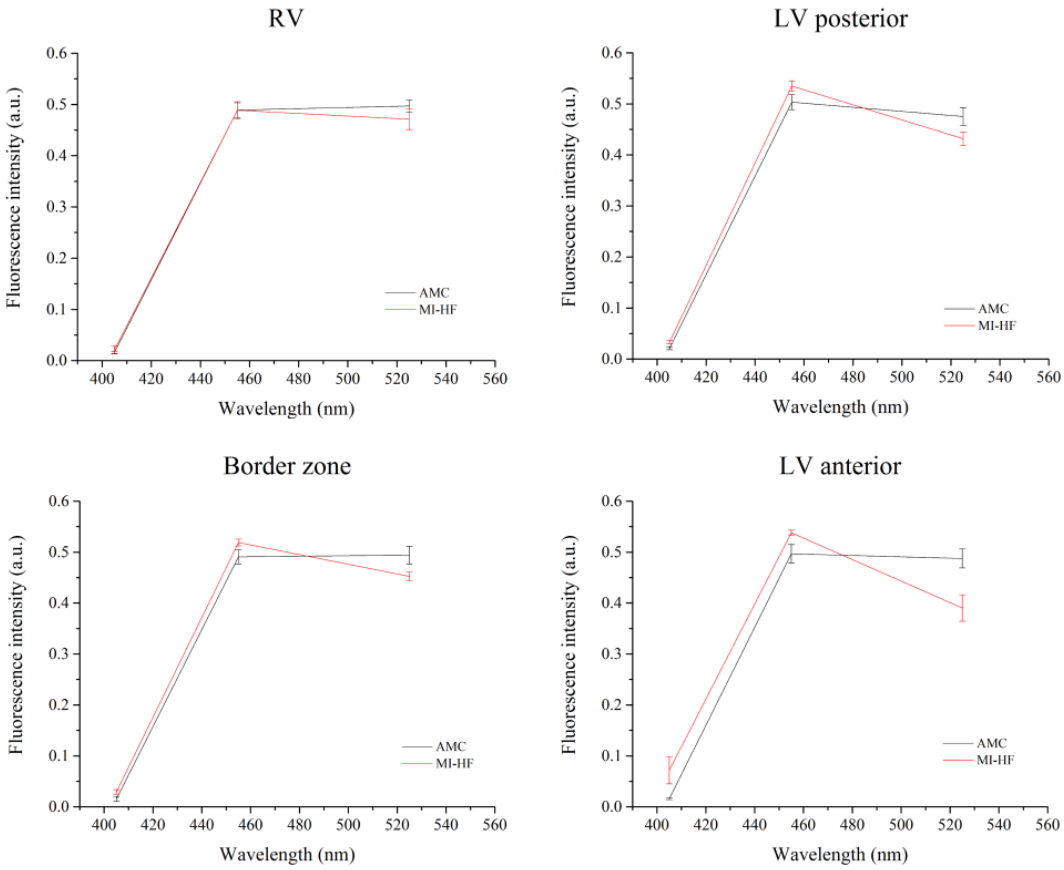

Figure 6.26 Relative autofluorescence in each region of interest for AMC and MI hearts, 2 weeks after MI surgery. As for week 1, data show a shift in the autofluorescence emission spectra towards shorter wavelengths, which is consistent with increased collagen content.

6.7.2.2.3 Autofluorescence lifetime measurements

Figure 6.27 shows the autofluorescence lifetime results for measurements realised 2 weeks after MI induction surgery. Our data indicates a significant increase in the mean autofluorescence lifetime of scar tissue (LV anterior) relative to healthy LV myocardium in all spectral channels, which can be traced back to significant increases in the long decay component and decreases in the contribution of the short decay to the autofluorescence profile in channels 2, 3 and 4. This increase is more pronounced than that observed for 1 week data, which suggests a greater contribution of collagen autofluorescence to the mean lifetime. In LV posterior, there is also an increase in the mean autofluorescence lifetime of channel 4 in MI-HF hearts, which we attribute to the presence of scar tissue in this area. With respect to the short decay component τ_1, which was provisionally associated with metabolic alterations in the tissue, changes in this parameter are more subtle than in week 1 data. In particular, detection channels 2 and 3 do not evidence any difference between AMC and MI-HF hearts that can suggest altered energetic state. However, in channel 4, this parameter is consistently shorter in MI-HF hearts, with statistical significance in the region of infarction (LV anterior), potentially reflecting an alteration in the metabolic state in this region.

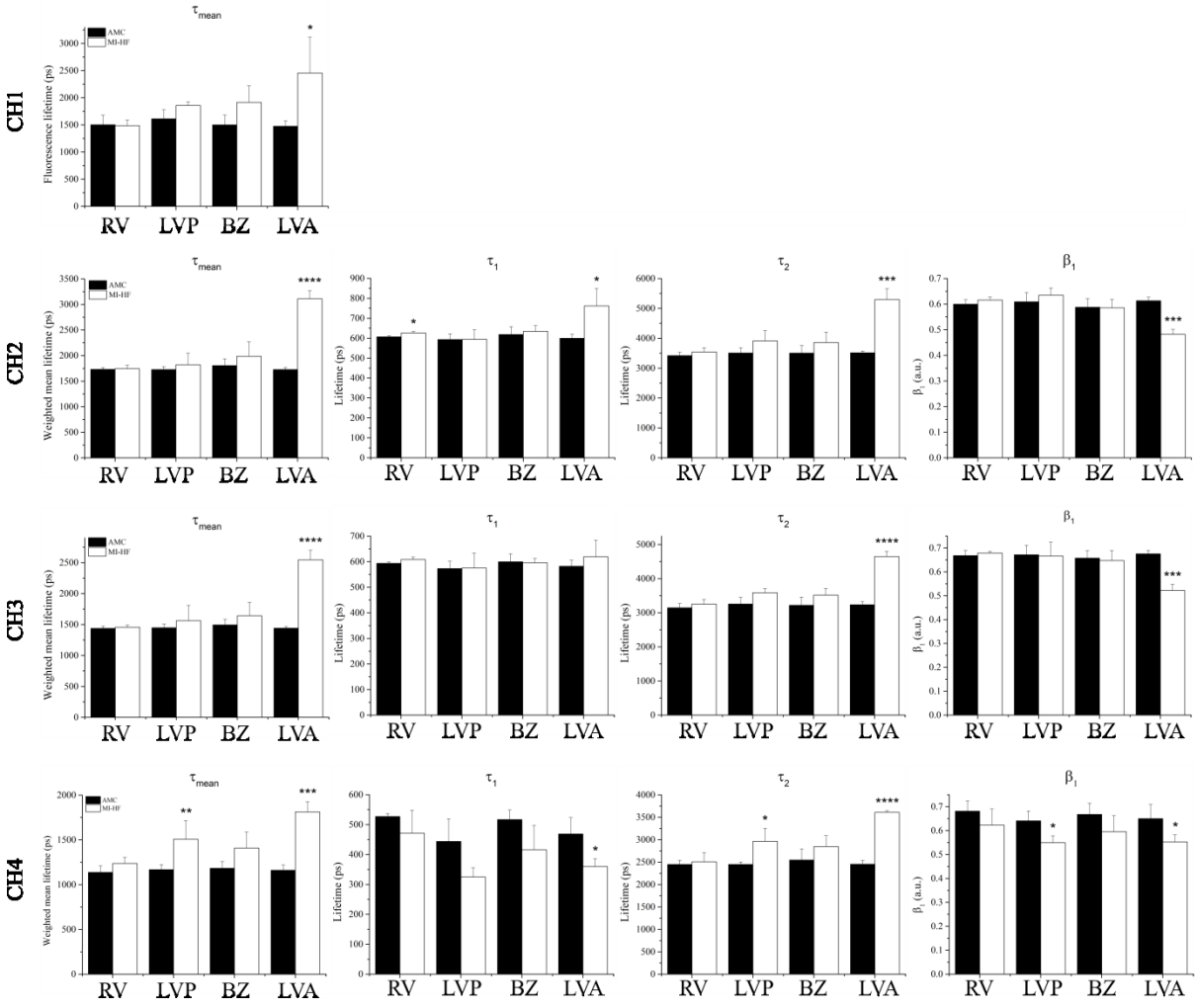

Figure 6.27 Autofluorescence lifetime parameters in each spectral detection channel, displayed by ROI, 2 weeks after MI induction. Results show a general increase in the mean autofluorescence lifetimes in the scar region of MI-HF relative to healthy AMC hearts, as a result of collagen deposition in this anatomical area, which is more prominent than for week 1 post-MI. RV – Right ventricle; LVP – Left ventricle posterior wall; BZ – border zone/septum; LVA – Left ventricle anterior wall/scar region.

6.7.2.2.4 Discriminant analysis

The results of the discriminant analysis applied to data collected two weeks after infarction are summarised in Table 6.8 and illustrated in Figure 6.28 as the scores of the two PC in each ROI. In general, our results yield good discrimination between healthy and diseased hearts in all regions investigated, with particular emphasis for the LV anterior, where the classification achieved 100% sensitivity and specificity and an AUC value of 1, denoting excellent classification performance. In the border zone region, the classification achieved good diagnostic accuracy (87.5%), although with lower sensitivity (77.8%) relative to the specificity (97.2%). In regions remote to the MI, i.e. RV and LV posterior, where changes in tissue are typically more subtle, classification produced lower diagnostic accuracy in comparison the scar tissue. Particularly in the RV, we achieved reasonable sensitivity and good specificity values (70 and 86%, respectively). In the LV posterior, the

classification produced high sensitivity (92%) which is likely due to the deposition of collagen and concomitant formation of scar tissue in this region, as discussed above.

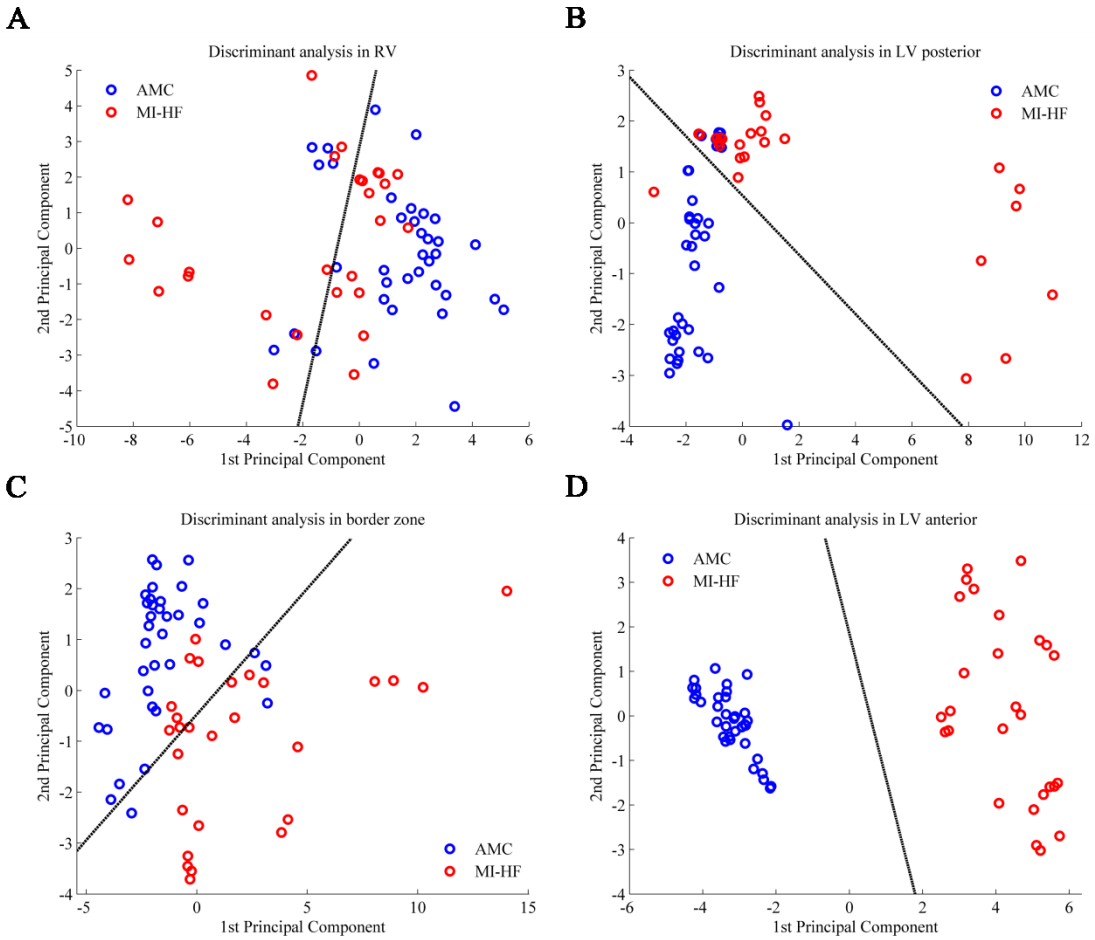

Figure 6.28 Results from PCA of all autofluorescence parameters measured 2 weeks post-MI for each ROI shown as scatter plots of the scores of the first two PC: a) RV, b) LV posterior, c) border zone and d) LV anterior. Black lines show the decision lines produced by LDA analysis. The two most relevant parameters (in descending order of importance) for the first and second principal components (PC1 and PC2, respectively) were as follows (see Table 6.4 for the list of parameters): **RV** – PC1: CH3 and CH2 I/CH3 I; PC2: CH2 τ_{mean} and CH3 τ_{mean}. **LV posterior** – PC1: CH1 R and CH1 I/CH3 I; PC2: CH2 R and CH3 τ_1. **Border zone** – PC1: CH1 I/CH3 I and CH1 R; PC2: CH4 τ_1 and CH4 β. **LV anterior** – PC1: CH2 τ_{mean} and CH2 τ_2; PC2: CH3 τ_1 and CH2 τ_1.

Table 6.8 Classification results of the LDA-PCA based algorithm applied to 2 week data, using the five most relevant PC.

	RV	LV posterior	Border zone	LV anterior
Variance in data (%)	90.7	94.9	94.4	98.0
Sensitivity (%)	70.4	92.6	77.8	100.0
Specificity (%)	86.1	83.3	97.2	100.0
Diagnostic accuracy (%)	78.2	88.0	87.5	100.0
AUC	0.91	0.90	0.94	1.00

6.7.2.3 4 weeks post-surgery

At week 4 post-surgery, scar tissue was clearly visible in anterior wall of the left ventricle in all specimens, although the border zone between healthier and damaged myocardium was still diffuse.

Hypertrophy of the heart was confirmed by a significant increase ($p < 0.05$) in heart to body weight ratio of MI-HF (3.89 ± 0.38 g/kg, n = 3) in comparison with AMC hearts (2.33 ± 0.22 g/kg, n = 3).

6.7.2.3.1 Diffuse reflectance measurements

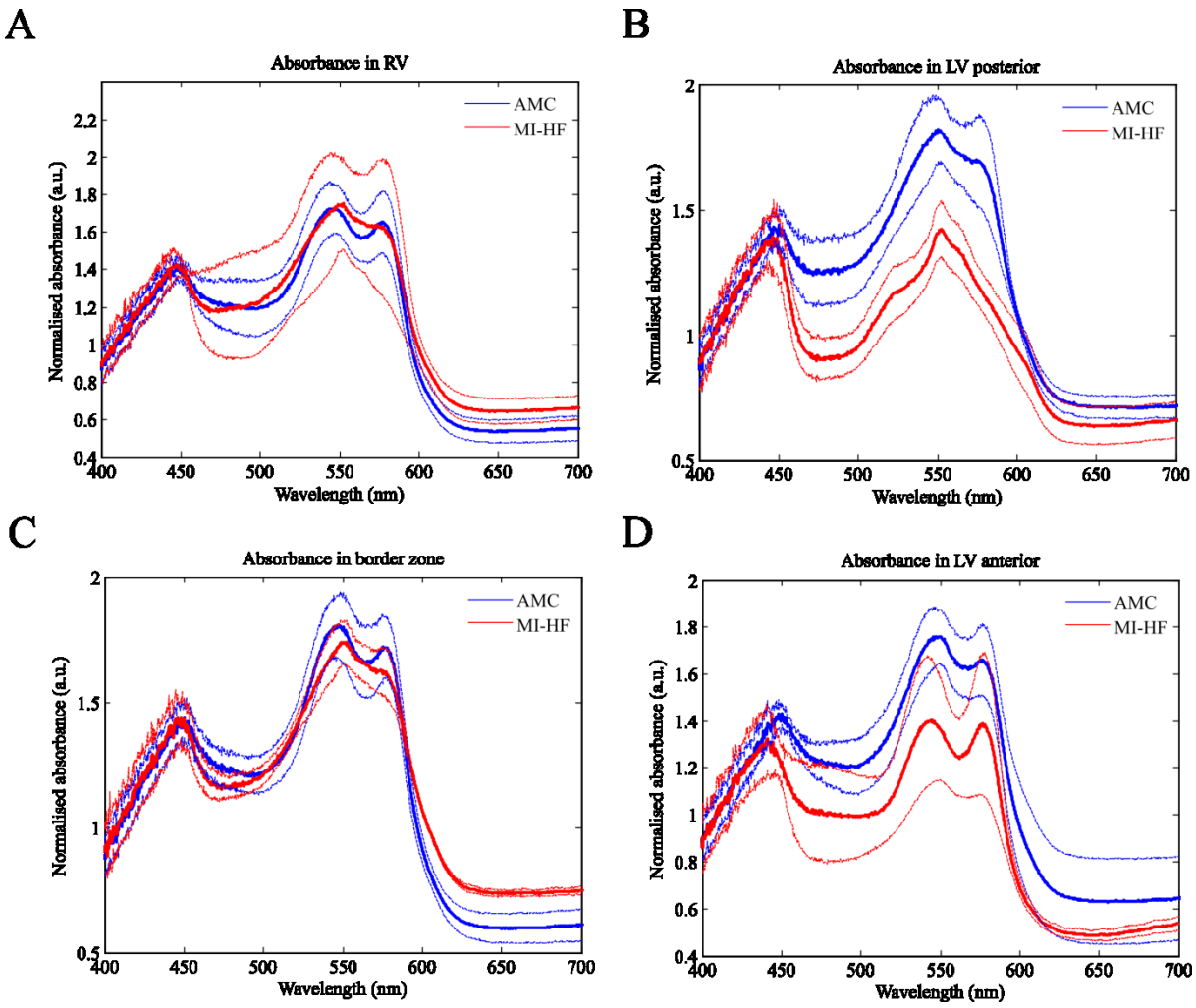

Figure 6.29 Diffuse reflectance spectra displayed as normalised tissue absorbance, 4 weeks post-infarction in (A) RV, (B) LV posterior, (C) Border zone, (D) LV anterior. Ticked solid lines indicate average and dashed lines indicate +/- 1 SD.

Figure 6.29 shows the average diffuse reflectance spectra of AMC and MI-HF specimens four weeks post-MI induction. These results indicate a decrease in tissue absorbance in MI-HF hearts in LV posterior and LV anterior but not in RV and border zone, where, in general, changes in the absorbance spectra are less evident. In agreement with our observations at weeks 1 and 2, AMC hearts present the double peak profile characteristic of oxygenated haemoglobin/myoglobin, although we note that this is less pronounced in the 4-week dataset. For example, LV posterior presents a single peak profile with maximum close to 550 nm with a shoulder at 580 nm, which are consistent with the presence of reduced cytochrome c and oxygenated haemoglobin/myoglobin in the tissue. The absorbance spectra of MI-HF hearts is, in general, more complex. In scar tissue (LV anterior), it presents a double peak profile with local maxima at ~540 nm and ~580 nm that are characteristic of oxygenated haemoglobin and myoglobin (see Figure 6.7). In contrast, the absorbance spectra in LV posterior appears to have

contributions from reduced cytochrome c (i.e. a shoulder at ~520 nm and a peak at ~550 nm) and deoxygenated haemoglobin and myoglobin (i.e. a smooth shoulder between 555 and 560 nm), which suggest poor tissue oxygenation in this region perhaps suggesting the presence of scar tissue. The spectral profiles of MI-HF in RV and border zone also present a single peak with maximum at ~550 nm, although there is a well-defined shoulder at ~580 nm, consistent with the oxygenated forms of haemoglobin and myoglobin.

6.7.2.3.2 Autofluorescence spectral measurements

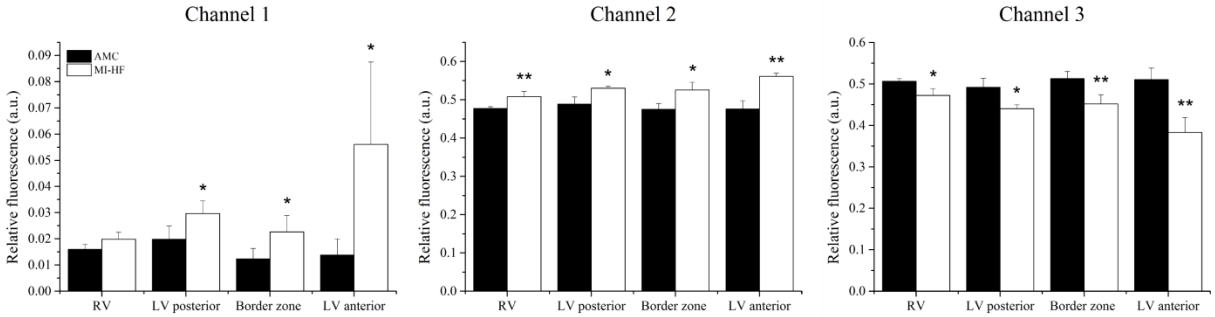

Figure 6.30 Relative autofluorescence contribution of each spectral detection channel in AMC and MI-HF hearts 4 weeks post-MI induction surgery, displayed by ROI.

Figure 6.30 and Figure 6.31 present the relative contribution of channels 1, 2 and 3 to the total autofluorescence signal arising from UV excitation. In agreement with the 1 and 2 week data, these results indicate an increase in the contribution of channels 1 and 2 to the autofluorescence signal, suggesting an increase in collagen content in MI-HF hearts. Although this increase is more clear in the scar region (LV anterior) where collagen deposition is expected to be more pronounced, significant increases can also be observed in regions remote to the infarction (RV and LV posterior) and border zone. We also note that changes in the border zone are similar to those observed in LV posterior, suggesting similar collagen proliferation in these regions. Since border zone measurements were realised in the area separating scar tissue and healthier myocardium, we would expect collagen increase in this regions to be roughly an average of that measured in RV and in LV anterior. Given the diffused scar tissue border observed in these hearts, as mentioned above, it is possible that measurements in these regions were predominantly realised in healthier myocardium, which would explain the relatively low increase in collagen content observed in this area.

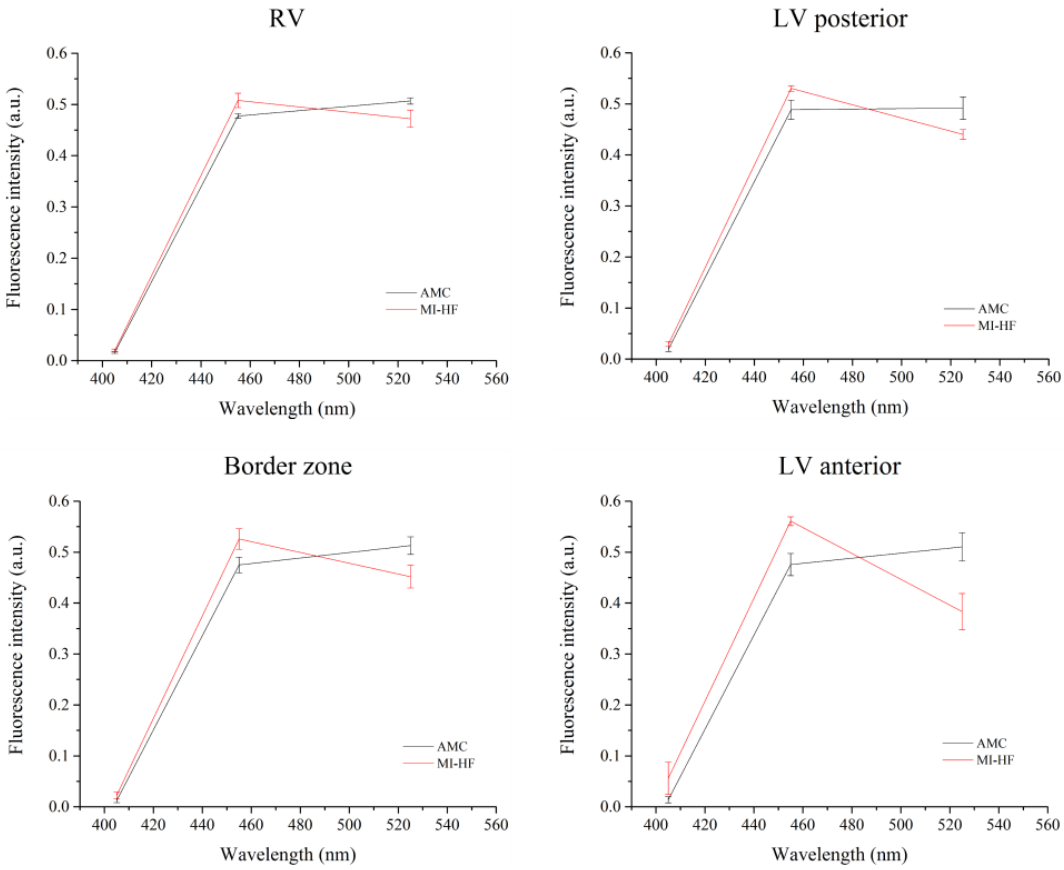

Figure 6.31 Relative autofluorescence in each region of interest for AMC and MI hearts, 4 weeks after MI surgery. Data show a shift in the fluorescence emission spectra towards short wavelengths in MI-HF relative to AMC hearts, in all anatomical regions of interest.

6.7.2.3.3 Autofluorescence lifetime measurements

Results of the autofluorescence lifetime data are plotted in Figure 6.32. In agreement with autofluorescence lifetime data of 1- and 2-week datasets, we observe a longer mean autofluorescence lifetime in scar tissue of MI-HF hearts relative to healthy LV myocardium, in all spectral detection channels. This increase is more pronounced than in weeks 1 and 2, potentially reflecting increased collagen concentration. Changes in NADH and FAD fluorescence lifetime may also be contributing to the mean autofluorescence lifetime, but this is hard to quantify in the presence of an apparent large increase in collagen content in the scar. In regions remote to the scar, in particular LV posterior, we observe changes in the short lifetime τ_1 of channels 3 and 4 that are opposite to changes induced by collagen proliferation and therefore may be related to alterations in the energetic state of the tissue. This is further emphasised by changes in the contribution of the short lifetime component β in these channels, which confirms previous results (see Figure 6.22) and are in agreement with our observations of the hypoxia Langendorff heart model (see Figure 6.16).

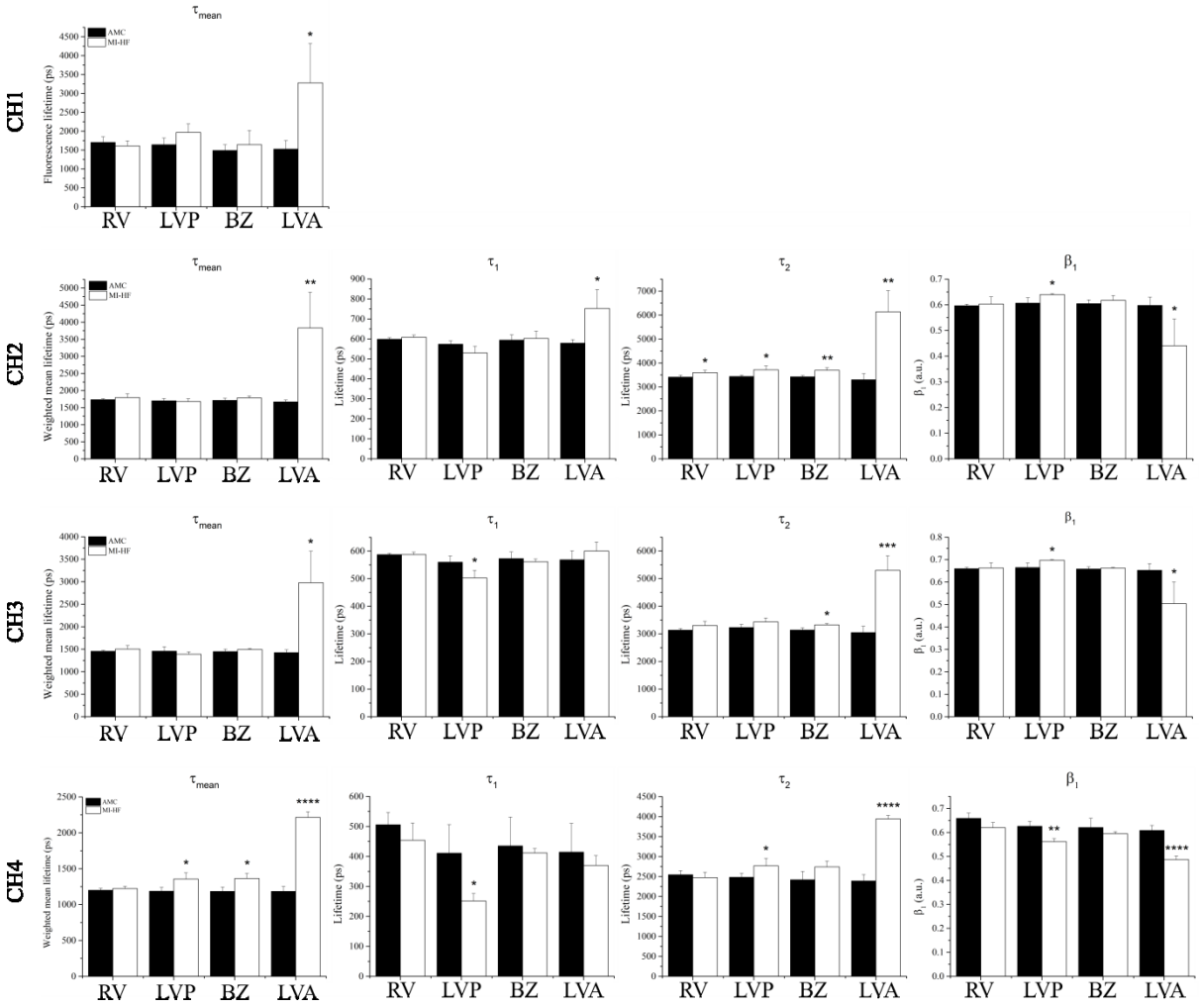

Figure 6.32 Autofluorescence lifetime parameters in each spectral detection channel, displayed by ROI, 4 weeks after MI induction. As a result of collagen deposition, changes in the mean autofluorescence lifetime in the region of infarction in all detection channels are now more prominent compared to weeks 1 and 2 post-infarction. Despite this large collagen increase, changes in short lifetime component τ_1 of channels 3 and 4 are still possible to observe in the remote non-infarcted myocardium, possibly due to alterations in the myocardial metabolism. RV – Right ventricle; LVP – Left ventricle posterior wall; BZ – border zone/septum; LVA – Left ventricle anterior wall/scar region.

6.7.2.3.4 Discriminant analysis

Classification results for 4-week data (see Figure 6.33 and Table 6.9) indicate excellent discrimination (specificity = 100%, sensitivity = 100% and AUC = 1) between AMC and MI-HF hearts in the region of infarction (LV anterior) and, more interestingly, in LV posterior, which is remote from the MI and therefore alterations in the spectroscopic parameters in this region are more subtle. In LV anterior, we observe a clear differentiation between the two groups (see Figure 6.33D), driven by the increase in collagen content in MI-HF hearts. In RV, we obtained a sensitivity of 81% and specificity of 86%, yielding a diagnostic accuracy of approximately 84%, and thus demonstrating a good classification performance considering the subtle differences in the autofluorescence parameters in this region. Finally, the performance of the classification in border zone was lower in comparison to other regions, due to poor sensitivity of the measurements (~62%) despite the very high specificity (>94%).

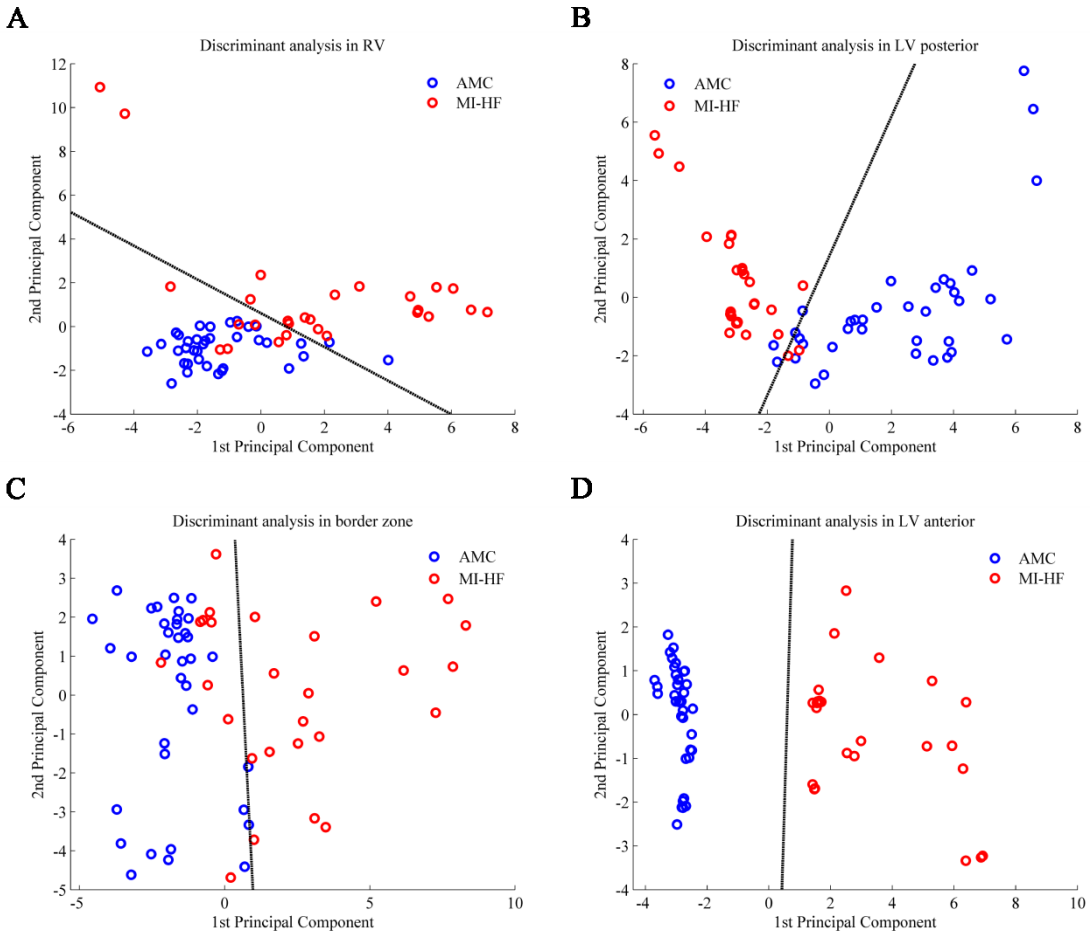

Figure 6.33 Results from PCA of all autofluorescence parameters measured 4 weeks post-MI for each ROI shown as scatter plots of the scores of the first two PC: a) RV, b) LV posterior, c) border zone and d) LV anterior. Black lines show the decision lines produced by LDA analysis. The two most relevant parameters (in descending order of importance) for the first and second principal components (PC1 and PC2, respectively) were as follows (see Table 6.4 for the list of parameters): **RV** – PC1: CH1 and CH1 I/CH3 I; PC2: CH3 τ_{mean} and CH2 τ_{mean}. **LV posterior** – PC1: CH3 R and CH2 I/CH3 I; PC2: CH2 τ_{mean} and CH3 τ_2. **Border zone** – PC1: CH3 R and CH1 I/CH3 I; PC2: CH3 τ_1 and CH3 τ_1. **LV anterior** – PC1: CH3 τ_2 and CH2 τ_2; PC2: CH3 τ_1 and CH4 τ_1.

Table 6.9 Classification results of the LDA/PCA based algorithm applied to 4 weeks data, using the five most relevant PC.

	RV	LV posterior	Border zone	LV anterior
Variance in data (%)	91.4	94.0	93.8	98.2
Sensitivity (%)	81.5	100.0	62.9	100.0
Specificity (%)	86.1	100.0	94.4	100.0
Diagnostic accuracy (%)	83.8	100.0	78.7	100.0
AUC	0.95	1.00	0.92	1.00

6.7.2.4 16 weeks post-surgery

Cardiac occlusion of the LAD produced a large transmural MI and thus formation of a well-defined scar in the anterior wall of the left ventricle in all specimens (see Figure 6.34). Hypertrophy of the remaining myocardium was confirmed by a significant increase ($p < 0.05$) in heart to body weight ratio in MI-HF animals (3.40 ± 0.60 g/kg, n = 6) compared to AMC animals (2.84 ± 0.45 g/kg, n = 6), in agreement with previous studies of this model [367]. Collagen content of the heart significantly increased in MI-HF animals compared to AMC (see Table 6.10 and Figure 6.34).

Table 6.10 Collagen content calculated from representative histology images. Statistical analysis between AMC and MI hearts was computed using a two-tailed Student t-test (n = 3).

	Collagen content assessed by PSR staining (%)		
	AMC	**MI-HF**	**p-value**
RV	4.5 ± 1.7	22.9 ± 4.2	0.0021
LV posterior	6.5 ± 2.0	35.5 ± 9.1	0.0057
Border zone	4.7 ± 0.7	28.3 ± 1.3	< 0.0001
LV anterior	2.6 ± 0.2	74.2 ± 5.0	< 0.0001

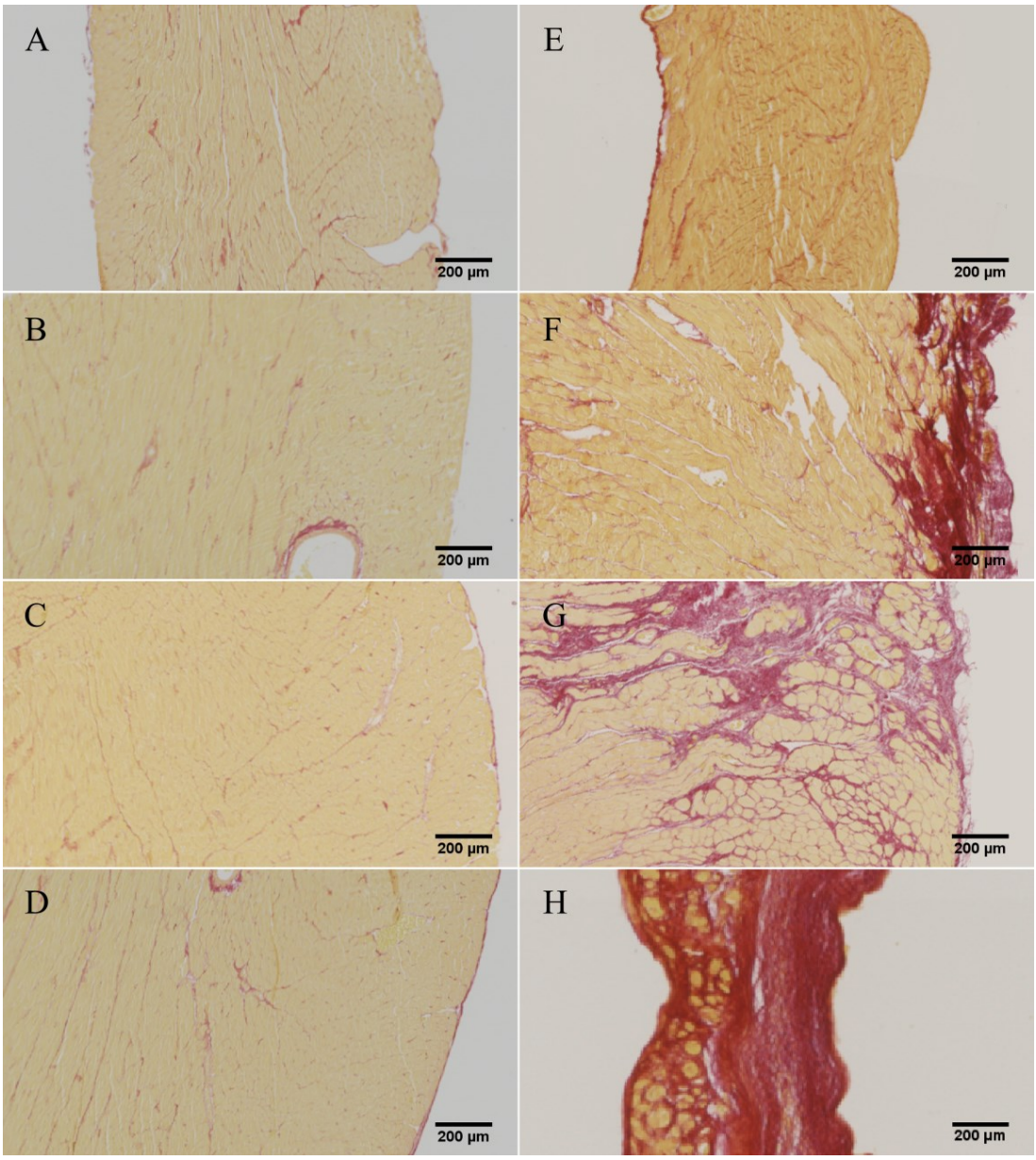

Figure 6.34 Representative histology images of AMC (left column) and MI-HF (right column) hearts 16 weeks post-MI induction in (A, E) RV, (B, F) LV posterior, (C, G) Border zone and (D, H) LV anterior. As expected, increase in interstitial collagen (coloured red) is more prominent in the region of infarction (panel H) and border zone (panel G) compared to non-infarcted muscle (panels E and F).

6.7.2.4.1 Diffuse reflectance measurements

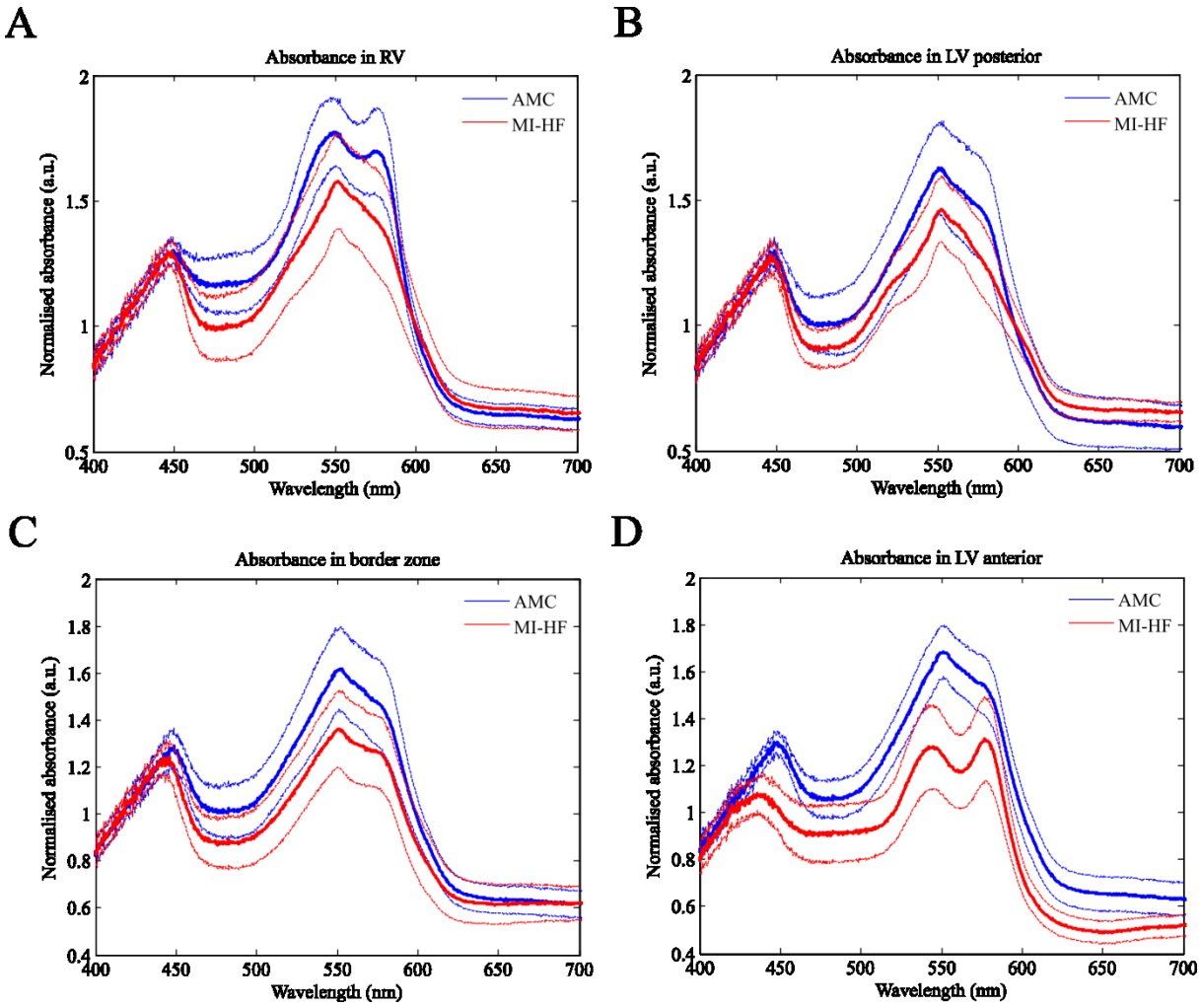

Figure 6.35 Diffuse reflectance spectra displayed as normalised tissue absorbance, 16 weeks post infarction in (A) RV, (B) LV posterior, (C) Border zone, (D) LV anterior. Ticked solid lines indicate average and dashed lines indicate +/- 1 SD.

Figure 6.35 illustrates the diffuse reflectance spectra of AMC and MI-HF hearts at 16 weeks post-infarction in all ROI, indicated as tissue absorbance. The results show an overall decrease in absorbance in MI-HF hearts, for all ROI, consistent with our observations at 1, 2 and 4 weeks post-infarction. In AMC hearts, the maximum absorption peak at ~550 nm is consistent with the presence of cytochrome c. There is also a shoulder at ~580 nm, which can be attributed to the presence of oxygenated haemoglobin and myoglobin in the tissue, as expected in healthy AMC hearts. This feature is most pronounced in the RV, where there is a well-defined peak at ~580 nm. In MI-HF hearts, differences in the diffuse reflectance spectra were observed for infarcted (LV anterior) compared to non-infarcted (RV and LV posterior) regions. In scar tissue (LV anterior in MI hearts), the diffuse reflectance spectrum shows hallmark oxygenated haemoglobin/myoglobin absorption features at ~540 nm and ~580 nm. We note that the cytochrome c absorption peak is no longer visible in the mean spectrum for scar tissue, which is consistent with the low concentration of mitochondria expected owing to cell loss and replacement with scar tissue. In regions remote to the MI, we observe

a single peak in the 500 – 600 nm band at ~550 nm consistent with cytochrome c accompanied by a smooth shoulder at ~580 nm consistent with oxygenated haemoglobin/myoglobin.

6.7.2.4.2 Autofluorescence spectral measurements

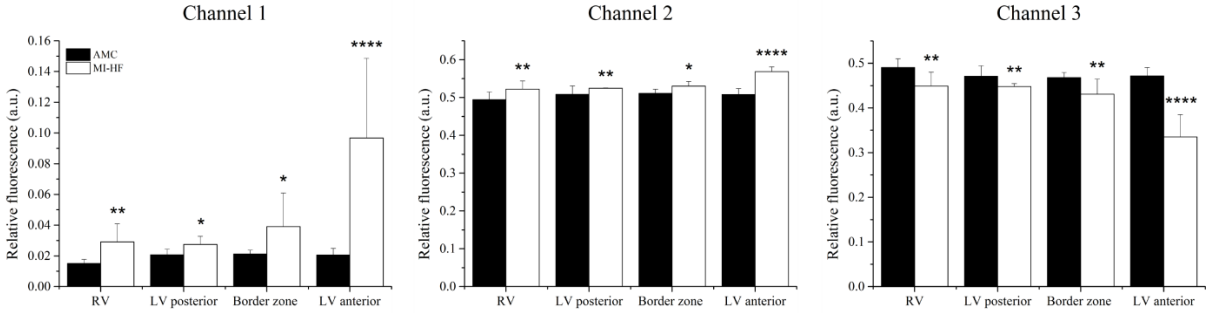

Figure 6.36 Relative autofluorescence contribution of each spectral detection channel in AMC and MI-HF hearts 16 weeks post-MI induction surgery, displayed by ROI.

Figure 6.36 and Figure 6.37 show the relative autofluorescence signal in each spectral channel for UV excitation by ROI and wavelength, respectively. The results indicate an increased contribution of channel 1 to the total fluorescence signal in MI-HF hearts in all regions, in agreement with our previous results. This increase is most significant in LV anterior where the scar tissue was formed. Our histology (see Table 6.10 and Figure 6.34) and previous histology [367] of this model has shown an increase in collagen type I in the scar, which, given its fluorescence emission spectrum (see Chapter 3), is consistent with the increase in fluorescence that we see in this channel. The increase in channel 1 contribution in sites remote to the MI, such as RV or LV posterior, also suggests an increase in collagen contribution in these regions, which is consistent with histology results and previous observations [3], [367]. We also observe an increase in the relative contribution of channel 2 in all regions, which is again consistent with an increase in collagen type I and its broad emission spectrum. As the total relative fluorescence signal must sum to one by definition, then the relative contribution of channel 3 to the total fluorescence signal therefore decreases for MI in all regions. The increase in collagen type I fluorescence is also apparent in Figure 6.37 as a shift in the fluorescence emission towards shorter wavelengths for all ROI and this is most pronounced for LV anterior.

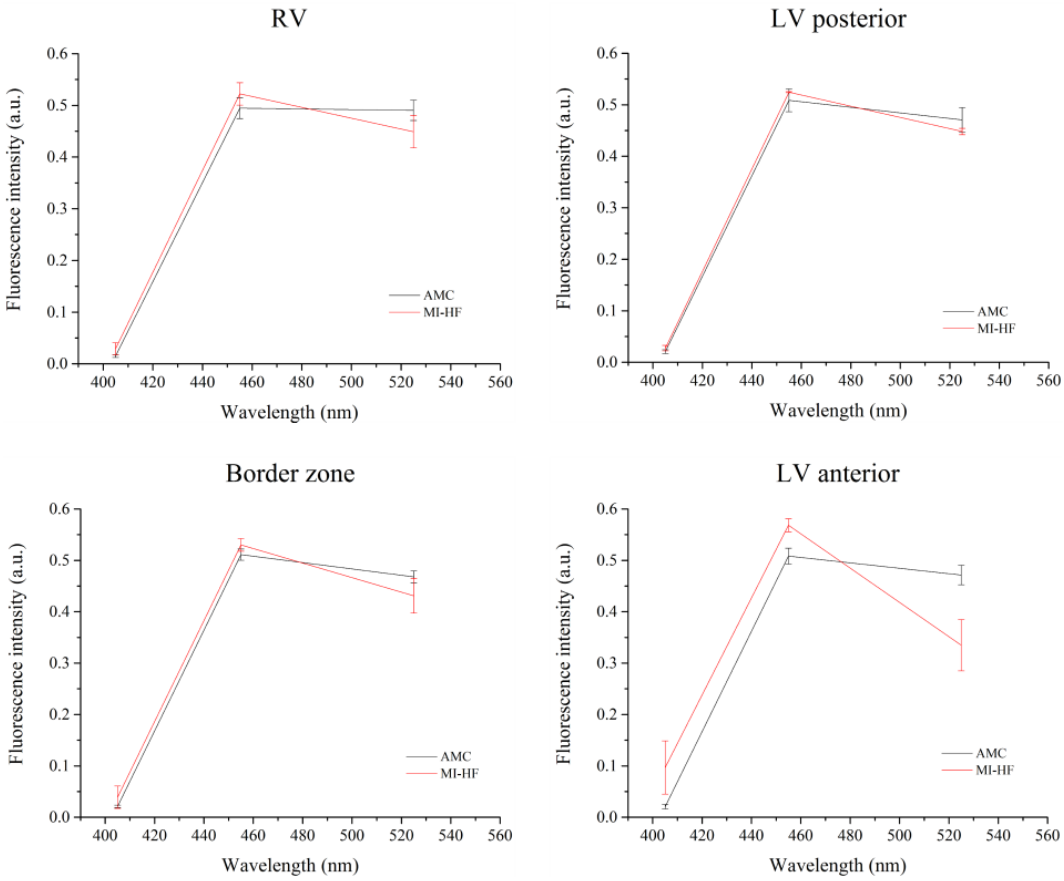

Figure 6.37 Relative autofluorescence in each region of interest for AMC and MI hearts, 16 weeks after MI surgery. Data show a shift in the fluorescence emission spectra of MI-HF hearts towards shorter wavelengths, as a results of collagen deposition following MI. This is more prominent in the region of infarction (bottom right panel).

6.7.2.4.3 Autofluorescence lifetime measurements

Results of the autofluorescence lifetime data are plotted in Figure 6.38. This data shows that MI-HF scar tissue (LV anterior) yields a longer mean autofluorescence lifetime compared to healthy LV myocardium in all detection channels. The increase in mean fluorescence lifetime in the LV anterior of MI-HF hearts is also reflected in all spectral channels in both the short (τ_1) and long (τ_2) decay components and as a decrease in the relative contribution of the short decay component (β). Changes in NADH or FAD fluorescence lifetimes may also be contributing to changes in the mean autofluorescence lifetime but this is challenging to quantify given the large increase in collagen autofluorescence in the infarcted regions scar (see Table 6.10 and Figure 6.34). Statistically significant increases in mean autofluorescence lifetime are also seen in all spectral channels for the border zone, which we again attribute to an increase in collagen type-I content in this region. In remotes sites from scar tissue, i.e. RV and LV posterior, we also observe statistically significant differences in decay profiles of channels 3 and 4. Particularly in channel 4, we see decreases in the short decay component τ_1 in both regions in MI-HF compared to AMC (see Figure 6.38 bottom row), which are in agreement with our previous results and thus we believe cannot be explained by increases in collagen type-I concentration but might be explained by alterations in tissue metabolism in these regions.

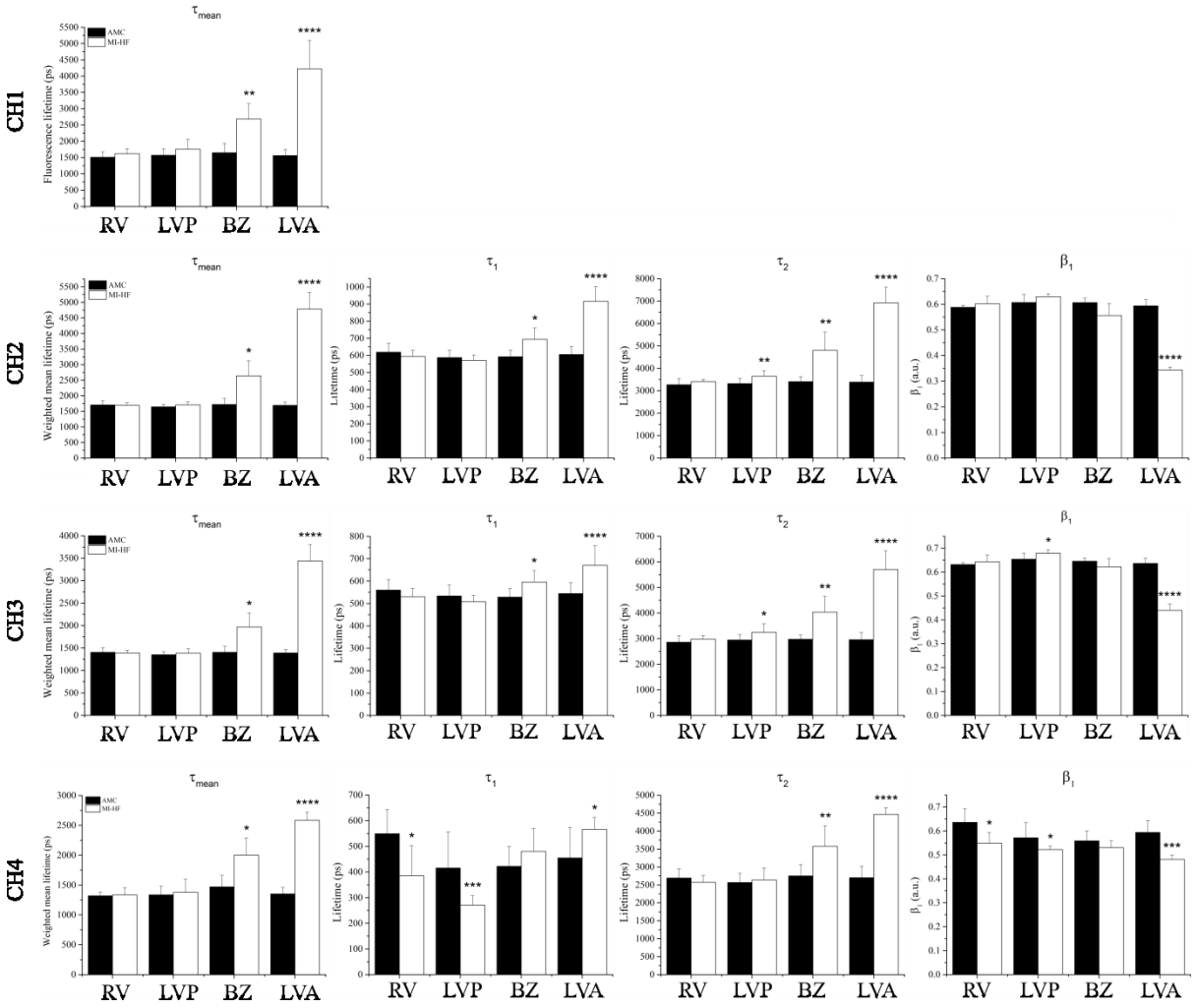

Figure 6.38 Autofluorescence lifetime parameters in each spectral detection channel, displayed by ROI, 16 weeks after MI induction. We observe a large increase in the mean autofluorescence lifetime of all detection channels in the scar region of MI-HF relative to AMC hearts, in consequence of a large increase in collagen content. It is still possible to observe a statistically significant decrease in the short lifetime component τ_1 of detection channel 4 (CH4) in the remote RV and LV posterior. RV – Right ventricle; LVP – Left ventricle posterior wall; BZ – border zone/septum; LVA – Left ventricle anterior wall/scar region.

6.7.2.4.4 Discriminant analysis

Differences between AMC and MI-HF hearts are most pronounced at 16 weeks after infarction, due to a large increase in collagen content, not only in the infarcted region, but also in the remote non-infarcted myocardium. Hence, we investigated the potential of all spectroscopic methods employed in our instrument to discriminate between healthy and infarcted hearts in each ROI. For the purpose of comparison between methods, we applied the classification algorithm separately to the following groups: diffuse reflectance; fluorescence intensity; all fluorescence data (both lifetime and intensity); diffuse reflectance and fluorescence intensity; diffuse reflectance and all fluorescence data. Figure 6.39 shows the scores of the first two PC for each ROI using all autofluorescence parameters and Table 6.11 summarises the results of the discrimination algorithm applied to all groups of measurements. Classification results show that all methods are well-suited to discriminate between healthy and diseased hearts in scar tissue (LV anterior), where the AUC values calculated from ROC

curves are close to 1 for all methods, and sensitivity and specificity range from 91 to 100% and 96 to 100%, respectively, demonstrating an excellent classification performance. In the border zone, the classification is more accurate when all fluorescence parameters (lifetime and intensity) are used - either in combination with diffuse reflectance (AUC = 0.96) or alone (AUC = 0.96) – in comparison to steady-state methods alone, i.e. diffuse reflectance or fluorescence intensity. Finally, in remote regions, i.e. RV and LV posterior, the best classification is achieved combining diffuse reflectance and fluorescence intensity parameters, with measured AUC of 0.99 and 0.84, respectively. Particularly in the RV, sensitivity and specificity values are high (93 and 100%, respectively) for this method. It should also be noted that for LV posterior the classification is poor in comparison to other regions, and thus sensitivity and specificity in this region are generally lower (76 to 87% and 61 to 71%, respectively).

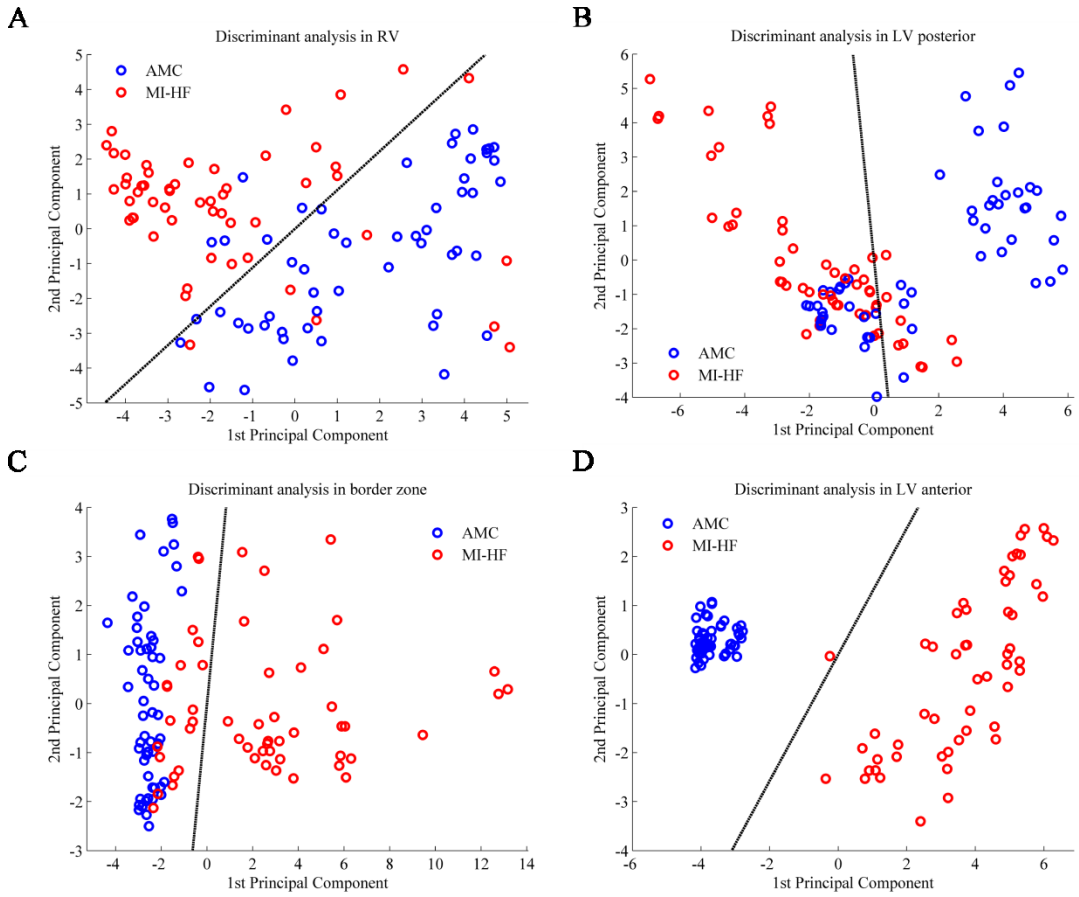

Figure 6.39 Results from PCA of all autofluorescence parameters measured 16 weeks post-MI for each ROI shown as scatter plots of the scores of the first two PC: a) RV, b) LV posterior, c) border zone and d) LV anterior. Black lines show the decision lines produced by LDA analysis. The two most relevant parameters (in descending order of importance) for the first and second principal components (PC1 and PC2, respectively) were as follows (see Table 6.4 for the list of parameters): **RV** – PC1: CH2 I/CH3 I and CH3 R; PC2: CH2 τ_2 and CH3 τ_2. **LV posterior** – PC1: CH3 R and CH1 I/CH3 I; PC2: CH3 τ_{mean} and CH2 τ_{mean}. **Border zone** – PC1: CH2 τ_{mean} and CH3 τ_{mean}; PC2: CH4 τ_1 and CH4 β. **LV anterior** – PC1: CH2 τ_{mean} and CH2 τ_2; PC2: CH1 I/CH2 I and CH1 I/CH3 I.

Table 6.11 Classification results of the LDA/PCA based algorithm applied to all autofluorescence and diffuse reflectance parameters and combinations of these parameters.

		RV	LV posterior	Border zone	LV anterior
Diffuse reflectance	**Variance in data (%)**	97.6	98.3	98.8	98.8
	Sensitivity (%)	86.7	80.0	82.2	100.0
	Specificity (%)	75.6	64.4	80.0	97.8
	Diagnostic accuracy (%)	81.1	72.2	81.1	98.9
	AUC	0.90	0.82	0.90	1.00
Fluorescence intensity	**Variance in data (%)**	100.0	100.0	100.0	100.0
	Sensitivity (%)	88.9	87.0	75.9	90.7
	Specificity (%)	92.6	61.1	100.0	100.0
	Diagnostic accuracy (%)	90.7	74.1	88.0	95.4
	AUC	0.96	0.82	0.90	1.00
Fluorescence data (lifetime + intensity)	**Variance in data (%)**	89.3	89.8	95.6	97.5
	Sensitivity (%)	92.6	75.9	87.0	98.2
	Specificity (%)	92.6	66.7	100.0	100.0
	Diagnostic accuracy (%)	92.6	71.3	93.5	99.1
	AUC	0.97	0.83	0.96	1.00
Diffuse reflectance + Fluorescence intensity	**Variance in data (%)**	90.8	91.5	92.7	95.3
	Sensitivity (%)	93.3	84.4	88.9	100.0
	Specificity (%)	100.0	68.9	82.2	95.6
	Diagnostic accuracy (%)	96.7	76.7	85.6	97.8
	AUC	0.99	0.84	0.92	1.00
Diffuse reflectance + Fluorescence data (lifetime + intensity)	**Variance in data (%)**	90.7	90.9	92.3	95.1
	Sensitivity (%)	88.9	84.4	91.1	100.0
	Specificity (%)	95.6	71.1	97.8	100.0
	Diagnostic accuracy (%)	92.2	77.8	94.4	100.0
	AUC	0.98	0.84	0.96	1.00

Finally, Table 6.12 shows the autofluorescence parameters in each ROI ranked by Cohen's d coefficient, calculated as described in section 6.7.1.4.5. In regions directly affected by the infarction, i.e. LV anterior scar tissue and at a lesser extent border zone, the best discrimination is provided by autofluorescence decay parameters, primarily associated with detection channels 2 and 3. In remote non-infarcted regions, i.e. RV and LV posterior, intensity-based parameters provide better discrimination than time-resolved data. Interestingly, in LV posterior the most discriminatory parameter is the short lifetime component τ_1 associated with FAD autofluorescence, which we provisionally associated with altered energetics.

Table 6.12 Fluorescence parameters ranked by Cohen's d coefficient. Parameters providing most discrimination between healthy and diseased hearts yield a larger coefficient. In general, lifetime-based parameters provide better discrimination in areas directly affected by the infarction (i.e. LV anterior and border zone) whilst steady-state parameters provide better discrimination in remote regions (i.e. RV and LV posterior).

RV		LV posterior		Border zone		LV anterior	
Parameter	**Cohen's d**	**Parameter**	**Cohen's d**	**Parameter**	**Cohen's d**	**Parameter**	**Cohen's d**
CH1 I/CH2 I	2.80	**CH4 τ_1**	3.21	**CH2 τ_2**	2.15	**CH2 τ_2**	13.47
CH3 R	2.46	**CH2 I/CH3 I**	2.55	**CH1 I/CH2 I**	2.14	**CH3 τ_2**	11.24
CH1 R	2.37	**CH3 R**	2.31	**CH3 τ_2**	2.06	**CH2 τ**	10.94
CH2 I/CH3 I	2.20	**CH2 R**	2.13	**CH2 I/CH3 I**	1.94	**CH4 τ**	9.77
CH2 R	2.03	**CH2 τ_2**	2.04	**CH3 R**	1.93	**CH3 τ**	9.57
CH1 I/CH3 I	1.99	**CH4 β**	1.63	**CH1 τ**	1.91	**CH4 τ_2**	9.15
CH4 β	1.76	**CH3 τ_2**	1.62	**CH4 τ_2**	1.83	**CH2 β**	8.86
CH4 τ_1	1.60	**CH1 I/CH2 I**	1.57	**CH4 τ**	1.80	**CH3 R**	7.68
CH3 τ_1	0.86	**CH1 I/CH3 I**	1.42	**CH2 τ**	1.78	**CH1 τ**	7.43
CH2 τ_2	0.77	**CH3 β**	1.33	**CH2 R**	1.66	**CH2 I/CH3 I**	6.88
CH2 τ_1	0.74	**CH1 R**	1.32	**CH3 τ**	1.65	**CH3 β**	6.08
CH3 τ_2	0.66	**CH2 β**	1.15	**CH1 R**	1.64	**CH1 R**	5.81
CH1 τ	0.57	**CH1 τ**	1.14	**CH2 τ_1**	1.57	**CH2 R**	5.52
CH4 τ_2	0.53	**CH3 τ_1**	1.14	**CH1 I/CH3 I**	1.49	**CH1 I/CH2 I**	5.48
CH2 β	0.48	**CH2 τ**	0.94	**CH3 τ_1**	1.40	**CH1 I/CH3 I**	4.79
CH3 β	0.41	**CH2 τ_1**	0.61	**CH2 β**	1.16	**CH2 τ_1**	4.17
CH3 τ	0.28	**CH3 τ**	0.51	**CH3 β**	0.66	**CH3 τ_1**	3.10
CH4 τ	0.19	**CH4 τ**	0.40	**CH4 β**	0.63	**CH4 β**	2.98
CH2 τ	0.17	**CH4 τ_2**	0.36	**CH4 τ_1**	0.52	**CH4 τ_1**	1.43

6.7.2.5 Discussion

In this section we have described the application of our instrument to an *in vivo* rat MI heart failure model. Due to absorption and scattering of both the excitation light and emitted fluorescence, our instrument is most sensitive to autofluorescence signal emitted near the surface of the heart, which can be a disadvantage in disease processes that vary with depth in the myocardium. However, it is known that myocardial infarction causes global alterations to the heart [371], [372] and thus measurements from the epicardial surface represent a potential approach to probe its metabolic and structural state. In the future, incorporation of the fibre-optics into cardiac catheters could facilitate these measurements also from the endocardial surface during a minimally-invasive procedure.

One of the major challenges in studies of the heart using autofluorescence or diffuse reflectance spectroscopy is related to the movement of the beating heart. The changing pressure between the probe and the heart surface can affect the blood content of the tissue in contact with the tip of the probe and this can influence the optical absorption. We chose a fluorescence measurement protocol with a duration spanning several cardiac cycles - typically 6 heart beats per acquisition - in order to average this effect. In addition, we performed three repeat measurements at each spatial location to achieve an average over multiple applications of the probe tip to the tissue surface.

Changes in the optical absorption caused by the mean pressure of the probe tip will influence the measured fluorescence intensity and diffuse reflectance spectrum most strongly. Ratios of the

fluorescence signal between different spectral detection channels will also be affected due to the change in absorption between channels. While the pressure of the probe may influence the mean depth that is probed, it should not greatly influence the fluorescence decay recorded, given that the acquisition is realised over a relatively narrow spectral band and the fluorescence lifetime readout is inherently ratiometric. Overall, we achieved relatively small standard deviations on the fluorescence lifetime parameters obtained from AMC hearts that indicates that any variation in lifetime caused by variations in probe pressure is small.

The diffuse reflectance spectrum of cardiac tissue is dominated by the absorption spectra of myoglobin and haemoglobin, which are the most abundant chromophores in the heart. Myoglobin and haemoglobin exhibit similar absorption spectra (see Figure 6.7) that are highly dependent on the tissue oxygenation [163], [164]. In the presence of oxygen, the absorption spectrum of haemoglobin presents a double peak profile, with local maxima at ~540 nm and ~576 nm, as shown in Figure 6.7. In contrast, in the absence of oxygen it exhibits a broader spectral profile with a single maximum peak at ~555 nm. Reduced and oxidised myoglobin present similar spectra to haemoglobin with slightly red-shifted absorption peaks. Other chromophores can also contribute to the absorption spectra of heart tissue, of which the most relevant is cytochrome c [162], [163]. As discussed in section 6.3.3, cytochrome c acts as electron carrier in the mitochondrial membrane in the respiratory chain and therefore can provide optical readouts of the metabolic activity. The absorbance spectrum of reduced cytochrome c exhibits a pronounced peak at ~550 nm (see Figure 6.7).

Our diffuse reflectance data are in general agreement with previous studies [3], [163]. We observed a decrease of absorption in MI-HF relative to AMC hearts in all time points studied, which we attribute to reduced blood content and, as consequence, decrease in haemoglobin and myoglobin concentrations in the tissue. Our data also suggests high levels of tissue oxygenation in the scar tissue. The presence of this characteristic haemoglobin/myoglobin double peak profile in infarcted myocardium was previously reported by others [7] two weeks after MI, which they attributed to some recovery of tissue oxygenation. An alternative explanation may be that these peaks arise due to absorption of light by oxygenated blood within the LV cavity, owing to the extensive cellular loss and consequent reduced wall thickness, which, in the 16 week data, was approximately 700 μm (see Figure 6.34).

A similar effect appears to be occurring in AMC hearts at weeks 1, 2 and 4 weeks post-MI, in which the average diffuse reflectance spectra are dominated by oxygenated haemoglobin and myoglobin absorption features (see Figure 6.19, Figure 6.24 and Figure 6.29, respectively). Interestingly, at 16 weeks post-MI, the characteristic double peak profile in the 500 – 600 nm band is only visible in the RV, while in the remaining regions we observed a single peak profile at ~550 nm - consistent with the

presence of reduced cytochrome c - accompanied by a smooth shoulder at ~580 nm that reveals the contribution to the spectra of oxygenated haemoglobin and myoglobin (see Figure 6.35). This difference potentially reflects an increased ventricular wall thickness in 16-week specimens, due to increased animal (and heart) size.

In general, the high level of oxygenation observed in AMC is not visible in MI-HF hearts (with the exception of scar tissue), which is consistent with the previously described [373] thickening of the remote non-infarcted myocardium wall, as consequence of the remodelling process following MI. Our data also suggest a decrease in tissue oxygenation from week 2, with particular emphasis for the LV posterior, where the characteristic absorption features of deoxygenated haemoglobin and myoglobin can be well distinguished. This may be the result of the decrease in tissue oxygenation as consequence of the reduced blood content after MI.

Our instrument recorded the autofluorescence emission into three spectral emission channels. For UV excitation, the relative signal in these three channels is in agreement with the fluorescence emission spectra acquired by others [3]. In their work, Ti et al. measured the autofluorescence spectra - excited at 337 nm - of infarcted and non-infarcted regions at weeks 1 to 4 after the MI induction surgery. They observed a general increase in autofluorescence intensity at week 1. Collagen-induced fluorescence was only visible 2 weeks after MI with a pronounced emission peak at ~400 nm, which was also present at 4 weeks. In our model, we observe an increase in the relative fluorescence in channel 1 from week 1, which suggests collagen proliferation immediately after infarction, particularly in the infarction region (LV anterior), but also at a lesser extent in sites remote to the MI, reflecting interstitial fibrosis. These results are in agreement with previous studies of the model [320], [338], [339], [374]. If we assume that the fluorescence signal in detection channel 1 arises predominantly from collagen, we can use the relative contribution of this channel to the total fluorescence signal as a quantitative measure of collagen content in all regions and at different time points after MI. The results, plotted in Figure 6.40, indicate a sharp increase in collagen content in the region of infarction (LV anterior) between weeks 1 and 2, in agreement with previously published results of Ti et al [3]. Interestingly, we did not observe a significant change in the channel 1 fluorescence signal from 2 weeks after the MI, suggesting that collagen deposition in this region occurs predominantly in the early stages of the disease. In contrast, our results suggest that collagen proliferation in RV occur predominantly at a later stage of disease progression, in agreement with previous observations [320], [333], potentially resulting from increased workload and consequent remodelling of the non-infarcted remote myocardium, as discussed previously in this chapter. With respect to border zone and LV posterior, our data suggests that collagen proliferation occurs immediately after MI, with no relevant variations in the detected signal after the first week. At 16 weeks, the mean relative increase in collagen concentration is 93.0% in RV, 32.7% in LV posterior,

84.5% in border zone and 372% in LV anterior, which is positively correlated ($r = 0.98$, $p < 0.05$) with qualitative observations of the histology data from this time point (see Table 6.10 and Figure 6.34). Overall, these results clearly demonstrate the sensitivity of our instrument to report structural changes in cardiac tissue, both in infarcted and non-infarcted remodelled regions.

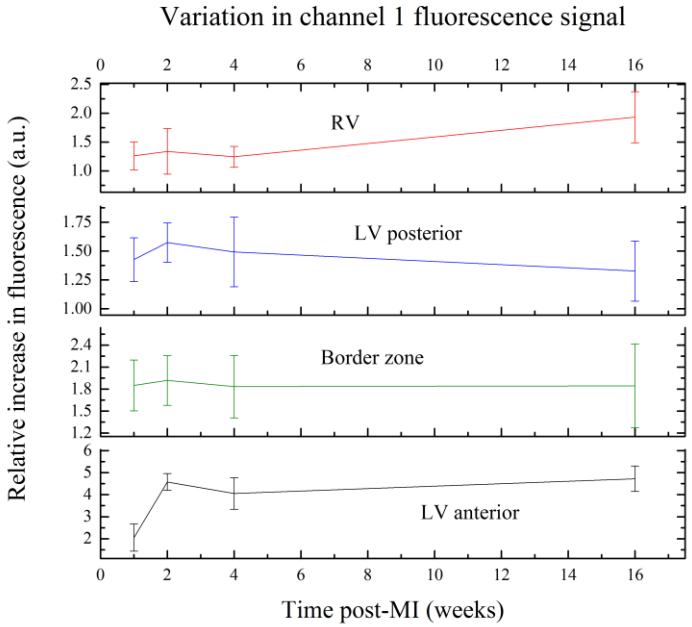

Figure 6.40 Relative collagen autofluorescence in MI-HF to AMC hearts in each ROI and at different time points after MI induction surgery.

We also observed an increase in the mean autofluorescence lifetime in scar tissue in all spectral channels, which becomes more prominent at later stages (see Figure 6.41). We believe this result can be explained by an increase in autofluorescence from collagen type I, given its broad emission spectrum (see Chapter 3) and its previously reported longer fluorescence lifetime. Previous studies of collagen fluorescence lifetime [122], [123] have demonstrated that collagen decay characteristics are highly dependent, not only of the excitation and emission spectra, but also of the source of collagen itself. Furthermore, in Chapter 3, we have also demonstrated that collagen type-I powder, albeit extracted from rat tail, yields a long and complex autofluorescence decay of approximately 6 ns. Using the cuvette-based time-resolved spectrofluorometer described in Chapter 3 with excitation light at 375 nm, we have measured the fluorescence lifetime of a decellularised heart, i.e. a cell-free heart presenting only the ECM scaffold, which consists predominantly of collagen fibrils. Measurements were realised at two emission wavelengths of interest - 455 nm and 525 nm - which correspond to approximately the channel centre wavelength of channels 2 and 3 of the single-point time-resolved spectrofluorometer used for this study. For these emission wavelengths we extracted mean lifetimes of 5.6 and 5.3 ns, respectively. These results are within the range of our collagen type I measurements and what has been previously reported by others [122], [123], [375], and thus confirms that collagen from myocardium ECM yields a longer autofluorescence lifetime compared to free and protein-bound NADH (0.4-0.5 ns and 1.0-3.0 ns respectively [1], [8], [78], [130]) and FAD (3.0 ns to 0.3 ns

respectively [77], [103]). A smaller increase in mean fluorescence lifetime in MI-HF border zone relative to infarct was observed, which is consistent with a smaller rise in collagen content in this region compared to the main infarct scar. This was particularly evident in the 16-week dataset (see Figure 6.41) when the scar was well-defined and the border between scar and healthier myocardium was easy to identify visually, thus facilitating the measurements in this region. Accordingly, the increase in the autofluorescence lifetime in border zone is not as pronounced at 1, 2 and 4 weeks post-MI, when scar was still diffuse, making it challenging to identify the border zone in these specimens. Interestingly, we note an increase in channel 1 autofluorescence lifetime with time also in AMC hearts (see Figure 6.41), which was also apparent in channels 2, 3 and 4 (data not shown). This variation potentially reflects an increased metabolic rate with time, given the increased animal (and heart) size, similar to our observations of diffuse reflectance data.

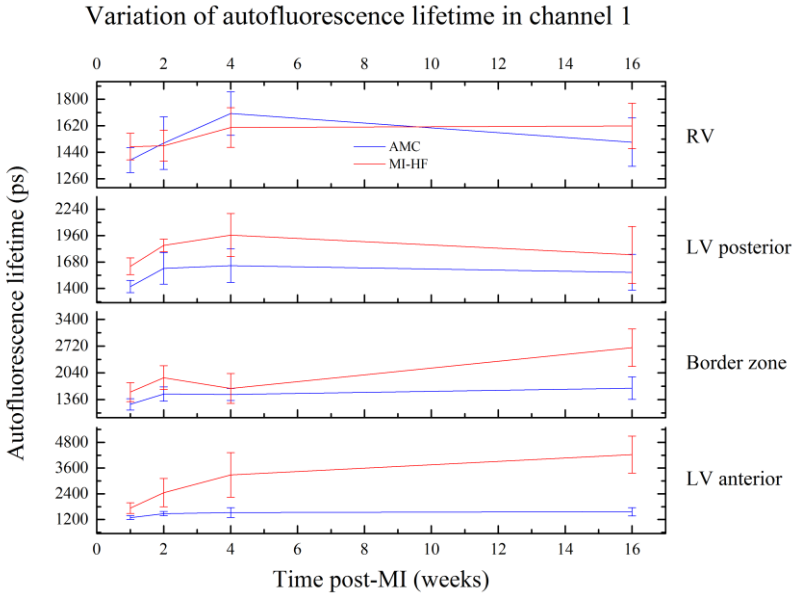

Figure 6.41 Autofluorescence lifetime measured in channel 1 in AMC and MI-HF hearts in each ROI and at different time points after MI induction surgery. A larger increase in the mean autofluorescence lifetime of collagen is observed in the region of infarction relative to non-infarcted regions,, where differences between AMC and MI-HF hearts are subtle.

We aimed to measure changes in the fluorescence lifetimes of NADH and FAD for all regions of the heart due to alterations in tissue metabolism. However, their emission spectra overlap strongly with the broad emission spectrum of collagen type I and thus it is challenging to quantify changes in NADH and FAD lifetime in tissue due to significant changes in collagen concentration and the corresponding changes in fluorescence lifetime, particularly at later stages of disease progression. Based on previous work by us (see section 6.6.2) and others [64], we would expect to measure a decreased fluorescence lifetime from NADH in poorly oxygenated tissue, such as scar. However, the considerable increase in collagen and its longer fluorescence lifetime, along with extensive cellular loss, masks any change in NADH lifetime in the scar region. In regions that are remote from the scar, where the absolute increase in collagen is less pronounced, e.g. LV posterior and RV, it is reasonable

to attribute the changes in fluorescence lifetime to changes in the fluorescence properties of intracellular fluorophores due to changes in energetics that are seen in heart failure. These changes are clearly visible at earlier stages of the disease progression after MI, when collagen deposition is not yet extensive. In particular, at week 1 post-MI we see a statistically significant decrease in the short lifetime component τ_1 of channels 2, 3 and 4 in the LV posterior viable myocardium in MI-HF compared to AMC ($p < 0.01$, $p < 0.05$ and $p < 0.01$, respectively). Similar changes are also visible at 4 and 16 weeks post-MI but are less pronounced (see Figure 6.42), likely due to the greater collagen deposition observed at these stages. These changes are most visible in detection channel 4, which, despite the extensive collagen proliferation (see Table 6.10, Figure 6.34 and Figure 6.42), still reports a statistically significant decrease in the short lifetime component τ_1 at 16 weeks in both RV and LV posterior viable myocardium in MI compared to AMC hearts ($p < 0.05$ and $p < 0.001$, respectively). The fluorescence signal of channels 2 and 3 is dominated by NADH autofluorescence and thus the short lifetime components in these channels are linked to free NADH [8]. In channel 4, the fluorescence signal arises predominantly from FAD autofluorescence and its the short lifetime component has previously been linked to protein-bound FAD [77]. Given the long fluorescence lifetime of collagen compared to NADH and FAD, we do not see how these changes can be attributed to additional collagen in the MI-HF heart. We therefore attribute them to tissue metabolic remodelling, with particular emphasis in the posterior wall of the LV MI-HF heart that causes a change in autofluorescence signal due to the increased work load and altered metabolic state. This concept of alteration in the energetic state in the failing heart is well-established [323], [326], [333].

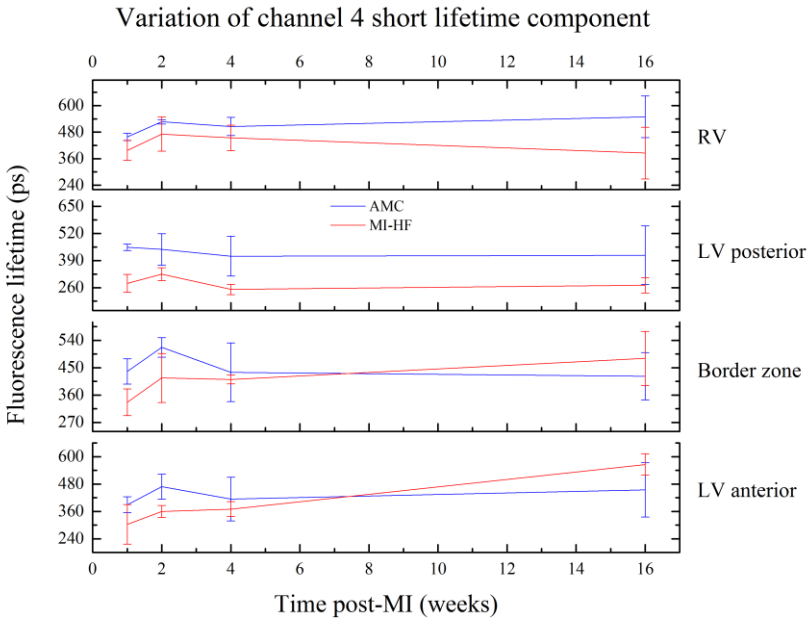

Figure 6.42 Short lifetime component τ_1 of detection channel 4 (associated with FAD autofluorescence) in AMC and MI-HF hearts in each ROI and at different time points after MI induction surgery. A shorter fluorescence lifetime of MI-HF relative to AMC hearts may indicate changes in myocardial metabolism as result of ventricular remodelling following MI.

Changes in the metabolic state of tissue are also known to affect the optical redox ratio of NADH to FAD fluorescence in biological tissues [77], [376], [377]. As discussed above, in our instrument, the redox ratio might, in principle, be estimated from the ratio of the fluorescence intensities measured in channels 2 and 3. However, although we were expecting to observe changes in the redox ratio in MI-HF hearts due to energetic alterations, as discussed above, the autofluorescence signals of channels 2 and 3 are "contaminated" by collagen type I autofluorescence, making it challenging to discern the origin of changes in the measurements, which could be structural or metabolic alterations of the tissue. This emphasizes the importance of any information concerning metabolic alterations in the tissue that can be provided by autofluorescence decay measurements that are not masked by structural changes, e.g. associated with collagen. Our measurements of the short lifetime component, particularly those associated with FAD autofluorescence are not confounded by changes in collagen autofluorescence and appear to indicate changes in the energetic state of the tissue. To summarise, our results suggest that the single-point time-resolved spectrofluorometer can read out both structural and energetic alterations in the tissue. Structural alterations associated with fibrosis can be indicated by both steady-state autofluorescence parameters (i.e. shift in the autofluorescence emission spectra towards shorter wavelengths) and time-resolved parameters (i.e. increase in the mean autofluorescence lifetime in all spectral channels). On the other hand, changes in the short lifetime components of channels 2, 3 and 4, with particular emphasis for the latter, appear to be associated with altered metabolism in the failing heart and can potentially provide information that is only available through time-resolved autofluorescence data.

To investigate the potential of our instrument to differentiate healthy from diseased myocardium we implemented a simple linear discrimination algorithm following data reduction employing PCA. In general, our results demonstrate excellent discrimination capabilities from the earliest stages of disease progression following MI. In particular, the classification results obtained at week 1 using solely autofluorescence parameters (see Table 6.7 and Figure 6.23) indicate that our instrument can clearly identify healthy and diseased myocardium even when alterations in cardiac tissue are subtle, such as those characteristic of early stages of disease. This is true not only for the region of infarction, but also in remote non-infarcted myocardium. In general, the discrimination between healthy and diseased myocardium was still high at 2, 4 and 16 weeks following MI, particularly in the infarcted tissue, where the diagnostic accuracy was always close to 100%. This is expected as in this model the scar yields more evident alterations than the remaining viable myocardium, particularly at 16 weeks post-infarction, when the scar is mature and could easily be identified visually due to its white colouration. Nonetheless, we observe a decrease in the classification performance at weeks 2, 4 and 16 relative to week 1. As discussed above, changes in the measured autofluorescence lifetime caused by collagen proliferation appear to be opposite to those caused by altered energetics, which may explain these results.

The discrimination algorithm was also applied to all combinations of spectroscopy methods employed by our instrument, in order to understand the potential of each of these techniques in cardiac diagnosis. For consistency between methods, the five most significant principal components were used as predictor variables in the discrimination matrix for all methods and for all combinations of methods. The results, presented in Table 6.11, show that all methods can provide excellent discriminant capabilities when applied directly to the infarcted region, which is expected, considering the magnitude of the changes in all parameters caused by proliferation of collagen. However, it is interesting to note that the best discriminant parameters in LV anterior - calculated through the Cohen's d coefficient (see Table 6.12) - are lifetime related parameters, which is consistent with the higher diagnostic accuracy calculated for classifications that include these parameters. In the border zone region, the accuracy of the classification decreased compared to that achieved for classification of scar. Our results show that steady-state methods alone provide a lower accuracy than when combined with time-resolved parameters. Classification results for LV anterior and border zone suggest that lifetime parameters are more sensitive to increase in collagen content - and therefore structural changes in the tissue - for the excitation and detection wavelengths used in this study. In sites remote to the MI, our results show that intensity based parameters provide better discrimination between healthy and diseased myocardium compared to lifetime based parameters. This is particularly evident in RV (see Table 6.12) and explains the classification results in this ROI, which show that fluorescence intensity parameters in combination with diffuse reflectance provide the most accurate tissue state classification. In LV posterior myocardium, it is interesting to observe that the best discrimination parameter is the short lifetime component extracted from the channel 4 autofluorescence decay. As discussed above, we believe that changes in this parameter do not reflect an increase in collagen content, but may explain the energetic impairment in the myocardium in post-MI heart failure. It is also relevant to point out that the best discriminant parameters given by the Cohen's d statistics in this ROI occur in channels 2, 3 and 4 - which include the emission wavelengths of NADH and FAD - and can also be associated to alterations in energetic state. As collagen proliferation is still observed through histology, we believe that the autofluorescence signal collected in this anatomical area is a result of both structural and metabolic changes.

6.8 Conclusions and summary

In this chapter, we presented an exploration of time-resolved spectrofluorometry and diffuse reflectance spectroscopy with a view to developing a new cardiac diagnostic tool.

We have studied the autofluorescence and diffuse reflectance signatures of cardiac tissue both *ex vivo* and *in vivo*. In particular, we characterised alterations in the autofluorescence properties of the myocardium in a Langendorff model of hypoxia and glucose deprivation that served as baseline readouts for *in vivo* investigations. In general, we measured longer autofluorescence lifetimes in

Langendorff compared to *in* vivo measurements, which can potentially reflect a switch in the preferential metabolic pathway from beta-oxidation in *in vivo* measurements to glycolysis in Langendorff measurements. More excitingly, we were able to translate *ex vivo* findings to an *in vivo* myocardial infarction heart failure model in rats, where we observed structural and metabolic alterations at different stages of disease progression, not only in the anatomical area of infarction but, more interestingly, also in remodelled myocardium remote from the scar where we report, for the first time, changes in the autofluorescence signal that we attribute to metabolic alterations within the myocardium. Structural alterations in the heart resultant from collagen proliferation are observed from the earliest stages after MI induction as an increase in the mean fluorescence lifetime in all spectral channels. The large increase in collagen content masks gross changes in the autofluorescence of NADH and FAD caused by altered metabolic state of the failing heart. These changes are observed as a decrease in the short lifetime of the autofluorescence decays associated with NADH and FAD and are more prominent at earlier stages after MI. Overall, our results demonstrate the potential of our instrument to characterise structural and metabolic changes in a failing heart *in vivo* without using exogenous labels.

Using a PCA-based discrimination algorithm we were also able to accurately distinguish healthy from diseased myocardium at all stages of disease progression investigated here, even in sites remote to the infarction where changes in tissue properties are more subtle. Despite the excellent results, we note that this is merely a first approach towards the development of a diagnostic algorithm to distinguish healthy from diseased myocardium, and thus further validation is required, particularly with respect to the number of datasets studied.

In the future, we envisage that this instrument could be applied not only during open-chest procedures, e.g. while the patient is still connected to a heart and lung machine, but also via incorporation of the fibre optic probe into coronary angiography or electrophysiology catheters. Catheter-based autofluorescence measurements have the potential to be relatively low cost compared to currently existing imaging modalities, such as PET or functional MRI, with the additional advantage that they can be performed without the need for contrast agents, e.g. during angioscopy or between catheter-based ablation procedures, to provide feedback to the clinician.

The work presented in throughout this chapter prompted the development of a clinically viable instrument to be used in open chest surgical procedures in humans, of which progress to date is briefly described below.

6.8.1 Towards *in vivo* measurements of the human heart during surgery

The results presented throughout this chapter prompted the development of a clinically viable instrument to realise the first in man study of time-resolved autofluorescence in open-chest procedures at the time of surgery. Our work suggests that our instrument can differentiate healthy from diseased myocardium in rats even when differences between the two regions are subtle. Yet, the question still remains: can we translate our findings to the human case? The goal of this first-in-man study is therefore to assess the viability and practicality of time-resolved autofluorescence measurements in cardiac procedures.

To this end, we have modified a clinical instrument previously used by our group [19], [38] to match the excitation and detection configuration of the time-resolved spectrofluorometer presented in Chapter 4 and used for the studies in this chapter. This new system is mounted on a clinically approved trolley for ease of deployment and transportation within the operating theatre.

In order to realise fluorescence detection in an operating theatre, there a few key issues that need to be addressed. The first refers to the operating theatre lighting that needs to stay on during the procedure which can cause an undesired level of background to our measurement. To suppress the background light, we have developed a stainless steel sheath with a conical shaped end that attaches to the distal end of the fibre-optic probe (see Figure 6.43A). This device includes a glass window (see Figure 6.43B, in blue) surrounded by two PTFE O-rings, positioned between the fibre-optic probe and the heart, so that the fibre optic is never in direct contact with the heart or blood. With this configuration, the distance between the tip of the probe and the heart will be fixed at 3 mm for all measurements.

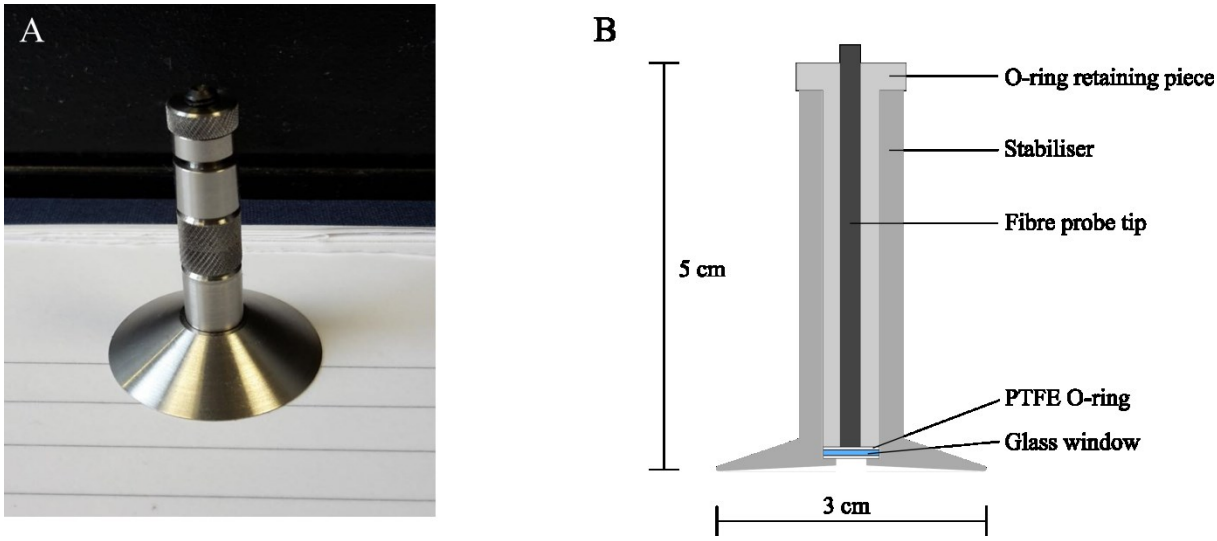

Figure 6.43 (A) Photograph and (B) cross-section diagram of the fibre probe stainless steel sheath. Figure 6.43B not drawn to scale.

The second issue refers to the irradiation with UV light that could potentially raise health and safety questions. Exposure to UV radiation has been shown to produce biological damage in the DNA of human cells [378] and promote the development of tumours in animal models [379]. This is more evident at shorter wavelengths, specifically the UVB and UVC range of the spectrum, i.e. up to 315 nm [86], [380]. Accordingly, we need to establish whether our instrument is safe regarding UV light delivery.

Approximately 98% of the solar UV exposure comes from the UVA range, i.e. from 315 to 400 nm, for which our skin provides a good protection against the potential harmful effects. However, the effects of UV exposure to the organs inside the body remain unclear and therefore this is still a potential source of concern. Because the wavelength used in our measurements is within the UVA range, we compared the dose provided by our system against that received during exposition to sunlight. The average UV power used in our measurements is typically around 1 μW at the sample. At 3 mm from the sample and considering 3 consecutive acquisitions of 1 second duration each, the corresponding average dose delivered to the sample is 78 $\mu J/cm^2$, which is equivalent to the UV dose of less than 10 seconds exposition to indirect sunlight through a north facing window during the morning of a clear sunny summer day in London. We note that a number of operating theatres use natural illumination for which the UV light dose delivered to internal organs in such conditions is greater than that delivered by our measurements. Furthermore, the ability for heart cells to reproduce is low and thus the development of cardiac tumours is extremely rare [381]. Overall, we consider that it is extremely unlikely that the UV light delivered by our system can induce malignancies in the heart. At the moment that this thesis is being written, our research application has been submitted to the Research Ethics Committee of the Royal Brompton Hospital, where measurements will take place. If approved, the first in man time-resolved fluorescence measurements should be realised in the early months of 2015.

7 Development of compact and low-cost detection instrumentation for single point time-resolved autofluorescence measurements

Despite recognised technological advances - see Chapter 4 - autofluorescence lifetime instrumentation can still be bulky and expensive. This limits the widespread application of this technique in clinical settings, where compact and user-friendly devices are required [140]. During the last few years, there has been a growing interest in identifying solutions that could increase the impact of fluorescence lifetime metrology and imaging, including for clinical research. These include the development of low-cost detection electronics for both time-domain [25], [382] and frequency-domain [52], [55] methods, lab-on-a-chip devices [47], compact illumination sources [51], [53] and fast and simple algorithms for lifetime determination [60], [64], [383], [384]. In Chapter 4 we introduced the development of a compact and portable autofluorescence lifetime single-point instrument that we successfully applied to the study of disease in biological tissue, as demonstrated in Chapters 5 and 6. Although the results were encouraging, there is still a lack of low-cost, compact and portable instruments that could be easily translated into clinical practice.

An alternative low-cost approach to fluorescence lifetime imaging and metrology was proposed by Colyer et al [55] in 2008. Essentially, this method utilises digital heterodyning between excitation and sampling frequencies - implemented in a Field Programmable Gate Array (FPGA) - to realise parallel acquisition by means of multiple sampling windows that are continuously sampling the fluorescence intensity decay and this has shown statistical accuracy comparable to the *gold standard* TCSPC technique for a fraction of the cost. In this chapter, a custom version of the Colyer method is presented, including detailed descriptions of the FPGA implementation and the development and characterisation of a low-cost Constant Fraction Discriminator (CFD) to be used with single-photon photomultipliers (PMT). The temporal accuracy of the FPGA and CFD implementations are then assessed using a well-characterised optical setup in our laboratory and compared against a TCSPC-based detection.

Outline

- Introduction of a low-cost time-resolved detection methodology.
- FPGA implementation of the low-cost detection.
- Characterisation of the FPGA implementation.

- Development and characterisation of a low-cost constant fraction discriminator.
- Evaluation of the low-cost fluorescence lifetime detection implementation and comparison against a gold-standard TCSPC-based setup, including preliminary results on the capability of this instrument in providing accurate fluorescence lifetime readings.

7.1 Time-resolved FPGA-based detection

Our detection algorithm is based on the method introduced by Colyer et al [55] in 2008. Although this method is commonly referred to as "digital frequency domain" (DFD), and thus categorised as a frequency domain technique, it effectively relies on temporal binning and single-photon detectors to acquire data. Traditional analogue frequency domain approaches or time-gated fluorescence lifetime techniques sequentially acquire phase-shifted or time-gated samples of the fluorescence signal. In contrast, the Colyer method introduced a detection architecture that relies on parallel acquisition implemented by means of multiple sampling windows that bin the fluorescence photons to realise acquisition with 100% duty cycle. Furthermore, as the detection algorithm can be completely implemented digitally, the modulation of the detected fluorescence occurs in each detection window and therefore the detectors do not require gain modulation. Hence, detectors that operate in the single-photon detection regime, such as PMT or single-photon avalanche diodes (SPAD), can be used.

A key feature of this method is that the excitation and sampling frequencies are not equal. Rather, the sampling frequency f_s must be slightly higher than the excitation frequency f_{exc} which generates a cross-correlation frequency f_{cc}, as defined in equation 7.1.

$$f_{cc} = |f_s - f_{exc}| \tag{7.1}$$

In practice, this means that the sampling window is continuously sliding throughout the excitation period and consequently the fluorescence emission. Hence, the phase shift between f_s and f_{exc} increases with time until they are in phase again. A diagram of this heterodyning process for one cross-correlation period is illustrated in Figure 7.1.

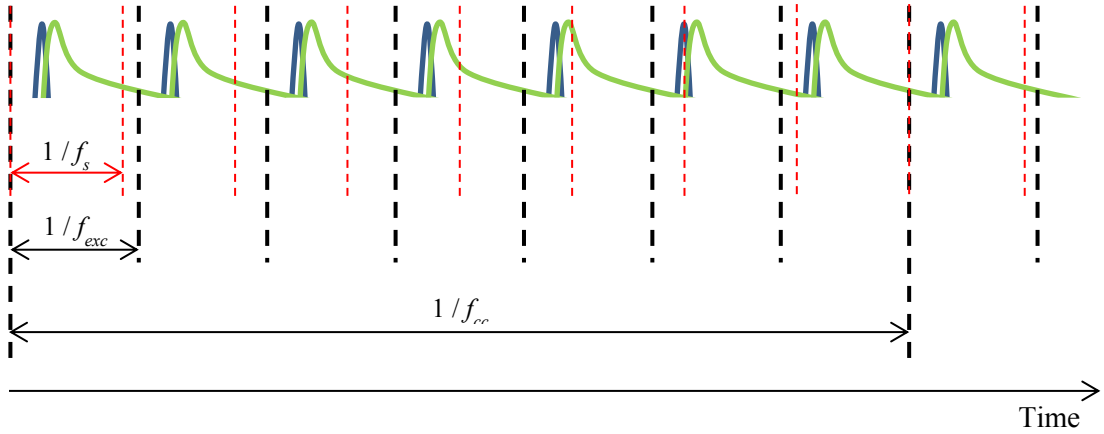

Figure 7.1 Schematics of the heterodyning between excitation and sampling frequencies. Laser excitation pulse is represented in blue and the fluorescence emission in represented in green. A sampling period is defined by the red dashed lines and an excitation period is defined by the black dashed lines.

To implement the parallel acquisition, a sampling period can be evenly divided into multiple detection windows that sample the decay at different phase offsets. An arbitrary number of windows can be used, although previous implementations of this method have only demonstrated 2 or 4-window architectures. The temporal resolution of the fluorescence acquisition improves with shorter sampling windows. Consequently, the more windows that are used, the greater will be the accuracy of the detection. Moreover, the temporal shift by the heterodyning effect allows sampling of the intensity decay in much finer steps compared to the width of the detection windows, further increasing the temporal resolution of the acquisition. The temporal shift Δt of each detection window at each sampling period is given by equation 7.2.

$$\Delta t = \frac{1}{f_{exc}} - \frac{1}{f_s} \tag{7.2}$$

Figure 7.2 illustrates a detection architecture using four detection windows.

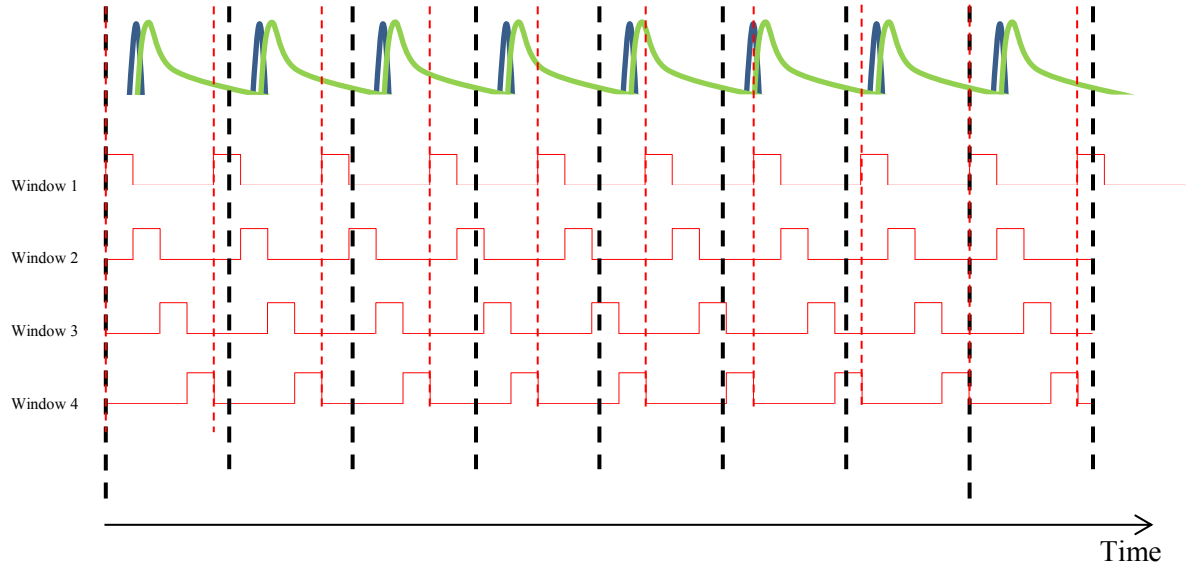

Figure 7.2 Principle of acquisition with multiple (n = 4) sampling windows. The sampling windows (in red) sample the excitation period continuously, with 100% duty cycle, so that no photons are lost during the acquisition window. The each sampling frequency, the phase offset between excitation and sampling frequencies increases, until they are in phase again.

When a photon generated event arrives from the detector, it will be picked up by one of the sampling windows and therefore no photons are lost during the acquisition period. Moreover, since the windows are generated digitally, there is virtually no switching time between sampling windows, leading to low electronic noise and therefore granting high accuracy measurements.

One of the greatest advantages of this acquisition method is that it can be fully implemented in relatively low-cost digital electronics, which can potentially increase its impact for clinical deployment or commercial development. The following section will describe the digital implementation of this approach on an FPGA board and discuss multiple acquisition architectures and their benefits and limitations.

7.2 Hardware implementation

In time domain fluorescence lifetime measurements, the illumination source, typically a laser, is usually operated in the MHz regime - ranging from 5 to 80 MHz - although operation at smaller frequencies is also common, specifically when nitrogen lasers or light emitting diodes (LED) are used for illumination [14], [20], [385]. Our approach aims to generate multiple detection windows within a sampling period. Ideally, as previously discussed, smaller detection windows are preferred as they can provide greater accuracy. However, this approach also relies on the heterodyning between excitation and sampling frequencies to realise the temporal resolution of the fluorescence acquisition. Since the sampling frequency runs slightly faster than the excitation frequency, and is therefore also in the MHz regime, the response time required by this architecture should be on the order of a few nanoseconds.

There are a few technologies that allow the implementation of this method in the nanosecond regime such as FPGAs or Application Specific Integrated Circuits (ASICs). The choice of technology should take in account several factors such as size, speed, power, cost and ease of deployment and use. FPGAs offer some advantages over ASIC particularly in terms of cost (ideal for rapid prototyping and limited production) and ease of development [386].

An FPGA is a highly specialised silicon chip that permits the programming of an arbitrary digital circuit to perform a specific function in hardware. Furthermore, it can be reprogrammed at any time after manufacturing [386], [387]. General FPGA platforms are available as starter or development kits at an affordable cost (~£200) for low speed operation (<500 MHz), and yet they can contain vast amount of programmable logic and features such as internal memory, embedded processors, digital signal processing blocks, multiple clocking structures, digital frequency synthesizers and high-speed I/O. One of the greatest advantages offered by FPGAs is their flexibility: a specific function can be rapidly implemented or reprogrammed. This means that multiple circuit layouts can be designed and rapidly loaded into the FPGA. For example, multiple designs, each featuring a different number of detection windows, can be developed and the FPGA can be rapidly reprogrammed to perform the specific functions required by the uploaded architecture. Hence, for the purposes of this project, an FPGA seems to be an ideal candidate to implement the fluorescence lifetime detection algorithm, as demonstrated by Colyer [55].

An FPGA configuration is specified using Hardware Description Language (HDL). An HDL should accurately model and describe a circuit from either the structural or behavioural point of view [386]. HDL greatly differs from general-purpose computer programming languages, such as C, Python or Java. These languages operate sequentially, i.e. operations are performed in sequential order, one at a time, and often one operation is dependent of the result of previous operations. In a digital system, such as an FPGA, multiple input and output ports are connected by customised wiring. If an input signal is changed, all lines associated with this signal are activated and a set of operations are initiated. These operations are performed in parallel and each operation will take a specific time to complete. Upon completion, the output port of each line is updated. This introduces the concepts of parallel processing, timing and propagation delay – the amount of time a specific line takes to complete a task – which cannot be described by common programming languages [386]. HDL can accurately model the hardware operation by incorporating the propagation delay and timing information and effectively describing the operations and the structural and logic implementation of a circuit. There are two widely used HDLs: Verilog and VHDL (Very high-speed integrated circuit HDL). Both languages offer specific benefits and limitations, but in general, their capabilities are quite similar. In this project, all HDL code was written in VHDL.

The specific FPGA selected for this project was a Spartan 3AN XC3S700AN (Xilinx, USA) available as a ready-to-use Starter Kit. This is a non-volatile FPGA platform evaluation board that includes multiple analogue and digital connectivity options and it is available for approximately £200. Among others, it includes the following key features, which are essential for the purposes of this project:

- **Clocks**
  - 50 MHz on board crystal oscillator
  - Open slot for a user-installed clock (a 133 MHz crystal oscillator was installed by the manufacturer)
  - SMA connector for interface with external clock line
  - Four Digital Clock Managers (DCM) for frequency synthesis
  - Eight global clock lines

- **Connectivity interfaces**
  - Two 9-pin RS232 serial ports
  - Two expansion connectors with both single ended and differential I/O
  - Multiple analogue and digital connectivity options, including ADC/DAC circuitry

Although this board allows great flexibility - e.g. the excitation frequency can either be generated on board or externally - it also imposes some constraints to the design. The most relevant is related to the frequency that can be generated using the on-board frequency synthesisers, which ranges from 5 to 320 MHz and is fundamentally limited by the bandwidth of the components. Although this range is wide enough to accept excitation frequencies traditionally used in fluorescence lifetime measurements (from 5 to 80 MHz), it can limit the number of detection windows used, particularly at higher excitation frequencies. Another disadvantage of this board is that, unlike other evaluation kits now available, it does not include a simple, integrated, ready-to-use and high-speed interface with an external device, e.g. laptop. Although it includes two RS232 connectors, this technology is limited in terms of speed – maximum transfer rate is typically 115.2 kB/s. An ideal solution would be Universal Serial Bus (USB) technology as it allows high-speed data transfer (up to 35 MB/s) and it is very well-established and available in all laptops or desktop personal computers. Because a USB interface for data transfer is not integrated in this FPGA board, an FPGA-USB communication structure was written to allow data output from the acquisition. This architecture is described in detail below in this report.

7.2.1 HDL implementation of the detection architecture

To implement the fluorescence lifetime detection architecture in HDL it is important to select an approach that minimises unstable path delays and structures in the FPGA. Therefore, two criteria should be taken into account, relative to the cross-correlation frequency f_{cc}:

1. The lower the value of f_{cc}, the greater will be the time for the sampling frequency f_s to have a phase shift equivalent to 2π relative to the excitation frequency f_{exc}. Hence, f_s will sample the fluorescence decay in finer steps, increasing the temporal resolution of the method.
2. For convenience and simplicity of the method, the value of f_{cc} should be an integer fraction of f_s, as defined in equation 7.3.

$$k = \frac{f_s}{f_{cc}} \tag{7.3}$$

The number k will define the number of sampling periods that fulfil a single cross-correlation period, thus defining also the number of bins in the fluorescence lifetime histogram as it is described below. From equations 7.1 and 7.3 we can derive the relation between excitation and sampling frequencies, defined in equation 7.4.

$$f_s = \frac{k}{(k-1)} f_{exc} \tag{7.4}$$

To implement multiple detection windows, a fast clock must be generated in HDL. This clock, f_w, is phase-locked and a multiple of f_s, as described by equation 7.5, where n_w defines the number of detection windows to be generated.

$$f_w = n_w f_s \tag{7.5}$$

Combining equations 7.4 and 7.5 we can then write f_w as function of the excitation frequency f_{exc}.

$$f_w = \frac{k n_w}{(k-1)} f_{exc} \tag{7.6}$$

The relation described in equation 7.6 is convenient to implement in hardware as f_s can easily be generated from frequency division of f_w.

The FPGA used for this project features multiple DCMs that provide means for frequency synthesis given a reference frequency. Each DCM can multiply an input frequency by a factor of α, defined as $\alpha = a / b$, where a and b are integers ranging from 1 to 32. One can use the excitation frequency f_{exc} as the reference frequency which is typically a direct output from a laser driver or a photodiode. In HDL, to implement the relation described in equation 7.6, a cascading DCM architecture needs to be used, as illustrated in Figure 7.3. Because having a cascading architecture can lead to increased propagation delays and undesired jitter, which can be of up to 2 ns at higher frequencies [388], the structure was limited to only two DCMs arranged in series. Jitter was minimised according to datasheet specifications, by adjusting the values of a_1, a_2, b_1 and b_2 such that $b_1 > b_2$.

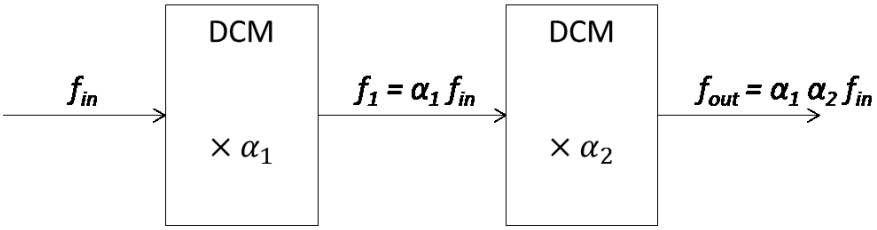

Figure 7.3 Clock architecture to generate multiple windows running at a frequency f_w.

As mentioned above, if f_{exc} is used as the input frequency, to generate f_w at the output, the relation described in equation 7.7 should be met.

$$\alpha_1 \alpha_2 = \frac{k n_w}{(k-1)} \leftrightarrow \frac{a_1}{b_1}\frac{a_2}{b_2} = \frac{k n_w}{(k-1)} \tag{7.7}$$

From this relation, a number of different heterodyning architectures can be implemented in HDL, either by changing the number of detection windows or the cross-correlation frequency. Table 7.1 summarises some possible combinations for an excitation frequency of 20 MHz.

Table 7.1 Possible HDL implementations of the fluorescence lifetime detection algorithm, at 20 MHz excitation frequency.

k	n_w	f_s (MHz)	f_w (MHz)	f_{cc} (MHz)
64	2	20.317	40.635	0.317
64	3	20.317	60.952	0.317
64	4	20.317	81.270	0.317
64	5	20.317	101.587	0.317
64	6	20.317	121.905	0.317
64	8	20.317	162.540	0.317
64	10	20.317	203.175	0.317
256	2	20.078	40.157	0.078

256	4	20.078	80.314	0.078

With respect to the number of detection windows n_w and bins k, this method yields two obvious limitations:

1. The number of detection windows n_w limits the number of bins k in the fluorescence intensity decay histogram.
2. At higher laser repetition rates, the number of windows that can be generated is limited due to frequency constraints. For example, at 80 MHz and 256 bins, a frequency f_w greater than 320 MHz would have to be generated to realise 4-window detection architecture, which is beyond the maximum operating frequency of the FPGA used in this implementation, i.e. 320 MHz.

Although these limitations impact the temporal resolution of the system, the digital heterodyning between excitation and sampling frequencies allows sampling of the fluorescence intensity decay in much finer steps than the width of the detection windows, thus increasing the temporal resolution (see equation 7.2). For example, at 20 MHz excitation, each bin in the fluorescence decay histogram corresponds to approximately 200 ps for $k = 256$, even though the width of each detection window is much larger than that, e.g. 12.45 ns in a 4-window architecture.

When a photon hits the detector, the voltage output is conducted to an FPGA digital input port. The FPGA recognises the event if the signal amplitude is higher than a threshold voltage for approximately 2 ns [389]. The input port can be configured to accept one of multiple logic levels, either single-ended - such as Transistor-Transistor Logic (TTL) or Complementary Metal–Oxide–Semiconductor (CMOS) - or differential - e.g. Positive Emitter-Coupled Logic (PECL). The voltage output waveform from single-photon light detectors varies with device. For example, in photon counting PMTs, the output signal is typically on the order of tens of millivolts (at 50 Ω), although the output current can vary from pulse to pulse due to the random nature of the PMT gain [390]. For time-critical applications, such as fluorescence lifetime measurements, the PMT output is usually routed to a constant fraction discriminator (CFD) that converts the PMT pulse into a logic level, typically TTL. Alternatively, SPAD detectors generally have a TTL output per each detected photon.

The logic to identify the time of arrival of a photon event is initiated once the signal from the detector is read by the FPGA input port. To generate a fluorescence lifetime histogram it is important to keep track not only of the detection window from which a photon is picked up, but also the phase shift between sampling and excitation frequencies. As previously mentioned, f_w evenly divides the sampling period in n_w windows, and thus can be used as input for a counter that identifies each window within a sampling period with a number ranging from 0 to $n_w - 1$. The photon event is picked

up by any of these detection windows and "tagged" with the corresponding counter value. To keep track of the phase shift between f_{exc} and f_s, an additional counter is implemented at the timescale of the sampling period. A schematic of the operation of the two counters in shown in Figure 7.4.

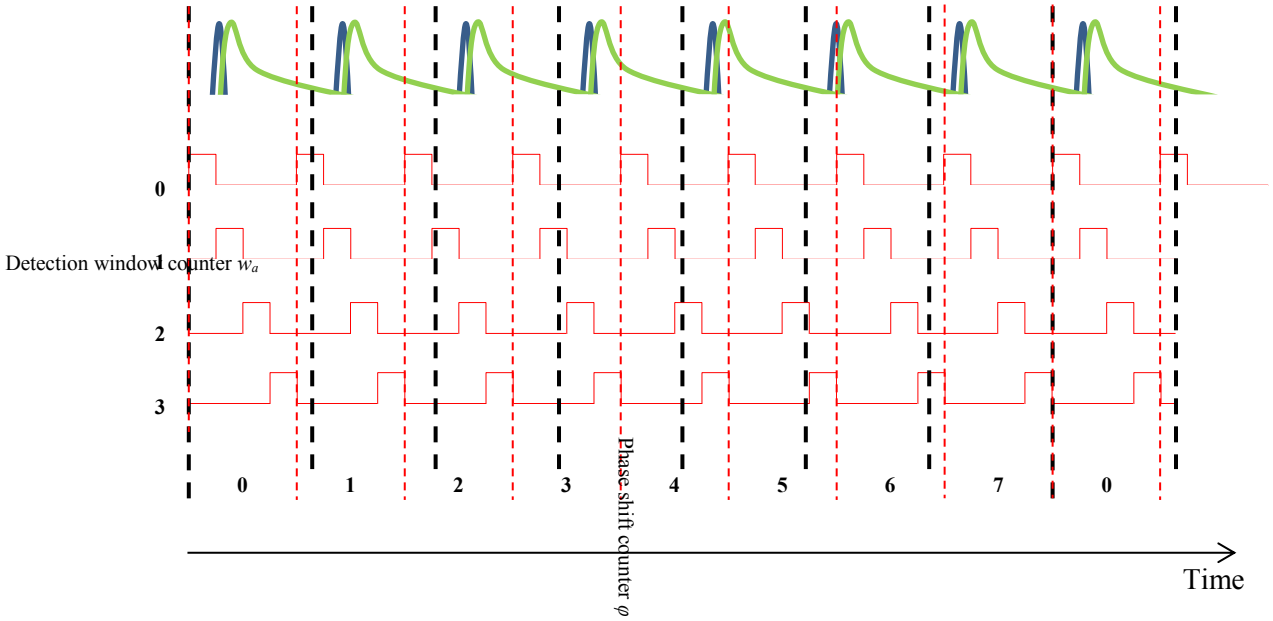

Figure 7.4 Schematic of a 4-window detection method showing the operation of the detection window and phase shift counters.

Each photon signal arriving at the FPGA is "tagged" with a corresponding window of arrival number, w_a, and phase shift counter φ. These values are then used to calculate the bin of arrival I for each photon, as defined by equation 7.8.

$$I(w_a, \varphi) = \left[(k-1) - \varphi + \frac{k \times w_a}{n_w}\right] mod\ k \tag{7.8}$$

The value of I is immediately transferred via USB to a computer for processing. Since I can assume values ranging from 0 to $k - 1$, the number of bits necessary to store a single value of I in HDL is given by equation 7.9.

$$n_{bits} = \log_2 k \tag{7.9}$$

The conditions previously defined for the cross-correlation frequency f_{cc} limit the maximum number of bins to 256, for this FPGA platform, which corresponds to 8 bits or 1 byte. This greatly simplifies the FPGA-USB communication as is discussed below.

When the acquisition is completed, a histogram of photon arrival times can be constructed. To verify our implementation, a Monte Carlo algorithm was developed to mimic the logic steps implemented in the FPGA and generate photon events that follow an exponential distribution, thus outputting fluorescence decay histograms. For simplicity, this algorithm does not take in consideration the dead time of the detection electronics timing constraints imposed by fluorescence lifetime experiments and the IRF is implemented as a delta function. Figure 7.5 shows the result of a Monte Carlo simulation of a single exponential fluorescence lifetime decay (τ = 5 ns), at 20 MHz, using an architecture with 8 detection windows and 64 bins, plotted in log scale.

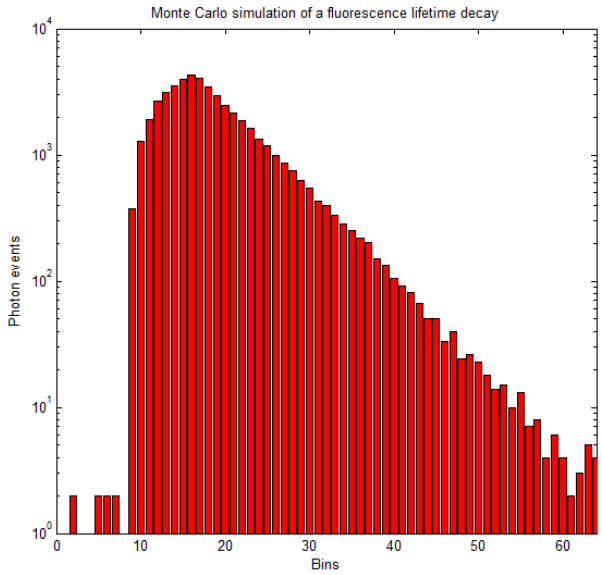

Figure 7.5 Monte Carlo simulation of a fluorescence lifetime decay with 50000 photons (k = 64; n_w = 8; f_{exc} = 20MHz; τ = 5 ns).

Figure 7.6 illustrates all steps to generate the method described above, using an excitation frequency of 20 MHz as input.

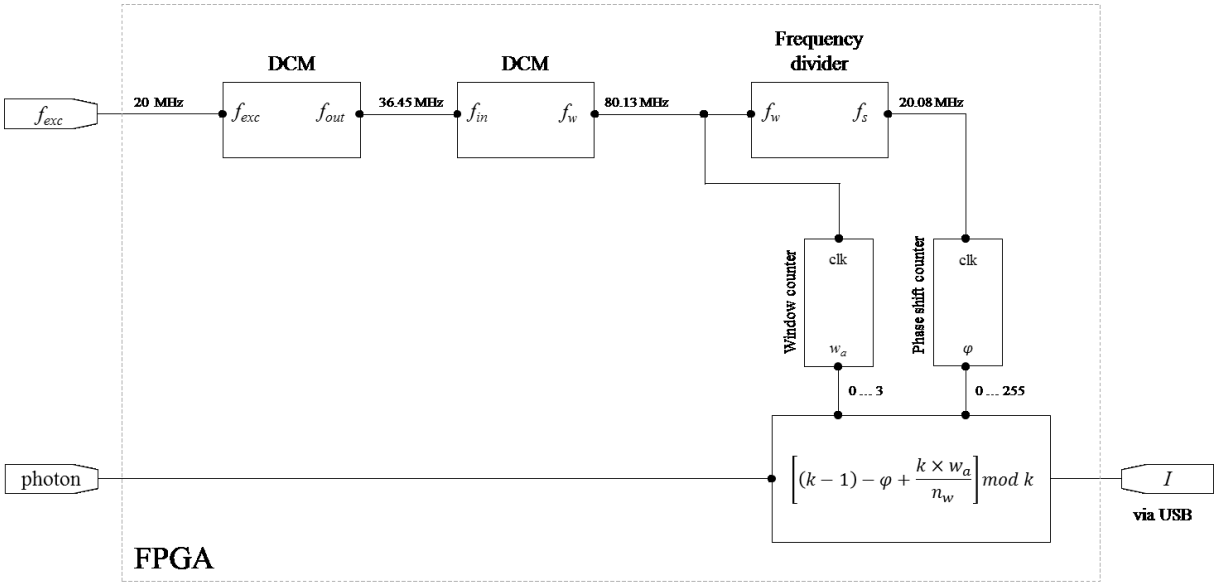

Figure 7.6 Simplified diagram of an HDL implementation of the fluorescence lifetime acquisition method, using 4 detection windows and 256 bins. Counters are incremented on the rising edge of the input frequencies.

Figure 7.7 illustrates a detailed HDL diagram of our implementation including complementary logic signals.

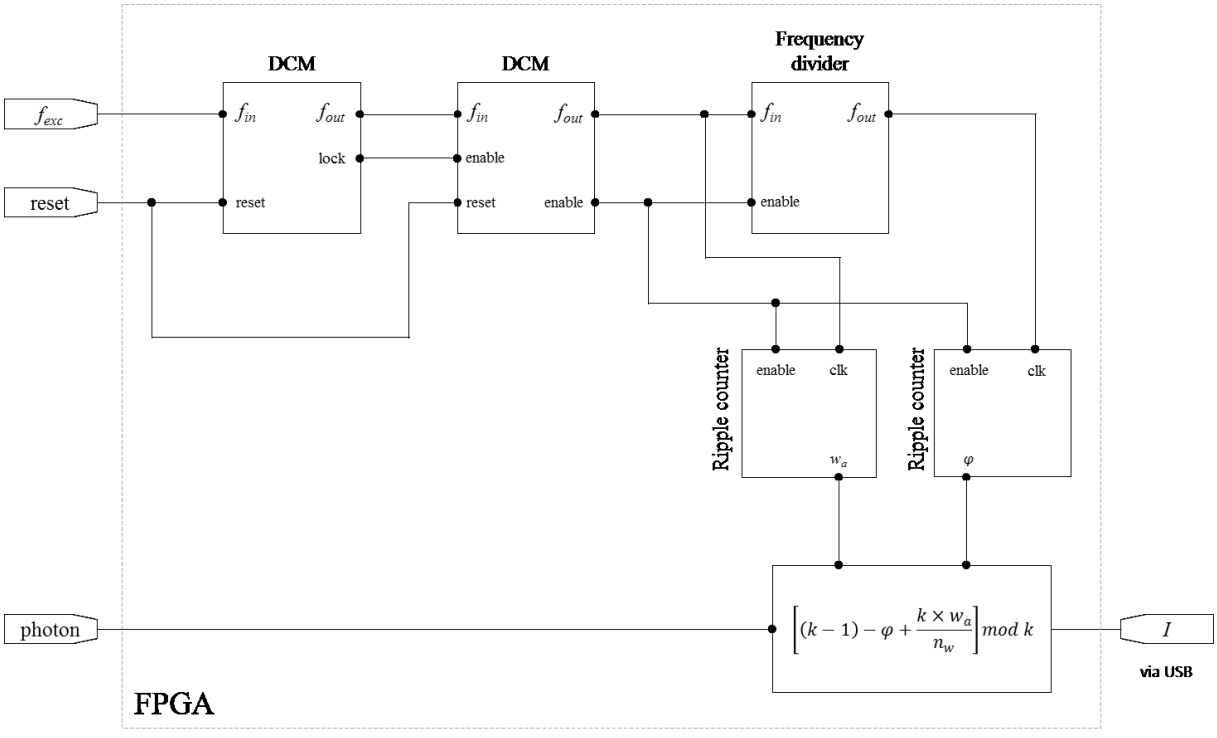

Figure 7.7 Detailed diagram of our HDL implementation.

7.2.2 Data transfer: FPGA-USB architecture

As discussed above, for each photon event, the FPGA outputs an 8-bit number (or lower) that corresponds to an index in the decay histogram. Since the FPGA does not have suitable structure to communicate directly to a computer via USB, an USB controller is necessary as an intermediate step.

USB communications consist of a host with USB support, typically a computer with USB controlling components and multiple ports downstream, and peripheral devices, all arranged in a tiered-star topology. The host controller formats data for transmitting on the bus and translates received data to a format that the operating-system (OS) can understand. Each peripheral device includes hardware and firmware to communicate with the host [391].

In the work described here, the USB architecture was implemented with a single peripheral device, consisting of the FPGA and an external USB controller (FT2232H Mini-Module, FTDI, UK) that includes the necessary hardware to allow communication with the host computer. The FT2232H Mini Module is a low-cost USB 2.0 Hi-Speed compatible module that handles all the USB signalling and protocols. Due to its compactness (35.58 x 29.15 mm) and very low cost (approximately £20), it is ideal for the purposes of this project. This device features two 8-bit channels for bidirectional communication and can operate in First In, First Out (FIFO) mode - incoming data is queued and leaves the queue by the arriving order. Within the FIFO operating mode, communication can be established either synchronously or asynchronously. The synchronous mode can transfer data at higher rates than the asynchronous mode (up to 60 MB/s against 20 MB/s), although it requires additional logic to implement the communication and the timing constraints are more stringent. The maximum count rate of single-photon detectors generally used in fluorescence lifetime measurements is typically of around a few MHz [30], [392], [393]. Furthermore, in photon-counting fluorescence lifetime techniques the count rate should be kept low - typically lower than 1% of the laser repetition rate, as discussed in Chapter 2 - to accommodate for the dead time of the detection electronics [29]. Hence, an asynchronous transfer suffices to transmit all data without losses.

Although the FT2232H chip allows data to be transferred between the FPGA and host in both directions, such a complex architecture was not found to be necessary for the purposes of this application. Therefore, the communication was only implemented in one way, allowing data to be passed from the FPGA to a computer. This architecture requires two logic signals for control and an additional bus with eight lines for data signals to be passed onto the USB controller. The FPGA-USB interface and port directionality is illustrated in the block diagram in Figure 7.8.

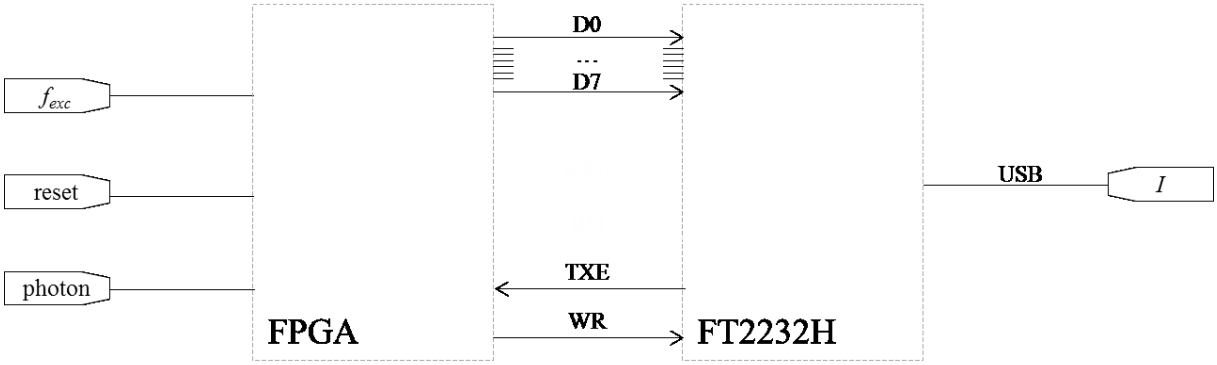

Figure 7.8 Block diagram illustrating the logic signals required to establish communication between the FPGA and the USB controller.

Table 7.2 summarises the operation of the control signals required to establish the communication.

Table 7.2 Logic signals involved in the FPGA - USB communication.

Signal	FPGA I/O	General function	Operation
D0…D7	Input/output	Data signals	
TXE	Input	Control signals for data transmission from the FPGA to the USB controller	When HIGH, data is not written into the FIFO. When LOW, data can be written into the FIFO by setting WR LOW
WR	Output		When goes from HIGH to LOW, data is transmitted via the FIFO buffer

In order to transfer data from the FPGA to the USB controller and vice-versa without losses and/or data corruption, strict USB timing specifications must be met. The following diagram illustrates the timing requirements for the asynchronous FIFO mode to transmit data from the FPGA to the USB controller.

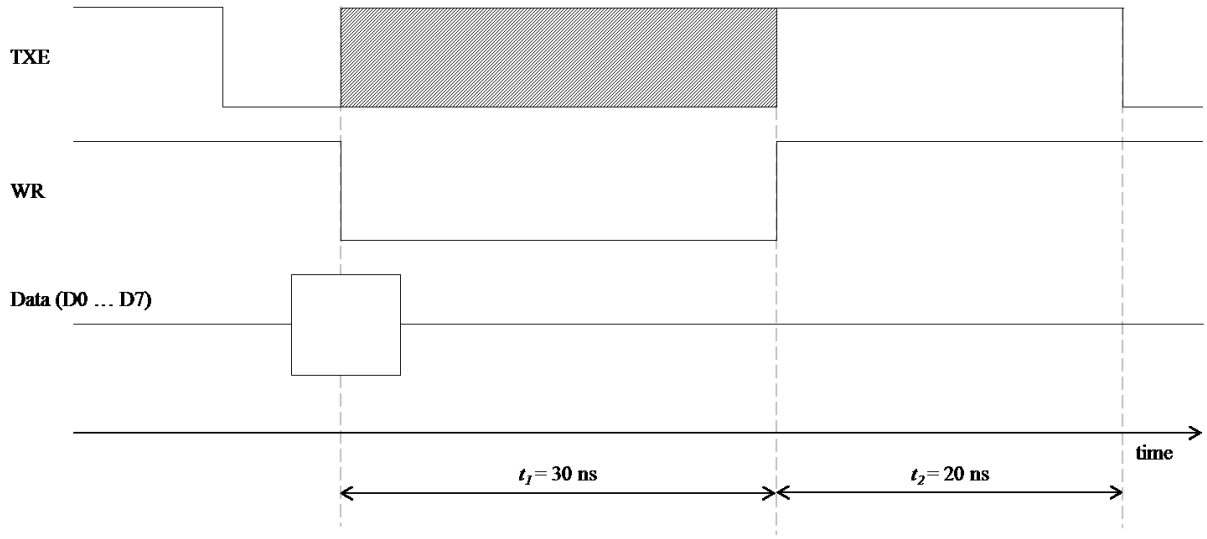

Figure 7.9 Timing diagram to write data to the USB controller after a photon event arrives the FPGA. Striped grey area in TXE line indicates a tri-state mode. Adapted from [394].

Data transmission from the FPGA to the USB controller is initiated after a photon event is detected at the FPGA input port. To meet the timing requirements, a synchronisation clock running at 30 MHz was generated. The FPGA, initially in *idle mode*, probes the TXE line. If this signal is LOW, data can be passed to the FIFO by setting WR line to LOW for at least 30 ns (t_1 in the timing diagram of Figure 7.9) or, equivalently, one synchronisation clock cycle. Once WR goes LOW, TXE enters in a tri-state mode (in grey in Figure 7.9) thus prohibiting transmission of new data to the FIFO. After the data is completely driven onto the FIFO, TXE will stay HIGH for further 20 ns (t_2), before eventually returning to LOW. Hence, data transmission is locked - i.e. new data is not written to the FIFO - from the moment WR is set to LOW and for a period of 50 ns. However, in practice, because the state machine is driven by a clock operating at 30 MHz, data transmission will effectively be locked for two clock cycles, i.e. approximately 66.6 ns, which corresponds to the time between writing the data to the FIFO and returning to *idle mode*, from which data can be transferred again. It should be noted that if two photon events occur simultaneously, i.e. within the dead time of the USB transmission, the second event will be lost if TXE remains HIGH. Figure 7.10 illustrates the state machine implemented in HDL to transmit data from the FPGA to a computer.

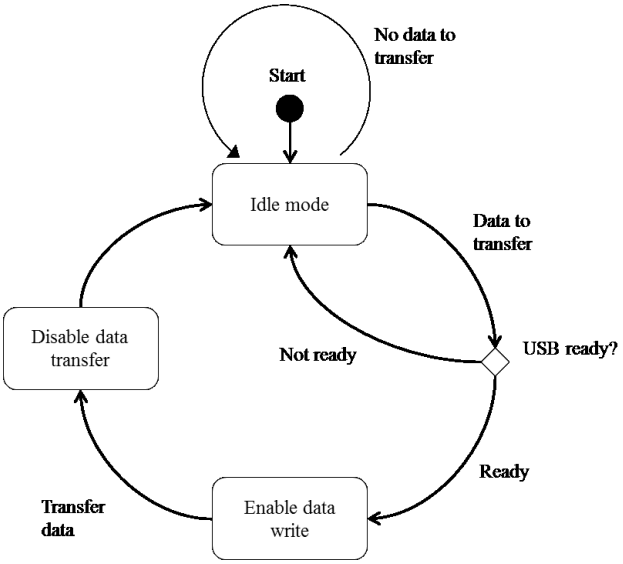

Figure 7.10 State machine implemented in the FPGA to accommodate the asynchronous transfer structure to the USB controller.

Figure 7.11 summarises the processes occurring in the FPGA from the arrival of a photon event until transmission of its time of arrival via USB.

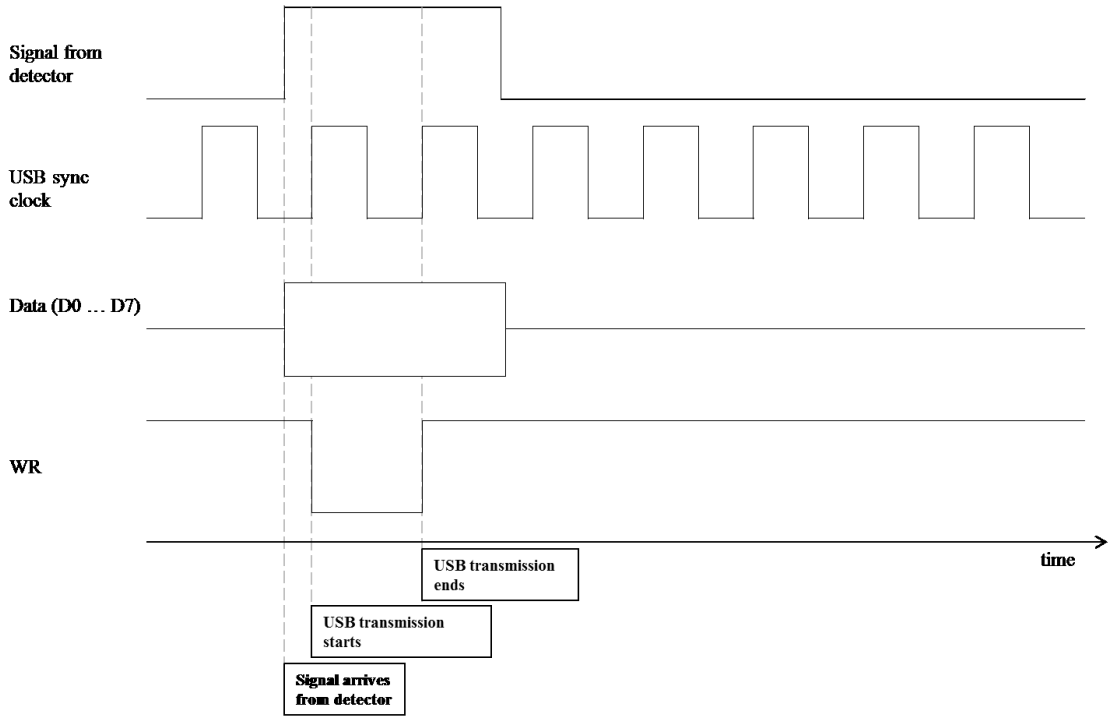

Figure 7.11 Timing diagram of processes occurring in the FPGA upon arrival of a photon signal from the detector.

7.2.3 Data acquisition

One of the key points related to data acquisition is the access to the USB interface from the host side. FTDI - the manufacturer of the FT2232H chip - provides a Dynamic-Link Library (DLL) that includes all the functions necessary to take control over the USB communication. Making use of the

DLL, there are a multitude of tools available for retrieving data from this system. The development of the software application must take into account the key aspects of ease of use and development, stability of the tool and cost. Hence, a custom acquisition program was developed in Python (Python Software Foundation, Python Language Reference, version 2.7), using its the native module Tkinter for the Graphic User Interface (GUI) and matplotlib [395] for plotting and related tools. Python is a high-level, free and open-source programming language that can be used for a wide variety of programming tasks, being particularly flexible to accommodate serial communications.

The application developed in Python features a user-friendly GUI that gives the user full control of the acquisition parameters, such as acquisition time or number of acquisitions. To configure the USB communication, functions provided in the DLL were used. Incoming data from the FPGA is retrieved by implementing a thread that constantly polls the FIFO buffer from the USB controller. Data arrives in packets that can contain a maximum of 65536 bytes and multiple packets can be read each second. Figure 7.12 illustrates the operation of this application.

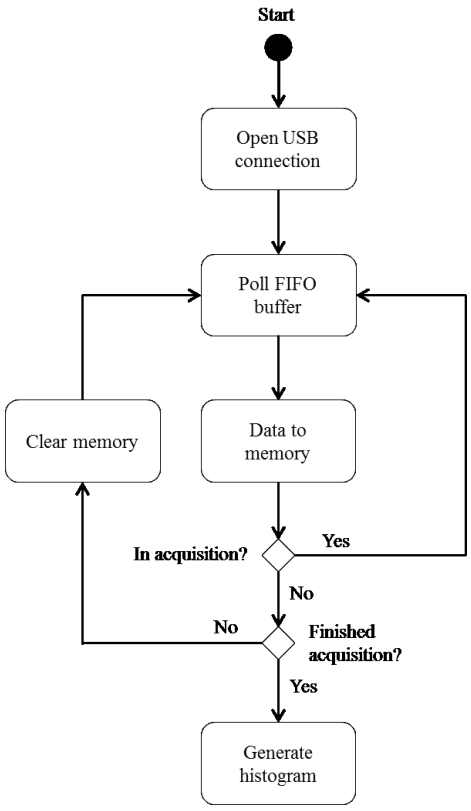

Figure 7.12 Flow diagram of data acquisition in Python.

Because the FIFO is read through a thread running in background, data can be temporarily available even if the user does not start an acquisition. Although, in this case, data is not stored for further

processing, it can be used to e.g. monitor the photon count rate on the fly. A screenshot of the user interface (UI) is shown in Figure 7.13.

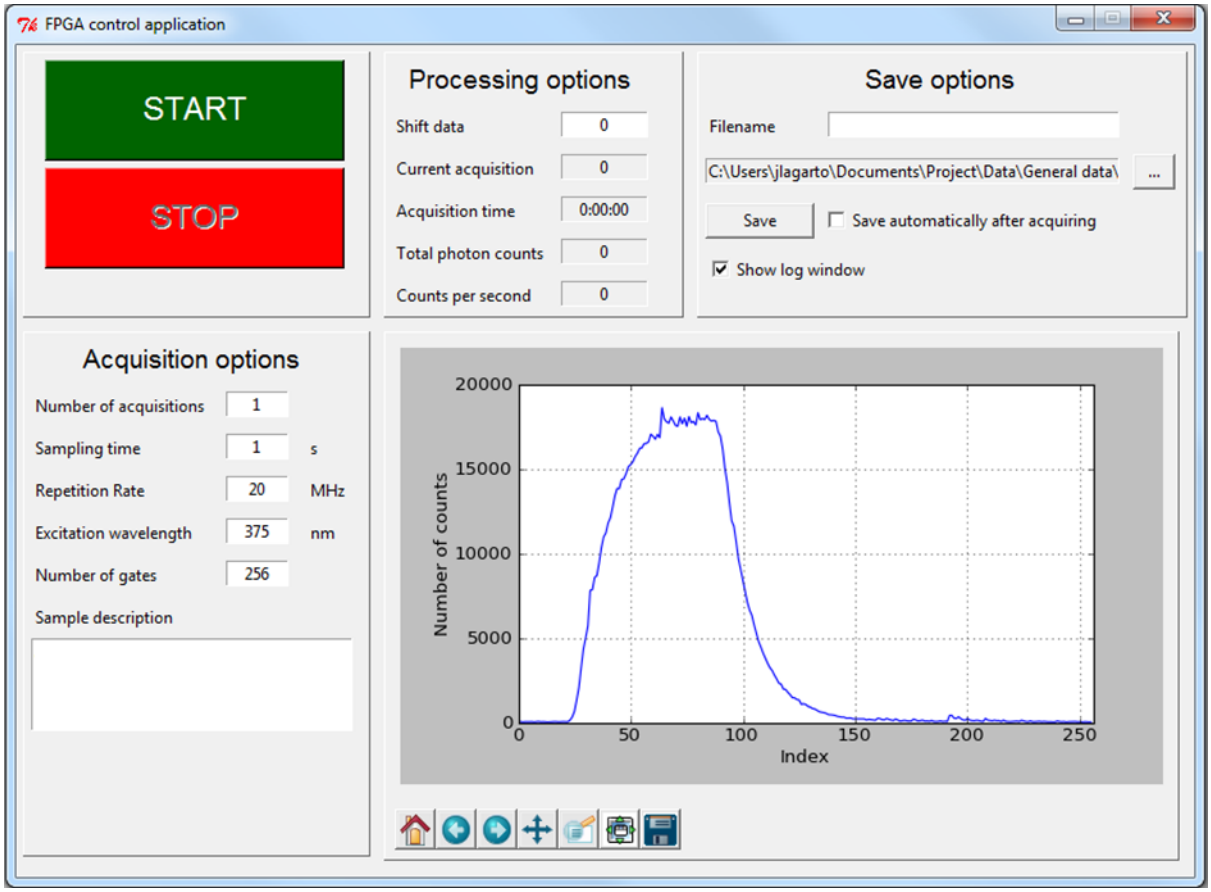

Figure 7.13 Front panel of the acquisition user interface.

A key feature of Python lies on its flexibility that allows the rapid development of small or large scale applications that otherwise could be time consuming. Therefore, although this application is limited to the interface with the detection system, it could easily and rapidly be extended to accommodate other systems within an optical instrument, e.g. the illumination setup, detectors or remote software interlock.

7.3 Characterisation of the detection method

In order to validate our implementation of this detection technique, the system - FPGA and USB controller - was characterised for different parameters. The following sections will present the results of this characterisation.

7.3.1 Linearity

Nonlinearity is one of the most important sources of errors in photon-counting techniques. Nonlinear errors in the acquisition can arise from: 1) synchronous noise in the detectors; 2) impedance mismatching in synchronisation; 3) detection cables or other timing delays and jitter in the detection

windows that cause non-uniformity of the detection gates. The latter is particularly relevant in the case of our implementation. As discussed earlier, the structure that generates the detection windows (as illustrated in Figure 7.3) is complex and a potential source of jitter. Although this can be minimised by following specific design recommendations for this architecture, it cannot be completely eliminated and will always be present in the circuit. Moreover, it becomes more relevant at higher frequencies [388]. In practice, a photon that arrives close to the interface of two sampling windows can be either picked by one or the other, depending on how much jitter the circuit yields.

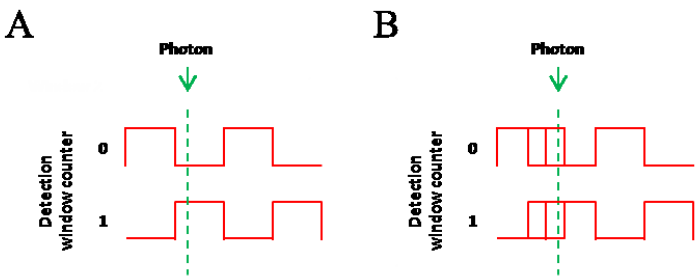

Figure 7.14. Photon event being detected in: (A) ideal conditions (B) sampling windows with jitter.

Figure 7.14A illustrates the detection of a photon event in an ideal system, i.e. with no jitter. In this case, the event will be detected by detection window 1. If the circuit is affected by jitter, as illustrated in Figure 7.14B, any of the sampling windows in the interface can detect the event. In an implementation with, e.g. 4 detection windows and 256 bins, this effect can cause a shift in the measurement equivalent to multiples of 64 bins, which potentially leads to IRF broadening and, by consequence, an increase in the uncertainty of the measurement. Although this is the primary source of errors in the acquisition, other sources can contribute to the uncertainty of the measurement, such as timing delays in the CFD, as discussed below, noise in detectors or jitter in the synchronisation signal.

To further investigate the linearity of the detection, white light from an asynchronous source was directed to the system at different intensities, which, in practice, corresponds to detection at different count rates. The results - plotted in Figure 7.15 - show a linear temporal response of the system to different levels of background light.

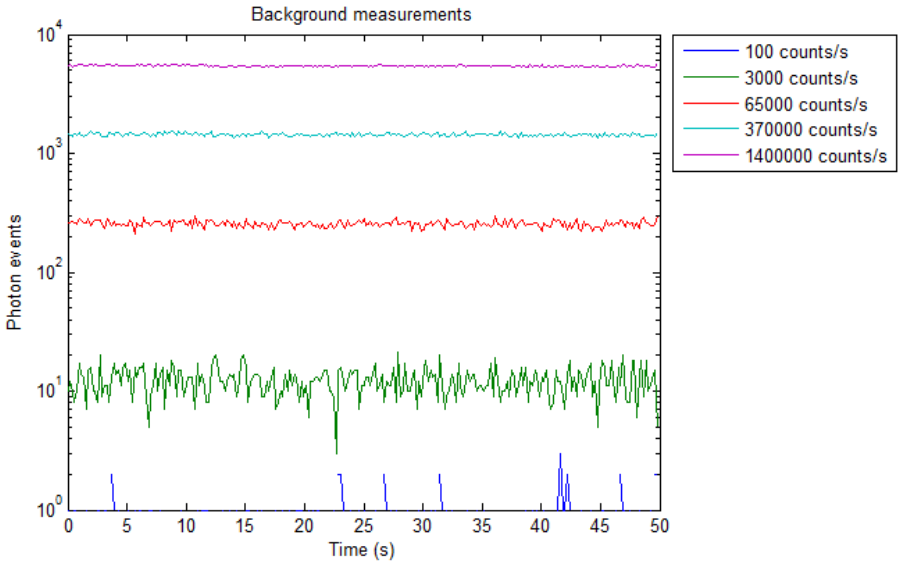

Figure 7.15 Background light measurements at different count rates. Flatness of the curves due to photons arriving in random timings indicate a linear response of the detection method.

7.3.2 Instrument response function

As discussed in Chapter 2, the photon distribution in a fluorescence lifetime measurement is the mathematical convolution of the sample's fluorescence intensity decay with the IRF. In an ideal optical system, the IRF is recorded as an exact replica of the laser excitation pulse and any deviations from this will broaden the IRF. Typically, the IRF broadening is mostly determined by the detector bandwidth or the laser pulse width. However, this is only true if the detection gates are shorter than the detector time response, laser pulse width and the temporal dispersion caused by the optical system, as the case of TCSPC measurements. In time-gated fluorescence lifetime methods, the width of the detection gates is typically greater than 1 ns, which is longer than any other contribution to the IRF. As discussed, our implementation makes use of a fast clock to generate detection gates. Since the maximum operating frequency of the FPGA is 320 MHz (see section 7.2.1), the absolute shortest gate width achievable corresponds to 3.125 ns. This is considerably larger than the temporal broadening caused by the optical setup, detectors and laser pulse shape, in the case of a short excitation pulse, as typically used in fluorescence lifetime experiments. Hence, the IRF of our instrument is primarily determined by the width of the detection gates, which can be calculated from equation 7.5. For example, using a 4-window and 256 bin architecture at 20 MHz excitation rate, the detection window frequency f_w is 80.313 MHz, corresponding to a gate width of 12.45 ns. The theoretical minimum width of an IRF in our instrument is defined as in equation 7.10:

$$IRF_{width} = \frac{1}{f_w} \tag{7.10}$$

Figure 7.16 shows the results of Monte Carlo simulations - parameters are discussed in the end of section 7.2.1 - for a sample with a very fast temporal response, e.g. a scatterer IRF, using different number of detection windows and assuming a δ excitation pulse. A total of 20000 photons were released in each simulation.

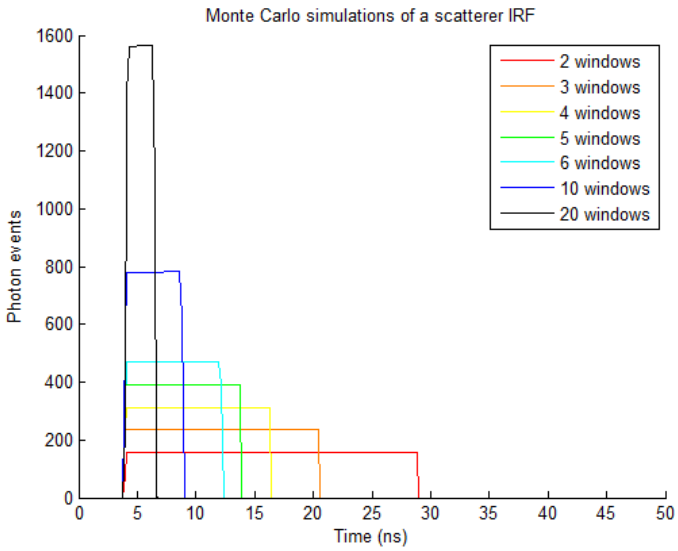

Figure 7.16 Monte Carlo simulation of a scatterer IRF at 20 MHz excitation. The number of bins was fixed at 256.

Figure 7.17 compares the full width at half maximum (FWHM) calculated from equation 7.10, extracted from Monte Carlo simulations (Figure 7.16) and measured experimentally.

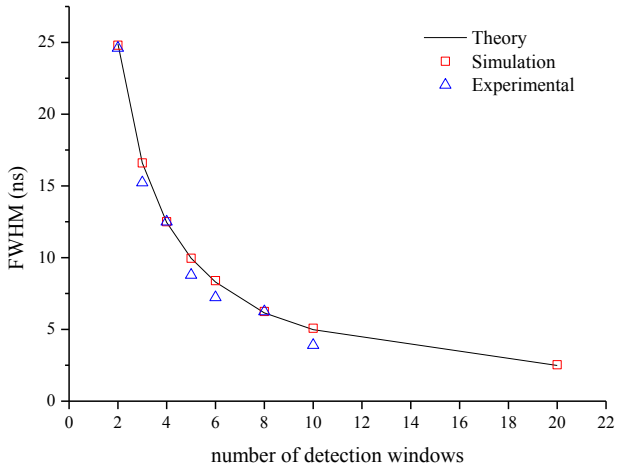

Figure 7.17 Comparison of the IRF FWHM for different number of windows. The number of bins of the histograms was 64 for $n_w = 8$ and 256 otherwise. The IRF was not measured experimentally for $n_w = 20$ as it would require the generation of a frequency greater than 320 MHz, which is beyond the FPGA operating frequency

Although Figure 7.17 demonstrates good agreement between theory (see equation 7.10), Monte Carlo simulations and experimental results ($r > 0.99$ and $p < 0.0001$ for all combinations), we can observe that in architectures that use a number of windows not a multiple of 4, the FWHM in experimental data is consistently lower than in theory or simulations. This is because our HDL implementation forces the calculation of the arrival bin - described in Equation 7.8 - to produce non-integer values. For example, in a 10-window architecture, if a photon has been captured by the 8th window of the 2nd sampling period, the bin of arrival would be 48.2. Although VHDL supports decimal dividers, its implementation is challenging and its operation is time-consuming within the hardware, thus leading to multiple timing errors in the final calculations. Figure 7.18 shows IRF measurements of a scattering sample of Ludox beads (420786-1L, Sigma-Aldrich, Canada) at 20 MHz excitation, using 4 and 10 detection windows.

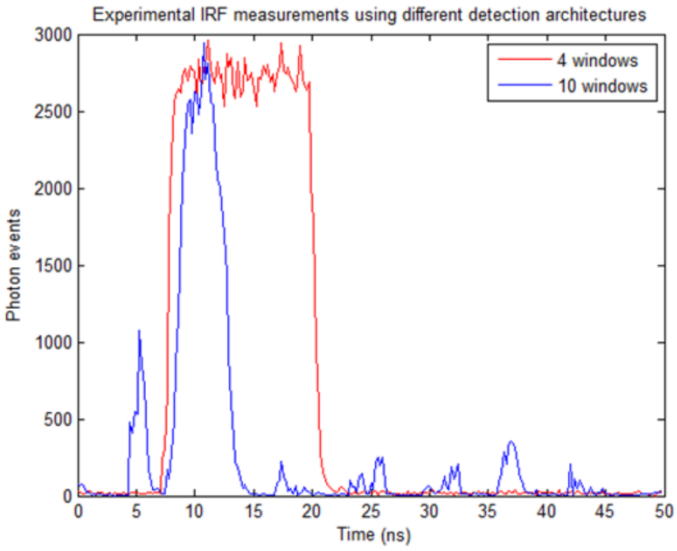

Figure 7.18 Experimental measurements of a scatterer IRF with 4 and 10 detection windows. Due to constraints in HDL, the 10-window architecture produces multiple timing errors

As demonstrated in Figure 7.18, the 10-window architecture features multiple peaks that are the result of timing errors and path delays in the FPGA due to the existence of non-integer arrival bins. In contrast, the 4-window detection architecture shows a well-defined curve with approximately 12.5 ns FWHM. Hence, for simplicity of the HDL implementation, architectures that do not meet the condition expressed in equation 7.11 were discarded.

$$\frac{k}{n_w} mod\ 2 = 0 \tag{7.11}$$

Table 7.3 summarises the configuration of three suitable architectures for fluorescence lifetime measurements.

Table 7.3 Suitable detection architectures for fluorescence lifetime acquisitions.

Architecture	Number of bins, k	Detection windows, n_w
1	64	8
2	256	2
3	256	4

It is important to have in mind that the architecture chosen for the measurements can depend on a number of factors but ultimately it is limited by the operation frequency of the FPGA. For example, at 40 MHz excitation, architecture 1 cannot be implemented as the detection frequency f_w would be greater than the maximum operating frequency of the FPGA, i.e. 320 MHz, hence forcing architectures 1 or 2 to be used. At 80 MHz, only architecture 2 can be used.

7.3.3 Count rate

The data transfer capabilities of our system were assessed using a frequency generator (TG2001, Thurlby Thandar Instruments Ltd, UK) to simulate photon events arriving at different frequencies. To verify the consistency of our method, the simulation was realised for different detection architectures, i.e. different number of bins and gates. It is relevant to point out that although this simulation does not reflect the real case, where photons arrive at random time intervals, it does represent a good approximation, particularly for count rates typically measured in fluorescence lifetime experiments. The results for three different architectures are plotted in Figure 7.19.

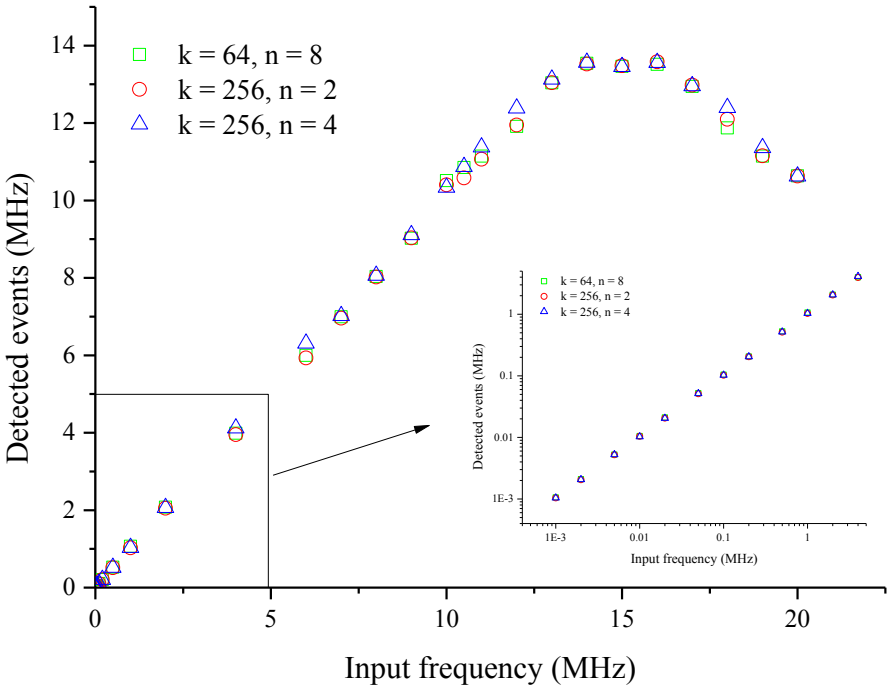

Figure 7.19 Detected events for different detection architectures at different detection frequencies.

Figure 7.19 shows that there is no significant variation in the count rate profile using different architectures, thus indicating that the number of detected events is independent of the number of sampling windows and bins. For lower count rates (≤ 13 MHz), all curves were fitted to a linear model. The fitting results - presented in Table 7.4 - demonstrate a linear response of the detection to the input frequency. Furthermore, the values extracted for the slopes (≈ 1) show that no events were lost during the acquisition process. This is true for a simulation of photon events arriving in known periodic intervals, larger than the dead time of the detection electronics. In the real case, even if the average time between consecutive events is much higher than the dead time, statistically there is a probability of a photon event to arrive within the dead time of the system, and therefore a fraction of the events will be lost.

Table 7.4 Results of the linear fitting for the range of detection frequency below 13 MHz (n = 21).

Architecture	Slope ± SEM	Pearson's r
k = 64, n = 8	1.011 ± 0.006	0.9996
k = 256, n = 2	1.024 ± 0.004	0.9998
k = 256, n = 4	1.006 ± 0.004	0.9998

In the range of input frequencies greater than 13 MHz, the detection reaches a saturation point and an event pile-up effect occurs, leading to a decrease in the detection efficiency. This corresponds to a dead time of approximately 75 ns which is lower than the theoretical dead time of the SPC-830

TCSPC acquisition card from Becker and Hickl [29] and is close to the dead time imposed by the state machine that drives the USB transmission, i.e. 66.6 ns (see section 7.2.2). It is interesting to verify that for input frequencies greater than 16 MHz, the number of detected events decreases. This is most likely due to interference with the state machine that implements the USB transfer and thus causing additional dead time in the detection.

To summarise, although the USB controller can operate at a maximum frequency of 20 MB/s in asynchronous mode, data transmissions greater than 13 MHz were achieved experimentally (see Figure 7.19), which is in close proximity to the expected value of 15 MHz (two 30 MHz cycles) imposed by our implementation (see section 7.2.2). Since fluorescence lifetime measurements have typical count rates on the order of hundreds of kHz, we believe that the limit that our method imposes is sufficient to realise fluorescence lifetime acquisitions in the linear region of the detection and therefore with maximum efficiency, i.e. with negligible loss of photons.

7.4 Development of low-cost constant fraction discriminator

In time-critical photon-counting applications, such as fluorescence lifetime measurements, it is essential to have a standardised output for each single photon event, both in time and amplitude. TCSPC already accommodates suitable electronic circuitry to convert the input signal from the detector into a logic pulse. The FPGA, however, cannot be triggered by a PMT analogue signal and therefore an additional translation step is needed between the detector and the FPGA, if a photon counting PMT is to be used. In fluorescence lifetime experiments or other applications that require precise and consistent measurements of the photon arrival times, the conversion of the PMT signal to a standardised output such as TTL is generally accomplished with fast constant fraction discriminators, which allow timing accuracy on the order of a few picoseconds.

As discussed in Chapter 2, theoretically, a CFD circuit seems relatively straightforward to develop: it can use cheap electronic components and well-established circuitry. However, PMT pulses have sub-nanosecond rise and fall times and operation at such high frequencies is critically dependent on the circuit design. Several factors can influence the behaviour of a high-speed electronic circuit. These include transmission line propagation and crosstalk, impedance mismatching, connector properties, delay, attenuation and ground inductance, among others [396]. The design of a circuit that meets such strict requirements comes at a cost and, typically, high-speed electronic circuitry is still expensive. In the case of CFD, along with circuit layout, some implementations also include an FPGA or microcontroller units (MCU) to provide a direct software interface with the circuit for e.g. adjusting voltage thresholds or pulse width. Altogether, commercially available CFDs are expensive devices - typically around £2000 for a single channel unit - and therefore are not suitable for a low-cost instrument, particularly for multichannel detection that would require multiple CFDs.

In the following section we present the development of an analogue CFD that minimises the timing requirements and the number of electronic components used, hence reducing the cost and the complexity of the implementation.

7.4.1 Methodology

This methodology is conceptually similar to others implemented in commercially available CFDs. Discrimination at a constant fraction of the pulse amplitude is achieved by comparing a PMT pulse with its filtered version. Because the two signals are proportional, variations in pulse amplitude will affect both equally. This principle is illustrated in Figure 7.20.

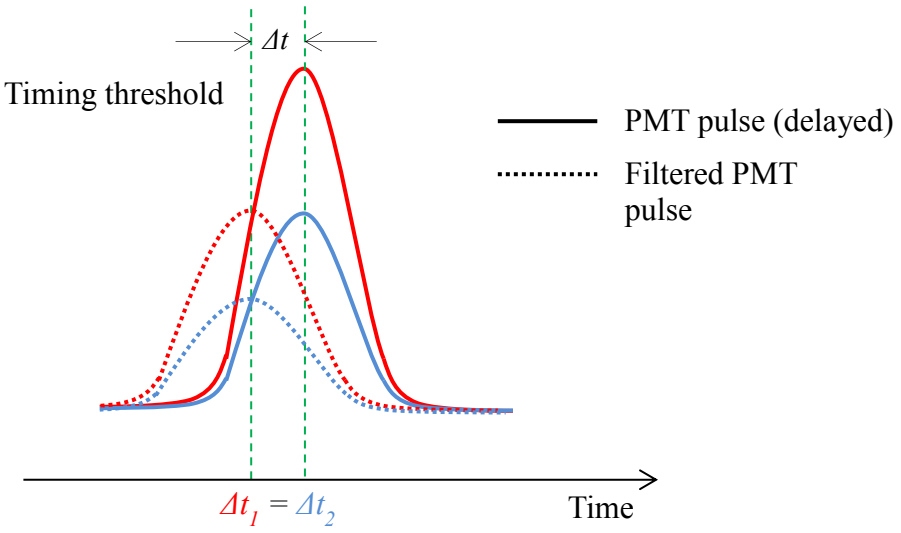

Figure 7.20 Constant fraction discrimination methodology illustrated for two pulses of different amplitude (solid red and solid blue). Dashed lines represent filtered version of the original PMT pulses.

The electronic circuitry to implement this method is similar to what has been discussed for conventional CFD approaches, see Chapter 2. A simplified diagram of the first stage of our implementation is shown in Figure 7.21. Here, the PMT pulse is split in two ways: one way is delayed and fed into the non-inverting input of a comparator (V_+) and the other is low-pass filtered and fed to the inverting input (V_-). The low-pass (LP) filter will attenuate the signal and introduce a phase delay. If the delay of the first line is properly adjusted, the two pulses will arrive at the comparator as illustrated in Figure 7.20. With this configuration, the comparator will effectively "see" a signal that is negative in the beginning and becomes positive following a fast transition. The comparator will trigger when the delayed pulse is greater than the filtered pulse, i.e. when $V_+ > V_-$. To avoid random triggering due to noise, a small voltage offset can be added to the inverting line. In contrast to a conventional CFD implementation, the PMT pulse is not fed onto a leading-edge discriminator for comparison against a voltage threshold. In our circuit, such discrimination is directly implemented by adjusting the voltage offset of the low-pass filtered signal. This approach reduces the number of

electronic components used and, more importantly, the complexity of the circuit, as there is no need to match the delay of the comparator that produces triggering at a constant fraction of the amplitude with a leading-edge output line.

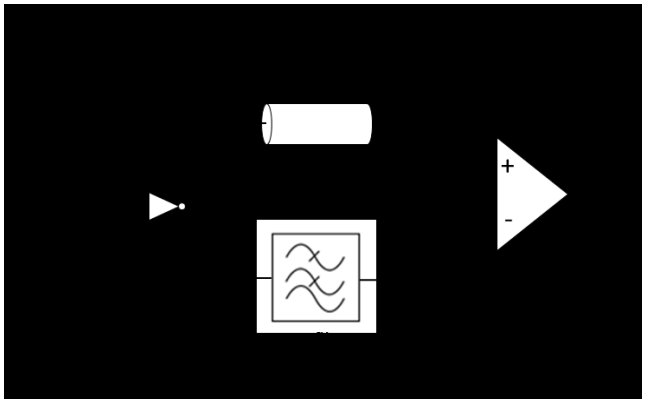

Figure 7.21 Simplified diagram of the input stage of our homemade CFD.

It is relevant to point out that this implementation requires the input pulse shape to be approximately constant from pulse to pulse, particularly with respect to rise time and FWHM, and also requires optimisation of critical parameters such as DC voltage offset at the inverting input, time delay and attenuation. Furthermore, it does not eliminate the amplitude dependency of the discrimination completely. Rather, this implementation brings the timing jitter to values that are negligible compared to the bin width of our detection architecture. A similar approach is implemented in a commercially available CFD from Sensl and the specified maximum timing jitter due to pulse amplitude variation for that device is 50 ps [397].

In theory, the best timing results are achieved when the two pulses arrive at the comparator as illustrated in Figure 7.20, i.e. if triggering occurs at the maximum amplitude of the LP filtered signal, as triggering is less likely to be affected by noise. However, it is challenging to achieve such timing precision and it would require the implementation of programmable delay lines that can offer timing adjustment on the order of a few picoseconds but, at the same time, would increase the complexity and cost of our implementation. We therefore adjusted the time delay by physically increasing or decreasing the length of the lines, aiming for triggering close to the maximum voltage at the inverting input.

The comparator used in our implementation, an ADCMP606 (Analog Devices, USA), requires a pulse width of at least 1 ns to trigger, therefore the delayed signal needs to be greater than the attenuated one for at least that period of time. Upon triggering, the comparator outputs a differential current-mode logic (CML) pulse of width equivalent to the time that the delayed pulse is greater than the attenuated pulse, which is approximately 1 ns. In terms of FPGA triggering circuitry, there are two

problems with this circuit: 1) the FPGA input ports do not support CML logic; 2) 1 ns pulse width is not sufficient to trigger a signal in the FPGA. To address the first issue, a voltage level translator was added to the circuit, to convert the signal from CML to low-voltage positive emitter-coupled logic (LVPECL). Pulse stretching was achieved using a D-type flip-flop with "feedback" to its reset line. In D-type flip-flops, the value at the input D is passed to the output Q upon triggering with a clock, see Figure 7.22A. Hence, the positive LVPECL was fed to both the clock and reset input ports of the flip-flop and the D-input was constantly fed with a DC voltage of 3.3 V. Upon arrival of this signal to the clock input, the output is set to a high state and will stay there until the diverted signal arrives at the reset input, thus bringing the Q output to a low state. By adjusting the delay between clock triggering and reset, one can control the output pulse width. The timing diagram for this pulse stretching method is presented in Figure 7.22B. Finally, for convenience, the differential output of the flip-flop is converted to a single-ended logic level, in this case low-voltage TTL (LVTTL). A simplified schematic of the CFD circuitry is illustrated in Figure 7.22C.

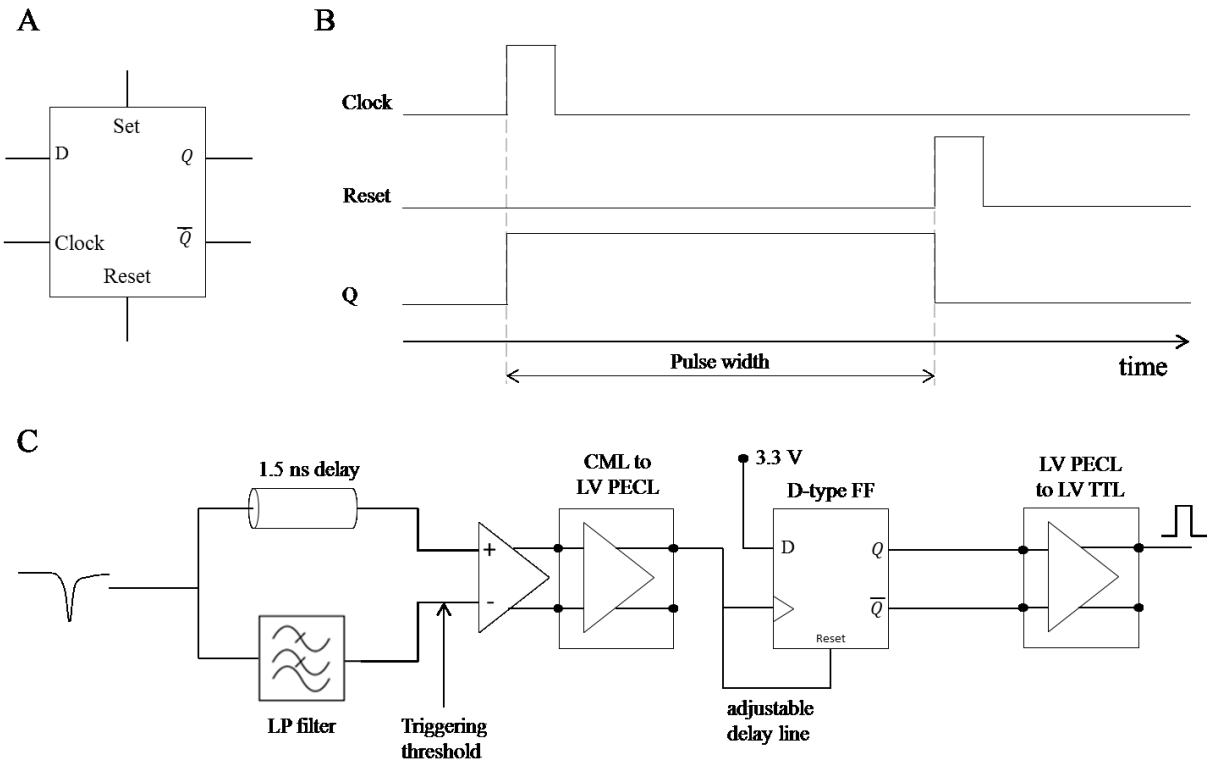

Figure 7.22 A) Schematic of a D-type flip-flop (***D***, flip-flop input; ***Q***, positive differential output; $\overline{Q}$, negative differential output); B) Timing diagram for pulse stretching; C) Simplified diagram of the CFD.

7.4.2 CFD characterisation

7.4.2.1 Time walk

The time walk of a CFD is defined as the timing jitter that results from fluctuation in the input pulse amplitude. Although in theory triggering occurs at a constant fraction of the maximum amplitude for each pulse, in practice, this requires the pulse shape to be fairly similar from pulse to pulse. In

particular, pulses with different rise times and FWHM will have different bandwidth and therefore will suffer different attenuation from the LP filter, leading to an uncertainty in the triggering time $t_{trigger}$, which can be defined as the time difference between the maximum amplitude of the delayed signal and the first time point where the delayed and attenuated signals have identical voltages. The bandwidth BW (or cutoff frequency) of an LP filter is given by equation 7.12 [396], where R and C refer to the values of the resistor and capacitor in the circuit, respectively.

$$BW = \frac{1}{2\pi RC} \tag{7.12}$$

The voltage across the capacitor when a step impulse - as approximation to the PMT signal - is applied at the input of an RC circuit is described by equation 7.13.

$$V(t) = V_0(1 - e^{-t/RC}) \tag{7.13}$$

Combining equations 7.12 and 7.13, one can calculate the relation between bandwidth and rise time of the pulse t_{rise}, which is defined as the time a signal takes to go from 10 to 90% of its maximum amplitude, the time-bandwidth relation is given by equation 7.14.

$$BW \cong \frac{0.35}{t_{rise}} \tag{7.14}$$

The parameters of the LP filter are therefore of great relevance as they define the pulse attenuation. Fast photon-counting PMTs used in fluorescence lifetime measurements have rise times typically between 0.5 ns for MCP-PMTs and 1 ns for standard PMTs [29]. This is equivalent to minimum and maximum bandwidths of approximately 350 and 700 MHz, respectively, according to equation 7.14. To achieve proper signal attenuation in this range of frequencies, we tested two LP filters with cutoff frequencies of approximately 530 and 723 MHz. For purposes of comparison between the two LP filter configurations, voltage signals at each input of the comparator were measured with an oscilloscope (TDS3032B, Tektronix, USA) sampling at 25 GHz. The time-walk uncertainty was assessed by measuring the average triggering time for both LP configurations (see Table 7.5).

Table 7.5 Triggering time measurements at using LP filter configurations. Oscilloscope triggering was set to 50 mV.

f_{cutoff} (MHz)	No. pulses	$t_{trigger} \pm \sigma$ (ns)	$\sigma/t_{trigger}$ (%)
530	254	0.87 ± 0.05	5.18
723	101	0.52 ± 0.02	4.17

Results show that both LP filter configurations introduce a small uncertainty of approximately 5% in the triggering time measurement. At the lowest cutoff frequency the uncertainty increases because there is a greater attenuation of the LP filtered signal, which brings its maximum voltage level to values close to the noise level. Hence, to minimise the time walk uncertainty, in our CFD implementation we used the LP filter with cutoff frequency of 723 MHz. The variation of voltage attenuation with signal frequency for this LP filter is shown in Figure 7.23.

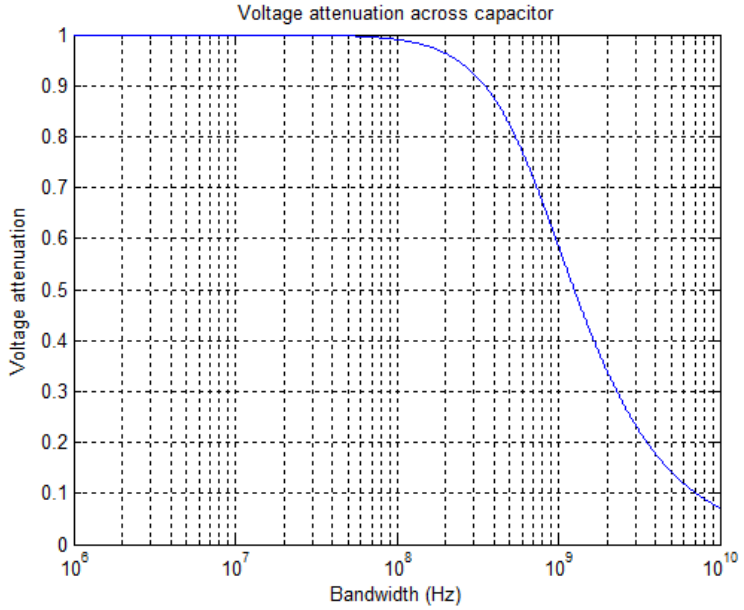

Figure 7.23 Simulated voltage attenuation across the capacitor in the RC circuit that implements the LP filter.

From Figure 7.23 we observe that voltage attenuation depends on the pulse bandwidth, which is a function of the rise time, as demonstrated in equation 7.14. To calculate the time walk uncertainty, we measured the rise time variation in one detector - the PMC-100-1 (Becker and Hickl, Germany) - of pulses with heights of 0.202 ± 0.133 mV (n = 14, mean ± SD). For this range of pulse heights we measured a rise time of 0.64 ± 0.07 ns which is equivalent to a range of frequencies within 500 to 600 MHz and voltage attenuation between 0.77 and 0.82, according to the plot in Figure 7.23. This represents approximately 5% variation in the amplitude of the attenuated pulse, which can explain the uncertainty in the experimental results presented in Table 7.5.

7.4.2.2 Voltage offset

True triggering at a constant fraction of the pulse height is achieved when the DC component at each comparator input is zero. In practice, this will obviously cause the comparator to trigger not only to light pulses but also to noise or other undesirable artefacts, such as reflections in the circuit. Therefore, a slightly positive voltage offset needs to be applied at the inverting input so that the voltage here is always higher than in the non-inverting input except when a true light signal arrives. A

voltage offset slightly above noise yields the best results. For higher voltage offsets, the device will increasingly operate as a leading-edge discriminator and the triggering time will mostly depend on the pulse amplitude. Ultimately, for very high voltage offsets, the threshold may not be reached by the signal and comparator will not trigger.

To investigate the influence of the voltage offset in our instrument, we measured the system IRF using Ludox beads, at different voltage offsets. Results for photon counts, FWHM and rise time are presented in Figure 7.24.

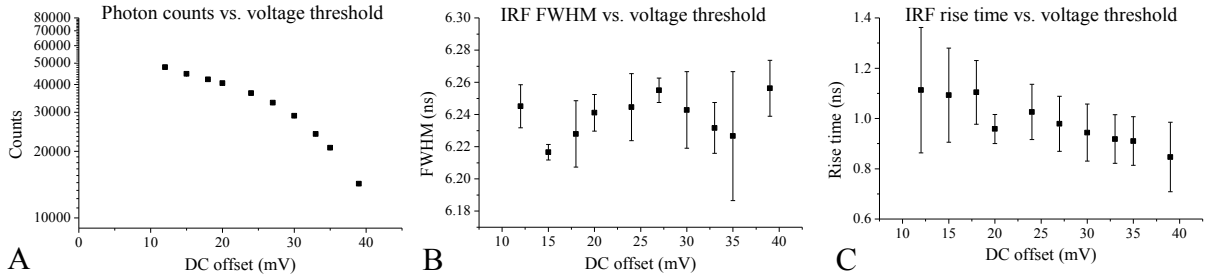

Figure 7.24 System dependence on the discriminator threshold voltage: (A) photon counts; (B) IRF FWHM; (C) IRF rise time. Measurements were realised using 375 nm excitation light at 40 MHz, with 4 detection windows and 256 bins.

For voltage thresholds below 10 mV, triggering due to noise becomes predominant and the shape of the IRF is lost. Thus, results for DC offset within this range are not shown. At higher voltage thresholds, the IRF assumes the shape of the detection gate of width equivalent to approximately one fourth of the sampling window, i.e. 6.25 ns, remaining approximately constant with increasing DC offset (see Figure 7.24B). As expected, we observe a decrease in photon counts with increasing DC offset, as less pulses will reach the minimum voltage that triggers the comparator, see Figure 7.24A.

With respect to rise time, we measured values of approximately 1 ns (Figure 7.24C), which is in accordance to what is expected from jitter introduced in the FPGA detection. As discussed previously, the architecture that generates the detection windows in the FPGA is a potential source of jitter in the circuit, which can go up to 2 ns, depending on the architecture and input frequency. Higher frequencies generate more jitter in the detection windows. Hence, the rise time of the IRF is greatly dependent on how much jitter is generated in the circuit and a rise time of approximately 1 ns falls within the expected range. It is also interesting to observe that the rise time decreases with increasing DC offset, see Figure 7.24C. A possible explanation may be related to pre-pulsing effects in the PMT. Pre-pulsing occurs when photons pass the photocathode without any interactions and thus are not converted in photoelectrons. For these photons, the conversion occurs when they first hit a dynode in the PMT. Although this phenomenon occurs for a minor fraction of the incident photons, it can generate a low amplitude pulse that appears before the *real* light pulse, as a result of fewer

interactions with the dynodes [398]. In our detection method, due to the width of the detection windows, pre-pulses and *real* light pulses are undistinguishable and this effect can translate in a longer rise time.

Overall, the voltage threshold applied to our CFD must balance all effects discussed above. Traditionally, the optimum voltage threshold corresponds to the point where pre-pulsing and background noise are minimised and photons from the *real* light pulse become dominant [29]. This occurs at the first inflexion point in the curve of photon counts against voltage threshold, which in our case corresponds to approximately 18 mV (see Figure 7.24A), calculated through the second order derivative (data not shown).

7.4.2.3 Jitter

Jitter is a time variant noise component that affects the phase of a signal and can be classified as either deterministic or random. Deterministic jitter refers to predictable or periodic deviations from the signal, whilst random jitter refers mainly to thermal noise, flicker noise or shot noise [399]. In the case of a non-periodic signal, as that of a PMT output pulse, only the random component is present. For convenience, random jitter will be designated as jitter hereafter.

Jitter is traditionally measured with a high bandwidth oscilloscope by setting the trigger to the zero cross level of the signal rising edge, or alternatively, to half of the maximum amplitude at the rising edge. An oscilloscope operating in *histogram mode* can trace a line profile at this level. The result will be a Gaussian distribution of the signal and jitter can be determined as the standard deviation of this profile. Figure 7.25 illustrates this measurement in a digital oscilloscope (TDS3032B, Tektronix, USA).

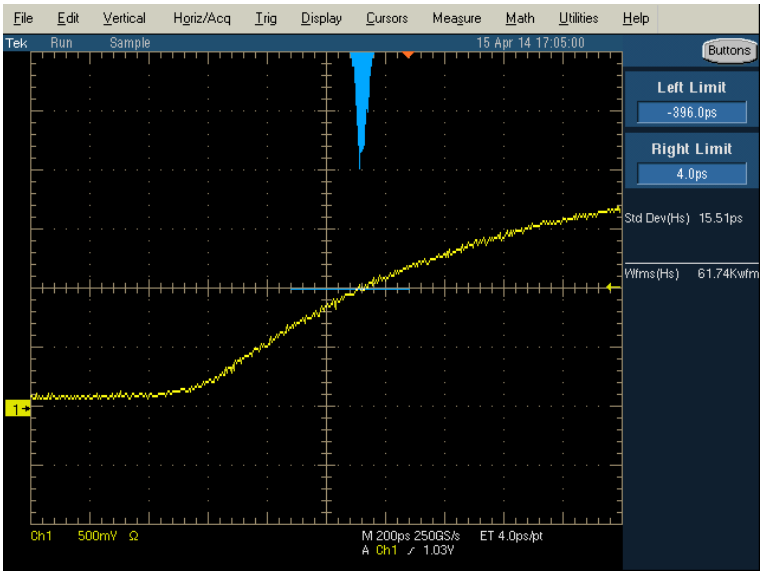

Figure 7.25 Jitter measurement of the CFD output. In blue, the Gaussian profile at half of the maximum amplitude in the rising edge. For an accurate measurement, the sampling rate of the oscilloscope must be adjusted to the maximum possible.

The jitter measured for over 60,000 CFD output pulses was 15.51 ps, which is negligible compared to the jitter introduced by other sources in the system.

7.4.2.4 Pulse width

As discussed previously in this report, the pulse width of the CFD output pulse is controlled by the feedback line between the reset and D inputs of the flip-flop, see Figure 7.22. To investigate the influence of the pulse width in a fluorescence measurement, a sample of a scatterer IRF (Ludox, Sigma Aldrich) was illuminated at 375 nm. The intensity of the excitation light was kept constant throughout these measurements. The response from the sample was measured using different delays in the feedback line and results of count rate variation with pulse width are plotted in Figure 7.26.

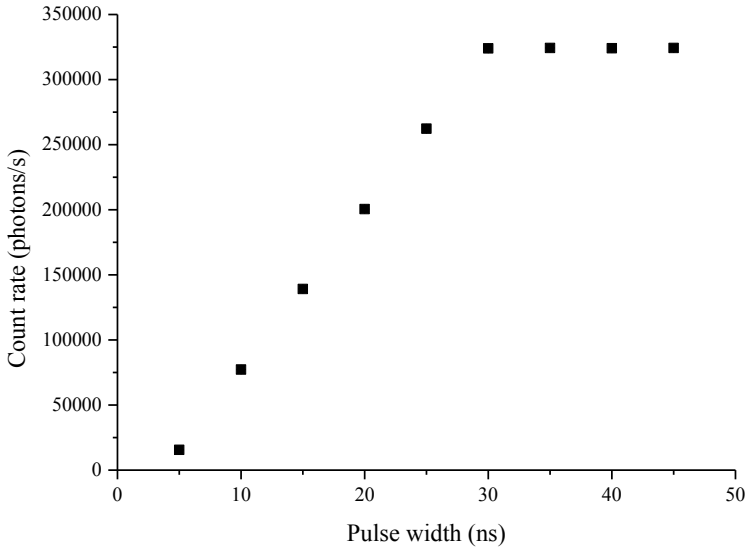

Figure 7.26 Variation of photon count rate width CFD output pulse width.

Results show that the count rate increases linearly with pulse width until saturation is reached, which occurs for a pulse width between 30 and 35 ns. This is consistent with our FPGA implementation that uses a 30 MHz clock (T ≈ 33.33 ns) to scan the input ports of the FPGA and transmit data via USB, see Figure 7.11. Therefore, if the pulse width is shorter than the clock period, there is a probability that the pulse is not read in the FPGA. In contrast, if the pulse width of CFD output signal is greater than the synchronisation clock period, the pulse will always be detected, thus explaining the saturation plateau. It is relevant to point out that the value of the pulse width effectively corresponds to the dead time of the CFD, as other pulses arriving at the flip-flop during this period are discarded due to the reset line. Nevertheless, if the pulse width is adjusted to a value immediately after saturation, i.e. 35 ns, such dead time is still shorter than the dead time of the USB transfer from FPGA to computer as measured experimentally (approximately 75 ns, see section 7.3.3), which means that the pulse width of the CFD does not restrict the maximum count rate of the instrument. Hence, all experiments reported hereafter were realised with a CFD pulse width of 35 ns. Figure 7.27 shows an oscilloscope snapshot of a single CFD output pulse. For n = 100 pulses, we measured a pulse width of 35.109 ± 0.015 ns, rise time of 1.735 ± 0.042 ns and fall time of 0.718 ± 0.014 ps (mean ± SD).

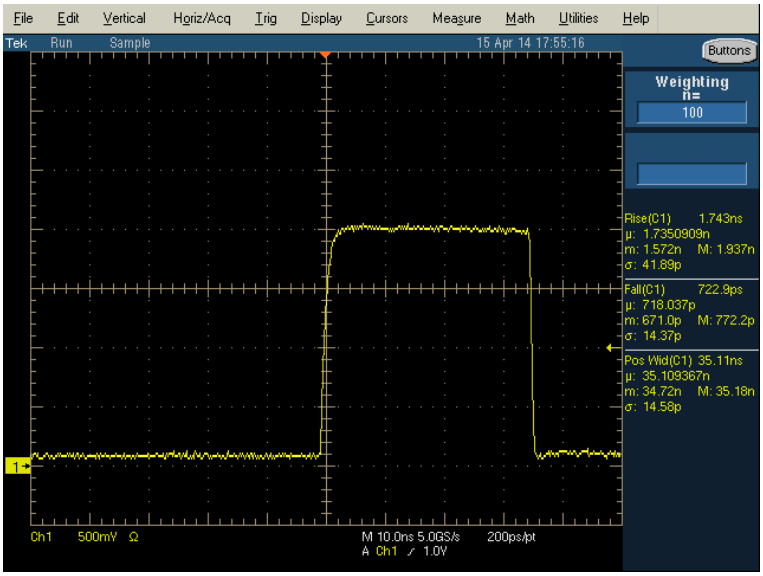

Figure 7.27 Oscilloscope snapshot of a CFD output pulse with 35 ns pulse width.

7.5 Experimental comparison with TCSPC

We investigated the capability of our instrument to make accurate fluorescence lifetime measurements by comparing our detection method with TCSPC. To establish a fair comparison between the two methods, we used the same optical setup - previously described in section 3.3.1.3 and in reference [128] - and only diverted the output signal of the PMT either to the FPGA (via the custom-made CFD presented in the previous section) or to the TCSPC card. All measurements were realised at 375 nm excitation and 40 MHz laser repetition rate. TCSPC settings were adjusted to provide 4096 bins in the

decay. In the FPGA, the detection was realised with 4 detection windows and 256 bins. For both methods, the IRF was measured at the excitation wavelength using Ludox beads (420786-1L, Sigma-Aldrich, Canada) suspended in water. The following sections present the results of this comparison.

7.5.1 Count rate

We compared the count rate capabilities of both detection methods by measuring the IRF from scattered light in Ludox beads. The intensity of the excitation was adjusted using the neutral density (ND) filters installed in the optical setup (see section 3.3.1.3), allowing measurement of detection frequencies within the typical range of fluorescence lifetime acquisitions. Results are plotted in Figure 7.28. From the linear fit to the data we extracted a slope of 0.9926 ± 0.0092 that indicates that under the same experimental conditions and within these count rates, the two systems detect the same number of photons. This is an expected result as in these measurements the average time between photons arriving at detection electronics is still far from the dead time of both methods, and thus all photons are detected.

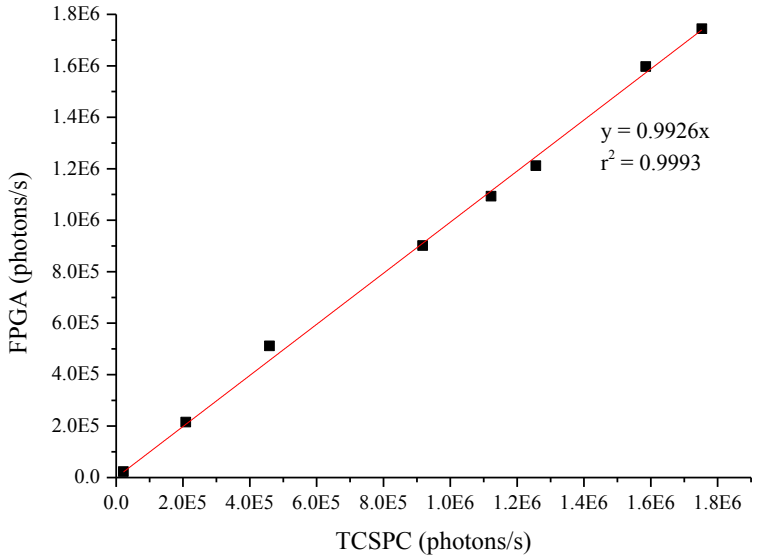

Figure 7.28 Count rate comparison between TCSPC and FPGA detections.

7.5.2 Fluorescence lifetime measurements of dyes

In order to check the temporal accuracy of both detection methods, two well characterised fluorescent dyes were measured: Stilbene-3 and NADH.

7.5.2.1 Stilbene-3

Stilbene-3 is excited in the UV and fluoresces strongly in the violet and blue ranges of the spectrum. A solution of 50 µM Stilbene-3 in purified water was measured with excitation at 375 nm, at room temperature. The detection wavelength was adjusted to 460 nm, which is close to the fluorescence emission peak of this dye, as measured experimentally, see Figure 7.29A.

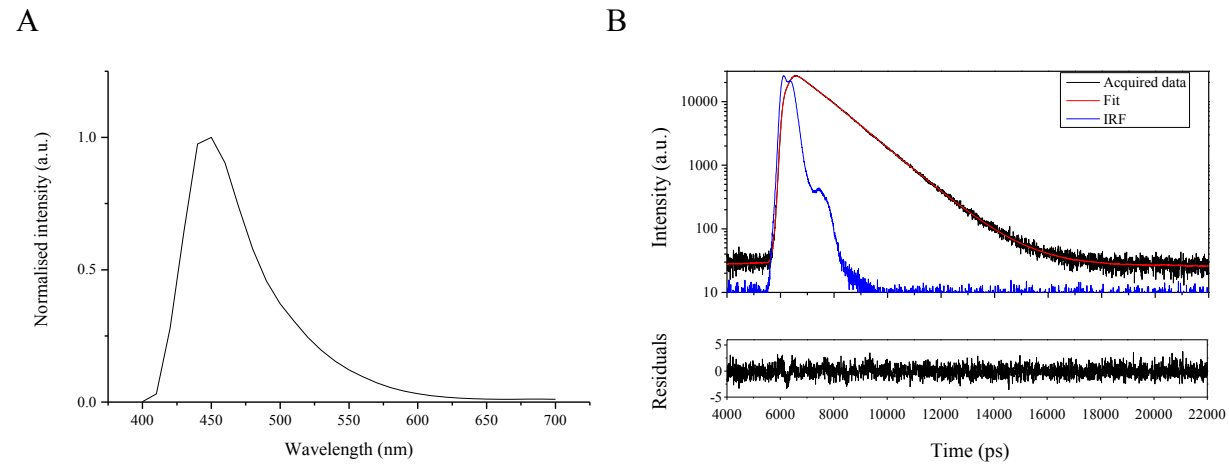

Figure 7.29 (A) Normalised fluorescence emission spectrum of Stilbene-3 at 375 nm excitation, acquired in 10 nm intervals, between 400 and 700 nm. (B) Fluorescence decay curve of Stilbene-3 measured with TCSPC, using 4096 bins.

The fluorescence lifetime extracted from TCSPC acquisition was 1.213 ± 0.009 ns (n = 3), which is consistent with lifetime values reported in literature [43], [234]. For the FPGA detection, we investigated the system's accuracy at different excitation intensities. Excitation light intensity was adjusted using the neutral density (ND) filters installed in the optical setup (see section 3.3.1.3). Fluorescence lifetime results are presented in Figure 7.30.

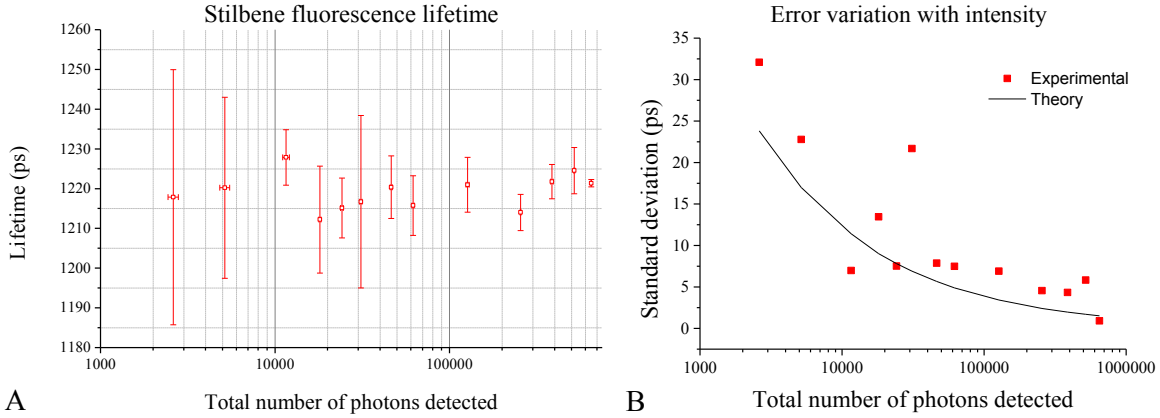

Figure 7.30 (A) Fluorescence lifetime of Stilbene measured at different excitation intensities (n = 3 for each data point); (B) Error variation with total intensity.

In Figure 7.30A, we observe that the fluorescence lifetime measured for Stilbene-3 is independent of the total number of photons collected. If we average all measurements, we obtain a lifetime of 1.219 ± 0.012 ns, which is in excellent agreement with the lifetime value measured with TCSPC. The photon economy and precision of our instrument is also investigated in Figure 7.30B, where we compare the experimental standard deviation (red squares) with the standard deviation (black line) calculated from equation 7.15 [400], where *N* denotes the total number of photons detected in each acquisition.

$$\sigma_\tau = \frac{\tau}{\sqrt{N}} \tag{7.15}$$

To first order, the precision of a measurement is determined by the system parameters, such as the number of detection windows and bins. These parameters define the width of the bins in the decay histogram and the resolution of the system and therefore can affect the accuracy of the lifetime determination. The plot in Figure 7.30B shows that, ultimately, the uncertainty in the fluorescence lifetime measurement is dependent of the total number of photons in the decay histogram.

7.5.2.2 NADH

NADH is a key cofactor for redox reactions and enzymatic metabolism. As discussed in Chapter 3, the excitation and emission spectra of NADH are well characterised: it has an absorption peak at 340 nm and emits short wavelength blue fluorescence. Its fluorescence lifetime is strongly dependent on the environment and presents two components that are commonly attributed to the extended and folded conformations of the molecule [8]. Free NADH in aqueous solution typically exhibits a mean lifetime between 400 and 500 ps [96]. Because of its short lifetime and dependence with temperature, as measured experimentally (see Chapter 3), NADH can provide a suitable test sample to verify the precision of our instrument to detect variations in fluorescence lifetime of the order of a few picoseconds, as those induced by temperature. Additionally, because it yields a complex fluorescence lifetime decay, it represents an opportunity to assess the ability of our system to resolve complex decay profiles, such as those typically found in tissue. We measured the fluorescence lifetime of NADH excited at 375 nm. Fluorescence was collected at 460 nm, which is close to the fluorescence emission peak. Results are presented in Figure 7.31. Both datasets were fitted a double exponential model and data presented in Figure 7.31A correspond to the weighted mean fluorescence lifetime. Figure 7.31C and D show the individual lifetime components extracted for each system.

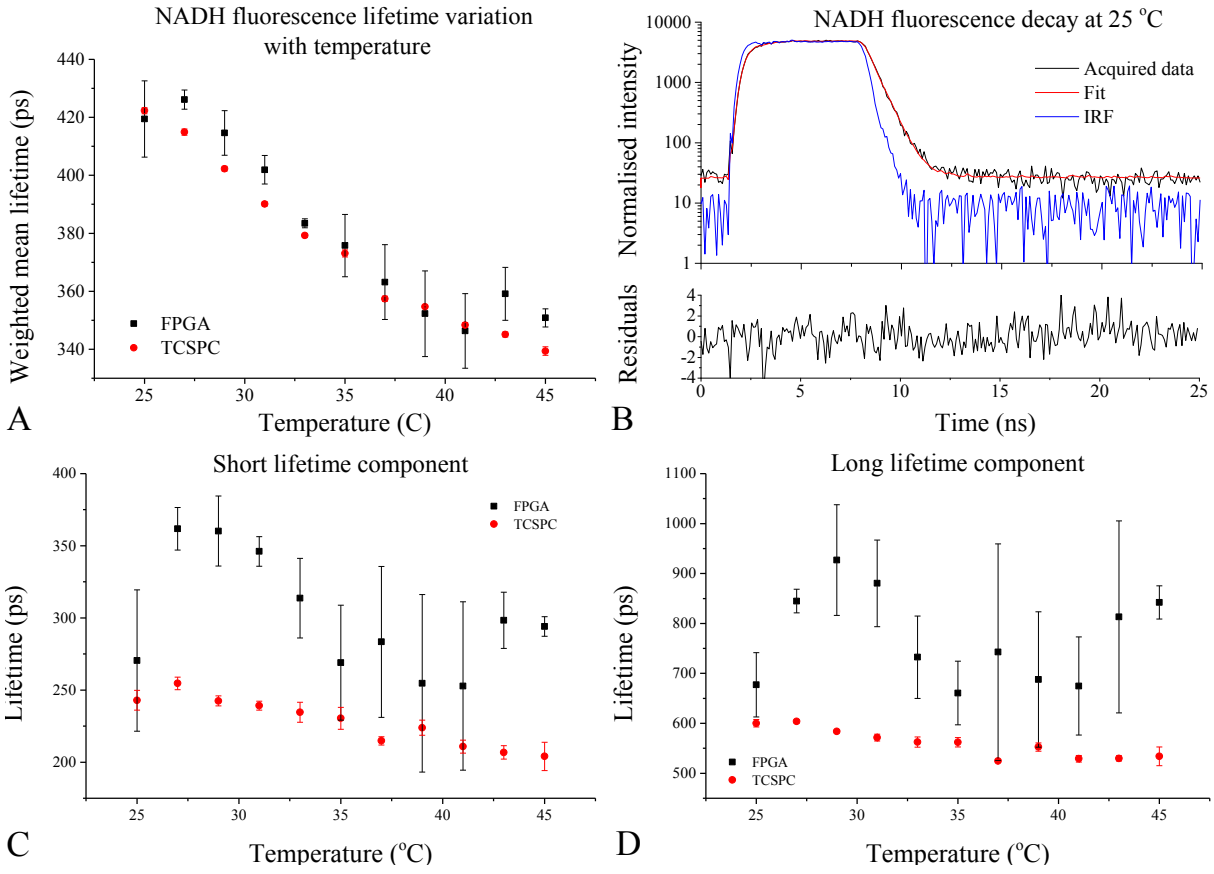

Figure 7.31 (A) Variation of NADH weighted mean fluorescence lifetime with temperature for TCSPC and FPGA detection methods; (B) FPGA fluorescence lifetime decay of NADH at 25 °C; (C) NADH short lifetime component; (D) NADH long lifetime component.

From Figure 7.31A, we verify that the weighted mean fluorescence lifetime measured with the FPGA is in good agreement with that extracted from TCSPC. Although the precision of the FPGA measurements is lower than in TCSPC (demonstrated by the larger error bars for FPGA measurements), results presented in Figure 7.31C and D show that even with detection windows of approximately 6.25 ns width, it is still possible to resolve a double exponential with lifetime components of 300 and 700 ps, as expected for NADH.

Overall, these results demonstrate the ability of our instrument to detect short lifetime variations even in cases where the width of the detection windows and bins of the decay histogram are much larger than the variation itself.

7.6 Conclusions and summary

This chapter presented the development of a low-cost detection approach for single point autofluorescence lifetime measurements that builds on the method introduced by Colyer et al [55]. In particular, we demonstrated the following improvements:

- Higher count rate capability (up to 13 MHz compared to approximately 2 MHz).
- Time of arrival of each photon is assigned on board, hence reducing data processing time.
- Implementation with a low-cost CFD.

With respect to count rate capabilities, the implementation of Colyer et al [55] utilises the on-board memory to store data relative to each incoming photon, i.e. window of arrival and phase shift. The information is then transferred to the computer in packets via USB at a maximum rate of 2 MHz, which is essentially imposed by the memory size: if the memory fills up within the dead time of the transmission (maximum of 6400 photons for every 3 ms), any additional photons arriving at the detectors are lost [55]. Our implementation utilises an alternative approach, in which the information relative to each photon (i.e. bin of arrival) is immediately transferred via USB. This approach guarantees maximum count rate of approximately 13 MHz - as demonstrated in Figure 7.19 - which is an improvement relative to the Colyer method and greater than the count rate capabilities of an SPC-830 TCSPC acquisition card from Becker and Hickl. In our approach, the maximum count rate is limited by our implementation of the USB data transmission, which could be enhanced by using a faster synchronisation clock (e.g. 100 MHz instead of 30 MHz) to drive the state machine that controls the USB transmission. This would allow fluorescence measurements with overall count rates up to 20 MHz, which is the maximum transmission rate allowed by the USB controller used in our system. Although in a fluorescence lifetime acquisition the photon count rate is typically within the kHz regime for single channel architecture, operation at higher detection frequencies can be relevant for multichannel detection, in which the fluorescence signal is spread across multiple wavelength ranges.

Another advantage of our implementation refers to the usage of a custom made and affordable CFD that minimises the timing requirements and the number of electronic components used and thus significantly reduces the cost of the detection in comparison to commercially available CFDs, which are typically available at a relatively high cost (~£2000). Although our CFD implementation introduces uncertainty in the triggering time of a PMT pulse, which is of about tens of picoseconds as demonstrated in section 7.4.2.1, this is still negligible compared to the jitter introduced by the generation of the sampling windows, which can go up to 2 ns, as discussed in section 7.2.1. The impact of using of low-cost CFDs can gain more relevance in a multispectral detection arrangement using photon counting PMTs.

The greatest disadvantage of our implementation relative to the original system refers precisely to the impossibility of realising parallel multispectral detection. In our method, this could be implemented

e.g. by using a second FPGA-USB interface with the USB controller to transmit the information of the channels from which photon events originated or by formatting the information from the detection channel and bin of arrival such that it could be transmitted in a single USB packet to the computer. With this configuration, no additional hardware would be needed and a maximum of 255 spectral channels could be used. Despite this limitation, it should be noted that this implementation was merely our first approach and therefore it should be regarded as a proof of concept. Hence, further optimisation is required before this detection methodology becomes attractive for autofluorescence measurements in clinical settings, particularly with respect to multispectral detection.

We experimentally characterised our implementation and the merits and limitations of the time-resolved measurement were discussed in detail. Overall, several sources can contribute to the broadening of the IRF with a concomitant increase of the uncertainty of the time-resolved measurement:

- Jitter in the generation of the sampling windows, which is inherent to the approach and can potentially lead non-uniformity of the bins.
- Path delays in the FPGA that can introduce timing errors in the measurement and create measurement artefacts in the IRF, as illustrated in Figure 7.17.
- Amplitude jitter of the pulse detection in the CFD.
- Other effects such as timing delays in the synchronisation and detection lines or random noise in the detectors, which are also common to other techniques, such as TCSPC.

We validated our detection algorithm against TCSPC on a previously described optical instrument that utilises a laser diode with short optical pulses (~70 ps) for illumination and a cooled photon-counting PMT that introduces near-zero afterpulsing artefacts in the measurement. The results showed that our instrument can describe single and complex exponential decays and, more interestingly, it can resolve lifetime variations on the order of a few picoseconds. Altogether, the detection system described in this chapter offers the following merits and limitations:

- **Merits**
  - Implementation at a much lower-cost than TCSPC: approximately 5% of the cost of a SPC-830 TCSPC acquisition card.
  - Compatible with different types of light source and single photon detectors.
  - High count rate capabilities (up to 13 MHz).
  - Compactness and portability.
  - Ability to resolve small lifetime variations.

- The uncertainty in the fluorescence lifetime measurement depends on the total number of photons in the decay histogram, as illustrated in Figure 7.30.

- **Limitations**
  - Complexity of the implementation.
  - Single channel operation.
  - Temporal resolution is limited by the operating frequency of the FPGA. In our case, the maximum operating frequency is 320 MHz, which e.g. limits the operation to 4 detection windows at 40 MHz excitation rate.

In the following chapter, the application of this system to biological samples is presented, using a low-cost illumination utilising cheap laser diodes and light delivery and collection via a fibre-optic bundle. If clinical practicality is demonstrated, we believe that such instrument could have significant potential for commercial development and clinical deployment.

8 A complete low-cost system for autofluorescence lifetime measurements of biological tissue

In the previous chapter, a low-cost detection methodology for fluorescence lifetime measurements was presented, building on a previous system implemented by Colyer et al [55]. A custom implementation and characterisation of this method were demonstrated against the "gold-standard" TCSPC-based detection using an optical setup previously developed in our laboratory. Despite the excellent agreement between the two detection methods, measurements were realised using an expensive picosecond pulsed illumination source and corresponding driver and a cooled photon-counting PMT that yields a low dark count rate and low afterpulsing. Altogether, these components have a combined cost of approximately £20,000 and therefore are not suitable for a low-cost implementation. In this chapter, the implementation of a complete low-cost instrument is explored, utilising cheap laser diodes with external modulation for excitation and a lower-cost non-cooled photon counting PMT. The development and characterisation of this instrument are presented, together with fluorescence lifetime measurements of reference fluorophores and preliminary data concerning the application of this system to autofluorescence lifetime measurements of biological tissues.

Outline

- Motivation.
- Development of a low-cost instrument for single-point time-resolved autofluorescence measurements of biological tissue.
- Instrument characterisation and calibration.
- Tissue autofluorescence lifetime measurements of lamb kidney.
- Conclusions and summary.

8.1 Motivation

In Chapter 4, we introduced the development of a compact and portable TCSPC-based time-resolved spectrofluorometer that was successfully used in clinical settings in the study of osteoarthritis and heart disease, as demonstrated in Chapters 5 and 6, respectively. Despite the encouraging results that prompted the development of a clinically viable instrument to be used in open chest surgical procedures in humans, of which progress to date was described at the end of Chapter 6, a major drawback that hampers further deployment of this instrument is related to its cost, as demonstrated in Table 8.1. For some applications, temporal resolution achieved with the instrument described in

Chapter 4 may not be necessary and so it is interesting to explore the practical implementation and performance of potentially lower cost instruments that provide lower cost resolution.

Table 8.1 Approximate cost of the time-resolved spectrofluorometer presented in Chapter 4.

Components	Quantity	Unit price (£)	Total (£)
Laser diodes	2	7000	14000
Laser diodes driver	1	7000	7000
PMTs	3	2000	6000
PMT driver (power supply and cooling circuitry)	2	1500	3000
Router	1	1000	1000
TCSPC module	1	17000	17000
Fibre-optic bundle	1	1000	1000
Other optical components (e.g. filter, mirrors, posts, etc…)	-	2000	2000
Other electronic components (e.g. computer, cables, etc…)	-	1000	1000
		Total	**51500**

Table 8.1 shows that the instrument presented in Chapter 4 costs over £50,000, which is mostly driven by the cost of the laser diodes and TCSPC acquisition card. The total cost of the instrument could be reduced by using a TCSPC module with lower temporal resolution, which is still approximately £7,000. The ultrafast laser diodes are state of the art instruments that provide short optical pulses of less than 100 ps duration, enabling TCSPC acquisition with sub-100 ps temporal accuracy, as discussed in Chapter 2. These could, in principle, be replaced by longer pulse alternatives if temporal resolution greater than 100 ps is sufficient. On the other hand, there are also components in the system that cannot be easily replaced by lower cost models, such as the fibre-optic bundle, optical filters or other optical parts. There is therefore scope for reducing the cost of this instrument, albeit at the cost of decreasing temporal resolution, particularly with respect to the TCSPC acquisition, which could be replaced by the detection method introduced in Chapter 7, light sources and detectors.

As discussed in Chapter 7, there has been a growing interest in identifying low-cost and compact solutions that could increase the impact of autofluorescence lifetime measurements in clinical research, with respect to excitation light sources and detectors. For illumination, both laser diodes and LEDs have found widespread deployment in biomedical applications in recent years. The attractiveness of laser diodes and LEDs is associated with their low-cost (components can be available for less than £50 at short wavelengths), low-power consumption and range of wavelengths available [1]. Furthermore, for fluorescence lifetime applications not requiring subnanosecond excitation pulses, laser diode and LED illumination can be implemented using a relatively simple driving circuit with external RF modulation, as in references [26], [51]–[54], [401]. Recent advances in LED technology have also introduced illumination using micro-LED arrays and its application in time-resolved measurements of fluorescence has been reported [47], [48], yet not in biomedical research.

For fluorescence lifetime applications requiring short optical excitation pulses, more sophisticated and accurate electronic circuitry are required, which can increase the cost of the devices. Accordingly, there are a range of commercial laser diodes and LEDs available providing picosecond optical pulses at specific wavelengths, such as those used in our time-resolved spectrofluorometer, described in Chapter 4. As demonstrated by Colyer et al [55], the detection method presented in Chapter 7 is not limited to picosecond excitation pulses and thus the expensive laser diodes can be replaced by lower cost models with external modulation providing longer pulses, which would reduce the total cost of the instrument.

With respect to detection of the autofluorescence signal, photon counting PMTs, SPAD or hybrid detectors can be used, as discussed in Chapter 2. In general, hybrid detectors yield the best characteristics for fluorescence lifetime acquisitions but they are more expensive than the alternatives and thus out of the scope of a low-cost instrument. Photon counting PMTs are attractive for fluorescence lifetime measurements due to their fast temporal response and high dynamic range [29]. The quality (i.e. SNR, afterpulsing and pulse profile) of a PMT response is inversely proportional to its cost, of which a significant fraction is related to the cooling instrumentation, which is used to reduce dark counts. Although low dark counts and afterpulsing are of importance in photon counting applications, both these effects can be accounted for, to some extent, by using appropriate fitting software. Uncooled photon counting PMTs are available for approximately £800 from Becker and Hickl, which is approximately three times less than the cost of the detectors used in our instrument (see Table 8.1). Furthermore, because cooling instrumentation and circuitry are not required, there is no need to use complex and expensive PMT drivers and instead a standard plug-top power supply could be used.

SPAD detectors can also be interesting options for a low-cost implementation. Although SPADs are typically avoided in fluorescence lifetime acquisitions due to their broader temporal response compared to PMTs and variable pulse width with wavelength and count rate [1], as discussed in Chapter 2, in our low-cost implementation such variations would be negligible compared to the width of the detection windows and thus these detectors could be used. Furthermore, SPADs can be manufactured at a much lower cost, as result of recent advances in complementary metal–oxide–semiconductor (CMOS) technology [402], and thus constitute an interesting alternative to photon counting PMTs. The limitations commonly associated with SPAD detectors, including low dynamic range and poor timing resolution (typically of hundreds of picoseconds FWHM), have also been subject of active investigation and remarkable progress has been made in recent years [403]–[405]. SPAD arrays can be of particular interest for multispectral detection, utilising a similar approach of that of spectrometers (see section 4.1.1.1), i.e. a grating or other dispersing element to separate the fluorescence emission according to its wavelength and a SPAD array to detect photons in different

wavelength channels. However, despite the advances and potential demonstrated in recent years, this is still an emerging technology that requires further optimisation before it can find commercial availability and widespread deployment, particularly with respect to fluorescence lifetime applications.

Despite the options available for low-cost illumination and detection, the number of instruments that can effectively be considered low-cost (i.e. using affordable light sources and detection instrumentation) is scarce and only a few reports of such instruments can be found in literature, e.g. [47]–[49], [52], of which a vast majority is still at an early stage of development and thus their potential has not yet been demonstrated in biomedical applications. Accordingly, there is still a lack of compact and portable autofluorescence lifetime instrumentation that could be implemented inexpensively and be rapidly translated into clinical practice. In this chapter, the implementation of a complete low-cost system is presented, utilising modulated laser diodes for excitation and standard uncooled photon counting PMTs, in combination with the detection method presented in Chapter 7, for time-resolved detection of the autofluorescence signal. In this is proof-of-concept study, the potential of this system to find inherent optical contrast in biological samples is demonstrated. In the following sections a detailed description of the development and characterisation of this instrument is provided, including comparison against the cuvette-based time-resolved spectrofluorometer described in section 3.3.1.3.

8.2 Development of a low-cost system for single point time-resolved autofluorescence measurements of tissue

8.2.1 Optical setup

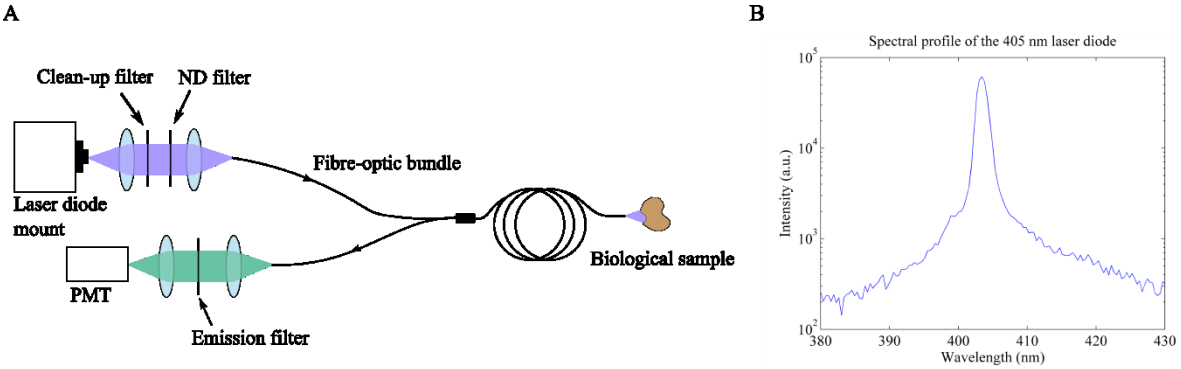

Figure 8.1 (A) Optical layout and electronic configuration of the low-cost single-point time-resolved fluorometer. (B) Spectral profile of the 405 nm diode. Measurements were carried out on a USB-2000 compact spectrometer (USB-2000+, Ocean Optics, USA) using the fibre-optic probe for light delivery.

The optical layout of the instrument is illustrated in Figure 8.1A. Excitation light was provided by a single-mode laser diode (Changchun New Industries, China) with centre wavelength at 405 nm (see Figure 8.1B) and maximum output power of 100 mW in CW operation, which was fitted on a

temperature-controlled laser diode mount (TCLDM9, Thorlabs, USA) providing suitable interfaces for external RF modulation, which was provided by a benchtop function generator (TG2001, Thurlby Thandar Instruments Ltd, UK), and current control, which will be discussed in detail in section 8.2.2. To reduce thermal effects in the diode, a temperature controller (TED200, Thorlabs, USA) was used. This is because, in laser diodes, the emission centre wavelength and threshold current are sensitive to temperature variations and thus temperature control is necessary to maintain stability of the output power and emission wavelength [232], [406]. A clean-up filter (LD01-405/10-25, Semrock, USA) was placed in the excitation path to suppress noise from spontaneous emission in the diode. When necessary, neutral density (ND) filters were also placed in the excitation path to adjust the optical power at the sample. To facilitate excitation light delivery to biological samples, the beam was directed into a fibre-optic probe, identical to that described in section 4.2.2. It should be noted that the optical fibres previously used for white light delivery and collection were not used in this setup, as in this case, we were not interested in the diffuse reflectance spectrum. Fluorescence light from the sample was collected by the detection fibres and delivered to the detection arm, where a set of lenses were used to focus the light onto the photocathode of a photon counting PMT (PMH-100, Becker and Hickl, Germany). A band-pass filter (FF03-525/50-25, Semrock, USA) was positioned in front of the detector to remove any residues of excitation light and to restrict fluorescence detection to the range of wavelengths between 500 to 550 nm. Finally, the output signal of the PMT was converted into a logic pulse using our homemade CFD (see section 7.4) and then fed to the FPGA input port to realise time-resolved detection. To maintain synchronicity in the system, a TTL-based clock operating at the same frequency as the laser diode modulation was provided by the function generator to the FPGA and used as reference clock to generate the sampling windows (see section 7.2).

A schematic of the electronic configuration implemented in this instrument is illustrated in Figure 8.2.

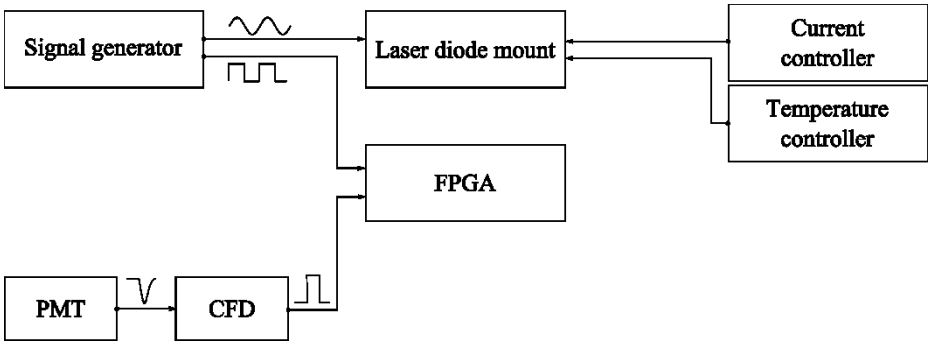

Figure 8.2 Electronic configuration concerning modulation and temperature stability of the laser diode and detection of the fluorescence signal.

8.2.2 Laser diode modulation

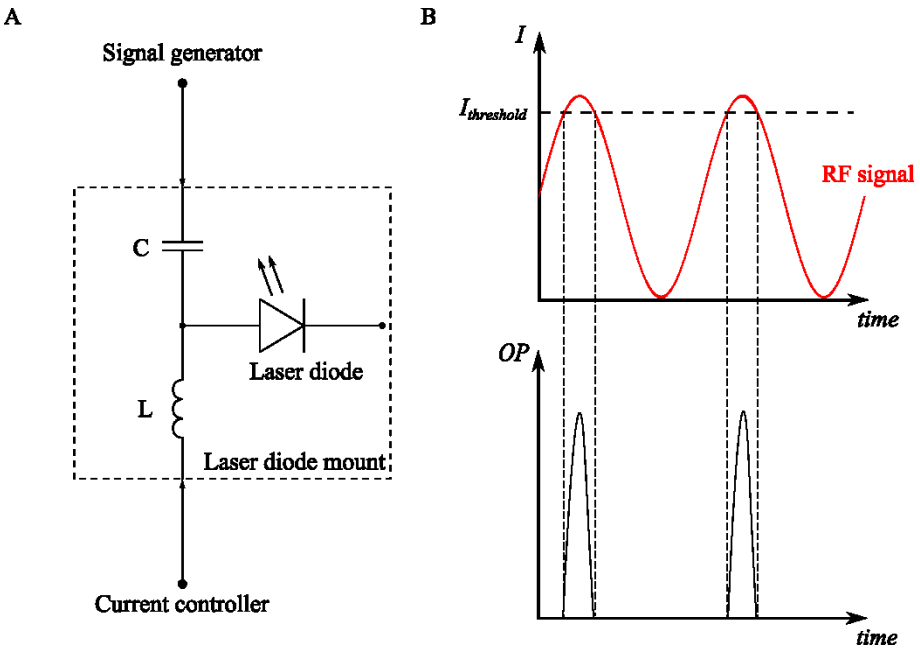

Figure 8.3 (A) Schematic representation of the bias-tee circuit inside the laser diode mount. The RF and DC signals were provided externally using a function generator and a current controller, respectively. (B) Diagram showing the laser diode operation showing injected current (top) and output optical power (OP) (bottom).

In gain-switched lasers, such as those of the instrument presented in Chapter 4, optical pulses are generated by modulating the laser diode with a brief current pulse that will bring the carrier density to above the lasing threshold. If the injected current is sufficiently high, stimulated emission of photons will occur faster than absorption, resulting in depletion of the carriers. If the current pulse is sufficiently shorter, the carrier density will not exceed the lasing threshold again, which results in a single short optical pulse. Despite its simplicity, this process requires stable circuitry and fine tuning of key parameters such as modulation waveform and current level and therefore, in practice, optical pulses with less than 100 ps width are difficult to achieve. As discussed previously in this chapter, although such short optical pulses can provide better temporal accuracy, they are not required to realise fluorescence lifetime acquisitions using the detection method presented in Chapter 7. Hence, in our implementation we aimed for the shortest optical pulses achievable using a sinusoidal modulation and adjusting the current level such that the laser was operating close to the lasing threshold. Low-cost illumination was implemented by modulation of a CW laser diode, which cost approximately £50. Modulation was achieved using a bias-tee network, which exists inside the laser diode mount (see Figure 8.3A). The principle of operation of this circuit is as follows: an electrical current provided by an external controller (LDC220, Thorlabs, USA) is sent through an inductive low-pass filter (LPF) that only allows the DC component to pass through the diode; in contrast, an RF signal provided by a function generator (TG2001, Thurlby Thandar Instruments Ltd, UK) bypasses the LPF and directly couples an AC component to the diode. The capacitor at the RF input removes any DC

component in the RF signal. This configuration superimposes the RF signal with the DC component at the input of the laser diode and thus its optical output power is modulated accordingly. Pulsed operation was achieved by coupling a 20 MHz sinusoidal waveform ($V_{pp} \approx 8$ V) to the RF input and adjusting the DC component so that the injected current was higher than the threshold current for a brief period, thereby generating short optical pulses. A schematic representation of this principle is illustrated in Figure 8.3B and its practical demonstration presented in section 8.3.1, which includes a comparison between different waveforms. In order to maintain the shape and width of the optical pulse, the RF and DC signals were adjusted before each experiment and maintained constant throughout the measurements. As mentioned, the optical power at the sample was adjusted using ND filters in the excitation path (see Figure 8.1A).

8.3 Instrument characterisation and calibration

8.3.1 Instrument response function

As discussed in the previous section, the low-cost laser diode was modulated using a sinusoidal waveform at 20 MHz. Optical pulses were achieved by fine tuning the current offset so that the current flowing through the laser was close to the gain threshold ($I_{threshold} < 35$ mA). Figure 8.4A shows a typical optical pulse measured using a fast photodiode (SV2-FC, Thorlabs, USA). Light from the laser diode was delivered to the photodiode using the fibre-optic bundle and therefore these measurements also reflect temporal broadening due to modal dispersion in the fibre, which is approximately 130 ps, as calculated in section 4.3.3. For these pulses, we calculated a FWHM of 3.07 ± 0.36 ns and rise time (10 to 90% of the pulse amplitude) of 1.52 ± 0.08 ns. The corresponding IRFs is shown in Figure 8.4B, for which we calculated a FWHM of 12.50 ± 0.09 ns and 2.35 ± 0.21 ns rise time.

For comparison, identical measurements were realised using the 375 nm laser diode installed in the cuvette-based system and the fibre-optic extension to deliver and collect light from the sample (see section 3.3.1.3). For this laser diode, we calculated a FWHM of 0.48 ± 0.06 ns and rise time of 0.25 ± 0.05 ns and a corresponding IRF with 12.35 ± 0.04 ns FWHM and 1.74 ± 0.08 ns rise time.

These results show that the optical pulses provided to the sample by the low-cost modulated laser diode are approximately one order of magnitude longer than those provided by the state of the art laser diode, which translates essentially in a longer IRF rise time (~600 ps) and, similarly, fall time. In practice, despite the increase in FWHM and longer edges, the pulses generated by this configuration enabled fluorescence lifetime measurements with good temporal accuracy and comparable to that of TCSPC-based measurements using picosecond optical pulses, as demonstrated in sections 8.3.2 and 8.4.

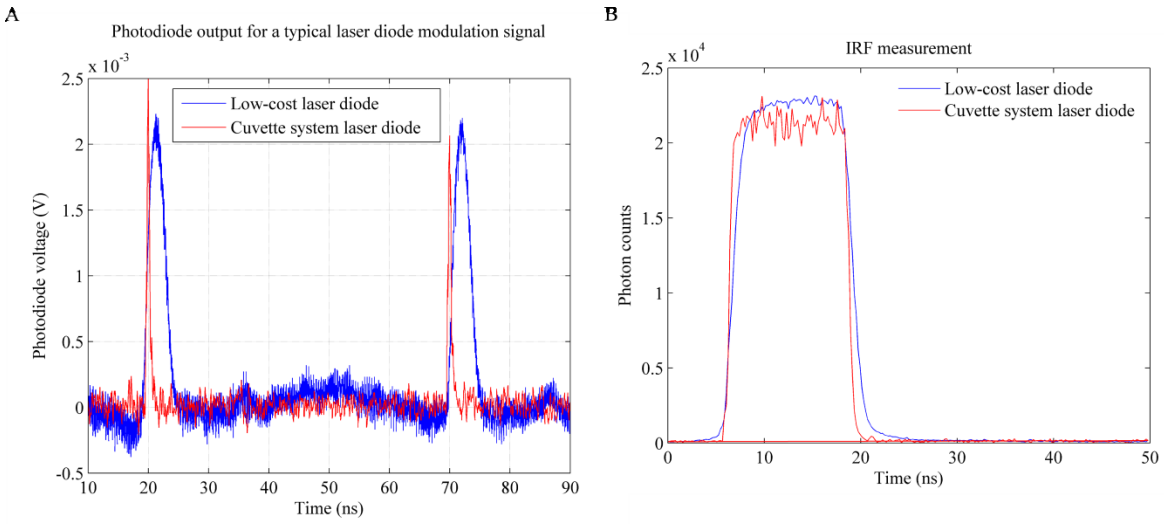

Figure 8.4 (A) Typical optical output of our modulated laser diode (in blue) and comparison with a commercially available laser diode installed in the cuvette-based system (in red). Pulses were measured with a fast photodiode with approximately 2 GHz bandwidth and 150 ps rise and fall times. In both measurements, light was delivered to the photodiode using a fibre-optic probe. (B) Corresponding IRF measurements of scattering Ludox beads.

It should be noted that the input signal for the laser diode required fine adjustment before each experiment and thus the shape and width of the optical pulse could change between different experiments. A limitation of this implementation concerns the function generator used to modulate the diode, which was operating at its maximum output frequency and consequently the signal was found to be jittery and unstable and thus not ideal for our circuit. In particular, we found that at 20 MHz the waveform changed with amplitude and offset. Figure 8.5 shows two 20 MHz sinusoidal waveforms generated with different amplitudes and DC voltage offsets, at the output of the frequency generator. Interestingly, the "distorted" sinusoidal signal (in blue in Figure 8.5) was found to provide shorter optical pulses in comparison to a regular sinusoidal input, possibly due to the faster rising edge and lower FWHM, resulting in the gain being less time above the lasing threshold.

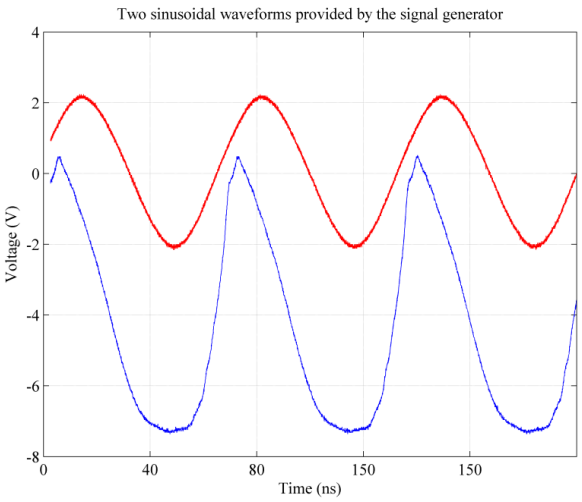

Figure 8.5 Two sinusoidal waveforms provided by the function generator at 20 MHz. The signal in blue can be used to achieve shorter optical pulses. Red curve: V_{pp} = 4.32 V; V_{DC} = 0 .80 V; f = 20 MHz. Blue curve: V_{pp} = 7.88 V; V_{DC} = -3.42 V; f = 20 MHz.

For comparison purposes, the laser diode was modulated using the "distorted" waveform illustrated in Figure 8.5 (V_{pp} = 7.88 V) and different current offsets. The results presented in Figure 8.6 shows the IRF broadening with increasing offset, which is an expected result as increasing the offset translates in a longer period above the gaining threshold, ultimately leading to longer optical pulses. This also emphasises the need to maintain a consistent waveform during an experiment, so that the IRF does not change and eventually results in wrong estimations of the fluorescence lifetime.

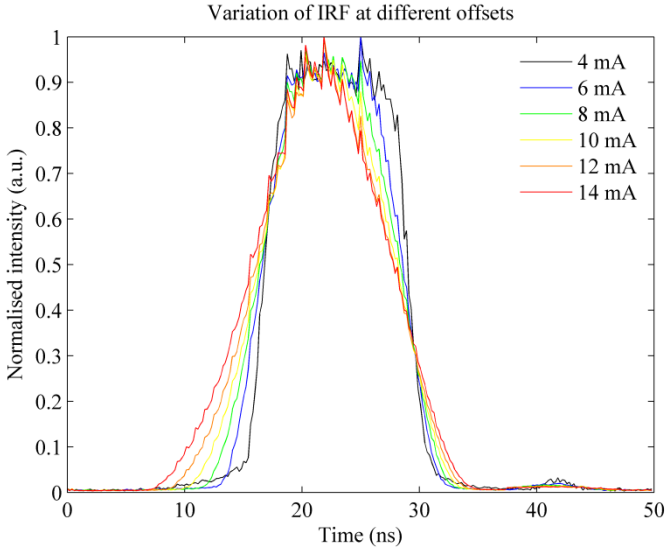

Figure 8.6 Variation of IRF shape and width with current offset. The input waveform is illustrated in Figure 8.5 (in blue).

8.3.2 Fluorescence lifetime measurements of reference fluorophores

8.3.2.1 Single exponential decays

The temporal accuracy of the low-cost instrument was verified against the cuvette-based time-resolved spectrofluorometer described in section 3.3.1.3, by measuring a number of fluorescent dyes presenting single exponential decay characteristics.

In both instruments, measurements were carried out using 405 nm excitation light at 20 MHz repetition rate, which was provided by the supercontinuum laser in the cuvette-based system (see section 3.3.1.3). Fluorescence light from the sample was collected at 525 nm centre wavelength. In the low-cost system, a band-pass filter was placed in front the detector to restrict the fluorescence detection to the range from 500 to 550 nm. The IRF was measured at the excitation wavelength using a scattering sample of Ludox beads (420786-1L, Sigma-Aldrich, Canada). It is relevant to point out that measurements in the cuvette-based system were carried out at the magic angle for detection and using vertically polarised excitation light, hence suppressing any contributions from fluorescence anisotropy to the fluorescence decay. In contrast, the low-cost system does not include suitable optics to realise polarisation-resolved excitation and emission and thus anisotropy can contribute to the measured fluorescence decay. Furthermore, in the low-cost system, light was delivered to the sample via a fibre-optic bundle, which further differentiates light delivery and collection in both systems. Measurements in the low-cost system were realised using two different detection architectures (see section 7.3.3), which, for convenience, will be identified as architecture 1 (4 detection windows and 256 bins) and 2 (8 detection windows and 64 bins). In the cuvette-system, TCSPC acquisition was realised using 1024 bins (10 bit ADC resolution). A total of 5 acquisitions were taken for each fluorophore. All datasets were fitted to a single exponential decay model using *FLIMfit* [42], an open-source software for analysis of fluorescence lifetime data written by our group. Results are presented in Table 8.2, showing mean ± standard deviation.

Overall, the fluorescence lifetimes extracted for these fluorophores are in good agreement between systems and, in the case of the low-cost system, between different detection architectures, which demonstrates the consistency of our implementation. As mentioned above, any deviations between systems can be related to anisotropy effects that can contribute to the fluorescence decay in the low-cost system but not in the cuvette-based system. These results demonstrate that it is possible to resolve single exponential decays with temporal accuracy comparable to TCSPC yet using nanosecond-wide excitation pulses.

Table 8.2 Average lifetimes of reference fluorophores in solution measured in the cuvette and low-cost systems. All measurements were realised at room temperature. All values are reported in nanoseconds (ns).

Fluorophore	Cuvette-based	Low–cost system	
	system	Architecture 1	Architecture 2
Coumarin 6	2.61 ± 0.01	2.64 ± 0.04	2.59 ± 0.02
Coumarin 153	4.68 ± 0.01	4.72 ± 0.05	4.72 ± 0.04
Coumarin 307	5.32 ± 0.01	5.38 ± 0.02	5.37 ± 0.03
Coumarin 314	3.52 ± 0.01	3.58 ± 0.05	3.53 ± 0.04
Fluorescein	4.06 ± 0.01	3.91 ± 0.03	4.10 ± 0.07

8.3.2.2 Double exponential decays

As demonstrated throughout this thesis, tissue autofluorescence typically exhibits complex decay profiles with multiple exponential components, which, in a simplistic approach, are commonly described by a double exponential decay model. Hence, in order to verify the ability of our instrument to resolve double exponential decays, well characterised fluorophores were measured, of which results are presented below.

8.3.2.2.1 FAD

As discussed in Chapter 3, FAD presents a bi-exponential fluorescence decay profile with relatively long lifetime components of approximately 2 and 4 ns, at room temperature. Hence, it represents a convenient test sample to verify the ability of our system to resolve complex exponential decays, such as those typically found in biological samples. A solution of 50 μM FAD in PBS was excited at 405 nm and the fluorescence was collected at 525 nm - using a band-pass filter (FF03-525/50-25, Semrock, USA) in the low-cost system - which is close to the fluorescence emission peak of the molecule, see Chapter 3. The laser repetition rate was set to 20 MHz and measurements were realised at room temperature. For measurements with the FPGA, we extracted a weighted mean fluorescence lifetime of 2.66 ns with individual components of 1.82 and 3.752 ns (χ^2 = 1.77), which are in reasonable agreement with TCSPC results under the same experimental conditions (τ_{mean} = 2.77 ns, τ_1 = 2.15 ns, τ_2 = 3.85 ns, χ^2 = 1.13) and with those presented in Chapter 3, using excitation light at 440 nm. These results show the potential of our system to measure complex decay profiles with long lifetime components.

8.3.2.2.2 Mixture of dyes: Coumarin 6 and Coumarin 307

To further verify the ability of our instrument to resolve double exponential decays, solutions containing mixtures of Coumarin 6 (τ = 2.5 ns) and Coumarin 307 (τ = 5.3 ns) at different relative proportions were measured and compared against measurements in the cuvette-based instrument, which serve as validation due to the high temporal accuracy of the measurements in this system. To achieve the desired proportions, the concentration of Coumarin 6 was kept fixed at ~6 μM and the concentration of Coumarin 307 in each solution was varied accordingly. Concentrations of the stock solutions of both dyes were calculated from absorbance measurements in the spectrophotometer (UV-3101PC, Shimadzu, Japan) using a molar extinction coefficient of 54 × 10^3 cm^{-1}/M at 460 nm for Coumarin 6 and 20 × 10^3 cm^{-1}/M at 460 nm for Coumarin 307 [407]. Fluorescence lifetime measurements were carried at 405 nm excitation and 20 MHz repetition rate with fluorescence detection at 525 nm centre wavelength. In the low-cost system, detection was realised using 4 detection windows and 256 bins. In the cuvette-system, TCSPC was realised using 4096 bins. Figure 8.7 compares the fluorescence lifetime curves measured in both instruments.

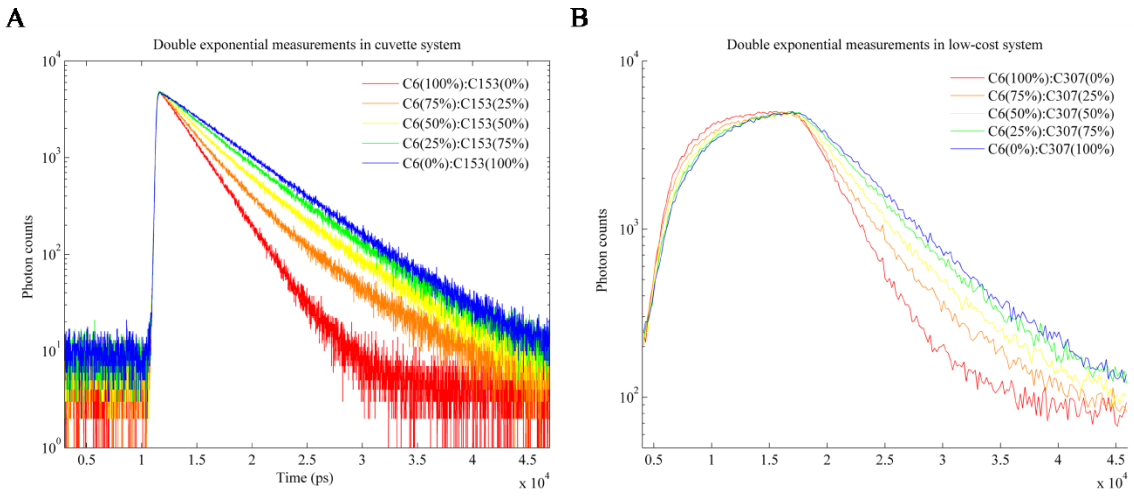

Figure 8.7 Fluorescence intensity decay profiles of mixture solutions of Coumarin 6 and Coumarin 307 measured in (A) the cuvette-based instrument and in (B) the low-cost system. The acquisition time was 5 s, in both instruments.

Analysis of the fluorescence lifetime decays was realised using *FLIMfit*. Results for the intensity weighted mean lifetimes are presented in Figure 8.8, including comparing with the expected results from theory.

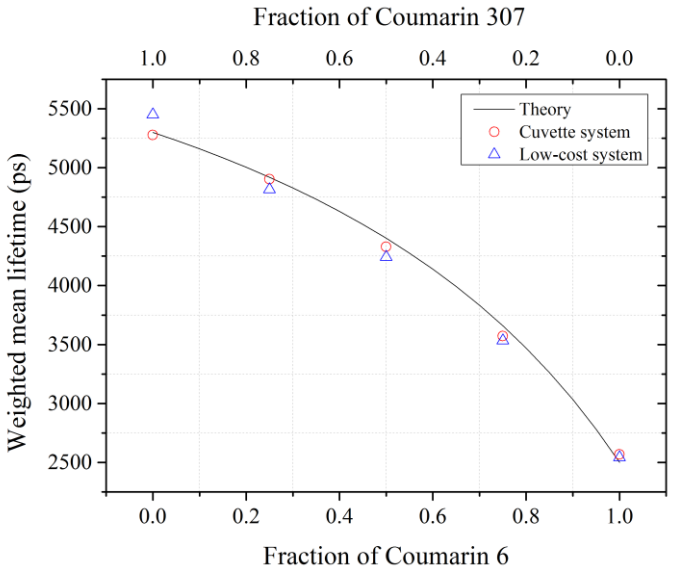

Figure 8.8 Intensity weighted mean fluorescence lifetimes of Coumarin 6 and Coumarin 307 solutions and comparison with values expected from theory. Data of pure solutions were fitted to a single exponential decay model, while data of mixture solutions were fitted to double exponential decay models. Analysis of data was realised using *FLIMfit*.

From Figure 8.8, we verify that the weighted mean fluorescence lifetime measured with the low-cost instrument is in excellent agreement with that measured in the cuvette-based system using TCSPC detection. This is in spite of the fact that TCSPC was realised with 4096 bins, which corresponds to a bin width of approximately 12 ps at 20 MHz against ~195 ps in the FPGA. With respect to the relative contributions of Coumarin 6 and Coumarin 307 to the fluorescence profiles, results show that the low-cost system can resolve the lifetime and relative proportions of both fluorophores although with lower accuracy than TCSPC (see Figure 8.9). Interestingly, the fitting produces an overestimation of

Coumarin 6 fluorescence lifetime with decreasing contribution from this fluorophore. In contrast, there is an underestimation of the Coumarin 307 fluorescence lifetime, which is more pronounced when this fluorophore is present in lesser amounts. This error is less apparent in TCSPC data. The number of photons detected during the acquisition of the data in the low-cost instrument (approximately 3.5×10^5 photons, on average) is lower than with TCSPC acquisition (approximately 2.0×10^6 photons, onn average), which results in a lower SNR (see Figure 8.7). This deviation can also be produced by the longer IRF of the low-cost system, which may reduce the sensitivity of the system for resolving complex decays.

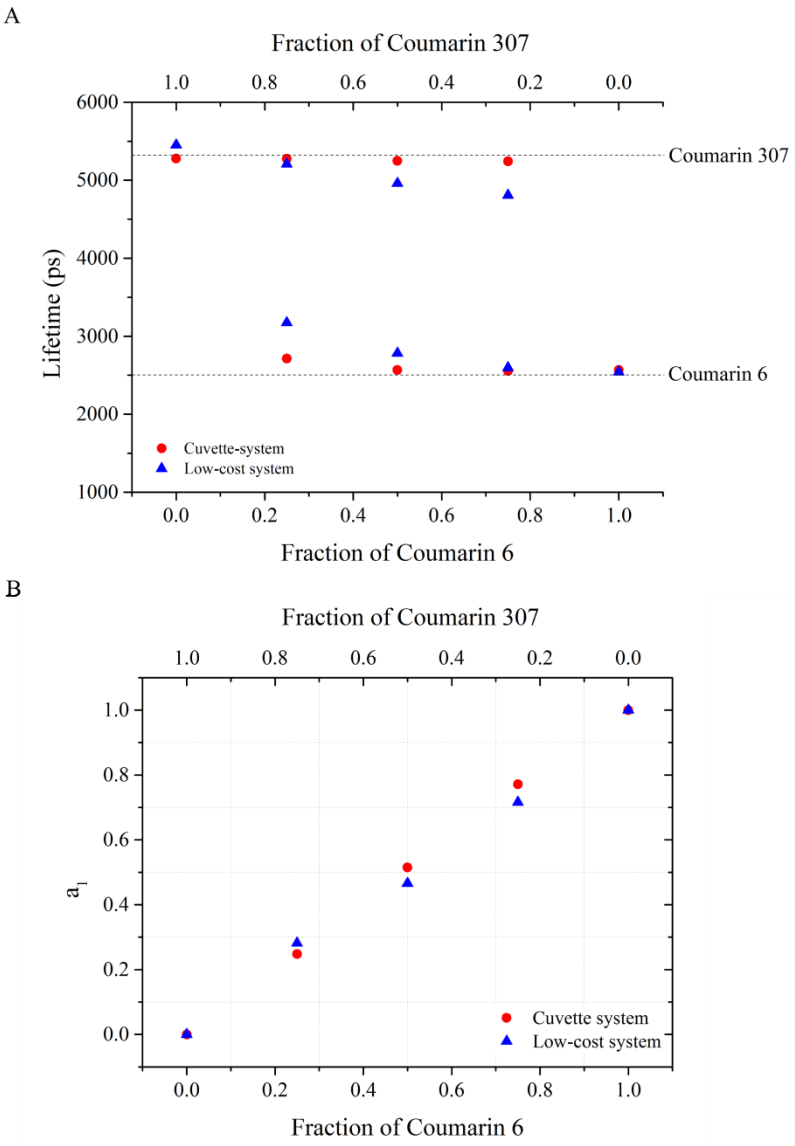

Figure 8.9 (A) Comparison between fluorescence lifetime components extracted for Coumarin 6 and Coumarin 307 measured with both instruments. Dashed lines represent the expected fluorescence lifetimes of pure Coumarin 6 (τ_{C6} = 2.5 ns)and Coumarin 307 solutions in ethanol (τ_{C307} = 5.3 ns). (B) Relative proportion of Coumarin 6 (a_1) calculated as described in section 2.4.

In summary, these results demonstrate that the low-cost instrument presented in this chapter can analyse single and double exponential decay profiles with reasonable accuracy. It was demonstrated

that, for complex decays profiles simulated using two fluorophores, it is possible to estimate the fluorescence lifetimes of each fluorophore contributing to the decay and their relative proportions with comparable results to TCSPC-based detection. As discussed in Chapter 4 and further demonstrated in Chapters 5 and 6, biological tissues exhibit complex multiexponential profiles, typically with more than two fluorophores. Because such complex profiles are difficult to analyse, more simplistic models using two exponentials are commonly used to describe data from biological specimens. Hence, the possibility of resolving double exponential decays using the low-cost instrument is of relevance towards its application to autofluorescence measurements of biological tissue, which is demonstrated in the following section.

8.4 Tissue autofluorescence measurements

In order to verify the suitability of our low-cost instrument to characterise the complex autofluorescence signal from biological specimens, the autofluorescence lifetimes of fresh lamb kidneys were measured using both the low-cost system and the cuvette-based TCPSC system. Lamb kidney can be easily acquired from the local abattoir and has a heterogeneous structure, comprising several different anatomical regions that can easily be identified within a small area (see Figure 8.10). This provides useful sources of autofluorescence lifetime contrast due to their different biochemical and structural compositions. Furthermore, the autofluorescence signal in kidney specimens has been associated with the presence of various types of collagens [408], lipofuscin granules [409] and NAD(P)H [409], [410], and therefore we should expect a strong autofluorescence signal at the excitation and emission wavelengths used in our experiments. We note, however, that despite all kidney samples being acquired fresh from the abattoir, there is no information regarding the time *post-mortem* at which these measurements were realised and therefore it is possible that the contribution of NAD(P)H to the autofluorescence signal is negligible. Overall, since our aim is to find contrast within the sample via its characteristic autofluorescence lifetime, lamb kidneys represent convenient test samples for our instrument.

The experiments reported below were realised using 405 nm excitation light at 20 MHz laser repetition rate. Fluorescence from the sample was collected with centre wavelength at 525 nm, as discussed previously in this chapter. In both systems, light was delivered and collected from the samples via a fibre-optic bundle. Detection in the low-cost system was realised using 4 detection windows and 256 bins. In the cuvette-system, TCSPC acquisition was realised with 1024 bins.

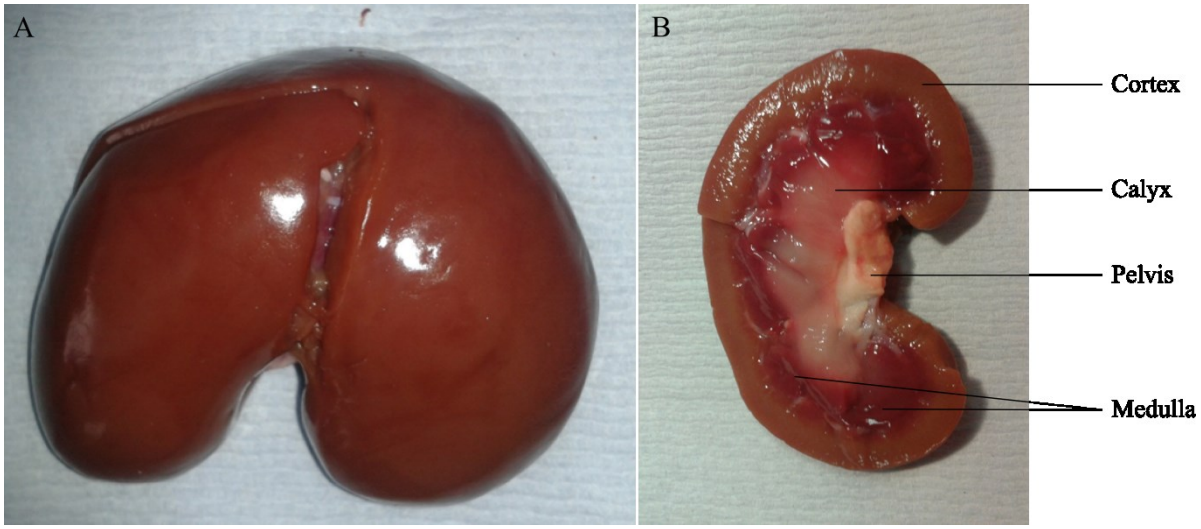

Figure 8.10 (A) External surface of lamb kidney. (B) Lamb kidney cut in half, revealing different anatomical regions of interest.

8.4.1 External surface of kidney

Initially, measurements were realised in the external surface of the kidney, by positioning the fibre-optic probe in the locations indicated in Figure 8.11. The probe tip was approximately 1 mm away from the tissue and a total of three measurements were taken in each location.

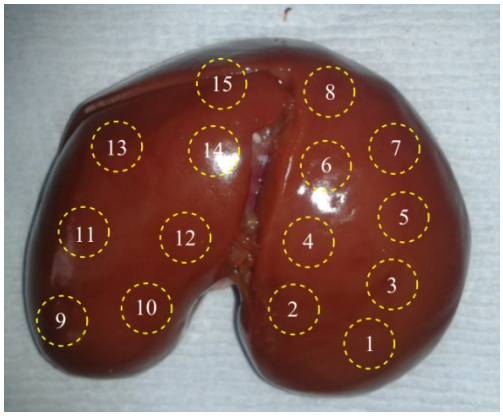

Figure 8.11 Location of the measurements in the external surface of the kidney.

As expected, the autofluorescence signal from lamb kidney yields a complex exponential decay profile, with at least three components. Table 8.3 compares the double and triple exponential fitting results of data collected with both instruments.

Table 8.3 Summary of the results produced by fitting double and triple exponential models to data collected in both instruments. Results show mean ± standard deviation (n = 15).

Parameter	Low-cost system (FPGA)		Cuvette-based system (TCSPC)	
	Double exponential	Triple exponential	Double exponential	Triple exponential
τ_1 (ns)	1.11 ± 0.10	0.76 ± 0.24	0.53 ± 0.03	0.20 ± 0.03
τ_2 (ns)	4.92 ± 0.26	3.32 ± 0.98	4.30 ± 0.16	1.70 ± 0.20
τ_3 (ns)	-	8.26 ± 1.12	-	6.93 ± 0.72
τ_{mean} (ns)	2.55 ± 0.15	2.66 ± 0.18	2.54 ± 0.15	2.73 ± 0.16
χ^2	2.58 ± 0.30	1.61 ± 0.31	2.11 ± 0.26	1.30 ± 0.08

The cuvette-based TCSPC results in Table 8.3 indicate the presence of a very short component (~ 200 ps) in the fluorescence decay, which can only be resolved by fitting three components to the TCSPC data. Indeed, the low-cost instrument fails to resolve this very short component and therefore the results for each component differ significantly from that of TCSPC, although the weighted mean lifetimes are in good agreement for tri-exponential fittings and in excellent agreement for double exponential fits. Overall, these results suggest that our instrument is not as sensitive to short lifetimes as the TCSPC measurement, possibly due to the longer rising and falling edges of the IRF compared to that using picosecond excitation pulses, as demonstrated in section 8.3.1. Since we have demonstrated the sensitivity of the detection method to short fluorescence lifetime decays using picosecond excitation pulses (see section 7.5.2.2), albeit at 40 MHz excitation frequency, it is possible that the longer excitation pulses used in this setup decreases the sensitivity of the detection to short decays. Nevertheless, the results presented in Figure 8.12, illustrating the spatial variation of the weighted mean fluorescence lifetime (extracted from a double exponential fitting model), demonstrate an excellent agreement between both setups, which is confirmed by the strong correlation between measurements for each position (see Figure 8.12B). To summarise, the autofluorescence lifetime variations read out by the "gold-standard" TCSPC setup can also be detected by the low-cost system, which is an encouraging step towards reading out intrinsic contrast in tissue with a low-cost approach. Typically, variations of autofluorescence lifetime in tissue due to disease can be on the order of a few hundreds of picoseconds (see Chapters 5 and 6), which is similar to the magnitude of the variations read out in this experiment, as illustrated in Figure 8.12A.

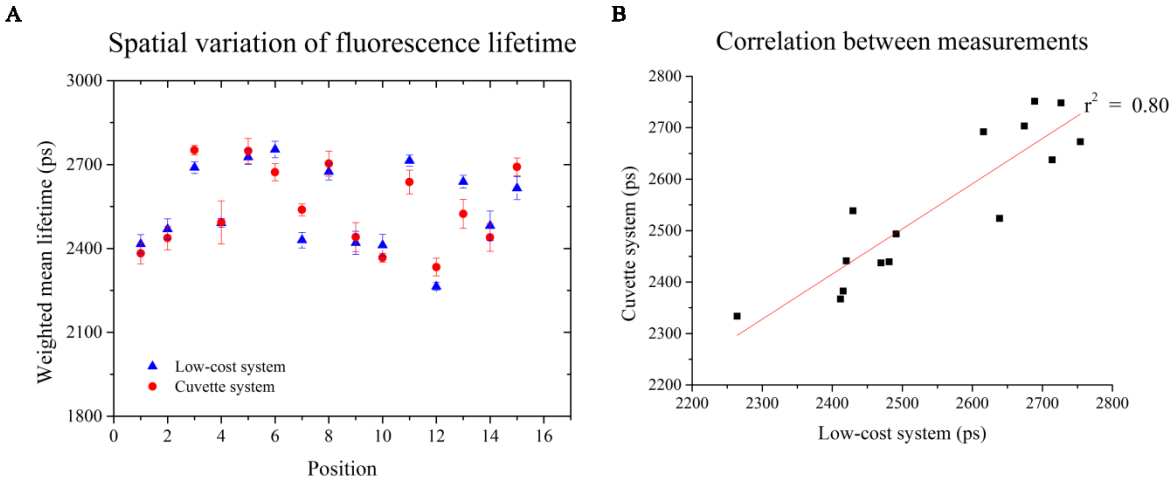

Figure 8.12 (A) Spatial variation of autofluorescence lifetime measured with both systems. Data shows the weighted mean lifetime extracted from a double exponential fitting. (B) Correlation between cuvette system and low-cost system for each position. A linear fit to the data output an r^2 of 0.80 or, similarly, a Pearson coefficient r of 0.89.

8.4.2 Internal structure of kidney

The results presented in the previous section demonstrate that the low-cost instrument can read out the mean autofluorescence lifetime from biological samples with comparable temporal accuracy of that provided by the TCSPC-based instrument. In this section, we aim to find intrinsic contrast between different structures that exist in a lamb kidney (see Figure 8.10B) using their characteristic autofluorescence lifetimes. For that purpose, a lamb kidney was cut in half, revealing (at least) four different structures that can be easily identified macroscopically and from which measurements were realised as indicated in Figure 8.13A. A total of three measurements were taken in each location and for each single acquisition the probe was taken away from the sample and repositioned, and thus the standard deviation of each measurement reflects also the variation of its location.

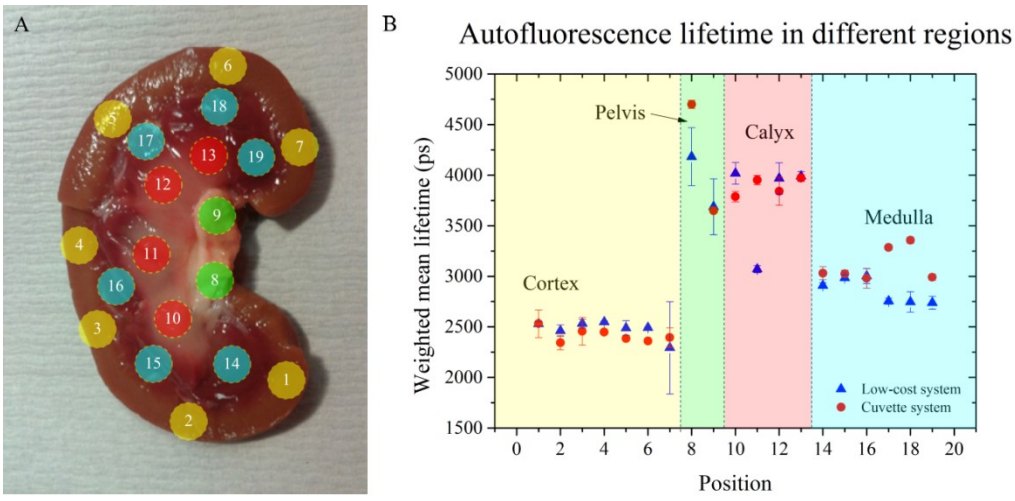

Figure 8.13 (A) Location of the measurements in each internal structure of a lamb kidney. Colour legend: cortex (yellow); pelvis (green); calyx (red); medulla (blue). Numbers and colours identify the position and region from each measurement was taken in Figure 8.13B. (B) Autofluorescence lifetime in different regions. Data show weighted mean fluorescence lifetime extracted from a double exponential fitting.

The results presented in Figure 8.13B show that both instruments measured different lifetimes for different structures, which is further confirmed when we average all acquisitions in each region (see Figure 8.14). Moreover, as in Figure 8.12A, we verify that variations of lifetime detected by the cuvette-based system are also detected by the low-cost instrument. In one particular measurement (position 11), we found a difference of approximately 1 ns between both systems. Because the standard deviation of this measurement with the low-cost system is low (~45 ps), it is possible that, rather than a difference between systems, this measurement reflects an acquisition from a different location in the tissue. Given the close proximity of the calyx to the medulla, it is likely that this measurement was taken inadvertently from the medulla, which would also explain the close fluorescence lifetime of this measurement with that of medulla. Overall, if we calculate the correlation between the average autofluorescence lifetimes extracted at each position from both systems, we achieve a Pearson coefficient *r* of 0.90, which is in close agreement to that extracted from previous measurements (see Figure 8.12) and demonstrates a strong correlation between measurements at each position in the two systems.

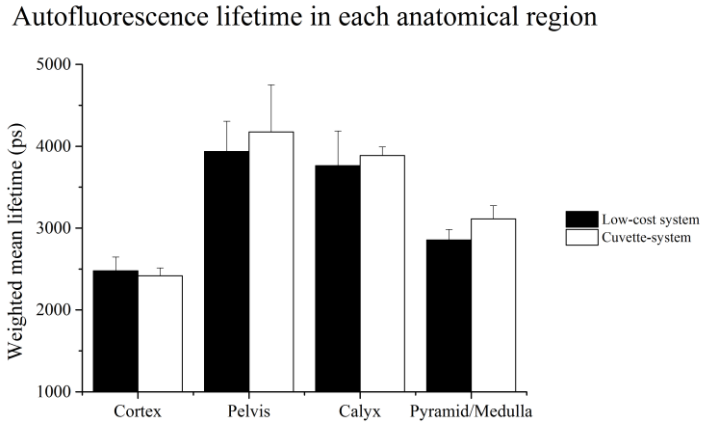

Figure 8.14 Average autofluorescence lifetime in each region, taking in consideration each single acquisition. Number of acquisitions in each region: cortex (n = 21); pelvis (n = 6); calyx (n = 12); medulla (n = 18).

Despite giving us a general idea of how the average autofluorescence lifetime varies between regions, the results presented in Figure 8.13B and Figure 8.14 do not provide any indication of how well can both systems separate out different regions through lifetime. For that purpose, one can use the Cohen's d coefficient, which was previously introduced in section 6.7.1.4.5, to quantitatively determine the separation between each region's data and therefore provide a robust comparison between the ability of each system to read out the intrinsic contrast in tissue. Alternatively, if one considers that the autofluorescence lifetime in each region is normally distributed over a number of repeated measurements, the resulting histogram can be fitted to a Gaussian profile and a qualitative interpretation of the data can be realised. Figure 8.15 shows the results of fitting Gaussian curves to histograms of the weighted mean lifetime and Table 8.4 shows the Cohen's d coefficient calculated for every combination of regions.

As expected, the results indicate that, in general, the cuvette-based TCSPC system provides better separation between regions of interest, which is demonstrated by the narrower and greater separation of the Gaussian profiles and higher Cohen's d coefficients. Nonetheless, Figure 8.15 demonstrates that the autofluorescence lifetime measured with the low-cost instrument provides sufficient contrast that allows clear separation of different anatomical regions, in particular cortex, medulla and calyx. It is also possible to separate out measurements of the pelvis with those of cortex and medulla, although it is challenging to differentiate pelvis from calyx, with both instruments. We also note that we achieved lower standard deviation for measurements of the medulla using the low-cost system, which translates in a narrower Gaussian profile compared to that produced by TCSPC measurements. Given the variation observed in the measurements of positions 17 to 19 (see Figure 8.13B), it is possible that these measurements were realised at different locations in the sample, therefore yielding different autofluorescence lifetimes. Overall, these results demonstrate that our low-cost instrument can read out intrinsic contrast in biological tissue by means of autofluorescence lifetime, although with lower accuracy than the cuvette-based TCSPC system.

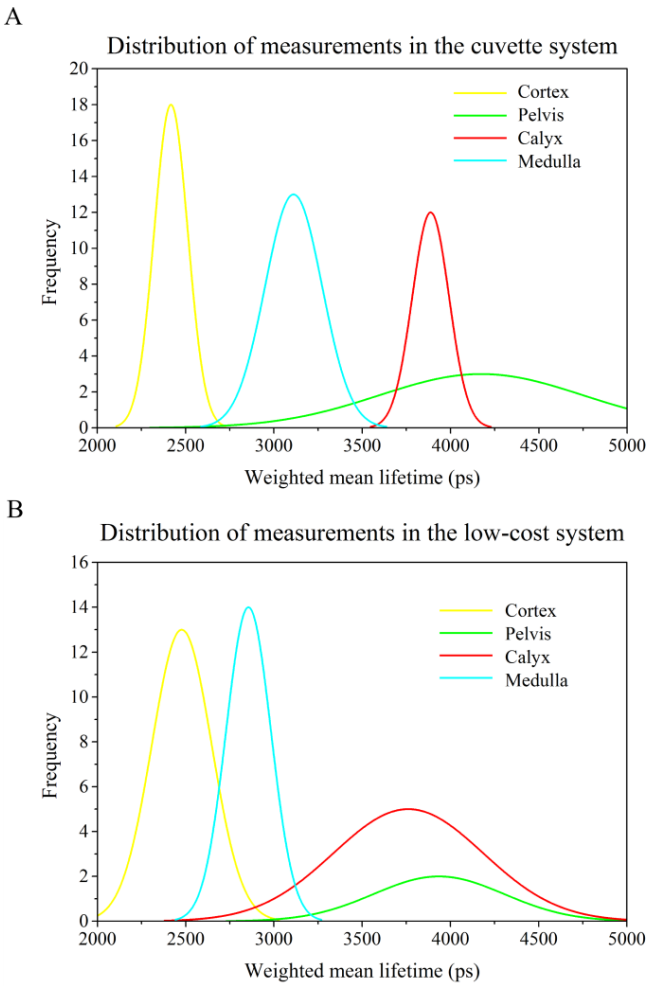

Figure 8.15 Autofluorescence lifetime distribution in each anatomical region measured with (A) the cuvette system and (B) the low-cost system. Curves presented are the result of Gaussian fits to the weighted mean lifetime histogram of all acquisitions.

Table 8.4 Cohen's d statistics for the low-cost system and the cuvette-system. Best separation in each pair of regions is highlighted in bold.

Regions	Low-cost system	Cuvette system
Cortex – Pelvis	**5.06**	4.25
Cortex – Calyx	3.97	**14.70**
Cortex – Medulla	2.53	**5.23**
Pelvis – Calyx	0.44	**0.63**
Pelvis – Medulla	**3.90**	2.51
Calyx – Medulla	2.90	**5.70**

8.5 Conclusions and summary

This chapter presented the implementation of a low-cost instrument for autofluorescence lifetime measurements of biological tissue, utilising inexpensive modulated laser diodes for excitation and standard uncooled photon counting PMTs in combination with custom electronic circuitry - presented in Chapter 7 - for time-resolved detection of the fluorescence signal. The potential of this instrument to read out intrinsic contrast in biological specimens was investigated and validated against a well-characterised cuvette-based time-resolved spectrofluorometer that utilises commercially available laser diodes providing picosecond optical pulses and "gold standard" TCSPC electronics to realise time-resolved detection of fluorescence with maximum temporal accuracy.

With respect to the illumination setup, our low-cost instrument utilises a cheap laser diode (cost ~£50), which is externally modulated by a function generator, providing a "distorted" sinusoidal waveform, and a current controller to achieve optical pulses of approximately 3 ns width. Although this pulse width corresponds to an order magnitude longer than that obtained from commercially available laser diodes, with this configuration we demonstrated that our instrument can realise time-resolved detection of fluorescence with comparable utility to TCSPC. This was primarily demonstrated by measuring a number of reference fluorophores presenting single exponential decay characteristics, from which decays were successfully described using two detection architectures (4 windows and 256 bins; and 8 windows and 64 bins). Here, it was interesting to note that the temporal accuracy of the measurements was not affected by altering the configuration of the detection. This is because the decrease in the number of detection windows is balanced by an increase in the number of times that each detection window samples the decay, with increasing offset, which translates in a greater temporal resolution.

We also verified the suitability of our system to resolve complex exponential decays by measuring a known fluorophore presenting two exponential components (FAD) and by creating mixture solutions of two fluorophores with single exponential characteristics, namely Coumarin 6 and Coumarin 307.

The results presented in section 8.3.2.2 demonstrate that the low-cost instrument can accurately describe these complex exponential decays and only minor deviations were found from measurements with the cuvette-based TCSPC system. The ability of our system to resolve double exponential decays is of great interest and relevance towards its application in biological studies. The autofluorescence of biological tissue is typically a complex signal, for which a number of fluorophores can contribute, as discussed in Chapters 3, 5 and 6. In an autofluorescence decay profile, this complexity translates into a great number of exponential components, which can reflect the number of fluorophores present in the tissue or, in a more complicated scenario, their conformations (e.g. NAD(P)H and FAD present double exponential decays, which are attributed to their stacked and open configurations [1]), protein-binding (e.g. NAD(P)H and FAD can bind to different proteins [1], [130]) or crosslinking (e.g. collagen). Obviously, it is challenging (not to say impossible) to discriminate between all these sources of signal in tissue and the usual pragmatic approach is to simplify the model so that the autofluorescence signal can be described by a small number of exponential components, typically two, e.g. [77], [78]. Hence, the ability of our instrument to resolve double exponential decays in the range of lifetimes analysed (2 to 5 ns) suggests potential to describe complex autofluorescence signals, which is an important step towards translation of this instrument into biomedical research applications.

Ultimately, the interest in autofluorescence for clinical research lies in its potential to provide label-free optical contrast and, therefore, the suitability of our low-cost instrument to read out intrinsic contrast in biological specimens was investigated. As a preliminary approach to the measurement of biological samples, we measured the autofluorescence lifetime of lamb kidney, which is a convenient test sample due to the number of internal structures that constitute sources of autofluorescence lifetime contrast. The results presented in section 8.4.2 indicate that our instrument can differentiate anatomical regions in kidney through the mean autofluorescence lifetime (using a double exponential decay model to fit the data) with precision comparable to TCSPC-based measurements, where both utilise a fibre-optic probe. This is confirmed by the strong correlation observed between measurements with each instrument. In summary, we have demonstrated that it is possible to read out intrinsic contrast in biological tissue using a low-cost instrument by means of time-resolved autofluorescence detection and with ability comparable to the leading techniques in the field, yet at significantly lower cost. The claim of low-cost is further demonstrated in Table 8.5, where we compare the cost of implementation of our instrument against the “gold standard” TCSPC system presented in Chapter 4, for one excitation wavelength and one detection channel.

Table 8.5 Summary of the approximate costs of the low-cost system and the single-point time-resolved spectrofluorometer presented in Chapter 4. Costs associated with optical elements, such as filters or mounts, were not included, as they are identical in both instruments.

Components	TCSPC-based system	Low-cost system
Laser diode and drivers	£14000	£2250 *
PMT	£2000	£800
PMT driver (power supply and cooling circuitry)	£1500	£10
TCSPC / FPGA & CFD	£17000	£300 **
Total	£34500	£3360

* includes laser diode, current and temperature controller, laser diode mount and signal generator.

** refers to cost of components only.

Table 8.5 demonstrates that our instrument, as it stands, can be implemented for less than 10% of the component cost of its "gold standard" version. This difference would significantly increase if more excitation wavelengths were to be used along with multispectral detection. Obviously, in both cases, there is scope to reduce the total costs. For example, in the TCSPC-based system, the PMT or TCPSC card could be replaced by lower cost models, which would reduce the cost of the instrument at the expense of its temporal accuracy. The cost of the low-cost system is mostly driven by the laser diode temperature and current controllers and if two excitation wavelengths were to be used, additional laser drivers would be required, which would further increase the cost of the implementation. An alternative approach to these drivers could include the development of custom circuitry that would allow driving more than one laser diode at fast modulation frequencies using a single board. With respect to the detection components, there is not an obvious alternative to replace the photon counting PMTs. An interesting alternative could consist in utilising SPAD arrays to detect the fluorescence signal, which could be used as a single large area detector. This approach would be particularly interesting for spectrally-resolved detection, utilising a similar method to that of spectrometers, i.e. by dispersing the incoming fluorescence light into the array, and multiple pixels of the array could be utilised to realise detection at a single wavelength. The usage of SPAD arrays for time-resolved detection of fluorescence has been previously reported by others, e.g. [27], [28], [47], [382], [411], albeit not in a multispectral configuration.

A limitation of the low-cost system is related to the function generator used to modulate the laser diode, which is operated at its maximum frequency and thus the output signal is severely distorted and unstable, as demonstrated in section 8.3. There are several commercially available low-cost alternatives to this function generator, e.g. from Novatech Instruments or Analog Devices, which can provide sine and TTL output signals with adjustable amplitude, phase shift and frequency up to 150 MHz. As an additional advantage, these function generators can be provided as printed circuit boards,

which can easily be controlled via a microcontroller unit board, such as Arduino, thus facilitating their integration within a system that needs to be compact, portable and user-friendly.

In conclusion, we have demonstrated the potential of our instrument to read out label-free optical contrast from biological tissue by means of autofluorescence lifetime. We have validated this low-cost instrument against a "gold standard" setup utilising picosecond pulsed excitation lasers and TCSPC-based detection and demonstrated comparable ability to resolve complex autofluorescence signals. It should be noted that our instrument is not intended to replace a TCSPC-based research system, such as the one presented in Chapter 4. Rather, it constitutes an alternative approach towards translation of autofluorescence lifetime instrumentation into clinical practice, where cost is more important than temporal accuracy, providing the latter is sufficient to readout inherent contrast. For example, if clinical practicality of this instrument is demonstrated, one could envisage its deployment in several facilities for the same total cost of a single TCSPC-based instrument, which would yield obvious benefits, including with respect to the amount of data generated for clinical research. The benefits of realising TCSPC-based detection are mostly associated with its greater temporal resolution in comparison with other methods. For example, if one wants to study the mechanisms associated with complex energetic alterations in the heart following myocardial infarction (as discussed in Chapter 6), a low-cost instrument may not be capable of resolving such complex autofluorescence signals and therefore an instrument providing greater temporal accuracy, such as TCSPC, should be used. However, in clinical practice, one key issue is to find label-free optical contrast in tissue that could aid clinicians in their decision-making processes. If a low-cost instrument can provide sufficient contrast to discern healthy from diseased tissue, then it could have significant potential for clinical deployment.

9 Conclusions and outlook

Fluorescence measurements of endogenous fluorophores can provide means of label-free optical contrast in biological specimens and thus represent an attractive alternative to currently existing diagnostic techniques that utilise exogenous (and potentially harmful) contrast agents, particularly for *in vivo* investigations. In this thesis, the development and application of autofluorescence and diffuse reflectance spectroscopy instrumentation were presented. This work aimed to assist the translation of these label-free techniques into clinical diagnosis of osteoarthritis and cardiac disease.

Chapter 2 introduced the underlying principles of fluorescence, including a review of the most widely employed techniques for fluorescence lifetime measurements. The concept of autofluorescence in biological specimens was introduced in Chapter 3, along with a review of the fluorescence properties of the most common endogenous fluorophores in biological tissue, with particular emphasis on NADH, FAD and collagen. Given the relevance of these fluorophores to our investigations, we characterised their fluorescence properties under physiological conditions, thereby providing baseline values of their parameters for our investigations of osteoarthritis and heart disease. Chapter 4 discussed the optical spectroscopy techniques most relevant to biological tissue, with particular focus on steady-state and time-resolved fluorescence spectroscopy and white light reflectometry. The advantages and limitations of these techniques were discussed and examples were given of their implementation in clinical research. Also in this chapter, the development of a fibre-optic probe-based instrument for single-point spectrally- and time-resolved fluorescence measurements was presented, together with data from its application to fluorescence lifetime reference fluorophores. Two such instruments were developed for deployment in autofluorescence studies of osteoarthritis and heart disease, presented in Chapter 5 and 6, respectively. In light of the significant cost of the instrument presented in Chapter 4, the last part of this thesis concerned the development of compact and portable fibre-optic probe-based instrumentation utilizing low-cost FPGA-based circuitry, inexpensive laser diodes and photon counting PMTs. A comprehensive description of the development and characterisation of this instrument was presented in Chapter 7 and Chapter 8 described its application to readout label-free optical contrast in biological tissue.

9.1 Autofluorescence lifetime studies of osteoarthritis

The experimental work presented in Chapter 5 aimed to investigate the clinical potential of time-resolved autofluorescence for the early diagnosis of osteoarthritis.

The diagnosis of osteoarthritis is currently based on physical examination and imaging of the joints, typically with X-Ray or Magnetic Resonance Imaging. These modalities can report on structural

alterations of the cartilage, although usually only at late stages of the disease progression, when the alterations in the tissue are no longer reversible. An alternative approach is the visual inspection of the cartilage via arthroscopy. However, this is a surgically invasive procedure that can lead to further disruption of the connective tissue and so is more commonly employed at later stages of osteoarthritis. Overall, there is still lack of non- or minimally-invasive tools that can detect early structural and biochemical changes in articular cartilage associated with osteoarthritis and which could potentially offer new prevention and treatment options. In Chapter 5, we explore the hypothesis that the autofluorescence lifetime of articular cartilage is sensitive to osteoarthritis-induced degradation. To this end, the autofluorescence properties of articular cartilage were characterised and the origins of the contrast were investigated using a number of different digestive enzymes to induce cartilage degradation. Initially, porcine articular cartilage explants were measured using 355 nm excitation light at 80 MHz. Our results demonstrated that the mean autofluorescence lifetime of enzymatically digested samples was significantly shorter than that of untreated cartilage samples. Given the long fluorescence lifetime measured for these samples, which we attributed to the presence of collagen type II, subsequent experiments were realised using a lower repetition rate (5 MHz), which necessitated the use of an excitation laser at a slightly longer wavelength (375 nm). In order to investigate the autofluorescence signal of cartilage in an environment closer to that found in joints, we induced localised lesions in the surface of porcine cartilage. Using 375 nm excitation, we consistently measured significant decreases in the autofluorescence lifetime of enzymatically treated samples compared to untreated samples. The decrease in autofluorescence lifetime was found to be more pronounced when samples were treated with bacterial collagenase, a strong enzyme that primarily degrades collagen (the predominant fluorophore in cartilage tissue) but also depletes aggrecan from the tissue. In order to understand the origin of the contrast, samples were treated with trypsin and retinoic acid, which are known to deplete aggrecan from the tissue while maintaining the collagen network intact. Our results demonstrate that treatment with these compounds significantly decreased the autofluorescence lifetime of cartilage and so changes in this parameter cannot be attributed exclusively to the degradation of the collagen matrix. This result represents an important step towards the validation of this technique in the early diagnosis of osteoarthritis, given that the early stages of disease progression are mainly characterised by loss of aggrecan while the collagen matrix is maintained relatively unchanged.

To progress our investigations towards the real physiological context, we worked to measure the autofluorescence lifetime of “naturally occurring” osteoarthritis (instead of enzymatically induced degradation) in murine knee joints. However, we did not observe contrast between healthy and damaged samples. A few hypotheses have been suggested to explain our results:

1. Although osteoarthritis developed naturally in the knee, it was artificially induced by cutting of the ligaments, which by itself can promote inflammation with concomitant proliferation of collagen to form scar tissue. Given the long autofluorescence lifetime of collagen, its proliferation in an inflammatory process could tend to increase the mean autofluorescence lifetime of cartilage – in contrast to the expected decrease caused by cartilage degradation.
2. In osteoarthritis, the medial region of the knee is typically more affected than the lateral region. Given the size of the samples and heterogeneity of the degradation, we were not able to identify any contrast between these regions due to the limited spatial resolution of our point probe instrument (~1 mm).
3. The cartilage of murine knee joints is very thin (~100 μm), therefore it is possible that excitation light could have travelled through its entire thickness and reached the subchondral bone underneath, which presents a mean autofluorescence lifetime comparable to that of healthy articular cartilage.

Finally, we also investigated the autofluorescence lifetime signature of human cartilage, both in samples treated with digestive enzymes and in samples where the disease developed naturally. In samples treated with retinoic acid, we measured a significant decrease in the mean autofluorescence lifetime relative to untreated samples at multiple emission wavelengths, which confirmed our previous results obtained using animal tissue. Here, we were able to distinguish between treated and untreated cartilage samples with sensitivity and specificity of 100% and 97%, respectively, which demonstrates the potential of our system to provide label-free contrast of degraded articular cartilage. We also aimed to read out intrinsic contrast in samples presenting naturally occurring degradation. However, we were unable to discriminate between healthier and damaged regions, most likely due the severe state of degradation presented by these samples over the entire cartilage area. Nonetheless, in general, the mean autofluorescence lifetimes measured in these samples were shorter than that typically measured in healthy untreated cartilage samples, which is an encouraging step towards the application of this technique in the detection of osteoarthritis. The biggest limitation of this investigation consisted of the lack of human samples presenting minor signs of degradation, as in early osteoarthritis. This is because such samples rarely become available. An alternative approach would be to measure cartilage samples from cadavers and we are currently working towards that end.

Given these observations and conclusions, work is currently underway to develop a clinically viable autofluorescence lifetime imaging arthroscope that can operate in parallel with existing techniques during arthroscopy. Given the great heterogeneity observed in naturally occurring osteoarthritic samples, we believe that an imaging modality is better suited to aid clinical diagnosis *in vivo* compared to a single point instrument. Once the clinical practicality and viability of this instrument is demonstrated in *ex vivo* samples, we aim to realise the first *in vivo* autofluorescence lifetime study of

articular cartilage in man, with a view to developing this technology for routine use in clinical diagnosis and monitoring of osteoarthritis.

9.2 Autofluorescence and diffuse reflectance studies of cardiac tissue

In Chapter 6 we explored the potential of time-resolved fluorescence spectroscopy and white light reflectometry to readout label-free contrast in cardiac disease, with a view to developing new cardiac diagnostic tools.

Using an *ex vivo* Langendorff rat model, the autofluorescence and diffuse reflectance signatures of cardiac tissue were investigated under different stress conditions, namely hypoxia and glucose deprivation. The autofluorescence readouts that accompany the metabolic stress induced by deprivation of oxygen or glucose were characterised to serve as a baseline for *in vivo* investigations of a myocardial infarction model in rats. Here, our investigations were focussed on the characterisation of the myocardium autofluorescence and diffuse reflectance signatures at 1, 2, 4 and 16 weeks post-infarction. Our results revealed structural and metabolic alterations at different stages of disease progression, not only in the anatomical area of infarction but, more excitingly, also in remodelled remote myocardium. Structural alterations in the myocardium are the result of collagen deposition as part of the healing process following infarction. Given the long fluorescence lifetime of collagen relative to NADH and FAD, the most predominant fluorophores in cardiac tissue, structural alterations are characterised by an increase in the mean autofluorescence lifetime of all spectral detection channels of the time-resolved spectrofluorometer used in the measurements - this is most pronounced at shorter emission wavelengths where collagen fluoresces most strongly. Given the large increase in collagen content in all regions investigated, particularly at later stages, changes in the autofluorescence signal due to metabolic alterations were less pronounced. We did, however, observe statistically significant decreases in the short lifetime τ_1 of the autofluorescence decays associated with NADH and FAD that cannot be explained by an increase in collagen content. These changes were most pronounced at the earliest stages of disease progression, when collagen deposition was not yet extensive, which suggests that they are indeed associated with metabolic remodelling of the myocardium. Furthermore, these changes were similar to those observed in the *ex vivo* Langendorff model following oxygen deprivation, which further supports this hypothesis. Interestingly, these changes were predominantly observed in regions remote from the scar where collagen deposition is less extensive, particularly in the posterior wall of the left ventricle, and can potentially reflect an increased workload of this region to maintain the overall function of the ventricle.

The potential of our instrument to discriminate healthy from diseased myocardium was also investigated and, in general, the results indicated excellent discrimination capabilities, not only in areas directly affected by the infarction but also in remote regions to the infarction, particularly at

earlier stages of disease progression. This result demonstrates the potential of our instrument to discriminate healthy from diseased myocardium, even when the differences between the two states are subtle.

The work presented in Chapter 6 prompted the development of a clinically viable instrument to realise single point measurements of the human heart *in vivo*, during open chest procedures. Although this is still ongoing work, we expect to realise the first in man time-resolved autofluorescence measurement in the early months of 2015. If clinical viability is demonstrated, this study could pave the way towards the translation of autofluorescence lifetime measurements into clinical practice in the context of cardiac diagnosis.

9.3 Low-cost instrumentation for single point time-resolved spectrofluorometry

The clinical impact of autofluorescence lifetime measurements for label-free diagnosis would be significantly enhanced if the cost of the instrumentation could be reduced below what is achievable with "gold-standard" commercial TCSPC-based technology. To this end, in Chapters 7 and 8 we presented an alternative approach to TCSPC-based autofluorescence lifetime measurements that builds upon a previously published detection methodology [55]. This new instrument utilises FPGA circuitry, relatively inexpensive laser diodes and photon counting PMTs. The potential of this instrument to read out label-free contrast in biological specimens was investigated against a well-characterised state-of-the-art TCSPC-based instrument, previously developed in our laboratory. The new low-cost instrument showed comparable temporal accuracy in the determination of reference fluorophore lifetimes or measurements of complex decays emanating from biological tissue. This instrument could potentially be implemented for approximately 10% of the cost of the "gold-standard" TCSPC-based version, which would significantly enhance the potential of autofluorescence lifetime metrology for clinical deployment and commercial development.

One current limitation of this instrument is the lack of spectral resolution that can be important for some applications, as in the case of heart disease. Hence, future work could explore e.g. SPAD technology to implement time-resolved detection in multiple spectral channels, which would further facilitate the translation of this technique into clinical practice.

9.4 Final remarks

In summary, the work presented in this thesis has demonstrated the potential of autofluorescence lifetime measurements to discriminate healthy and diseased tissue in osteoarthritis and heart disease. Progress has been made on both topics and work is now focussed on the translation of autofluorescence lifetime metrology to *in vivo* clinical measurements. In osteoarthritis, our work demonstrated the potential of autofluorescence lifetime to provide a label-free readout of early

changes in the cartilage matrix due to degradation, which is beyond current diagnostic techniques. Further work in this field is still required to increase the sample size (of *ex vivo* human samples) and assess the feasibility and viability of *in vivo* measurements. The ultimate goal of this project is to develop a clinically viable instrument to realise *in vivo* autofluorescence lifetime measurements during knee arthroscopy. With respect to cardiac tissue measurements, the work presented in this thesis has stimulated the development of a clinical instrument to readout myocardial metabolic and structural abnormalities during heart surgery. In the short term, the investigation will be focussed on understanding whether the contrast observed in animal models is reproducible in the human heart. Provided that the clinical viability of this instrument is verified in this preliminary study, we envisage that autofluorescence lifetime measurements could find wide application in cardiac diagnosis, either by monitoring the metabolic state of the heart during heart surgery or by aiding diagnosis via implementation of a less invasive catheter-based approach. In any case, the work presented in this thesis constitutes a first step towards the implementation of autofluorescence lifetime metrology as a label-free diagnostic tool for heart disease.

References

[1] J. R. Lakowicz, *Principles of Fluorescence Spectroscopy*, vol. 13, no. 2. Springer, 1999, p. 029901.

[2] M. Inaguma and K. Hashimoto, "Porphyrin-like fluorescence in oral cancer: In vivo fluorescence spectral characterization of lesions by use of a near-ultraviolet excited autofluorescence diagnosis system and separation of fluorescent extracts by capillary electrophoresis.," *Cancer*, vol. 86, no. 11, pp. 2201–11, Dec. 1999.

[3] Y. Ti, P. Chen, and W.-C. Lin, "In vivo characterization of myocardial infarction using fluorescence and diffuse reflectance spectroscopy.," *J. Biomed. Opt.*, vol. 15, no. 3, p. 037009, 2010.

[4] Y. Pu, J. Xue, W. Wang, B. Xu, Y. Gu, R. Tang, E. Ackerstaff, J. a Koutcher, S. Achilefu, and R. R. Alfano, "Native fluorescence spectroscopy reveals spectral differences among prostate cancer cell lines with different risk levels.," *J. Biomed. Opt.*, vol. 18, no. 8, p. 87002, Aug. 2013.

[5] E. Blatt, F. E. Treloar, K. P. Ghiggino, and R. G. Gilbert, "Viscosity and temperature dependence of fluorescence lifetimes of anthracene and 9-methylanthracene," *J. Phys. Chem.*, vol. 85, no. 19, pp. 2810–2816, Sep. 1981.

[6] M. Mycek, P. Urayama, K. Heyman, and M. Bussey, "Using POPOP's viscosity-dependent lifetime as a picosecond resolution standard in near-UV fluorescence lifetime imaging microscopy," in *Manipulation and Analysis of Biomolecules, Cells, and Tissues,*, 2003, vol. 4962, no. 734, pp. 143–150.

[7] R. Leenders, M. Kooijman, A. van Hoek, C. Veeger, and A. J. W. G. Visser, "Flavin dynamics in reduced flavodoxins," *Eur. J. Biochem.*, vol. 45, pp. 37–45, 1993.

[8] H. D. Vishwasrao, A. A. Heikal, K. A. Kasischke, and W. W. Webb, "Conformational dependence of intracellular NADH on metabolic state revealed by associated fluorescence anisotropy.," *J. Biol. Chem.*, vol. 280, no. 26, pp. 25119–26, Jul. 2005.

[9] T. S. Blacker, R. J. Marsh, M. R. Duchen, and A. J. Bain, "Activated barrier crossing dynamics in the non-radiative decay of NADH and NADPH," *Chem. Phys.*, vol. 422, pp. 184–194, Aug. 2013.

[10] T. Nakabayashi, S. Oshita, R. Sumikawa, F. Sun, M. Kinjo, and N. Ohta, "pH dependence of the fluorescence lifetime of enhanced yellow fluorescent protein in solution and cells," *J. Photochem. Photobiol. A Chem.*, vol. 235, pp. 65–71, May 2012.

[11] T. S. Blacker, Z. F. Mann, J. E. Gale, M. Ziegler, A. J. Bain, G. Szabadkai, and M. R. Duchen, "Separating NADH and NADPH fluorescence in live cells and tissues using FLIM.," *Nat. Commun.*, vol. 5, no. May, p. 3936, Jan. 2014.

[12] G. C. Tang, a Pradhan, and R. R. Alfano, "Spectroscopic differences between human cancer and normal lung and breast tissues.," *Lasers Surg. Med.*, vol. 9, no. 3, pp. 290–5, Jan. 1989.

[13] A. Pradhan, P. Pal, G. Durocher, L. Villeneuve, A. Balassy, F. Babai, L. Gaboury, and L. Blanchard, "Steady state and time-resolved fluorescence properties of metastatic and non-metastatic malignant cells from different species.," *J. Photochem. Photobiol. B.*, vol. 31, no. 3, pp. 101–12, Dec. 1995.

[14] M.-A. Mycek, K. T. Schomacker, and N. S. Nishioka, "Colonic polyp differentiation using time-resolved autofluorescence spectroscopy," *Gastrointest. Endosc.*, vol. 48, no. 4, pp. 390–394, 1998.

[15] P. J. Tadrous, J. Siegel, P. French, S. Shousha, E.-N. Lalani, and G. W. H. Stamp, "Fluorescence lifetime imaging of unstained tissues: early results in human breast cancer.," *J. Pathol.*, vol. 199, no. 3, pp. 309–17, Mar. 2003.

[16] P. Uehlinger, T. Gabrecht, T. Glanzmann, J.-P. Ballini, A. Radu, S. Andrejevic, P. Monnier, and G. Wagnières, "In vivo time-resolved spectroscopy of the human bronchial early cancer autofluorescence.," *J. Biomed. Opt.*, vol. 14, no. 2, p. 024011, 2009.

[17] P. A. A. De Beule, C. Dunsby, N. P. Galletly, G. W. Stamp, A. C. Chu, U. Anand, P. Anand, C. D. Benham, A. Naylor, and P. French, "A hyperspectral fluorescence lifetime probe for skin cancer diagnosis.," *Rev. Sci. Instrum.*, vol. 78, no. 12, p. 123101, Dec. 2007.

[18] Y. Ardeshirpour, V. Chernomordik, M. Hassan, R. Zielinski, J. Capala, and A. Gandjbakhche, "In vivo fluorescence lifetime imaging for monitoring the efficacy of the cancer treatment.," *Clin. Cancer Res.*, vol. 20, no. 13, pp. 3531–9, Jul. 2014.

[19] A. J. Thompson, S. Coda, M. B. Sørensen, G. Kennedy, R. Patalay, U. Waitong-Brämming, P. a a De Beule, M. a a Neil, S. Andersson-Engels, N. Bendsøe, P. M. W. French, K. Svanberg, and C. Dunsby, "In vivo measurements of diffuse reflectance and time-resolved autofluorescence emission spectra of basal cell carcinomas.," *J. Biophotonics*, vol. 5, no. 3, pp. 240–54, Mar. 2012.

[20] M. Lam, D. R. Yankelevich, S. L. Tinling, R. F. Gandour-edwards, W. L. Monsky, D. G. Farwell, and L. Marcu, "In vivo validation of a bimodal technique combining time-resolved fluorescence spectroscopy and ultrasonic backscatter microscopy for diagnosis of oral carcinoma," *J. Biomed. Opt.*, no. 17(11), 2012.

[21] J. Phipps, Y. Sun, R. Saroufeem, N. Hatami, and L. Marcu, "Fluorescence lifetime imaging microscopy for the characterization of atherosclerotic plaques," in *Proceedings-Society of Photo-Optical Instrumentation Engineers*, 2009, vol. 7161, p. 71612G.

[22] J. Phipps, Y. Sun, R. Saroufeem, N. Hatami, M. C. Fishbein, and L. Marcu, "Fluorescence lifetime imaging for the characterization of the biochemical composition of atherosclerotic plaques.," *J. Biomed. Opt.*, vol. 16, no. 9, p. 096018, Sep. 2011.

[23] J. E. Phipps, Y. Sun, M. C. Fishbein, and L. Marcu, "A fluorescence lifetime imaging classification method to investigate the collagen to lipid ratio in fibrous caps of atherosclerotic plaque.," *Lasers Surg. Med.*, vol. 44, no. 7, pp. 564–71, Sep. 2012.

[24] J. Park, P. Pande, S. Shrestha, F. Clubb, B. E. Applegate, and J. A. Jo, "Biochemical characterization of atherosclerotic plaques by endogenous multispectral fluorescence lifetime imaging microscopy.," *Atherosclerosis*, vol. 220, no. 2, pp. 394–401, Feb. 2012.

[25] C. J. De Grauw and H. C. Gerritsen, "Multiple Time-Gate Module for Fluorescence Lifetime Imaging," *Appl. Spectrosc.*, vol. 55, no. 6, 2001.

[26] G. T. Kennedy, D. S. Elson, J. D. Hares, I. Munro, V. Poher, P. M. W. French, and M. a a Neil, "Fluorescence lifetime imaging using light emitting diodes," *J. Phys. D. Appl. Phys.*, vol. 41, no. 9, p. 094012, May 2008.

[27] D. Li, J. Arlt, J. Richardson, R. Walker, A. Buts, D. Stoppa, E. Charbon, and R. Henderson, "Real-time fluorescence lifetime imaging system with a 32 x 32 0.12um CMOS low dark-count single-photon avalanche diode array," *Opt. Express*, vol. 18, no. 10, pp. 26–28, 2010.

[28] R. M. Field, S. Realov, and K. L. Shepard, "A 100 fps, Time-Correlated Single-Photon-Counting-Based Fluorescence-Lifetime Imager in 130 nm CMOS," *IEEE J. Solid-State Circuits*, vol. 49, no. 4, pp. 867–880, Apr. 2014.

[29] W. Becker, *The bh TCSPC Handbook*. 2008.

[30] Becker & Hickl GmbH, "PMC-100 datasheet."

[31] M. Wahl, "Time-Correlated Single Photon Counting." Picoquant, pp. 1–14.

[32] W. Becker, a Bergmann, M. a Hink, K. König, K. Benndorf, and C. Biskup, "Fluorescence lifetime imaging by time-correlated single-photon counting.," *Microsc. Res. Tech.*, vol. 63, no. 1, pp. 58–66, Jan. 2004.

[33] I. Bugiel, K. Konig, and H. Wabnitz, "Investigation of Cells by Fluorescence Laser Scanning Microscopy with Subnanoscond Time Resolution," *Lasers Life Sci.*, vol. 3, no. 1, pp. 47–53, 1989.

[34] W. Becker, A. Bergmann, and H. Gmbh, "Lifetime Imaging Techniques for Optical Microscopy," *Time*, pp. 1–41, 2003.

[35] R. Patalay, C. Talbot, Y. Alexandrov, I. Munro, M. a a Neil, K. König, P. M. W. French, A. Chu, G. W. Stamp, and C. Dunsby, "Quantification of cellular autofluorescence of human skin using multiphoton tomography and fluorescence lifetime imaging in two spectral detection channels.," *Biomed. Opt. Express*, vol. 2, no. 12, pp. 3295–308, Dec. 2011.

[36] R. Patalay, C. Talbot, Y. Alexandrov, M. O. Lenz, S. Kumar, S. Warren, I. Munro, M. a a Neil, K. König, P. M. W. French, A. Chu, G. W. H. Stamp, and C. Dunsby, "Multiphoton multispectral fluorescence lifetime tomography for the evaluation of basal cell carcinomas.," *PLoS One*, vol. 7, no. 9, p. e43460, Jan. 2012.

[37] A. J. Thompson, "Developing endoscopic instrumentation and techniques for in vivo fluorescence lifetime imaging and spectroscopy," 2012.

[38] S. Coda, A. J. Thompson, G. T. Kennedy, K. L. Roche, L. Ayaru, D. S. Bansi, G. W. Stamp, A. V Thillainayagam, P. M. W. French, and C. Dunsby, "Fluorescence lifetime spectroscopy of tissue autofluorescence in normal and diseased colon measured ex vivo using a fiber-optic probe.," *Biomed. Opt. Express*, vol. 5, no. 2, pp. 515–38, Feb. 2014.

[39] D. Chorvat and A. Chorvatova, "Spectrally resolved time-correlated single photon counting: a novel approach for characterization of endogenous fluorescence in isolated cardiac myocytes.," *Eur. Biophys. J.*, vol. 36, no. 1, pp. 73–83, Dec. 2006.

[40] D. Elson, J. Requejo-Isidro, I. Munro, F. Reavell, J. Siegel, K. Suhling, P. Tadrous, R. Benninger, P. Lanigan, J. McGinty, C. Talbot, B. Treanor, S. Webb, A. Sandison, A. Wallace, D. Davis, J. Lever, M. Neil, D. Phillips, G. Stamp, and P. French, "Time-domain fluorescence lifetime imaging applied to biological tissue.," *Photochem. Photobiol. Sci.*, vol. 3, no. 8, pp. 795–801, Aug. 2004.

[41] J. Mcginty, N. P. Galletly, C. Dunsby, I. Munro, D. S. Elson, J. Requejo-isidro, P. Cohen, R. Ahmad, A. Forsyth, A. V Thillainayagam, M. A. A. Neil, P. French, and G. W. Stamp, "Wide-field fluorescence lifetime imaging of cancer," *Opt. Express*, vol. 1, no. 2, pp. 124–135, 2010.

[42] S. C. Warren, A. Margineanu, D. Alibhai, D. J. Kelly, C. Talbot, Y. Alexandrov, I. Munro, M. Katan, C. Dunsby, and P. M. W. French, "Rapid global fitting of large fluorescence lifetime imaging microscopy datasets.," *PLoS One*, vol. 8, no. 8, p. e70687, Jan. 2013.

[43] D. S. Elson, J. A. Jo, and L. Marcu, "Miniaturized side-viewing imaging probe for fluorescence lifetime imaging (FLIM): validation with fluorescence dyes, tissue structural proteins and tissue specimens.," *New J. Phys.*, vol. 9, no. 07, p. 127, Jan. 2007.

[44] H. Sparks, S. Warren, J. Guedes, N. Yoshida, T. C. Charn, N. Guerra, T. Tatla, C. Dunsby, and P. French, "A flexible wide-field FLIM endoscope utilising blue excitation light for label-free contrast of tissue.," *J. Biophotonics*, vol. 11, pp. 1–11, Feb. 2014.

[45] D. D.-U. Li, S. Ameer-Beg, J. Arlt, D. Tyndall, R. Walker, D. R. Matthews, V. Visitkul, J. Richardson, and R. K. Henderson, "Time-domain fluorescence lifetime imaging techniques suitable for solid-state imaging sensor arrays.," *Sensors*, vol. 12, no. 5, pp. 5650–69, Jan. 2012.

[46] M. Zhao, Y. Li, and L. Peng, "FPGA-based multi-channel fluorescence lifetime analysis of Fourier multiplexed frequency-sweeping lifetime imaging.," *Opt. Express*, vol. 22, no. 19, pp. 23073–85, Sep. 2014.

[47] B. R. Rae, J. Yang, J. Mckendry, Z. Gong, D. Renshaw, J. M. Girkin, E. Gu, M. D. Dawson, and R. K. Henderson, "A Vertically Integrated CMOS Microsystem for Time-Resolved Fluorescence Analysis," vol. 4, no. 6, pp. 437–444, 2010.

[48] Y. Wang, B. R. Rae, R. K. Henderson, Z. Gong, J. Mckendry, E. Gu, M. D. Dawson, G. a. Turnbull, and I. D. W. Samuel, "Ultra-portable explosives sensor based on a CMOS fluorescence lifetime analysis micro-system," *AIP Adv.*, vol. 1, no. 3, p. 032115, 2011.

[49] H. Wang, Y. Qi, T. J. Mountziaris, and C. D. Salthouse, "A portable time-domain LED fluorimeter for nanosecond fluorescence lifetime measurements.," *Rev. Sci. Instrum.*, vol. 85, no. 5, p. 055003, May 2014.

[50] R. D. Spencer and G. Weber, “MEASUREMENTS OF SUBNANOSECOND FLUORESCENCE LIFETIMES WITH A CROSS-CORRELATION PHASE FLUOROMETER,” *Ann. N. Y. Acad. Sci.*, vol. 158, no. 1 Electronic As, pp. 361–376, May 1969.

[51] P. Herman, B. P. Maliwal, H. J. Lin, and J. R. Lakowicz, “Frequency-domain fluorescence microscopy with the LED as a light source.,” *J. Microsc.*, vol. 203, no. Pt 2, pp. 176–81, Aug. 2001.

[52] M. J. Booth and T. Wilson, “Low-cost, frequency-domain, fluorescence lifetime confocal microscopy.,” *J. Microsc.*, vol. 214, no. Pt 1, pp. 36–42, Apr. 2004.

[53] a D. Elder, J. H. Frank, J. Swartling, X. Dai, and C. F. Kaminski, “Calibration of a wide-field frequency-domain fluorescence lifetime microscopy system using light emitting diodes as light sources.,” *J. Microsc.*, vol. 224, no. Pt 2, pp. 166–80, Nov. 2006.

[54] P. Herman and J. Vecer, “Frequency domain fluorometry with pulsed light-emitting diodes.,” *Ann. N. Y. Acad. Sci.*, vol. 1130, pp. 56–61, Jan. 2008.

[55] R. A. Colyer, C. Lee, and E. Gratton, “A Novel Fluorescence Lifetime Imaging System That Optimizes Photon Efficiency,” *Microsc. Res. Tech.*, vol. 213, no. August 2007, pp. 201–213, 2008.

[56] G. A. Wagnieres, J. C. Mizeret, A. Studzinski, and H. van den Bergh, “Endoscopic Frequency-Doamin Fluorescence Lifetime Imaging for Clinical Cancer Photodetection: Apparatus Design.,” 1995, vol. 2392, pp. 42–54.

[57] U. S. Dinish, P. Gulati, V. M. Murukeshan, and L. K. Seah, “Diagnosis of colon cancer using frequency domain fluorescence imaging technique,” *Opt. Commun.*, vol. 271, no. 1, pp. 291–301, Mar. 2007.

[58] C. Stringari, J. L. Nourse, L. a Flanagan, and E. Gratton, “Phasor fluorescence lifetime microscopy of free and protein-bound NADH reveals neural stem cell differentiation potential.,” *PLoS One*, vol. 7, no. 11, p. e48014, Jan. 2012.

[59] B. K. Wright, L. M. Andrews, M. R. Jones, C. Stringari, M. a Digman, and E. Gratton, “Phasor-FLIM analysis of NADH distribution and localization in the nucleus of live progenitor myoblast cells.,” *Microsc. Res. Tech.*, vol. 75, no. 12, pp. 1717–22, Dec. 2012.

[60] C. Stringari, R. a Edwards, K. T. Pate, M. L. Waterman, P. J. Donovan, and E. Gratton, “Metabolic trajectory of cellular differentiation in small intestine by Phasor Fluorescence Lifetime Microscopy of NADH.,” *Sci. Rep.*, vol. 2, p. 568, Jan. 2012.

[61] R. J. Woods, S. Scypinski, L. J. C. Love, and H. A. Ashworth, “Transient digitizer for the determination of microsecond luminescence lifetimes,” *Anal. Chem.*, pp. 1395–1400, 1984.

[62] J. a Jo, Q. Fang, T. Papaioannou, and L. Marcu, “Fast model-free deconvolution of fluorescence decay for analysis of biological systems.,” *J. Biomed. Opt.*, vol. 9, no. 4, pp. 743–52, 2004.

[63] A. H. A. Clayton, Q. S. Hanley, and P. J. Verveer, “Graphical representation and multicomponent analysis of single-frequency fluorescence lifetime imaging microscopy data.,” *J. Microsc.*, vol. 213, no. Pt 1, pp. 1–5, Jan. 2004.

[64] G. I. Redford and R. M. Clegg, “Polar plot representation for frequency-domain analysis of fluorescence lifetimes.,” *J. Fluoresc.*, vol. 15, no. 5, pp. 805–15, Sep. 2005.

[65] M. Köllner and J. Wolfrum, “How many photons are necessary for fluorescence-lifetime measurements?,” *Chem. Phys. Lett.*, vol. 200, no. 1–2, pp. 199–204, Nov. 1992.

[66] H. E. Grecco, P. Roda-Navarro, and P. J. Verveer, “Global analysis of time correlated single photon counting FRET-FLIM data,” *Opt. Express*, vol. 17, no. 8, p. 6493, Apr. 2009.

[67] R. Alford, H. M. Simpson, J. Duberman, G. C. Hill, M. Ogawa, C. Regino, H. Kobayashi, and P. L. Choyke, “Toxicity of Organic Fluorophores Used in Molecular Imaging : Literature Review,” vol. 8, no. 6, pp. 341–354, 2009.

[68] B. Chance, P. Cohen, F. Jobsis, and B. Schoener, “Intracellular oxidation-reduction states in vivo,” *Science (80-.).*, vol. 137, no. 3529, pp. 499–508, 1962.

[69] S. Andersson-Engels, J. Johansson, U. Stenram, K. Svanberg, and S. Svanberg, “Malignant tumor and atherosclerotic plaque diagnosis using laser-induced fluorescence,” *IEEE J. Quantum Electron.*, vol. 26, no. 12, pp. 2207–2217, 1990.

[70] G. A. Wagnieres, W. M. Star, and B. C. Wilson, “In Vivo Fluorescence Spectroscopy and Imaging for Oncological Applications,” *Photochem. Photobiol.*, vol. 68, no. 5, pp. 603–632, 1998.

[71] M.-A. Mycek, P. Urayama, W. Zhong, R. D. Sloboda, K. H. Dragnev, and E. Dmitrovsky, “Fluorescence Spectroscopy and Imaging for Noninvasive Diagnostics: Applications to Early Cancer Detection in the Lung Mary-Ann,” *Proc. SPIE-OSA Biomed. Opt.*, vol. 5141, no. 2003, pp. 70–80, Oct. 2003.

[72] E. M. Gill, A. Malpica, R. E. Alford, A. R. Nath, M. Follen, R. R. Richards-Kortum, and N. Ramanujam, “Relationship between collagen autofluorescence of the human cervix and menopausal status.,” *Photochem. Photobiol.*, vol. 77, no. 6, pp. 653–8, Jun. 2003.

[73] K. Konig, K. Schenke-layland, I. Riemann, and U. A. Stock, “Multiphoton autofluorescence imaging of intratissue elastic fibers,” vol. 26, pp. 495–500, 2004.

[74] D. Chorvat, M. Cagalinec, and J. Kirchnerova, “Mitochondrial Autofluorescence Induced by Visible Light in Single Rat Cardiac Myocytes Studied by Spectrally Resolved,” vol. 14, no. 2, pp. 220–230, 2004.

[75] B. Li and S. Xie, “Autofluorescence excitation-emission matrices for diagnosis of colonic cancer,” vol. 11, no. 25, pp. 3931–3934, 2005.

[76] W. H. Yong, P. V Butte, B. K. Pikul, J. A. Jo, Q. Fang, T. Papaioannou, K. L. Black, and L. Marcu, “Distinction of brain tissue, low grade and high grade glioma with time-resolved fluorescence spectroscopy,” pp. 1255–1263, 2006.

[77] M. C. Skala, K. M. Riching, A. Gendron-Fitzpatrick, J. Eickhoff, K. W. Eliceiri, J. G. White, and N. Ramanujam, “In vivo multiphoton microscopy of NADH and FAD redox states, fluorescence lifetimes, and cellular morphology in precancerous epithelia.,” *Proc. Natl. Acad. Sci. U. S. A.*, vol. 104, no. 49, pp. 19494–9, Dec. 2007.

[78] M. C. Skala, K. M. Riching, D. K. Bird, A. Gendron-Fitzpatrick, J. Eickhoff, K. W. Eliceiri, P. J. Keely, and N. Ramanujam, “In vivo multiphoton fluorescence lifetime imaging of protein-bound and free nicotinamide adenine dinucleotide in normal and precancerous epithelia.,” *J. Biomed. Opt.*, vol. 12, no. 2, p. 024014, 2007.

[79] P. V Butte, B. K. Pikul, A. Hever, W. H. Yong, K. L. Black, and L. Marcu, “Diagnosis of meningioma by time-resolved fluorescence spectroscopy.,” *J. Biomed. Opt.*, vol. 10, no. 6, p. 064026, 2010.

[80] H. B. Manning, M. B. Nickdel, K. Yamamoto, J. L. Lagarto, D. J. Kelly, C. B. Talbot, G. Kennedy, J. Dudhia, J. Lever, C. Dunsby, P. French, and Y. Itoh, “Detection of cartilage matrix degradation by autofluorescence lifetime.,” *Matrix Biol.*, vol. 32, no. 1, pp. 32–8, Jan. 2013.

[81] A. T. Shah, M. Demory Beckler, A. J. Walsh, W. P. Jones, P. R. Pohlmann, and M. C. Skala, “Optical metabolic imaging of treatment response in human head and neck squamous cell carcinoma.,” *PLoS One*, vol. 9, no. 3, p. e90746, Jan. 2014.

[82] OMLC, “Optical properties spectra,” 2001. [Online]. Available: http://omlc.ogi.edu/spectra. [Accessed: 05-Nov-2014].

[83] F. W. J. Teale and G. Weber, “Ultraviolet Fluorescence of the Aromatic Amino Acids,” *Biochem. J.*, vol. 1, no. 1, pp. 476–482, 1954.

[84] T. Torikata, Leslie S. Forster, Robert E. Johnson, and J. A. Rupley, “Lifetimes and NADH quenching of tryptophan fluorescence in pig heart cytoplasmic malate dehydrogenase,” *J. Biol. Chem.*, vol. 254, no. 9, pp. 3516–3520, 1979.

[85] T. Torikata, L. S. Forster, C. C. O’Neal, and J. a. Rupley, “Lifetimes and NADH quenching of tryptophan fluorescence in pig heart lactate dehydrogenase,” *Biochemistry*, vol. 18, no. 2, pp. 385–390, Jan. 1979.

[86] F. E. Ahmed, R. B. Setlow, E. Grist, and N. Setlow, “DNA damage, photorepair, and survival in fish and human cells exposed to UV radiation.,” *Environ. Mol. Mutagen.*, vol. 22, no. 1, pp. 18–25, Jan. 1993.

[87] H. Andersson, T. Baechi, M. Hoechl, and C. Richter, “Autofluorescence of living cells,” vol. 191, no. July, pp. 1–7, 1998.

[88] Y. Wu and J. Y. Qu, “Autofluorescence spectroscopy of epithelial tissues.,” *J. Biomed. Opt.*, vol. 11, no. 5, p. 054023, 2006.

[89] Y. A. Ushenko, A. D. Arkhelyuk, M. I. Sidor, V. T. Bachynskyi, and O. Y. Wanchuliak, “Laser polarization autofluorescence of endogenous porphyrins of optically anisotropic biological tissues and fluids in diagnostics of necrotic and pathological changes of human organs.,” *Appl. Opt.*, vol. 53, no. 10, pp. B181–91, Apr. 2014.

[90] W. Ying, “NAD+/NADH and NADP+/NADPH in cellular functions and cell death: regulation and biological consequences.,” *Antioxid. Redox Signal.*, vol. 10, no. 2, pp. 179–206, Feb. 2008.

[91] B. Chance, B. Schoener, R. Oshino, and F. Itshak, “Oxidation-Reduction Ratio Studies of Mitochondria in Freeze-trapped,” 1979.

[92] A. Mayevsky, T. Manor, E. Pevzner, A. Deutsch, R. Etziony, N. Dekel, and A. Jaronkin, “Tissue spectroscope: a novel in vivo approach to real time monitoring of tissue vitality.,” *J. Biomed. Opt.*, vol. 9, no. 5, pp. 1028–45, 2004.

[93] A. Mayevsky and G. G. Rogatsky, “Mitochondrial function in vivo evaluated by NADH fluorescence : from animal models to human studies,” 2007.

[94] A. Mayevsky and B. Chance, “Oxidation-reduction states of NADH in vivo: from animals to clinical use.,” *Mitochondrion*, vol. 7, no. 5, pp. 330–9, Sep. 2007.

[95] M. Ranji, S. Kanemoto, M. Matsubara, M. a Grosso, J. H. Gorman, R. C. Gorman, D. L. Jaggard, and B. Chance, “Fluorescence spectroscopy and imaging of myocardial apoptosis.,” *J. Biomed. Opt.*, vol. 11, no. 6, p. 064036, 2013.

[96] J. R. Lakowicz, H. Szmacinski, K. Nowaczyk, and M. L. Johnson, “Fluorescence lifetime imaging of free and protein-bound NADH.,” *Proc. Natl. Acad. Sci. U. S. A.*, vol. 89, no. 4, pp. 1271–5, Feb. 1992.

[97] T. G. Scott, R. D. Spencer, N. J. Leonard, and G. Weber, “Emission Properties of NADH. Studies of Flurorescence Lifetimes and Quantum Efficiencies of NADH, AcPyADH, and Simplified Synthetic Models,” *J. Am. Chem. Soc.*, vol. 7302, no. 1968, 1970.

[98] B. R. A. Stinson, A. Tg, and J. J. Holbrook, “Equilibrium Binding of Nicofinamide Nucleotides to Lactate Dehydrogenases,” pp. 719–728, 1973.

[99] C. A. Ghiron, M. R. Eftink, J. K. Waters, and D. W. Emerich, “Fluorescence studies with malate dehydrogenase from rhizobium japonicum 3I1B-143 bacteroids: a two-tryptophan containing protein,” in *Biochemistry*, 1990, vol. 1204, pp. 179–183.

[100] B. Zelent, T. Troxler, and J. M. Vanderkooi, “Temperature dependence for fluorescence of beta-NADH in glycerol/water solution and in trehalose/sucrose glass.,” *J. Fluoresc.*, vol. 17, no. 1, pp. 37–42, Jan. 2007.

[101] A. J. Walsh, K. M. Poole, C. L. Duvall, and M. C. Skala, “Ex vivo optical metabolic measurements from cultured tissue reflect in vivo tissue status.,” *J. Biomed. Opt.*, vol. 17, no. 11, p. 116015, Nov. 2012.

[102] A. J. Walsh, R. S. Cook, H. C. Manning, D. J. Hicks, A. Lafontant, C. L. Arteaga, and M. C. Skala, “Optical metabolic imaging identifies glycolytic levels, subtypes, and early-treatment response in breast cancer.,” *Cancer Res.*, vol. 73, no. 20, pp. 6164–74, Oct. 2013.

[103] M. S. Islam, M. Honma, T. Nakabayashi, M. Kinjo, and N. Ohta, “pH Dependence of the Fluorescence Lifetime of FAD in Solution and in Cells.,” *Int. J. Mol. Sci.*, vol. 14, no. 1, pp. 1952–63, Jan. 2013.

[104] T. Nakabayashi, M. S. Islam, and N. Ohta, “Fluorescence decay dynamics of flavin adenine dinucleotide in a mixture of alcohol and water in the femtosecond and nanosecond time range.,” *J. Phys. Chem. B*, vol. 114, no. 46, pp. 15254–60, Nov. 2010.

[105] P. a. W. van den Berg, K. A. Feenstra, A. E. Mark, H. J. C. Berendsen, and A. J. W. G. Visser, “Dynamic Conformations of Flavin Adenine Dinucleotide: Simulated Molecular Dynamics of the Flavin Cofactor Related to the Time-Resolved Fluorescence Characteristics,” *J. Phys. Chem. B*, vol. 106, no. 34, pp. 8858–8869, Aug. 2002.

[106] P. WAHL, J.-C. AUCHET, A. J. W. G. VISSER, and C. VEEGER, “A Pulse Fluorometry Study of Lipoamide Dehydrogenase. Evidence for Non-Equivalent FAD Centers,” *Eur. J. Biochem.*, vol. 50, no. 2, pp. 413–418, Jan. 1975.

[107] N. Nakashima, K. Yoshihara, F. Tanaka, and K. Yagi, “Picosecond fluorescence lifetime of the coenzyme of D-amino acid oxidase.,” *J. Biol. Chem.*, vol. 255, no. 11, pp. 5261–3, Jun. 1980.

[108] F. Tanaka, N. Tamai, and I. Yamazaki, “Picosecond-resolved fluorescence spectra of D-amino-acid oxidase. A new fluorescent species of the coenzyme.,” *Biochemistry*, vol. 28, no. 10, pp. 4259–62, May 1989.

[109] M. D. Shoulders and R. T. Raines, “Collagen structure and stability.,” *Annu. Rev. Biochem.*, vol. 78, pp. 929–58, Jan. 2009.

[110] E. J. Miller and S. Gay, *Structural and Contractile Proteins Part D: Extracellular Matrix*, vol. 144, no. 1983. Elsevier, 1987.

[111] M. G. Patino, M. E. Neiders, S. Andreana, B. Noble, and R. E. Cohen, “Collagen: an overview.,” *Implant Dent.*, vol. 11, no. 3, pp. 280–5, Jan. 2002.

[112] P. Bornstein and H. Sage, “Structurally distinct collagen types,” *Annu. Rev. Biochem.*, no. 49, pp. 957–1003, 1980.

[113] K. T. Weber, “Cardiac interstitium in health and disease: the fibrillar collagen network.,” *J. Am. Coll. Cardiol.*, vol. 13, no. 7, pp. 1637–52, Jun. 1989.

[114] W. Cheng, R. Yan-hua, N. Fang-gang, and Z. Guo-an, “The content and ratio of type I and III collagen in skin differ with age and injury,” *African J. Biotechnol.*, vol. 10, no. 13, pp. 2524–2529, 2011.

[115] E. Schwartz, F. A. Cruickshank, C. C. Christensen, J. S. Perlish, and M. Lebwohl, “COLLAGEN ALTERATIONS IN CHRONICALLY SUN-DAMAGED HUMAN SKIN,” *Photochem. Photobiol.*, vol. 58, no. 6, pp. 841–844, Dec. 1993.

[116] D. Eyre, “Cross-Linking in Collagen and Elastin,” *Annu. Rev. Biochem.*, vol. 53, no. 1, pp. 717–748, Jan. 1984.

[117] A. Uchiyama, T. Ohishi, M. Takahashi, K. Kushida, T. Inoue, M. Fujie, and K. Horiuchi, “Fluorophores from aging human articular cartilage.,” *J. Biochem.*, vol. 110, no. 5, pp. 714–8, Nov. 1991.

[118] R. Richards-Kortum and E. Sevick-Muraca, “Quantitative optical spectroscopy for tissue diagnosis.,” *Annu. Rev. Phys. Chem.*, vol. 47, pp. 555–606, Jan. 1996.

[119] M. P. Rebecca Richards-Kortum, Rebekah Drezek, Konstantin Sokolov, Ina Pavlova, “Survey Of Endogenous Biological Fluorophores,” in *Handbook of Biomedical Fluorescence*, B. Rogue and M.-A. Mycek, Eds. CRC Press, 2003.

[120] J. Zhang, R. Chen, W. Liu, Z. Chen, L. Shu, and Y. Liu, “The spectra character of photodegraded the pyridinoline cross-links by Hypocrellin B,” *J. Phys. Conf. Ser.*, vol. 277, p. 012016, Jan. 2011.

[121] H. B. Manning, “The Expression and Cross-Linking of Collagens,” Imperial College London, 2006.

[122] L. Marcu, D. Cohena, J. I. Maarek, W. S. Grundfesta, T. Development, and C. M. C. L. Angeles, “Characterization of Type I , II , III , IV , and V collagens by time-resolved laser-induced fluorescence spectroscopy,” vol. 3917, pp. 93–101, 2000.

[123] P. Ashjian, A. Elbarbary, P. Zuk, D. a DeUgarte, P. Benhaim, L. Marcu, and M. H. Hedrick, "Noninvasive in situ evaluation of osteogenic differentiation by time-resolved laser-induced fluorescence spectroscopy.," *Tissue Eng.*, vol. 10, no. 3–4, pp. 411–20, 2004.

[124] S. Andersson-Engels, J. Johansson, K. Svanberg, and S. Svanberg, "Fluorescence imaging and point measurements of tissue: applications to the demarcation of malignant tumors and atherosclerotic lesions from normal tissue.," *Photochem. Photobiol.*, vol. 53, no. 6, pp. 807–14, Jun. 1991.

[125] W. R. GRAY, L. B. SANDBERG, and J. A. FOSTER, "Molecular Model for Elastin Structure and Function," *Nature*, vol. 246, no. 5434, pp. 461–466, Dec. 1973.

[126] B. D. P. Thornhill, "Separation of a Series of Chromophores and Fluorophores Present in Elastin," *Biochem. J.*, no. 147, pp. 215–219, 1975.

[127] K. Koenig and H. Schneckenburger, "Laser-induced autofluorescence for medical diagnosis.," *J. Fluoresc.*, vol. 4, no. 1, pp. 17–40, Mar. 1994.

[128] H. B. Manning, G. T. Kennedy, D. M. Owen, D. M. Grant, A. I. Magee, M. A. A. Neil, Y. Itoh, C. Dunsby, and P. French, "A compact, multidimensional spectrofluorometer exploiting supercontinuum generation.," *J. Biophotonics*, vol. 1, no. 6, pp. 494–505, Dec. 2008.

[129] C. Dunsby, P. M. P. Lanigan, J. McGinty, D. S. Elson, J. Requejo-Isidro, I. Munro, N. Galletly, F. McCann, B. Treanor, B. Önfelt, D. M. Davis, M. a a Neil, and P. M. W. French, "An electronically tunable ultrafast laser source applied to fluorescence imaging and fluorescence lifetime imaging microscopy," *J. Phys. D. Appl. Phys.*, vol. 37, no. 23, pp. 3296–3303, Dec. 2004.

[130] Q. Yu and A. a. Heikal, "Two-photon autofluorescence dynamics imaging reveals sensitivity of intracellular NADH concentration and conformation to cell physiology at the single-cell level," *J. Photochem. Photobiol. B Biol.*, vol. 95, no. 1, pp. 46–57, Apr. 2009.

[131] N. Ramanujam, "Fluorescence Spectroscopy In Vivo," pp. 20–56, 2000.

[132] A. Glasfeld, "Biochemistry: The Chemical Reactions of Living Cells, 2nd Edition (David E. Metzler)," *J. Chem. Educ.*, vol. 81, no. 5, p. 646, May 2004.

[133] P. Mitchell and J. Moyle, "Estimation of membrane potential and pH difference across the cristae membrane of rat liver mitochondria.," *Eur. J. Biochem.*, vol. 7, no. 4, pp. 471–84, Feb. 1969.

[134] M. F. C. Abad, G. Di Benedetto, P. J. Magalhães, L. Filippin, and T. Pozzan, "Mitochondrial pH monitored by a new engineered green fluorescent protein mutant.," *J. Biol. Chem.*, vol. 279, no. 12, pp. 11521–9, Mar. 2004.

[135] S. Ogikubo, T. Nakabayashi, T. Adachi, M. S. Islam, T. Yoshizawa, M. Kinjo, and N. Ohta, "Intracellular pH sensing using autofluorescence lifetime microscopy.," *J. Phys. Chem. B*, vol. 115, no. 34, pp. 10385–90, Sep. 2011.

[136] B. BAUMGARTEN and J. HONES, "SPECTROSCOPIC INVESTIGATION OF DIH YDRONICOTIN AMIDES-II. DIHYDRONICOTINAMIDE ADENINE DINUCLEOTIDE COMPLEXES WITH DEHYDROGENASES," *Photochem. Photobiol.*, vol. 47, no. 2, pp. 201–205, Feb. 1988.

[137] B. S. S. Anand and N. Sujatha, "Fluorescence quenching effects of hemoglobin on simulated tissue phantoms in the UV–Vis range," *Meas. Sci. Technol.*, vol. 23, no. 2, p. 025502, Feb. 2012.

[138] V. N. Petushkov, I. H. M. van Stokkum, B. Gobets, F. van Mourik, J. Lee, R. van Grondelle, and A. J. W. G. Visser, "Ultrafast Fluorescence Relaxation Spectroscopy of 6,7-Dimethyl-(8-ribityl)-lumazine and Riboflavin, Free and Bound to Antenna Proteins from Bioluminescent Bacteria," *J. Phys. Chem. B*, vol. 107, no. 39, pp. 10934–10939, Oct. 2003.

[139] I. J. Bigio and J. R. Mourant, "Ultraviolet and visible spectroscopies for tissue diagnostics: fluorescence spectroscopy and elastic-scattering spectroscopy.," *Phys. Med. Biol.*, vol. 42, no. 5, pp. 803–14, May 1997.

[140] L. Marcu, "Fluorescence lifetime in cardiovascular diagnostics.," *J. Biomed. Opt.*, vol. 15, no. 1, p. 011106, 2010.

[141] R. Y. Kwong and E. K. Yucel, “Cardiology patient pages. Computed tomography scan and magnetic resonance imaging.,” *Circulation*, vol. 108, no. 15, pp. e104–6, Oct. 2003.

[142] L. W. Dobrucki and A. J. Sinusas, “PET and SPECT in cardiovascular molecular imaging.,” *Nat. Rev. Cardiol.*, vol. 7, no. 1, pp. 38–47, Jan. 2010.

[143] S. B. Cantor, M. F. Mitchell, G. Tortolero-Luna, C. S. Bratka, D. C. Bodurka, and R. Richards-Kortum, “Cost-effectiveness analysis of diagnosis and management of cervical squamous intraepithelial lesions.,” *Obstet. Gynecol.*, vol. 91, no. 2, pp. 270–7, Feb. 1998.

[144] I. Georgakoudi, W. L. Rice, M. Hronik-Tupaj, and D. L. Kaplan, “Optical spectroscopy and imaging for the noninvasive evaluation of engineered tissues.,” *Tissue Eng. Part B. Rev.*, vol. 14, no. 4, pp. 321–40, Dec. 2008.

[145] P. A. Oberg, T. Sundqvist, and A. Johansson, “Assessment of cartilage thickness utilising reflectance spectroscopy.,” *Med. Biol. Eng. Comput.*, vol. 42, no. 1, pp. 3–8, Jan. 2004.

[146] R. Sanders, H. C. Gerritsen, A. Draaijer, P. M. Houpt, and Y. K. Levine, “Confocal fluorescence lifetime imaging of free calcium in single cells.,” *J. Fluoresc.*, vol. 4, no. 4, pp. 291–4, Dec. 1994.

[147] S. Weiss, “Fluorescence Spectroscopy of Single Biomolecules,” *Science (80-.).*, vol. 283, no. 5408, pp. 1676–1683, Mar. 1999.

[148] K. Carlsson and A. Liljeborg, “Confocal fluorescence microscopy using spectral and lifetime information to simultaneously record four fluorophores with high channel separation,” vol. 185, no. January, pp. 37–46, 1997.

[149] S. Huang, A. A. Heikal, and W. W. Webb, “Two-photon fluorescence spectroscopy and microscopy of NAD(P)H and flavoprotein.,” *Biophys. J.*, vol. 82, no. 5, pp. 2811–25, May 2002.

[150] G. T. Kennedy, H. B. Manning, D. S. Elson, M. A. A. Neil, G. W. Stamp, B. Viellerobe, F. Lacombe, C. Dunsby, and P. French, “A fluorescence lifetime imaging scanning confocal endomicroscope.,” *J. Biophotonics*, vol. 3, no. 1–2, pp. 103–7, Jan. 2010.

[151] M. Rajadhyaksha, S. González, J. M. Zavislan, R. R. Anderson, and R. H. Webb, “In vivo confocal scanning laser microscopy of human skin II: advances in instrumentation and comparison with histology.,” *J. Invest. Dermatol.*, vol. 113, no. 3, pp. 293–303, Sep. 1999.

[152] K. J. Busam, C. Charles, G. Lee, and a C. Halpern, “Morphologic features of melanocytes, pigmented keratinocytes, and melanophages by in vivo confocal scanning laser microscopy.,” *Mod. Pathol.*, vol. 14, no. 9, pp. 862–8, Sep. 2001.

[153] S. Woutersen, “Femtosecond Mid-IR Pump-Probe Spectroscopy of Liquid Water: Evidence for a Two-Component Structure,” *Science (80-.).*, vol. 278, no. 5338, pp. 658–660, Oct. 1997.

[154] T. E. Matthews, I. R. Piletic, M. A. Selim, M. J. Simpson, and W. S. Warren, “Pump-probe imaging differentiates melanoma from melanocytic nevi.,” *Sci. Transl. Med.*, vol. 3, no. 71, p. 71ra15, Feb. 2011.

[155] D. Huang, E. A. Swanson, C. P. Lin, J. S. Schuman, W. G. Stinson, W. Chang, M. R. Hee, T. Flotte, K. Gregory, and C. A. Puliafito, “Optical coherence tomography.,” *Science*, vol. 254, no. 5035, pp. 1178–81, Nov. 1991.

[156] U. Morgner, W. Drexler, F. X. Kärtner, X. D. Li, C. Pitris, E. P. Ippen, and J. G. Fujimoto, “Spectroscopic optical coherence tomography,” *Opt. Lett.*, vol. 25, no. 2, p. 111, Jan. 2000.

[157] W. Drexler and J. G. Fujimoto, “State-of-the-art retinal optical coherence tomography.,” *Prog. Retin. Eye Res.*, vol. 27, no. 1, pp. 45–88, Jan. 2008.

[158] C. H. Liu, B. B. Das, W. L. Sha Glassman, G. C. Tang, K. M. Yoo, H. R. Zhu, D. L. Akins, S. S. Lubicz, J. Cleary, and R. Prudente, “Raman, fluorescence, and time-resolved light scattering as optical diagnostic techniques to separate diseased and normal biomedical media.,” *J. Photochem. Photobiol. B.*, vol. 16, no. 2, pp. 187–209, Oct. 1992.

[159] P. J. Caspers, G. W. Lucassen, and G. J. Puppels, “Combined in vivo confocal Raman spectroscopy and confocal microscopy of human skin.,” *Biophys. J.*, vol. 85, no. 1, pp. 572–80, Jul. 2003.

[160] M. D. Keller, E. Vargis, N. de Matos Granja, R. H. Wilson, M.-A. Mycek, M. C. Kelley, and A. Mahadevan-Jansen, “Development of a spatially offset Raman spectroscopy probe for breast tumor surgical margin evaluation.,” *J. Biomed. Opt.*, vol. 16, no. 7, p. 077006, Jul. 2011.

[161] K. Sokolov, M. Follen, and R. Richards-Kortum, “Optical spectroscopy for detection of neoplasia.,” *Curr. Opin. Chem. Biol.*, vol. 6, no. 5, pp. 651–8, Oct. 2002.

[162] R. S. Balaban, V. K. Mootha, and a Arai, “Spectroscopic determination of cytochrome c oxidase content in tissues containing myoglobin or hemoglobin.,” *Anal. Biochem.*, vol. 237, no. 2, pp. 274–8, Jun. 1996.

[163] A. E. Arai, C. E. Kasserra, P. R. Territo, A. H. Gandjbakhche, and R. S. Balaban, “Myocardial oxygenation in vivo: optical spectroscopy of cytoplasmic myoglobin and mitochondrial cytochromes.,” *Am. J. Physiol.*, vol. 277, no. 2 Pt 2, pp. H683–97, Aug. 1999.

[164] E. Häggblad, T. Lindbergh, M. G. D. Karlsson, H. Casimir-Ahn, E. G. Salerud, and T. Strömberg, “Myocardial tissue oxygenation estimated with calibrated diffuse reflectance spectroscopy during coronary artery bypass grafting.,” *J. Biomed. Opt.*, vol. 13, no. 5, p. 054030, 2008.

[165] J. Eng, R. M. Lynch, and R. S. Balaban, “Nicotinamide adenine dinucleotide fluorescence spectroscopy and imaging of isolated cardiac myocytes.,” *Biophys. J.*, vol. 55, no. 4, pp. 621–30, Apr. 1989.

[166] J. Venius, D. Labeikyt, and V. Strazdait, “Investigation of human heart tissue extracts by spectroscopic methods,” no. 3, pp. 53–58, 2006.

[167] M. Ranji, S. Member, M. Matsubara, B. G. Leshnower, R. H. Hinmon, D. L. Jaggard, B. Chance, L. Fellow, R. C. Gorman, and J. H. Gorman, “Quantifying Acute Myocardial Injury Using Ratiometric Fluorometry,” vol. 56, no. 5, pp. 1556–1563, 2009.

[168] J. Venius, S. Bagdonas, E. Zurauskas, and R. Rotomskis, “Visualization of human heart conduction system by means of fluorescence spectroscopy.,” *J. Biomed. Opt.*, vol. 16, no. 10, p. 107001, Oct. 2011.

[169] J. Venius, S. Bagdonas, E. Žurauskas, and R. Rotomskis, “Time-resolved fluorescence spectroscopy of the heart tissues,” *Lith. J. Phys.*, vol. 51, no. 4, pp. 370–376, 2011.

[170] C. W. Han, C. R. Chu, N. Adachi, A. Usas, F. H. Fu, J. Huard, and Y. Pan, “Analysis of rabbit articular cartilage repair after chondrocyte implantation using optical coherence tomography,” *Osteoarthr. Cartil.*, vol. 11, no. 2, pp. 111–121, Feb. 2003.

[171] W.-F. T. Lai, C.-H. Chang, Y. Tang, R. Bronson, and C.-H. Tung, “Early diagnosis of osteoarthritis using cathepsin B sensitive near-infrared fluorescent probes,” *Osteoarthritis Cartilage*, vol. 12, no. 3, pp. 239–44, Mar. 2004.

[172] A. Johansson, T. Sundqvist, J.-H. Kuiper, and P. Å. Öberg, “A spectroscopic approach to imaging and quantification of cartilage lesions in human knee joints.,” *Phys. Med. Biol.*, vol. 56, no. 6, pp. 1865–78, Mar. 2011.

[173] J. M. Maarek, L. Marcu, M. C. Fishbein, and W. S. Grundfest, “Time-resolved fluorescence of human aortic wall: use for improved identification of atherosclerotic lesions.,” *Lasers Surg. Med.*, vol. 27, no. 3, pp. 241–54, Jan. 2000.

[174] H. Yabushita, B. E. Bouma, S. L. Houser, H. T. Aretz, I.-K. Jang, K. H. S. C. R. Kauffman, M. Shishkov, D.-H. Kang, E. F. Halpern, and G. J. Tearney, “Characterization of Human Atherosclerosis by Optical Coherence Tomography,” *Circulation*, vol. 106, no. 13, pp. 1640–1645, Sep. 2002.

[175] I.-K. Jang, G. J. Tearney, B. MacNeill, M. Takano, F. Moselewski, N. Iftima, M. Shishkov, S. Houser, H. T. Aretz, E. F. Halpern, and B. E. Bouma, “In vivo characterization of coronary atherosclerotic plaque by use of optical coherence tomography.,” *Circulation*, vol. 111, no. 12, pp. 1551–5, Mar. 2005.

[176] M. Chandra, J. Scheiman, D. Heidt, D. Simeone, B. McKenna, and M.-A. Mycek, “Probing pancreatic disease using tissue optical spectroscopy.,” *J. Biomed. Opt.*, vol. 12, no. 6, p. 060501, 2007.

[177] A. R. Tumlinson, L. P. Hariri, U. Utzinger, and J. K. Barton, "Miniature endoscope for simultaneous optical coherence tomography and laser-induced fluorescence measurement.," *Appl. Opt.*, vol. 43, no. 1, pp. 113–21, Jan. 2004.

[178] S. Yuan, C. A. Roney, J. Wierwille, C.-W. Chen, B. Xu, G. Griffiths, J. Jiang, H. Ma, A. Cable, R. M. Summers, and Y. Chen, "Co-registered optical coherence tomography and fluorescence molecular imaging for simultaneous morphological and molecular imaging.," *Phys. Med. Biol.*, vol. 55, no. 1, pp. 191–206, Jan. 2010.

[179] D. Lorenser, B. C. Quirk, M. Auger, W.-J. Madore, R. W. Kirk, N. Godbout, D. D. Sampson, C. Boudoux, and R. A. McLaughlin, "Dual-modality needle probe for combined fluorescence imaging and three-dimensional optical coherence tomography.," *Opt. Lett.*, vol. 38, no. 3, pp. 266–8, Feb. 2013.

[180] Z. Huang, H. Lui, D. I. McLean, M. Korbelik, and H. Zeng, "Raman spectroscopy in combination with background near-infrared autofluorescence enhances the in vivo assessment of malignant tissues.," *Photochem. Photobiol.*, vol. 81, no. 5, pp. 1219–26, 2005.

[181] M. S. Bergholt, W. Zheng, K. Lin, K. Y. Ho, M. Teh, K. G. Yeoh, J. B. Y. So, and Z. Huang, "Combining near-infrared-excited autofluorescence and Raman spectroscopy improves in vivo diagnosis of gastric cancer.," *Biosens. Bioelectron.*, vol. 26, no. 10, pp. 4104–10, Jun. 2011.

[182] G. Zonios, L. T. Perelman, V. Backman, R. Manoharan, M. Fitzmaurice, J. Van Dam, and M. S. Feld, "Diffuse reflectance spectroscopy of human adenomatous colon polyps in vivo.," *Appl. Opt.*, vol. 38, no. 31, pp. 6628–37, Nov. 1999.

[183] R. Mallia, S. S. Thomas, A. Mathews, R. Kumar, P. Sebastian, J. Madhavan, and N. Subhash, "Oxygenated hemoglobin diffuse reflectance ratio for in vivo detection of oral pre-cancer.," *J. Biomed. Opt.*, vol. 13, no. 4, p. 041306, 2013.

[184] J. W. Spliethoff, D. J. Evers, H. M. Klomp, J. W. van Sandick, M. W. Wouters, R. Nachabe, G. W. Lucassen, B. H. W. Hendriks, J. Wesseling, and T. J. M. Ruers, "Improved identification of peripheral lung tumors by using diffuse reflectance and fluorescence spectroscopy.," *Lung Cancer*, vol. 80, no. 2, pp. 165–71, May 2013.

[185] W. Lohmann and E. Paul, "In situ detection of melanomas by fluorescence measurements.," *Naturwissenschaften*, vol. 75, no. 4, pp. 201–2, Apr. 1988.

[186] P. Calzavara-Pinton, "Reflectance Confocal Microscopy for In Vivo Skin Imaging," *Photochem. ...*, pp. 1421–1430, 2008.

[187] K. S. Nehal, D. Gareau, and M. Rajadhyaksha, "Skin imaging with reflectance confocal microscopy.," *Semin. Cutan. Med. Surg.*, vol. 27, no. 1, pp. 37–43, Mar. 2008.

[188] J. C. T. Braga, M. P. Macedo, C. Pinto, J. Duprat, M. D. Begnami, G. Pellacani, and G. G. Rezze, "Learning reflectance confocal microscopy of melanocytic skin lesions through histopathologic transversal sections.," *PLoS One*, vol. 8, no. 12, p. e81205, Jan. 2013.

[189] J. W. Wilson, S. Degan, M. A. Selim, J. Y. Zhang, and W. S. Warren, "In vivo pump-probe microscopy of melanoma and pigmented lesions," vol. 8226, p. 822602, Feb. 2012.

[190] J. W. Wilson, L. Vajzovic, F. E. Robles, T. J. Cummings, P. Mruthyunjaya, and W. S. Warren, "Imaging microscopic pigment chemistry in conjunctival melanocytic lesions using pump-probe laser microscopy.," *Invest. Ophthalmol. Vis. Sci.*, vol. 54, no. 10, pp. 6867–76, Jan. 2013.

[191] M. Mogensen, L. Thrane, T. M. Jørgensen, P. E. Andersen, and G. B. E. Jemec, "OCT imaging of skin cancer and other dermatological diseases.," *J. Biophotonics*, vol. 2, no. 6–7, pp. 442–51, Jul. 2009.

[192] B. J. Vakoc, D. Fukumura, R. K. Jain, and B. E. Bouma, "Cancer imaging by optical coherence tomography: preclinical progress and clinical potential," *Nat. Rev. Cancer*, vol. 12, no. 5, pp. 363–368, Apr. 2012.

[193] C. a Banzhaf, L. Themstrup, H. C. Ring, M. Mogensen, and G. B. E. Jemec, "Optical coherence tomography imaging of non-melanoma skin cancer undergoing imiquimod therapy.," *Skin Res. Technol.*, vol. 20, no. 2, pp. 170–6, May 2014.

[194] S. Devpura, K. N. Barton, S. L. Brown, O. Palyvoda, S. Kalkanis, V. M. Naik, F. Siddiqui, R. Naik, and I. J. Chetty, "Vision 20/20: the role of Raman spectroscopy in early stage cancer detection and feasibility for application in radiation therapy response assessment.," *Med. Phys.*, vol. 41, no. 5, p. 050901, May 2014.

[195] L. Mavarani, D. Petersen, S. F. El-Mashtoly, A. Mosig, A. Tannapfel, C. Kötting, and K. Gerwert, "Spectral histopathology of colon cancer tissue sections by Raman imaging with 532 nm excitation provides label free annotation of lymphocytes, erythrocytes and proliferating nuclei of cancer cells.," *Analyst*, vol. 138, no. 14, pp. 4035–9, Jul. 2013.

[196] Y. Sun, J. Phipps, D. S. Elson, H. Stoy, S. Tinling, J. Meier, B. Poirier, F. S. Chuang, D. G. Farwell, and L. Marcu, "Fluorescence lifetime imaging microscopy: in vivo application to diagnosis of oral carcinoma.," *Opt. Lett.*, vol. 34, no. 13, pp. 2081–3, Jul. 2009.

[197] S. Cheng, R. M. Cuenca, B. Liu, B. H. Malik, J. M. Jabbour, K. C. Maitland, J. Wright, Y.-S. L. Cheng, and J. a. Jo, "Handheld multispectral fluorescence lifetime imaging system for in vivo applications," *Biomed. Opt. Express*, vol. 5, no. 3, p. 921, Feb. 2014.

[198] I. Georgakoudi, B. C. Jacobson, J. Van Dam, V. Backman, M. B. Wallace, M. G. Müller, Q. Zhang, K. Badizadegan, D. Sun, G. a. Thomas, L. T. Perelman, and M. S. Feld, "Fluorescence, reflectance, and light-scattering spectroscopy for evaluating dysplasia in patients with Barrett's esophagus," *Gastroenterology*, vol. 120, no. 7, pp. 1620–1629, Jun. 2001.

[199] Y. Ti and W.-C. Lin, "Optical Characterization of Myocardial Infarction: An in vivo Study," *Biomed. Opt.*, p. BTuF41, 2008.

[200] J. L. Schroeder, M. Luger-Hamer, R. Pursley, T. Pohida, C. Chefd'hotel, P. Kellman, and R. S. Balaban, "Short communication: Subcellular motion compensation for minimally invasive microscopy, in vivo: evidence for oxygen gradients in resting muscle.," *Circ. Res.*, vol. 106, no. 6, pp. 1129–33, Apr. 2010.

[201] V. Studer, J. Bobin, M. Chahid, S. H. S. Mousavi, E. Candes, and M. Dahan, "Compressive Fluorescence Microscopy for Biological and Hyperspectral Imaging," *Proc. Natl. Acad. Sci. U. S. A.*, vol. 104, no. 51, pp. 20167–72, Jan. 2012.

[202] N. Ramanujam, "Fluorescence spectroscopy of neoplastic and non-neoplastic tissues.," *Neoplasia*, vol. 2, no. 1–2, pp. 89–117, 2000.

[203] L. Marcu, "Fluorescence lifetime techniques in medical applications.," *Ann. Biomed. Eng.*, vol. 40, no. 2, pp. 304–31, Mar. 2012.

[204] W. R. Lloyd, R. H. Wilson, S. Y. Lee, M. Chandra, B. McKenna, D. Simeone, J. Scheiman, and M.-A. Mycek, "In vivo optical spectroscopy for improved detection of pancreatic adenocarcinoma: a feasibility study.," *Biomed. Opt. Express*, vol. 5, no. 1, pp. 9–15, Dec. 2013.

[205] M. Al-Salhi, V. Masilamani, T. Vijmasi, H. Al-Nachawati, and a P. VijayaRaghavan, "Lung cancer detection by native fluorescence spectra of body fluids--a preliminary study.," *J. Fluoresc.*, vol. 21, no. 2, pp. 637–45, Mar. 2011.

[206] R. Rajasekaran, P. R. Aruna, D. Koteeswaran, G. Bharanidharan, M. Baludavid, and S. Ganesan, "Steady-state and time-resolved fluorescence spectroscopic characterization of urine of healthy subjects and cervical cancer patients.," *J. Biomed. Opt.*, vol. 19, no. 3, p. 37003, Mar. 2014.

[207] M.-A. E. J. Ortner, B. Ebert, E. Hein, K. Zumbusch, D. Nolte, U. Sukowski, J. Weber-Eibel, B. Fleige, M. Dietel, M. Stolte, G. Oberhuber, R. Porschen, B. Klump, H. Hörtnagl, H. Lochs, and H. Rinneberg, "Time gated fluorescence spectroscopy in Barrett's oesophagus.," *Gut*, vol. 52, no. 1, pp. 28–33, Jan. 2003.

[208] N. Kollias, G. Zonios, and G. N. Stamatas, "Fluorescence spectroscopy of skin," *Vib. Spectrosc.*, vol. 61, no. 1–2, pp. 17–23, Aug. 2002.

[209] M. Cardenas-Turanzas, J. A. Freeberg, J. L. Benedet, E. N. Atkinson, D. D. Cox, R. Richards-Kortum, C. MacAulay, M. Follen, and S. B. Cantor, "The clinical effectiveness of optical spectroscopy for the in vivo diagnosis of cervical intraepithelial neoplasia: where are we?," *Gynecol. Oncol.*, vol. 107, no. 1 Suppl 1, pp. S138–46, Oct. 2007.

[210] M. A. Bennet, P. R. Richardson, J. Arlt, A. McCarthy, G. S. Buller, and A. C. Jones, "Optically trapped microsensors for microfluidic temperature measurement by fluorescence lifetime imaging microscopy," *R. Soc. Chem.*, pp. 3821–3828, 2011.

[211] H. C. Gerritsen, R. Sanders, A. Draaijer, C. Ince, and Y. K. Levine, "Fluorescence lifetime imaging of oxygen in living cells," *J. Fluoresc.*, vol. 7, no. 1, pp. 11–15, Mar. 1997.

[212] H.-J. Lin, P. Herman, and J. R. Lakowicz, "Fluorescence lifetime-resolved pH imaging of living cells.," *Cytometry. A*, vol. 52, no. 2, pp. 77–89, Apr. 2003.

[213] D. R. Yankelevich, D. Ma, J. Liu, Y. Sun, Y. Sun, J. Bec, D. S. Elson, and L. Marcu, "Design and evaluation of a device for fast multispectral time-resolved fluorescence spectroscopy and imaging.," *Rev. Sci. Instrum.*, vol. 85, no. 3, p. 034303, Mar. 2014.

[214] L. Marcu, Q. Fang, J. a Jo, T. Papaioannou, A. Dorafshar, T. Reil, J.-H. Qiao, J. D. Baker, J. a Freischlag, and M. C. Fishbein, "In vivo detection of macrophages in a rabbit atherosclerotic model by time-resolved laser-induced fluorescence spectroscopy.," *Atherosclerosis*, vol. 181, no. 2, pp. 295–303, Aug. 2005.

[215] Y. Sun, J. Park, D. N. Stephens, J. a Jo, L. Sun, J. M. Cannata, R. M. G. Saroufeem, K. K. Shung, and L. Marcu, "Development of a dual-modal tissue diagnostic system combining time-resolved fluorescence spectroscopy and ultrasonic backscatter microscopy.," *Rev. Sci. Instrum.*, vol. 80, no. 6, p. 065104, Jun. 2009.

[216] J. Phipps, N. Hatami, Z. Galis, J. D. Baker, M. C. Fishbein, and L. Marcu, "A fluorescence lifetime spectroscopy study of matrix metalloproteinases -2 and -9 in human atherosclerotic plaque," *J. Biophotonics*, vol. 4, no. 9, pp. 650–658, 2011.

[217] L. Marcu, J. a Jo, Q. Fang, T. Papaioannou, T. Reil, J.-H. Qiao, J. D. Baker, J. a Freischlag, and M. C. Fishbein, "Detection of rupture-prone atherosclerotic plaques by time-resolved laser-induced fluorescence spectroscopy.," *Atherosclerosis*, vol. 204, no. 1, pp. 156–64, May 2009.

[218] P. V Butte, A. N. Mamelak, M. Nuno, S. I. Bannykh, K. L. Black, and L. Marcu, "Fluorescence lifetime spectroscopy for guided therapy of brain tumors.," *Neuroimage*, vol. 54 Suppl 1, pp. S125–35, Jan. 2011.

[219] J. Swartling, S. Pålsson, P. Platonov, S. B. Olsson, and S. Andersson-Engels, "Changes in tissue optical properties due to radio-frequency ablation of myocardium.," *Med. Biol. Eng. Comput.*, vol. 41, no. 4, pp. 403–9, Jul. 2003.

[220] B. Yu, H. L. Fu, and N. Ramanujam, "Instrument independent diffuse reflectance spectroscopy.," *J. Biomed. Opt.*, vol. 16, no. 1, p. 011010, 2011.

[221] A. A. Stratonnikov and V. B. Loschenov, "Evaluation of blood oxygen saturation in vivo from diffuse reflectance spectra.," *J. Biomed. Opt.*, vol. 6, no. 4, pp. 457–67, Oct. 2001.

[222] E. Gussakovsky, O. Jilkina, Y. Yang, and V. Kupriyanov, "Hemoglobin plus myoglobin concentrations and near infrared light pathlength in phantom and pig hearts determined by diffuse reflectance spectroscopy.," *Anal. Biochem.*, vol. 382, no. 2, pp. 107–15, Nov. 2008.

[223] G. Zonios and A. Dimou, "Modeling diffuse reflectance from semi-infinite turbid media: application to the study of skin optical properties.," *Opt. Express*, vol. 14, no. 19, pp. 8661–74, Sep. 2006.

[224] S.-H. Tseng, C.-K. Hsu, J. Yu-Yun Lee, S.-Y. Tzeng, W.-R. Chen, and Y.-K. Liaw, "Noninvasive evaluation of collagen and hemoglobin contents and scattering property of in vivo keloid scars and normal skin using diffuse reflectance spectroscopy: pilot study.," *J. Biomed. Opt.*, vol. 17, no. 7, p. 077005, Jul. 2012.

[225] T. Lindbergh, E. Häggblad, H. Ahn, E. Göran Salerud, M. Larsson, and T. Strömberg, "Improved model for myocardial diffuse reflectance spectra by including mitochondrial cytochrome aa3, methemoglobin, and inhomogenously distributed RBC.," *J. Biophotonics*, vol. 4, no. 4, pp. 268–76, Apr. 2011.

[226] T. Lindbergh, M. Larsson, Z. Szabó, H. Casimir-Ahn, and T. Strömberg, "Intramyocardial oxygen transport by quantitative diffuse reflectance spectroscopy in calves.," *J. Biomed. Opt.*, vol. 15, no. 2, p. 027009, 2013.

[227] C. P. Brown, J. C. Bowden, L. Rintoul, R. Meder, A. Oloyede, and R. W. Crawford, “Diffuse reflectance near infrared spectroscopy can distinguish normal from enzymatically digested cartilage,” *Phys. Med. Biol.*, vol. 54, no. 18, pp. 5579–94, Sep. 2009.

[228] C. P. Brown, C. Jayadev, S. Glyn-Jones, a J. Carr, D. W. Murray, a J. Price, and H. S. Gill, “Characterization of early stage cartilage degradation using diffuse reflectance near infrared spectroscopy,” *Phys. Med. Biol.*, vol. 56, no. 7, pp. 2299–307, Apr. 2011.

[229] N. Lue, J. W. Kang, C.-C. Yu, I. Barman, N. C. Dingari, M. S. Feld, R. R. Dasari, and M. Fitzmaurice, “Portable optical fiber probe-based spectroscopic scanner for rapid cancer diagnosis: a new tool for intraoperative margin assessment.,” *PLoS One*, vol. 7, no. 1, p. e30887, Jan. 2012.

[230] T. J. Pfefer, K. T. Schomacker, M. N. Ediger, and N. S. Nishioka, “Multiple-fiber probe design for fluorescence spectroscopy in tissue.,” *Appl. Opt.*, vol. 41, no. 22, pp. 4712–21, Aug. 2002.

[231] T. Papaioannou, N. Preyer, Q. Fang, H. Kurt, M. Carnohan, R. Ross, A. Brightwell, G. Cottone, L. Jones, and L. Marcu, “Performance evaluation of fiber optic probes for tissue lifetime fluorescence spectroscopy,” *Proc. SPIE*, vol. 4958, pp. 43–50, 2003.

[232] B. E. A. Saleh and M. C. Teich, *Fundamentals of Photonics*, vol. 13. Wiley-Interscience, 1991, pp. 1–982.

[233] J. L. Charlton and J. Saltiel, “An analysis of trans-stilbene fluorescence quantum yields and lifetimes,” *J. Phys. Chem.*, vol. 81, no. 20, pp. 1940–1944, Oct. 1977.

[234] D. J. Kelly, S. C. Warren, S. Kumar, J. L. Lagarto, B. T. Dyer, A. Margineanu, E. W.-F. Lam, C. Dunsby, and P. M. W. French, “An automated multiwell plate reading flim microscope for live cell autofluorescence lifetime assays,” *J. Innov. Opt. Health Sci.*, vol. 7, no. 5, p. 1450025, Jan. 2014.

[235] ISS, “Fluorescence lifetime standards.” [Online]. Available: http://www.iss.com/resources/reference/data_tables/FL_LifetimeStandards.html. [Accessed: 11-Sep-2014].

[236] R. W. K. Leung, S.-C. A. Yeh, and Q. Fang, “Effects of incomplete decay in fluorescence lifetime estimation.,” *Biomed. Opt. Express*, vol. 2, no. 9, pp. 2517–31, Sep. 2011.

[237] A. S. Kristoffersen, S. R. Erga, B. Hamre, and O. Frette, “Testing Fluorescence Lifetime Standards using Two-Photon Excitation and Time-Domain Instrumentation: Rhodamine B, Coumarin 6 and Lucifer Yellow.,” *J. Fluoresc.*, vol. 24, no. 4, pp. 1015–24, Jul. 2014.

[238] N. Boens, W. Qin, N. Basaric, J. Hofkens, M. Ameloot, U. Hasselt, D. Building, J. Pouget, J. Lefe, B. Valeur, F.-P. Cedex, E. Gratton, N. D. Silva, I. I. Building, Y. Engelborghs, K. Willaert, A. Sillen, A. J. W. G. Visser, A. Van Hoek, J. R. Lakowicz, H. Malak, I. Gryczynski, A. G. Szabo, and D. T. Krajcarski, “Fluorescence Lifetime Standards for Time and Frequency Domain Fluorescence Spectroscopy,” vol. 79, no. 5, pp. 2137–2149, 2007.

[239] K. Dowling, M. J. Dayel, M. J. Lever, P. M. French, J. D. Hares, and a K. Dymoke-Bradshaw, “Fluorescence lifetime imaging with picosecond resolution for biomedical applications.,” *Opt. Lett.*, vol. 23, no. 10, pp. 810–2, May 1998.

[240] D. Fixler, Y. Namer, Y. Yishay, and M. Deutsch, “Influence of Fluorescence Anisotropy on Fluorescence Intensity and Lifetime Measurement: Theory, Simulations and Experiments,” vol. 53, no. 6, pp. 1–12, 2006.

[241] T. He, Z. Xue, M. V. y Alvarado, K. K. Wong, W. Xie, and S. T. C. Wong, “Nonlinear motion compensation using cubature Kalman filter for in vivo fluorescence microendoscopy in peripheral lung cancer intervention.,” *J. Biomed. Opt.*, vol. 18, no. 1, p. 16008, Jan. 2013.

[242] “Osteoarthritis in General Practice,” 2013.

[243] J. H. Ryu, A. Lee, M. S. Huh, J. Chu, K. Kim, B.-S. Kim, K. Choi, I. C. Kwon, J. W. Park, and I. Youn, “Measurement of MMP Activity in Synovial Fluid in Cases of Osteoarthritis and Acute Inflammatory Conditions of the Knee Joints Using a Fluorogenic Peptide Probe-Immobilized Diagnostic Kit,” *Theranostics*, vol. 2, no. 2, pp. 198–206, Jan. 2012.

[244] A. Naumann, J. E. Dennis, A. Awadallah, D. A. Carrino, J. M. Mansour, E. Kastenbauer, and A. I. Caplan, "Immunochemical and Mechanical Characterization of Cartilage Subtypes in Rabbit," *J. Histochem. Cytochem.*, vol. 50, no. 8, pp. 1049–1058, Aug. 2002.

[245] A. D. Pearle, R. F. Warren, and S. a Rodeo, "Basic science of articular cartilage and osteoarthritis," *Clin. Sports Med.*, vol. 24, no. 1, pp. 1–12, Jan. 2005.

[246] J. Malda, J. C. de Grauw, K. E. M. Benders, M. J. L. Kik, C. H. a van de Lest, L. B. Creemers, W. J. a Dhert, and P. R. van Weeren, "Of mice, men and elephants: the relation between articular cartilage thickness and body mass.," *PLoS One*, vol. 8, no. 2, p. e57683, Jan. 2013.

[247] D. Eyre, "Collagen of articular cartilage," *Arthritis Res.*, vol. 4, no. 1, pp. 30–5, Jan. 2002.

[248] J. Martelpelletier, "Pathophysiology of osteoarthritis," *Osteoarthr. Cartil.*, vol. 12, pp. 31–33, 2004.

[249] A. Johansson, J.-H. Kuiper, T. Sundqvist, F. Persson, C. Speier, D. D'Alfonso, J. B. Richardson, and Å. Öberg, "Spectroscopic measurement of cartilage thickness in arthroscopy: ex vivo validation in human knee condyles.," *Arthroscopy*, vol. 28, no. 10, pp. 1513–23, Oct. 2012.

[250] J. Kinnunen, S. Saarakkala, M. Hauta-kasari, P. Vahimaa, and J. S. Jurvelin, "Optical spectral reflectance of human articular cartilage - relationships with tissue structure , composition and mechanical properties," vol. 2, no. 5, pp. 583–587, 2011.

[251] J. Kinnunen, J. S. Jurvelin, J. Mäkitalo, M. Hauta-Kasari, P. Vahimaa, and S. Saarakkala, "Optical spectral imaging of degeneration of articular cartilage.," *J. Biomed. Opt.*, vol. 15, no. 4, p. 046024, 2014.

[252] G. Spahn, H. Plettenberg, H. Nagel, E. Kahl, H. M. Klinger, T. Mückley, M. Günther, G. O. Hofmann, and J. a Mollenhauer, "Evaluation of cartilage defects with near-infrared spectroscopy (NIR): an ex vivo study," *Med. Eng. Phys.*, vol. 30, no. 3, pp. 285–92, Apr. 2008.

[253] I. Afara, I. Prasadam, R. Crawford, Y. Xiao, and A. Oloyede, "Non-destructive evaluation of articular cartilage defects using near-infrared (NIR) spectroscopy in osteoarthritic rat models and its direct relation to Mankin score," *Osteoarthritis Cartilage*, vol. 20, no. 11, pp. 1367–73, Nov. 2012.

[254] G. Li, M. Thomson, E. Dicarlo, X. Yang, B. Nestor, M. P. G. Bostrom, and N. P. Camacho, "A Chemometric Analysis for Evaluation of Early-Stage Cartilage Degradation by Infrared Fiber-Optic Probe Spectroscopy," *Appl. Spectrosc.*, vol. 59, no. 12, pp. 1527–1533, Dec. 2005.

[255] L. Marcu, M. C. Fishbein, J.-M. I. Maarek, and W. S. Grundfest, "Discrimination of Human Coronary Artery Atherosclerotic Lipid-Rich Lesions by Time-Resolved Laser-Induced Fluorescence Spectroscopy," *Arterioscler. Thromb. Vasc. Biol.*, vol. 21, no. 7, pp. 1244–1250, Jul. 2001.

[256] T. Glanzmann, J.-P. Ballini, H. van den Bergh, and G. Wagnières, "Time-resolved spectrofluorometer for clinical tissue characterization during endoscopy," *Rev. Sci. Instrum.*, vol. 70, no. 10, p. 4067, 1999.

[257] J. A. Jo and L. Marcu, "Laguerre-based method for analysis of time-resolved fluorescence data: application to in-vivo characterization and diagnosis of atherosclerotic lesions," vol. 11, no. 2, pp. 1–22, 2009.

[258] C. Talbot, *Temporal and Spectral Resolution of Tissue Autofluorescence*, no. December. 2006.

[259] H. B. Manning, "Development of multi-dimensional fluorescence metrology and application to cartilage degradation in arthritis."

[260] M. Valiyaveettil, J. S. Mort, and C. a McDevitt, "The concentration, gene expression, and spatial distribution of aggrecan in canine articular cartilage, meniscus, and anterior and posterior cruciate ligaments: a new molecular distinction between hyaline cartilage and fibrocartilage in the knee joint.," *Connect. Tissue Res.*, vol. 46, no. 2, pp. 83–91, Jan. 2005.

[261] A. F. Steinert, S. C. Ghivizzani, A. Rethwilm, R. S. Tuan, C. H. Evans, and U. Nöth, "Major biological obstacles for persistent cell-based regeneration of articular cartilage," *Arthritis Res. Ther.*, vol. 9, no. 3, p. 213, Jan. 2007.

[262] E. B. Hunziker, “Articular cartilage repair: basic science and clinical progress. A review of the current status and prospects.,” *Osteoarthritis Cartilage*, vol. 10, no. 6, pp. 432–63, Jun. 2002.

[263] A. J. Sophia Fox, A. Bedi, and S. a Rodeo, “The basic science of articular cartilage: structure, composition, and function,” *Sports Health*, vol. 1, no. 6, pp. 461–8, Nov. 2009.

[264] M. Müller-Gerbl, E. Schulte, and R. Putz, “The thickness of the calcified layer of articular cartilage: a function of the load supported?,” *J. Anat.*, vol. 154, pp. 103–11, Oct. 1987.

[265] L. J. Sandell and T. Aigner, “Articular cartilage and changes in arthritis. An introduction: cell biology of osteoarthritis.,” *Arthritis Res.*, vol. 3, no. 2, pp. 107–13, Jan. 2001.

[266] S. D. Bos, P. E. Slagboom, and I. Meulenbelt, “New insights into osteoarthritis: early developmental features of an ageing-related disease.,” *Curr. Opin. Rheumatol.*, vol. 20, no. 5, pp. 553–9, Sep. 2008.

[267] L. Han, A. J. Grodzinsky, and C. Ortiz, “Nanomechanics of the Cartilage Extracellular Matrix.,” *Annu. Rev. Mater. Res.*, vol. 41, pp. 133–168, Jul. 2011.

[268] J. Riesle, a P. Hollander, R. Langer, L. E. Freed, and G. Vunjak-Novakovic, “Collagen in tissue-engineered cartilage: types, structure, and crosslinks.,” *J. Cell. Biochem.*, vol. 71, no. 3, pp. 313–27, Dec. 1998.

[269] D. R. Eyre, M. a Weis, and J.-J. Wu, “Articular cartilage collagen: an irreplaceable framework?,” *Eur. Cell. Mater.*, vol. 12, pp. 57–63, Jan. 2006.

[270] C. Kiani, L. Chen, Y. J. Wu, A. J. Yee, and B. B. Yang, “Structure and function of aggrecan.,” *Cell Res.*, vol. 12, no. 1, pp. 19–32, Mar. 2002.

[271] P. J. Roughley, “The structure and function of cartilage proteoglycans,” *Eur. Cell. Mater.*, vol. 12, pp. 92–101, Jan. 2006.

[272] A.-M. Malfait, R.-Q. Liu, K. Ijiri, S. Komiya, and M. D. Tortorella, “Inhibition of ADAM-TS4 and ADAM-TS5 prevents aggrecan degradation in osteoarthritic cartilage.,” *J. Biol. Chem.*, vol. 277, no. 25, pp. 22201–8, Jun. 2002.

[273] H. W. Von den Hoff, G. P. van Kampen, and J. K. van der Korst, “Proteoglycan depletion of intact articular cartilage by retinoic acid is irreversible and involves loss of hyaluronate.,” *Osteoarthritis Cartilage*, vol. 1, no. 3, pp. 157–66, Jul. 1993.

[274] A. Poole, R, M. Kobayashi, T. Yasuda, S. Laverty, F. Mwale, T. Kojima, T. Sakai, C. Wahl, S. El-Maadawy, G. Webb, E. Tchetina, and W. Wu, “Type II collagen degradation and its regulation in articular cartilage in osteoarthritis.,” *Ann. Rheum. Dis.*, vol. 61 Suppl 2, no. fig 1, pp. ii78–81, Nov. 2002.

[275] D. T. Felson, “Epidemology of hip and knee osteoarthritis,” *Epidemliologic Rev.*, vol. 10, no. 1, pp. 23–32, Jan. 1988.

[276] H. Lorenz and W. Richter, “Osteoarthritis: cellular and molecular changes in degenerating cartilage.,” *Prog. Histochem. Cytochem.*, vol. 40, no. 3, pp. 135–63, Jan. 2006.

[277] D. T. Felson, “Developments in the clinical understanding of osteoarthritis.,” *Arthritis Res. Ther.*, vol. 11, no. 1, p. 203, Jan. 2009.

[278] D. T. Felson, “The epidemiology of knee osteoarthritis: results from the Framingham Osteoarthritis Study.,” *Semin. Arthritis Rheum.*, vol. 20, no. 3 Suppl 1, pp. 42–50, Dec. 1990.

[279] M. Blagojevic, C. Jinks, a Jeffery, and K. P. Jordan, “Risk factors for onset of osteoarthritis of the knee in older adults: a systematic review and meta-analysis.,” *Osteoarthritis Cartilage*, vol. 18, no. 1, pp. 24–33, Jan. 2010.

[280] M. J. Janusz, E. B. Hookfin, S. a Heitmeyer, J. F. Woessner, a J. Freemont, J. a Hoyland, K. K. Brown, L. C. Hsieh, N. G. Almstead, B. De, M. G. Natchus, S. Pikul, and Y. O. Taiwo, “Moderation of iodoacetate-induced experimental osteoarthritis in rats by matrix metalloproteinase inhibitors.,” *Osteoarthritis Cartilage*, vol. 9, no. 8, pp. 751–60, Nov. 2001.

[281] G. Murphy and H. Nagase, “Reappraising metalloproteinases in rheumatoid arthritis and osteoarthritis: destruction or repair?,” *Nat. Clin. Pract. Rheumatol.*, vol. 4, no. 3, pp. 128–35, Mar. 2008.

[282] M. W. Lark, E. K. Bayne, J. Flanagan, C. F. Harper, L. A. Hoerrner, N. I. Hutchinson, I. I. Singer, S. A. Donatelli, J. R. Weidner, H. R. Williams, R. A. Mumford, and L. S. Lohmander, “Aggrecan degradation in human cartilage. Evidence for both matrix metalloproteinase and aggrecanase activity in normal, osteoarthritic, and rheumatoid joints.,” *J. Clin. Invest.*, vol. 100, no. 1, pp. 93–106, Jul. 1997.

[283] N. Miosge, K. Waletzko, C. Bode, F. Quondamatteo, W. Schultz, and R. Herken, “Light and electron microscopic in-situ hybridization of collagen type I and type II mRNA in the fibrocartilaginous tissue of late-stage osteoarthritis.,” *Osteoarthritis Cartilage*, vol. 6, no. 4, pp. 278–85, Jul. 1998.

[284] J. R. Lakowicz, *Principles of Fluorescence Spectroscopy*, vol. 13, no. 2. Springer, 2006, p. 029901.

[285] C. R. Chu, M. Szczodry, and S. Bruno, “Animal models for cartilage regeneration and repair.,” *Tissue Eng. Part B. Rev.*, vol. 16, no. 1, pp. 105–15, Feb. 2010.

[286] S. Ronken, M. P. Arnold, H. Ardura García, a Jeger, a U. Daniels, and D. Wirz, “A comparison of healthy human and swine articular cartilage dynamic indentation mechanics.,” *Biomech. Model. Mechanobiol.*, vol. 11, no. 5, pp. 631–9, May 2012.

[287] M. I. Rowley, P. R. Barber, A. C. C. Coolen, and B. Vojnovic, “Bayesian analysis of fluorescence lifetime imaging data,” *Sci. York*, vol. 7903, pp. 790325–790325–12, 2011.

[288] P. M. van der Kraan, E. L. Vitters, H. M. van Beuningen, L. B. van de Putte, and W. B. van den Berg, “Degenerative knee joint lesions in mice after a single intra-articular collagenase injection. A new model of osteoarthritis.,” *J. Exp. Pathol. (Oxford).*, vol. 71, no. 1, pp. 19–31, Feb. 1990.

[289] G. J. van Osch, P. M. van der Kraan, E. L. Vitters, L. Blankevoort, and W. B. van den Berg, “Induction of osteoarthritis by intra-articular injection of collagenase in mice. Strain and sex related differences.,” *Osteoarthritis Cartilage*, vol. 1, no. 3, pp. 171–7, Jul. 1993.

[290] D. J. Harrington, “Bacterial Collagenases and Collagen-Degrading Enzymes and Their Potential Role in Human Disease,” vol. 64, no. 6, pp. 1885–1891, 1996.

[291] S. M. Botter, G. J. V. M. van Osch, J. H. Waarsing, J. C. van der Linden, J. a N. Verhaar, H. a P. Pols, J. P. T. M. van Leeuwen, and H. Weinans, “Cartilage damage pattern in relation to subchondral plate thickness in a collagenase-induced model of osteoarthritis.,” *Osteoarthritis Cartilage*, vol. 16, no. 4, pp. 506–14, Apr. 2008.

[292] M. Durigova, H. Nagase, J. S. Mort, and P. J. Roughley, “MMPs are less efficient than ADAMTS5 in cleaving aggrecan core protein.,” *Matrix Biol.*, vol. 30, no. 2, pp. 145–53, Mar. 2011.

[293] D. J. Buttle, C. J. Handley, M. Z. Ilic, J. Saklatvala, M. Murata, and a J. Barrett, “Inhibition of cartilage proteoglycan release by a specific inactivator of cathepsin B and an inhibitor of matrix metalloproteinases. Evidence for two converging pathways of chondrocyte-mediated proteoglycan degradation.,” *Arthritis Rheum.*, vol. 36, no. 12, pp. 1709–17, Dec. 1993.

[294] C. R. Flannery, C. B. Little, C. E. Hughes, and B. Caterson, “Expression of ADAMTS homologues in articular cartilage.,” *Biochem. Biophys. Res. Commun.*, vol. 260, no. 2, pp. 318–22, Jul. 1999.

[295] C. J. Handley, G. M. Winter, M. Z. Ilic, J. M. Ross, C. Anthony Poole, and H. Clem Robinson, “Distribution of newly synthesized aggrecan in explant cultures of bovine cartilage treated with retinoic acid.,” *Matrix Biol.*, vol. 21, no. 7, pp. 579–92, Nov. 2002.

[296] E. S. Yansen, N. Y. Ignatieva, S. V Averkiev, A. B. Shekhter, V. V Lunin, and E. N. Sobol, “Changes in proteoglycan subsystem of cartilage as a result of infrared-laser treatment,” *LASER Phys.*, vol. 15, no. 12, pp. 1660–1663, Jul. 2005.

[297] A. W. Thomas and F. L. Seymour-Jones, “THE HYDROLYSIS OF COLLAGEN BY TRYPSIN,” *J. Am. Chem. Soc.*, vol. 45, no. 6, pp. 1515–1522, Jun. 1923.

[298] M. H. Gregory, N. Capito, K. Kuroki, A. M. Stoker, J. L. Cook, and S. L. Sherman, “A review of translational animal models for knee osteoarthritis.,” *Arthritis*, vol. 2012, p. 764621, Jan. 2012.

[299] S. S. Glasson, T. J. Blanchet, and E. a Morris, “The surgical destabilization of the medial meniscus (DMM) model of osteoarthritis in the 129/SvEv mouse.,” *Osteoarthritis Cartilage*, vol. 15, no. 9, pp. 1061–9, Sep. 2007.

[300] S. Kamekura, K. Hoshi, T. Shimoaka, U. Chung, H. Chikuda, T. Yamada, M. Uchida, N. Ogata, a Seichi, K. Nakamura, and H. Kawaguchi, “Osteoarthritis development in novel experimental mouse models induced by knee joint instability.,” *Osteoarthritis Cartilage*, vol. 13, no. 7, pp. 632–41, Jul. 2005.

[301] Y. Sun, D. R. Mauerhan, J. S. Kneisl, H. James Norton, N. Zinchenko, J. Ingram, E. N. Hanley, and H. E. Gruber, “Histological examination of collagen and proteoglycan changes in osteoarthritic menisci.,” *Open Rheumatol. J.*, vol. 6, pp. 24–32, Jan. 2012.

[302] D. Loeuille, I. Chary-Valckenaere, J. Champigneulle, A.-C. Rat, F. Toussaint, A. Pinzano-Watrin, J. C. Goebel, D. Mainard, A. Blum, J. Pourel, P. Netter, and P. Gillet, “Macroscopic and microscopic features of synovial membrane inflammation in the osteoarthritic knee: correlating magnetic resonance imaging findings with disease severity.,” *Arthritis Rheum.*, vol. 52, no. 11, pp. 3492–501, Dec. 2005.

[303] B. L. Proffen, M. McElfresh, B. C. Fleming, and M. M. Murray, “A comparative anatomical study of the human knee and six animal species.,” *Knee*, vol. 19, no. 4, pp. 493–9, Aug. 2012.

[304] B. Bresnihan, G. Cunnane, P. Youssef, G. Yanni, O. Fitzgerald, and D. Mulherin, “Microscopic measurement of synovial membrane inflammation in rheumatoid arthritis: proposals for the evaluation of tissue samples by quantitative analysis.,” *Br. J. Rheumatol.*, vol. 37, no. 6, pp. 636–42, Jun. 1998.

[305] A. Ghodsi, “Dimensionality Reduction A Short Tutorial,” 2006.

[306] P. R. Peres-Neto, D. a. Jackson, and K. M. Somers, “How many principal components? stopping rules for determining the number of non-trivial axes revisited,” *Comput. Stat. Data Anal.*, vol. 49, no. 4, pp. 974–997, Jun. 2005.

[307] S. Prahl, “Optical Absorption of Hemoglobin,” 1999. [Online]. Available: http://omlc.ogi.edu/spectra/hemoglobin/summary.html. [Accessed: 28-Jan-2014].

[308] P. Liu, Z. Zhu, C. Zeng, and G. Nie, “Specific absorption spectra of hemoglobin at different PO2 levels: potential noninvasive method to detect PO2 in tissues.,” *J. Biomed. Opt.*, vol. 17, no. 12, p. 125002, Dec. 2012.

[309] G. N. Kiefer, K. Sundby, D. McAllister, N. G. Shrive, C. B. Frank, T. Lam, and N. S. Schachar, “The effect of cryopreservation on the biomechanical behavior of bovine articular cartilage.,” *J. Orthop. Res.*, vol. 7, no. 4, pp. 494–501, Jan. 1989.

[310] M. Szarko, K. Muldrew, and J. E. Bertram, “Freeze-thaw treatment effects on the dynamic mechanical properties of articular cartilage.,” *BMC Musculoskelet. Disord.*, vol. 11, p. 231, Jan. 2010.

[311] K. Muldrew, K. Novak, H. Yang, R. Zernicke, N. S. Schachar, and L. E. McGann, “Cryobiology of articular cartilage: ice morphology and recovery of chondrocytes.,” *Cryobiology*, vol. 40, no. 2, pp. 102–9, Mar. 2000.

[312] K. F. Almqvist, L. Wang, C. Broddelez, E. M. Veys, and G. Verbruggen, “Biological freezing of human articular chondrocytes.,” *Osteoarthritis Cartilage*, vol. 9, no. 4, pp. 341–50, May 2001.

[313] B. a Rogers, C. L. Murphy, S. R. Cannon, and T. W. R. Briggs, “Topographical variation in glycosaminoglycan content in human articular cartilage.,” *J. Bone Joint Surg. Br.*, vol. 88, no. 12, pp. 1670–4, Dec. 2006.

[314] K. Thygesen, J. S. Alpert, and H. D. White, “Universal definition of myocardial infarction.,” *J. Am. Coll. Cardiol.*, vol. 50, no. 22, pp. 2173–95, Nov. 2007.

[315] A. S. Go, D. Mozaffarian, V. L. Roger, E. J. Benjamin, J. D. Berry, M. J. Blaha, S. Dai, E. S. Ford, C. S. Fox, S. Franco, H. J. Fullerton, C. Gillespie, S. M. Hailpern, J. a Heit, V. J. Howard, M. D. Huffman, S. E. Judd, B. M. Kissela, S. J. Kittner, D. T. Lackland, J. H. Lichtman, L. D. Lisabeth, R. H. Mackey, D. J. Magid, G. M. Marcus, A. Marelli, D. B. Matchar, D. K. McGuire, E. R. Mohler, C. S. Moy, M. E. Mussolino, R. W. Neumar, G. Nichol, D.

K. Pandey, N. P. Paynter, M. J. Reeves, P. D. Sorlie, J. Stein, A. Towfighi, T. N. Turan, S. S. Virani, N. D. Wong, D. Woo, and M. B. Turner, *Heart disease and stroke statistics--2014 update: a report from the American Heart Association.*, vol. 129, no. 3. 2014, pp. e28–e292.

[316] M. G. Friedrich, "Tissue characterization of acute myocardial infarction and myocarditis by cardiac magnetic resonance.," *JACC. Cardiovasc. Imaging*, vol. 1, no. 5, pp. 652–62, Sep. 2008.

[317] D. Baykut, M. M. Gebhard, H. Bölükoglu, K. Kadipasaoglu, S. Hennes, O. H. Frazier, and a Krian, "Online detection of myocardial ischemia by near infrared spectroscopy with a fiberoptic catheter.," *Thorac. Cardiovasc. Surg.*, vol. 49, no. 3, pp. 162–6, Jun. 2001.

[318] B. L. Troy, J. Pombo, and C. E. Rackley, "Measurement of Left Ventricular Wall Thickness and Mass by Echocardiography," *Circulation*, vol. 45, no. 3, pp. 602–611, Mar. 1972.

[319] J. Suzuki, T. Sakamoto, K. Takenaka, K. Kawakubo, K. Amano, H. Takahashi, I. Hasegawa, T. Shiota, Y. Hada, and T. Sugimoto, "Assessment of the thickness of the right ventricular free wall by magnetic resonance imaging in patients with hypertrophic cardiomyopathy.," *Br. Heart J.*, vol. 60, no. 5, pp. 440–5, Nov. 1988.

[320] J. P. Cleutjens, M. J. Verluyten, J. F. Smiths, and M. J. Daemen, "Collagen remodeling after myocardial infarction in the rat heart.," *Am. J. Pathol.*, vol. 147, no. 2, pp. 325–38, Aug. 1995.

[321] "Heart - Cross section (diagram)." [Online]. Available: http://www.patient.co.uk/diagram/heart-cross-section-diagram. [Accessed: 11-Oct-2014].

[322] C. L. Gibbs, "Cardiac Energetics," *Physiol. Rev.*, vol. 58, no. 1, pp. 174–254, 1978.

[323] S. Neubauer, "The failing heart--an engine out of fuel.," *N. Engl. J. Med.*, vol. 356, no. 11, pp. 1140–51, Mar. 2007.

[324] W. C. Stanley, F. a Recchia, and G. D. Lopaschuk, "Myocardial substrate metabolism in the normal and failing heart.," *Physiol. Rev.*, vol. 85, no. 3, pp. 1093–129, Jul. 2005.

[325] J. M. Huss and D. P. Kelly, "Review series Mitochondrial energy metabolism in heart failure : a question of balance," vol. 115, no. 3, 2005.

[326] T. Doenst, T. D. Nguyen, and E. D. Abel, "Cardiac metabolism in heart failure: implications beyond ATP production.," *Circ. Res.*, vol. 113, no. 6, pp. 709–24, Aug. 2013.

[327] C. K. Mathews, V. H. K. E., and K. G. Ahern, *Biochemistry*, 3rd ed. (I. San Francisco, Calif. : Addison-Wesley, 2000.

[328] A. Tzagoloff, *Mitochondria*. Plenum Press, 1982.

[329] T. M. Dall, T. D. Blanchard, P. D. Gallo, and A. P. Semilla, "The economic impact of Medicare Part D on congestive heart failure.," *Am. J. Manag. Care*, vol. 19, no. 6 Suppl, pp. s97–100, May 2013.

[330] S. a Dosh, "Diagnosis of heart failure in adults.," *Am. Fam. Physician*, vol. 70, no. 11, pp. 2145–52, Dec. 2004.

[331] Y. Sun and K. T. Weber, "Infarct scar: a dynamic tissue.," *Cardiovasc. Res.*, vol. 46, no. 2, pp. 250–6, May 2000.

[332] W. M. Blankesteijn, E. Creemers, E. Lutgens, J. P. Cleutjens, M. J. Daemen, and J. F. Smits, "Dynamics of cardiac wound healing following myocardial infarction: observations in genetically altered mice.," *Acta Physiol. Scand.*, vol. 173, no. 1, pp. 75–82, Sep. 2001.

[333] I. Stefanon, M. Valero-Muñoz, A. A. Fernandes, R. F. Ribeiro, C. Rodríguez, M. Miana, J. Martínez-González, J. S. Spalenza, V. Lahera, P. F. Vassallo, and V. Cachofeiro, "Left and right ventricle late remodeling following myocardial infarction in rats.," *PLoS One*, vol. 8, no. 5, p. e64986, Jan. 2013.

[334] J. N. Cohn, R. Ferrari, and N. Sharpe, "Cardiac remodeling—concepts and clinical implications: a consensus paper from an international forum on cardiac remodeling," *J. Am. Coll. Cardiol.*, vol. 35, no. 3, pp. 569–582, Mar. 2000.

[335] M. a. Pfeffer and E. Braunwald, “Ventricular remodeling after myocardial infarction. Experimental observations and clinical implications,” *Circulation*, vol. 81, no. 4, pp. 1161–1172, Apr. 1990.

[336] B. I. Jugdutt, “Ventricular remodeling after infarction and the extracellular collagen matrix: when is enough enough?,” *Circulation*, vol. 108, no. 11, pp. 1395–403, Sep. 2003.

[337] A. R. Lyon, V. O. Nikolaev, M. Miragoli, M. B. Sikkel, H. Paur, L. Benard, J.-S. Hulot, E. Kohlbrenner, R. J. Hajjar, N. S. Peters, Y. E. Korchev, K. T. Macleod, S. E. Harding, and J. Gorelik, “Plasticity of surface structures and β(2)-adrenergic receptor localization in failing ventricular cardiomyocytes during recovery from heart failure.,” *Circ. Heart Fail.*, vol. 5, no. 3, pp. 357–65, May 2012.

[338] J. S. Hochman and B. H. Bulkley, “Expansion of acute myocardial infarction: an experimental study,” *Circulation*, vol. 65, no. 7, pp. 1446–1450, Jun. 1982.

[339] L. W. Eaton and B. H. Bulkley, “Expansion of acute myocardial infarction: its relationship to infarct morphology in a canine model,” *Circ. Res.*, vol. 49, no. 1, pp. 80–88, Jul. 1981.

[340] H. F. Weisman, D. E. Bush, J. a. Mannisi, M. L. Weisfeldt, and B. Healy, “Cellular mechanisms of myocardial infarct expansion,” *Circulation*, vol. 78, no. 1, pp. 186–201, Jul. 1988.

[341] R. Bussani, a Abbate, G. G. L. Biondi-Zoccai, a Dobrina, a M. Leone, D. Camilot, M. P. Di Marino, F. Baldi, F. Silvestri, L. M. Biasucci, and a Baldi, “Right ventricular dilatation after left ventricular acute myocardial infarction is predictive of extremely high peri-infarctual apoptosis at postmortem examination in humans.,” *J. Clin. Pathol.*, vol. 56, no. 9, pp. 672–6, Sep. 2003.

[342] W. J. McKenna, A. Kleinebenne, P. Nihoyannopoulos, and R. Foale, “Echocardiographic measurement of right ventricular wall thickness in hypertrophic cardiomyopathy: Relation to clinical and prognostic features,” *J. Am. Coll. Cardiol.*, vol. 11, no. 2, pp. 351–358, Feb. 1988.

[343] R. Ventura-Clapier, A. Garnier, and V. Veksler, “Energy metabolism in heart failure.,” *J. Physiol.*, vol. 555, no. Pt 1, pp. 1–13, Mar. 2004.

[344] M. N. Sack, T. A. Rader, S. Park, J. Bastin, S. A. McCune, and D. P. Kelly, “Fatty Acid Oxidation Enzyme Gene Expression Is Downregulated in the Failing Heart,” *Circulation*, vol. 94, no. 11, pp. 2837–2842, Dec. 1996.

[345] T. Ide, H. Tsutsui, S. Hayashidani, D. Kang, N. Suematsu, K. -i. Nakamura, H. Utsumi, N. Hamasaki, and a. Takeshita, “Mitochondrial DNA Damage and Dysfunction Associated With Oxidative Stress in Failing Hearts After Myocardial Infarction,” *Circ. Res.*, vol. 88, no. 5, pp. 529–535, Mar. 2001.

[346] A. P. Koretsky, L. A. Katz, and R. S. Balaban, “Determination of pyridine nucleotide fluorescence from the perfused heart using an internal standard.,” *Am. J. Physiol.*, vol. 253, no. 4 Pt 2, pp. H856–62, Oct. 1987.

[347] D. Chorvat, J. Kirchnerova, M. Cagalinec, J. Smolka, a Mateasik, and a Chorvatova, “Spectral unmixing of flavin autofluorescence components in cardiac myocytes.,” *Biophys. J.*, vol. 89, no. 6, pp. L55–7, Dec. 2005.

[348] J. J. Holbrook and R. G. Wolfe, “Malate Dehydrogenase. X. Fluorescence Microtitration Studies of D-Malate, Hydroxymalonate, Nicotinamide Dinucleotide, and Dihydronicotinamide-Adenine Dinucleotide Binding by Mitochondrial and Supernatant Porcine Heart Enzymes,” vol. 11, no. 13, pp. 2499–2502, 1963.

[349] J. E. Churchich, “Recognition of partially-folded mitochondrial malate dehydrogenase by GroEL. Steady and time-dependent emission anisotropy measurements.,” *Protein Sci.*, vol. 7, no. 12, pp. 2587–94, Dec. 1998.

[350] A. Chorvatova, F. Elzwiei, A. Mateasik, and D. Chorvat, “Effect of ouabain on metabolic oxidative state in living cardiomyocytes evaluated by time-resolved spectroscopy of endogenous NAD(P)H fluorescence,” *J. Biomed. Opt.*, vol. 17, no. 10, p. 101505, 2012.

[351] C. a Brautigam, J. L. Chuang, D. R. Tomchick, M. Machius, and D. T. Chuang, “Crystal structure of human dihydrolipoamide dehydrogenase: NAD+/NADH binding and the structural basis of disease-causing mutations.,” *J. Mol. Biol.*, vol. 350, no. 3, pp. 543–52, Jul. 2005.

[352] M. Iwata, Y. Lee, T. Yamashita, T. Yagi, S. Iwata, A. D. Cameron, and M. J. Maher, "The structure of the yeast NADH dehydrogenase (Ndi1) reveals overlapping binding sites for water- and lipid-soluble substrates.," *Proc. Natl. Acad. Sci. U. S. A.*, vol. 109, no. 38, pp. 15247–52, Sep. 2012.

[353] H.-W. Wang, Y.-H. Wei, and H.-W. Guo, "Reduced Nicotinamide Adenine Dinucleotide (NADH) Fluorescence for the Detection of Cell Death," *Anticancer. Agents Med. Chem.*, vol. 9, no. 9, pp. 1012–1017, Nov. 2009.

[354] R. M. Bell, M. M. Mocanu, and D. M. Yellon, "Retrograde heart perfusion: the Langendorff technique of isolated heart perfusion.," *J. Mol. Cell. Cardiol.*, vol. 50, no. 6, pp. 940–50, Jun. 2011.

[355] R. Hober and J. Hober, "Experiments on the absorption of organic solutes in the small intestine of rats," *J. Cell. Comp. Physiol.*, vol. 10, no. 4, pp. 401–422, Dec. 1937.

[356] A. N. Wick, T. N. Morita, and L. Joseph, "The Oxidation of Mannitol.," *Exp. Biol. Med.*, vol. 85, no. 1, pp. 188–190, Jan. 1954.

[357] S. M. Nasrallah and F. L. Iber, "Mannitol absorption and metabolism in man.," *Am. J. Med. Sci.*, vol. 258, no. 2, pp. 80–8, Aug. 1969.

[358] D. R. Saunders and H. S. Wiggins, "Conservation of mannitol, lactulose, and raffinose by the human colon.," *Am. J. Physiol.*, vol. 241, no. 5, pp. G397–402, Nov. 1981.

[359] E. Margoliash and N. Frohwirt, "Spectrum of horse-heart cytochrome c.," *Biochem. J.*, vol. 71, no. 3, pp. 570–2, Mar. 1959.

[360] K. A. Schenkman, D. R. M. Arble, D. H. Burns, and E. O. Feigl, "Optical Spectroscopic Method for in Vivo Measurement of Cardiac Myoglobin Oxygen Saturation," vol. 53, no. 3, 1999.

[361] K. a Schenkman, D. R. Marble, D. H. Burns, and E. O. Feigl, "Myoglobin oxygen dissociation by multiwavelength spectroscopy.," *J. Appl. Physiol.*, vol. 82, no. 1, pp. 86–92, Jan. 1997.

[362] J. Bowen, "The absorption spectra and extinction of myoglobin," no. d, pp. 235–245, 1948.

[363] J. P. Headrick, J. Peart, B. Hack, A. Flood, and G. P. Matherne, "Functional properties and responses to ischaemia-reperfusion in Langendorff perfused mouse heart," *Exp. Physiol.*, 2001.

[364] P. Marambio, B. Toro, C. Sanhueza, R. Troncoso, V. Parra, H. Verdejo, L. García, C. Quiroga, D. Munafo, J. Díaz-Elizondo, R. Bravo, M.-J. González, G. Diaz-Araya, Z. Pedrozo, M. Chiong, M. I. Colombo, and S. Lavandero, "Glucose deprivation causes oxidative stress and stimulates aggresome formation and autophagy in cultured cardiac myocytes.," *Biochim. Biophys. Acta*, vol. 1802, no. 6, pp. 509–18, Jun. 2010.

[365] J. Tong, Y. Cao, Y. Hotta, N. Ishikawa, H. Nishimaki, K. Masuda, C. L. Yang, K. Kasai, and G. Itoh, "Cardiomyocyte Apoptosis Induced in Langendorff Preparation of Isolated Guinea-Pig Heart Perfused with Krebs-Henseleit Solution Deprived of Glucose , with and without Oxygen Supply," no. 1, pp. 143–151.

[366] E. Takimoto and D. a Kass, "Role of oxidative stress in cardiac hypertrophy and remodeling.," *Hypertension*, vol. 49, no. 2, pp. 241–8, Feb. 2007.

[367] A. R. Lyon, K. T. MacLeod, Y. Zhang, E. Garcia, G. K. Kanda, M. J. Lab, Y. E. Korchev, S. E. Harding, and J. Gorelik, "Loss of T-tubules and other changes to surface topography in ventricular myocytes from failing human and rat heart.," *Proc. Natl. Acad. Sci. U. S. A.*, vol. 106, no. 16, pp. 6854–9, Apr. 2009.

[368] P. Whittaker, R. a Kloner, D. R. Boughner, and J. G. Pickering, "Quantitative assessment of myocardial collagen with picrosirius red staining and circularly polarized light.," *Basic Res. Cardiol.*, vol. 89, no. 5, pp. 397–410, 1994.

[369] J. Schindelin, I. Arganda-Carreras, E. Frise, V. Kaynig, M. Longair, T. Pietzsch, S. Preibisch, C. Rueden, S. Saalfeld, B. Schmid, J.-Y. Tinevez, D. J. White, V. Hartenstein, K. Eliceiri, P. Tomancak, and A. Cardona, "Fiji: an open-source platform for biological-image analysis," *Nat Meth*, vol. 9, no. 7, pp. 676–682, Jul. 2012.

[370] A. Thompson, H. Manning, M. Brydegaard, S. Coda, G. Kennedy, R. Patalay, U. Waitong-Braemming, P. De Beule, M. Neil, S. Andersson-Engels, Y. Itoh, N. Bendsøe, C. Dunsby, K. Svanberg, and P. M. French,

"Hyperspectral fluorescence lifetime fibre probe spectroscopy for use in the study and diagnosis of osteoarthritis and skin cancer," in *Optical Biopsy IX*, 2011, vol. 7895, p. 78950G–78950G–10.

[371] H. F. Weisman, D. E. Bush, J. a. Mannisi, and B. H. Bulkley, "Global cardiac remodeling after acute myocardial infarction: A study in the rat model," *J. Am. Coll. Cardiol.*, vol. 5, no. 6, pp. 1355–1362, Jun. 1985.

[372] L. H. Opie, P. J. Commerford, B. J. Gersh, M. A. Pfeffer, and N. England, "Controversies in Cardiology 4," vol. 367, 2006.

[373] N. F. Voelkel, R. A. Quaife, L. A. Leinwand, R. J. Barst, M. D. McGoon, D. R. Meldrum, J. Dupuis, C. S. Long, L. J. Rubin, F. W. Smart, Y. J. Suzuki, M. Gladwin, E. M. Denholm, and D. B. Gail, "Right ventricular function and failure: report of a National Heart, Lung, and Blood Institute working group on cellular and molecular mechanisms of right heart failure.," *Circulation*, vol. 114, no. 17, pp. 1883–91, Oct. 2006.

[374] V. Caorsi, C. Toepfer, M. B. Sikkel, A. R. Lyon, K. MacLeod, and M. a Ferenczi, "Non-linear optical microscopy sheds light on cardiovascular disease.," *PLoS One*, vol. 8, no. 2, p. e56136, Jan. 2013.

[375] Y. H. Li, J. C. Yue, and G. P. Cai, "Fluorescence characterization of type I collagen from normal and silicotic rats and its quenching dynamics induced by hypocrellin B.," *Biopolymers*, vol. 42, no. 2, pp. 219–26, Aug. 1997.

[376] J. Y. Yager, R. M. Brucklacher, and R. C. Vannucci, "Cerebral oxidative metabolism and redox state during hypoxia-ischemia and early recovery in immature rats.," *Am. J. Physiol.*, vol. 261, no. 4 Pt 2, pp. H1102–8, Oct. 1991.

[377] B. Y. M. R. Duchen and T. J. Biscoe, "Mitochondrial function in type i cells isolated from rabbit arterial," pp. 13–31, 1992.

[378] J. G. Peak, M. J. Peak, R. S. Sikorski, and C. A. Jones, "INDUCTION OF DNA-PROTEIN CROSSLINKS IN HUMAN CELLS BY ULTRAVIOLET and VISIBLE RADIATIONS: ACTION SPECTRUM," *Photochem. Photobiol.*, vol. 41, no. 3, pp. 295–302, Mar. 1985.

[379] N. Bech-Thomsen and H. C. Wulf, "CARCINOGENIC and MELANOGENIC EFFECTS OF A FILTERED METAL HALIDE UVA SOURCE and A TUBULAR FLUORESCENT UVA TANNING SOURCE WITH OR WITHOUT ADDITIONAL SOLAR-SIMULATED UV RADIATION IN HAIRLESS MICE," *Photochem. Photobiol.*, vol. 62, no. 4, pp. 773–779, Oct. 1995.

[380] G. Horneck, "Quantification of biologically effective environmental UV irradiance.," *Adv. Space Res.*, vol. 26, no. 12, pp. 1983–94, Jan. 2000.

[381] K. Y. Lam, P. Dickens, and A. C. Chan, "Tumors of the heart. A 20-year experience with a review of 12,485 consecutive autopsies.," *Arch. Pathol. Lab. Med.*, vol. 117, no. 10, pp. 1027–31, Oct. 1993.

[382] D. Mosconi, D. Stoppa, L. Pancheri, L. Gonzo, and A. Simoni, "CMOS Single-Photon Avalanche Diode Array for Time-Resolved Fluorescence Detection," *2006 Proc. 32nd Eur. Solid-State Circuits Conf.*, pp. 564–567, Sep. 2006.

[383] M. a Digman, V. R. Caiolfa, M. Zamai, and E. Gratton, "The phasor approach to fluorescence lifetime imaging analysis.," *Biophys. J.*, vol. 94, no. 2, pp. L14–6, Jan. 2008.

[384] F. Fereidouni, A. Esposito, G. A. Blab, and H. C. Gerritsen, "A modified phasor approach for analyzing time-gated fluorescence lifetime images," *J. Microsc.*, 2011.

[385] P.-C. Jiang, W. S. Grundfest, and O. M. Stafsudd, "Quasi-real-time fluorescence imaging with lifetime dependent contrast.," *J. Biomed. Opt.*, vol. 16, no. 8, p. 086001, Aug. 2011.

[386] Pong P. Chu, *RTL Hardware design using VHDL*. Wiley-IEEE Press, 2006, p. 694.

[387] R. Sass and A. G. Schmidt, *Embedded systems design with platform FPGAa*. Elsevier, 2010, p. 389.

[388] Xilinx, "Using Digital Clock Managers (DCMs) in Spartan-3 FPGAs," 2006.

[389] Xilinx, “Spartan-3A FPGA Family,” 2010.

[390] Becker & Hickl GmbH, “How (and why not) to Amplify PMT Signals.”

[391] J. Axelson, *USB Complete: The Developer’s Guide*, Fourth. Lakeview Research, 2009, pp. 1–504.

[392] ID Quantique, “id100 Series Datasheet.”

[393] M. P. Devices, “PDM Series datasheet.”

[394] F. T. D. I. Ltd, “FT2232H Dual High Speed USB to Multipurpose UART / FIFO IC,” 2012.

[395] J. D. Hunter, “Matplotlib: A 2D graphics environment,” *Comput. Sci. Eng.*, vol. 9, no. 3, pp. 90–95, 2007.

[396] P. Horowitz, “The Art of Electronics,” *Am. J. Phys.*, vol. 58, no. 7, p. 702, 1990.

[397] Sensl, “HRM-CFD Programmable Constant Fraction Discriminator User Manual,” 2011.

[398] P. B. Coates, “A theory of afterpulse formation in photomultipliers and the prepulse height distribution,” *J. Phys. D. Appl. Phys.*, vol. 6, no. 16, pp. 1862–1869, Oct. 1973.

[399] J. Hagedorn and F. Alicke, “How to Measure Total Jitter (TJ),” 2012.

[400] M. G. Bulmer, *Principles of Statistics*, Second., vol. 13, no. 2. Dulmer, 1966, pp. 56–59.

[401] A. D. Elder, J. Swartling, S. M. Matthews, K. Yunus, J. H. Frank, and C. F. Kaminski, “Fluorescence Lifetime Imaging Using Cheap LEDs as Illumination: Application in Microchannels,” *Laser Applilcations to Chem. Secur. Environ. Anal.*, p. TuE9, 2006.

[402] a. Rochas, M. Gani, B. Furrer, P. a. Besse, R. S. Popovic, G. Ribordy, and N. Gisin, “Single photon detector fabricated in a complementary metal–oxide–semiconductor high-voltage technology,” *Rev. Sci. Instrum.*, vol. 74, no. 7, p. 3263, 2003.

[403] A. Gulinatti, I. Rech, P. Maccagnani, M. Ghioni, and S. Cova, “Improving the performance of Silicon Single Photon Avalanche Diodes,” 2011, vol. 8033, pp. 803302–803302–11.

[404] a. Gulinatti, I. Rech, F. Panzeri, C. Cammi, P. Maccagnani, M. Ghioni, and S. Cova, “New silicon SPAD technology for enhanced red-sensitivity, high-resolution timing and system integration,” *J. Mod. Opt.*, vol. 59, no. 17, pp. 1489–1499, Oct. 2012.

[405] A. Gulinatti, I. Rech, P. Maccagnani, S. Cova, and M. Ghioni, “New silicon technologies enable high-performance arrays of Single Photon Avalanche Diodes.,” *Proc. Soc. Photo. Opt. Instrum. Eng.*, vol. 8727, May 2013.

[406] J. I. Pankove, “Temperature Dependence of Emission Efficiency and Lasing Threshold in Laser Diodes,” *IEEE J. Quantum Electron.*, pp. 119–122, 1968.

[407] G. A. Reynolds and K. H. Drexhage, “New coumarin dyes with rigidized structure for flashlamp-pumped dye lasers,” vol. 13, no. 3, pp. 3–6, 1975.

[408] K. Yoshioka, M. Tohda, T. Takemura, N. Akano, K. Matsubara, a Ooshima, and S. Maki, “Distribution of type I collagen in human kidney diseases in comparison with type III collagen.,” *J. Pathol.*, vol. 162, no. 2, pp. 141–8, Oct. 1990.

[409] M. S. Viegas, T. C. Martins, F. Seco, and a do Carmo, “An improved and cost-effective methodology for the reduction of autofluorescence in direct immunofluorescence studies on formalin-fixed paraffin-embedded tissues.,” *Eur. J. Histochem.*, vol. 51, no. 1, pp. 59–66, 2007.

[410] R. N. Raman, C. D. Pivetti, D. L. Matthews, C. Troppmann, and S. G. Demos, “Quantification of in vivo autofluorescence dynamics during renal ischemia and reperfusion under 355 nm excitation.,” *Opt. Express*, vol. 16, no. 7, pp. 4930–44, Mar. 2008.

[411] D. E. Schwartz, E. Charbon, and K. L. Shepard, “A Single-Photon Avalanche Diode Array for Fluorescence Lifetime Imaging Microscopy,” vol. 43, no. 11, pp. 2546–2557, 2008.

Appendix A: Derivation of Equation 4.2

At the sample plane, we can assume that the excitation light provided by a fibre-optic probe has a circular profile and, likewise, the fluorescence signal can be detected from a circular region. Assuming identical fibre geometry, the two circular regions have identical radius *r*. Furthermore, one can consider the collection fibre to be at a position equal to two times the radius of a single fibre, which is identified as *d* in Figure A0.1.

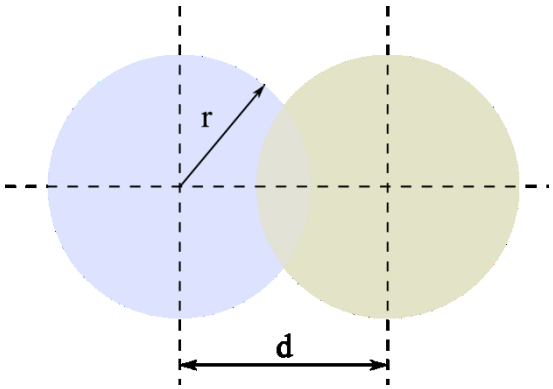

Figure A0.1 Schematic of two overlapping circles of equal radii r and with their centres separated by a distance d.

The overlapping area in the centre of Figure A0.1 is symmetric. Hence, by working with only one circle and applying some basic geometry we can divide the overlapping region in two areas defined by points OAB and OABP, as shown in Figure A0.2.

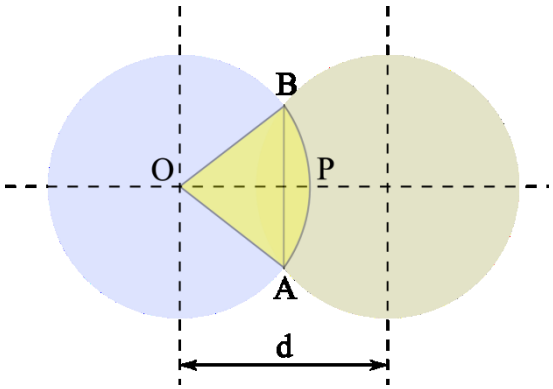

Figure A0.2 Basic geometry in the region of intersection.

By calculating the areas of OABP and OAB, one can find the area of ABP, which is corresponds to half of the overlapping area of the two circles. The area of the sectors OABP is given by equation A.1:

$$A_{OABP} = \frac{\theta}{2} r^2 \tag{A.1}$$

where and r is the radius of the circle and θ is the centre angle of the triangle AOB, in radians, as defined in equation A.2.

$$\cos\theta = \frac{d}{2r} \leftrightarrow \theta = \cos^{-1}\left(\frac{d}{2r}\right) \tag{A.2}$$

The area of the triangle OAB can be calculated through simple trigonometry, as illustrated in Figure A0.3.

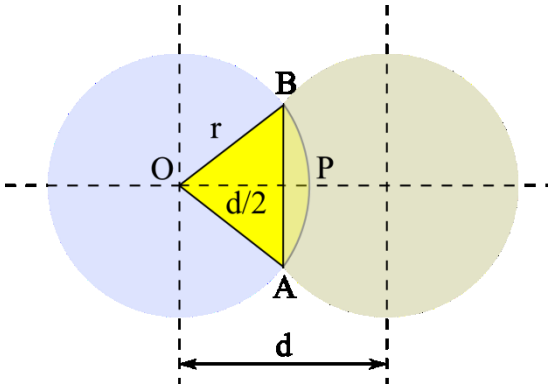

Figure A0.3 Simplification of the geometry to find the area of the triangle OAB.

The area of the triangle is then given by equation A.3.

$$A_{OAB} = \frac{d}{2}\sqrt{r^2 - \frac{d^2}{4}} \tag{A.3}$$

Combining equations A.1, A.2 and A.3, we find the area of the sector ABP.

$$A_{ABP} = \frac{r^2}{2}\cos^{-1}\left(\frac{d}{2r}\right) - \frac{d}{2}\sqrt{r^2 - \frac{d^2}{4}} \tag{A.4}$$

The area of intersection of the two circles is twice the area of ABP.

$$A_{overlap} = r^2\cos^{-1}\left(\frac{d}{2r}\right) - d\sqrt{r^2 - \frac{d^2}{4}} \tag{A.5}$$